



**HAL**  
open science

# The structure, morphology, and surface texture of debris avalanche deposits : field and remote sensing mapping and analogue modelling

Engielle Mae Paguican

► **To cite this version:**

Engielle Mae Paguican. The structure, morphology, and surface texture of debris avalanche deposits : field and remote sensing mapping and analogue modelling. Earth Sciences. Université Blaise Pascal - Clermont-Ferrand II, 2012. English. NNT : 2012CLF22255 . tel-00794267

**HAL Id: tel-00794267**

**<https://theses.hal.science/tel-00794267>**

Submitted on 25 Feb 2013

**HAL** is a multi-disciplinary open access archive for the deposit and dissemination of scientific research documents, whether they are published or not. The documents may come from teaching and research institutions in France or abroad, or from public or private research centers.

L'archive ouverte pluridisciplinaire **HAL**, est destinée au dépôt et à la diffusion de documents scientifiques de niveau recherche, publiés ou non, émanant des établissements d'enseignement et de recherche français ou étrangers, des laboratoires publics ou privés.

N° d'Ordre : D. U. 2255

**Université Blaise Pascal**  
U.F.R. Sciences et Technologies

**ECOLE DOCTORALE DES SCIENCES FONDAMENTALES**  
N° 721

**T H E S E**  
présentée pour obtenir le grade de  
**DOCTEUR D'UNIVERSITÉ**  
*Spécialité: Volcanologie*

Par **PAGUICAN, Engielle Mae**  
Master

**The Structure, Morphology, and Surface Texture of  
Debris Avalanche Deposits: Field and Remote Sensing  
Mapping and Analogue Modelling**

9 July 2012

**Jury :**

*Examiner :*

Raphael PARIS

— Université Blaise Pascal

*Reviewers :*

Jean-Luc SCHNEIDER

— Université Bordeaux

Anne LE FRIANT

— Institut de Physique du Globe de Paris

Thomas OOMMEN

— Michigan Technological University

*Advisor :*

Benjamin VAN WYK DE VRIES

— Université Blaise Pascal

Alfredo Mahar Francisco LAGMAY

— University of the Philippines

*For Daddy Tim, Mommy Vangie, Ivan Grace and Gareth*

## Acknowledgements:

I want to give my biggest thanks to my supervisor, Dr Benjamin van Wyk de Vries, who has always made me feel that I am in control over my academic life but he is available for support, guidance and advise if needed. It is a dream come true to have worked with you, BossChiefBen! Thank you for helping me get some funding to continue my work, and for giving me the opportunity to travel, share my work and meet people. I appreciate the travel opportunities a lot! Thank you for making me a ‘more international” PhD student. I also want to thank Dr Mahar Lagmay and Dr Carlo Arcilla for their efforts on having my MOA signed.

A BIG-BIG Thanks to My Family: Daddy Tim, Mommy Vangie, Ivan Grace, relatives and friends who supported me 100 percent on my dream of becoming a scientist. And to my “other half”, my partner, my travel buddy, my red knight - Gareth Fabbro who showered me with all the love, encouragement, and support I needed. I love you.

My desire of becoming a good scientist started with The Philippine Society of Youth Science Clubs (PSYSC) fourteen years ago. In PSYSC, I have met my lifetime friends who walked with me in the halls of learning and shared my dreams, laughter, and sorrow.

My PhD has been an opportunity for academic and personal growth. Along the way, I met people who took care of me like I am part of the family. Among those are: My Family in Clermont-Ferrand: BCBen-MomFran-Max-Eva-Flori-Nora; My family in Buhi, Ate Analiza-Jerry Morada and Family; and My Family in Buffalo:SirCaco-MumEliza-Isla-Ciaran; and for Serge and Jennifer Bravinder for providing me a roof for a month.

PhD would not be exciting without the company of other PhDs and everyone in the Lab, my officemates a.k.a my partymates: Gareth, BRap-tiste, Deniz, Asmaa-Manu, Oscar-Amelie, Gabi-your car is the best! Yannick, Camille, Manon and Nabaz.

I stayed in NIGS for about five months during the fieldwork at Iriga and I want to thank the people in the Administration Office, Ate Che-Che, Ate Lexie, Kuya Ronel for your efforts in helping me. Most especially to Gerard “Kuya Titan” Quina for being a field partner, for being with me every step of the way, and for never letting me walk alone. Also thanks to my NIGS friends, April Lim, Cathy Abon, Meryl Calibo, and Grace Bato for their field assistance and friendship in NIGS. I have to give thanks for the logistic support of Dr Arcilla who favored me a lot while I was in NIGS.

I am grateful to the reviews and mostly positive comments of my Jury: Dr Raphael Paris, Dr Thomas Oomen, Dr Jean-Luc Schneider and Dr Anne Le Friant and careful review of of our Iriga Paper which is Chapter 2 of this

work by Prof Jocelyn McPhie, Lee Siebert and an anonymous reviewer, and Chapter 6 by Dr Onur Kose.

This work is a result of the co-tutelle PhD program between the Universite Blaise Pascal and the University of the Philippines. As the first co-tutelle student under this program, I have been to a complete spectrum of procedural and bureaucratic issues from immigration to day-to-day survival, making this whole thing a self-sacrifice in itself. Despite all these, I am more than thankful for I have grown stronger and I have had the opportunity to learn more, appreciate the simplest things and look at life at its brighter side. And I dedicate this work to those who have shared with me their precious time and knowledge and in one way or another eased the burden.

Funding I got from this work was provided by the French Embassy in Manila, the EIFFEL Excellence Scholarship, the UBP International Office and the Doctoral School. I thank everyone from the embassy who assisted me and whom I have met among those are Mlle Isabelle Epailard, Mlle Julie Blazy, and Mlle Anais Bouquelloen.

Lastly, I offer my most fervent thanks to the most gracious Infant Jesus of Prague: O most gracious Infant Jesus, in humble adoration I offer You most fervent thanks for all the blessings You have bestowed upon me. I shall always praise Your ineffable mercy and confess that You alone are my God, my helper, and my protector. Henceforth my entire confidence shall be placed in You. Everywhere will I proclaim Your mercy and generosity, so that Your great love and the great deeds which You perform may be acknowledge by all. May devotion to Your most Holy Infancy extend more and more in the hearts of all Christians and may all who experience Your assistance persevere in returning unceasing gratitude to Your most Holy Infancy to which be praise and glory for all eternity. Amen.



## Abstract:

Flank collapse generates avalanches and large landslides that significantly change the shape of a volcano and alter the surrounding landscape. Most types of volcanoes experience flank collapse at some point during their development. In the Philippines, for example, the numerous volcanoes with breached edifices belong to the cone, subcone, and massif morphometric classes. Debris avalanches occur frequently on both volcanic and non-volcanic terrains making it an important geologic event to consider for hazard assessment.

Debris avalanche deposits (DAD) preserve surface and internal structures, morphology, and texture that can be used to determine transport type, deformation history, causal mechanism, and emplacement kinematics. However, natural DAD are often too vast and chaotic-seeming in the field so that structural and morphological mapping by remote sensing is a good complement to studying them.

This study describes and analyses recurrent structural and morphological features of analogue models and natural DAD at Mt Iriga and Guinsaigon (Philippines), and uses several other examples at Mt Meager (Canada), and Storegga Slide (Norway). The study explores the use of analogue models as landslide kinematics, dynamics, and emplacement and causal mechanism indicators. Hummocks are identified as a key structural element of DAD.

Hummocks, a major DAD topographic feature, are formed as the mass in motion slides and evolves by progressive spreading and break up. Internally, high angle normal faults dissect hummocks and merge into low angle shear zones at the base of the slide zone. Hummock size distribution is related to lithology, initial position, and avalanche kinematics. Hummocks provide information on the transport conditions and initial composition of the landslide. Their geometry (size and shape), internal structures, and spatial distribution are kinematic indicators for landslides from development until emplacement and provide a framework for interpreting emplacement dynamics.

Experiments with curved analogue ramps show the development of an area of accumulation and thickening, where accelerating materials reach a gently sloped depositional surface. Experiments with straight ramps show a longer slides with continued extension by horst and graben structures and transtensional grabens. A thickened mass is found to subsequently remobilise and advance by secondary collapse. This set of experiments show that failure and transport surface morphology can influence the emplacement mechanism, morphology, and avalanche runout.

Structural and morphological mapping by remote sensing, and description of recurrent features at the remote and previously unmapped Süphan Dağı (Turkey), Cerro Pular-Pajonales (Argentina), and Tacna (Peru) DAD

suggest scenarios, causes, triggering and emplacement mechanisms of these DAD. These are used to explain their avalanche kinematics and dynamics.

Mapping DAD is a necessary step for identifying past events and existing hazards in specific areas. Identifying and describing the DAD structures and morphology will help understand the kinematics and dynamics of the emplaced avalanches.

**Keywords:** debris avalanche deposits; hummocks; structural and morphological mapping, analogue modelling; remote sensing; Mt Iriga; Guinsaigon; Mt Meager; Storegga landslide; Süphan Dağı (Turkey); Cerro Pular-Pajonales (Argentina); Tacna (Peru)

---

## Résumé:

Les effondrements de flanc déclenchent de larges avalanches de débris et glissements de terrain, provoquant ainsi une modification de la pente du volcan et altérant le paysage. Les différents types de volcans subissent des effondrements de flanc lors de leur développement. Aux Philippines, par exemple, les volcans présentant des brèches sont les cônes, sub-cônes et volcans massifs. Les avalanches de débris affectent les édifices volcaniques et non-volcaniques ; leur étude constitue donc un enjeu primordial pour l'évaluation des risques naturels.

Les dépôts d'avalanche de débris (DAD) présentent des structures de surface et internes, des morphologies et des textures pouvant être utilisés pour déterminer le type de transport, les mécanismes de déformation et les vitesses d'emplacement de l'avalanche de débris. Cependant, sur le terrain, les DAD sont souvent vastes et chaotiques, ainsi l'apport de la télédétection complète l'étude de terrain en apportant une vision d'ensemble de l'avalanche.

Notre étude s'intéresse à la structure et morphologie des DAD par l'utilisation de modèles analogiques et en contexte naturel via l'étude du Mt Iriga et Guinsaugon aux Philippines et à travers d'autres sites dans le monde (Mt Meager, Canada; Storegga Slide, Norvège). L'étude de la vitesse de mise en place, de la dynamique et des mécanismes de déformation des avalanches de débris s'est faite via la modélisation analogique. Il apparaît ainsi que la formation de "hummocks" est un processus clé dans la structuration des DAD.

Les "hummocks" sont des parties massives du volcan arrachées lors de l'avalanche de débris et qui se disloquent au fur et à mesure de son avancée. Cette dislocation des "hummocks" s'effectue via l'apparition de failles normales à fort pendage qui fusionnent avec les zones de cisaillement à faible pendage situées à la base du glissement. Les "hummocks" fournissent des informations sur les conditions de transport et la composition initiale de l'avalanche. Leur géométrie (taille et forme), leur structure interne et leur distribution spatiale sont des indicateurs de la vitesse du développement de l'avalanche. Ils permettent d'interpréter sa dynamique de mise en place.

Les expériences analogiques utilisant une rampe courbée montrent le développement de zones d'accumulation et d'épaississement à l'endroit où les matériaux atteignent une surface de dépôt à faible pente. Les expériences avec des rampes rectilignes montrent de plus long glissement. L'extension de ces avalanches est accommodée par des structures en horst et graben ainsi qu'en transtension. Le dépôt consécutif à l'avalanche peut être remobilisé lors d'effondrements secondaires. L'ensemble de ces expériences montre que la morphologie de la surface de glissement influence les mécanismes de mise en place, l'extension spatiale et la structure de l'avalanche.

La cartographie structurale et morphologique acquise par télédétection ainsi que la description de caractéristiques récurrentes sur plusieurs DAD, difficiles d'accès et jusqu'ici non cartographiés (Süphan Dağı (Turkey), Cerro Pular-Pajonales (Argentina), and Tacna (Peru)), a permis de préciser les scénarios, les causes et les facteurs de mise en place des DAD.

La cartographie des DAD est une étape nécessaire pour retracer les évènements passés et estimer les risques naturels dans une zone spécifique. L'identification et la description des morphologies et structures des DAD devraient permettre la compréhension des mécanismes de mise en place de l'avalanche.

# Contents

<b>1</b>	<b>Introduction</b>	<b>1</b>
1.1	Introduction . . . . .	2
1.2	Motivation of the Present Work . . . . .	4
1.3	This Thesis . . . . .	5
1.4	The Philippines . . . . .	6
1.5	The Philippine Volcanoes . . . . .	7
1.5.1	Spatial Distribution of Philippine Volcanoes . . . . .	7
1.5.2	Morphometry and Evolution of Philippine Volcanoes . . . . .	12
1.5.3	Evolution . . . . .	17
<b>2</b>	<b>Controls and emplacement of the Iriga DAD</b>	<b>23</b>
2.1	Abstract . . . . .	24
2.2	Introduction . . . . .	24
2.3	Regional Setting . . . . .	25
2.4	Mt Iriga . . . . .	27
2.5	Methods and Terms . . . . .	28
2.6	Mt Iriga Morphology . . . . .	28
2.6.1	Iriga DAD1 Geometry, Structure, and Morphology . . . . .	29
2.6.2	Iriga DAD1 Lithology and Stratigraphy . . . . .	31
2.6.3	Buhi DAD2 Geometry, Structure, and Morphology . . . . .	35
2.6.4	Buhi DAD2 Lithology and Stratigraphy . . . . .	37
2.7	Discussion . . . . .	43
2.7.1	Comparison of the Iriga DAD1 and Buhi DAD2 . . . . .	43
2.7.2	Collapse Mechanism . . . . .	44
2.7.3	Mode of Transport . . . . .	45
2.7.4	Substrate Incorporation . . . . .	47
2.7.5	Mobility . . . . .	48
2.8	Conclusions . . . . .	48
<b>3</b>	<b>Hummocks: how they form and how they evolve</b>	<b>51</b>
3.1	Abstract . . . . .	52
3.2	Introduction . . . . .	52
3.3	Methodology . . . . .	54
3.3.1	Analogue Models . . . . .	54
3.3.2	Model Set-Up and Parameters . . . . .	55
3.3.3	Scaling . . . . .	57
3.4	Results . . . . .	60

3.4.1	Standard Experiment . . . . .	60
3.4.2	Model Avalanche Class . . . . .	60
3.4.3	Surface Morphology and Structures . . . . .	60
3.4.4	Plan View Shape . . . . .	63
3.4.5	Subsurface Deformation . . . . .	65
3.4.6	Hummocks . . . . .	66
3.4.7	Sequence of Events . . . . .	71
3.5	Discussion . . . . .	71
3.5.1	Avalanche Characteristics . . . . .	72
3.5.2	Hummock Description . . . . .	72
3.5.3	Avalanche Stages and Hummock Formation . . . . .	74
3.5.4	Structural Models: Layers and Structural Interface . . . . .	78
3.6	Conclusions . . . . .	78
<b>4</b>	<b>The anatomy of avalanche hummocks</b>	<b>81</b>
4.1	Abstract . . . . .	82
4.2	Introduction . . . . .	82
4.2.1	Hummock Interpretations . . . . .	83
4.2.2	Hummock Types . . . . .	84
4.2.3	Iriga volcano and her DADs . . . . .	84
4.2.4	Objectives . . . . .	86
4.3	Methodology . . . . .	86
4.4	Results . . . . .	86
4.4.1	Hummock Exploration and Accounting . . . . .	87
4.4.2	Field Description . . . . .	89
4.5	Discussion . . . . .	95
4.6	Conclusions . . . . .	96
<b>5</b>	<b>The development of structures in avalanches</b>	<b>99</b>
5.1	Abstract . . . . .	100
5.2	Introduction . . . . .	100
5.3	Model Set-up . . . . .	102
5.4	Scaling . . . . .	103
5.5	Reproducibility, Model Limitation, Initiation . . . . .	108
5.6	Results . . . . .	108
5.6.1	The Curved Ramp Experiments: Set 1 . . . . .	110
5.6.2	The Inclined Straight Ramp Experiments: Set 2 . . . . .	112
5.6.3	Natural Debris Avalanche Deposits . . . . .	116
5.7	Discussion . . . . .	124
5.7.1	Morphology and Structures in Curved- and Straight- Based Analogue Slides . . . . .	124

5.7.2	Development of Structures and Evolution of Morphology in Large Debris Slides . . . . .	127
5.7.3	Implications of Analogue Morphology and Structure on Natural Prototypes . . . . .	128
5.8	Conclusions . . . . .	128
<b>6</b>	<b>Structural and morphological mapping of DAD</b>	<b>131</b>
6.1	Abstract . . . . .	132
6.2	Introduction . . . . .	132
6.2.1	Structures and Morphological Features in Analogue and Natural DAD . . . . .	133
6.2.2	Remote Sensing and GIS in Mapping DAD . . . . .	133
6.2.3	Objectives and Limitations . . . . .	136
6.3	Study Sites . . . . .	136
6.3.1	Cerro Pular-Pajonales (Chile-Argentina) . . . . .	136
6.3.2	Süphan Dağı (Turkey) . . . . .	137
6.3.3	Tacna (Peru) . . . . .	138
6.4	Methodology . . . . .	139
6.4.1	Data Gathering and building the GIS . . . . .	139
6.4.2	Topographic Modelling: SRTM DEM and ASTER GDEM	139
6.4.3	Colour Composites: Landsat ETM+ . . . . .	139
6.4.4	RS and GIS Interpretation and Surface Mapping . . . . .	141
6.5	Results . . . . .	141
6.5.1	Cerro Pular-Pajonales . . . . .	141
6.5.2	Süphan Dağı . . . . .	144
6.5.3	Tacna . . . . .	147
6.6	Dynamics and Kinematics . . . . .	152
6.6.1	Cerro Pular-Pajonales . . . . .	152
6.6.2	Süphan Dağı . . . . .	152
6.6.3	Tacna . . . . .	155
6.7	Conclusion . . . . .	155
<b>7</b>	<b>Summary and future work</b>	<b>157</b>
7.1	Introduction . . . . .	158
7.2	The Philippine Volcanoes . . . . .	158
7.3	Iriga volcano (Philippines) and her 2 DAD . . . . .	159
7.4	Hummocks: How They Form, What They Mean, and Anatomy	160
7.5	Structures in Long-Runout Avalanches and Large Landslides .	161
7.6	Mapping Remote DAD . . . . .	162
7.7	Future Work . . . . .	162

---

A Philippine Volcanoes	165
B Avalanche class and hummock types	205
C Hummock size versus distance	207
D Curved and straight ramp experiments	209
Bibliography	213

# List of Figures

1.1	Debris avalanches . . . . .	2
1.2	Search and rescue operations at Guinsaugon, southern Leyte, Philippines . . . . .	5
1.3	The Philippines . . . . .	9
1.4	Evolutionary trend of the Central American and southern Central Andes volcanoes . . . . .	13
1.5	The morphometry of Philippine volcanoes . . . . .	15
1.6	Summit contours for Philippine volcanoes according to class .	16
1.7	Evolutionary trend of the Philippine volcanoes . . . . .	18
2.1	Tectonic map of the Philippines and regional map of Mt Iriga	26
2.2	The two Mt Iriga DAD . . . . .	31
2.3	Iriga collapse scar and hummocks . . . . .	32
2.4	Iriga DAD1 lithologies and structures . . . . .	33
2.5	Bulldozer facies at the distal edge of Iriga DAD1 . . . . .	35
2.6	Stratigraphic correlations in Iriga DAD1 and Buhi DAD2 . . .	36
2.7	Internal deformation within Buhi DAD2 . . . . .	38
2.8	Mingled and mixed units in Buhi DAD2 . . . . .	39
2.9	The lower part of Buhi DAD2 . . . . .	40
2.10	Buhi DAD2 lithologies . . . . .	41
2.11	Mt Iriga vs analogue volcanoes built on strike-slip faults . . .	47
3.1	Hummocks at the two Iriga DAD . . . . .	53
3.2	Analogue model set-up . . . . .	56
3.3	Avalanche classes and hummock types . . . . .	61
3.4	3D avalanche development and hummock formation . . . . .	62
3.5	Subsurface avalanche structures . . . . .	65
3.6	Increasing line plot of hummock area . . . . .	67
3.7	Line graph of hummock area vs distance from summit . . . . .	68
3.8	Hummock spatial distribution during avalanche . . . . .	69
3.9	Hummock formation and degree of faulting during avalanche emplacement . . . . .	70
3.10	Structural models of hummock formation . . . . .	77
4.1	Mt Iriga and her 2 DAD with hummock type locations . . . . .	85
4.2	Increasing size plot of DAD1, DAD2 and analogue hummocks	87
4.3	Hummock DAD1 and DAD2 size vs distance . . . . .	88
4.4	The Lady Backhoe's hummock . . . . .	90

4.5	The Captain's Slide Hummock . . . . .	91
4.6	The Lava Topping Hummock . . . . .	93
4.7	The Ignimbrite Topping Hummock . . . . .	94
4.8	The anatomy of a hummock . . . . .	96
5.1	Analogue long runout slides set-up . . . . .	102
5.2	Curved ramp analogue avalanches . . . . .	103
5.3	Straight ramp analogue avalanches . . . . .	105
5.4	Structural and morphological development in straight ramp models with thinner deposit . . . . .	115
5.5	Structural and morphological development in straight ramp models thicker deposit . . . . .	117
5.6	The Guinsaigon Rockslide-Debris Avalanche (Philippines) . .	121
5.7	The Meager Rockslide Avalanche (Canada) . . . . .	123
5.8	The Storegga Slide (Norway) . . . . .	126
5.9	Natural tongue-like runout deposits and rib-ridge morphology	129
6.1	Cerro Pular-Pajonales DAD and vicinity . . . . .	142
6.2	Cerro Pular-Pajonales DAD (in detail) . . . . .	143
6.3	Süphan Dağı DAD . . . . .	147
6.4	The Western and Eastern Süphan Dağı DAD . . . . .	148
6.5	Tacna DAD . . . . .	150
6.6	Tacna DAD (in detail) . . . . .	151
6.7	Süphan Dağı vs analogue models of volcanoes built on strike- slip faults . . . . .	154
A.1	Apo . . . . .	166
A.2	Babuyan Claro . . . . .	167
A.3	Balut . . . . .	168
A.4	Banahaw . . . . .	169
A.5	Bulusan . . . . .	170
A.6	Cabalian . . . . .	171
A.7	Cagua . . . . .	172
A.8	Camiguin de Babuyan . . . . .	173
A.9	Cancanajag . . . . .	174
A.10	Corregidor Complex . . . . .	175
A.11	Cuernos de Negros . . . . .	176
A.12	Didicas . . . . .	177
A.13	Hibok-hibok . . . . .	178
A.14	Iriga . . . . .	179
A.15	Isarog . . . . .	180
A.16	Kalatungan . . . . .	181

---

A.17 Kanlaon . . . . .	182
A.18 Labo . . . . .	183
A.19 Leonard Massif . . . . .	184
A.20 Makaturing . . . . .	185
A.21 Malinao . . . . .	186
A.22 Malindig . . . . .	187
A.23 Mandalagan . . . . .	188
A.24 Maripipi . . . . .	189
A.25 Mariveles-Limay-Samat . . . . .	190
A.26 Matutum . . . . .	191
A.27 Mayon . . . . .	192
A.28 Musuan . . . . .	193
A.29 Natib . . . . .	194
A.30 Negron . . . . .	195
A.31 Parangan . . . . .	196
A.32 Parker . . . . .	197
A.33 Pinatubo . . . . .	198
A.34 Ragang . . . . .	199
A.35 San Cristobal . . . . .	200
A.36 Silay . . . . .	201
A.37 Sinumaan . . . . .	202
A.38 Smith . . . . .	203
A.39 Vulcan Biliran . . . . .	204
B.1 Chosen analogue models that best represent the recurrent morphology and structures in the three sets of experiments: Set 1, Set 2, and set 3 with their classified avalanche classes and the type of hummocks formed in each of the classes. . . . .	206
C.1 Line plot of the hummock sizes sorted according to its distance away from the source. . . . .	208
D.1 Analogue slides using the curved ramp, Set 1. Parameters used are presented in Table 2. . . . .	210
D.2 Analogue slides using the straight ramp, Set 2. Parameters used are presented in Table 3. . . . .	211



# List of Tables

1.1	Philippine volcano population per status and spatial distribution	10
1.2	Philippine volcanoes morphometric data . . . . .	22
3.1	List of scaling variables . . . . .	55
3.2	Definition and values of the independent dimensionless variables	58
5.1	Scaling variables for Set 1 and Set 2 . . . . .	107
5.2	Model labels, parameters, and cohesion of material and source box used for Set 1. . . . .	109
5.3	Model labels, parameters, and cohesion of material and source box used for Set 2 . . . . .	110
6.1	Landsat characteristics . . . . .	134
6.2	Literally known colour composites used as guide in the colour composition and lineament delineation. . . . .	140



CHAPTER 1

# Introduction

---



Figure 1.1: Debris Avalanches. **A** Guinsaugon DAD; **B** Mt Meager DAD. The source areas are marked by stars. Enclosed in circles are the scales.

## 1.1 Introduction

Volcano morphology reflects the effects of aggradational and degradational processes on the edifice (Grosse et al., 2009; van Wyk de Vries et al., 2007). These processes can continuously change the morphology and shape of volcanoes and can sometimes lead to flank instability. When a volcano is unstable, it is more likely to experience structural failure and collapse (McGuire, 1996).

Flank collapses are caused by a number of factors: tectonic activity (Lagmay et al., 2000; Vidal N. and Merle O., 2000), internal growth by magmatic intrusion (Donnadieu and Merle, 1998; Tibaldi, 2001), weakening by hydrothermal alteration (Reid et al., 2001; van Wyk de Vries and Francis, 1997) and gravitational spreading (Borgia et al., 1992; van Wyk de Vries and Francis, 1997; van Wyk de Vries et al., 2000). One or a combination of earthquakes (Montaldo et al., 1996), magmatic intrusions (Elsworth and Voight, 1996; Voight et al., 1983), and meteoric events (van Wyk de Vries et al., 2000) can trigger collapses. Failure of destabilized volcano flanks and mountain ranges can generate debris avalanches and large landslides (Fig. 1.1). Avalanches can reshape mountains by leaving collapse scars on the edifice and depositing voluminous debris avalanche deposits (DAD) on the lower slopes and even further beyond.

Hazards of debris avalanches and large landslides are significant at both active and extinct volcanoes. The high mobility and very long runouts of avalanches cause high human and material loss, directly or indirectly. Avalanches are capable of burying large tracts of land, damming rivers that can catastrophically drain into floods and lahars and cause devastating tsunamis if they reach lakes and seas. Examples are collapse-induced lahars at Casita, Nicaragua; tsunamis induced by collapse at Mayu-yama, Japan (Bernard et al., 2009; Evans et al., 2007; Kerle and van Wyk de Vries, 2001; Siebert,

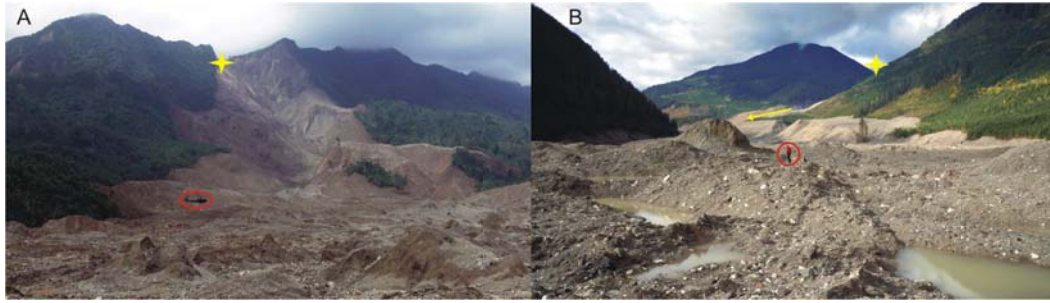


Figure 1.1: Debris Avalanches. **A** Guinsaugon DAD; **B** Mt Meager DAD. The source areas are marked by stars. Enclosed in circles are the scales.

## 1.1 Introduction

Volcano morphology reflects the effects of aggradational and degradational processes on the edifice (Grosse et al., 2009; van Wyk de Vries et al., 2007). These processes can continuously change the morphology and shape of volcanoes and can sometimes lead to flank instability. When a volcano is unstable, it is more likely to experience structural failure and collapse (McGuire, 1996).

Flank collapses are caused by a number of factors: tectonic activity (Lagmay et al., 2000; Vidal N. and Merle O., 2000), internal growth by magmatic intrusion (Donnadieu and Merle, 1998; Tibaldi, 2001), weakening by hydrothermal alteration (Reid et al., 2001; van Wyk de Vries and Francis, 1997) and gravitational spreading (Borgia et al., 1992; van Wyk de Vries and Francis, 1997; van Wyk de Vries et al., 2000). One or a combination of earthquakes (Montaldo et al., 1996), magmatic intrusions (Elsworth and Voight, 1996; Voight et al., 1983), and meteoric events (van Wyk de Vries et al., 2000) can trigger collapses. Failure of destabilized volcano flanks and mountain ranges can generate debris avalanches and large landslides (Fig. 1.1). Avalanches can reshape mountains by leaving collapse scars on the edifice and depositing voluminous debris avalanche deposits (DAD) on the lower slopes and even further beyond.

Hazards of debris avalanches and large landslides are significant at both active and extinct volcanoes. The high mobility and very long runouts of avalanches cause high human and material loss, directly or indirectly. Avalanches are capable of burying large tracts of land, damming rivers that can catastrophically drain into floods and lahars and cause devastating tsunamis if they reach lakes and seas. Examples are collapse-induced lahars at Casita, Nicaragua; tsunamis induced by collapse at Mayu-yama, Japan (Bernard et al., 2009; Evans et al., 2007; Kerle and van Wyk de Vries, 2001; Siebert,

2002); tsunamis in Tenerife, Canary Islands, triggered by the Guimar debris avalanche (Giachetti et al., 2011); and effects on the landscape and sedimentation of western Taranaki, New Zealand (Procter et al., 2009).

Debris avalanche genesis and transport are poorly understood but evidence and triggering mechanisms may be preserved within their deposit morphology and structures. Thus, identification and mapping of DAD structures, morphology, and texture are essential to understand their emplacement mechanism and dynamics.

DAD are large scale and sometimes inaccessible so the use of remote sensing for structural and morphological mapping is necessary. Bathymetric and geophysical data such as at St Vincent, West Indies (Le Friant et al., 2009), Lesser Antilles Arc (Deplus et al., 2001), and Piton des Neiges shield volcano, Reunion Island (Bachèlery et al., 2003; Lénat et al., 2001; Oehler et al., 2004) were also used for recognising and studying offshore debris avalanches. Topographic expression and contrasted spectral properties are helpful to recognise DAD morphology, structures, and extent, and constrain their emplacement properties (e.g. Francis and Wells, 1988; Kervyn et al., 2008; Wadge et al., 1995).

A comprehensive structural and morphological mapping and analysis of Parinacota, Lastarria, Ollague, Aucanquilcha, Lullaillaco, Socompa, and Tetivicha (Central Andes of Chile, Argentina and Bolivia); Blackhawk, Chaos Jumbles and Martinez Mountain (California, USA); Carlson (Idaho, USA); and Mombacho (Nicaragua) debris avalanches were done by Shea and van Wyk de Vries (2008). Ground truth for the structures and morphological features on Socompa are provided by Kelfoun et al. (2008); van Wyk de Vries et al. (2002, 2001); Wadge et al. (1995), on Mombacho by Kelfoun et al. (2008), and on Parinacota and Ollague by Clavero et al. (2004, 2002). Some field-based studies such as on the Cantal volcano, France (Schneider and Fisher, 1998); Iwasegawa and Kaida DAD, Japan (Takarada et al., 1999); Roque Nublo DAD, Gran Canaria, Spain (Mehl and Schmincke, 1999); Parinacota, Northern Chile (Clavero et al., 2002); Mombacho, Nicaragua (Shea et al., 2008); and Chimborazo, Ecuador (Bernard et al., 2008) focus on lithology and structure descriptions as a way to understand DAD transport and emplacement.

Analogue models recreating natural systems at laboratory scale (Merle and Borgia, 1996; Ramberg, 1981) are also employed for understanding avalanches. Analogue avalanches have been made to study the morphology, structure, and internal distribution of stratified material (e.g. Shea and van Wyk de Vries, 2008). Some particular studies focus on the occurrence and significance of longitudinal ridges, hummocks and flow bands (Cassie et al., 1988; Dufresne and Davies, 2009; McColl and Davies, 2011); and the effects of substrata and basement fault movement on the volcano edifice (Andrade and van Wyk de

Vries, 2010; Cecchi et al., 2005; Lagmay et al., 2000; Mathieu and van Wyk de Vries, 2011; Merle and Borgia, 1996; Shea and van Wyk de Vries, 2008; van Wyk de Vries and Francis, 1997; van Wyk de Vries et al., 2000; Wooller et al., 2009, 2004).

Numerical modelling are also used to study transport processes (Campbell, 1989; Campbell et al., 1995; Kelfoun and Druitt, 2005; Pouliquen and Renault, 1996; Staron et al., 2001), development of DAD structures (Thompson et al., 2010), emplacement (Davies et al., 2010; Dufresne et al., 2010; Kelfoun and Druitt, 2005) and dynamics (Friedmann et al., 2006) of debris avalanches.

A database of volcanic and non-volcanic mass movement deposits is compiled to give the scientific community a useful tool and access to the state of research concerning volcanic sector and mountain slope collapse processes, debris and rock avalanche runout mechanisms, numerical modelling and hazard assessments (Dufresne, 2009). It is a part of the Volcano Global Risk Identification and Analysis Project (VOLGRIPA).

## 1.2 Motivation of the Present Work

On 17 February 2006, the  $\sim 20$  million  $\text{m}^3$  (Lagmay et al., 2006) Guinsaigon rockslide-debris avalanche buried a whole village killing 1,221 people and displacing approximately 19,000 (Guthrie et al., 2009). It was one of the most disastrous landslides in Philippine history (Catane et al., 2008) and the most devastating single-event landslide to have occurred worldwide since the Casita volcano rock avalanche-debris flow triggered by typhoon Mitch in Nicaragua in 1998 (Evans et al., 2007; Kerle and van Wyk de Vries, 2001).

The Guinsaigon avalanche may have been a result of progressive failures and tectonic weakening, as the Philippine Fault Zone traverses the area (Guthrie et al., 2009). Intense precipitation and an almost synchronous seismic event closely preceding the landslide may have triggered the collapse of this structurally weak part of the mountain range. The landslide mobility was increased by the presence of rice paddy fields in the valley bottom.

It started when a block slide transformed into an avalanche, leaving behind a deep, wedge-shaped scarp, a debris-flow-type marginal deposit over  $3.2 \text{ km}^2$  and a runout of 4.1 km, damming 4 streams on its way (Catane et al., 2007). The debris avalanche deposit is described as having a hummocky topography and pressure ridges (Catane et al., 2008; Guthrie et al., 2009).

My first hand experience at the rescue operations of the Guinsaigon rockslide-debris avalanche (Fig. 1.2) gave a deep realisation on the importance of studying avalanches in tectonically active areas like the Philippines and even in considerably stable landmasses. An effective method to mitigate



Figure 1.2: My photo during the 2006 Guinsaugon rockslide debris avalanche search and rescue operations.

debris avalanche risks is to learn to recognise the structures, morphology, and surface textures of avalanches and large landslides, and understand their roles and effects in the emplacement and transport mechanisms of such events.

This thesis attempts to use this approach at understanding avalanches. Clear examples of natural DAD structures and morphology at Mt Iriga, Guinsaugon, Mt Meager and Storegga are complemented with those created by laboratory analogue avalanches. In particular, the spatial distribution, formation, evolution, and internal characteristics of hummocks and the development of structures and morphological features in long runout landslides are described in detail.

### 1.3 This Thesis

The dissertation starts with an introduction (Chapter 1) to the tectonics and geology of the Philippines. A major part discussed is on the spatial distribution, morphometry and evolution of the Philippine volcanoes. At the end of

the chapter, a classification system for Philippine volcanoes based on individual volcano morphometry and evolutionary trends is presented.

Chapter 2 presents a detailed investigation on the volcano-tectonic controls of the debris avalanches at Mt Iriga, a volcano with two DAD. Fieldwork supplemented by aerial photographs has provided the basis for the morphological mapping of an ancient debris avalanche deposit on the southwest flank of the volcano, and the mapping of the previously known recent debris avalanche.

Studying the Iriga DAD has laid the foundation for further studies concentrating on the morphological and structural features in DAD. In particular, work at Mt Iriga led to the investigation of a prominent large landslide and avalanche feature, the hummocks. Analogue modelling in Chapter 3, explores how these hummocks form and what they mean.

The anatomy of hummocks (Chapter 4) relates the lessons learned from Chapter 3 to the natural hummock cross-sections and detailed descriptions at Iriga DAD. Natural hummock prototypes of the different avalanche classes observed in the analogue experiments will be presented in this chapter.

Curved and straight ramp analogue avalanches (Chapter 5) aims to describe in detail the development of avalanche structures and morphology for analogue avalanches with different sliding base morphology. Findings from analogue modelling are compared with the DAD features of Mt Iriga and Guinsaigon (Philippines), Mt Meager (Canada) and Storegga Slide (Norwegian margin).

In Chapter 6: Case studies presents the remotely sensed morphological and structural mapping of previously unmapped DAD at three locations including Cerro Pular-Pajonales in Chile-Argentina, Süphan Dağı in Turkey and a large long-runout landslide in Tacna, Peru. Lastly, in Chapter 7 a summary and suggestions for future work is given.

## 1.4 The Philippines

The Philippine archipelago (Fig. 1.3) is made up of a collage of insular arcs, ophiolitic suites, continental rocks, and sedimentary basins (Aurelio, 2000; Aurelio M and R, 2002; Barrier et al., 1991) in two distinct geologic entities: the North Palawan Block and the Philippine Mobile Belt (Gervasio, 1967). It is a result of the subduction of the Philippine Sea Plate under the Eurasian and Indo-Australian Plates.

Opposing subduction zones (Fig. 1.3) control the Philippine tectonics (Aurelio, 2000; Barrier et al., 1991): trenches on the west (Manila, Negros, Cotabato and Sulu trenches) subduct eastward and trenches on the east (the Philippine and East Luzon trenches) have westward vergence. Collision zones

mark the northern and southern extremities as well as the western margin of the archipelago. Taiwan is a result of the collision of the western edge of the Philippine Sea Plate with the continental margin of Eurasia; Mindoro-Panay resulted when the North Palawan Block collided with the central portion of the Philippine Mobile Belt; and the Moluccas Sea double-vergent subduction caused the convergence and collision of two active volcanic arcs. These subduction and collision zones result in the Philippine mobile belt, an actively deforming zone in between the two active systems (Fig. 1.3) (Gervasio, 1967).

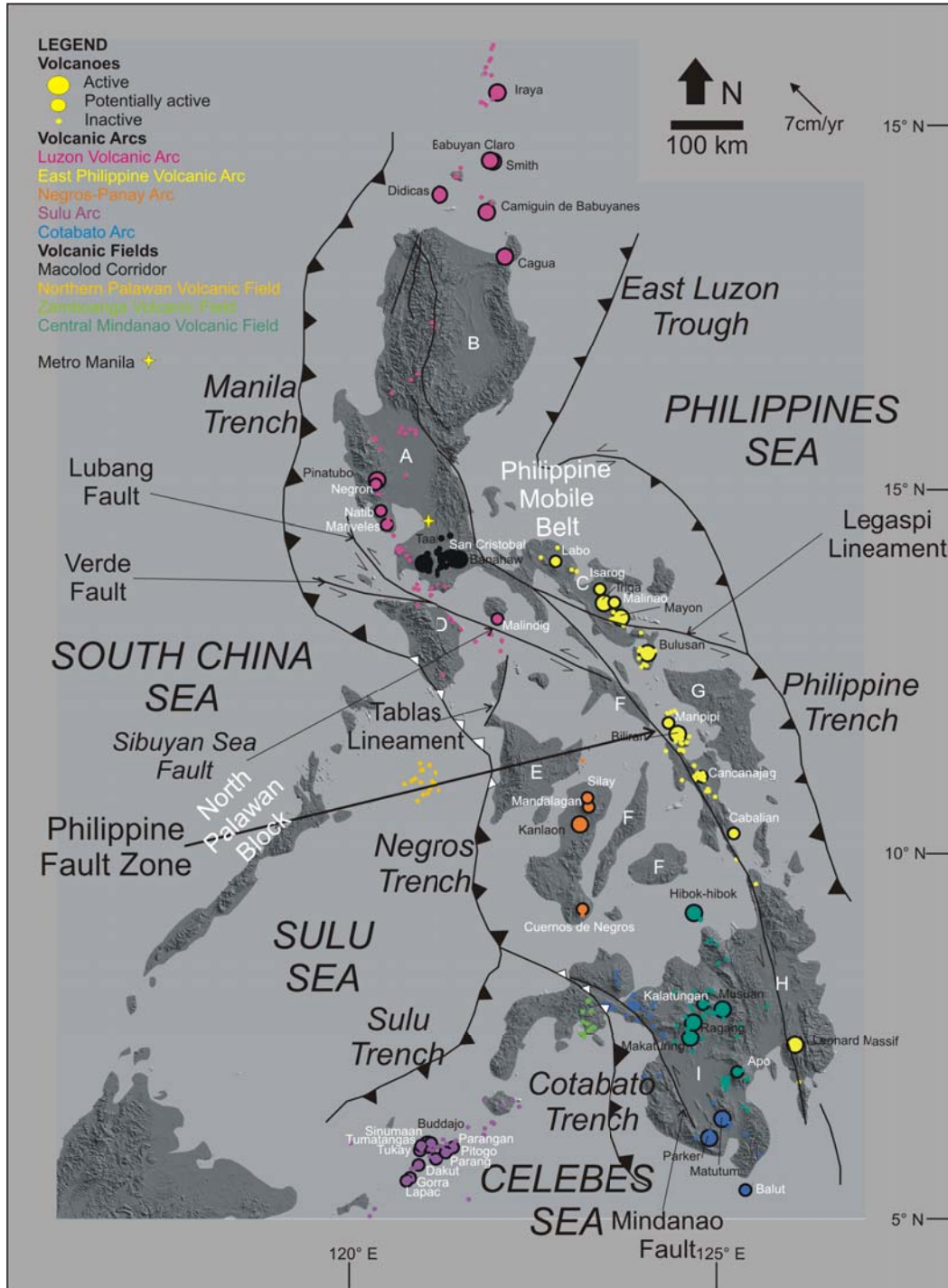
Major strike-slip faults further complicate the terrain (Fig. 1.3) (Aurelio, 2000; Barrier et al., 1991): the left-lateral Philippine Fault traverses the whole archipelago offsetting mountain ranges, sedimentary basins and lithologic markers; the Valley Fault System runs through most parts of Metropolitan Manila; the Macolod Corridor influences the alignment of scoria cones, maars and recent volcanoes south of Manila including Taal volcano; the left-lateral offshore Lubang-Verde Fault System played a role during the transition from subduction along the Manila Trench to the collision in the Mindoro-Palawan-Panay area; the Sibuyan Sea Fault as a transtensional branch of the Philippine Fault relayed to the Verde Passage Fault; the Tablas Lineament that is a tectonic boundary between the North Palawan micro-continental block and the western edge of the Philippine Mobile Belt; the Legaspi Lineament that is a splay of the Philippine Fault that continues to the Philippine Trench; and the left lateral with normal component Mindanao Fault.

Within the mobile belt are sedimentary basins (Fig. 1.3) (Aurelio M and R, 2002), generally oriented N-S including: the structurally-controlled Ilocos-Central Luzon and Agusan-Davao Basins, the asymmetric west-dipping Cagayan Valley Basin, the Samar Basin, and the Cotabato Basin flanked by the active volcanic arcs of Cotabato and central Mindanao. NW-oriented basins are the Mindoro Basin juxtaposed with the South China Sea ophiolitic crust, and the Southern Luzon-Bicol Basin controlled by the Philippine Fault. NE-oriented basins are the asymmetric Iloilo Basin and the Visayan Sea Basin that unconformably overlies on volcanoclastic basement.

## 1.5 The Philippine Volcanoes

### 1.5.1 Spatial Distribution of Philippine Volcanoes

Activity along the subduction zones is reflected through the distribution of the active volcanic arcs (Aurelio M and R, 2002). Except for the East Luzon Trough, five trenches bounding the archipelago have corresponding volcanic belts (Fig. 1.3): the East Philippine Volcanic Arc for the Philippine Trench;



the Luzon Volcanic Arc for the Manila Trench; the Negros-Panay Arc for the Negros Trench; the Cotabato Arc for the Sulu Trench; and the Sulu-Zamboanga Arc for the Cotabato Trench. The Philippines has four volcanic fields: Macolod Corridor, Palawan Volcanic Field, Zamboanga Volcanic Field and Central Mindanao Volcanic Field. The Plio-Quaternary volcanoes that make up these arcs and volcanic fields are classified by (PHIVOLCS-DOST, 2002) into active, potentially active, and inactive volcanoes (Tables 1.1, 1.2). Active volcanoes are those that have erupted within the last 600 y (historic) or within the last 10,000 y based on datable materials. Morphologically young-looking volcanoes without historical records of eruption are classified as potentially active and the weathered and eroded volcanoes as inactive. Table 1.1 lists the number of volcanoes classified as active, potentially active, and inactive volcanoes in each of the volcanic arcs and volcanic fields. Described below are the five volcanic arcs and four volcanic fields.

#### 1.5.1.1 The Luzon Volcanic Arc

The Luzon Arc consists of a 1200 km-long chain of stratovolcanoes and volcanic necks extending from eastern Taiwan to Mindoro (Castillo and Newhall, 2004). It resulted from the subduction of the South China Sea along the Manila Trench since the Early Miocene (Balce et al., 1982; Knittel and Defant, 1988; Maury et al., 1992; Teng, 1990; Yumul et al., 2003). The K-Ar dates from the Bataan front arc volcanoes to the volcanic rocks exposed in Mindoro range from 1.7 to 0.1 Ma (Defant et al., 1990; Yumul et al., 2000).

---

Figure 1.3 (*preceding page*): The Philippines has two geologic entities (written in white letters), the more stationary North Palawan Block and the more tectonically active Philippine Mobile Belt located between the opposing subduction of the west-dipping Philippine and East Luzon trenches and east-dipping Manila, Negros, Cotabato and Sulu trenches (Aurelio, 2000; Barrier et al., 1991). Solid triangles are active subduction zones while open triangles are active collision fronts. Also shown are some of the major strike-slip faults: the Philippine Fault Zone, the Lubang-Verde and Sibuyan Faults; the sedimentary basins: Ilocos-Central Luzon (A), Cagayan Valley Basin (B), Southern Luzon-Bicol Basin (C), Mindoro Basin (D), Iloilo Basin (E), Visayan Sea Basin (F), Samar Basin (G), Agusan-Davao Basins (H), and the Cotabato Basin (I); and in colour the volcanoes of the arcs corresponding to the trenches: Luzon Volcanic Arc, East Philippine Volcanic Arc, Cotabato Arc and Sulu-Zamboanga Arc; and volcanic fields: Macolod Corridor, Palawan, Zamboanga and Central Mindanao.

	Active	Potentially Active	Inactive	Total
<b>Volcanic Arcs</b>				
Luzon Volcanic Arc	7	4	65	<b>76</b>
East Philippine Volcanic Arc	5	6	64	<b>75</b>
Negros-Panay Arc	1	3	2	<b>6</b>
Cotabato Arc	2	1	56	<b>59</b>
Sulu-Zamboanga Arc	1	9	39	<b>49</b>
<b>Volcanic Fields</b>				
Macolod Corridor	2	1	48	<b>51</b>
Palawan Volcanic Field	0	0	16	<b>16</b>
Zamboanga Volcanic Field	0	0	12	<b>12</b>
Central Mindanao Volcanic Field	4	2	63	<b>69</b>
<b>Total</b>	<b>22</b>	<b>26</b>	<b>365</b>	<b>413</b>

Table 1.1: Number of active, potentially active and inactive volcanoes for the different volcanic arcs and volcanic fields of the Philippines.

#### 1.5.1.2 The East Philippine Volcanic Arc

This arc extends from Bicol to eastern Mindanao (e.g. [Andal et al., 2005](#); [McDermott et al., 2005](#)). Magmatism and recent volcanism in the area is related to the westward subduction of the Philippine Sea plate along the Philippine Trench ([Castillo and Newhall, 2004](#); [Sajona et al., 1994](#)). The Leyte segment is a 250 km-long NW-SE belt of volcanoes from Biliran to Panaon islands. The Lower Oligocene-Lower Miocene rocks in the northeastern Mindanao segment have erupted after an increase in the angle of subduction of the oceanic crust along the Philippine Trench ([Mitchell et al., 1986](#)).

#### 1.5.1.3 The Negros-Panay Arc

The Negros-Panay Volcanic Arc is a 260 km N-S belt with four volcanoes in the island of Negros and two small island volcanoes east of Panay Island. Mt Canlaon is the only active volcano, although potentially active Mt Mandalagan and Cuernos de Negros have active fumaroles. This arc is produced by subduction of the Sulu Sea crust along the Middle Miocene Negros Trench.

#### 1.5.1.4 The Cotabato Arc

This arc is produced by subduction of the Celebes Sea crust along the Cotabato Trench since the Late Miocene ([Aurelio, 2000](#)). Rocks in this area can have holeiite to tholeiite-calk-alkaline to exclusively calk-alkaline affinities

with K-Ar ages of about 30 Ma (Pubellier et al., 1991). Adakite rocks have a Miocene age (Sajona et al., 1994).

#### 1.5.1.5 The Sulu Arc

The Sulu Arc is defined by a northeast-trending linear chain of small volcanic islands along the boundary between the Sulu and Celebes Seas, west of Mindanao island. Geochemically, basalts and basaltic andesites (Castillo et al., 2002) from the arc have varying degrees of HFSE enrichment. This is a result of the variable amount of mixing between enriched South China Sea intraplate lavas and depleted Sulu seafloor basalts mantle end-components within a compositionally heterogeneous mantle wedge (Castillo et al., 2007).

#### 1.5.1.6 The Macolod Corridor

The Macolod Corridor is a 40-km wide, NE-SW area of approximately 200 monogenetic volcanoes with two distinct clusters of scorias and maars (Calibo et al., 2009). These clusters of volcanoes were generated by a counter-clockwise block rotation in southwestern Luzon that is linked to the opposite motions of the subducting South China Sea under the Manila Trench on the west and the strike-slip Philippine Fault on the east coupled with shearing from the Verde Fault (Fig. 1.3). This block rotation resulted in localised extension along the sides of the blocks that led to the partial melting of the crust (Calibo et al., 2009; Galgana et al., 2007).

#### 1.5.1.7 The Palawan Volcanic Field

The geomorphologically young Palawan Volcanic Field is probably the largest exposure of basaltic lava flows in the Philippine archipelago (Arcilla et al., 2003). This volcanic field is not influenced by recent subduction processes due to the absence of trenches in its surroundings. It also postdates collision of Northern Palawan with the Proto-Philippine arc (Arcilla et al., 2003). The high field strength element concentrations of the lavas show gradation with those of the South China Basin Seamounts and primitive Jolo arc rocks suggesting cogenetic origins from geochemically enriched sources (Arcilla et al., 2003).

#### 1.5.1.8 The Zamboanga Volcanic Field

The Pliocene-Quaternary Zamboanga volcanic field is on the south side of the eastern portion of the Zamboanga Peninsula (Fig. 1.3) (Sajona et al., 1996).

It is linked to the southward subduction of the Oligocene-Miocene Sulu Sea back-arc basin along the Sulu Trench.

### 1.5.1.9 The Central Mindanao Volcanic Field

The Central Mindanao Volcanic Field is the most extensive field of active volcanoes in the Philippines (Sajona et al., 1993). Several seismic studies (Besana et al., 1997; HK and YP, 1980; Pubellier et al., 1991) and reconnaissance petrologic investigations (e.g. Maury et al., 1996; Sajona et al., 1994, 1993; Sajona F.G. et al., 1997) have suggested that this volcanic field is associated with remnants of the subducted Molluca Sea Plate under parts of Mindanao island. Parental magmas of the central Mindanao volcanic field most likely came from the mantle wedge metasomatized by fluids dehydrated from subducted sediments and oceanic crust (Castillo et al., 1999). Based on geographic and structural setting, tectonic, and geochemistry, volcanoes in central mindanao has a northwest migration of volcanism and Camiguin is the northernmost extension of this volcanic field (e.g. Castillo et al., 1999; Corpuz, 1992; Sajona et al., 1994; Sajona F.G. et al., 1997).

## 1.5.2 Morphometry and Evolution of Philippine Volcanoes

Grosse et al. (2009) presented a quantitative morphometric classification and interpretation of evolutionary trends for arc volcanoes (see Fig. 1.4). In their work, morphometric analysis of two contrasting arcs, Central America and the southern Central Andes, was used to interpret processes operating during volcano construction.

A similar morphometric analysis is presented here for the Philippine volcanoes. The analysis aims to obtain quantitative morphological data of the active and potentially active volcanoes in the Philippines and interpret possible shape evolution trends. Also, it will hopefully add to the global documentation of volcanoes and give useful information on the factors controlling volcano shape and evolution, especially in areas with high erosion rates like the Philippines.

The morphometric analysis uses the Morvolc code (Grosse et al., 2012, 2009). It focuses only on the 39 morphologically young-looking active and potentially active volcanoes and uses the 90 m resolution Shuttle Radar Topography Mission (SRTM) digital elevation model (DEM) to compute and define parameters for size: height, width and volume; plan shape: ellipticity and irregularity; and profile shape: height-width ratio, summit width-basal width ratio and slope.

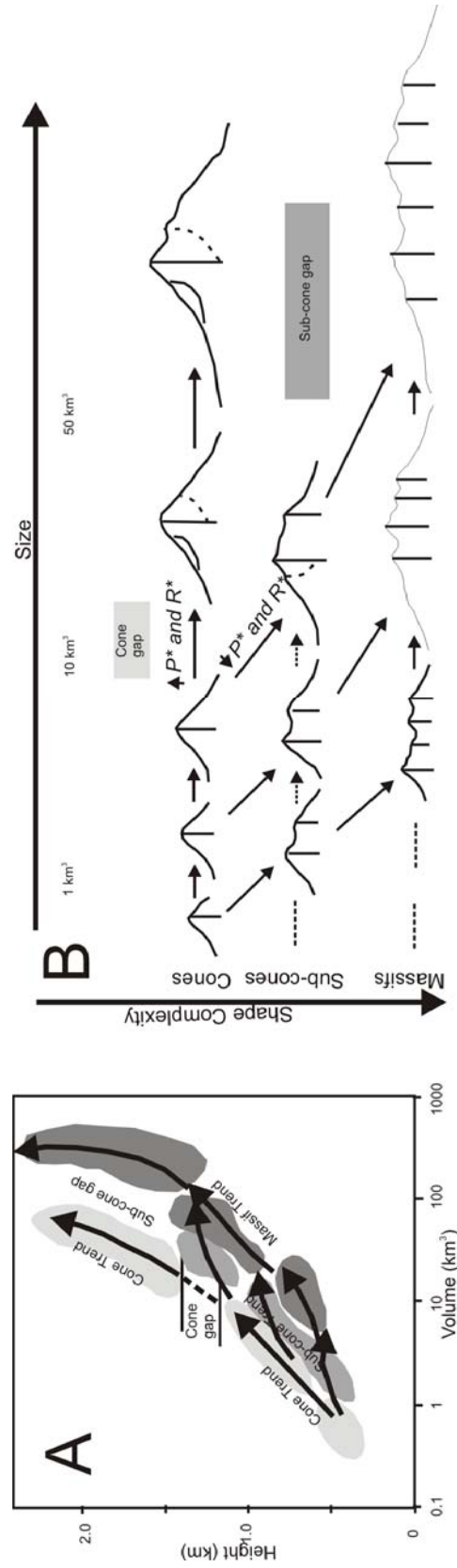


Figure 1.4: Evolutionary trends of the Central American and southern Central Andes volcanic edifices (taken from Grosse et al., 2009). **A** Evolutionary trends of the three main types of volcanic edifices and **B** Evolutionary growth paths starting from small simple cone. P\* is pressure and R\* is resistance balance.

### 1.5.2.1 The MORVOLC code

Morvolc is an interactive data language (IDL) code developed by (Grosse *et al.*, 2012, 2009) for characterising volcano morphometry. The extent of each volcano is manually delineated mostly by following the breaks in slope around the edifice base also considering the extent of deposits, using DEM-derived slope maps, 3D surfaces and shaded relief images. Thus, far-reaching fall and flow products are not considered in the delineation, just the visible edifice. A 3D basal surface is then calculated from the edifice outline using a least-square criterion and this is used to estimate volume and height parameters. Elevation contour lines are then generated from the DEM, and a summit region is defined at the elevation where the edifice starts flattening out.

### 1.5.2.2 Morphometric Parameters

Morvolc generates an array of morphometric parameters for detailed quantification and characterisation of volcano morphology including the size, shape, and morphometric ratios considered here (Table 1.2). The edifice and summit outlines give the basal and summit areas and average basal and summit widths. Height and volume are computed using the edifice outline and the 3D basal surface. Plan shape is characterised by the shape of the elevation contours, quantified into two dimensionless shape descriptor indices: ellipticity index (ei) and irregularity index (ii), which estimate and quantify contour elongation and complexity, respectively, starting at a value of 1 for circular and regular contours. Profile shape of the volcanic edifice is summarised with two ratios of size parameters: the height/basal width ratio ( $H/W_B$ ) estimates the edifice steepness, and the summit width/basal width ratio ( $W_S/W_B$ ) estimates the truncation of the edifice and shows the relative importance of the summit region.

### 1.5.2.3 Quantitative Morphometry of Philippine Volcanoes

The active and potentially active volcanoes of the Philippines have a wide variety of sizes and shapes (Table 1.2, Fig. 1.5-1.6). Their edifice heights vary from 150 to 2090 m and their volumes range from 0.4 to 550 km<sup>3</sup>. Edifice shapes vary from smooth, steep and conical to very irregular and flat.

The edifices can be grouped into three main classes according to their size (basal width and volume), profile steepness ( $H/W_B$ ) and plan shape (average ii and ei) (Fig. 1.5E): cones, subcones and massifs; a subclass of breached edifices is also identified. Considering basal width and volume, two size groups can be defined, small and large (Fig. 1.5A, B, C). Small edifices have basal widths  $\leq 10$  km and volumes  $\leq 20$  km<sup>3</sup>. Large edifices have basal widths

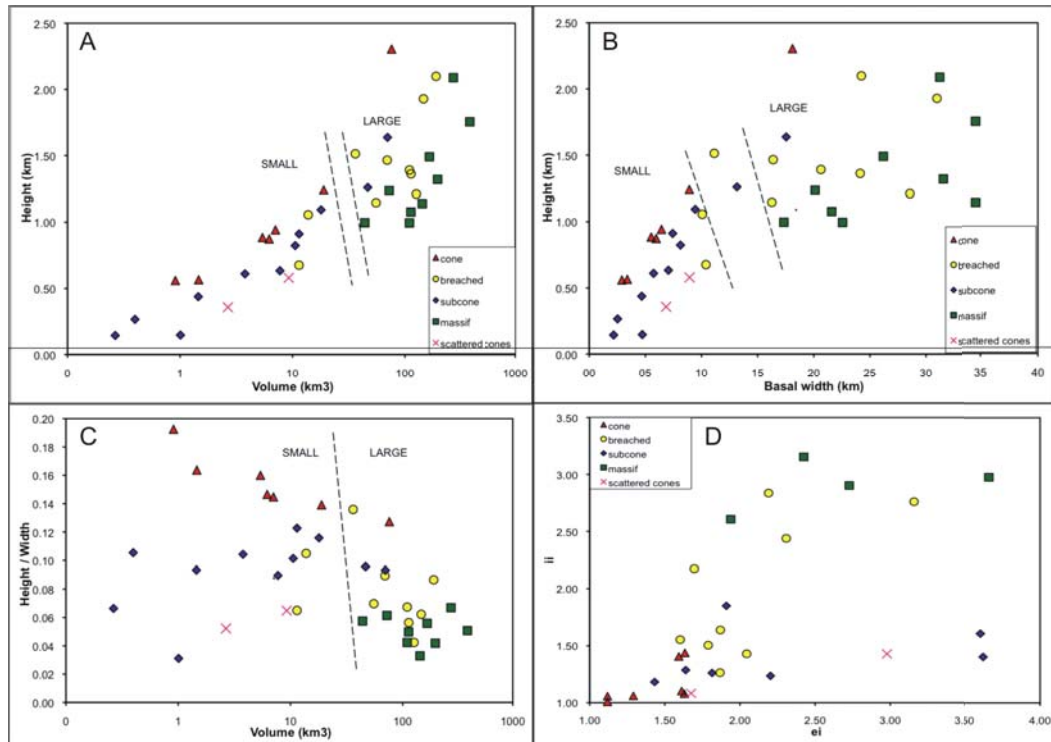


Figure 1.5: Morphometry of Active and Potentially Active Volcanoes in the Philippines. Plot of volcano shape: height against **A** volume and **B** Basal width, and **C** height and basal width ratio against volume. Legend is the same as in A-B and C; volcano complexity: **C** irregularity index against ellipticity index.

$\geq 15$  km and volume  $\geq 30$  km<sup>3</sup>. Two volcanoes, Banahaw and Kalatungan have intermediate basal widths but are large considering their volumes. Their heights are in the higher end of the spectrum for the cone and subcone classes, respectively.

Edifices classified as cones ( $n=7$ ) are steep, with  $H/W_B \geq 0.13$ . They have circular and regular plan shapes, having low  $ei$  (average  $ei \approx 1.7$ ) and  $ii$  (average  $ii \leq 1.1$ ) values, although two edifices are more irregular, Maripipi, because of strong erosion, and Bulusan as it is a vent of a caldera system. Most cones are small, except for large and very active Mayon.

Massifs ( $n=9$ ) are large volcanoes with low  $H/W_B$  ( $\leq 0.07$ ). Their plan shapes are very irregular (average  $ii < 2.6$ ), with intermediate to high ellipticity (average  $ei < 1.9$ ).

Subcones ( $n=11$ ) have shape parameters with intermediate values. They have  $H/W_B$  ratios mostly between 0.08 and 0.12 and average  $ii$  values between

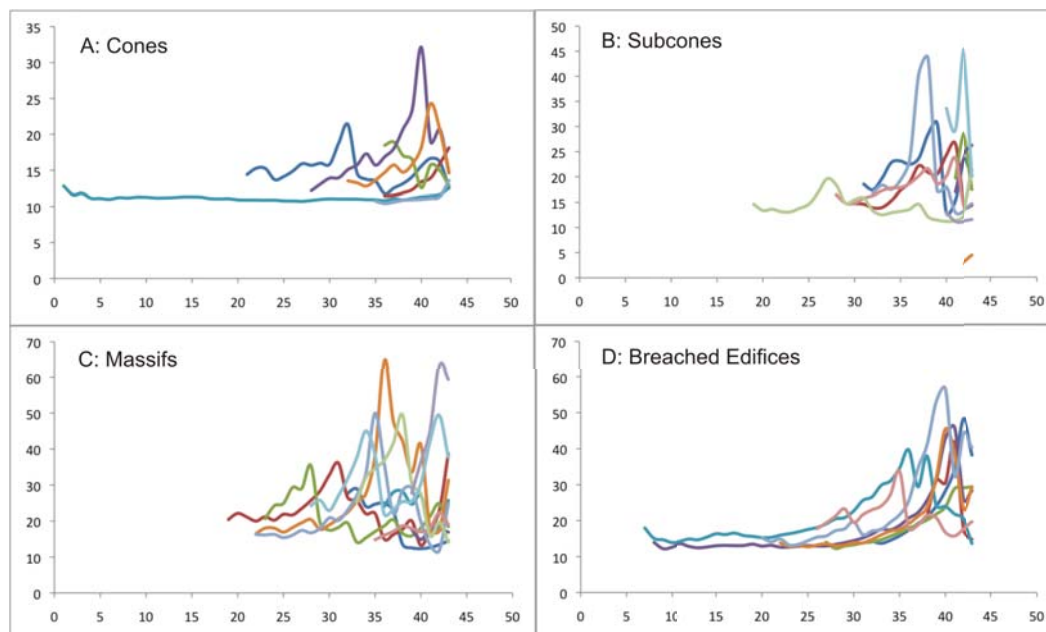


Figure 1.6: Line plot of the summit contours (pegged on the highest elevation contour) vs irregularity index ( $ii$ ). Irregularity Indices of the Summit Contours grouped according to classes: **A** Cones; **B** Subcones; **C** Massifs; and **D** Breached Edifice, a subclass that can include cones, subcones or massifs.

1.2 and 1.8; their average  $ei$  values are very variable. Most subcones are small.

Ten volcanoes have breached edifices, qualitatively defined by collapse-scars and horseshoe-shaped summits. These edifices can be grouped into a morphometric subclass; they are edifices belonging to any of the three main classes that show breaching. They have variable  $H/W_B$  ratios mostly below 0.12, within the range of subcones (3 edifices) and massifs (6 edifices); only Banahaw has a high  $H/W_B$  ratio within the range of cones. They have a variable  $ei$  values and intermediate to high  $ii$  values (average  $ii < 1.2$ ). Most breached edifices are large, only Cagua and Iriga are small. It is difficult to distinguish breached edifices quantitatively because their morphometric parameters are variable as a result of their different ‘pre-breaching’ edifice morphologies. Their common feature is the horseshoe shape of their summits. Thus, their uppermost elevation contours generally have very high  $ii$  and  $ei$  values. Figure 1.6 shows height vs  $ii$  graphs of different edifice types. Breached edifices have increasing irregularity towards the summit.

Two small and very low edifices, Parangan and Sinumaan can be considered as a separate class of scattered cones. Makaturing is seen as a large example of this group (see Appendix A).

### 1.5.3 Evolution

From the morphometric data and classification (Fig. 1.5, 1.7) of the Philippine volcanoes into cones, subcones, massifs, and breached edifices, an evolutionary trend is suggested. The wide variety of volcano sizes and shapes may represent different growth stages. At the earliest stage of volcano formation, an edifice can either be a cone if it has a simple morphology and a single summit vent or a subcone if it has more than one eruption centre. The cone can continue to grow by eruption from its single vent and deposition of products on its flanks resulting in an increase in height and volume (Fig. 1.3B) without a change or addition of vents, thus maintaining its simple conical shape. Conversely, it can grow new domes on its flank or its eruption centre can migrate evolving into a subcone. Small cones and subcones can grow into larger cones and subcones if no further complexities arise, or they can grow wider into massifs if their complexities increase.

During growth from small to larger cones (e.g. Mayon) or to a subcone or massif, the chance of structural failure of the edifice increases. This increase in probability can be due to growth of the volcano by magma intrusion or weakening of its edifice by hydrothermal alteration or if the volcano is spreading due to its volume and size over a substratum that is too weak to support it. These causes happen during the development of a volcano. Large landslides leave large collapse scars on the volcano summit and abruptly change the shape of the volcano, having a very irregular summit shape, for example.

From this suggested volcano evolution trend, we have an idea on whether a certain volcano is likely to be affected by breaching and at what particular stage of evolution it is based on its morphometry. These morphological trends should be integrated with geological, geophysical and geochemical data in the future works to improve the volcano evolution models, all the more in trying to find out whether a volcano is prone to structural failure and breaching.

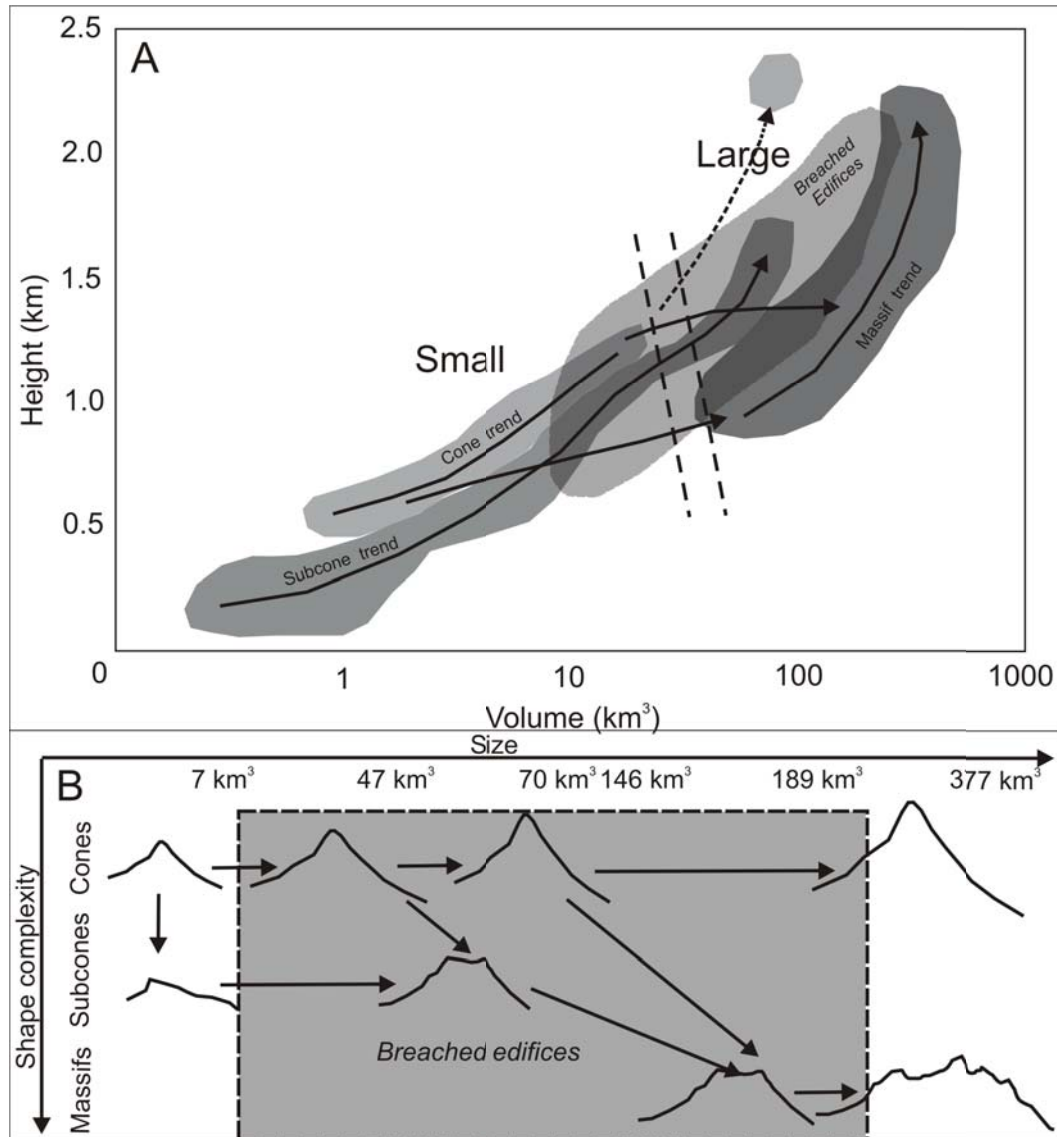


Figure 1.7: Morphometric evolution trends of Philippine volcanoes. **A** Fields of the four main types of volcanic edifices based on the plot of volcano height against volume and **B** possible evolutionary growth paths starting from either a small cone with a single vent or a small subcone with multiple eruption centres or domes (modified from (Grosse et al., 2009)).



	Status	Size Class	Shape Class	Basal			Height km	Volume km <sup>3</sup>	EI Avg	II Avg	H/W ratio	W/W ratio	Slope Mean (flank)
				Width km	Width km	Width km							
Malindig	potentially active	small	subcone	9.44	1.09	17.95	1.81	1.26	0.12	0.1	13.51		
Matutum	active	large	subcone	17.55	1.64	69.98	1.43	1.18	0.09	0.01	11.05		
Musuan	active	small	subcone	2.52	0.27	0.4			0.11		10.9		
Vulcan Biliran	active	small	subcone	7.05	0.63	7.74	3.61	1.61	0.09	0.15	14.66		
Didicas	active	small	subcone (elongate)	4.73	0.15	1.01	3.63	1.4	0.03	0.4	6.35		
Apo	potentially active	large	massif	31.22	2.09	269.2			0.07	0.12	10.29		
Cuernos de Negros	potentially active	large	massif	34.57	1.76	376.91	2.42	3.15	0.05	0.24	10.73		
Labo	potentially active	large	massif	20.12	1.24	72.35	2.73	2.9	0.06	0.36	11.07		
Leonard Massif	active	large	massif	21.6	1.08	112.88			0.05		15.92		
Makaturing	active	large	massif	22.57	0.99	109.64			0.04		10.74		
Mandalagan	potentially active	large	massif	26.2	1.49	164.96	1.94	2.61	0.06	0.23	11.1		
Negron	potentially active	large	massif	17.34	1	43.9			0.06		15.83		

	Status	Size Class	Shape Class	Basal			Volume km <sup>3</sup>	EI Avg	II Avg	H/W ratio	W/W ratio	Slope Mean (flank)
				Width km	Height km	II Avg						
Parker	active	large	massif	31.54	1.32	195.08	3.67	2.98	0.04	0.04	9.78	
Pinatubo	active	large	massif	34.58	1.14	142.51			0.03	0.03	8.29	
Banahaw	int/large	active	breached cone	11.14	1.51	36.17	1.87	1.64	0.14	0.15	16.85	
Cagua	active	small	breached subcone	10.4	0.68	11.43			0.07	0.2	10.24	
Iriga	active	small	breached subcone	10.07	1.06	13.79	1.87	1.26	0.1	0.03	9.58	
Isarog	potentially active	large	breached subcone	30.97	1.93	146.13	1.6	1.55	0.06	0.05	5.19	
Kanlaon	active	large	breached subcone	24.24	2.1	188.79	2.04	1.43	0.09	0.08	10.94	
Malinao	potentially active	large	breached subcone	16.38	1.47	69.49	1.79	1.5	0.09	0.09	12.13	
Mariveles-Limay-Samat	potentially active	large	breached subcone	24.14	1.36	113.24	1.7	2.17	0.06	0.15	9.06	
Ragang	active	large	breached subcone	20.64	1.39	109.66	2.31	2.44	0.07	0.2	11.84	
Natib	potentially active	large	breached massif	28.57	1.21	126.05	2.19	2.84	0.04	0.14	8.32	
Silay	potentially active	large	breached massif	16.27	1.15	55.3	3.16	2.76	0.07	0.22	13.82	

	Status	Size Class	Shape Class	Basal			II		Slope	
				Width km	Height km	Volume km <sup>3</sup>	Avg	ratio	ratio	Mean (flank)
Parangan	potentially active	small	scattered cones	6.85	0.36	2.67	1.67	1.08	0.05	5.03
Simumaan	potentially active	small	scattered cones	8.94	0.58	9.25	2.98	1.43	0.06	7.39

Table 1.2: Morphometric parameters for the active and potentially active volcanoes of the Philippines. Not in the list are the active volcanoes: Buddajo, Taal and Iraya and the potentially active volcanoes: Lapac, Parang, Tukay and Tumatangas. All except Taal are volcanoes too small to be accurately analysed with the SRTM DEM. Given are the calculated basal width, height, volume,  $H/W_B$  and  $W_S/W_B$  ratios, average slopes and average ellipticity and irregularity indices. The lack of data for the ellipticity (ei) and irregularity indices (ii) and edifice truncation ( $W_S/W_B$ ) is because in many volcanoes, there are very few and/or unrepresentative closed elevation contours resulting in values that are not meaningful.

CHAPTER 2

**Volcano-tectonic controls and  
emplacement kinematics of the  
Iriga debris avalanches  
(Philippines)**

---

## 2.1 Abstract

Mt Iriga in southeastern Luzon is known for its spectacular collapse scar possibly created in 1628 AD by a 1.5 km<sup>3</sup> debris avalanche, spread over 70 km<sup>2</sup> and dammed the Barit River to form Lake Buhi. The collapse has been ascribed to a non-volcanic trigger related to a major strike-slip fault under the volcano. Using a combination of fieldwork and remote sensing, we have identified a similar size, older debris avalanche deposit (DAD) to the southwest of the edifice that originated from a sector oblique to the underlying strike-slip fault. Both deposits cover wide areas of low, waterlogged plains, to a distance of about 16 km for the oldest and 12 km for the youngest. Hundreds of m wide, and up to 50 m high hummocks of intact conglomerate, sand, and clay units derived from the base of the volcano show that the initial failure planes cut deep into the substrata. In addition, large proportions of both DAD consist of ring-plain sediments that were incorporated by soft-sediment bulking and extensive bulldozing. An ignimbrite unit incorporated into the younger Buhi DAD forms small (less than 5 m high) discrete hummocks between the larger ones. Both debris avalanches slid over water-saturated soft sediment or ignimbrite, and spread out on a basal shear-zone, accommodated by horst and graben formation and strike-slip faults in the main mass. The observed faults are listric and flatten into a well-developed basal shear zone. This shear zone contains substrate material and has a diffuse contact with the intact substrata. Long, transport-normal ridges in the distal parts are evidence of compression related to deceleration and bulldozing. The collapse orientation and structure on both sectors and DAD constituents are consistent with predictions from analogue models of combined transtensional faulting and gravity spreading. Iriga can serve as a model for other volcanoes, such as Mayon, that stand in sedimentary basins undergoing transtensional strike-slip faulting.

Keywords: Mt Iriga, debris avalanche deposit, volcano-tectonics, transtensional faulting, emplacement kinematics

## 2.2 Introduction

Flank destabilization may occur during the development of a stratovolcano. Such destabilisation may be caused by tectonic activity (Lagmay et al., 2000; Vidal N. and Merle O., 2000), internal growth by magmatic intrusion (Donnadieu and Merle, 1998; Tibaldi, 2001) or weakening by hydrothermal alteration (Reid et al., 2001; van Wyk de Vries and Francis, 1997) and gravitational spreading (Borgia et al., 1992; van Wyk de Vries and Francis, 1997). Failure of destabilized volcano flanks can generate large debris avalanches, triggered

by one or a combination, of earthquakes (Montaldo et al., 1996), magmatic intrusions (Elsworth and Voight, 1996; Voight et al., 1983), and meteoric events (van Wyk de Vries et al., 2000). Evidence and triggering mechanisms of volcanic debris avalanches may be preserved within the debris avalanche deposits (DAD).

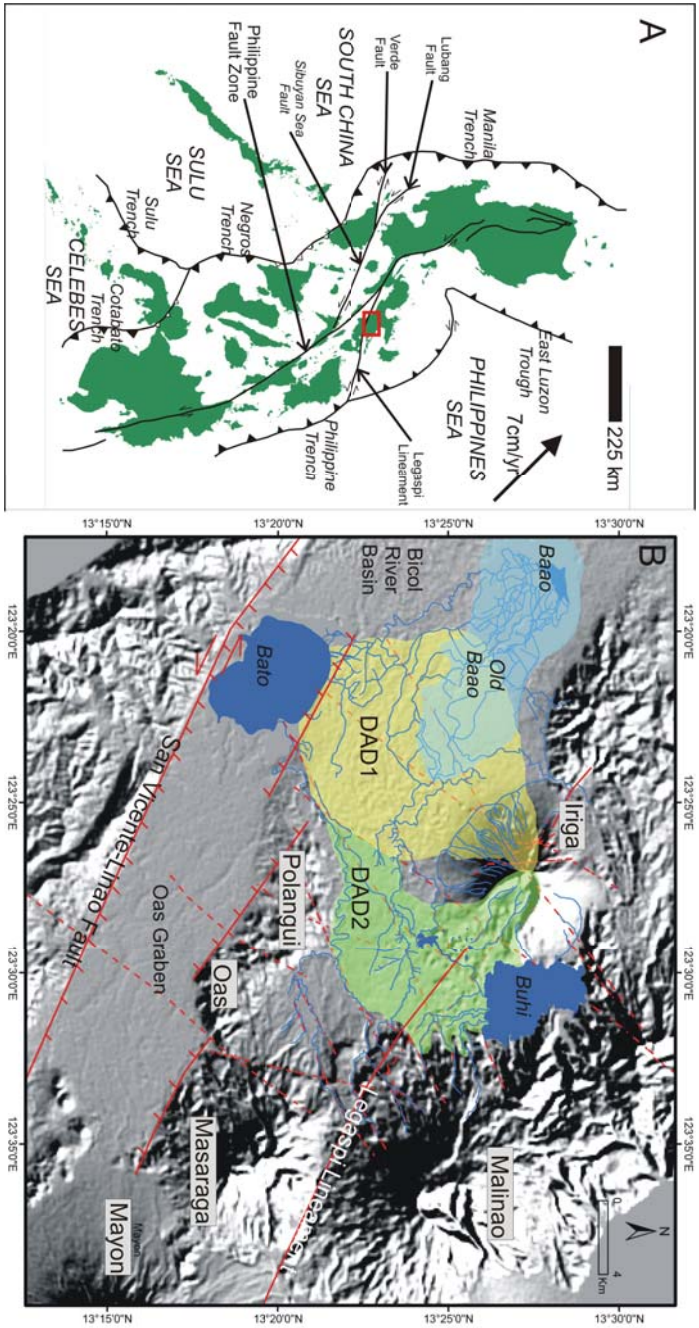
The hazard of landslides, rockslide avalanches, and debris flows on active and even extinct volcanoes can be significant. Examples are the 1998 avalanche and debris flow at Casita, Nicaragua that killed ~2,500 people (Kerle and van Wyk de Vries, 2001, e.g.), mass movements on the Monts Dore volcano in the French Massif Central over the last century (Bernard et al., 2009), and the collapse of Mayu-yama lava dome at the Unzen Volcanic Complex, Japan in 1792 (Siebert, 2002).

We have studied the lithology, structure, and texture of the Mt Iriga DAD in the Philippines and investigate the causes, timing of events, and mode of emplacement. Mt Iriga is a particularly useful case as it was the source of a young, possibly historic DAD (Aguila et al., 1986; Belousov et al., 2011), and it has well-preserved source and depositional areas, as well as extensive local erosion and artificial excavations that expose the deposit structure. Many intact volcanoes are in a similar geological environment to Iriga, for example, Mayon, Concepción, Merapi, and Pacaya, so it provides a widely applicable model.

## 2.3 Regional Setting

Opposing subduction zones control the tectonic environment in the Philippines: oceanic plates on the west subduct eastward and those on the east have westward vergence (Aurelio, 2000). The opposing subduction has generated the Philippine Fault (Fig. 2.1A), demarcated into northern, central, and southern segments (Aurelio, 2000). A number of splays (Fig. 2.1B) propagate from the central segment and cut the Bicol Volcanic Arc, including: the Legaspi Lineament, a northwest-striking left-lateral strike-slip fault that extends over 40 km (Aurelio et al., 1997) from the northern slope of Mt Mayon across Mt Iriga; the San Vicente-Linao Fault that bounds the southern margin of Lake Bato and extends towards the southern slopes of Mt Mayon (Bureau of Mines and Geosciences, 1963; Lagmay et al., 2005; Travaglia and Baes, 1979); and the normal faults on the northernmost margin of Lake Bato that terminate at the western foot of Mt Mayon (Lagmay et al., 2005). The north-western extension of the Legaspi Lineament also crosses the Bicol River Basin. This basin is the catchment area for both water and sediment from several volcanoes in the Bicol Volcanic Arc (Bureau of Mines and Geosciences, 1981).

Figure 2.1: **A** Tectonic map of the Philippines and the location of Mt Iriga (red box). Structures are from [Barrier et al. \(1991\)](#) and [Aurelio \(2000\)](#). Hachured lines are active subduction zones and those with open triangles are active collision fronts. Arrow indicates the direction and velocity of the Philippine Sea Plate. **B** SRTM shaded relief map of Mt Iriga and vicinity showing its two DAD, Mounts Malinao, Masaraga, Polangui-Oas, Mayon, the Oas Graben, the Lakes Buhí, Bato, Baao and older Baao, the Bicol River Basin (BRB). The regional faults are shown (red polylines): northwest-trending Legaspi Lineament, San Vicente-Linao Fault, the normal faults on the northern boundary of Lake Bato, and the northeast-trending structures.



The general stratigraphy around Mt Iriga can be summarised as follows: (1) a basement of Cretaceous to Paleogene accreted oceanic basalts and island arc rocks (Aurelio 2000); (2) Late Miocene to Early Pliocene laminated calcarenite exposed along the northern boundaries of the Oas graben and the southern foot of the Polangui-Oas mountains (Lagmay et al. 2005); (3) the Pliocene to Pleistocene age Polangui Volcanic Complex (Aurelio 2000); (4) the Quaternary volcanoes that form the Polangui, Oas, Malinao and Masaraga mountains, and the landforms on the northern and eastern ends of Lake Buhi (Fig. 2.1B). These volcanoes are composed principally of basaltic to dacitic lavas and pyroclastic deposits; (5) the youngest beds are composed of alluvium in the Bicol River Basin and the Mt Iriga deposits described below.

## 2.4 Mt Iriga

Mt Iriga (locally known as Mt Asog) stands 1,196 m asl in the near-sea-level Bicol River Basin. The towns of Iriga and Buhi are located on its western and eastern slopes, respectively. The volcano is well known for its southeast-elongated avalanche scar generated by a 1.5 km<sup>3</sup> collapse that spread as a rockslide-debris avalanche over an area of 70 km<sup>2</sup> (Aguila et al. 1986). The DAD dammed the Barit River and formed Lake Buhi. The DAD shows no evidence of contemporaneous magmatic activity, suggesting a non-volcanic trigger for the sector collapse event (Aguila et al., 1986). Aguila et al. (1986) suggested the collapse to have happened in 1628 AD but Belousov et al. (2011) gave an age of about 500 AD. We have also found a large, older DAD to the south of Mt Iriga described below. This deposit is very briefly mentioned in Moriya (1994). We call the younger DAD the Buhi DAD2, and the older one is called the Iriga DAD1.

The Pleistocene to Recent olivine-pyroxene-phyric basalt and pyroxene-phyric, pyroxene hornblende-phyric and hornblende-phyric andesite lavas of Mt Iriga are intercalated with pyroclastic and lahar deposits (Panem and Cabel, 1998). Within the Buhi DAD2 collapse scar on Mt Iriga is a more recent scoria-tuff cone and a large lava flow, composed of hornblende-pyroxene-phyric basalt. A small phreatic eruption was reported in the first half of the 17th century. Lahar and epiclastic deposits that merge with sand and clay of the Bicol River Basin dominate the lower slopes of Mt Iriga. Around its eastern base, a thick sequence of silicic pumiceous pyroclastic flow deposits of unknown origin is intercalated with alluvium and Mt Iriga-derived epiclastic deposits (Aguila et al., 1986).

## 2.5 Methods and Terms

The main units within the older and younger DAD were mapped in order to establish a general stratigraphy and determine the relative chronology of volcano edifice development. We also searched for field evidence of regional faults and investigated deformation structures in the DAD. Field mapping of the DAD structures is hampered by vegetation, erosion, and subsequent deposition, and by the fact that the features occur on a large scale. In order to deal with the scale problem, we used for mapping the Shuttle Radar Topography Mission (SRTM) and Advanced Spaceborne Thermal Emission and Reflection Radiometer (ASTER) satellite images, Google Earth, and a terrain model extracted by digital photogrammetry of 1:25,000-scale aerial photographs with a spatial resolution of 10 m. We separated each DAD into proximal, medial, and distal zones for ease of description, although it should be noted that changes in structures and facies are gradational. Charred wood for radiocarbon dating from the eastern pumice-rich ignimbrite was collected. All the information was compiled and interpreted in a geographical information system, ARCGIS<sup>®</sup> Software (available as an electronic supplement).

We use the term “block facies” for the large coherent blocks from the collapsed edifice that vary from several to hundreds of meters in width, as well as their coarsely fractured equivalents. Such usage follows [Glicken \(1996\)](#), [Siebert \(2002\)](#) and the more recent discussion in [Bernard et al. \(2009\)](#). Block facies can be composed of lava, pyroclastic rocks, lahar deposits, conglomerate, sand, and gravel, where the original stratigraphy is preserved and where there is no mixing of lithologies.

The DAD “mixed facies” is a breccia of fine clay to boulders of different origin. It is considered to be the blended parts of the DAD that mantle and surround the block facies ([Glicken, 1996](#)). There are a large proportion of fine components in which the larger blocks are supported, but generally there is a continuous range of clast size so that no matrix and clast populations can be differentiated (e.g [Bernard et al., 2009](#), and references therein). We do not distinguish any “matrix facies” ([Bernard et al., 2009](#); [Glicken, 1996](#)), as all parts of the deposit can be assigned to either the mixed or block facies.

## 2.6 Mt Iriga Morphology

Large areas around the southwest, south and east of Mt Iriga have hummocky morphology related to the two DAD. The older Iriga DAD1 forms the relief to the south and southwest, underlying Iriga City, and the well-known Buhi DAD2 forms the eastern and southeastern morphology (Fig. 2.2A).

The morphology of Mt Iriga differs in different sectors. The northeastern and southwestern slopes of the volcano are smoother than the northwestern and southeastern sectors that contain the source areas for the two DAD. There are prominent northwest- and northeast- trending lineaments, including the Legaspi Lineament (Fig. 2.1B), that have orientations consistent with the regional stress regime.

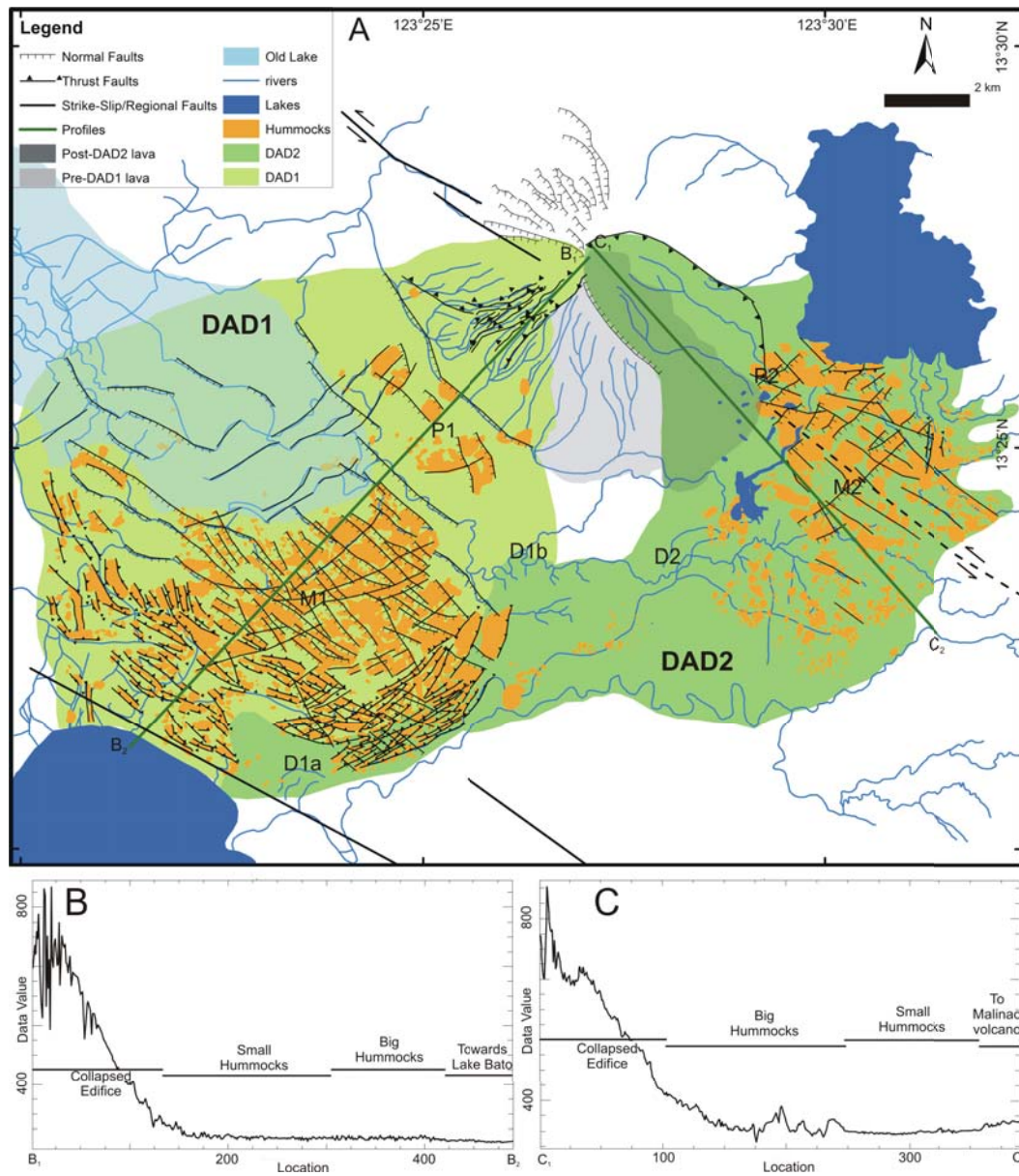
### 2.6.1 Iriga DAD1 Geometry, Structure, and Morphology

The Iriga DAD1 produced an amphitheatre that is now mostly in-filled by subsequent eruptive products (Fig. 2.1B, 2.2A). The fan-shaped DAD1 deposit is 16 km long and 12 km wide, covering an area of 118 km<sup>2</sup>. It has an estimated volume at 2 km<sup>3</sup>, assuming a pre-collapse edifice summit at 1,300 m asl (Fig. 2.3A). The DAD1 has a very hummocky topography (Fig. 2.2A, 2.3B).

The long ridges are mostly oriented normal to the transport direction (Fig. 2.2A). The ridges are formed of contorted, remobilised and bulked substrate sequences that are repeated vertically, suggesting the presence of thrusts or folds. The long ridges represent a “bulldozer” facies (Belousov *et al.*, 1999).

In the medial and proximal areas, exposed hummock cross-sections show mostly normal faults that form horsts and grabens and a few thrust and strike-slip faults. Normal faults have greater displacement and become less steeply dipping from the centre to the edge of the hummock (Fig. 2.4A). Faults cut steeply through the upper to middle part of hummocks that are composed of coarse block facies (Fig. 2.4A-B). These faults broaden downwards into diffuse shear zones in brecciated, unconsolidated, and finer mixed facies in the lower part of the hummocks (Fig. 2.4C). Toward the base of the hummocks, at the level of the surrounding inter-hummock surface, horizontal bands, folds and fluid-like mingling and mixing of layers are observed. Centimetre- to meter-scale clay and ignimbrite blocks are fractured and fragmented into jigsaw crack and jigsaw-fit textures, and dismembered along their long axis. Such blocks have elongate lens-like domains with fracture patterns that indicate horizontal stretching (Fig. 2.4E-G). In river outcrops where the base of the deposit is exposed, there are zones of horizontal lenticular and boudinaged bands that indicate local stretching and shearing along horizontal and inclined planes (Fig. 2.4B-C). Beds in the sedimentary substrate are contorted and incorporated into the lower part of the DAD1 (Fig. 2.4F-G), resulting in fluid-like mingling of lithologies (Fig. 2.5A-C).

The DEM profiles (Fig. 2.2B) show that DAD1 is dominantly distally raised, using the classification of Shea and van Wyk de Vries (2008). The



hummocks in DAD1 do not decrease in plan-view size with distance. In the western half of the DAD1, current elevation is about 5 m lower than in the southeastern side and there are very few hummocks. This area used to be part of Lake Baao, and is frequently flooded, so any DAD1 deposits are covered with sediments. The presence of distal DAD1 in the southwestern area requires that the debris avalanche passed over this area.

### 2.6.2 Iriga DAD1 Lithology and Stratigraphy

The DAD1 sequence (Fig. 2.6) comprises: a substrate that consists mainly of unconsolidated to weakly consolidated clay and sand, and conglomerate and gravel closer to the volcano; the DAD unit; and an overlying 3-10 m-thick unit of basaltic-andesite and silicic tephra that mantles the proximal to medial areas. The DAD1 block facies is found in the proximal hummocks at the foot of the volcano and in the medial hummocks whereas the DAD1 mixed facies predominates in hummock outcrops in the medial and distal areas and in between the proximal hummocks. Sedimentary substrate is found intact in proximal and medial hummocks and fragmented in the long ridge-shaped hummocks that dominate the distal margins.

The block facies consists of brecciated lavas, best exposed in little-deformed torevia-like hummocks near the edifice and in the cores of some

---

Figure 2.2 (*preceding page*): **A** Hummock distribution map, avalanche scarps, structures in Iriga DAD and river systems and lakes around the volcano. These are mapped from field data, the 1988 aerial photographs, SRTM, ASTER-GDEM radar images, Google Earth, and topographic maps. The sites of each stratigraphic column (Fig. 2.6) and bulldozer facies (Fig. 2.5) are located at P1, P2 (proximal), M1, M2 (medial), and D1a, D1b, D2 (distal) for DAD1 and DAD2, respectively. Both DAD are roughly fan-shaped with lobate distal margins. Iriga DAD1 is within the Bicol River Basin, the main catchment of rivers flowing from Iriga, Malinao, and Masaraga volcanoes as well as waters from Lake Buhi. Hummocks are drawn as orange polygons and ridges are delineated as black lines. Ridges in DAD1 are mostly thrust faults (with triangles) in the distal margin and normal faults (ticks) in the proximal and medial zones. DAD2 is dominated by strike-slip and normal faults parallel to the active basement faults in the proximal and medial areas and a few thrust faults occur near the topographic barriers. **B** Height Profile of Iriga DAD1 shows higher hummocks in the distal portion (distally raised). **C** Height Profile of Buhi DAD2 shows higher hummocks in the proximal area (proximally raised). Locations of profiles are plotted as yellow polylines in Figure 2.2A.

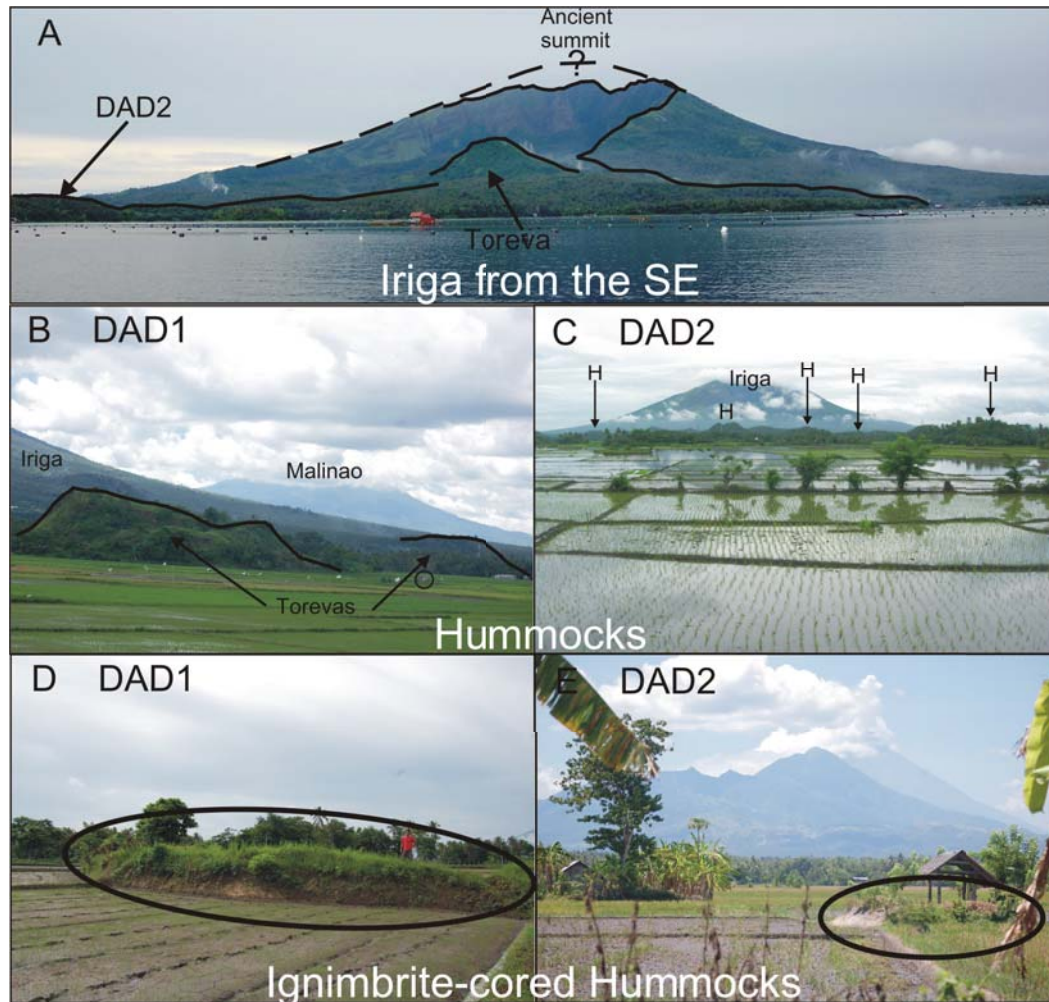


Figure 2.3: **A** View of the southeastern collapse amphitheatre and inferred edifice prior to the first collapse of Mt Iriga. Note the large torea block on DAD2 standing above the debris field. **B** General view of the DAD1 torea blocks from the western plains with a small hut (circled) as scale. **C** View from the southeast looking over the saturated surface of DAD2 with the hummocks (H) in the distance. **D** Photo of ignimbrite-cored small hummock (circled) in the eastern part of DAD1. **E** View, looking southeast on DAD2 including a small ignimbrite-cored (circled) hummock sticking out of paddy field with Masaraga and Mayon in the distance.

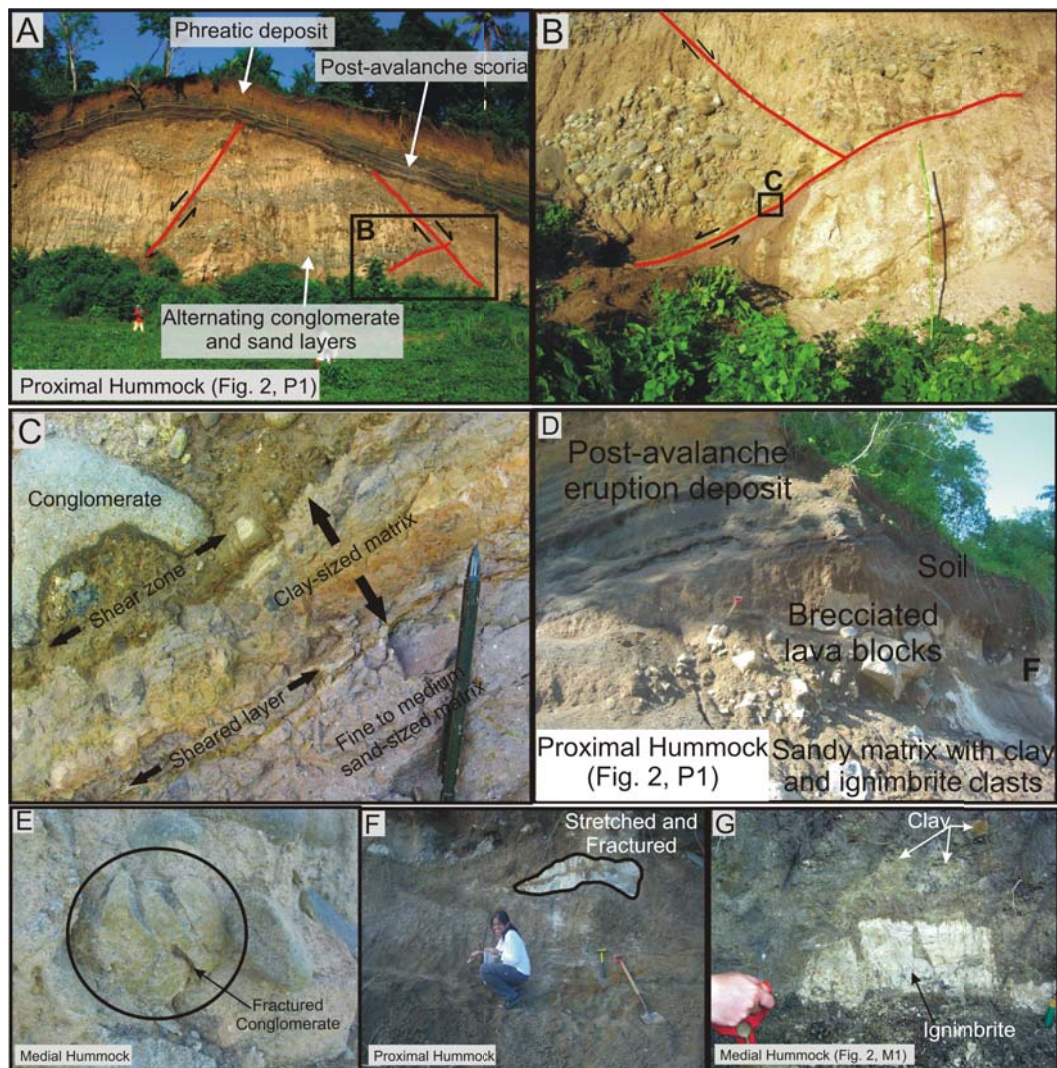
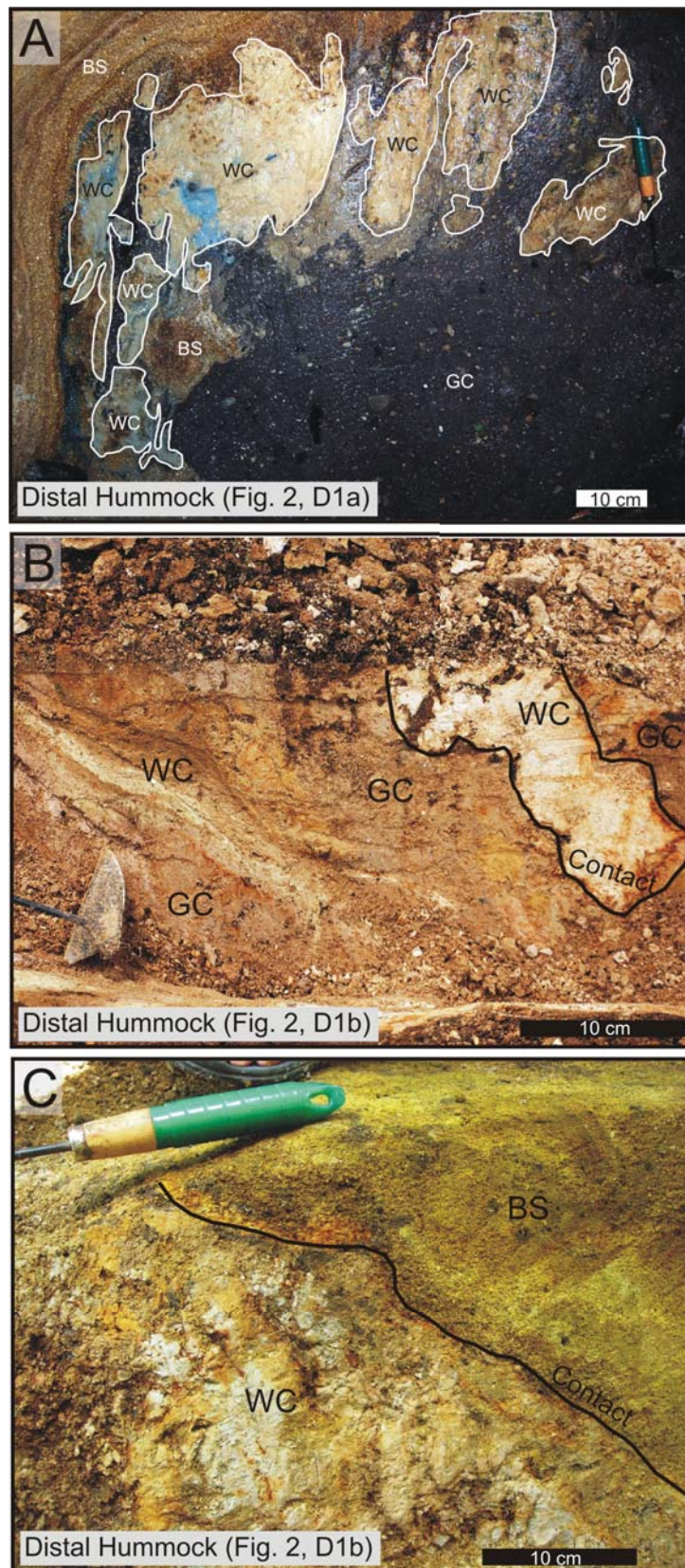


Figure 2.4: DAD1 lithologies and structures. **A** Large proximal hummock of DAD1 that is entirely made of alternating conglomerate and sand layers displaced by normal faults and mantled by post-collapse eruption deposits. **B** Displaced alternating conglomerate and sand layers cut by normal listric that illustrate the extensional dynamics forming the hummocks. **C** Close up of extensional low angle shear zone cutting the lower clay and conglomerate layers. **D** Hummock mantled by alternating scoria deposits and about 0.3 m thick phreatic eruption deposit. A soil layer between the hummock and the alternating scoria signifies that scoria eruptions happened sometime after the avalanche. **E** Fracturing in cobbles near the base of a hummock. **F**, **G** Clasts of stretched and fractured ignimbrite and clay blocks within the DAD.



medial hummocks in the centre of the DAD (Point P1, Fig. 2.2A). Jigsaw cracks and impact marks are observable on some lava blocks. Hummocks of block facies composed of sand and conglomerate are also found in the medial zone (Fig. 2.4A-B), whereas in the distal area, hummocks are composed entirely of mixed facies.

Below and between the proximal hummocks there is mixed facies composed predominantly of a poorly sorted breccia that is probably derived from block and ash flow deposits. In the medial zone, a layer of mixed facies composed of clasts of fractured clay and pumiceous ignimbrite underlies and surrounds the block facies (Fig. 2.4D-G). The distal DAD contains a block facies of rounded cobbles in sand matrix that we interpret as remobilised lahar deposits.

In the distal zone, the DAD base is not sharp and instead, there is an interval in which the mixed facies and sedimentary substrata are mixed and mingled. The distal zone substrata consist of folded white and grey clay beds and sandy layers that are well exposed near the DAD margins in the Niño Jesus and Iriga rivers (Fig. 2.5A-C). The lithologies are unlithified and deformable by hand pressure. The folds are chaotic, disharmonic, and changes in dip suggest fold wavelengths from centimetres to several tens of meters. Measuring the fold orientations was not possible due to the lack of clear bedding planes.

In general, the original pre-avalanche stratigraphic sequence from the volcano is preserved in the DAD. In the eastern portions of the DAD there are small hummocks, up to a few meters high and tens of meters long, composed of remobilised pumice-rich ignimbrite that are also commonly seen in DAD2 (Fig. 2.3D). This ignimbrite is an additional stratigraphic element present only on the eastern side of the volcano, and underlies most of the distal Mt Iriga post-DAD1 sequence.

### 2.6.3 Buhi DAD2 Geometry, Structure, and Morphology

The Buhi DAD2 extends to the southeast and is about 12 km long and 11 km wide. It has a fan-shape with an asymmetric distal margin; a lobe extends

---

Figure 2.5 (*preceding page*): Bulldozer facies at the distal edge of DAD1 with the alternating white- (WC) and grey- (GC) coloured clays and brown sand (BS) of very contorted beds. **A** Shows a sequence of steeply dipping strata at point D1a in Figure 2.2A. **B** Photo of similar steep and contorted strata in a cut between P1 and D1b in Figure 2.2A. **C** Close up of the more regular contact between the disrupted white clay and brown sand layer. Edges of the white clay layer are traced.

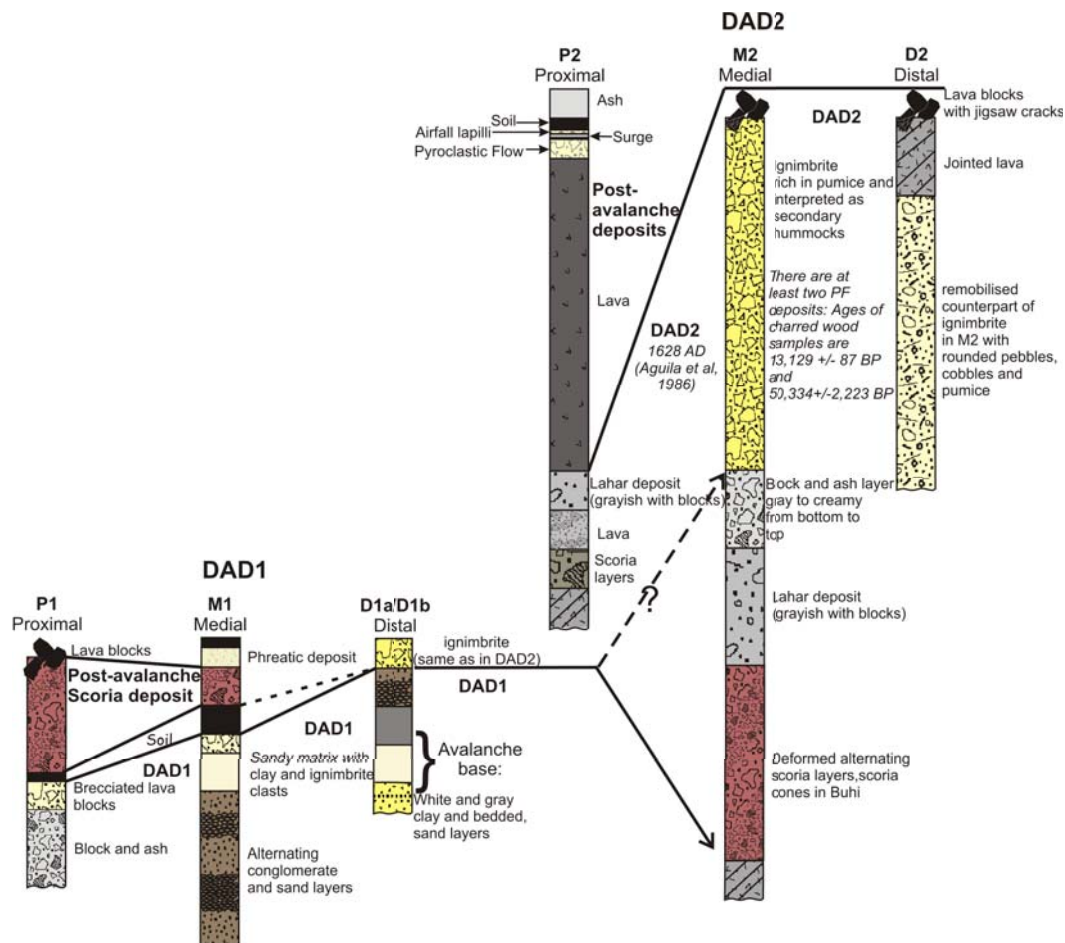


Figure 2.6: Stratigraphic columns and correlations in DAD1 and DAD2 of Mt Iriga with locations plotted in Figure 2.2A.

8 km west of the main body covering an area of about 70 km<sup>2</sup> and leaving a hummock field with small lakes and depressions (Fig. 2.2A). The opposing slope of Malinao volcano has constrained the debris avalanche path (Fig. 2.1B, 2.2A). The source amphitheatre is prominent and fresh. Buhi DAD2 is covered by a thin soil and is not affected by the frequent and widespread floods of the Bicol River Basin because of its higher elevation. Iriga River that drains Lake Buhi has cut a gorge down to the base of the deposit.

The DAD2 hummocks are elongate and mostly oriented parallel to the transport direction. Hummock height and area decrease with distance (Fig. 2.2A, C). Most of them are conical (Fig. 2.3C); some smaller hummocks have flat tops (Fig. 2.3E). One 2.5 km-wide torea block stands at the eastern base of the edifice. The DAD2 topographic profile is dominantly proximally raised, using the classification of Shea and van Wyk de Vries (2008).

Quarry cross sections through hummocks expose partly brecciated units that are cut by normal faults and thrust and strike-slip faults. The faults seen as flower structures are best observed in sequences with lavas and interbedded pyroclastic deposits (Fig. 2.7C-D). In Buhi town, the scoria-dominated hummocks are cut by steep to near-vertical faults that strike N45E and have throws up to several meters, forming horsts and grabens. This strike is that of regional faults, raising the possibility that some post-emplacment regional deformation may have affected the avalanche. However, these faults are restricted to the hummocks, and they are more probably transport-related structures. Their strike could be pre-avalanche topography controlled by regional structures. Such sensitivity to underlying structures is shown in the Socompa DAD (e.g. [Shea and van Wyk de Vries, 2008](#)).

In addition to local deformation along the faults, pervasive internal deformation in the form of boudinage, microfaults and fractures is also present at the edge and in the lower parts of the flatter hummocks (Fig. 2.7B). Local mingling is shown by diapir-like structures at well-exposed contacts in the upper part of hummocks (Fig. 2.8A-B). Mingling is better developed lower down. Intimate mixing of lithologies at their contacts also increases downwards, producing the mixed facies.

In some well-exposed hummock margins, domains of the pumice-rich ignimbrite are elongated with stretched clasts or mingled with brecciated block-and-ash flow or lava facies (Fig. 2.8A). In addition, some outcrops near the DAD margin showed an intimate fluidal texture with mingling of the block-and-ash flow deposit intimately mingled with scoria layers. In some hummocks, lenses of red ash are included within the block-and-ash flow layers. These may be stretched and boudinaged bases or tops of units.

In outcrops of the lower several meters of the DAD, there are horizontal bands of different lithologies, such as clay, sand, gravel, conglomerate, pumice-rich ignimbrite and mixed facies (Fig. 2.9A). In Iriga River (Fig. 2.9B), the DAD2 base has a sharp contact with a conglomerate substrate at one place, but a diffuse fluidal contact elsewhere above a clay-rich substrate. Above the conglomerate substrate, the lowest part of the DAD unit is a foliated zone and overlain by a 10 cm- to 1 m-thick interval of cobbles and rounded clay clasts, followed by another foliated layer, and then a clay-rich interval that merges into the mixed facies of the DAD.

#### 2.6.4 Buhi DAD2 Lithology and Stratigraphy

The Buhi DAD2 sequence (Fig. 2.6) comprises: the volcanic and sedimentary substrata; the DAD2 unit; and post-DAD2 eruption deposits. A post-DAD2 cone and lava cover about 9 km<sup>2</sup> of the amphitheatre (Fig. 2.2A).

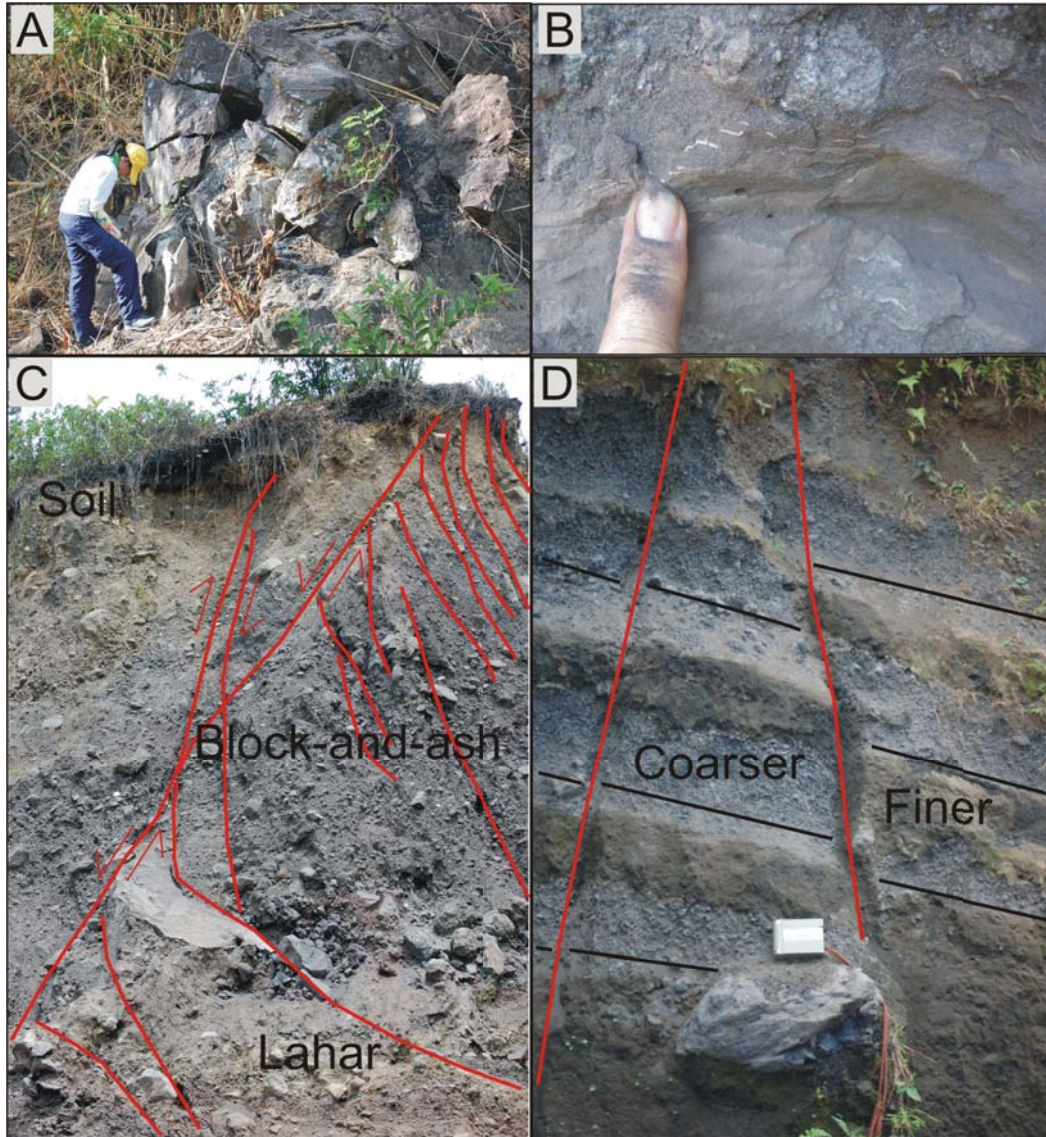


Figure 2.7: Internal deformation within DAD2 hummocks. **A** Large-scale spaced jigsaw cracks in the lava block facies. **B** Small-scale deformation in mixed lahar and block and ash facies. Note the small faults picked out by the white ash layer. **C** Faults in hummocks dissecting the block and ash and lahar layers. **D** Faults displacing layers within scoria cones transported by the avalanche.

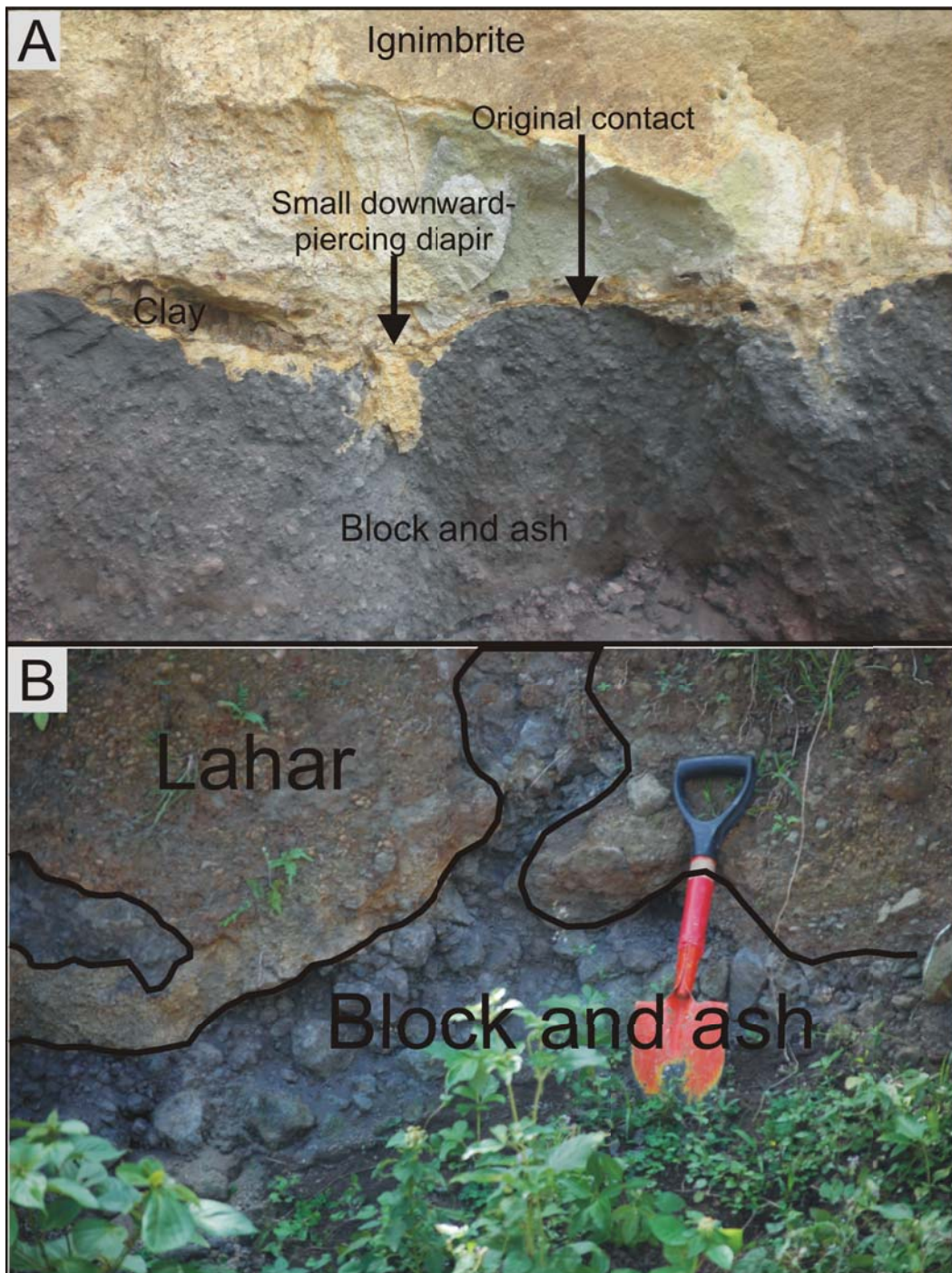


Figure 2.8: Mingling, and limited mixing of units within DAD2. **A** Contact between pumice-rich ignimbrite and block and ash facies, showing small diapirs of the ignimbrite descending into the lower layer, but a general preservation of the contact (small scale deformation in B is within this lower layer). **B** Inter-fingering of the blocky part of the block and ash (lower) layer with the upper laharic layer.

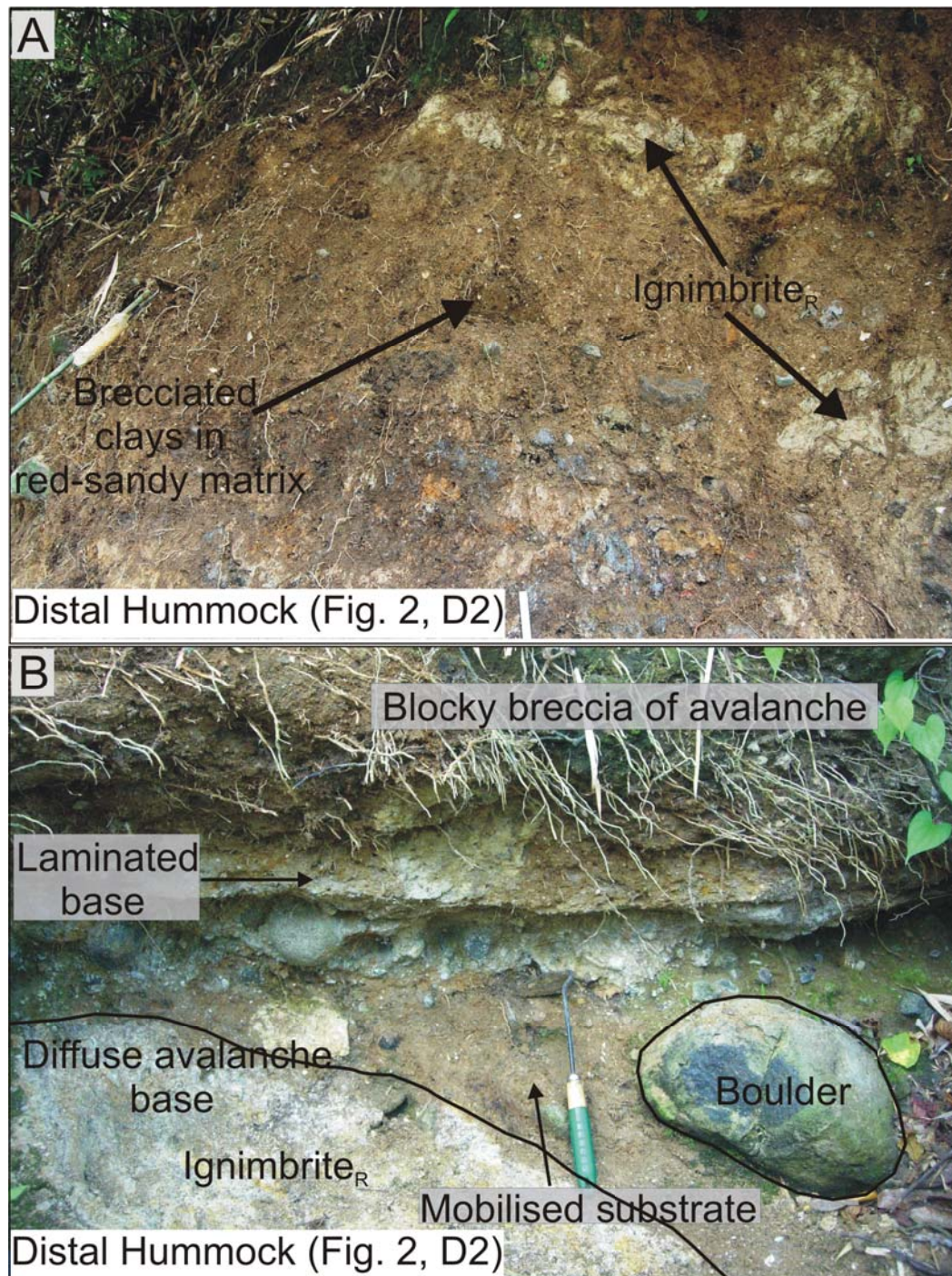


Figure 2.9: **A** The substrate-dominated lower part of DAD2 composed of stretched blocks of remobilised ignimbrite (ignimbrite<sub>R</sub>) seen as clasts with clays, sands and gravel, and no distinct contact. **B** Horizontally-banded base with conglomerates and lahar materials, broken lava, and mixed clay on top of consolidated gravel and pyroclastic flow layers.

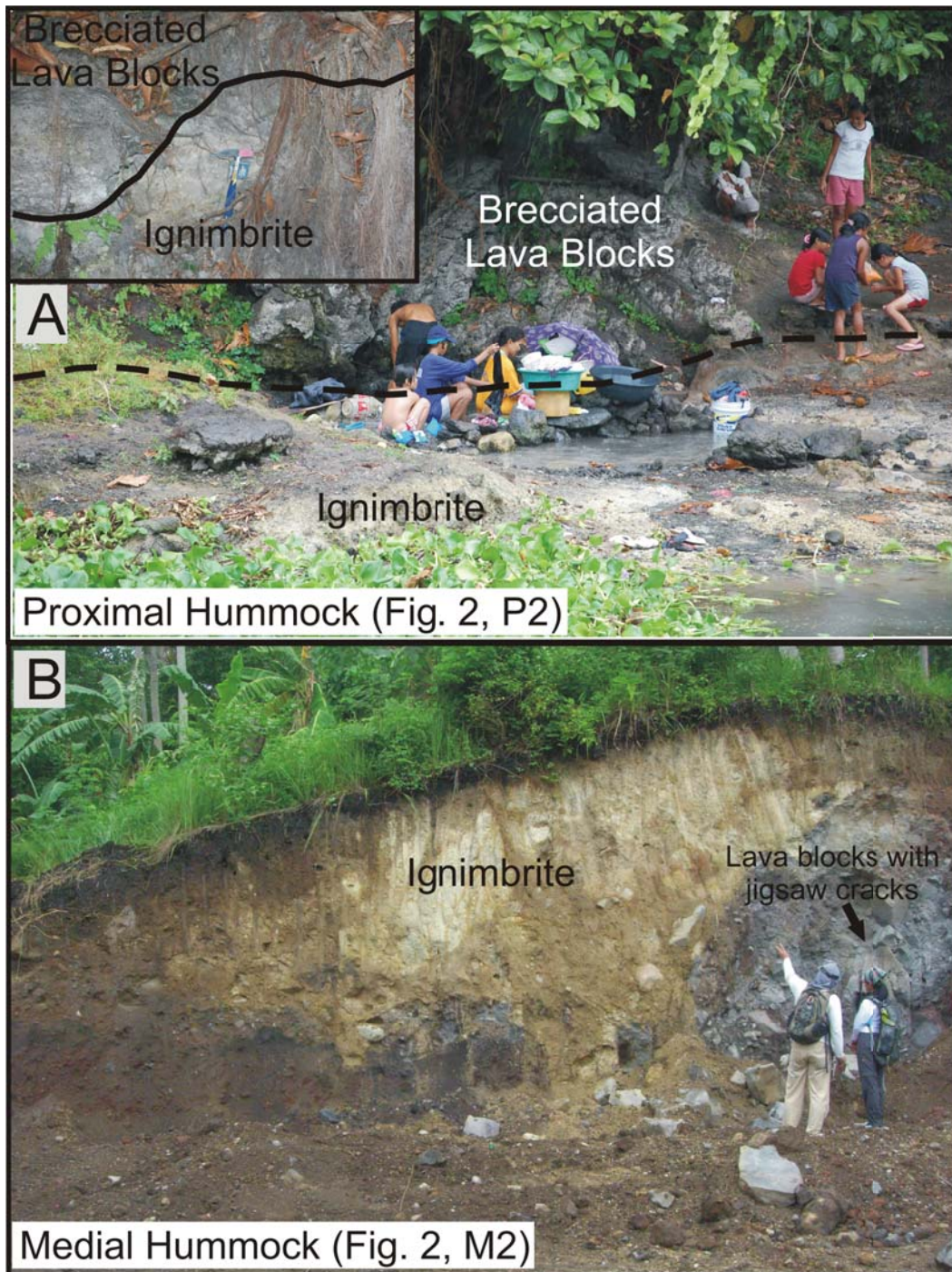


Figure 2.10: Illustration of DAD2 lithologies. **A** The block facies composed of lava blocks overlying (without soil layer) the ignimbrite. Inset shows a detail of hummock dominated by lava breccia and underlying ignimbrite. **B** Lava block inclusions with jigsaw cracks included in the ignimbrite.

DAD2 contains a block facies of brecciated lava (Fig. 2.7A), block-and-ash flow deposits, and pumice-rich ignimbrite. Clear and sharp stratigraphic contacts between units within blocks are preserved in hummock cores. Toward hummock edges, contacts are deformed and the units are mingled in diapir-like features and intimately mixed along contacts (Fig. 2.7A-B, 2.8A-B). The DAD2 mixed facies is composed of fragments of pumice-rich ignimbrite, clasts derived from the block-and-ash flow deposits, alluvial conglomerate, more angular clasts from the abundant lahar deposits, soil, and clay (Fig. 2.9A-B). Conglomerate and components sourced from the abundant substrate sequences are found incorporated into the lower part of the deposit (Fig. 2.9A-B).

In the amphitheatre, there is a large outcrop of pale grey dacitic lava that was originally part of the upper edifice and is probably a toreva block. At the amphitheatre edge, there are other toreva blocks made of alternating massive and clinker-dominated lava units, like those in the upper edifice. In the proximal hummock exposures, there are similar lava units with interbedded scoria. Some hummocks in the proximal and medial areas include block-and-ash flow deposits and reverse graded units of rounded clasts interbedded with cross-bedded sand, which we interpret as a lahar unit (Fig. 2.7C). This unit can be up to 15 m thick. In some hummocks, the block-and-ash flow deposits are directly overlain by about 3 m of pumice-rich ignimbrite (Fig. 2.8A).

The thick ignimbrite layer found in and under the DAD comprises at least two units: a greyish unit with a minimum radiocarbon age of  $50,000 \pm 2,200$  BP, and a cream-coloured unit with an uncalibrated radiocarbon age of  $13,000 \pm 87$  BP. The younger unit contains stretched soil and clay blocks, and blocks of older ignimbrite that were incorporated during the younger unit's emplacement.

In the proximal and medial area hummocks, the ignimbrite layer occurs beneath the lava and scoria block facies (Fig. 2.10A). In some exposure of the block facies, lava clasts are in contact with clasts of the younger ignimbrite and there is no mingling of the units (Fig. 2.10B). In the medial to distal areas, this ignimbrite layer is commonly exposed in the areas between the hummocks. Its surface comprises low, rounded hummocks (a few meters high and tens of meters long) locally capped by isolated lava blocks (Fig. 2.3E). We interpret these as a late-formed, secondary hummocks formed in the stretched zones between the main hummocks, where isolated blocks of intact stratigraphy are preserved.

In the distal areas the DAD2 stratigraphy has: an upper unit containing angular to rounded pebble to cobble-sized clasts of similar texture and lithology to the block and ash deposits as well as pumice in an ashy matrix (Fig. 2.9B). Underneath this unit, the DAD contains a lava-derived breccia

with jigsaw cracks and impact marks. The lower part of the DAD is made of a mixed facies predominantly composed of the pumice-rich ignimbrite and incorporated sedimentary substrata.

In the distal zone, the substratum is composed of clay, sand, gravel, and the pumice-rich ignimbrite. Nearer to the volcano, the substrate sediments are coarser and lahar units formed of cobbles, boulders and gravel are common, and interbedded with the ignimbrite.

## 2.7 Discussion

### 2.7.1 Comparison of the Iriga DAD1 and Buhi DAD2

The newly recognised southwestern Iriga DAD1 spread freely, with no topographic barrier. In contrast, the southeastern, younger DAD2 was partially confined and deflected. Clay-rich sediment, conglomerate, and sand were involved in the DAD1 initial failure mass, indicating that the failure plane cut below the volcanic edifice. This is similar to the emplacement scenario at Mombacho (Shea and van Wyk de Vries, 2008; van Wyk de Vries and Francis, 1997), and Socompa (van Wyk de Vries et al., 2001). DAD1 ran over a plain underlain by water-saturated fine alluvial and lacustrine sediments, a situation that led to bulking and significant bulldozing. DAD2 contains a large proportion of ignimbrite that was probably part of the original failure; it was also bulked by incorporation of ignimbrite and clay-rich sediment in more distal areas.

The two DAD are similar in terms of several characteristics. Both display normal faults consistent with a horst-graben model proposed for the formation of hummocks (e.g. Glicken, 1996; Shea and van Wyk de Vries, 2008). Both have thrust faults in distal locations. Blocks in the block facies in both DAD exhibit impact marks and brecciation. Shear zones are concentrated at the bases of both DAD, and less deformed layers above exhibit normal and strike-slip faults. The lower layer in each DAD has been subjected to strong simple shear at the base; basal contacts are ductile shear zones marked by foliations and folds. Pure shear affected the DAD body, which was a dominantly brittle mass and deformed by faults. Neither DAD has any evidence of particle rotation or rollover even in distal, sediment-dominated areas, consistent with the idea that the mass slid rather than rolled or flowed.

Large amounts of substrata below the volcanic edifice were included in the initial collapse volume and significant clay-rich sediment was incorporated during emplacement. Substrate was mobilised and entrained into the debris avalanches en masse, as shown by the diffuse basal zones, and the domains

of substrata preserved in the deposit. DAD1 and DAD2 do not display any evidence of magmatic activity related to collapse. The collapse directions of both DAD are also consistent with a fault-related cause (e.g. [Lagmay et al., 2000](#); [Wooller et al., 2009](#)). Both DAD preserve the general stratigraphic sequence of the initial failure mass. A pre-avalanche sequence of sedimentary and volcanic units including the block-and-ash flow deposits and lavas, are preserved within DAD1, the pumice-rich ignimbrite occurs in the eastern distal margin. The DAD2 stratigraphy of alternating sequences of basaltic and andesitic units is also preserved. Preservation of the initial stratigraphy is possible only if the transport involved a non-turbulent, translational mechanism without large-scale mixing.

The two DAD differ in some respects. DAD1 hummocks are mainly oriented tangential to the edifice boundary, whereas DAD2 hummocks are elongate and their long axes are roughly parallel to the transport direction. Jigsaw crack textures are common in blocks in the block facies of DAD1, but they are very common in the lava blocks in DAD2. DAD1 had a deep failure plane that cut into the volcanic substrate leading to an initial basal layer with lava, conglomerates, and clays, whereas DAD2 had a shallower failure plane restricted to the volcano, and partly slid on a pumice-rich ignimbrite layer. DAD1 is distally raised, having horsts and grabens in the medial zone and thrusts and folds in the distal zone. DAD2 is proximally raised, horsts and grabens occur in the medial and the distal zones and thrusts and folds are limited to areas adjacent to topographic barriers.

### 2.7.2 Collapse Mechanism

A significant proportion of sedimentary substrate was incorporated intact as hummocks in Iriga DAD1 (Fig. 2.4A-C). As indicated above, this indicates that the collapse failure cut into the volcano substrata. The substrata-derived components incorporated in the DAD, and the sediments known to exist in the Bicol River Basin, are all unconsolidated soft sediments. Consequently, volcano gravitational spreading is likely to have occurred at Mt Iriga (e.g. [Andrade and van Wyk de Vries, 2010](#); [Borgia et al., 2000](#); [Shea et al., 2008](#); [van Wyk de Vries and Borgia, 1996](#); [van Wyk de Vries and Francis, 1997](#)) and the spreading may have developed instability leading to collapse. The general pre-volcanic land surface and the substrata both dip gently to the south into the Bicol River Basin and this slope may have influenced the southerly direction of the DAD1 collapse ([Wooller et al., 2004](#)).

In addition, regional faults may be important, as Mt Iriga is cut by an active strike-slip fault related to the formation of the Bicol Basin ([Aurelio et al., 1997](#); [Lagmay et al., 2000](#)) (Fig. 2.1B). Movement along this basement

fault may have led to collapse on both sides of the volcano as shown by the analogue models (Fig. 2.11C-E) of Mathieu and van Wyk de Vries (2011), Lagmay et al. (2000) and (Wooller et al., 2009). The asymmetry and north-westly elongation of the volcano edifice, and the orientation of lineaments on the summit and flanks are also consistent with observations of analogous volcanoes (Fig. 2.11C-E) undergoing strike-slip deformation (Lagmay et al., 2000; Mathieu and van Wyk de Vries, 2011; Wooller et al., 2009).

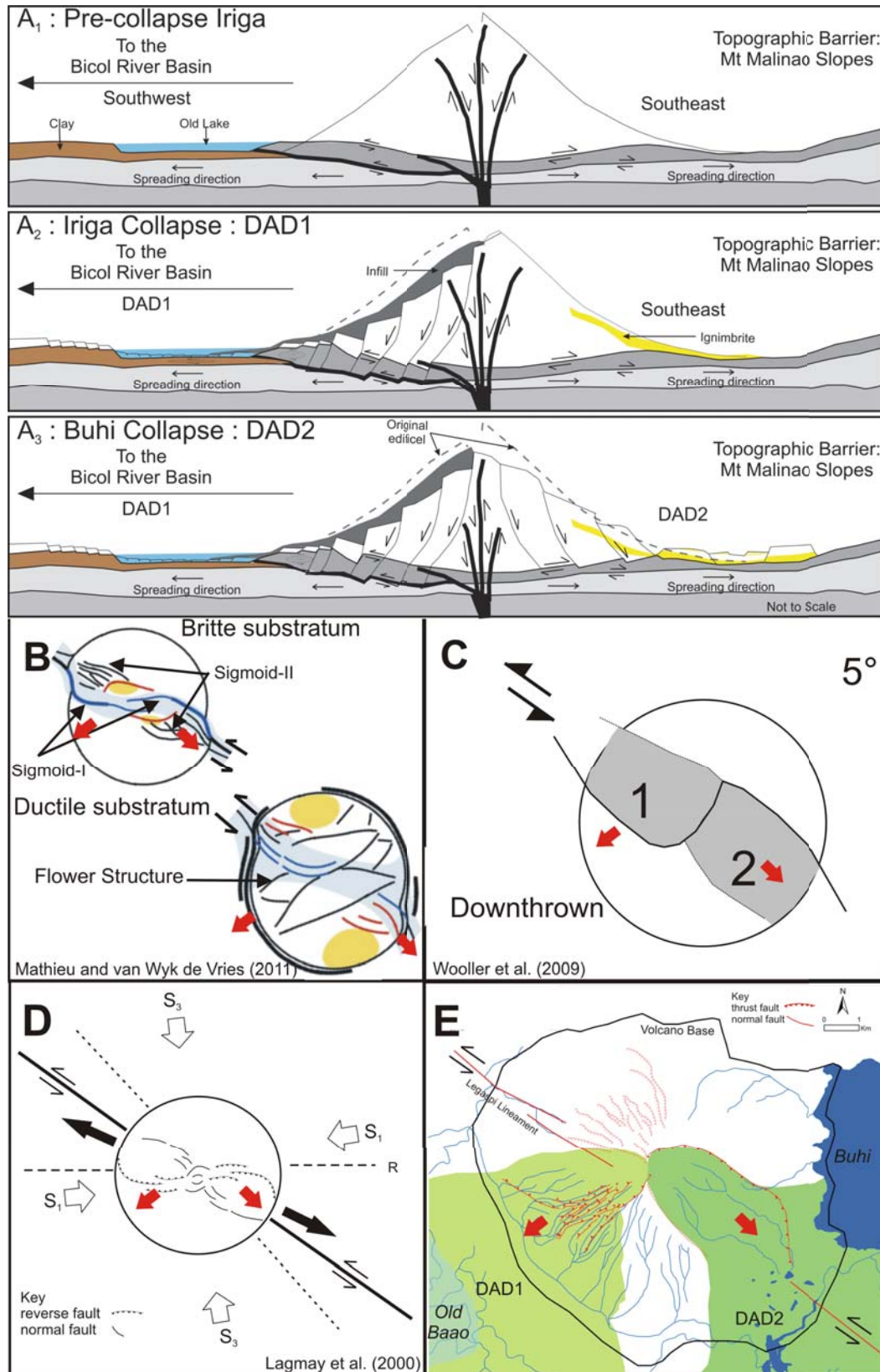
Most probably, the two collapses are related to progressive deformation of the edifice by the underlying fault and gravity spreading of Mt Iriga into the Bicol River Basin. Comparison of Mt Iriga structures (Fig. 2.11B) with the predictive models of fault-driven edifice collapse (Wooller et al., 2009) (Fig. 2.11C-E) suggests that a vertical left-lateral strike-slip fault, with a probable  $5^\circ$  to  $10^\circ$  of obliquity located very near the centre of the cone could have caused the instability of the Mt Iriga edifice.

### 2.7.3 Mode of Transport

Both DAD exhibit strongly developed basal shear zones, horst and graben structures, frontal thrusts and folds that suggest a translational slide transport mode in which simple shear was concentrated at the base. In this mode, the bulk of the rock mass travels as an extending and thinning wedge above the low resistance basal layer. The hummocks are evidence of the thinning by horst and graben formation. The low abundance of jigsaw cracked blocks in both DAD is an evidence of an overall extensional regime, in which few collisions occurred as blocks moved apart.

Lahar units, fluvial conglomerate, and sand and clay units normally located at the volcano foot dominate the DAD distal areas. Deposits of the original upper parts of the edifice are restricted to the proximal areas and make up the toreva blocks. This pattern is also observed in the Socompa DAD (Wadge et al., 1995), and it indicates momentum transfer from the rear to the front of the debris avalanche (Andrade and van Wyk de Vries, 2010; van Wyk de Vries et al., 2001).

A reconstruction of Mt Iriga with both sector collapses in place is presented in Figure 2.11A. Extensional dynamics during the transport of DAD1 is inferred from the predominance of normal fault-bound hummocks in the proximal and medial zone. The long dimensions of the hummocks are generally aligned normal to the transport direction, suggesting extension mainly in the transport direction. The elongate thrust-cored lateral ridges at the margins indicate compression at the edge of the spreading mass. Extension in the medial zone is shown at outcrop scale by stretched clasts of clay, ash, and lapilli within the hummock block facies and in the mixed facies (Fig. 2.4F-G).



The western side of DAD1 is lower in elevation and a lake probably existed there (Fig. 2.1B, 2.2A). In this area of few and small hummocks, there was either no DAD deposition, or it has subsequently been eroded, or it has been covered by younger sediments (Fig. 2.11A). On the eastern side of DAD1, the deposit is continuous and there is a predominance of compressive structures and incorporated sediments. Thus, DAD1 event was dominated by extension in the main body of the mass and compression at the margins where bulking occurred.

DAD2 also shows mainly extension in the proximal and medial zones, and the hummocks lack a dominant orientation, indicating spreading in all directions. Compressional structures in the distal zone indicate confinement and deflection by topographic barriers.

### 2.7.4 Substrate Incorporation

DAD1 includes substantial amounts of substrata either originating from the initial slide and found in the large hummocks composed of sedimentary units

---

Figure 2.11 (*preceding page*): **A** Reconstructed cross-section of Mt Iriga and mechanism of DAD formation. A1 Pre-collapse Mt Iriga with the strike-slip flower structure, and ductile substrata being extruded. A2 The first collapse resulted in Iriga DAD1. The scar was then infilled by lava, lahar, tephra, and scoria deposits (gray strip on the SW flank). On the SE flank is a deposit of the pumice-rich ignimbrite (yellow strip). A3 Shallower collapse structures on the SE flank of Mt Iriga accommodated the sliding of this part of the edifice, DA2. The yellow polygon on the southeast side is the ignimbrite unit that served as the basal layer for DAD2. **B** Morphology and strike of structures in sinistral strike-slip experiments by Mathieu and van Wyk de Vries (2011) showing the locations of the Sigmoid-I faults that curve at the summit of the cone and Sigmoid-II in the upper cone. Figure at the lower left is with the addition of a ductile layer with flower structures in the northern and southern flanks of the cone. **C** Summary sketch of transtensional deformation in analogue models with 5° of obliquity from Wooller et al. (2009) with predicted collapse order that is matched by Mt Iriga. **D** Structures at Mt Iriga from the predictive model for cones overlying left-lateral strike-slip faults of Lagmay et al. (2000). **E** The structural pattern on the flank and synthetic faults generated at acute angles to the main strike-slip shear of Mt Iriga are similar to those outlined in (B), (C) and (D) suggesting that a strike-slip with slight dip movement may have led to its instability, and subsequent collapse. The red arrows indicate direction of Mt Iriga collapses.

(Fig 2.4A-C), or incorporated into the base of the DAD by rip-off or bulldozing mechanisms. Evidence of this bulking is well exposed at the base of the distal elongate hummocks (Fig. 2.5A-C). The sequence of alternating conglomerate and sand layers, and the upper units of lava blocks and block-and-ash flow layers formed an initial abrasive basal layer that eroded proximal substrata, and bulldozed the substrate sediments, incorporating them into the avalanche. The strong deformation of clay-rich substrate layers suggests that this substrate was susceptible to liquefaction (Fig 2.5, 2.9). After liquefaction, substrata would be incorporated by development of shear planes below the original base. The DAD1 had a low resistance basal slide plane (Figs. 2.4, 2.5). In contrast, ignimbrite and scoria layers served as the proximal basal layer of the DAD2 avalanche, allowing a low-friction initial slide (Fig. 2.10). It subsequently moved over and partly incorporated an ignimbrite-dominated substrate.

We note that at the Mombacho El Crater slide, the mass ran over a non-saturated sedimentary substrate with limited erosion and bulking (Shea and van Wyk de Vries, 2008). The other Mombacho DAD (Las Isletas) ran over an ignimbrite like the Buhi DAD2 that it incorporated and which behaved as a low-resistance layer (Shea and van Wyk de Vries, 2008). As Las Isletas was emplaced into a lake, here the substrata, like at Iriga, was probably saturated. This may indicate that saturation is an important condition for bulking sediment during debris avalanche emplacement.

### 2.7.5 Mobility

The DAD1 probably had a greater initial volume and therefore a higher failure mass potential energy. Considering a collapse height of 1,200 m, the apparent friction,  $H/L$ , is 0.07 for DAD1 and 0.10 for DAD2. If Mt Iriga had a higher pre-collapse summit of 1,300 m (Fig. 2.3A), this ratio will be about 0.08 for DAD1, which still suggests it was a more mobile avalanche than DAD2. The dimensionless ratio of the area to the volume,  $A/V^{2/3}$ , for both DAD is within the typical values for volcanic and non-volcanic avalanches, at approximately 68 and 53, respectively (Dade and Huppert, 1998). A more saturated substrate may have resulted in the Iriga DAD1 having a broader and wider runout.

## 2.8 Conclusions

Iriga DAD1 is an older DAD of similar size to the known Buhi DAD2, and occurs to the southwest of Mt Iriga. It originated from a sector oblique to the strike-slip fault that passes through the volcano. Both debris avalanches

spread out over wide areas of low plains to a distance of about 16 km for DAD1 and 12 km for DAD2. Normal faults that form horsts and grabens within the hummocks demonstrate extension during spreading. Both DAD exhibit evidence that suggest non-turbulent translational sliding. Hummocks composed of only sedimentary facies (sand and conglomerate) in the proximal to medial areas of DAD1 show that the initial failure included the edifice base and that the failure plane cut deep into the substrata.

In addition, a large proportion of DAD1 consists of unconsolidated sediments incorporated by bulking and extensive bulldozing. The low depositional slopes of DAD1, as well as bulking-related bulldozing, led to the predominance of compressional structures at the distal margins. The thick ignimbrite deposit below and within DAD2 provided a basal, low-friction layer for this debris avalanche. The steeper depositional slope of DAD2 resulted in longitudinal spreading and thinning, whereas DAD1 ran over a flat plain and spread widely.

The collapses of Mt Iriga possibly resulted from destabilisation by combined strike-slip faults and gravity spreading and suggest that such collapses can cut deep into the substrata, generating large volumes and long runouts. The orientation and structure of both the younger and older failure scars are consistent with those generated in analogue models involving a vertical-strike slip fault with about  $5^\circ$  obliquity.

Knowledge of the link between basement structures and debris avalanches will help in understanding edifice instability and may be used to target priority areas for volcanic sector hazard mapping. Nearby, Mayon volcano could potentially suffer the same fate as Mt Iriga, with debris avalanches generated to the west and southeast. Like at Mt Iriga, such failures would occur on sliding sectors cutting the edifice, the substrata, and the volcano foot, and such structures would potentially develop slowly before any collapse. A critical element to consider in predicting runouts and areas covered is the nature of the substrate and its degree of saturation. The role played by substrate wetness also suggests that runouts could differ between wetter and dryer periods of the year.



CHAPTER 3

**Hummocks: how they form and  
how they evolve in rockslide  
debris avalanches**

---

### 3.1 Abstract

Hummocks are characteristic topographic features of fast or sluggishly emplaced landslides and rockslide-debris avalanches. Such features are particularly common on volcanic rockslide-debris avalanches. We use scaled analogue models to study the formation of hummocks and explore their importance for understanding landslide kinematics and dynamics. The models are designed specifically to replicate large-scale volcanic collapse, but are relevant to many non-volcanic settings. We characterise hummocks in terms of their spatial distribution and internal structure and determine their evolution from slide initiation to the final arrest. Hummocks initially form by extensional faulting as a landslide begins to move. As motion continues, individual large blocks develop and move apart creating an initial hummock distribution. Hummock size is a function of position in the initial mass, modified by subsequent hummock deformation and break up. The initial distribution consists of small hummocks at the front and larger ones at the back. After the initial stages of break up, as the mass spreads, individual hummocks tend to get wider, but may decrease in height. During spreading, hummocks can continue to break up or can merge and form bigger hummocks. The internal structure of a typical hummock is that of normal faults that flatten into low angle detachments at the hummock base, where they merge with a basal shear zone. When landslides become compressive by confinement or on meeting gentler slopes, hummocks may bunch together. Also, thrusting in such conditions creates a new generation of long anticlinal hummocks. In the areas of landslide internal transverse movement, elongate hummocks will develop between strike-slip flower structures. All these model structures are consistent with field observations and suggest a general brittle-slide emplacement for most landslide avalanches. Where hummocks do not form, and where there is absence of any fault-like feature in the avalanche deposit, a more fluidal flow type of emplacement is possible. Hummocks can be used as kinematic indicators, and can indicate how a landslide has evolved from its initial failure. They can also be used for reconstructing initial failures and provide a framework with which to study emplacement dynamics.

Keywords: Hummocks, Avalanche, Large Landslides, Analogue Modelling, Horst and Graben Structures

### 3.2 Introduction

Hummocks are morphological features seen as mounds and ridges that characterize large landslides and debris avalanches. Hummocks are seen on most

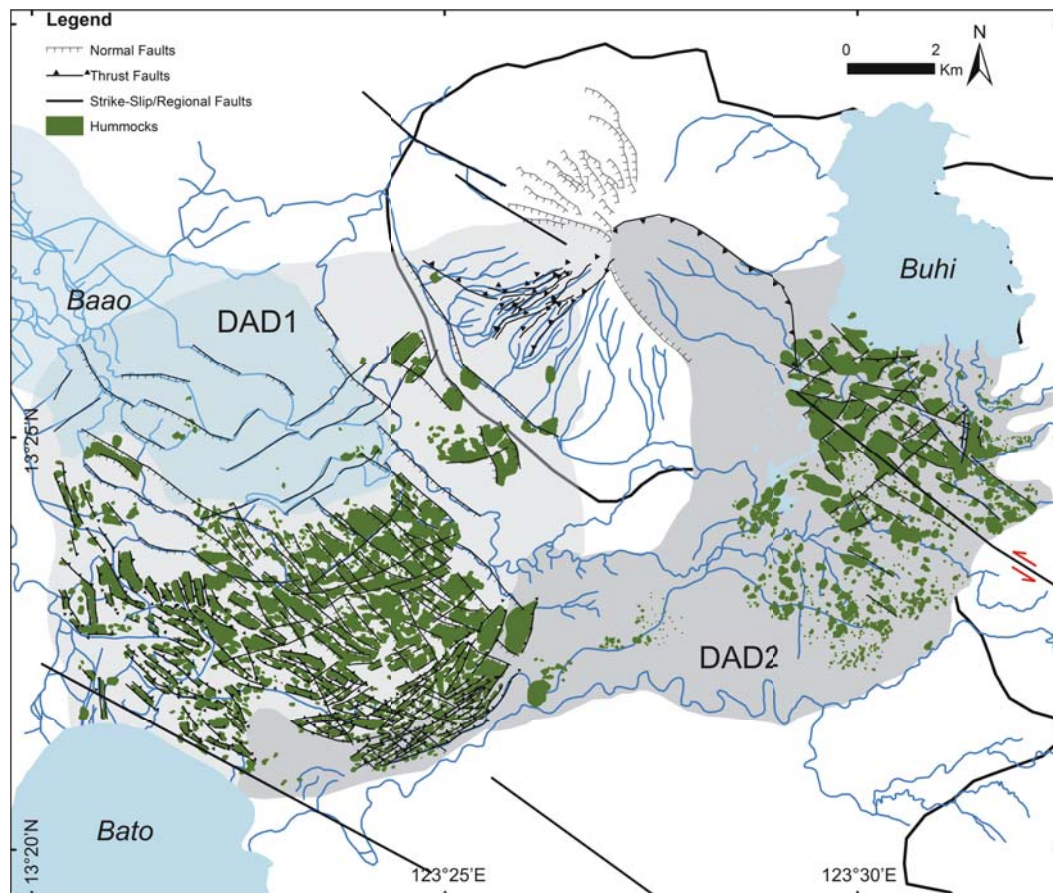


Figure 3.1: Iriga Volcano and her two DADs ((Paguican et al., 2011) showing the regional faults, water bodies: Lakes Baao, Buhi and Bato, hummocks, DAD structures-faults and ridges.

sub-aerial and submarine mass movements on the Earth and also on other planets. They are especially common on volcanic mass movements, for example, the Iriga debris avalanches (Fig. 3.1). The hummock family includes torevas, which are large tilted and rotated blocks left within or at the foot of the failure scar. Torevas can reach up to several kilometers in size and can disaggregate on their downhill sides into smaller hummocks (Francis et al., 1985; Lucchitta, 1979; Wadge et al., 1995). Often steep-sided in the downslope direction, the proximal sides of torevas are often filled in by post collapse material (Glicken, 1991). Downslope of the torevas are smaller hummocks. These can have radial or transverse orientation with respect to the landslide transport direction. This arrangement has been explained to be due to basal shear resistance when hummocks are either slowed and sculpted by adjacent faster moving material parallel to the flow direction (Glicken, 1986, 1991),

stretched during transport (Dufresne, 2009), and compressed by deceleration when an avalanche encounters topographic irregularities (Eppler et al., 1987) or water bodies (Siebert et al., 1995). Their shape has also been attributed to structures formed as the mass spreads (Shea and van Wyk de Vries, 2008), suggesting a link between hummock shape and the spreading kinematics.

Hummocks can thus, form from horst and graben structures during lateral spreading of an avalanche (Voight et al., 1981, 1983), or by the separation of individual avalanche blocks rafted in finer grained material (Crandell, 1861; Glicken, 1986, 1996). Their height and number density often decrease away from source (Crandell, 1861; Glicken, 1986, 1996; Siebert, 1984; Ui, 1983), as fact that has been often explained by progressive disaggregation of debris avalanche blocks (Takarada et al., 1999; Ui and Glicken, 1986).

Prominent elongated, sub-parallel alignments hummock trains can be remnants of longitudinal ridges (Dufresne and Davies, 2009). The longitudinal ridges are probably remnants of hummocks dissected by transport parallel strike-slip faults related to lateral velocity changes (Andrade and van Wyk de Vries, 2010; Shea and van Wyk de Vries, 2008).

Using analogue models, we study the evolution and spatial distribution of hummocks in large-scale volcanic landslides. Internal and surface structures and morphology of the mass movements are characterized with the aim to understand the formation and geometry of hummocks and to explore their use as an indicator of landslide kinematics and dynamics.

## 3.3 Methodology

### 3.3.1 Analogue Models

Most avalanche analogue or numerical model studies have focused on understanding the transport and emplacement mechanisms of landslides (Campbell, 1989; Campbell et al., 1995; Kelfoun and Druitt, 2005; Pouliquen and Renaut, 1996; Staron et al., 2001) and verifying models of granular flow assumed to operate in such events (Denlinger and Iverson, 2001; Iverson and Denlinger, 2001). Recent analogue models by Shea and van Wyk de Vries (2008) and Andrade and van Wyk de Vries (2010) explored the kinematics of rockslides by describing deposit structure and morphology of the upper brittle layer from the early stages of collapse towards the final phase of material runout. These models use either a polished surface to simulate a low basal friction contact, or a ductile basal layer to simulate basal ductile deformation. The main mass of the landslide is modeled by a granular sand and plaster mix.

In our models, we assume, like Andrade and van Wyk de Vries (2010),

Definition	Unit	Value	Nature (N)	Model (M)	Ratio (M/N)
Edifice height	$h$	m	1300	0.11	$8.5 \times 10^{-5}$
Edifice radius	$R$	m	4000	0.15	$3.8 \times 10^{-5}$
Edifice cohesion	$C$	Pa	$10^4$	250	$0.025 \times 10^{-5}$
Edifice density	$\rho$	$\text{kg m}^{-3}$	2200	1500	0.7
Basal layer angle	$\alpha$	rad	p	p/6	0.17
Basal layer length	$D$	m	8000	0.18	$2.3 \times 10^{-5}$
Basal layer vertex distance	$d$	m	?	0	–
Basal layer thickness	$T$	m	200	0.01	$5 \times 10^{-5}$
Basal layer viscosity	$\mu$	Pa s	$10^7$	20000	0.002
Basal layer density	$\gamma$	$\text{kg m}^{-3}$	1400	1000	0.7
Failure and deposition slope	$\beta$	°	0°-45°	0°, 3°, 5°	0°-0.1°
Velocity	$V$	$\text{m s}^{-1}$	100	$10^{-6}$	10–7
Time	$t$	t	60	> 3600	> 60
Gravity acceleration	$g$	$\text{m s}^{-2}$	9.8	9.8	1

Table 3.1: List of scaling variables

a basal ductile layer and a frictional deformation regime of the main body. In the model, there are basically two deformational regimes: simple shear is concentrated in the ductile base and the brittle body stretches or contracts in predominantly pure shear. The analogue models record the continuous movement of a low-viscosity basal silicone layer spreading over an unconfined transport zone. In some models, a lubricating oil layer that simulates a very low viscosity basal slide plane underlies the basal viscous silicone layer. These models provide a hybrid between the smooth slide models and the viscous basal models.

### 3.3.2 Model Set-Up and Parameters

We use as a standard model a volcanic cone made of sand and plaster, silicone and oil (Fig. 3.2) as used, and scaled, for example by [Andrade and van Wyk de Vries \(2010\)](#); [Delcamp et al. \(2008\)](#); [Mathieu and van Wyk de Vries \(2011\)](#).

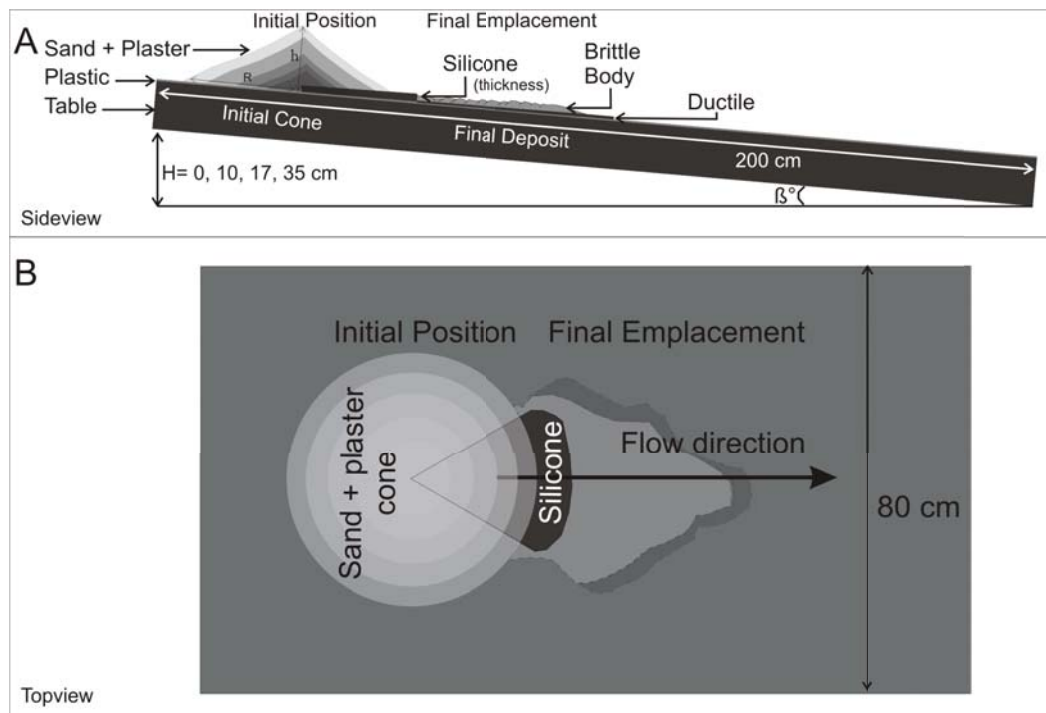


Figure 3.2: Analogue model set-up and illustration of geometrical parameters in **A** vertical view and **B** plan view. Constants and scaling parameter values are given in Tables 3.1 and 3.2.

Sand and plaster represent the edifice, silicone is the underlying ductile strata, and oil (when used) is the highly lubricated sliding base. The sand-plaster mix has cohesion and internal friction scaled to be similar to most rocky materials of volcanic slopes. By adding plaster, cohesion is raised as described by [Donnadieu and Merle \(1998\)](#). The silicone layer simulates the low viscosity basal layer in spreading stratovolcanoes and flank collapses ([Andrade and van Wyk de Vries, 2010](#); [Cecchi et al., 2005](#); [van Wyk de Vries and Francis, 1997](#); [van Wyk de Vries et al., 2000](#); [Wooller et al., 2004](#)). This layer is often consists of mobilized sediments, volcanoclastic, and altered rocks. The oil placed under the silicone in some experiments decreases friction between the sliding basal layer and the plastic sheet, thus speeding up sliding. In such cases, simple shear is concentrated in the oil layer and the rest deforms by pure shear stretching. This layer represents a possibly very low resistance layer that could be present at an avalanche base (e.g. [Siebert, 1984](#); [Thompson et al., 2010](#)).

The failure angle of the landslide (i.e. its initial plan shape) and inclination of transport and depositional areas are also taken into account in the

analogue models (see Table 3.1 for the scaling variables). Failure occurs in the edifice when the basal layer deformation induced by the cone load and pressure gradient creates stresses greater than the strength of the sand or sand and plaster. The collapsing material then slides and spreads downslope on a plastic-covered table that can be inclined up to  $10^\circ$ . In each model experiment, initiation and deposition slopes are fixed at  $0^\circ$ ,  $3^\circ$ ,  $5^\circ$  or  $10^\circ$ .

Three sets of experiments were made. Set 1 used pure sand of negligible cohesion (0 Pa) with oil under 1 or 2 cm of silicone (see Table 3.2 for dimensionless ratios). Set 2 used different cohesion granular layers with sand and plaster proportions of: 3:1 (250 Pa); 1:1 (500 Pa), 1:3 (750 Pa) and has oil under 1-2 cm of silicone built. Set 3 has the same ratio of cone material as in Set 2 but underlain by 1 cm of silicone without lubrication. In some of the experiments, model cones are topped with pure plaster to enhance visibility of structures formed after collapse.

In total, 45 experiments were completed. There were 9 experiments for Set 1, 24 for Set 2 and 12 for Set 3. Sequential photographs (plan view) were taken to record the development of surface structures. Vertical sections were made for the Set 1 experiments to view internal deformation within the landslide field. Repetition of the same experiments with identical initial parameters showed the same geometric, morphologic, and dynamic characteristics, thus demonstrating reproducibility.

### 3.3.3 Scaling

The scaling procedure used in the analogue experiments is the same as in previous models that simulate flank destabilization and catastrophic volcano collapses (Andrade and van Wyk de Vries, 2010; Donnadieu and Merle, 1998; Lagmay et al., 2000; Vidal N. and Merle O., 2000). Geometric, kinematic, and dynamic scaling between the analogue experiment and real stratovolcanoes are calculated based on parameters listed in Table 3.1.

Scaling determines the conditions necessary for proportional correspondence between geometric features and forces acting in nature and in the laboratory. According to the Buckingham theorem, ten independent dimensionless variables must be defined and need to be similar between models and nature. Five of the variables are geometrically and closely similar, defined in Table 3.2. Five kinematic and dynamic variables are calculated using the gravitational ( $F_G$ ), inertial ( $F_I$ ), failure resistance ( $F_R$ ), and viscous ( $F_V$ ) forces acting on both natural and analogue models defined as:

Dimensionless variable	Definition	Equation	Value			$\frac{M_1}{N}$	$\frac{M_2}{N}$	$\frac{M_3}{N}$	
			Nature	Model ( $M_1$ )	Model ( $M_2$ )				Model ( $M_3$ )
$\pi_1$	Edifice (height / radius)	$\frac{h}{R}$	0.3	0.7	0.7-0.9	0.8	$\sim 1$	$\sim 1$	$\sim 1$
$\pi_2$	Basal layer thickness/ Edifice height	$\frac{T}{h}$	0.1-0.2	0.1-0.2	0.1	0.1-0.2	$\sim 1$	$\sim 1$	$\sim 1$
$\pi_3$	Basal layer length/ Edifice radius	$\frac{D}{R}$	1.3-2	1.2	1-1.1	1.2	$\sim 1$	$\sim 1$	$\sim 1$
$\pi_4$	Basal layer vertex distance/ Edifice radius	$\frac{d}{R}$	?	0	0	0	-	-	-
$\pi_5$	$a$ angular distance	$\frac{\alpha R}{h}$	1.6-10.8	0.7	0.6-0.8	0.7	$\sim 1$	$\sim 1$	$\sim 1$
$\pi_6$	Edifice/ Basal layer density	$\frac{\rho}{\gamma}$	1-1.6	1.5	1.5	1.5	$\sim 1$	$\sim 1$	$\sim 1$
$\pi_7$	Gravitational/ Viscous forces	$\frac{FG}{FV}$	168-375	291	291-397	317	$\sim 1$	$\sim 1$	$\sim 1$
$\pi_8$	Frictional/ Viscous forces	$\frac{FR}{FV}$	32-36	186-276	178-361	168	$\sim 1$	$\sim 1$	$\sim 1$
$\pi_9$	Inertial/ Viscous forces	$\frac{FI}{FV}$	1.3-132	$3 \times 10^{-4}$ - $3 \times 10^{-5}$	$3 \times 10^{-4}$ - $3 \times 10^{-5}$	$3 \times 10^{-4}$ - $3 \times 10^{-5}$	low	low	low
$\pi_{10}$	Inertial/ Gravity forces	$\frac{FI}{FG}$	0.8-0.00352	$9 \times 10^{-7}$ - $9 \times 10^{-8}$	$9 \times 10^{-7}$ - $7 \times 10^{-8}$	$8x \times 10^{-7}$ - $8 \times 10^{-8}$	low	low	low

Table 3.2: Definition and values of the independent dimensionless variables (after Andrade and van Wyk de Vries, 2010).

$$F_G = \rho \times g \times h \quad (3.1)$$

$$F_I = \rho \times V^2 \quad V \text{ is the process velocity} \quad (3.2)$$

$$F_V = \frac{\mu}{t} \quad t \text{ is the process time} \quad (3.3)$$

$$F_R = C + \frac{h}{R} \left( 2\frac{F_G}{3} - F_V \right) \quad (3.4)$$

$C$  is the edifice cohesion and  $R$  is the edifice radius, assuming a Navier-Coulomb failure.

The densities of sand layers comprising the model cone layers were similar and averaged at  $1500 \text{ kg m}^{-3}$ . Our scaling procedure considers the difference in the average bulk density of a volcanic edifice estimated at  $2200 \text{ kg m}^{-3}$  (Williams et al. 1987), and a basal pumice-rich ignimbrite, or sediment with densities in the range of  $1400$  to  $2100 \text{ kg m}^{-3}$  (Bell 2000). The heights of the analogue cones are 12, 11, and 11-15 cm for Set 1, Set 2, and Set 3 experiments, respectively. Each one is built with slopes of  $25$ - $30^\circ$ , the angle of repose of stratocones. The model cones for Set 1 and Set 3 experiments have a radius of 15 cm, and for Set 2, 16 to 17.5 cm. Each model is scaled with respect to the radius of the Socompa and Mombacho volcanoes that are both gravitational spreading volcanoes with major landslides with their basal perimeters defined by breaks in slope and associated thrust-fold belts (van Wyk de Vries and Francis, 1997; van Wyk de Vries et al., 2001).

The low-viscosity ductile basal layer of the analogue models is composed of equilateral silicone pieces, 18 cm in length and has a varying thickness of about 15 percent of the model cone height. The vertex of the silicone is always placed at the centre of the cone to ensure that edifice collapse includes the summit. The edges of the silicone define the lateral limits of the subsequent collapse amphitheater.

Sand and plaster cohesion were scaled to the cohesion of volcanic rocks that range from  $10^6$  to  $10^8$  Pa for intact basalts and other lavas, and  $10^2$ - $10^5$  Pa for volcanic ash and tephra (Afrouz, 1992; Bell, 2000) and  $10^4$  to  $10^7$  Pa for both lavas and tephra. There is no direct measurement for the basal layer viscosity during catastrophic collapses, but it may be estimated in the order of  $10^7$  Pa from numerical analysis and simulations of debris avalanche flows (Andrade and van Wyk de Vries, 2010; Dade and Huppert, 1998; Kelfoun and Druitt, 2005; Sousa and Voight, 1995). The analogue silicone has a viscosity of  $\sim 10^4$  Pa and the oil  $\sim 10^{-1}$ .

## 3.4 Results

### 3.4.1 Standard Experiment

The experiments generally result in shorter runout than in the natural counterpart as at a late stage deformation becomes very slow, however the morphology and structures observed are similar to those observed in large-scale landslide deposits and are seen to remain similar in those experiments that attained scaled natural run outs (Fig. 3.1, Appendix D). Despite changing variables and configurations in the sets of experiments, there are recurrent morphological features and structures that are developed across most experiments. The structures produced are thus general features, and their appearance does not depend strongly on thickness of silicone or cohesion of the brittle layer.

Deformation of the analogue cones starts as soon as they are constructed and ends when deformation is almost negligible and overall morphology remains invariable. The rates of deformation depend mainly on the silicon viscosity, the presence of an oil layer and to the lesser extent the sand-plaster mixture cohesion. Experiments that have long runout are stopped when the analogue landslide reaches the end of the table setup.

### 3.4.2 Model Avalanche Class

Model avalanches can be of three classes and can develop three types of hummock morphology and structure (Fig. 3.3, Appendix D): Class A avalanches have progressive spreading and extension. Class B avalanches undergo progressive spreading but have a localized early compression phase related to the spreading proximal zone pushing against a decelerating distal area. Class C avalanches have late-stage compression only at the distal portion of the deposition zone. Individual avalanches can change from one type to another during their development.

### 3.4.3 Surface Morphology and Structures

There are two major zones identified in our experiments (Fig. 3.3, 3.4, 3.5): The collapse zone, which is equivalent to the *toreva* domain of Andrade and van Wyk de Vries (2010), and the depositional zone, formed when the avalanche progresses out of the amphitheater limits, laterally and longitudinally spreading out material at its base. These two zones are generally separated by a major graben that Andrade and van Wyk de Vries (2010) also observed. This graben is an arcuate depression perpendicular to the slide direction. It separates the area of larger *toreva*-like hummocks from the zone with smaller hummocks (Fig. 3.3, 3.4, 3.5).

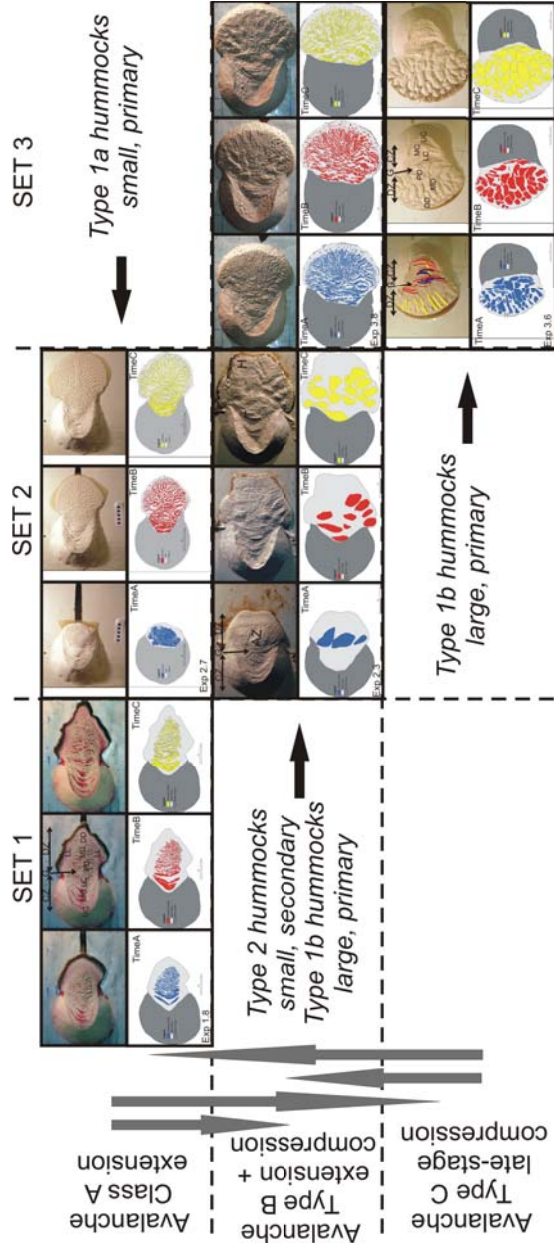


Figure 3.3: Development of analogue avalanches. Five analogue models that represent the three sets of experiments are grouped according to avalanche classes and the resulting hummock types: one for Set 1, two for each Set 2 and Set 3. Avalanches can be of Class A with progressive spreading and extension resulting in progressively broken, primary, smaller hummocks, Hummock Type 1a; Avalanche Class B for progressive spreading with compression in some areas resulting in a wider range of hummock size, Hummock Type 1b and 2; or Avalanche Class C for progressive sliding with late-stage compression resulting in increasing hummock size, Hummock Type 1b. Grey arrows indicate that during an avalanche, hummocks can start big and break during extension or they can merge sometime during its development. For each experiment, three photos representing the avalanche evolution and hummock development are in the first row, with their hummocks, debris field and depositional zone delineations below for statistical analysis of hummock area and spatial distribution. Morphological features are labeled and delineated in some experiments: collapse zone (CZ) and its upper (UC), medial (MD) and lower (LC) areas; depositional zone (DZ) and its proximal (PD), medial (MD) and distal (DD) areas; the graben (G); accumulation zone (AZ) in the PD, MD or DD, ridges (R), torevas (T) and hummocks (H); and the surface structures: normal (red), thrust (blue) and strike-slip (yellow) faults.

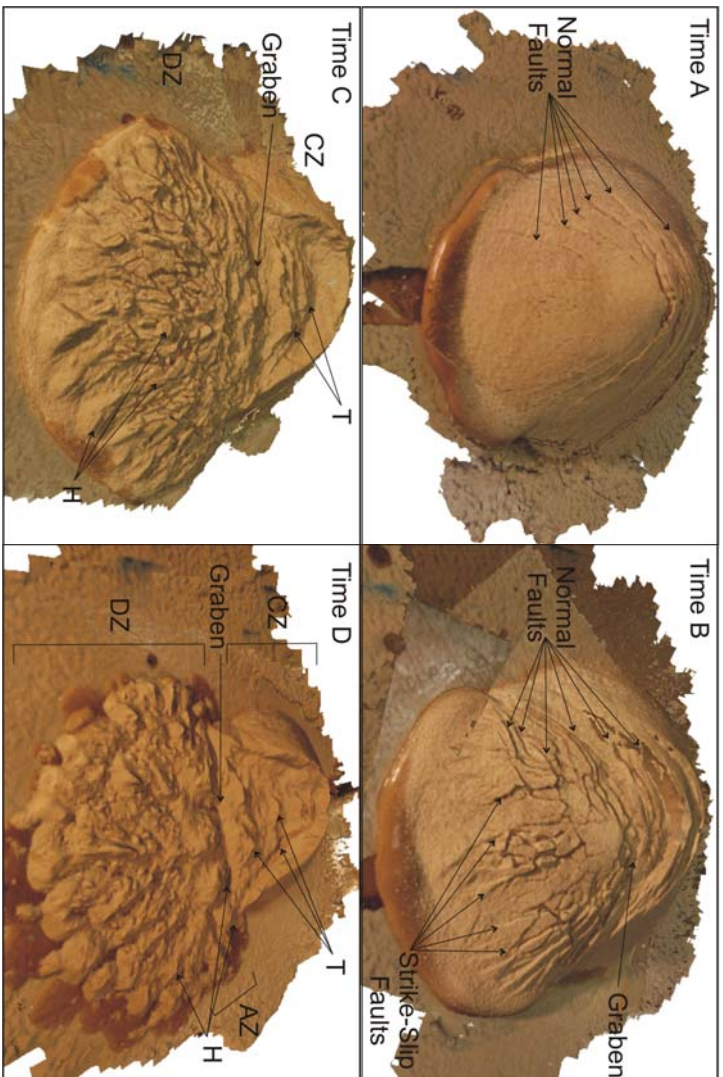


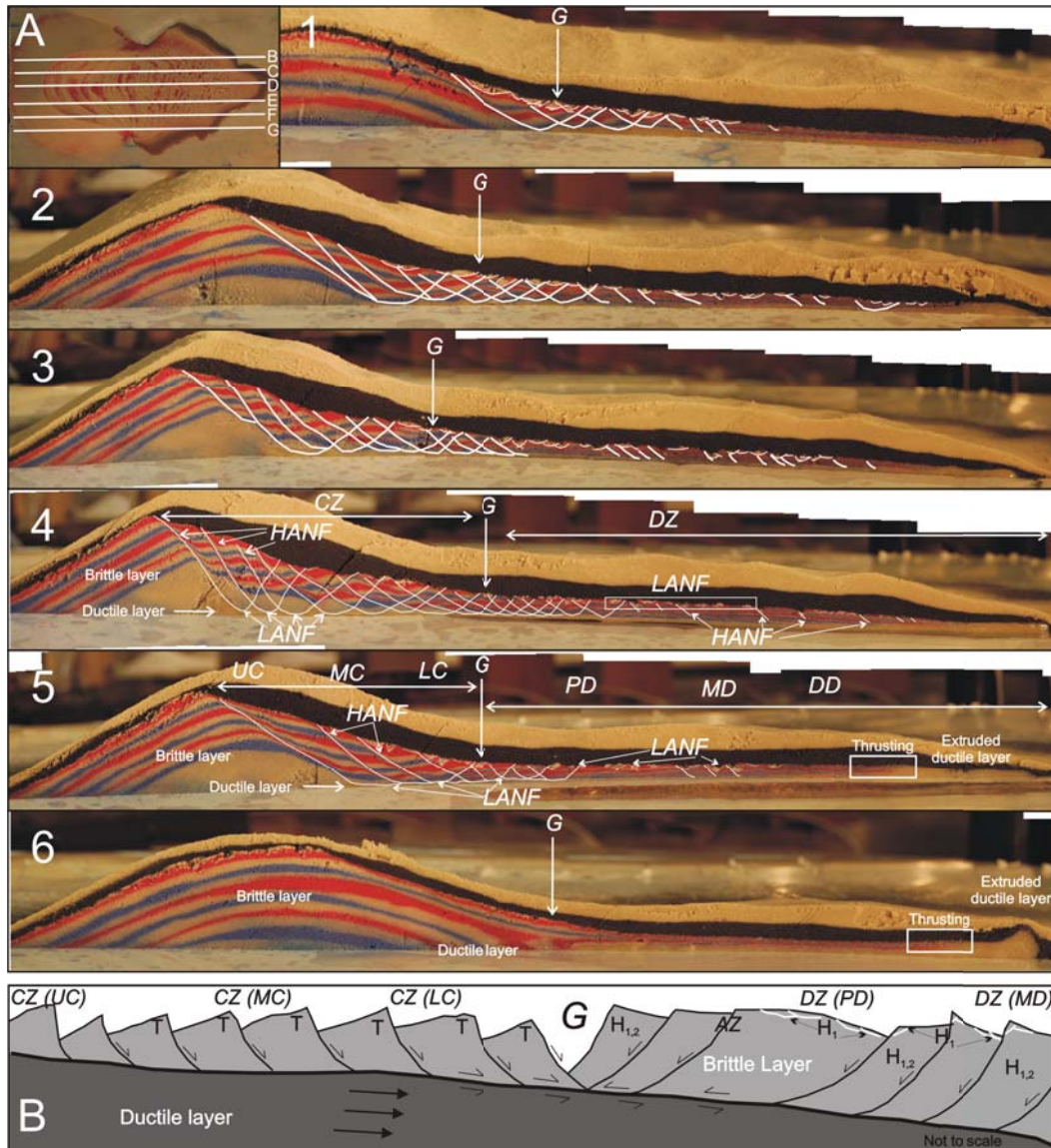
Figure 3.4: A 3D example of structural and morphological development of an avalanche and formation of hummocks during its evolution (ARC 3D webservice by the VISICS research group, Belgium). Time **A** formation of normal faults and movement along these cause edifice extension downwards by sliding; Time **B** collapse of more edifice materials near the summit and formation of more normal faults in the collapse (CZ) and depositional (DZ) zones. Movement along these faults spreads the materials further down with the graben forming as the edifice materials come out of the amphitheatre limits towards a gentler slope; At Time **C**, torevas (T) formed since the earlier stages are more evident and the materials at the base spreads both to the lateral and downslope direction. Hummocks in the DZ are well formed at this stage; and at Time **D**, the avalanche spreads and hummocks break up.

The collapse zone is further subdivided into: the upper, the middle, and the lower collapse areas (Fig. 3.3). The upper collapse area is composed primarily of summit material dominated by normal faults oriented perpendicular to the slide direction. The middle collapse area is where numerous strike-slip faults appear and the lower collapse zone is where arcuate normal faults convex towards the volcanic cone, are dominant. Irregularities of elevation profile in the collapse zone are due to foreva tilting and rotation. The depositional zone is subdivided into: the proximal, medial, and distal areas. It is where forevas and blocks break up as the landslide spreads laterally and longitudinally. Prominent features in this zone are the lateral levees, ridges, and hummocks (Fig. 3.3). The depositional zone, like the collapse zone, is cut by normal, strike-slip and thrust faults. Normal faults appear in extension-dominated areas, where they accommodate basal shearing, tilting, and rotation of the sliding materials. They also appear in the medial to distal depositional zones as the deposits spread further. Thrust faults dominate in the proximal and distal accumulation zones where the materials approach gentler slopes or when spreading wanes. Thrust faults at the frontal margin are caused by compression as margins resist spreading. Arcuate transtensional faults form along the sliding direction because of differential forward movement of the deposit combined with lateral spreading.

Hummocks and forevas are observed in all experiments (Fig. 3.3). Large hummock trains in Set 2 and 3 experiments are parallel to the slide direction. In Set 1, they are transverse and curved towards the frontal margins. For the Set 2 and 3 with 1:1 ratio of sand and plaster, both large and small hummocks form and superimposed on the same area. Large hummocks are elongated whereas the smaller hummocks are equant. Only small and rounded hummocks are observed in experiments with the less cohesive, pure sand cone material, Set 1 experiment.

#### 3.4.4 Plan View Shape

Avalanche deposits produced in the Set 1 and Set 2 experiments with oil have long runout equaling that of natural deposits, whereas Set 3 without the oil have a short runout and with a wide depositional zone (Fig. 3.3, 3.8). The presence of the oil layer and low cohesion of the cone edifice in the experiments influences the landslide runout shape and length (Exp. 1.6, 1.8 in Fig. 3.3). On the other hand, the absence of oil and higher cohesion dampens spreading of the avalanche front. Instead, there is enhanced lateral spreading that generates a wide depositional zone (Exp. 2.3, 3.6, 3.8, in Fig. 3.3). Lobes can form at the frontal and lateral ends of each landslide deposit and the lobe shape can vary (Fig. 3.3). Experiments with oil produce landslide



deposits with irregular lobes. Those without lubrication have symmetrical, more rounded, and more regular lobes. This is attributed to the presence of oil layer as the reduced friction by lubrication of the silicone affects the basal- and upper- layer spreading rate on both lateral and frontal margins.

### 3.4.5 Subsurface Deformation

Vertical cuts (Fig. 3.5A), parallel to the main sliding direction, reveal the avalanche internal structure. The collapse and depositional zones are dissected by normal faults and are separated by a graben. Strike-slip faults, at times arcuate towards the frontal margin are difficult to see in this view but are clear in Figure 3.3. In the collapse zone, listric normal faults converge into the ductile shear zone. The listric normal faults accommodate the sliding, tilting, and rotation of the blocks in the collapse zone.

In the depositional zone the listric faults are more shallowly dipping and more closely spaced. In the topmost part of the brittle distal layer there are also shallower and minor low angle normal faults that accommodate the sliding, tilting, and rotation of smaller blocks. These produce the secondary small hummocks that appear like detachment blocks gliding on top of the

---

Figure 3.5 (*preceding page*): Subsurface **A** vertical view parallel to slide direction of an analogue avalanche and **B** interpretation. **A** is a plan view image for the locations of the cross sections 1-6. The different sub-areas for collapse and depositional zones and graben are in 1-6. The analogue has an upper brittle layer where normal faults are evident and a ductile layer underneath with varying thickness throughout the avalanche area. High angle normal faults (HANF) in the upper brittle layer become listric and converge into a low angle normal fault (LANF). These faults accommodate the sliding, tilting and rotation of edifice blocks in the collapse zone forming the torevas and their smaller counter part, first-order: Type 1 and the second-order Type 2 hummocks. On the topmost part of the brittle layer are shallower low angle normal faults that accommodate the sliding, tilting and rotation of minor blocks at the very top forming the Type 2 hummocks. **H** shows a cross-section interpretation of an avalanche. From the collapse zone towards the proximal deposition zone, brittle shearing dominates as ductile shearing only occurs in the upper part of the thinning silicone. From the medial towards the distal deposition zone, however, ductile shearing dominates resulting in the thrusting of both the silicone and thinning or thickening of the sand-plaster layer. Adding layers of black and white sand preserves the original surface of the debris avalanche.

debris field or sometimes stranded on top of the larger hummocks.

The graben is a transition point of the normal faults between the collapse and depositional zones. It is where sliding toerevas start to break up as the landslide spreads into a wider depositional zone or where toerevas accumulate as they approach a gentler slope. In general, the dip of normal faults decreases with depth and distance from the summit. This is shown by listric faults that converge in the boundary of the upper brittle layer and the underlying ductile layer in the collapse zone. The shallow normal faults do not reach this boundary in the depositional zone. The high and low angle normal faults in the collapse zone create the toerevas. In the depositional zone, they create hummocks. Figure 3.5B shows a cross-sectional interpretation and morphology of these structures.

### 3.4.6 Hummocks

In this study, each experiment is divided into three stages: initial, development, and final deposition. Experiments that best represent the recurrent morphology and structures are chosen and presented in Figure 3.3 and Appendix D. Their hummocks and debris fields are delineated. Using statistical analysis, hummock area, spatial distribution and factors affecting it are explored for patterns that aid to investigate their types and evolution throughout the landslide-avalanche development.

#### 3.4.6.1 Characterization

There are two types of hummocks formed in the experiments (Fig. 3.3, 3.5): the Type 1, primary hummocks and the Type 2, secondary hummocks. Type 1 hummocks are of two classes: Type 1a are the small and generally equant hummocks formed early on through the initial development stages of faulting, and may undergo minor breakup during emplacement; and Type 1b are the larger and often elongated hummocks. Type 2 forms on top and alongside the larger, Type 1b hummocks. Type 1b hummocks develop from original landslide blocks that became stretched and flattened and they may also grow from the accretion of blocks.

#### 3.4.6.2 Exploratory Statistics

A line graph of increasing hummock area (Fig. 3.6) shows that experimental avalanches can produce either a highly contrasting or a gradually changing population of hummock type. Small hummocks, Type 1a and Type 2 (Exp 1.8, 2.7, 2.3, 3.8) resulting from class A and B avalanches (extension during

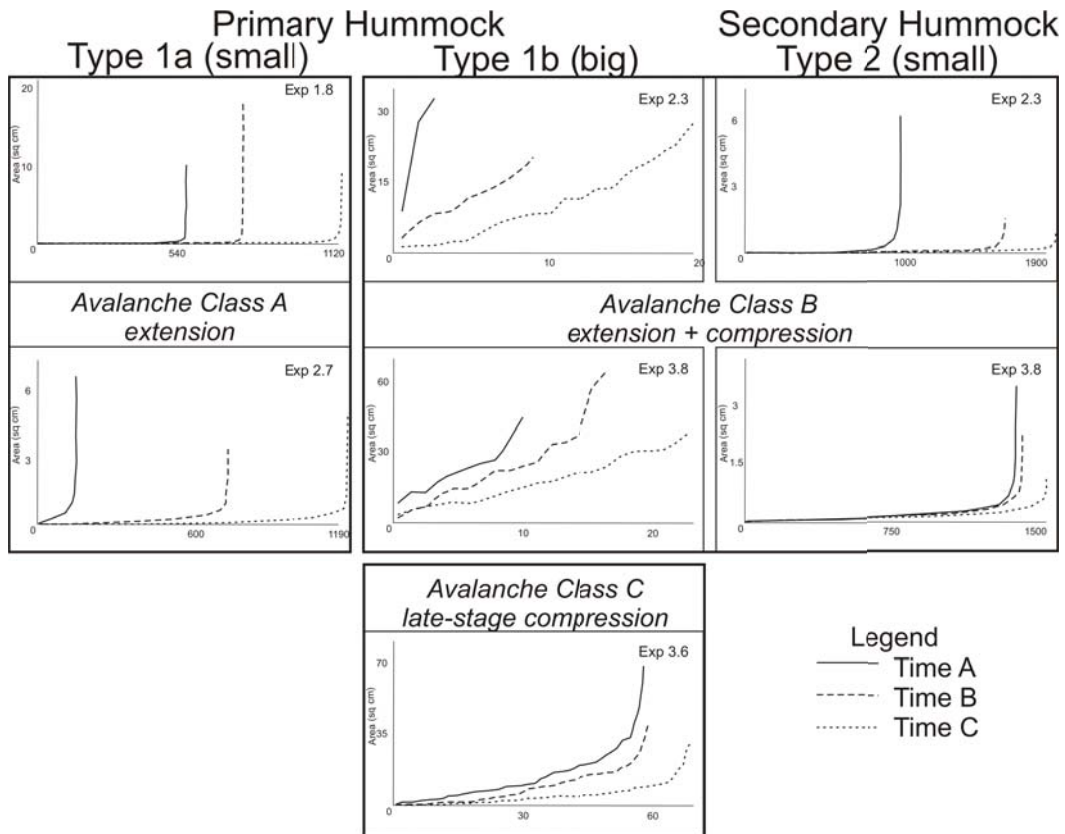


Figure 3.6: Increasing line plot of hummock area. Avalanches can produce either or a combination of a large number of small hummocks or a very low count of big hummocks. Small hummocks, regardless of whether they are primary or secondary can be highly contrasting having mostly of very small and very few large hummocks. Sizes of type 2 hummocks, however, exhibit a gradual change in slope implying that for avalanches that produce larger hummocks (compression-dominated avalanches), their hummocks are of similar sizes during transport.

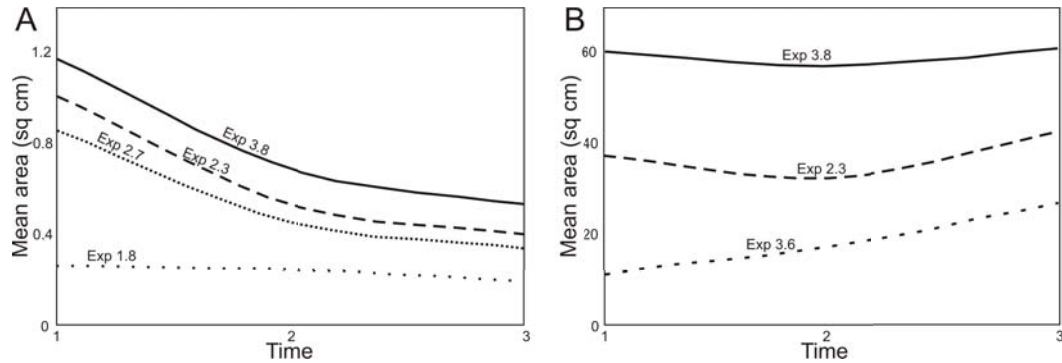


Figure 3.7: Line graph showing mean areas of hummocks with respect to distance from the summit (the greater the time, the farther the hummocks are from the source). Type 1 (A) and Type 2 (B) hummocks will always tend to break up, due to spreading and extension during an avalanche emplacement. However, they can start to merge and form increase in size once undergoes compression.

avalanche) tend to have very high frequency of small and very few big hummocks. This is seen by the very abrupt change in slope on Figure 3.6. Type 1b hummocks (Exp 2.3, 3.8, 3.6) produced by class B and C analogue avalanches (with compression at some point during the avalanche) exhibit gently sloping graphs, indicating that within certain stages during the avalanche, the hummocks are of restricted range of sizes. In general, hummock population may decrease as their size increases or populations increase as they progressively break up.

During an avalanche, types 1a and 2, small hummocks always tend to break-up and disintegrate if they have lower cohesion (Fig. 3.7A, Appendix D) as shown by an overall decrease in hummock size. However, as an avalanche wanes or when cone materials block the spreading of silicone at the front of the avalanche causing compression, hummocks can merge and integrate materials (Fig. 3.7B, Appendix D) forming the larger hummocks during compression. This results in larger hummocks at the medial to distal margins.

### 3.4.6.3 Spatial Distribution

Hummock spatial distribution is recorded by taking the centre of each hummock. The elongation and direction of the ellipse (Fig. 3.8) represents the general direction and orientation in which the hummocks form and separate. In general, this follows the plan view shape of the debris avalanche deposit itself.

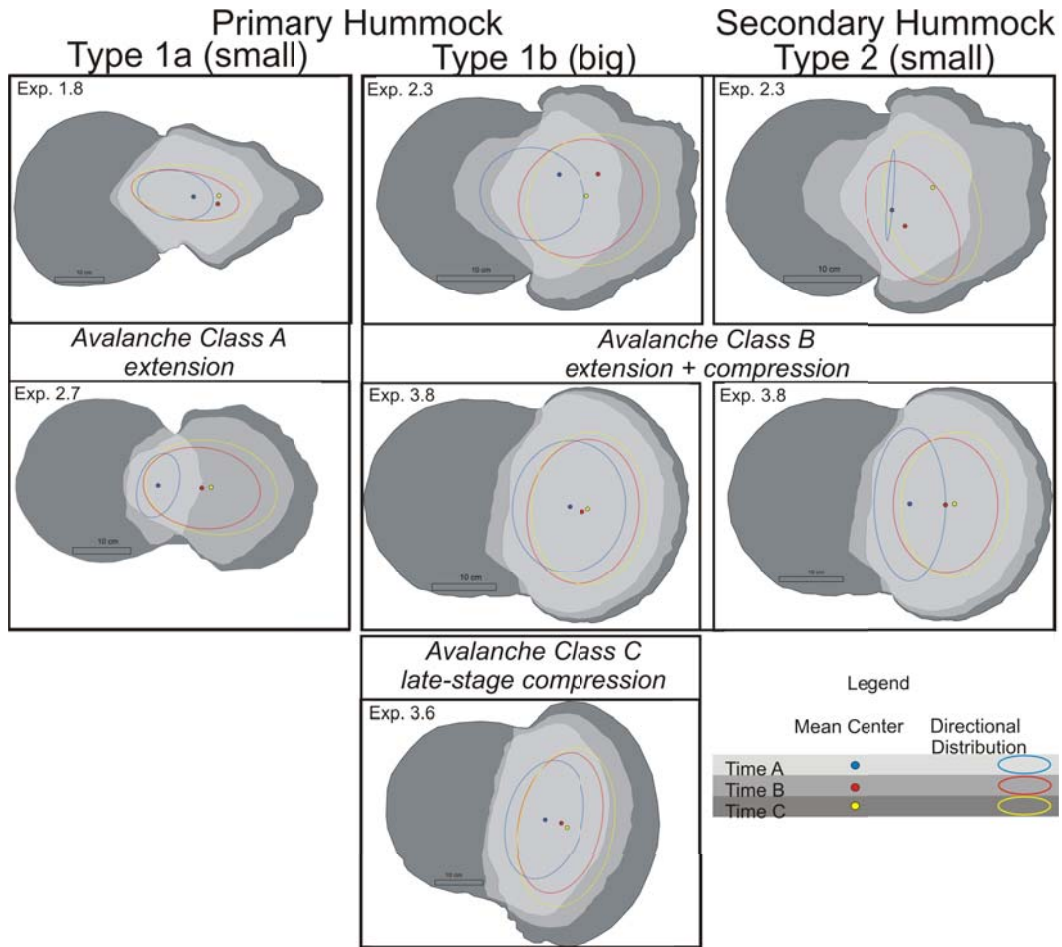


Figure 3.8: Trend of the directional ellipses and mean centers. The directional ellipses show the lateral or longitudinal formation direction of hummocks and the mean centre is the centre point of the central hummock.

The mean centre (Fig. 3.8) shows the point where the central hummock moves at each stage of the experiment. In general, these trends allow visualization of the link between central hummocks, overall direction of movement and avalanche flow direction. The trend in the directional ellipse and mean centre of the hummock areas show that spreading occurs mostly parallel to the long axis, downslope-spreading of the avalanche if the material is less cohesive and lubricated whereas dominantly lateral for high basal friction and more cohesive experiments.

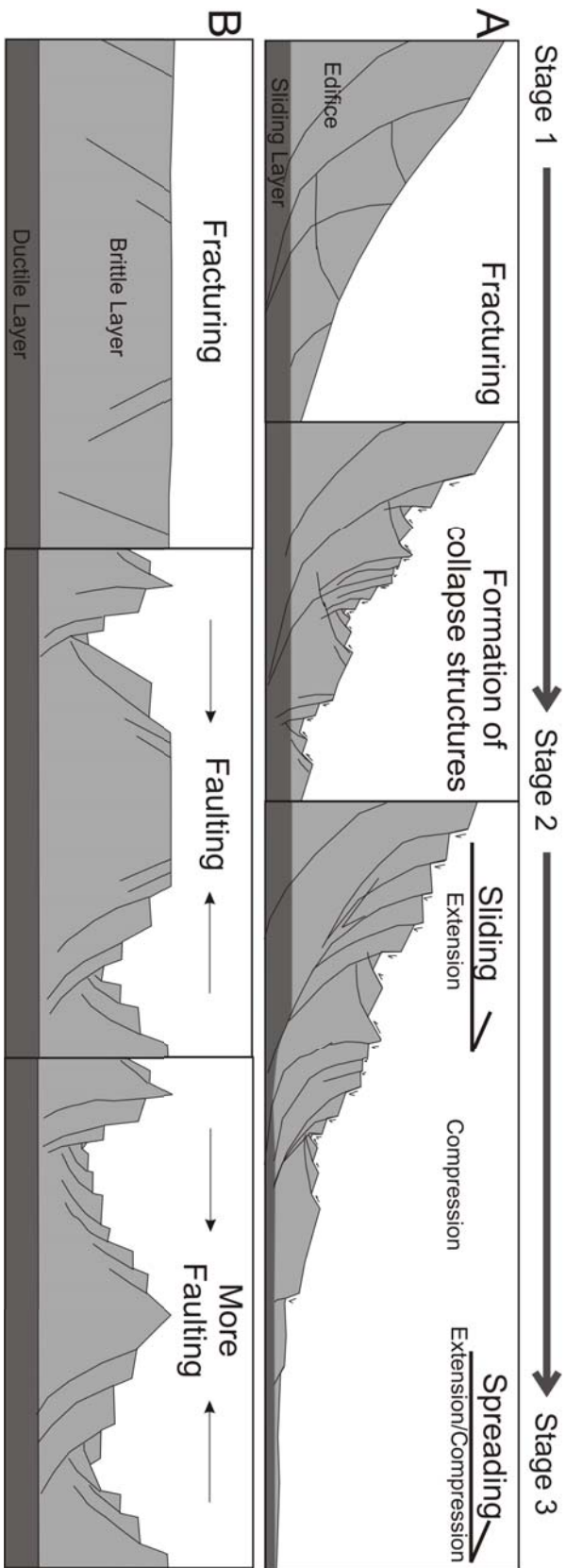


Figure 3.9: The different stages of avalanche emplacement showing an interpretation of hummock formation **A** and degree of faulting **B**.

### 3.4.7 Sequence of Events

The development of a rockslide debris avalanche model can be subdivided into three stages depending on the structures and morphological features that form. These are the slide initiation, development, and final emplacement. A discussion regarding these stages is presented in this section with accompanying diagrams (Fig. 3.4, 3.9) that show the development of the overall morphological and structural features and the formation and evolution of hummocks.

#### 3.4.7.1 Slide Initiation

Fractures begin to develop at the onset of edifice collapse. As soon as the underlying silicone layer in the experiments begins to stretch, sliding initiates and transforms early fractures into faults. These faults define the amphitheater walls (Fig. 3.4A, 3.9) and also accommodate the extension of edifice blocks as the avalanche spreads outwards. Blocks may become torevas if they remain intact in the collapse zone or proximal area of the depositional zone. If broken into smaller blocks, they become hummocks in the depositional zone. Transtensional faults in the collapse zone start to appear early on. This slide initiation stage is also described by Andrade and van Wyk de Vries (2010).

#### 3.4.7.2 Development Stage

The collapse, depositional zones, and horst and graben structures in an avalanche become obvious during the development stage (Fig. 3.4B-C, 3.9). More normal faults form and edifice materials slide in both zones. Large blocks and torevas at the lower part spread more, break up, and form the smaller hummocks (Type 1a, 2). Some torevas remain intact and some can accumulate and combine with neighboring ones forming the larger Type 1b hummocks.

#### 3.4.7.3 Final Stage

During the final stage, Type 2 detachment hummocks become evident whereas torevas in the collapse zone remain as they are. In the depositional zone, hummocks can break up or remain intact as the avalanche continues to spread. The ductile layer may build up at the margin where a thrust brittle upper layer forms compression ridges.

## 3.5 Discussion

To understand what hummocks are and how they are formed, their existence and relationship with other structural and morphological features within an

avalanche field must first be recognized. From the analogue models, we observe hummocks to form in all experiments but their final spatial distribution, size, elongation, and morphology can vary (Fig. 3.2).

### 3.5.1 Avalanche Characteristics

Analogue avalanche models constructed in this study develop a similar and consistent set of structures. In all the experiments, collapse and depositional zones are separated by a graben (Andrade and van Wyk de Vries, 2010) and faults dissect the entire mass (Fig. 3.3-3.5). In the collapse zone, large listric faults form the main failure plane of the avalanche. From the middle towards the base of the collapse zone, transtensional and compressional faults appear as the collapsing mass spreads outwards (Fig. 3.3-3.5). The areas between the faults are the hummocks.

The depositional field has three areas: the proximal, medial, and distal areas. Size, orientation, elongation, and spatial distribution of the hummocks are different in each of these areas and are controlled by varying emplacement conditions.

In experiments where a less cohesive pure sand cone stands on an inclined plane, and the base is oil-lubricated, progressive but gradual spreading and thinning of the avalanche is observed (Fig. 3.3). On the other hand, in more cohesive models of sand and plaster cones on a gently inclined plane, regardless of lubrication at the base (Fig. 3.3), higher friction and resistance to slide result in an accumulation area within the depositional zone. Hummocks are formed from the broken edifice blocks that slid, tilted or rotated as the avalanche progresses.

### 3.5.2 Hummock Description

#### 3.5.2.1 Morphology

Hummocks can be characterized according to their basal shape, surface morphology, and orientation with respect to flow and slide direction. The basal shape of hummocks can be equant, circular, rectangular or elliptical. Hummock deformation and shape after initial formation depends on the velocity distribution and the strain field of the avalanche. Their initial shapes stretch along acceleration and contract on the deceleration directions. Hummock elongation is a product of initial shape and subsequent deformation that can be either dominantly parallel, perpendicular or randomly oriented with respect to flow direction. The surface morphology of hummocks can be flat topped or pointed, ridged, or rounded. Densely faulted hummocks can create pinnacle-topped features (Fig. 3.9B).

Generally, circular-based and flat-topped hummocks are formed in rapidly emplaced long runout models whereas elongated and pinnacle hummocks form in experiments of cohesive avalanche material with moderate runout. The slope angle of collapse base, cohesion, and lubrication can influence the runout length, lateral or longitudinal spreading direction, shape, and orientation of individual hummocks.

### 3.5.2.2 Types

We identify different hummock types based on their size and development (Fig. 3.3): Type 1a are the first order small hummocks; Type 1b are the first-order large, elongated hummocks; and Type 2 are the second-order small, polygonal hummocks that formed after and raft over the Type 1b hummocks. The extensional faulting of avalanche deposits forms the first-order hummocks. Small-scale shear faulting or brittle fracturing separating and detaching stretched upper layers of the larger primary hummocks forms the Type 2. They may be the internal equivalents of boudinage type blocks, of stretched and separated competent layers, such as seen in many avalanche hummock cuts (e.g. Figure 5F in [Shea and van Wyk de Vries, 2008](#)), or (e.g. Figure 4 in [Bernard et al., 2009](#)), or in other avalanche analogue models ([Shea and van Wyk de Vries, 2008](#)).

From the vertical cross sections, we observe that high angle normal faults in the upper brittle layer converge into low angle normal faults towards the lower part, accommodating the sliding, tilting, and rotation of edifice blocks forming the Type 1 hummocks. The shallower low angle normal faults or brittle fractures on the topmost part of the brittle layer serve as a décollement interface of the different lithologies forming the Type 2 hummocks.

### 3.5.2.3 Trends in Size and Spatial Distribution

Hummocks can have a low population density with a large size distribution as generally the case for Type 1b or high population but with a small size distribution as in the case for deposits with dominant small hummocks, Type 1a and 2. If a model avalanche produces large hummocks, the difference in size distribution is minimal. On the other hand, if smaller hummocks form, their size range is broad with most hummocks at the lower end of the size spectrum. In this case there are very few that are at the large end of the size spectrum.

As an avalanche develops, hummocks can decrease in number but increase in size or they can increase in number but decrease in size. At the final stage, however, hummock population is more often higher compared to the early stages indicating that hummocks do break up during sliding development.

A progressively spreading and thinning avalanche body, class A is dominated by extension with the largest hummocks confined to the lower collapse zone and proximal depositional zone. The smaller hummocks spread all over the depositional zone as in Iriga (DAD 2, Fig. 3.1) (Paguican et al., 2011). In class B exhibiting hummock type 1b and 2, and class C avalanche experiments where there is substantial compression due to frontal restriction, for example, the biggest hummocks can be located anywhere in the depositional zone forming the accumulation zones. This is clearly observed at the Tetivicha avalanche, Bolivia (Shea and van Wyk de Vries, 2008) and Iriga debris avalanche deposits (Fig. 3.1) (Paguican et al., 2011).

### 3.5.3 Avalanche Stages and Hummock Formation

From the analogue models, it is clear that hummock formation is intimately linked to the development of the avalanche. At the first stage, normal listric faults accommodate the extension by sliding and rotation of blocks. These blocks are the initial hummocks. Then during transport, the avalanche may spread freely or may encounter barriers and topographic constraints such as other topography. During this stage, hummock population develops and evolves.

#### 3.5.3.1 From Landslide to Hummocks

The low angle normal faults at the base and the high angle normal faults at the upper layer converge creating the sliding plane. This plane facilitates most of the sliding, tilting and rotation of edifice blocks as the body spreads down the amphitheater. The major normal faults limit the boundaries of the collapse amphitheater. Near the amphitheater base and outside of its limits, edifice materials will start to spread laterally as well as longitudinally. As the sliding plane activates and initiates sliding, brecciation and faulting in the edifice occurs and blocks are formed by the upper normal faults. As the collapsing edifice mass moves down, extension of the upper layers above the slide plane induces normal faulting, generating horsts and grabens. The faulted blocks become the building blocks of hummocks as the whole mass spreads.

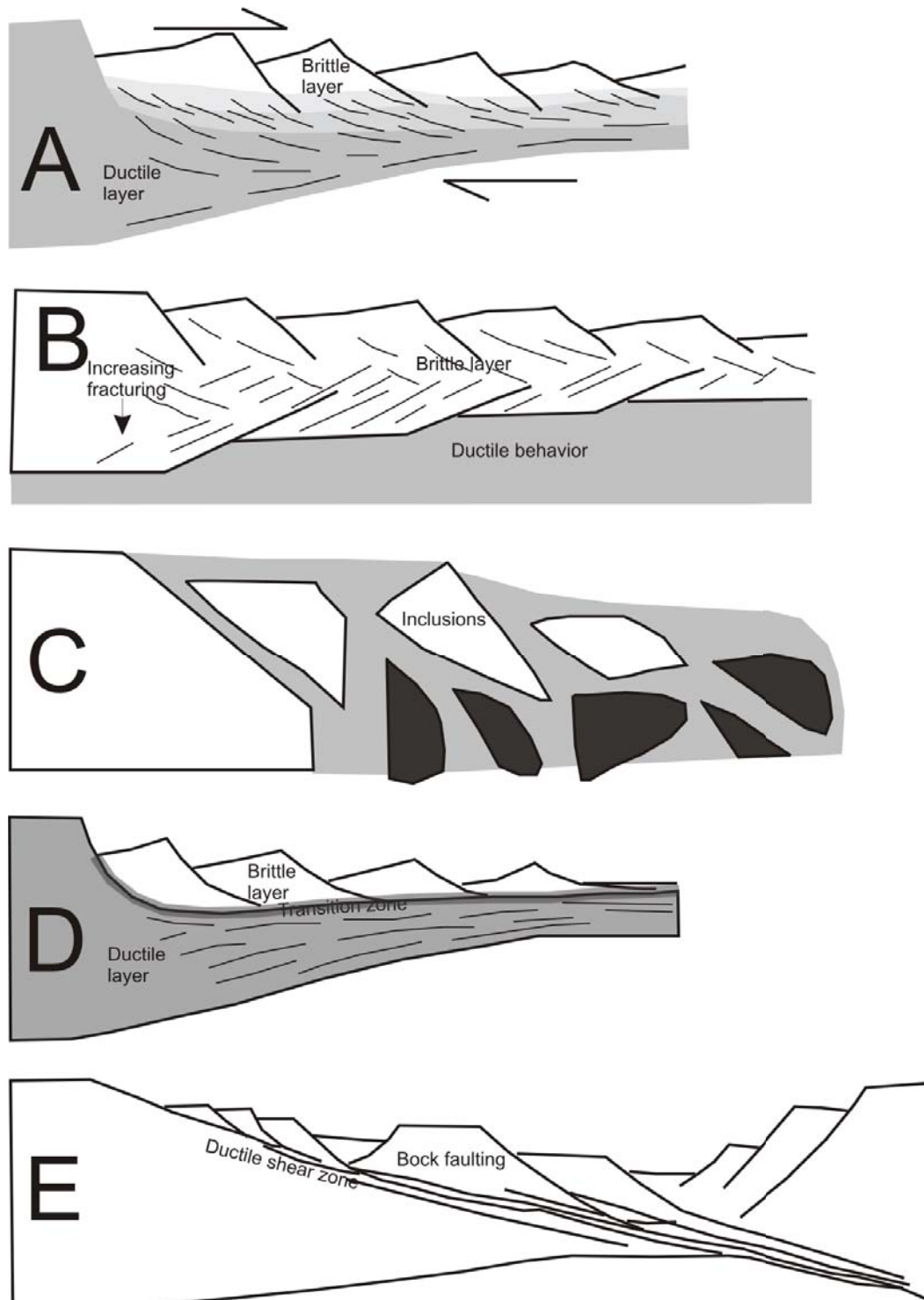
As the edifice materials come out of the amphitheatre and into the depositional zone, debris will spread and extend not only downslope but also laterally. As the materials approach the gentler slope at the piedmont, proximal materials accumulate, creating ridges oriented perpendicular to the flow. As more materials slide down from the edifice, these materials are pushed to spread further, where extensional or compressional structures may dominate depending on the topography and morphology of the depositional zone.

Naturally, extension happens on unconfined depositional environments with regular topography. On the other hand, compressional features such as ridges parallel, sub-parallel or perpendicular to the flow direction may develop in confined environments. These ridges may form distal accumulation zones if frontal debris is compressed in the distal front. Distal accumulation zones may be remobilized into lahars or could remobilize as secondary slides, as at So-compa (Kelfoun et al., 2008). High angle normal faults and tension fractures are not clearly rooted to the basal layer in the depositional zone, their strain is taken up by diffuse deformation in the lower brittle zone, or on structures too small to observe at the model scale. Spreading and increasing extension by block sliding, tilting, and rotation is the stage when hummocks are developed. As spreading wanes, hummocks can break and move farther apart as in avalanches resulting in Type 1a and 2 hummocks or move closer as in those forming the Type 1b hummocks. Figure 3.4 observed the juxtaposition of type 1b as well as the break up of the Types 1a and 2 hummocks such as in Parinacota (Clavero et al., 2002). There are also shallower, minor low angle normal faults and fractures that penetrate the topmost brittle layer. Like the major normal faults, these minor low angle normal faults accommodate the sliding, tilting and rotation of the upper most layer of the original edifice layer forming the Type 2 hummocks.

A clearly observable structure during the DAD models development is the presence of a graben that separates the collapse and depositional zones. It is formed when down-sliding blocks approach gentler slopes. In cross section, antithetic normal faults start to appear within this zone (Fig. 3.5B). This is also how depressions in the depositional zone are formed (Andrade and van Wyk de Vries, 2010).

### 3.5.3.2 The Role of Normal Faults

The existence of high angle normal faults and major low angle normal faults at the collapse zone is a consequence of the geometry of the sliding mass and the brittle and ductile layers present. These faults accommodate the sliding, tilting, rotation and gliding of hummocks. At the main failure plane, low angle normal faults relay with the high angle normal faults. This is the contact where the base of the brittle blocks slides on a coherent interface with the ductile basal layer. Relative movements of the blocks are accommodated by pervasive deformation in the ductile layer under this interface. High angle normal faults in the collapse zone are generally rooted in the basal layer although this is not the case for those in the shallower depositional zone that do not clearly extend down to the silicone, rather they pass into a lower brittle horizontal stretching area.



Layering within the avalanche, with an incoherent layer at the top such as the upper ignimbrite layer or the lower block and ash layer at Iriga DAD2, Philippines (Paguican et al., 2011) generates an internal decollement causing minor low angle normal faulting over the discontinuity. If there is a pre-existing discontinuity between layers allowing the upper layer to glide over the lower layer, this decollement may take up the deformation. Rotational movement of the upper layer could also generate sliding at the interface. These internal avalanche structures exist as result of layer interface that could be caused by a major internal structure or by a contrasting stratigraphy (Fig. 3.10). Below are the structural models of this layer interface deformation following those brittle and ductile layer interactions and effects on extending crust by Brun and Choukroune (1983).

### 3.5.3.3 Degree of Stretching

During the development of the landslide and evolution of hummocks, the scale variation of stretched portions is observed. The width, thickness, and volume of the active area change during stretching. The normal listric faults in the collapse zone decreases in dip as it approaches the depositional zone, especially in the medial towards the distal areas where it disappears or probably becomes more horizontal by instantaneous stretching in the very thin ductile layer (Fig. 3.9A).

There are three degrees of stretching (Fig. 3.9) during avalanche and hummock formation and they gradually change from Stage 1 to 3 according to increasing degree of stretching (Fig. 3.9A) and normal faulting (Fig. 3.9B) from modified main structural occurrences of stretching in the crust by Brun and Choukroune (1983). Stage 1 is when fractures and shallow high angle normal faults start to appear. Stage 2 and 3 is when extension continues and fracturing intensifies, probably when edifice separates into blocks with faulting more dense and more steeply dipping towards the centre of the moving block.

---

Figure 3.10 (*preceding page*): Structural models of the brittle and ductile layer interface and its effect on hummock formation, using an extensional tectonic model (Brun and Choukroune, 1983). These provide a model for hummock formation: **A**: deformation with progressive transition between brittle and ductile layers; **B**: hummock structure controlled by original discontinuities within the brittle layer; **C**: complete disaggregation into blocks with injection of avalanche matrix in between; **D**: deformation with sharp transition between brittle and ductile layers; and **E**: hummock formation with a detachment-type fault.

Movement along these faults causes the displacement of the brittle layers. At this stage, the tension forces are strong enough to cause the upper brittle layer to split apart, dropping down the centre block relative to its adjacent flanking blocks forming grabens and horst, respectively. This could create steeply dipping walls parallel to slide direction. This is what happens when the hummocks form. Variation in the thickness of the upper brittle and basal ductile layers begins in Stage 2, and is more evident and widely observable in Stage 3. During the final stage, hummocks tend to spread instead of break apart. The basal ductile layer is thinner towards the summit area and most of it has been extruded towards the frontal margins. Structures shown in the cross-sections (Fig. 3.5) are those of late stage 4 when the avalanche is nearly fully stretched.

### 3.5.4 Structural Models: Layers and Structural Interface

Five structural models (Fig. 3.10) based on the models of stretched crust by Brun and Choukroune (1983). These models are established on a combination of continuous and discontinuous processes:

1. Deformation with progressive vertical transition from purely brittle deformation at the top to purely ductile deformation at the base.
2. Hummock structure controlled by original discontinuities within the brittle layer with deformation that is purely on the upper brittle layer. In this model, fracture frequency may increase with depth, low angle faults exist and the base may show ductile behavior and serve as a sliding layer;
3. Complete disaggregation into blocks with injection of avalanche matrix in between;
4. Deformation with sharp transition between brittle and ductile layers; and
5. Hummock formation with a detachment-type fault. Deformation results from a combination of a low-dipping ductile shear zone and block faulting above.

## 3.6 Conclusions

Hummocks are the morphological expression of brittle layer deformation due to spreading in landslides and avalanches. They are principally the stretched

remains of tilted and rotated blocks of the original failure volume. In general, both landslide-avalanches and hummocks initiate and evolve in a similar way. Landslides and avalanches start with fracturing and faulting of the failure area (or for a volcano, the edifice). As strain increases, the upper landslide layer can split apart, forming grabens and horsts, and creating steeply dipping escarpments parallel to the slide direction. Normal and strike-slip faults accommodate the sliding, tilting and rotation of blocks that later evolve into hummocks. These faults also accommodate the extension and spreading within hummocks. Therefore, hummocks are formed by extension of the avalanche, with the hummocks spreading and moving apart as the avalanche spreads. They can also move together or compress, or new ridge-like hummocks can form due to avalanche constriction by topography. The morphology and spatial distribution of hummocks are dependent on the interplay of the number density of normal, thrust and strike-slip faults, which is a function of strain and material properties such as cohesion and the nature of a ductile sliding layer. Hummock shape and size depends first on the original position in the initial landslide and the first-formed structures. The hummock shape changes with subsequent spreading, break-up or merger. During landsliding, hummocks can break up, resulting in higher number density, on the other hand hummock merger during compression can reduce number density. At the last stages of emplacement, hummocks can either break or remain intact while spreading farther apart from each other, and can themselves spread, increasing their surface area. The structures within avalanche deposits and hummocks indicate that they form by extension and are consistent with a general slide model where pure shear stretching dominates in the upper brittle part and simple shear is concentrated at the base. When hummocks and fault-like features are not formed, a more fluidal flow type of emplacement could be possible.

Lastly, we call primary hummocks in large landslides and avalanches, type 1, that can be divided into two main groups: The type 1a small hummocks, which are generally found toward the front, and type 1b large hummocks that are initially formed from the initial landslide toereva blocks, and are found in the proximal and medial zones. Type 1b hummocks can also form by coalescence during compressive or arrest stages.

The type 2 hummocks are secondary features formed by a boudinage-like process during layer parallel stretching. They can exist on or around the type 1 hummocks, and are generally seen as single blocks of more consolidated material.

Avalanches that spread freely have large numbers of small type 1a and few large type 1b hummocks. Avalanches that become constrained tend to preserve the larger type 1b and tend to have accompanying type 2 secondary

ones. The analogue models presented here allow the visualization of the development of landslide-avalanche hummocks and provide a structural and kinematic sequence of their formation. This can then be used to understand natural avalanche hummock structure and distribution, and thus obtain the emplacement history. Hummocks are a useful tool for understanding avalanche emplacement.

CHAPTER 4

# The anatomy of avalanche hummocks

---

## 4.1 Abstract

Hummocks are topographic features of large landslides, rockslide-debris avalanches formed as the mass in motion slides, spreads, and break up. Hummocks are found in many landslides and avalanches especially on volcanic ones. Hummock size, shape, and spatial distribution vary between and within deposits. Brittle faulting in the main moving mass forms hummocks. Such a universal structure, which has such clear variations to the deformation process, should provide information on landslide emplacement conditions. We study well-preserved and well-sectioned hummocks in the Iriga rockslide-debris avalanches (Philippines), to characterise the internal hummock structure and relate hummocks to the landslide-avalanche behaviour. The hummocks initiated from an initial landslide masses by extensional strike-slip faulting and evolved by progressive spreading. Once formed, hummocks remain as discrete entities that spread by extensional faulting. In hummocks, the upper and outer surface is destabilised by minor slumps, and scree formation that form a rubbly carapace. The central parts of a hummock are dissected by high angle normal faults that descend into listric shear zones as they merge into a low angle shear zones in the landslide basal slide zone. In the upper part of hummocks, second-order smaller hummocks can form when the layers parallel to the thinning boudinage generates blocks. The type of stretch structure depends on lithology and coherent interface (generally lava flows) or incoherent interface (like ignimbrite blocks). The study shows that hummock size distribution is not related to distance but could be related to lithology, initial position, and avalanche kinematics. In conclusion, hummocks do not provide clear evidence of fragmentation during transport, as they are the intact blocks survivors, but do provide information on the transport conditions and initial composition of the landslide.

Keywords: Hummocks, Debris Avalanches, Large Landslides, Faults, Iriga volcano

## 4.2 Introduction

Hummocks are structural features that are related to strain and the particular deformation regime in landslides and debris avalanche deposits (DAD). Hummocks are remains of initial failure blocks that slide, tilt, and rotate down a slope. They stand prominent above the rest of the deposit and are found spread all over the debris fields with both the collapse scar and depositional zones. Hummock cuts expose the internal structure of debris avalanches preserved after its final depositional stage.

### 4.2.1 Hummock Interpretations

Hummocks, hillocks, toma or cresta and molards all refer to debris cones or mounds described in several non-volcanic and volcanic debris avalanches with or without associated magmatic (Bezymianny-type) and phreatic (Bandai-type) eruptions. They are also present on debris flows as in Osceola Mudflow (Vallance and Scott, 1997), Teteltzingo deposit (Carrasco-Núñez, 1993), and the Pilcaya debris-flow deposit (Capra and Macías, 2000). DAD have a distinct, irregular, hummocky, small depression topography with longitudinal and transverse ridges commonly prominent (Glicken, 1982; Siebert, 1984). Most hummocks are made up of brecciated segments of the former failure area and make up a facies called avalanche block facies (Crandell et al., 1984; Mimura and Kawachi, 1981; Siebert et al., 1987). An opposing matrix facies generally constitutes the inter-hummocks area.

Hummocks have been described and interpreted in various situations. The peculiar conical mounds of loose rocks in the 1903 Frank slide deposit were said to represent the relicts of debris ridges partly destroyed by flying rocks (McConnell and Brock, 1904). The “little Fujiyamas” on the Mageik slide from Novarupta, Alaska were interpreted as a result of in place fragmentation of large boulders (Griggs, 1920). In the 1881 Elm slide deposit, Switzerland, Heim (1932) suggested that hummocks form when the slide mass thinned out as it entered the wider part of the valley forming the mounds by dilation. Goguel and A (1972) and Mollard and Janes (1984) refer the debris cones and conical mounds of broken slide rock deposited along the typically lobate margin of rock avalanche spoil debris in the French Alps as molards.

Toma, the term used for the hills in Tamins rockslide by Abele (1974) or Cresta hills, for the Flims rockslide deposit were interpreted to be in-situ outcropping basement by Heim (1981). However, studies by Cadisch (1944); Nabholz (1954); Pavoni (1968); Remenyik (1959) and (Scheller, 1970) suggested that these mounds of intensively crushed materials with preserved sedimentary structures (von Poschinger and Kippel, 2009) have no connection with the underlying rocks but are distinct elements within the gravel mass.

Laboratory experiments by Cassie et al. (1988) suggest that molards form when cohesionless soil with a certain percentage of fines are vibrated causing particle segregation. Coarser particles are then expelled from the top forming rounded mounds. The radially aligned hummocks in debris avalanche deposits are proposed to be remnants of longitudinal ridges (Dufresne and Davies, 2009).

A continuum of hummock morphologies include: hummocks when the length to height (L/H) ratio is less than or equal to 10, ridges if greater than 10 and flow bands if L/H is in hundreds (Dufresne and Davies, 2009).

Andrade and van Wyk de Vries (2010) proposed that hummocks dissected by faults with deformation at the scale of grains create the longitudinal ridges and shear bands. Paguican et al. (2011) suggest that hummocks, avalanches, and large landslides evolve in the same way. They start with fracturing and normal faulting of the edifice for avalanches, and edifice blocks for hummocks. Extension forces the upper brittle layer to split, stretching and dropping a block relative to its adjacent blocks, forming the horst and graben structures during landslide spreading.

### 4.2.2 Hummock Types

Analogue modelling of flank avalanches by (previous chapter of this thesis) resulted in three types of hummocks in large landslides and avalanches: the primary small and more or less equant Type 1a hummocks; the primary elongated and larger Type 1b hummocks; and the secondary small hummocks that raft over and in between Type 2 hummocks. Vertical cuts of the models revealed high angle normal faults that accommodate the sliding, tilting and rotation of edifice blocks as it spreads down the analogue volcano forming the primary small (Type 1a) and large (Type 1b) hummocks. Sharp discontinuities and decollement on the upper most part of the analogue deposits also show low angle normal faults that accommodates the sliding over of the uppermost layer on the relatively more rigid layer underneath it on the brittle part of the deposit forming the Type 2 hummocks. In this case, the decollement may not be a fault as it is a pre-existing discontinuity between layers. On the other hand, it could be a fault resulting from a large-magnitude extension accommodating the rotational movement of the upper layer.

### 4.2.3 Iriga volcano and her DADs

One of the best places to study the inside and surface of hummocks for their geometry, structure, and deformation is at Iriga volcano (Philippines). It is a volcano in the southeast northern island of Luzon that stands partly on substrata weak enough to spread on opposite sides of the volcano. Both of the DAD at Iriga volcano are well preserved but also erosion and human excavation are extensive, exposing hummock anatomy.

Iriga DAD1 on the southwest and Buhi DAD2 on the southeast flanks originate from sectors oblique to the strike of the main active strike-slip basement (Fig. 4.1). The older Iriga DAD1 was caused by gravitational spreading and movement of the underlying fault that created major sub-horizontal thrust faults at the base of the edifice progressively pushing and extruded the substratum outwards, creating a weak surface and by an equally important

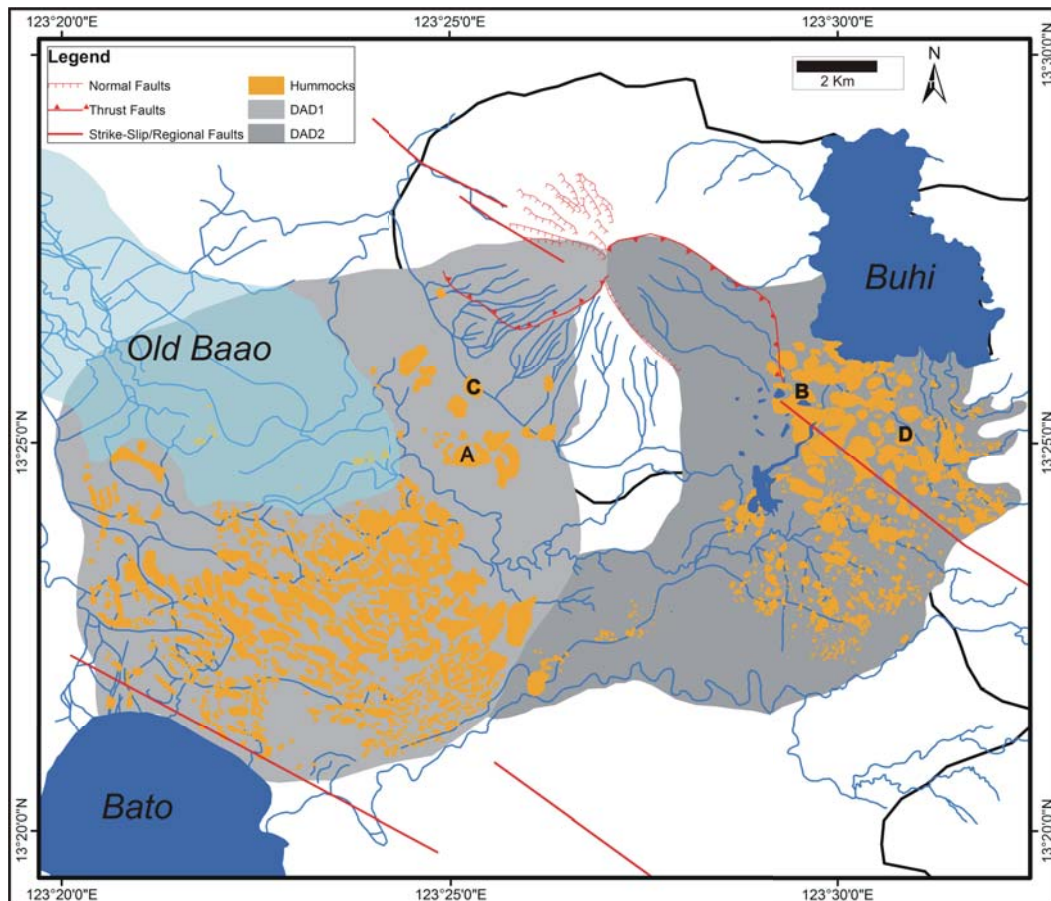


Figure 4.1: Iriga Volcano and her two DADs (Paguican et al., 2011) and the location of featured hummocks. In red polylines are the structures that caused and resulted from the edifice collapses. In blue are the water bodies that have significant roles in the development and emplacement of the avalanches and their hummocks: Iriga river system; and Lakes Old Baao and Bato for DAD1 (yellow polygon) on the southwest and Lake Buhi for DAD2 (green polygon) on the southeast. Locations of the hummocks are shown as A for Lady Backhoe (Fig. 4.4); B for Captain's Slide (Fig. 4.5); C for the Lava Topping (Fig. 4.6); and D for the ignimbrite Topping (Fig. 4.7).

faulting at its base. This regional basement faults also caused the younger Buhi DAD2. Most probably, the conditions for the two collapses are related to progressive deformation of the edifice by the underlying fault, associated with gravity spreading into the basin. Tectonic or volcanic seismicity may have triggered both of the collapses (Paguican et al., 2011). Iriga DAD1 spread freely over a water-saturated area dominated by fine alluvial and lacustrine sediments, leading to bulking and significant bulldozing. Iriga DAD1 hummocks are composed of clay-rich sediments, conglomerates, and sands. Buhi DAD2, on the other hand was confined and deflected by 8 km towards the west by the Malinao edifice and had an important proportion of ignimbrite incorporated in the failure base. Both DAD are useful in studying avalanches and large landslides created by faults underlying volcanoes. Hummocks in both DADs are similar but contrast in some aspects and characteristics making them a good place to study hummocks of different causal, transportation and emplacement mechanism travelling on different sliding surfaces (Paguican et al., 2011).

#### 4.2.4 Objectives

This study describes the anatomy of hummocks at Iriga DAD1 and Buhi DAD2. And unveil the record of information on the transport conditions and initial composition, and emplacement and causal mechanism of large slides.

### 4.3 Methodology

Fieldwork was carried out around the Iriga volcano DAD where quarries allowed us to study the lithology and structure within the hummocks. Select type hummocks are presented here to describe internal structures. We use remote sensing, aerial photograph interpretation and digital elevation analysis, and GIS to supplement our over-all description on the morphology (size, shape and distribution) and spatial distribution of the hummocks. Exploratory and spatial distribution statistics were done for Iriga and compared to those of analogue models.

### 4.4 Results

We characterise hummocks at Iriga volcano according to their basal shape, surface morphology, and elongation with respect to flow direction (Fig. 4.1). Hummocks of Iriga DAD1 have mostly an elongated base as opposed to those

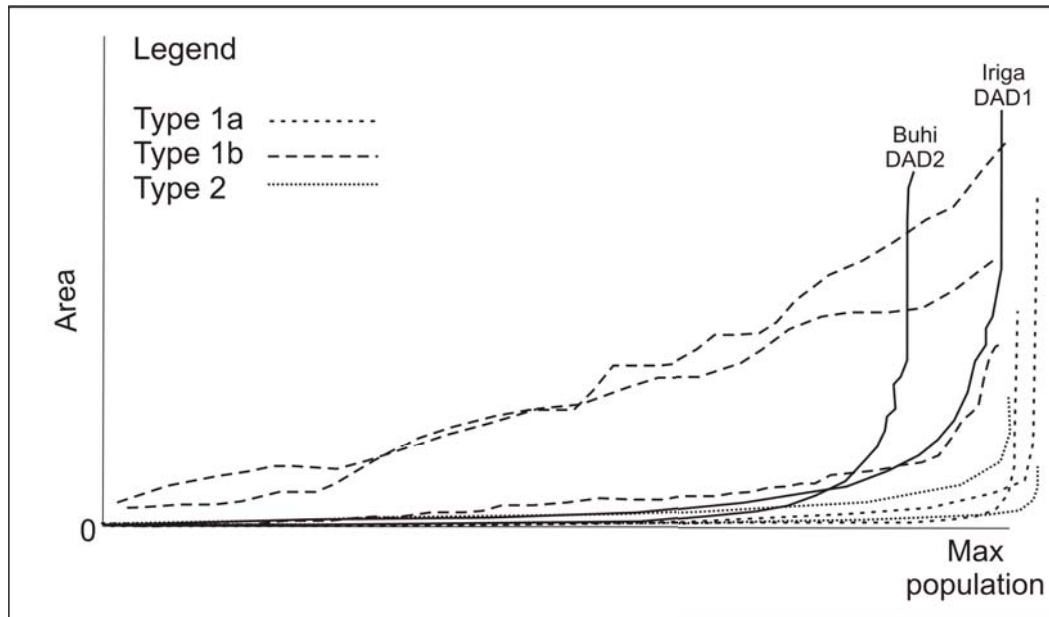


Figure 4.2: Increasing size plot of Iriga DAD1, Buhi DAD2 and analogue avalanche hummocks (previous chapter of this thesis).

of Buhi DAD2, which have the circular base. Based on the hummock elongation direction, those in DAD1 are dominantly perpendicular to flow direction while those in DAD2 dominantly flow parallel except near the deposit edges where the hummocks are randomly oriented. Probably as an effect of DAD2 deflection as it reached the Malinao edifice.

#### 4.4.1 Hummock Exploration and Accounting

A line graph of increasing hummock size for Iriga DAD1 and Buhi DAD2 (Fig. 4.2) yields a pattern that goes well with those plots of analogue hummock models. Iriga DAD1 is dominated by the larger Type 1b hummocks. They are big (several 100s m), and elongated, with relatively gently sloped line plot compared to Buhi DAD2. On the other hand, Buhi DAD2 has characteristics of the small either Type 1a or Type 2 and large Type 1b hummocks. The plot shows a relatively steeper line showing an abrupt change from having a lot of small hummocks to very few big hummocks. Buhi DAD2 has a high number of small hummocks. Most of these are those ignimbrite-cored, secondary hummocks (Type 2) and a few primary large hummocks (Type 1b) especially in the proximal and medial depositional zones.

Plotting the size of hummocks (y) against their distance from the source

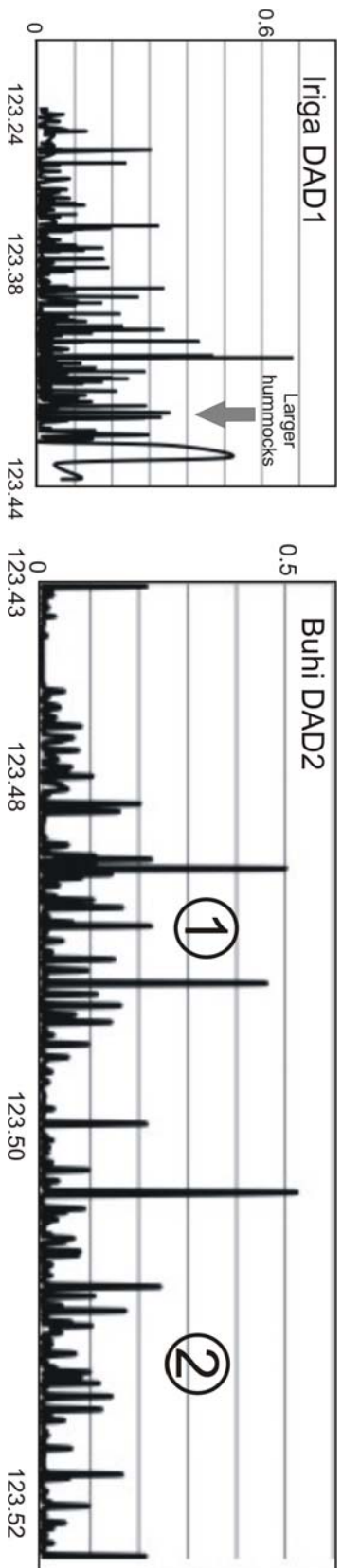


Figure 4.3: Spatial Distribution of Iriaga DAD1 and Buhi DAD2 Hummocks showing the change of hummock size ( $y$ ) with respect to its longitudinal location as distance from source ( $x$ ). Iriaga DAD1 has larger hummocks in the distal area while Buhi DAD2 has big hummocks in the proximal and medial depositional zones and another group in the distal area.

(x) (Fig. 4.3) shows that the Iriga DAD1 has its larger hummocks in the distal depositional zone just like in the potting of Type 1b hummocks D while Buhi DAD2 has 2 groups of large hummocks. This means that during the evolution of the older debris avalanche at Iriga, these large Type 1b hummocks may have formed at the distal area of the depositional zone due to some late-stage compression probably as the travelling debris meets with the higher elevation of the southwest boundary of the Polangui-Oas Mountains that served as a topographic barrier. In the case of Buhi DAD2, there are two areas with big hummocks. The first group is the group that contains the torevia blocks and primary, large hummocks that is breaking up as the avalanche spreads and the second group at the distal area might be representing the group that is due to confinement by the Malinao edifice as a topographic barrier.

#### 4.4.2 Field Description

Hummocks are quarried at Iriga DAD1 and Buhi DAD2 exposing the internal structures of both debris avalanche deposits. Structural and lithologic layer sequence mapping and detailed description of some chosen hummocks is presented here.

##### 4.4.2.1 CASE 1: Lady Backhoe's Hummock Faulting (Type 1b Hummock; Fig. 4.4, 4.8A)

A quarry in the proximal area of Iriga DAD1 (Pt. A, Fig. 4.1) deposition zone exposes a complete cross-section of a hummock. There is an overlying mantle of post-avalanche scoria and tephra, and a soil layer. The hummock is composed of alternating conglomerate and sand on top of clay and sand layers (Fig. 4.4A, 4.4C) at the base. The upper conglomerate beds are displaced by listric normal faults. These faults become less steeply dipping from the centre towards the edges of the hummock. The faults are composed of narrow shear zones that broaden into diffuse shear zones as they pass into the more clayey lower layer (Fig. 4.4D). Faults also penetrate up to the basal clay-rich layer of the avalanche hummock (Fig. 4.4E-F) showing a continuous deformation even under the shear zone shown in Figure 4.4D. The Lady Backhoe hummock is elongated and densely faulted but not dense enough to cause external destabilisation and scree formation at its base (Fig. 4.8A).

##### 4.4.2.2 CASE 2: Captain's Slide: A hummock break-up (Type 1a Hummock; Fig. 4.5, 4.8B)

Captain's Slide hummock (Fig. 4.5) is in the DAD2 proximal deposition zone (Pt. B, Fig. 4.1). A part of the hummock has slid putting the lives and

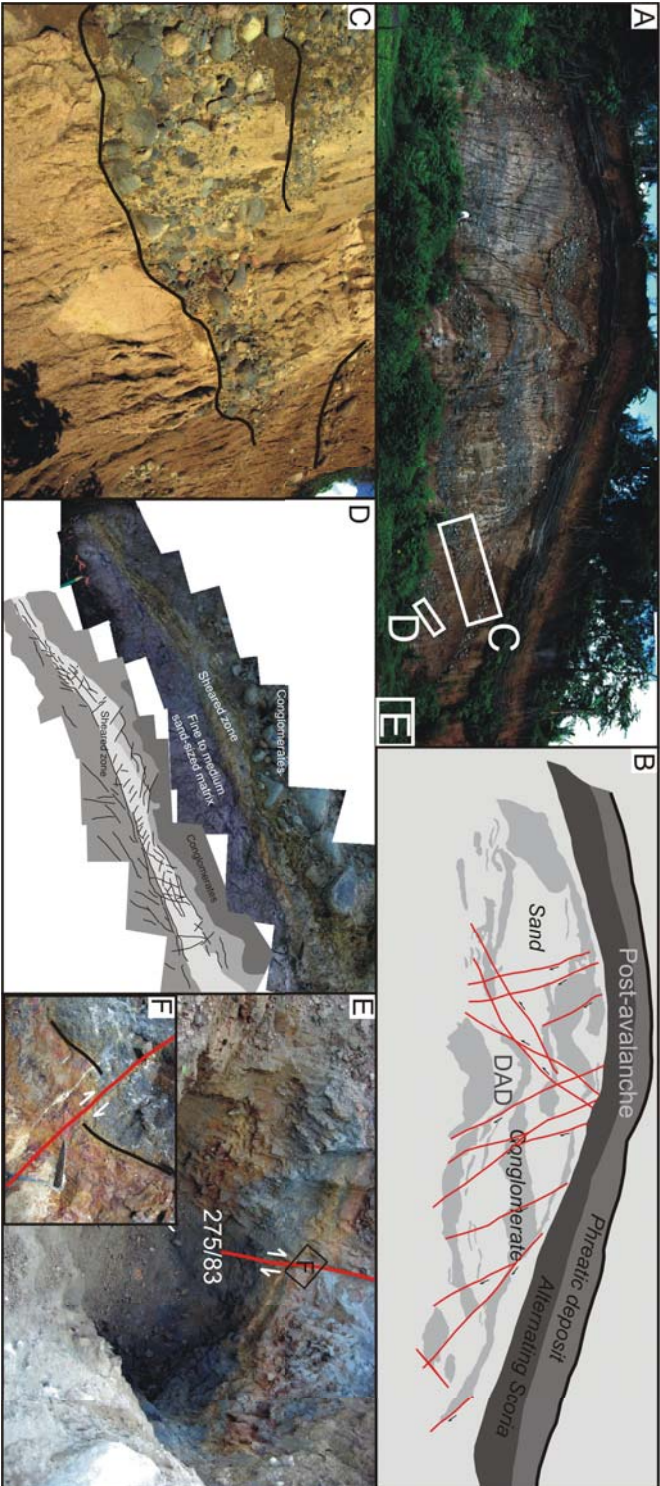


Figure 4.4: The Lady Backhoe's Hummock Faulting (proximal depositional zone, DAD1). **A** is the hummock's vertical cut showing displaced layers of cobbles and sand-sized deposits by the normal faults. Locations of **C**, **D**, and **E** are in white boxes. **B** is a sketch of the internal layers and faults (red polylines) of this hummock. **C** shows the orientation of cobbles as it was originally deposited prior to the avalanche that remobilized them. **D** is a low angle shear zone. It shows the interface between the upper brittle layer and the lower ductile layer of DAD1. **E** is the basal ductile layer of DAD1. It shows that there is continuous deformation under the shear zone shown in **D** and therefore, faults penetrate up to the ductile layer of an avalanche. **F** shows the slickenside in the ductile layer drawn in box **E**.

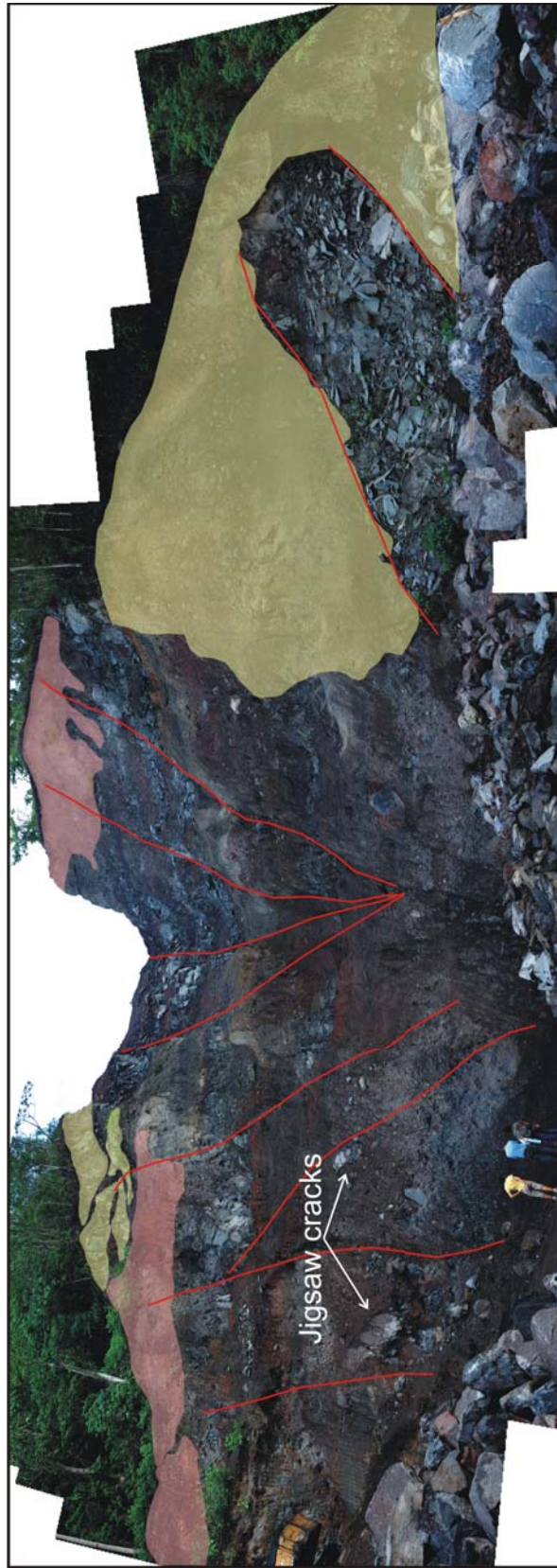


Figure 4.5: The Captain's Slide Hummock (proximal depositional zone, DAD2) showing how normal faults can cause a hummock to break up. In red polylines are some normal faults dissecting the hummock. Movement by extension, sliding for example along these faults, cause the hummock to break up and evolve into smaller hummocks. A hummock is still unstable after its emplacement because of these normal faults.

properties of people living around it at risk of rock falls that they decided to quarry the whole hummock. The ongoing quarry exposes the internal layers and structures of the hummock. The hummock is of displaced layers of jointed lava at the bottom, and displaced alternating layers of lava with auto-brecciated sub-layers, and scoria layers at the top. Like in Lady Backhoe's hummock, numerous normal faults dissect these layers. The more steeply dipping are at the centre and becomes less steeply dipping at the edge. At the edges, slumped layers of brecciated lava are observed (Fig. 4.5 in yellow polygon). This loose and angular lava material may have been caused by extension along the outer normal faults causing them to slide down. The brecciation of lava with observed jigsaw cracks within lava blocks included in the DAD indicate that brecciation and collision happened both at initiation and during transport although, not producing a turbulent flow because the original layering of the volcano edifice has been preserved but displaced by local faults. This hummock shows that normal faults within hummocks can destabilise and cause hummock block break-ups by minor slumping and scree formation on its upper and outer surface (Fig. 4.8B).

#### **4.4.2.3 CASE 3: The Lava Topping (Type 2 Hummock on a coherent interface; Fig. 4.6, 4.8C)**

The Lava Topping hummock is in the lower collapse zone of DAD1 (Pt. C, Fig. 4.1). It is made up of brecciated lava blocks at the top and block and ash layer at the bottom. In this exposure, low angle normal faults are delineated on the upper part of the block and ash layer that may have accommodated the relative movement and stretching of the lavas on top. The stretched lava is considered as a Type 2 hummock on top of the block and ash layer. The boundary between these two layers shows a coherent interface between the stretched lavas on top and faulted block and ash layer below (Fig. 4.8C). The presence of brecciated lava with impact marks and the absence of jigsaw cracks at least in the upper brecciated lava layer, indicate brecciation at the initiation of the landslide and a non-turbulent flow during transport.

#### **4.4.2.4 CASE 4: The Ignimbrite-Topping (Type 2 Hummock on an incoherent interface; Fig. 4.7, 4.8D)**

This hummock exposes the upper three lithologies of the DAD2 medial zone (Pt. D, Fig. 4.1): a block and ash unit with some parts laharic reworking towards the base; and two thick pumice-rich ignimbrite deposits. There is a first grey deposit, and a second cream-coloured one that entrains blocks of the grey ignimbrite. Both have elongated and flattened soil and clay clasts

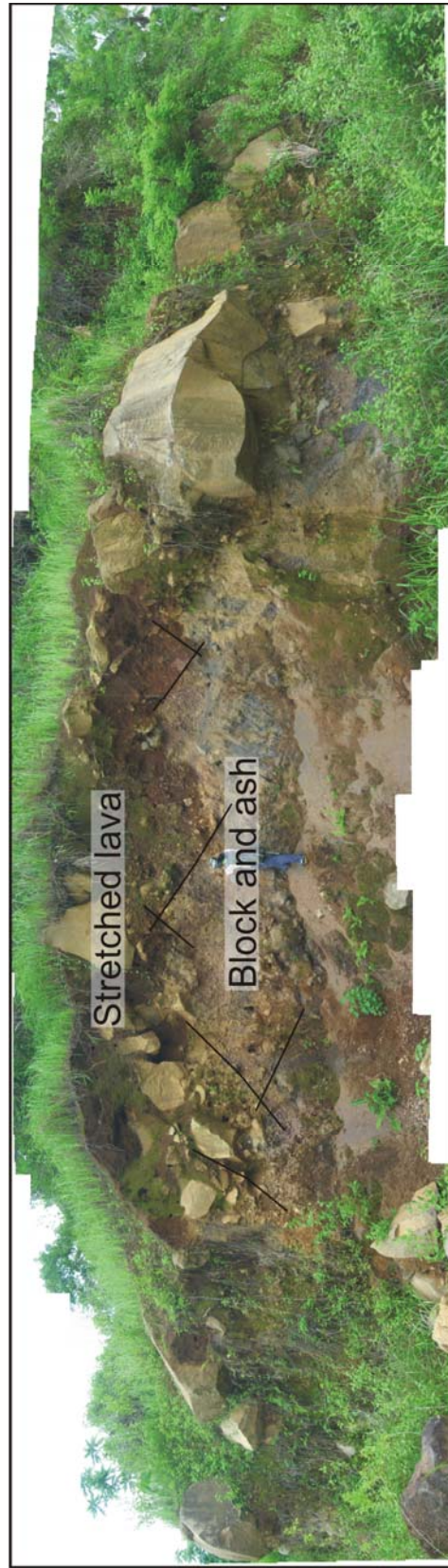


Figure 4.6: The Lava Topping hummock (lower collapse zone, DAD1) shows a coherent interface between the stretched lavas on top and faulted block and ash layer below. These low angle normal faults in black polylines in the block and ash layer accommodated the relative movement of the lavas on top. Here, the stretched lava is considered as a Type 2 hummock floating on top of the block and ash layer.

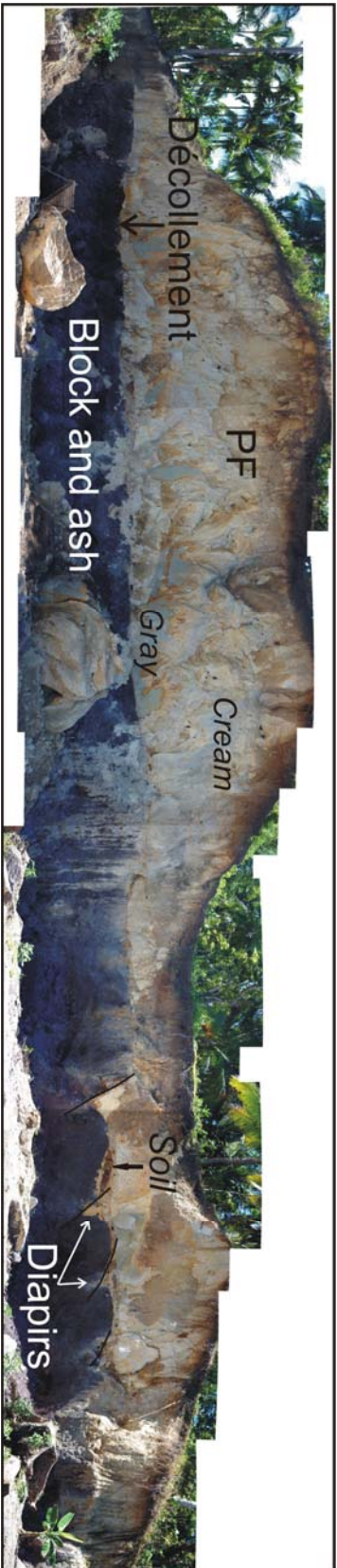


Figure 4.7: The ignimbrite Topping hummock (medial depositional zone, DAD2) shows an incoherent interface between the upper pyroclastic flow deposit layer and the underlying block and ash layer. Extension is by the sliding movement of the overlying deposit. The overlying ignimbrite layer is a Type 2 hummock gliding over the block and ash layer of the DAD during the avalanche.

parallel to the depositional plane. These ignimbrite layers are also found on the plains all around the volcano and on the debris field. In some places, they are exposed as small, rounded hummocks a meter high. The overlying ignimbrite layer is a Type 2 hummock gliding over the block and ash layer of the DAD during the avalanche (Fig. 4.8D). The hummock is cut through by a quarry, an incoherent interface, a very sharp contact at very low-angle, almost horizontal between the ignimbrite and the underlying block and ash deposit is seen. Diapir structures exist at points where the two layers are displaced by faults. This decollement is considered as a low-angle normal fault if sliding at the base of the upper ignimbrite layer is a large-magnitude extension accommodating rotational movement of the upper layer. However, the sharp boundary between two layers may not be a low angle normal fault if it is a pre-existing discontinuity between layers allowing the upper layer to glide over the lower layer.

## 4.5 Discussion

Hummocks are made of slid, tilted or rotated edifice blocks containing the displaced original layers of the collapsed failure zone. The normal faults within hummocks cause the displacement of hummock layers leading to hummock break-up and spreading (Fig. 4.8A-B) or destabilisation causing the outer and top layer to slide and slump down and form scree deposits at the bottom. As the density of faulting increases, a more pointed and smaller hummocks form. On the other hand, lesser faulting can cause minor breaking up and less destabilised elongated or bigger hummocks (Fig. 4.8A-B). The different lithologies within hummocks are separated by either a coherent or incoherent boundaries (Fig. 4.8C-D). These boundaries accommodate the sliding, tilting and rotation of the blocks in an avalanche forming the primary hummocks. They also accommodate the extension and spreading of the top most brittle part of a hummock and of the avalanche upper brittle layer that forms the secondary hummocks. The incoherent boundary between the upper and lower layers that allows for a gliding of the upper layer may or may not be a normal fault. The discontinuity is a normal fault if it is a result of large displacement during extension. However, it may not be a fault if it is a pre-existing boundary between the two layers. Hummocks are formed by extension and spreading of collapsed edifice during the avalanche. Compression happens only when the avalanche is confined by a topographic barrier such as in Buhi DAD2 or when it enters a body of water such as in Iriga DAD1. The type of edifice materials, and the density of existing structures that dissects and destabilises the entire hummock control the size, shape, and morphology of

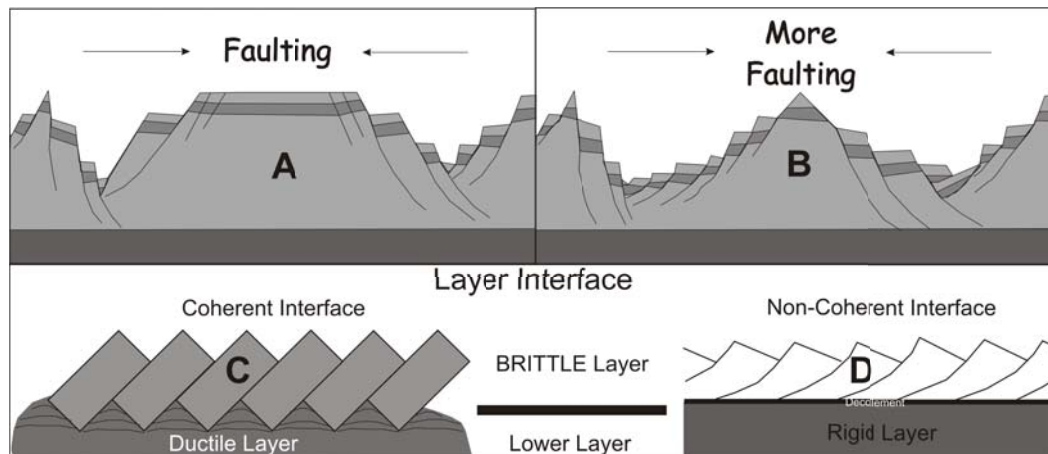


Figure 4.8: The Anatomy of a Hummock. **A** (Case 1, The Lady Backhoe Hummock) and **B** (Case 2, The Captain's Slide Hummock) shows how hummocks evolve from bigger blocks into smaller hummocks and how a primary hummock can be destabilised by increasing fault density and extension during sliding and spreading. **C** (Case 3, The Lava Topping Hummock) and **D** (Case 4, The ignimbrite Topping Hummock) show the types of interface that may exist between the layer boundaries. So far, we only know that non-coherent interface exists in the avalanche (as shown by Hummock 1: The Lady Backhoe) but both can exist for the boundary between a Type 1a or 1b hummocks and a Type 2 hummock (as shown by Hummocks 3 and 4: The Lava Topping and The ignimbrite Topping).

avalanches. Its elongation is dependent on whether there is a uniform extensional forces acting on the hummocks, forming the more rounded-based hummocks such as in Buhi DAD2 or if an avalanche extension is slower in one direction probably by waning extension or compression, and a stronger and lubricated extension on the other direction resulting in elongated hummocks such as in Iriga DAD1.

## 4.6 Conclusions

In conclusion, the internal structures that accommodate the sliding, tilting, and rotation of edifice blocks in avalanches are the same subsurface structures in hummocks only at a more localized level. The normal faults in the hummocks, like in the avalanche are high angle in the upper brittle layer that broadens into shear zone towards the base. They become less steeply dipping from the centre of the hummock towards the edges. If extension is strong

---

enough in these faults, stability occurs by slumping forming scree at the top and outer surface or cause the layers to split apart, dropping parts of the block leading to hummock break-up and thus, in these case hummock gets smaller. Type 2 hummocks indeed, occur in nature, such as stretch lava block layer in Iriga DAD1 and the ignimbrite layer of Buhi DAD2. In an avalanche, the formation of hummock Type 1a and Type 1b is by an incoherent interface, having listric normal faults that accommodate the stretching and spreading of the edifice. Within an avalanche, however, a Type 2 hummock results from either a coherent such as in Lava Topping hummock or incoherent interface as in ignimbrite Topping hummock of two layers with varying lithology in the upper most part of the brittle layer of an avalanche. All these hummock internal structures all point down to hummock being evidence to the idea that avalanches form by extension. And that hummock develops from extension during an avalanche when the deposit forms horst and graben structures.



CHAPTER 5

**The development of structures  
in analogue and natural debris  
avalanches and large landslides**

---

## 5.1 Abstract

All types of landslides and rockslide-debris avalanches present a plethora of internal structures that are also well observed on the surface. Many of the surface features are interpretable as faults and folds that can be used to determine deformation history and kinematics of emplacement. We present two sets of simple ramp-slide experiments of reduced basal friction laboratory rockslides, equivalent to a highly deformed simple shear layer, with plug-flow. We call these analogue slides. The experiments used a curved ramp where materials accelerate until reaching a gently-sloped depositional surface and a constantly inclined straight ramp with a more regular slope and longer slides. We use a detailed description of structures, their sequential formation, and deposit morphology to investigate the transport type and deformation chronology from slide initiation to final stop. Results using a curved ramp show accumulation and thickening where the slope decreases. The thickened mass then further remobilises and advances by secondary collapse of the thickened mass. Such a stop-start process may be important in many mountainous avalanches where there are rapid changes in slope. We observed that frontal accumulation is produced during flow as materials at the front move slower relative to those in the medial and proximal zones and helps maintain a thicker mass that flow further. When the front destabilizes, secondary collapse happens. On a constantly inclined straight ramp, analogue slides show continued extension by horst and graben structures forming a rib-and-ridge morphology and transtensional grabens. Strike-slip shearing at the levees and sets of compression and extension structures in the middle are observed in both set-ups.

We compare the analogue slides kinematics and dynamics to the natural examples. The 2006 Guinsaugon rockslide debris avalanche (Philippines), the 2010 Mt Meager rockslide debris avalanche (Canada), and Storegga Slide (Norwegian margin) and find that frontal accumulation and secondary avalanching, and spreading by progressive mass failure occurs. The failure surface morphology can influence the emplacement mechanism, morphology, and runout of large landslides and avalanches.

Keywords Avalanches, landslides, analogue models, secondary slides, retrogressive mass failure, Guinsaugon (Southern Leyte, Philippines), Mt Meager (British Columbia, Canada), Storegga Slide (Norway)

## 5.2 Introduction

Analogue models recreating natural systems at laboratory scale (Merle and Borgia, 1996; Ramberg, 1981) are important for understanding natural phe-

nomena and have been used in geology to study structural and tectonic features. In rockslide avalanches, however, some studies have explored on the morphology, structures, and internal distribution of stratified material (e.g. [Andrade and van Wyk de Vries, 2010](#); [Shea and van Wyk de Vries, 2008](#)).

Most ramps use different shapes and dimensions with various granular materials to study the transport physics and emplacement dynamics numerically directly ([Kelfoun and Druitt, 2005](#)) or indirectly ([Campbell, 1989](#); [Campbell et al., 1995](#); [Pouliquen and Renaut, 1996](#); [Staron et al., 2001](#)).

[Andrade and van Wyk de Vries \(2010\)](#) looked at the structures associated with toreva formation and its subsequent break up. Torevas are formed by: (1) Sliding initiated by fracturing of the volcanic flank; (2) formation of collapse structure, a trapezoidal block bounded by an undisturbed sliding block front but high fracturing at the back; (3) progressive sliding and thinning of mega blocks creating more collapse structures; (4) formation of horsts lined by two antithetic normal faults forming trapezoidal blocks where further fracturing can result into pyramidal blocks; (5) deceleration and arrival of toreva blocks on low-angle surface forming smaller hummock that undergo intense closely-spaced normal faulting in the direction of sliding.

[Shea and van Wyk de Vries \(2008\)](#) examined the morphology and structures of 13 natural rockslide avalanche deposits and made simple and well-constrained experiments of reduced basal friction and low runout that focus on the formation of deposit structures and morphology to investigate the transport type and deformation chronology of the upper brittle layer. Variations in the sliding surface curvature, lateral profile, roughness, and material cohesion can reproduce the majority of rockslide-avalanche deposit features. They also proposed a fourfold avalanche classification based on the texture: (1) hummocky due to cohesion differences of initial layering or (2) non-hummocky or ridged for homogeneous material, and kinematics: (3) dominantly extensional or (4) dominantly compressional. A brittle plug-flow model or basal slide-dominated model where spreading by pure shear, and faulting fits both the natural and model rockslide avalanches.

This work presents and describes the structures and morphological features observed in the two sets of analogue experiments and three natural avalanches and large landslides including the 2006 Guinsaigon rockslide avalanche (Philippines), the 2010 Mt Meager rockslide debris avalanche (Canada), and Storegga Slide (Norwegian margin) through structural maps interpreted from remotely sensed images and existing literatures. The experiments concentrate on the detailed description, formation chronology, and evolution of observed structural and morphological characteristics to gain insights into the transport type and deformation history in the natural prototypes. This structural to dynamics approach has been used in tectonic and volcano-tectonic analogue

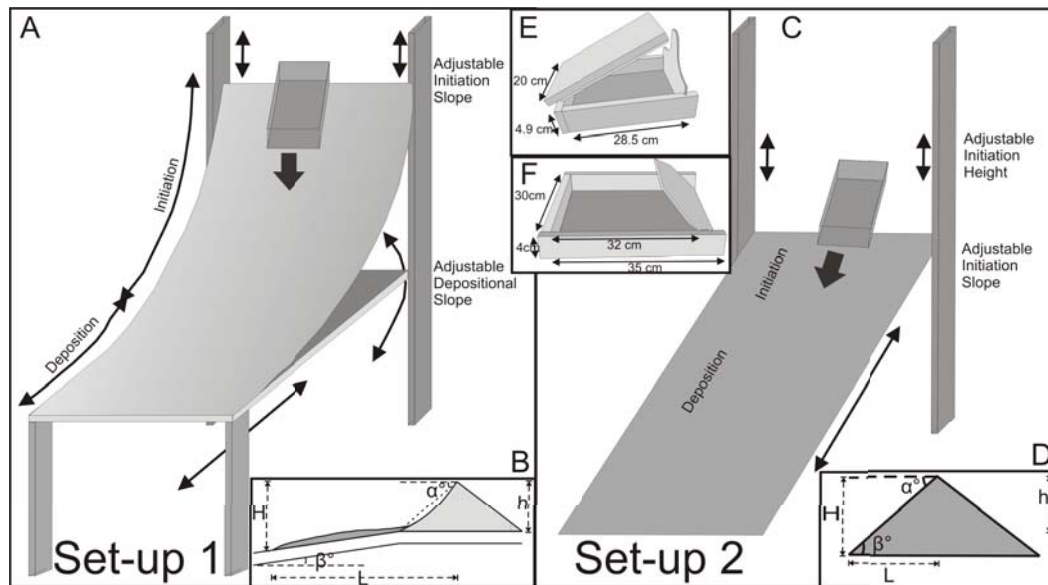


Figure 5.1: Analogue slides set-up. A, B Curved Ramp configuration for Set 1: the initiation and deposition slopes can be varied. C, D Inclined Straight Ramp configuration for Set 2: both the initiation,  $\alpha$  and deposition slopes,  $\beta$  can be changed with height of initiation. E Source Box 1 with a simpler geometry. F Source Box 2 with inclined trapdoor and open lid.

models for a long time (Merle and Borgia, 1996; Shea and van Wyk de Vries, 2008).

### 5.3 Model Set-up

Models must represent the failure, transport, and emplacement plane. Failure occurs on a surface slope that is above or equal to the basal friction angle of the sliding material. The dynamics of the natural basal layer is still not completely understood and is simulated by a low-friction surface of the polished steep ramp.

This study uses the experimental set-up of Shea and van Wyk de Vries (2008) built with flexible 2 mm thick, 150 cm wide, and 300 cm long aluminium sheet (Fig. 5.1). In contrast to the pure sand used previously, we use powder-size ( $< 100 \mu\text{m}$ ) and coloured sand-size spherical glass beads for Set 1 and Set 2, respectively. Unlike sand, this material is sensitive to several factors such as electrostatic interactions and humidity, which introduce a small cohesion and allow for the formation of surface fault scarps. The aluminium sheet has relatively low basal friction angle and does not induce electrostatic interactions

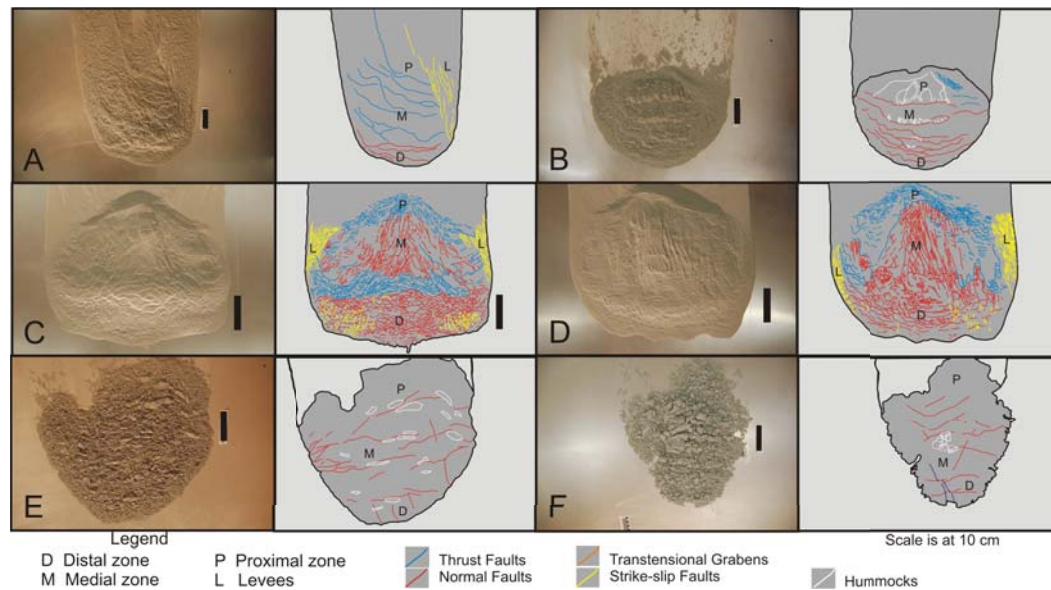


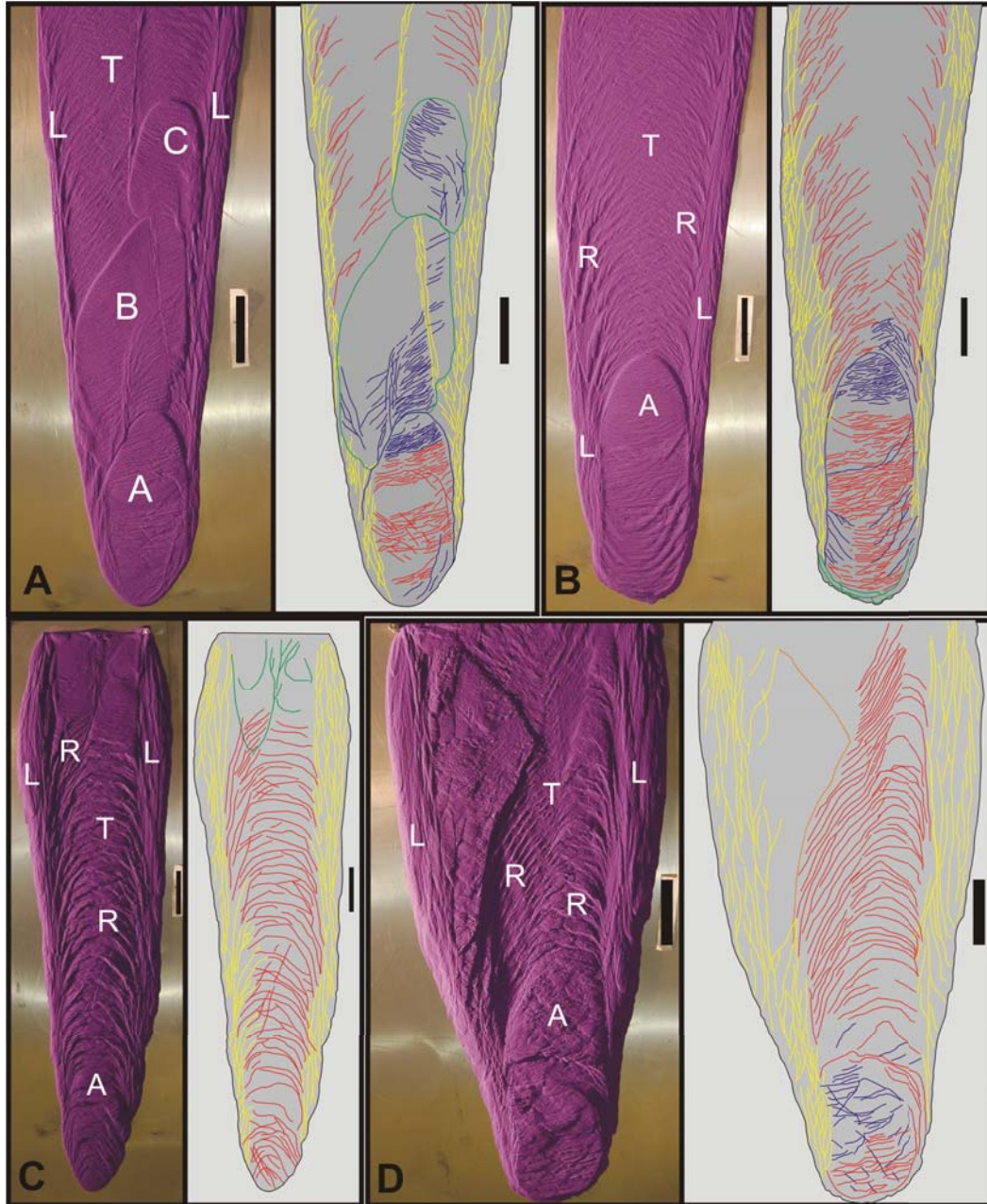
Figure 5.2: Set 1: Curved ramp analogue avalanches using the powder-size glass beads. Source slopes are at  $35^\circ$ ,  $45^\circ$ , and  $55^\circ$ ; deposition slopes are at  $0^\circ$ ,  $10^\circ$ , and  $18^\circ$ ; and volume of glass beads at  $1000$  and  $2000 \text{ cm}^3$

with the sliding material, replicating the equivalent of highly deformed simple shear basal layer in a plug-flow-type configuration (Shea and van Wyk de Vries, 2008).

There are two sets of analogue slides: Set 1 is on a curved ramp (Fig. 5.2, Appendix D) where materials accelerate until they reach a gently sloped depositional surface; and Set 2 on constantly inclined straight ramp (Fig. 5.3, Appendix D) with a more regular slope. Two source boxes of different volumes and dimensions are used: Box 1 (Fig. 5.1E) of simple geometry for better tracking of deformation with straight trapdoor and a compressive lid tightly closed and tied to the lower part, and Box 2 (Fig. 5.1F) with inclined trapdoor and open lid.

## 5.4 Scaling

Geometric and dynamic parameters must be scaled to guarantee maximum similarity between reality and laboratory analogue models. This allows determination of the conditions necessary to ensure proportional correspondence between forces acting in nature and those acting in laboratory environment (Ramberg, 1981). Accordingly, 12 dimensionless numbers serve to compare dynamic and geometric features in both nature and laboratory.



Most physical quantities can be expressed with the primary dimensions of length [L], mass [M] and time [T], except for those that are dimensionless and do not require unit specifications. The following three groups affect the system (Table 5.1):

1. Variables related to the deposit geometry and sliding environment: horizontal runout  $L$ , deposit thickness  $e$ , area  $A$ , width  $W$ , total fall height  $H$ , fall height from source to beginning of depositional surface  $h$ , the failure surface average slope  $\alpha$ , the depositional surface average slope  $\beta$ , and the initial volume  $V$ ;
2. Variables associated with intrinsic material properties: density  $\rho$ , cohesion  $\tau_0$ , and internal friction angle  $\theta$ ;
3. Dynamic variables: basal friction angle  $\gamma$ , flow velocity  $\mu$ , and gravity  $g$ .

The best-known geometrical and structural parameters in natural examples (1) are handled with most confidence and are best constrained in the models. Variables (2) and (3) are poorly understood if not unknown in natural avalanches limiting the scaling possible for dynamic comparisons. However, general cautious statements on model responses to changing parameters should be made to natural cases. Both model and natural prototypes deform in the strain rate insensitive frictional regime so velocity and strain rate scale differences should not be significant within this regime (Middleton and Wilcock, 1994).

To allow a simple and well-defined model for avalanches, certain essential variables including  $\tan \alpha$ ,  $\tan \beta$ ,  $\tan \theta$ ,  $L$ ,  $H$ ,  $A$ ,  $V$ ,  $\tau_0$ ,  $\rho$ , and  $g$  must be selected and some do not change significantly and so are taken as constants.

---

Figure 5.3 (*preceding page*): Set 2: Inclined straight ramp analogue avalanches using the sand-size glass beads. Experiments of this set have longer runouts. The deposit is made up of its levees (L), proximal to medial depositional areas as a translation zone (T) where the horst and graben and rib-and-ridge morphology (R) are usually observed, and in the distal depositional area is the deposit head that is an accumulation zone of most materials (A) that when over-steepened may destabilise into secondary ‘mini’ slides (green line). Several accumulation zones (B, C) may also exist in the medial area. The recurrent structures are strike-slip faults (yellow lines), normal faults (red lines), transtensional graben limits (orange lines), and thrust faults (blue lines). Scale of the figure is at 10 cm.

Repetitive variables:  $V$ ,  $\rho$ ,  $g$  have independent dimensions and less interesting behaviour than others (Middleton and Wilcock, 1994). Combining  $L$ ,  $H$ ,  $A$ ,  $V$ ,  $\tau_0$ ,  $\tan \alpha$ ,  $\tan \beta$ , and  $\tan \theta$  with these three variables produces the dimensionless pi ( $\pi$ ) numbers.  $\tan \alpha$ ,  $\tan \beta$ , and  $\tan \theta$  are expressed as  $[L] [L^{-1}]$  and are dimensionless. Thus, the first pi ( $\pi$ ) numbers are:  $\pi_1 = \tan \alpha$  or dimensionless acceleration;  $\pi_2 = \tan \beta$  or dimensionless deceleration; and  $\pi_3 = \tan \theta$ , stays constant and will be ignored.

To scale the length, the function:  $f(L) = L$  with exponent of 1,  $V$ ,  $\rho$ , and  $g$  is used. The dimensions are:  $[L]^1 [L^3]^a [ML^{-3}]^b [LT^{-2}]^c$ . For the products to be dimensionless, the sum of the exponents from  $[L]$ ,  $[M]$ ,  $[T]$  must be 0:

$$\begin{aligned} 1 + 3a - 3b + c &= 0 && \text{for L} \\ b &= 0 && \text{for M} \\ -2c &= 0 && \text{for T, } c = 0 \\ \text{Hence, } a &= -\frac{1}{3} \end{aligned}$$

In this way we define:

$$\pi_4 = \frac{L}{V^{1/3}}, \quad \text{dimensionless runout} \quad (5.1)$$

Scaling of  $\tau_0$  is as follows:

$$f(\tau_0) = \tau_0, V, \rho, g;$$

We choose to give  $\tau_0$  the exponent 1. The dimensions are:

$$\begin{aligned} -1 + 3a + 3b + c &= 0 && \text{for L} \\ 1 + b &= 0 && \text{for M, so } c = -1 \\ -2 - 2c &= 0 && \text{for T, so } c = -1 \\ \text{Hence, } a &= -\frac{1}{3} \end{aligned}$$

Thus:

$$\pi_5 = \frac{\tau_0}{\rho g V^{1/3}}, \quad \text{dimensionless resistance} \quad (5.2)$$

To those five pi numbers we can add:

$$\pi_6 = \frac{H}{V^{1/3}}, \quad \text{dimensionless initial energy} \quad (5.3)$$

Variables	Dimensions	Nature	Analogue Models	Max Scaling
$L$ : avalanche runout	[L]	100 km	0.003 km	$L^* = \Omega * T^* = 1/300$
$H$ : total fall height	[L]	5000 m	$\sim 1$ m	1/100
$h$ : fall height before arrival on depositional slope	[L]	3000 m	0.9 m	1/500
$W$ : deposit width	[L]	20000 m	0.7 m	1/3
$A$ : covered area	[L <sup>2</sup> ]	700 km <sup>2</sup>	$\sim 1$ m <sup>2</sup>	1/10 <sup>6</sup>
$V$ : volume	[L <sup>3</sup> ]	100 km <sup>3</sup>	$5.25 \times 10^{-12}$ km <sup>3</sup>	$\sim 1/10^{12}$
$e$ : deposit thickness	[L]	300 m	0.03 m	1/5000
$w$ : avalanche velocity	[LT <sup>-1</sup> ]	100 ms <sup>-1</sup>	1 ms <sup>-1</sup>	$\Omega^* = 1/20$
$\emptyset$ : clast diameters	[L]	50 m	600 $\mu$ m	1
$\rho$ : material density	[ML <sup>-3</sup> ]	2600 kg m <sup>-3</sup>	1600 kg m <sup>-3</sup>	1
$g$ : gravity	[LT <sup>-2</sup> ]	9.81 m s <sup>-2</sup> on earth	9.81 m s <sup>-2</sup> on earth	1
$\theta$ : internal friction angle	-	30°	33°	1
$t$ : placement time	[T]	500 sec	2-3 sec	$T^*=1/15$
$\gamma$ : basal friction angle	-	30°	55°	$\sim 1$
$\alpha$ : failure plane average slope	-	50°	45°	$\sim 1$
$\beta$ : depositional surface average slope	-	30°	18°	$\sim 1$
$\tau_0$ : cohesion	[ML <sup>-1</sup> T <sup>-2</sup> ]	100000 Pa	250 Pa	-547861

Table 5.1: List of scaling variables involved in rockslide avalanche motion and emplacement, and their maximum dimensions both in nature and in the analogue models Set 1 and Set 2.

Its inverse can be considered as a factor of dimensionless volume:

$$\pi_7 = \pi_6' = \pi_6^{-1} \quad (5.4)$$

$$\pi_8 = \frac{e}{V^{1/3}}, \quad \text{dimensionless width} \quad (5.5)$$

$$\pi_9 = \frac{A}{H^2}, \quad \text{dimensionless area} \quad (5.6)$$

$$\pi_{10} = \frac{H}{L}, \quad \text{characterizes the mobility of the avalanche} \quad (5.7)$$

Length, width, and thickness are the geometric parameters quantified. Other morphological parameters including: the influence of initiation and deposition slopes, material cohesion and volume to the geometry, morphology such as hummocks and levees, and structural features and faults are described qualitatively. Filmed experiments serve to analyze the evolution of deformation.

## 5.5 Reproducibility, Model Limitation, Initiation

Each time the boxes are filled, manual shaking compacts the particles minimizing inter-granular spaces and ensures minimum grain remobilization during tilting. To avoid electrostatic charges, sliding surfaces are cleaned with an antistatic product after each experiment. The gate of the box is then released discharging materials all at once. Depending on the slope, materials may slide out of the box in varying speed and in several collapse pulses. In order for the results to be interpreted, each experiment must have two to three replicates and must show the same geometric, morphologic, and dynamic characteristics for the same set-up of input parameters.

## 5.6 Results

For Set 1: curved ramp, there are a total of 110 experiments (Fig. 5.2, Appendix D) and for Set 2: inclined straight ramp, there are 31 analogue slides (Fig. 5.3, Appendix D), which are measured and characterized in detail. The configurations on labelling, parameters, material cohesion, and source box types are given in Table 5.2 and 5.3. The general plan view shape of the deposit, common morphology and recurrent structures, and how these were influenced by the initiation configurations of the source box, slope, and height are described in detail below.

$H = 73$ cm	$H = 46$ cm	$H = 63$ cm	$H = 114$ cm
<b>Low cohesion</b>		<b>Cohesive</b>	
<b>Box 1</b>		<b>Box 2</b>	
$\alpha = 35^\circ, 45^\circ, 55^\circ$	$\alpha = 35^\circ, 45^\circ, 55^\circ$	$\alpha = 35^\circ, 45^\circ, 55^\circ$	$\alpha = 45^\circ, 55^\circ$
$\beta = 0^\circ, 10^\circ, 18^\circ$	Set 1.1 (44)	Set 1.3 (20)	Set 1.4 (24)
$\beta = 10^\circ$	Set 1.2 (12)		
$\beta = 18^\circ$			Set 1.5 (10)

*Note: In parentheses are the replicate counts.*

Table 5.2: Model labels, parameters, and cohesion of material and source box used for Set 1.

H (m)	Volume (cm <sup>3</sup> )	Box 1	Box 2
		Replicates R1	Replicates R1
1.1	1000	2.1 (3)	2.3 (2)
	2000	2.2 (8)	2.4 (4)
1.2	1000	2.5 (2)	2.7 (2)
	2000	2.6 (3)	2.8 (3)
1.3	1000	2.9 (1)	2.11 (1)
	2000	2.10 (1)	2.12 (1)

*Note: In parentheses are the replicate counts.*

Table 5.3: Model labels, parameters, and cohesion of material and source box used for Set 2

## 5.6.1 The Curved Ramp Experiments: Set 1

### 5.6.1.1 Plan view Shape

The analogue deposits using the curved ramp range from elongated tongue-like (Fig. 5.2A) with parallel eastern and western margins for lower angle source slopes to single-lobe wider depositional areas for a high angle source slope (Fig. 5.2B-F). Irregular-edged deposits are found in experiments that produced hummocks (Fig. 5.2F) and those with minor spreading tongues at the margins (Fig. 5.2C-D). All experiments resulted in having a single major lobe. Those made from less cohesive materials have more regular edges. Most of the experiments are laterally elongated having greater lateral than longitudinal spreading and a compressed deposit at the main body in the depositional zone.

### 5.6.1.2 Deposit Morphology

Analogue slides have the following morphological features: (1) Levees: L; (2) Accumulation zones in the proximal: P, medial: M and distal: D zones; (3) Terraces and Steps; (4) Secondary Slides; and (5) Hummocks. These features may develop and transform from one to another during the sliding and at the final emplacement of materials.

Moving levees (Fig. 5.2A, C-D) can form as soon as the material slides out of the box and reaches the depositional area but their eventual preservation depends on the amount and supply of materials. They can contain numerous strike-slip faults sub-parallel to sliding direction produced by the difference in

velocity between edge and centre area.

Accumulation zones (Fig. 5.2A-D) are formed in the proximal, medial, or distal areas. Accumulation in the proximal area is a result of the arrival of faster-moving, later mobilised material that impacts and thrusts frontal deposits. Medial zones usually have the thickest deposit due to thrusting and thickening as sliding materials go through a change of slope from the steeper initiation to the gentler deposition slopes. An added constraint from the earlier deposited material thickens the medial zone. Also, as in the proximal zone, arrival of later mobilised material. Materials from the proximal accumulation zone thrust over the medial area at a later time can mask early-formed structures (Fig. 5.2A-D). Normal faults with strike-slip component parallel to sliding direction indicate extension towards the lateral margins (Fig. 5.2C-D) or perpendicular direction by materials spreading down slope (Fig. 5.2B, E-F). The deposit can be well-spread in the medial zone such as in Figures 5.2A, E-F or can have a decreasing thickness from the middle towards both lateral sides as in Figures 5.2C-D indicating lateral spreading during transport. The distal accumulation zone (Fig 5.2A, C-D) forms when frontal spreading slows down but sliding and deposition of later materials continues in the medial and proximal zones. Thrusting of later materials is evident in the formation of thrust lobes strictly piled one on top of the other. The frontal area is dominated by side normal faults and central thrusts. The steep front side has small collapses or secondary slides that spread materials further downslope in thin ripply lobes (Fig. 5.2C-D). This terminal collapses occur mostly at the edges of the lobes. Destabilization of a thick accumulation zone by spreading and normal faulting can lead to secondary slides (Fig. 5.2A, C-D) and terraces steps (Fig. 5.2B).

Terraces (Fig. 5.2B) or “steps” form when a proximal to medial accumulation zone confined by the levees results in a relatively greater vertical displacement between two adjacent blocks. The faults perpendicular to slide direction accommodates the extension of the thicker deposit leaving the more stable blocks behind while materials at its front spread. White lines in Figure 5.2B indicate jigsaw-like cracks formed from the collision of accumulation blocks against each other. Further movement in Figure 5.2B would most probably result in the breaking of blocks and into a hummocky topography such as in Figure 5.2E-F.

Hummocks (Fig. 5.2E-F) range from large and elongated to small and rounded. They result when sliding materials form blocks. They may originate even earlier, when material is still in the box. Larger hummocks are elongated perpendicular to flow direction. Within hummocks jigsaw cracks is observed. These may result from the impact during emplacement when there is no clear stress direction or from multiple cracking by constantly chang-

ing stresses and fractures by collision with other materials. These fractures accommodate extension within the blocks during sliding and hummocks deformation (Fig. 5.2F). A hummock can also disintegrate or merge as it interacts with imperfections in the sliding surface.

### 5.6.1.3 Recurrent Structures

Recurrent surface structures in analogue deposits are: (1) Strike-slip, (2) Thrust, and (3) Normal faults. Each of these structures appears and dominates at certain stages during the initiation, development, and final deposition of materials. Strike-slip faults dominate in the levees. They are manifestations of the difference in velocity of the sliding central body of deposit and of the lateral sides. Strike-slip faults are also observed in the medial zone as an effect of the sliding of materials past each other. Thrust Faults are usually in the proximal accumulation zones as a result of the slumping and emplacement of additional deposits onto previously emplaced materials. Normal Faults are found in the whole avalanche deposit and are observed delimiting the terraces and steps. They form the transtensional grabens within the medial zone as well as secondary sliding on the edges of accumulation zones. These extensional features are manifestations of the extension and spreading movement of materials towards the lateral and frontal edges.

### 5.6.1.4 Influence of Initial Experiment Configuration to the Final Emplacement

Longer runouts result from a steeper initiation slope. The thickness of the deposit is dependent on volume. A greater volume of material regardless of the width of the source box or smaller volume of material on a smaller source box can result to a thicker deposit. Comparing the deposits using source box 1 and 2, the latter has initially thicker materials even before its release while source box 2 is wider so initially material is thinner on its release until its transport.

## 5.6.2 The Inclined Straight Ramp Experiments: Set 2

### 5.6.2.1 Plan view Shape and Thickness

The plan view of the deposit is tongue-shaped and can have two general forms: triangular, and rectangular. Triangular-shaped deposits (Fig. 5.3C-D) can have a pointed distal accumulation zone (A) and a wider upper translational zone (T) like in Figure 5.3C or a narrow distal edge and a very wide

translational zone like in Figure 5.3D. Rectangular-shaped deposits have near-parallel lateral levees (L) and longer runouts (Fig. 5.3A-B). Deposition can be evenly spread with some transtensional grabens in between (Fig. 5.3C-D) or non-uniform with accumulation zones at the distal margin and a thin deposit in the translational zone (Fig. 5.3A-B).

### 5.6.2.2 Deposit Morphology and Recurrent Structures

There are three important zones in the analogue slide experiments (Fig. 5.3): (1) translation zone, T; (2) accumulation zone, A; and (3) levees, L. Important morphologic features in these experiments are the (4) late-stage accumulation lobes, B, C; (5) rib-and-ridge morphology, R; and (6) transtensional grabens (orange lines) in the translation zone where spreading is greatest; and the (7) secondary 'mini' slides (green lines) in the distal margins where accumulation is thickest due to compression. In plan view, each of these zones consists of recurrent structures including normal faults (red), thrust faults and folds (blue), and strike-slip faults (yellow). These give clues on the kinematics of these types of landslides.

The translation zone is where failed materials move downslope by sliding or translation on top of the basal shear surface (aluminium ramp). Within the translation zone there are recurrent structures and morphologic features including: (1) perpendicular or sub-perpendicular normal faults that can form horst and graben structures, the rib-and-ridge morphology, or transtensional grabens. Pure normal faults can be oriented perpendicular to spreading direction or with an obliquely. Transtensional grabens (Fig. 5.3D) form when an portion of deposit detaches from materials behind; (2) thrust faults are located at the boundary of the translation and accumulation zones as later materials are thrust over earlier deposits (Fig. 5.3A-B, D) or at the proximal translation zone as the last bits of materials are emplaced until movement ceases. Subsequent thrusting by multiple pulses in the slide can result into lobes that can mask initial structures and morphologic features. In this case, sliding is lubricated by earlier deposits and continues until stopped by an obstacle. Subsequent lobes can have drag-like features on their sides that are preserved as levees. Compression starts when spreading at the front lobe starts to wane and the materials at the back catch up with the accumulating front lobe. This drags some portions resulting in folds and thrusting. This accumulated and compressed material may thicken enough to be destabilized and may spread further with the production of normal faults (Fig. 5.3B).

The lobe-like accumulation zone (Fig. 5.3A-B, D) forms when sliding wanes at the distal end and lateral margins and incoming material is thinned or depleted. Within this zone there are recurrent structures: (1) thrust-fold

structures, and (2) normal faults that can lead to (3) secondary 'mini' slides at the margins. Thrust faults and folds form when the movement of materials at the side and at the front slow down but those at the middle and rear portions are still fast moving (Fig. 5.3A-B, D) creating drag-like features. Normal faults in this area imply extension of the thicker deposit causing secondary 'mini' slides. Sub-perpendicular to the sliding direction, normal faults occur to accommodate the compression by the incoming sliding material or from lateral constraints by the levees and the spreading of material towards the free space. When over-accumulated and over steepened materials at the edge of the frontal lobes become unstable, secondary 'mini' slides (Fig. 5.3B) occur.

Levees form as soon as the materials begin to slide down. Most of the materials, however, will accumulate in the middle and slide further leaving thin levees along the way. The differentiated movement form the extensional features in the levees. The levees have (1) pure strike-slip faults that are in the outer edge, (2) inner faults with both strike-slip and normal components (oblique-slip motion) that lead to a rib-ridge morphology seen in the inner portion of the levees. These are usually in the proximal part of the translation zone.

The rib-ridge morphology shows repeating ridges elongated perpendicular or sub-perpendicular to sliding direction. It is a result of the translated horst and graben structure in well-spread deposits with generally uniformly thick materials (Fig. 5.3C). Extensional features like this form when a normal fault opens up and the downthrown block continues to slide until stable while the upthrown block is generally stable. Transtensional grabens (Fig. 5.3D) in thick deposits form when a thick mass of deposit on the downslope block detaches itself from a more stable upper part leaving a window of thinner deposit in between them. Transtensional graben is a manifestation of extensional movement that starts as normal faults with a strike-slip component.

### 5.6.2.3 Sequence of Events

Sliding is initiated by opening the source box, which allows the materials to slide down. There are two types of material transport during sliding from initiation until translation and emplacement: materials progressively leave the source box and slide downslope (Fig. 5.4), or they can come out as a thick deposit in single or multiple pulses and materials are translated downslope (Fig. 5.5).

Most experiments resulted in a depositional zone with an accumulation and a translation sub-zones. The accumulation zone is the head-like part on the distal end where most of the earlier materials are emplaced and the translation zone is where materials are transported by sliding or translation

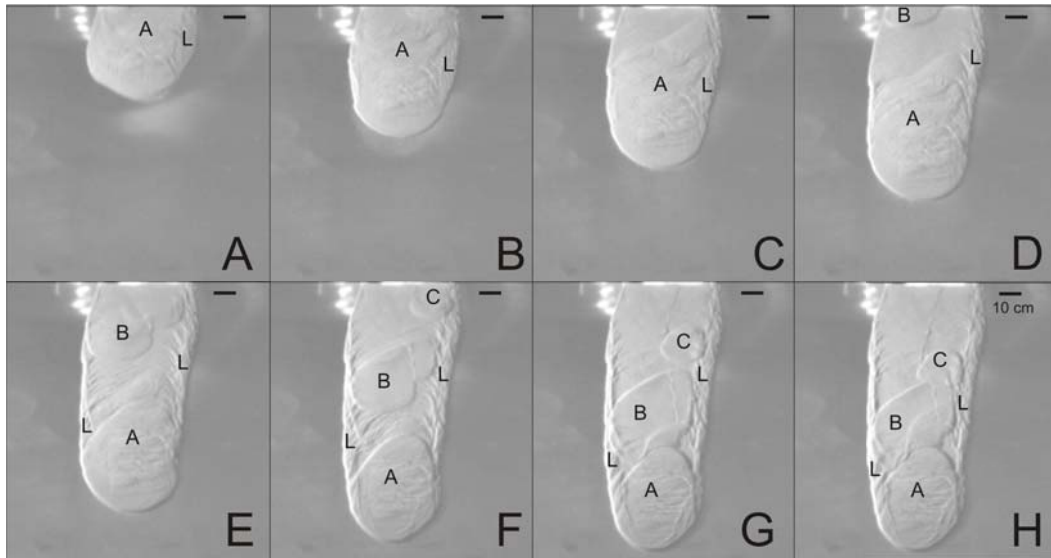


Figure 5.4: Evolution of morphology and development of structures in relatively thinner avalanche deposit showing the formation of an accumulation zone at the distal margin while leaving behind a translation zone in the proximal and medial depositional areas. During release, the materials had a retrogressive discharge as indicated by the pulses. The following is the sequence of structure development for this experiment: A First pulse of materials leave a thick sheet of deposit (A) with radiating structures, strike slip faults formed as the materials are spreading. B Materials continue to slide forming levees (L) with a many strike-slip faults. C Materials spread mostly downwards and to the lateral sides. Oblique strike-slip faults form in the levees. D The sliding of materials towards the front and the pushing of materials at the back causes compressive structures in the middle of the depositional area. Normal faults accommodate sliding in the medial area forming an accumulation zone (A) in the distal part. Meanwhile, a new pulse of material starts to slide (B). E The relatively slower movement of materials at the front than at the middle and back results in an accumulation of materials in the front lobe, now forming its head. As the bulk of deposit is being transported down, movement of the strike-slip with normal movement in the medial area leaves a thin layer of material behind while thrusting materials at the rear portion of the distal head. The new materials from the second pulse (B) also masks previously emplaced deposits in the proximal area. F The distal head slides more slowly, while second pulse materials slides faster by the reduced friction provided by the earlier emplaced material on its base. This results in increased compression between the two lobes. At this point, a third pulse of materials starts to slide down (C). *(continued on next page)*

Figure 5.4: (*continued from previous page*) G There is little spreading by the distal area. The lubricated second pulse materials (B) however, continue to spread until stopped by distal accumulation zone (A). There is increased compression between these two areas, at this point that pushes the distal end to spread. The stress causes the drag-like features, probably folds on the eastern end of the distal lobe. Although the third pulse materials is very thin, it still slides down due to lubrication by earlier emplaced materials until stopped and merges with the second accumulation lobe (B).

in the proximal zone. The earlier materials released from the source box (Fig. 5.4A), which have slid down the ramp (Fig. 5.4B), will lubricate the path for the succeeding materials as shown by Mangeney et al. (2010). This results in longer runout of late-emplaced materials. As materials at the distal front slow down, the lubricated later materials at the proximal portion become compressed and thrust (Fig. 5.4C-D). This shapes the distal accumulation zone (Fig. 5.4D). As the frontal spreading wanes, more and more materials are constrained at the back. Depending on the number of sliding pulses, accumulation lobes may be formed at the back of the distal accumulation zone (Fig. 5.4E-G). Subsequent arrival of material can also be emplaced on top of the earlier deposit masking out previously emplaced structures and morphology (Fig. 5.4F-G). Translation and sliding continues while the frontal margins stop moving then later materials may still be lubricated and slide and this causes drag structures and folds (Fig. 5.4F-H).

When material continuously slides out of the source box, a well-spread, uniformly thicker deposit is formed in the translation zone (Fig. 5.5A-B). As materials are transported out from the source box, extensional features strike-slip and transtensional faulting occur on both sides forming the levees, and in the middle translation zone (Fig. 5.5B-H). Normal faults start to form accommodating extension and horst and graben structures with separate blocks. At this stage, the lower blocks continue to slide but the upper blocks come to rest progressively from rear to front (Fig. 5.5F-J). This creates the rib-and-ridge morphology. Unstable accumulation areas may experience secondary 'mini' slides accommodated by normal faults and spread even further (Fig. 5.5I-J).

### 5.6.3 Natural Debris Avalanche Deposits

There are three natural avalanches presented here: The Guinsaugon Rockslide Avalanche, Philippines (Fig. 5.6), the Meager Rockslide-Debris Avalanche, Canada (Fig. 5.7) and Storegga Slide in the Norwegian margin (Fig. 5.8). Their deposit geometry, and surface morphology are interpreted from remotely sensed images and existing field and geophysical data. Descriptions from

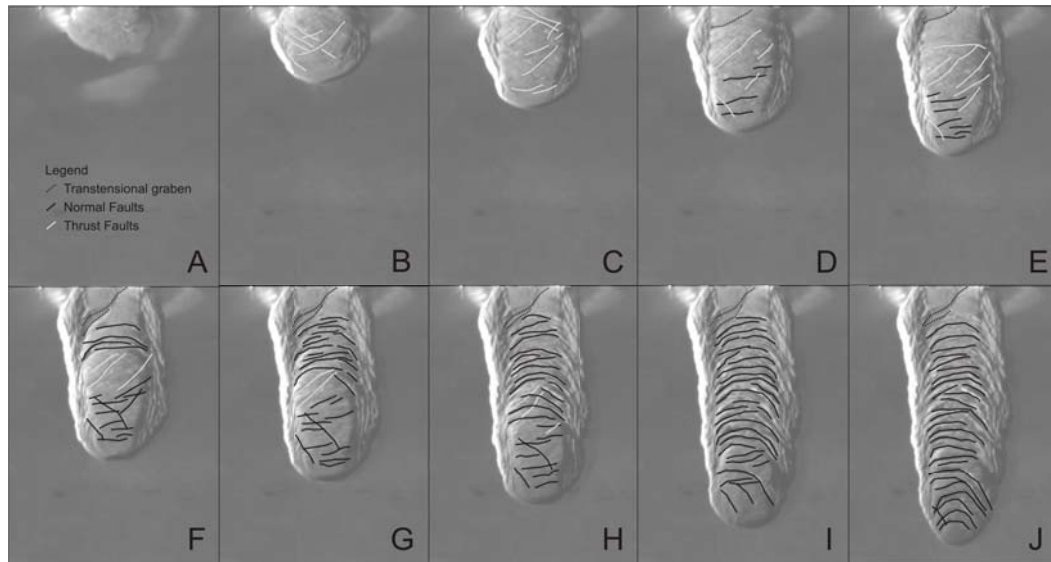


Figure 5.5: Evolution of morphology and development of structures in relatively thicker avalanche deposit. After being released out of the source box, material spreads into a uniformly thick deposit until longitudinal spreading wanes and eventually stops. The evolution and progression of structures is as follows: A After initiation, materials slid forming a lobe at the front. More materials are in the central where there is limited spreading capacity of the materials than at the sides and front. B Compression from the fast-moving rear materials form the oblique structures. Levees (on both lateral sides) with strike slip faults start to form that will remain stable until the end. C More materials slid out of the box resulting in more strike slip faults on both levees. To accommodate the Compression from the rear and shearing at the levees, create oblique structures (thrust faults) in the main body of the slide while the front lobe continuously slides and spreads deposits downward. D A more developed compression structures appears in the main body while normal faults add more extension and spreading at the distal area of the deposit slide. A normal faults that will open up and create a transtensional graben is initiated. E The whole deposit continuous to slide. Just below where the transtensional graben is initiated, continues sliding compresses more materials in the medial area (M) resulting in more thrust faults. More normal faults also develop in the distal area to accommodate spreading of materials downward. (*Continued on the next page*)

Figure 5.5: (*Continued from previous page*) F Movement and downward spreading in the levees continue by strike-slip faulting. Normal fault in the proximal area opens up accommodating downward spreading of materials and forming a transtensional graben. Sliding at this part, compresses more materials in the main body, particularly in the medial towards the distal area. Accumulated materials in the distal and in the proximal areas continue to slide and spread by normal faulting. In the distal area, the head of the deposit start to form. G The proximal towards the medial areas continue to form normal faults that accommodate spreading in these areas. At the same time, the distal area also continue to spread accommodated by the existing normal faults. H-J Strike-slip faults continue to accommodate spreading of materials in the levees. More normal faults form to accommodate the spreading of the main sliding body. H An oblique normal fault is generated. I Further movement of the distal area destabilizes the distal end of the main sliding body I-J that causes major spreading, probably a collapse accommodated by the normal faults at the distal front.

previous works will give an idea of their emplacement dynamics.

### 5.6.3.1 The Guinsaugon Rockslide-Debris Avalanche (Southern Leyte, Philippines)

On 17 February 2006, the most disastrous landslide event in Philippine history occurred along a steep fault scarp of the Philippine Fault zone at Guinsaugon, Saint Bernard, Southern Leyte (Fig. 5.6A) killing 1,221 people. The deposit has covered an area of three million m<sup>2</sup> and a distance of 4 km from the crown to its toe. The thickness is 6-7 m near the toe and 30 m at the base of the fault scarp with volume of around 15-20 million m<sup>3</sup>. The main sliding plane of the avalanche is a prominent north-northeast oriented plane at the head of the landslide intersected at an angle by a smaller planar feature. The debris avalanche deposit is composed of volcanic rocks of the Calian Formation, and breccias produced by the movement of the Philippine Fault. Triggering factors of the avalanche are rainfall and a 2.6 magnitude earthquake (Catane et al., 2008; Guthrie et al., 2009; Lagmay et al., 2006).

Some common morphology and recurrent structures in the curved ramp set of experiments are observed in the Guinsaugon rockslide-debris avalanche deposit, such as the terraces and steps (Fig. 5.6B-C), secondary slides (Fig. 5.6D), distal accumulation zone (Fig. 5.6E), normal and strike-slip faults (Fig. 5.6F-G), and hummocks (Fig. 5.6H). These features are presented in a simple plan view drawing (Fig. 5.6I). Figure 5.6J (modified from Catane et al. 2008) shows the curved basal ramp that influences the production of the common

features in the curved ramp experiments.

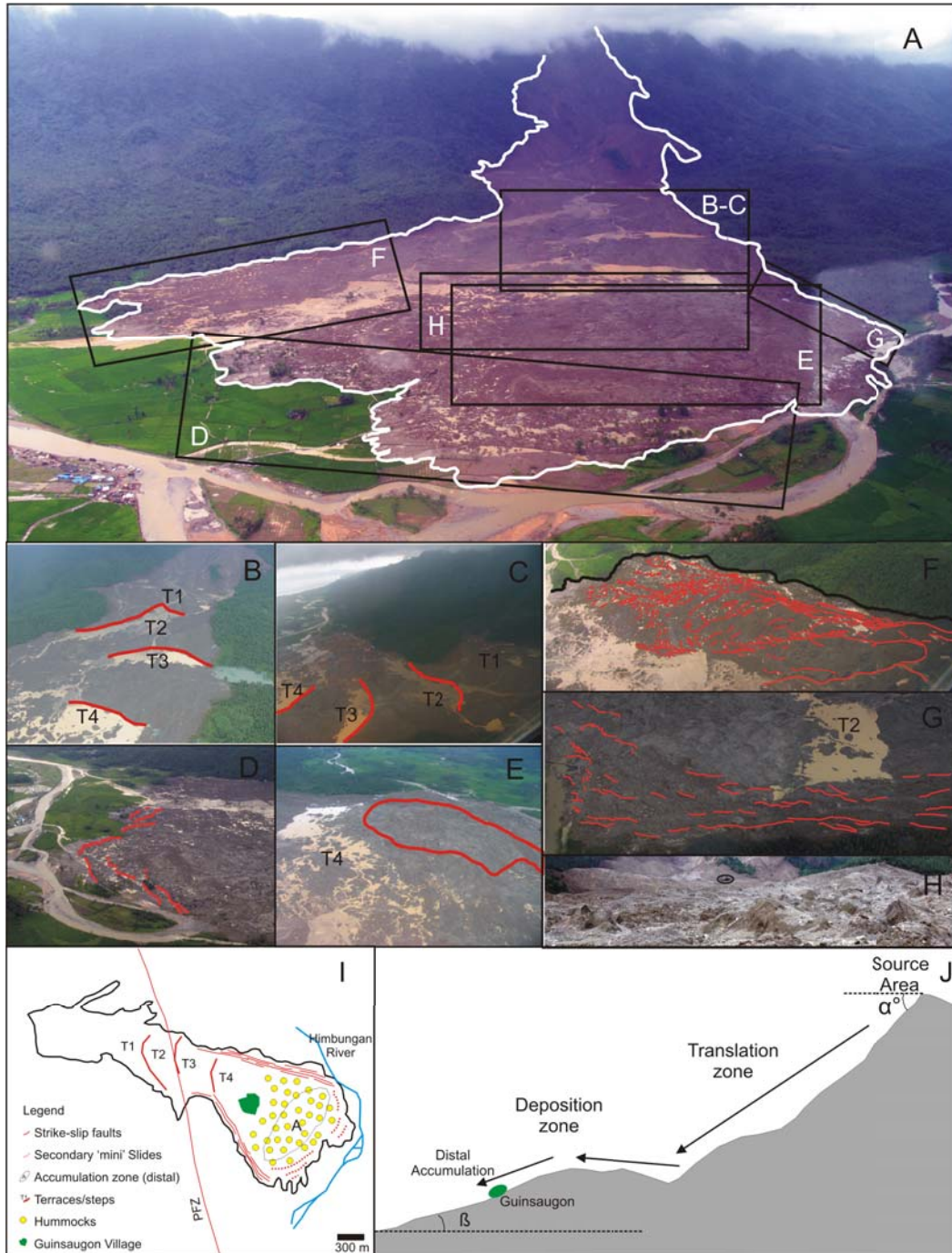
### 5.6.3.2 Meager Rock Avalanche (British Columbia, Canada)

Mt Meager is the youngest member of the Mount Meager Volcanic Complex, at the northern limit of the Cascade magmatic arc together with other Pacific Northwest volcanoes including Baker, Rainier, St Helens, Hood, and Shasta. It is arguable the most landslide-prone region in Canada (Friele and Clague, 2009; Friele et al., 2008). The volcanic activity at these centres is a product of Juan de Fuca plate oceanic subduction beneath the continental North America (Hickson 1994).

On 6 August 2010, one of the largest landslide worldwide since 1945 and one of the three largest in the Canadian Cordillera in historical times (Evans, 2006; Guthrie and Evans, 2007; Lipovsky et al., 2008) occurred resulting in an evacuation of the 1500 residents of Pemberton, 65 km downstream of the slide source. It originated when a detached rock mass from the secondary peak of Mt Meager collapsed into a rock avalanche and impacted the weathered and saturated flanks of the volcano. Undrained loading of the sloping flank caused a rapid evacuation of the entire flank with a strong horizontal force incorporating a significant volume of material, and forming a highly mobile debris flow.

The disintegrating mass travelled down Capricorn Creek at a velocity of  $64 \text{ m s}^{-1}$  (Guthrie et al., 2012). When it encountered the opposing wall of the Meager Creek, 7.8 km from the source, there was a super-elevation causing a run-up of 270 m above the valley floor and the deflection of the landslide debris to 3.7 km upstream and 4.9 km downstream into the Lillooet River valley (Fig. 5.7A-B) (Guthrie et al., 2012). This blocked the Lillooet River for a couple of hours, approximately 10 km from the collapse source. Deposition at the Capricorn-Meager confluence also dammed Meager Creek for about 19 h creating a lake 1.5 km long that burst into flood by over-topping (Guthrie et al., 2012). Post-event digital elevation model estimated the initial volume of the collapsing mass to be  $48.5 \times 10^6 \text{ m}^3$ , height of 2183 m, and total length of 12.7 km. This yields  $H/L = 0.172$  and a travel angle of  $9.75^\circ$  (Guthrie et al., 2012).

The Meager rockslide avalanche has bends and barriers resulting in a confined slide with deflections and run ups as opposed to the free-spreading nature in the set of experiments. Still, some prominent well-preserved areas in this avalanche deposit have morphological and structural features mapped out to be similar to those in the analogue slides (Fig. 5.7B). Some of these are: thrust fault-dominated accumulation zone deposited just as when the avalanche meets a confinement by the Meager Creek Barrier (Fig. 5.7C); the medial



accumulation zone delineated with strike-slip faults and thrust faults located in the more gentle slopes of the depositional zone (Fig. 5.7D); and the distal accumulation zone that shows thrusting of bulldozed material from the river bed that the avalanche has crossed as it was emplaced at the distal-most front and the main debris avalanche materials at the rear part of this area (Fig. 5.7E).

The sliding basal plane topography is given in Figures 5.7B and 5.7F. Profile of the whole Mt Meager slide (Fig. 5.7F) from collapse to depositional areas (Fig. 3 of Guthrie et al., 2012) and basal slide topography of the area where the three key areas are located (Fig. 14 of (Fig. 14 of Guthrie et al., 2012) et al. 2012) show that the slide is on a curved basal ramp before the Meager Creek Barrier and a more straight basal ramp on the depositional area down towards the Lilloet river.

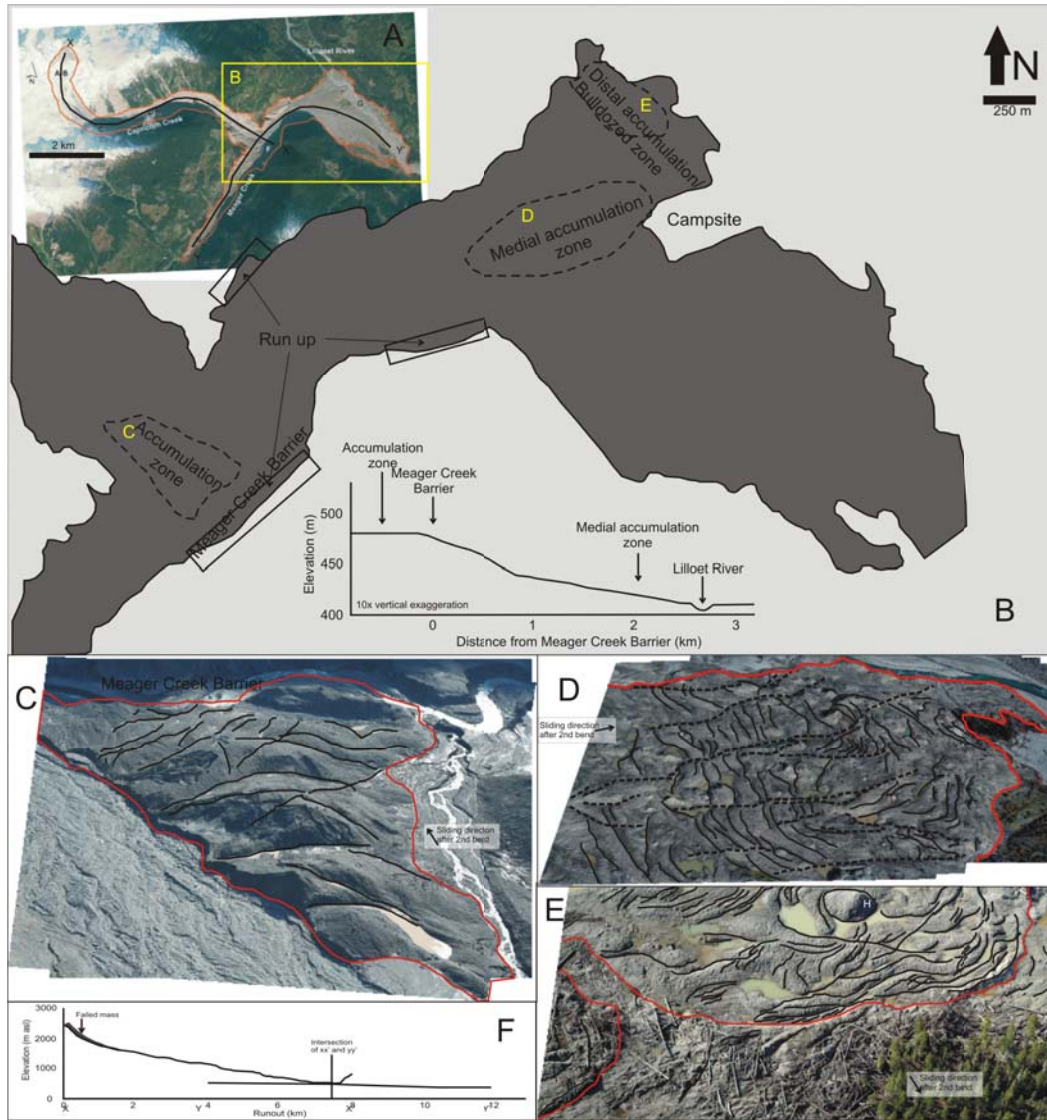
### 5.6.3.3 Storegga Slide (Norwegian margin)

The development of the Storegga depression separates the North Sea Fan in the south from the Vøring Plateau to the north. The detailed architecture of its immediate surrounding is a result of a large number of paleoslides that occurred intermittently since late Pliocene times (Evans et al., 2005; Nygård et al., 2005). Numerous regional models relating to the triggering mechanisms and scenarios have been proposed including: excess pore pressures caused by gas-hydrate dissociation due to sea level or water-temperature change (Mienert et al., 2005) and offshore earthquakes (Atakan and Ojeda, 2005).

The Storegga slide (Fig. 5.8A) occurred about 8200 y ago involving

---

Figure 5.6 (*preceding page*): The Guinsaugon Rockslide-Debris Avalanche Deposit (Southern Leyte, Philippines). A Oblique view of the different areas showing its morphological (B-C, D, E, H) and structural (F, G) features similar to those in analogue models: B-C Terraces or steps; D Secondary slides; E Distal accumulation zone; F-G Extensional structures including normal and strike-slip faults; H Hummocks; and I Simplified plan view map with the morphological and structural features. The outline of the debris avalanche deposit is from Guthrie et al. 2009. Drawn in north-south red line crossing the avalanche is the Philippine Fault Zone (PFZ). In blue lines at the toe of the deposit is the Himbungan River. J Cross section view showing the landslide ramp of the Guinsaugon rockslide-debris avalanche (modified from Catane et al. 2008). The configuration is the same as the Curved ramp experiment, Set1.



3000 km<sup>3</sup> volume of material and affected an area of 9000 km<sup>2</sup> (Kvalstad et al., 2005). The upper headwall has a length of about 300 km and the northwest boundary of the deposition zone extends about 800 km towards northwest (Berg et al., 2005; Bryn et al., 2005). Bathymetric and slide scar morphology (Fig. 5.8A-F) by Kvalstad et al. (2005) and a shaded relief map (Fig. 5.8G-H) from the multi-beam bathymetry (Færseth and Sætersmoen, 2008), show the slide consisting of repeating series of large, slightly inclined terraces forming steps with heights of 50-350 m and a distance between scarps of 5 to 10 km along the northern flank to more than 50 km in the central deep part of the slide (Fig. 5.8B-H) creating the rib-and-ridge morphology. Seismic sections in this area show the reverse and normal faults forming the horst and graben structures orthogonal to slide direction. This is interpreted to be by progressive softening of the weak marine clay base layer, retrogressively migrating upslope and laterally during sliding.

Although the mechanism that initiated the slide is not well understood, the first event according to Bryn et al. (2002) was followed by successively smaller slides. In some areas sediments have moved as flows, whereas in others they remain as more or less coherent blocks. While the slides are generally in tectonic terms, extensional features and numerous zones of compression can

---

Figure 5.7 (*preceding page*): The Meager Rockslide Avalanche (British Columbia, Canada). A Inset is a plan view map of the Mt Meager rockslide avalanche. Delineated in solid black line are elevation profiles xx' from the collapse source to the two bends and up to the Meager Creek Barrier and yy' from the barrier towards both direction of confinement and slide deflection. In yellow box is the location of an outlined part of the slide presented in B, a simplified plan view outline of the rockslide avalanche showing the three areas with prominent morphological and structural features similar to those in analogue models: C accumulation zone as a result of the Meager creek Barrier that resulted into thrusting of later materials onto previously emplaced deposits; D medial accumulation zone as a result of sliding at a more regular gentle slope and waning of spreading at its front; and E distal accumulation of bulldozed river material formed with the incorporation of the riverbed made of sand and pebbles by bulldozing that occurs at the front of the distal depositional zone. F Cross section view showing the landslide ramp of the Mt Meager rockslide avalanche. Basal slide morphology from the source to the Meager Creek Barrier is more similar to the curved ramp experiments while the second part from barrier to further downslope is more similar to the straight ramp models. A, B and F are taken and modified from Guthrie et al. (2012).

be seen where individual flows and slide lobes terminate.

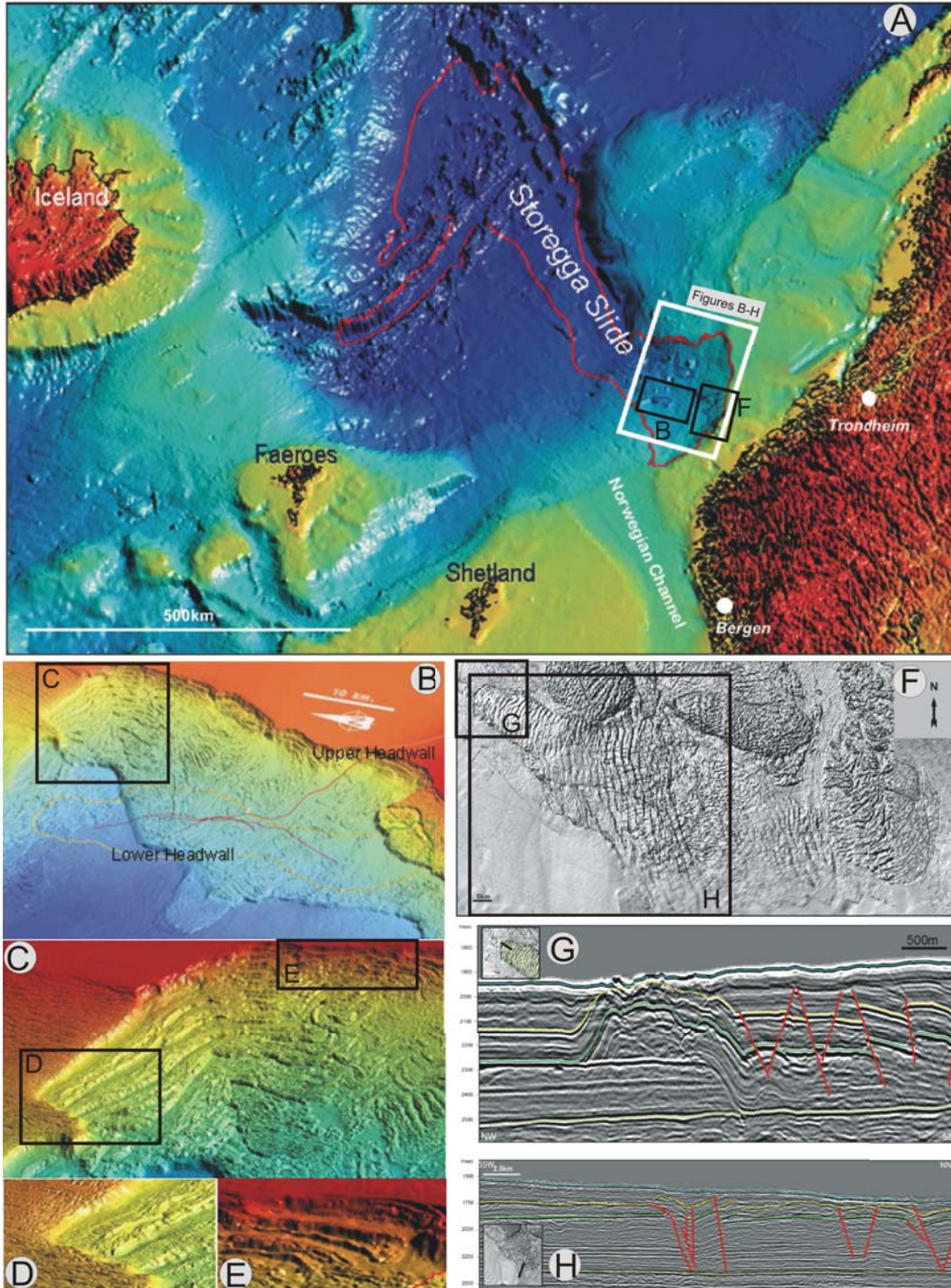
## 5.7 Discussion

### 5.7.1 Morphology and Structures in Curved- and Straight-Based Analogue Slides

Curved and inclined straight ramp experiments resulted in different analogue avalanche deposits in terms of plan shape, morphology, and structures. A curved sliding base results in a fan-shaped depositional area with shorter but wider runout probably because of the sudden change in the sliding slope and deposition slope (Fig. 5.2). The lateral accumulation zone is thickest in the middle towards distal zones. A straight sliding base, however, results in a tongue-shaped depositional area. It can have a well-spread, longer and narrower runouts with parallel levees or depositional area that has a wider proximal zone and narrowing towards the distal portion.

Both sets of experiments resulted in a morphology and structure that are very similar but may have developed and evolved in very different ways and different mechanisms. The main features are: the presence of (1) levees on the lateral margins of the deposits, (2) accumulation zones, (3) subsequent lobes emplaced on top and masking pre-existing structures, (4) secondary ‘mini’ slides, and structures including: (5) thrust-fold structures, (6) strike-slip faults, and (7) normal faults.

Levees form because of the difference in material velocity during spreading. The materials in the middle move faster than those at the lateral sides. Both sets of experiments have accumulation zones formed at different stages and sites. Curved experiments have a single accumulation zone formed in the middle towards the distal depositional area as a result of material thrusting where there is a change from the steeper initiation towards a gentler depositional slope. On the other hand, straight-based experiments have accumulation zones mostly on the distal area as frontal spreading wanes but later materials continue to spread faster. Subsequent accumulation zones can form at the proximal and medial portions and can mask earlier deposit morphology and structures. Over-steepened accumulation zones can be destabilised by further spreading resulting in secondary ‘mini’ slides. Common structures also occur in the deposit. Areas where there is compression and thrusting are dominated by thrust faults. Folds are commonly seen in the frontal accumulation zones when the middle part of moves faster dragging with it the remaining parts of the deposit. Extensional structures also occur over the whole depositional area indicating spreading towards the lateral sides and towards the



frontal edge. Strike-slip faults dominate the lateral edges in the translation zone towards frontal edge for the inclined straight-based experiments and at the lateral edges of the main depositional zone for curved ramp experiments.

On the other hand, there are also morphological features and surface structures unique to each of the two slide types such as: the existence of the (1) terraces or steps, and (2) hummocks in the curved ramp experiments; and the (3) rib-and-ridge structures and (4) transtensional graben in straight ramp experiments.

Terraces and steps form in slightly cohesive experiments where the accumulated deposits extend by normal faulting progressively leaving stable blocks in the proximal towards the medial zones while the adjacent side facing the downslide direction is displaced by normal faulting and continues to spread. The blocks that form the terraces are bigger, usually thicker and with greater vertical displacement between adjacent blocks compared to those forming the hummocks. A terrace block can be faulted during spreading and displacement breaking into hummocks. This is the same mechanism that forms the rib-and-ridge ‘thumbprint’ morphology in the straight ramp experiments with elongated but thinner horsts and the transtensional grabens. In transtensional grabens, however, the graben is wider and can have thicker deposit as

---

Figure 5.8 (*preceding page*): The Rib-and-ridge morphology of the Prehistoric Storegga Slide. A Bathymetric map of the southern Norwegian Sea and the Norwegian margin area with outline of the Storegga Slide as modified from [Færseth and Sætersmoen \(2008\)](#). In black boxes are locations of B and F; B Bathymetric image of the Ormen Lange area (from [Gauer et al. 2005](#)) with locations of C in the black box; C Upper headwall with slide blocks forming the rib-and-ridge morphology of the slide (from [Gauer et al., 2005](#)) with locations of D to E in black boxes; D and E are the repeating series of horst and graben structures orthogonal to slide direction (from [Gauer et al., 2005](#)); F Shaded relief map from the multi-beam bathymetry showing the reverse and normal faults that are orthogonal to slide direction on the surface of the slump (from [Færseth and Sætersmoen, 2008](#)). The boxes are locations for G and H; G W-E oriented seismic section of the fault-bend folding associated with the frontal ramp and associated reverse faults east of the ramp; H N-S oriented seismic section across the southern lateral margin of the slump. Along this part of the slump margin, the detachment climbs from an intra Naust bedding plane horizon (light green) below the slump, across lithological layers to the top of the Tampen Slide in the footwall to the south, to form a steep lateral ramp. Reflections in G and H: Seabed in blue; Top Tampen Slide in yellow; Base Tampen Slide in green (from [Færseth and Sætersmoen, 2008](#)).

it can contain the rib-and-ridge within it. The grabens in the rib-and ridge morphology have thinner deposits than the grabens by transtensional faulting because these are formed by detachment and then translation of the downside adjacent horsts and ridges.

### 5.7.2 Development of Structures and Evolution of Morphology in Large Debris Slides

General plan view and morphology of curved and straight ramps are different and unique structures do occur in each set of experiments. Curved ramps result in deposits that are wider but shorter than the longer but narrower straight-based experiments. Lateral spreading is greater in curved experiment because the steep initiation slope and gentler depositional zone cause waves of materials to be deposited and thrust one on top of the other on the proximal to medial part of the accumulation zone. On curved ramps, extensional features are found in the middle towards distal depositional zone as secondary spreading of the thickened mass occurs on its over-steepened margins. In contrast, straight ramp experiments show sliding and progressive translation of material resulting in longer runout with more frontal rather than lateral spreading. The proximal part is dominated by extension but as the frontal margin starts to wane, compressional features, and accumulation of materials start to occur. Destabilisation by secondary 'mini' slides at the edges still occurs to a small extent. Transtensional graben in the medial or proximal area or a series of horsts and graben-like structures called the rib-and-ridge morphology are the dominant feature that contrasts with the compressed and thickened deposits in the curved ramps.

Based on the Guinsaigon rockslide-debris avalanche basal plane topography and structures and morphology similar to the analogue models, the slide resulted in a thickened medial up to distal depositional area. The thickened mass in the medial depositional zone will later form the terraces and steps (Fig. 5.6B-C) the normal faults within it results in vertical extension movement as it spreads. The distal accumulation zone (Fig. 5.6E) because it is a thick mass moving on top of a saturated layer of the rice paddies, will remobilise generating the secondary slides (Fig. 5.6D). During motion, normal and strike-slip faults (Fig. 5.6F-G), and hummocks (Fig. 5.6H) continue to accommodate the sliding and spreading of deposit.

In the Meager rockslide avalanche, there was thrusting of debris when the slide met the Meager Creek Barrier (Fig. 5.7C) during the avalanche emplacement. The medial accumulation zone, unlike the upper accumulation zone has a few prominent strike-slip faults in addition to its thrust faults (Fig. 5.7D). This area is in a gentler less confined depositional zone so materials

are relatively more free to spread towards side of the campsite (Fig. 5.7B) or downslope following the flow of the Lilloet river. During the debris spreading on the distal area, some debris that successfully crossed the Lilloet river has bulldozed thru the river bend incorporating within it sand and gravel thrusting towards the frontal edge as the debris is losing energy to inundate any further areas (Fig. 5.7E).

The repeating series of large, slightly inclined terraces forming horst and graben structures orthogonal to slide direction, rib-and-ridge morphology (Fig. 5.8B-F) in the Storegga slide off of Norway happened in response to the progressive and retrogressive softening upslope and laterally of the weak marine clay base layer. Progressive spreading and extension continued in some areas as flows and as more or less coherent blocks in other areas as slides. Compression structures appear at the termination points of these flows and slide lobes.

### 5.7.3 Implications of Analogue Morphology and Structure on Natural Prototypes

Experiments show that the shape of the basal ramp affects the morphology and structures that form in the deposits. These surface features in natural avalanche deposits can be used to identify the underlying ramp shape and the translation and emplacement kinematics in avalanches. Tongue-like and longer runouts result from slides with higher inclined slopes. On the other hand, fan-shaped deposits result from avalanches and slides with an abrupt change in the initiation and deposition slopes. The shape and morphology of the deposit is also affected by the coherence of the collapsed material. Incoherent and monolithologic materials on a smooth and straight failure surface for example can form the tongue-like long runout deposits such as in the Lullailaco southern avalanche (Fig. 5.9A) and Socompa rockslide-debris avalanche (Fig. 5.9B), and the rib-and-ridge thumbprint such as at the Storegga slide (Fig. 5.8), the South Nation River slide (Fig. 5.9C) in 1971 (Quinn et al. 2011) and ice break up from the failing Larsen ice shelf in Antarctica (Fig. 5.9D) (Quinn et al. 2007) while those with coherent blocks will most likely result into terraces and steps, hummocks and fan-shaped deposits such as in Guinsaigon rockslide debris avalanche (Fig. 5.6).

## 5.8 Conclusions

The shape of an avalanche path affects the structural features and morphology of the deposit. The structures are formed progressively as the avalanche slides

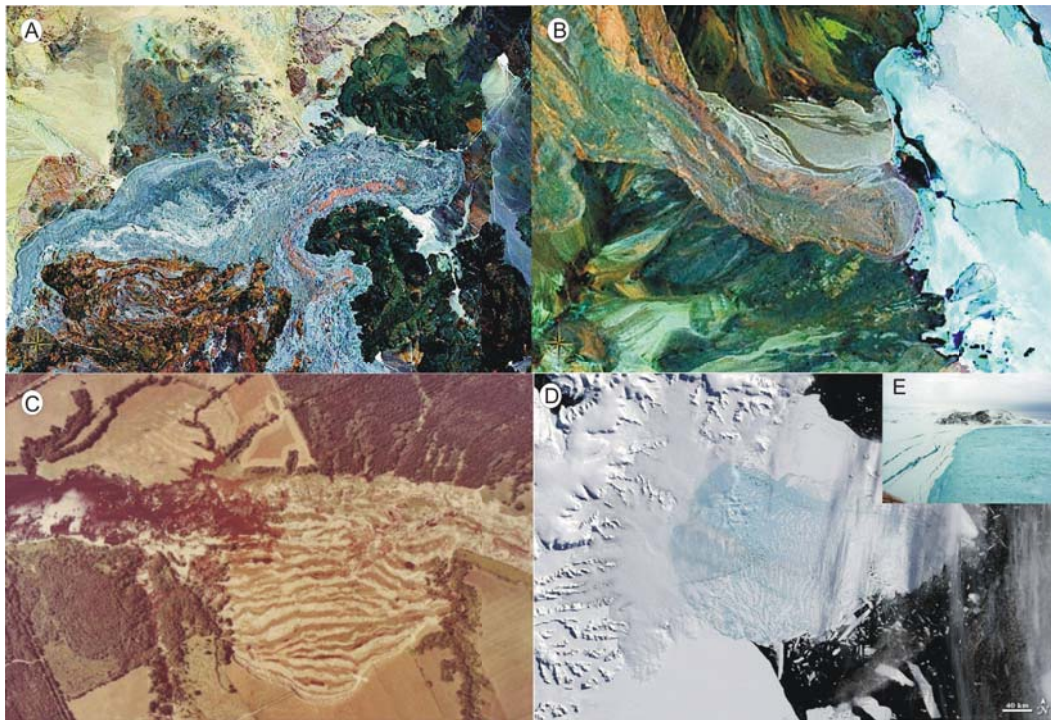


Figure 5.9: Natural examples of the tongue-like long runout deposits and rib-and-ridge morphology formed on a smooth and straight failure surface. Tongue-like long runout deposits at A Llullaillaco southern avalanche and B Socompa rockslide-debris avalanche, and the rib-and-ridge morphology of the C South Nation River slide (Quinn et al. 2011) and D Larsen ice shelf in Antarctica (Quinn et al. 2007). Inset in E is a closer view of the faults that accommodate the breaking and disintegration of the ice shelf.

down. The deposit thus reflects the evolution of the slide. Slides and avalanches on curved ramps (Set 1) and the Guinsaigon rockslide-debris avalanche deposit result into fan-shaped deposits with displacement of coherent blocks creating terraces or steps, and hummocks. Materials start to accumulate at the base of the initiation zone and thicken where the slope decreases (depositional zone) forming the medial accumulation zone. Frontal accumulation during flow occurs as materials at the front move slower relative to those in the medial and proximal zones. This helps maintain a thicker mass that can be remobilised by secondary sliding.

Incoherent and monolithologic materials on a smooth and straight failure surface (Set 2) experiments and the Storegga slide can form the tongue-like longer runouts with rib-and-ridge morphology. The stability of the proximal and instability of the distal sides of the block form transtensional grabens.

Most materials accumulate in the distal portion making up the head of the deposit. The features that differentiate the curved and straight ramps imply that during emplacement, extension and spreading by sliding and translation dominate in avalanches and large landslides until sliding at the distal zones wanes and thrusts and folds start to form, resulting in accumulation zones.

Curved and straight basal slide ramps will always generate strike-slip faults in the levees and in the medial zone during spreading. Thrust faults result from a deceleration in the distal margin while material in the proximal and medial areas is still sliding. Folds in the distal zone are caused by the interaction and drag from late-emplaced material sliding next or over previously emplaced materials. Normal faults appear anywhere in the deposit where extension during material spreading occurs and large displacement along them creates the transtensional graben, rib-and-ridge morphology, and secondary slides. Secondary slides happened in Guinsaigon (Fig. 5.6) rockslide-debris avalanches. Such processes may be important in many mountainous avalanches where there are rapid changes in slope.

Description of these structural features and morphology in large landslides and avalanche deposits help in understanding the transport type, emplacement mechanism, and deformation history of the natural prototypes. It also gives insights on what to expect shall a natural avalanche with a curved basal layer or a large landslide with a straight base and incoherent monolithic material happen.

CHAPTER 6

**Structural and morphological  
mapping of large landslides and  
debris avalanche deposits  
(DAD)**

---

## 6.1 Abstract

The identification and characterisation of the surface features of debris avalanche deposits (DAD) by remote sensing is an important component for studying possible scenarios for debris avalanche causes, their triggering and their emplacement mechanisms. This is especially so for large, unmapped or little known volcanic or non-volcanic DAD.

This chapter presents three previously little known DAD at Süphan Dağı (Turkey), Cerro Pular-Pajonales (Chile-Argentina), and Tacna (Peru) using remote sensing (RS) and geographical information system (GIS) methods. Data used are the: SRTM and ASTER DEM and LANDSAT multispectral images, as well as Google Earth. A detailed description is presented of the important features such as: the collapse scars, DAD extent, levees, hummocks, lobes, ridges, and morphological features such as the rib-ridge morphology, accumulation zones, and frontal “mini slides”, as well as structures: normal, thrust and strike-slip faults.

The interpretation is based on experience gained from structural and morphological mapping of laboratory analogue avalanches as well as from field knowledge gained at the Iriga and the Guinsaigon (Philippines), and the Meager (Canada) DAD.

From interpretation of the structural and morphological features, a scenario for each debris avalanche emplacement is given. Such DAD are often too big and too seemingly chaotic to be successfully studied in the field. The synoptic view that remote sensing and GIS provide an excellent good way of looking at the deposits of such big events and a standardised approach allows the comparison of different events. Mapping these deposits is a necessary step for the identifying hazard for large-scale landslides.

Keywords: Süphan Dağı (Turkey), Cerro Pular-Pajonales (Chile-Argentina), Tacna (Peru), debris avalanche, remote sensing, GIS, morphometric and structural mapping, SRTM, Landsat

## 6.2 Introduction

Avalanches can occur on the slopes of volcanic and non-volcanic terrains. They can involve rocks, sediments, snow and ice, or a combination of any of these at different scales (Hunger, 2006). Volcanic debris avalanches can cover several hundreds of square kilometers, travel long distances (Shea et al., 2008; Stoopes and Sheridan, 1992), and reshape volcanoes (Dufresne and Davies, 2009). Avalanches can directly or indirectly cause human and property loss by generating subsidiary events like tsunamis, damming, lahars, or magma re-

lease (Siebert, 1984; Siebert et al., 1987; Voight and Elsworth, 1997). Debris avalanches occur on structurally weakened volcanoes and mountains depending on the deformation types, duration, and intensities (Shea et al., 2008), and can be triggered by short timescale events (Dufresne and Davies, 2009).

### 6.2.1 Structures and Morphological Features in Analogue and Natural DAD

Most analogue avalanche studies are concerned with understanding the transport and emplacement mechanisms of landslides (Campbell, 1989; Campbell et al., 1995; Kelfoun and Druitt, 2005; Pouliquen and Renaut, 1996; Staron et al., 2001) and verifying models of granular flow (Denlinger and Iverson, 2001; Iverson and Denlinger, 2001). Recent small-scale analogue models that replicate the natural avalanches provide a conceptual view on the formation of the structural and morphological features on the avalanches and are used to explore their kinematics and dynamics (Andrade and van Wyk de Vries, 2010; Shea and van Wyk de Vries, 2008). Earlier in this thesis, the description and characterisation of the morphology and structures from the early stages of collapse towards the final phase of material runout were performed with the assumption that a simple shear regime operates in the upper brittle layer and a pure shear in the basal ductile layer.

Thus, Chapters 3 and 5 of this thesis characterised and discussed the formation, evolution, and importance of hummocks as a prominent topographic feature in large landslides and debris avalanches, and of recurrent structures and morphology in long runout landslides. The prominent and recurrent deposit morphology and structures in curved and straight ramp models are compared to the natural DAD at Mt Iriga, Mt Meager, Storegga and Guinsaigon in Chapters 2, 4, and 5 of this thesis. An in-depth look at how the hummocks form and what they mean is presented in Chapter 3. In plan view, curved ramp experiments produce more laterally spreading and relatively thicker deposits compared to the tongue-like, and longer runout of the straight ramp experiments. Strike-slip faults, thrust faults and fold, and perpendicular or sub-perpendicular to slide direction normal faults are recurrent structures, together with the translation and accumulation zones, levees on the lateral sides and secondary 'mini' slides on the over-steepened front, hummocks, transtensional grabens, and rib-ridge morphology.

### 6.2.2 Remote Sensing and GIS in Mapping DAD

Most applications of RS in geology involve the delineation of structures, discrimination of different rock and soil types and resource exploration (Kruse

	Characteristic	Landsat TM	Landsat ETM+
Spectral region	Visible and reflected IR	0.45 to 2.35 $\mu\text{m}$	0.45 to 2.35 $\mu\text{m}$
	Panchromatic		0.52 to 0.90 $\mu\text{m}$
	Thermal IR	10.5 to 12.5 $\mu\text{m}$	
Spectral bands		7	8
Terrain coverage	East to west	185 km	185 km
	North to south	170 km	170 km
Ground resolution cell	Visible and reflected IR	30 $\times$ 30 m	30 $\times$ 30 m
	Panchromatic		15 $\times$ 15 m
	Thermal IR	120 $\times$ 120 m	60 $\times$ 60 m

Table 6.1: Landsat characteristics

and Dietz, 1991). The wide area coverage of the data in connection with their long-term availability allows analysis of the spatial dynamics within larger areas of large-scale events such as debris avalanches and large landslides even in inaccessible areas. The capability for the RS data to be used in recognising and mapping DAD extent and constrain their emplacement processes (Francis and Wells, 1988; Wadge et al., 1995) is particularly important in studying such events. A DAD has a recognisable topography and contrasted spectral properties with the adjacent areas. GIS improve the quality and power of geological interpretation and analysis of RS data. The capacity of GIS to perform spatial and statistical calculations is important for natural hazard assessments.

### 6.2.2.1 Optical Remote Sensing

The availability of multi-spectral, optical, and high-resolution data and the advanced capabilities of digital image processing techniques to enhance interpretable images have increased the potential and accuracy of delineating geological structures (Drury, 1987), and DAD features. The existing multi-spectral Landsat satellite systems are useful for mapping lithologies designed to investigate natural resources with special focus on vegetation coverage, lithology, and mineral exploration (Crippen and Blom, 2001; Yousif and Shehid, 1999).

Many geological studies have employed Thematic Mapper (TM) and Enhanced TM+ data to discriminate the various lithologies, lineaments, and minerals. Spectral characteristics of TM bands (Table 6.1), with its advanced multispectral scanning and earth resources sensor designed for higher image resolution, sharper spectral separation, improved geometric fidelity, and greater radiometric accuracy and resolution than the MSS sensor are suitable for

mapping lithology and alteration zones in regions where bedrock is exposed. Landsat 5-TM is useful for vegetation and soil moisture studies, and discriminating between rock and mineral types (<http://www.satimagingcorp.com>). Hydrothermal alteration areas may be distinguishable using the ratio of TM band 5 and 7 (Podwysocki et al., 1982; Prost, 1980; Rowan and Kahle, 1982).

Landsat-7 Enhanced TM (ETM+) has a panchromatic, thermal, and reflective bands of 15, 60, and 30 m per pixel ground resolution that covers the visible green to near-IR portion of the electromagnetic spectrum (Table 6.1). It is in the mid-infrared, particularly helpful for discriminating among types of rock formations and offers a very high resolution mapping capability for volcanic features. Image enhancement techniques and colour compositions of multi-spectral data sets create the false colour and the true colour composites that improve the visual appearance and increase interpretation accuracy.

### 6.2.2.2 Radar Remote Sensing

Optical RS data can be supplemented by a DEM that can be converted to a shaded relief image with varying sun azimuths and angles and height exaggerations (Drury, 1987; Lillesand and Kiefer, 1979; Strandberg, 1967). A DEM data has seven elements useful for geological interpretation: tone, texture, pattern, size, shadow, shape, and association (Gupta, 1991; Lillesand and Kiefer, 1979). These elements reflect the surface morphology, soil moisture, vegetation cover, and drainage pattern of an area that can give information rock type, structure, process, and time.

In a shaded relief image, tone, the grey level of a certain pixel of the image, is the primary basic element. It is the proportion of the deviation angle from the normal incident of light from the sun and so, depends on its slope and aspect. Other elements like texture and patterns are arrangements of tone that reflect the elevation or slope and aspect.

The National Aeronautics and Space Administration's (NASA) SRTM launched in 11 February 2000 aimed at producing digital topographic data for 80% of Earth's land surfaces. It used both a C-band of 5.8 cm wavelength and X-band of 3-cm wavelength radar separated by a 60 m long mast to produce 1-arc second and 3-arc second spatial resolution data for the USA and the rest of the world. NASA's Jet Propulsion Laboratory processed the topographic data.

Since its release in 2002, SRTM data became an essential source of information for volcano-tectonic studies such as large-scale structural mapping of volcanic features (e.g. Grosse et al., 2009; Kervyn et al., 2008; Lagmay and Valdivia, 2006) and evaluate models for volcano instability such as sector collapse and gravitational spreading. Although this dataset was resampled into from

30 m to 90 m losing some morphological information, it does not preclude quantitative discrimination of volcanoes on the basis of their morphology and still made a significant contribution to the study of volcanic forms and volcanic hazard assessment (Wright et al., 2006). Structures appear as either linear features for faults or curvilinear for underlying domes in an image (Drury, 1987; Lillesand and Kiefer, 1979; Strandberg, 1967). Visual interpretation for geology is an effective method and needs a skillful interpreter (Gupta, 1991).

### 6.2.3 Objectives and Limitations

Identification and mapping of DAD can help understand the mechanism and triggering factors of the collapse and assess the related hazards. Remote RS structural and morphological mapping provide much needed information on rockslide avalanche kinematics and can give an idea on the original topography of the source and depositional areas, and possibly, the source material characteristics.

This part of the study will apply what has been learned in doing RS structural and morphological mapping on natural the DAD at Iriga and Guinsaigon (Philippines) and Mt Meager (Canada) rockslide-debris avalanches and analogue experiments. The aim is to identify, map, and characterise morphological features and structures to discuss the emplacement mechanism and the implications for hazards and monitoring needs of previously unmapped DAD at Süphan Dağı, Cerro Pular-Pajonales, and Tacna. For these areas, field analyses are beyond the scope of this study and while future fieldwork is anticipated, each area is difficult to access and hard to work in, so that RS will remain the principle information source in geographic space. The technique, iproposed here, can be applied to other inaccessible volcanoes and may contribute to the improvement of understanding DAD and corresponding assessment of hazards.

## 6.3 Study Sites

### 6.3.1 Cerro Pular-Pajonales (Chile-Argentina)

Cerro Pular, a massive stratovolcano with a volume of more than 13 km<sup>3</sup> and height of 6200 m along with its major satellite vent Cerro Pajonales at 5900 m at the south is classified as an unusually large sub-cone by the morphometric analysis of Grosse et al. (2009). It forms a 12-km northeast to southwest high volcanic ridge (Smithsonian Inst Bull Global Volcanism Network 6/1990 and 1/1991). Cerro Pajonales is the youngest feature of the volcanic complex with evidence of Holocene activity. The Cerro Pular-Pajonales are the two

major centres that form the southern and most recent part of the Cerros de Coransoque that forms a drainage divide between Salar de Atacama basin and Salar de Pular basin.

The volcanic ridge shows evidence for a long volcanic history such as extensive lava flows on the lower flanks and several craters along the crest of the ridge (<http://volcano.oregonstate.edu/oldroot/CVZ/pularpajon/index.html>). Laguna Pajonales, a small lake is on the southern part of Cerro Pular. Lavas from Cerro Pular-Pajonales are well preserved at lower elevations and glaciated at the upper levels.

### 6.3.2 Süphan Dağı (Turkey)

Süphan Dağı is the 2nd highest volcano in Turkey on the northern shores of Turkey's largest lake, the Lake Van. This large volcano together with the fissure flooding of Malazgirt graben (Fig. 6.3A-B) were volcanic events in the Quaternary. The Süphan Dağı basal products consist of numerous eruptive centers formed by domes with thick lava flows (Innocenti et al., 1980) and minor pyroclastics of calc-alkaline affinity. The most recent are the obsidian domes and lava flows (Innocenti et al., 1980). Perlite domes and explosion breccia ramparts such as Nernek Dağı and Mustafa Hill (Fig. 6.3A-B), and Aygörgölü maar (Fig. 6.3A-B), a 1.5 km wide, low-rimmed depression related to the phreato-magmatic eruptions of Süphan Dağı (Innocenti et al., 1980) are on the southern margin of the volcano.

Süphan Dağı and its vicinity represent a post-Miocene tectonic depression in a convergence zone of the Anatolian-Iranian block and the Arabian plate. This geodynamic setting is expressed in a very complex structural context where folds, transcurrent and tensional elements have been developing from the Cretaceous up to present. This structural evolution is connected with the development of volcanism showing various volcanic characters and petrogenetic affinities since the Miocene. The main structural trend strikes NE to NNE with second fracture system transverse to it at NW to WNW. The margins of Süphan Dağı are controlled by tensional fractures and faults that modify the volcano shape and represent the main magma feeding system during the Pliocene and Quaternary that fits into the regional compressional regime in the area (Innocenti et al., 1980). Süphan Dağı is a volcano related to a tail-crack structure at the SE termination point of the 50 km long NE-striking Süphan Fault and terminate in a maar volcano emplaced on the fault side (Adiyaman et al., 1998). Two others terminate into curved faults that are interpreted as an open tail-cracks at fault end forming the curved ends and the open crack underneath the volcano as well, similar to patterns described in the Ethiopian rift (Chorowicz et al., 1994).

Potassium-Argon dates for Süphan Dağı range from 2 to about 0.1 million years, but the latest basaltic eruption occurred about 10,000 y ago (Yilmaz Y. et al., 1998). During the latest stage of activity, voluminous basaltic lava flows travelled as far as 30 km from the summit.

### 6.3.3 Tacna (Peru)

Two regional structures: the Incapuquio Fault System and the Sama-Calientes Fault run through the Tacna landslide area. The Incapuquio fault system is an Oligocene left lateral (Jacay et al. 2002), straight, and well-delineated fault about 200 km as traced on SRTM DEM and aerial photographs. In the field, it that cut through various relief, bedrock, and alluvial deposits (Audin et al., 2006). Temporary seismic networks employed in the area indicate crustal seismicity on Incapuquio fault system suggesting ongoing tectonic activity by a near vertical fault (David et al., 2004).

Associated with the Incapuquio fault system is the 50 km long Sama-Calientes Fault system. It is an emergent thrust fault that affects the Holocene terraces and offsets a series of brown to white layers in a natural trench visible along the dry valley in Calientes town (see Fig. 3C of Audin et al., 2006). The Sama-Calientes Fault runs near Calientes town, upstream of Tacna and cuts through the active flood plain of the Caplina River Valley. This fault forms a km long emergent thrust with major flexures in the Huaylillas Formation (25-9 Ma by Roperch et al., 2006). Last surface ruptures are within the youngest river terrace near the village of Calientes and also within the Pedregal Plain (Audin et al., 2006). The trace of the fault follows some folds and reverse faults that offset terraces in the active drainages (dry secondary rivers) or the sediments of the Pliocene Calientes Formation (Fig. 3C of Audin et al., 2006), Moquegua units (Oligocene to Neogene) or the Early Miocene Huaylillas Formation (Fig. 3A and 4 of Audin et al., 2006)(Figs. 3A and 4 of Audin et al. 2006). Calientes fault segment has post Pliocene activity indicated by the folds in the Calientes Formation. Well-preserved scarp dipping steeply to the south and affecting the Huaylillas Formation are observed along the foothill of Pedregal Plain (Audin et al., 2006) but are barely followed through the Cerrillos Negros between Pedregal (west) and Lagayache (east) Plains. It is the distal zone of a major rock avalanche coming from the Cerro Caquilluco giant landslide area uphill.

## 6.4 Methodology

### 6.4.1 Data Gathering and building the GIS

Remotely sensed SRTM DEM (<http://srtm.csi.cgiar.org>), ASTER GDEM (<http://asterweb.jpl.nasa.gov/>), and Landsat ETM+ for Cerro Pular-Pajonales and Tacna and TM Mosaic for Süphan Dağı (<http://edcns17.cr.usgs.gov>) imagery covering the target areas were downloaded. These images were opened, post-processed, and visually inspected using the ENVI<sup>®</sup> software to study the structures, morphology and topography of each areas.

Topographic modelling for DEM and colour composites for optical RS data are performed to available data sets. After enhancing the geological and geomorphologic features in the images, they are stored in a geo-database for easy presentation and facilitate the morphological and structural interpretation and mapping.

### 6.4.2 Topographic Modelling: SRTM DEM and ASTER GDEM

Topographic modelling for DEM data is made by converting them into shaded relief and hillshade images for a 3D depiction of the terrain. During the process, the sun azimuth and sun angle are changed to enhance and generate hillshade images. These processes accentuate the structural grain and discontinuities in the topography, highlighting the geologic structures. Several different light direction orientations from different sun azimuth and sun angle values should be chosen subsequently while investigating the imagery for the same region, in order not to miss structural features obscured by certain light directions.

### 6.4.3 Colour Composites: Landsat ETM+

Generating the true and false colour composites for the Landsat mosaic images show and enhance the surface features in the areas of interest. The colour composite image enhancement is done by creating images from a combination of image band data displayed in red, green, and blue display channels (Drury, 2001; Liu and Mason, 2009). Different bands were combined guided by Table 2 to map out deposits and confirm structures and morphological features. True colours in RGB often show more contrast in surface features.

RGB display	Red	Green	Blue	Extra	Reference
4:7:6	Structural ment differentia- tion	linea- Hydrothermal alteration	Temperature trast	con-	Rothery 1987
7:5:4	Intrusive/ drothermal alterations	hy- Gabbro	Vegetation		Rothery 1987
7:4:2	Vegetation	Vegetation		Radiometric cor- rection important	Chica-Olmo 2002
4:7:5	Granites, MnO as brown areas	FeO, redish/ brighter Clay minerals are brighter	Clay minerals are brighter	Radiometric cor- rection important	Chica-Olmo 2002
7:4:2	Pink background	Monzogranite grayish-green	Sedimentary units in bluish-grey	Sedimentary and volcanic units are separated	Abdelhamid, and Rabba 1994
4:7:2	Orange-red ground	back- FeO is yellow			Jingyuan and Xuc- man 1991
4:7:3	Orange-pink ground	back- FeO is yellow			Jingyuan and Xuc- man 1991

Table 6.2: Literally known colour composites used as guide in the colour composition and lineament delineation.

### 6.4.4 RS and GIS Interpretation and Surface Mapping

Processed and enhanced satellite images were interpreted to extract their most striking morphometric and structural characteristics. Geological features such as sedimentary mounds, volcanic cones, maars, lava flows, and water bodies (e.g. lakes) are identified and delineated as shape files in the GIS. Other features such as the collapse scar, lobes, hummocks, areas with a rib-ridge morphology and en-echelon fractures, and normal, thrust and strike-slip faults are also recorded.

Identification and mapping of features is entirely based on visual interpretation, common sense, knowledge from the structural and morphological mapping at Iriga, Guinsaugon, Storegga, and Meager slides as well as from analogue model examples. These features are identified based on topographic expressions on the DEM and spectral contrast on the Landsat images as a result of the difference in vegetation cover, morphology, and structures with other adjacent deposits. The DAD extents are inferred from the distribution of these structural and morphological features.

Faults and lineaments are identified as clear and straight segments. In dissected terrains, they are identified by the abrupt tonal changes, and contrasting tonal corridors. On a regional scale, lineaments are rectilinear or gently curved alignments of topographic features [Hobbs \(1911\)](#). Some morphologic structures may be linked together as a lineament. Independent of topography, straight lineaments can be sub-vertical-normal faults (e.g. [Shea and van Wyk de Vries, 2008](#); [Wise et al., 1985](#)). Curvilinear structures, in general, are dipping less steeply. Lineaments are attributed to a statistical significance on the level of a set of parallel linear elements and grouped in lineament swarms. Tightly disposed parallel lines are replaced by one main lineament. This is confirmed by doing routine analysis, looking at different shaded relief images processed from different viewing angles (different sun and angle azimuth).

## 6.5 Results

### 6.5.1 Cerro Pular-Pajonales

Deposits and sediments of the southern to eastern sides of Cerro Pular Pajonales are flanked by Salin, Tarque, Agua Delgada, Aracar, and Arizaro volcanoes (Fig. 6.1A). In between these volcanoes is the Salar de Pular and an area of rough, hummocky topography, assumed to be a DAD (Fig. 6.1A-B, 6.2). The Cerro Pular-Pajonales ridge is scarp-shaped, probably the trace of the old Cerro Pular debris avalanche scar (Fig. 6.1A-C).

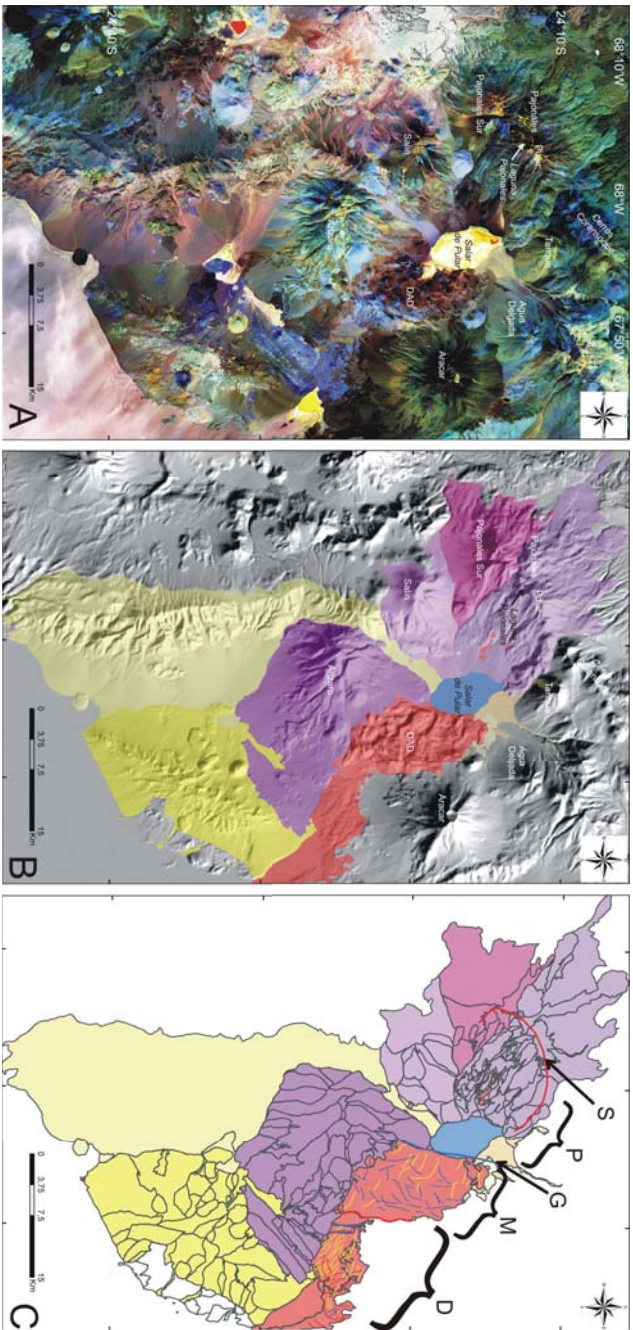


Figure 6.1: Cerro Pular-Pajonales DAD and its vicinity **A** Landsat ETM+ with Cerro Pular-Pajonales DAD in the middle and and the surrounding volcanic centres. **B** Volcano and sedimentary units grouped according to its nearest volcanic centre (polygons in shades of violet) as a possible source draped over a SRTM DEM. **C** Geological and morphological features delineated to extract the Cerro Pular-Pajonales DAD (red polygon). Those related to a possible batholith (2, 3) and recent sediments coming down from volcanic center 10, 8, 12 are in yellow, and water bodies (i.e. salt lake) in blue. The DAD itself has three zones proximal (P), medial (M); and distal (D) zones and the collapse scar (S, thick red polyline); and graben (G, thick blue polyline on the southern boundary of Salar de Pular) are also shown. Structures including the normal (red), thrust (blue), and strike-slip faults (yellow); Graben (G), secondary slide (SS) and transtensional graben (TG) are drawn on the debris avalanche surface.

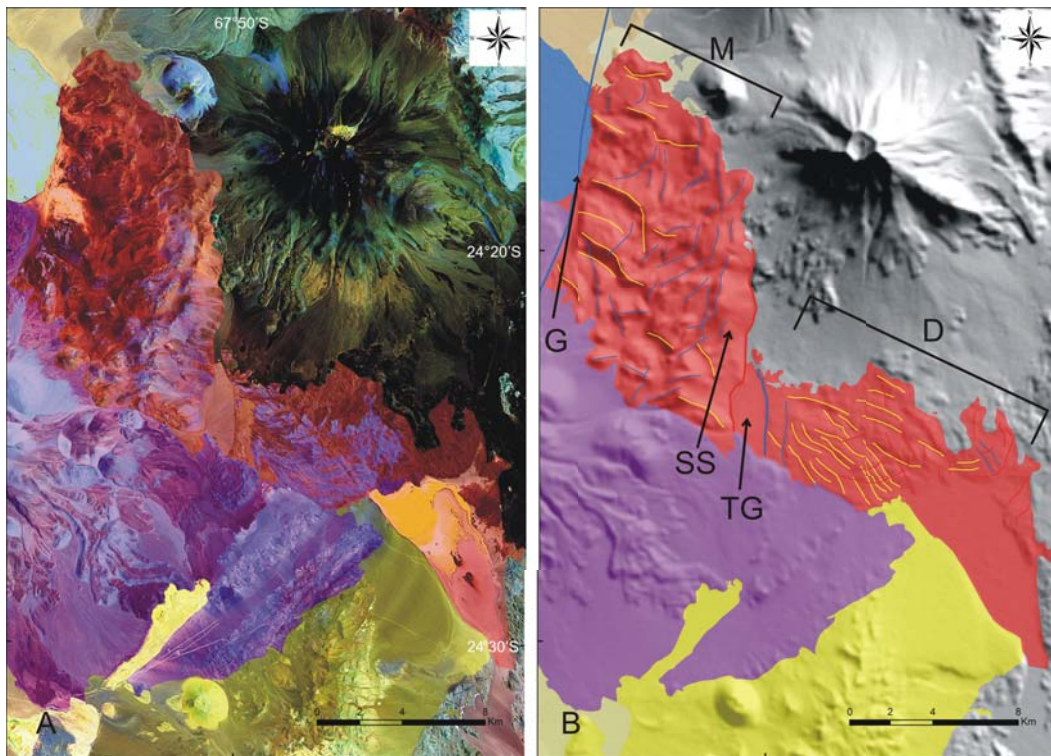


Figure 6.2: Cerro Pular-Pajonales DAD. **A** Landsat ETM+ image of the DAD (in red), showing the hummocky topography in the medial part (upper, left-closer from source) and the smoother, thinner deposit in the distal zone (lower, right-farther from source). **B** DAD draped on a DEM. Structures including the normal (red), thrust (blue), and strike-slip faults (yellow), and the graben (G), secondary slide (SS) and transtensional graben (TG) are drawn.

All geologic and morphologic features and structures such as lava flow and deposits with different spectral signatures and surface textures from its adjacent areas are delineated (Fig. 6.1C). These features are then grouped according to the nearest source area for volcanic deposits (Fig. 6.1B-C). Those left with unique surface texture, morphology and structures similar to those of the natural and analogue DAD are identified to be part of the DAD (red polygon in Fig. 6.1-6.2).

### 6.5.1.1 Geometry of the DAD

For organization of detailed description, the 50-km long Cerro Pular-Pajonales DAD is divided into three zones: the proximal (P), medial (M), and distal (D) areas. Based on the more recent deposits from the surrounding volcanic

centres that cover most of the DAD, this must be an old avalanche deposit (probably several million years old).

Recent deposits from Cerro Pular, Cerro Pajonales, and Cerro Pajonales Sur cover the proximal area nearest to the source (for about 20 km). The other half of the entire DAD runout, for 28 km is the only visible part DAD. This area consist the DAD medial and distal depositional zones with its lateral sides covered by the deposits from Arizaro, Agua Delgada, and Aracar volcanoes.

From the definition of [Shea and van Wyk de Vries \(2008\)](#), the Cerro Pular-Pajonales DAD is proximally raised with irregular edges, as the thickest part is the medial zone and not the distal zone. The medial zone is also wider at about 14 km and thins to about 6 km across downslope in the distal zone.

### 6.5.1.2 Structures and Morphology of the DAD

Downslope of the Pular-Pajonales scar-shaped ridge (thick red polyline, Fig. 6.1B-C) is a smoother surface of volcanics that descends toward the Salar de Pular. The Proximal zone of the DAD, also its translation zone has a smooth surface. Thus, this area is also covered by recent deposits. At the edge of the proximal zone is a depression, Salar de Pular. The southern boundary of this lake and the northern edge of the thicker, medial zone is a prominent structure, probably a graben. The thicker deposit in the medial zone has strike-slip faults (yellow polylines, Fig. 6.1C, 6.2B) parallel to the assumed transport direction. In the medial zone are thrust faults (blue polylines, Fig. 6.1C, 6.2B) normal to the sliding direction. On the front-most edge of the medial zone is a very steep and thick deposit. In general, the thick medial zone is dominated by compressional structures with some extension nearer the source and at the over steepened front. A thin deposit extends from the steep front interpreted as a secondary collapse. This forms the distal zone of the DAD. Flow bands and strike-slip faults dominate the thinner, more smooth-textured distal depositional zone.

### 6.5.2 Süphan Dağı

On the northern side of Süphan Dağı, two probable DAD were mapped (Fig. 6.3-6.4): the western and eastern Süphan Dağı DAD. The west-east elongated volcano has a trace of scars opening towards the NW and NE that are traversed with either of the NE- or NW- trending regional structures (Fig. 6.3C). To trace the extents of the two DAD, all geological features such as lava flows and sedimentary features adjacent to the volcano are delineated (Fig. 6.3A) and grouped into the two DAD and a non-DAD deposit (Fig. 6.3B) that includes the sedimentary deposits on the northeast side of the volcano and the post-

collapse deposits that mantle some parts of the DAD in the translation zones. The geometry, morphology, and structures in both DAD are identified and described below.

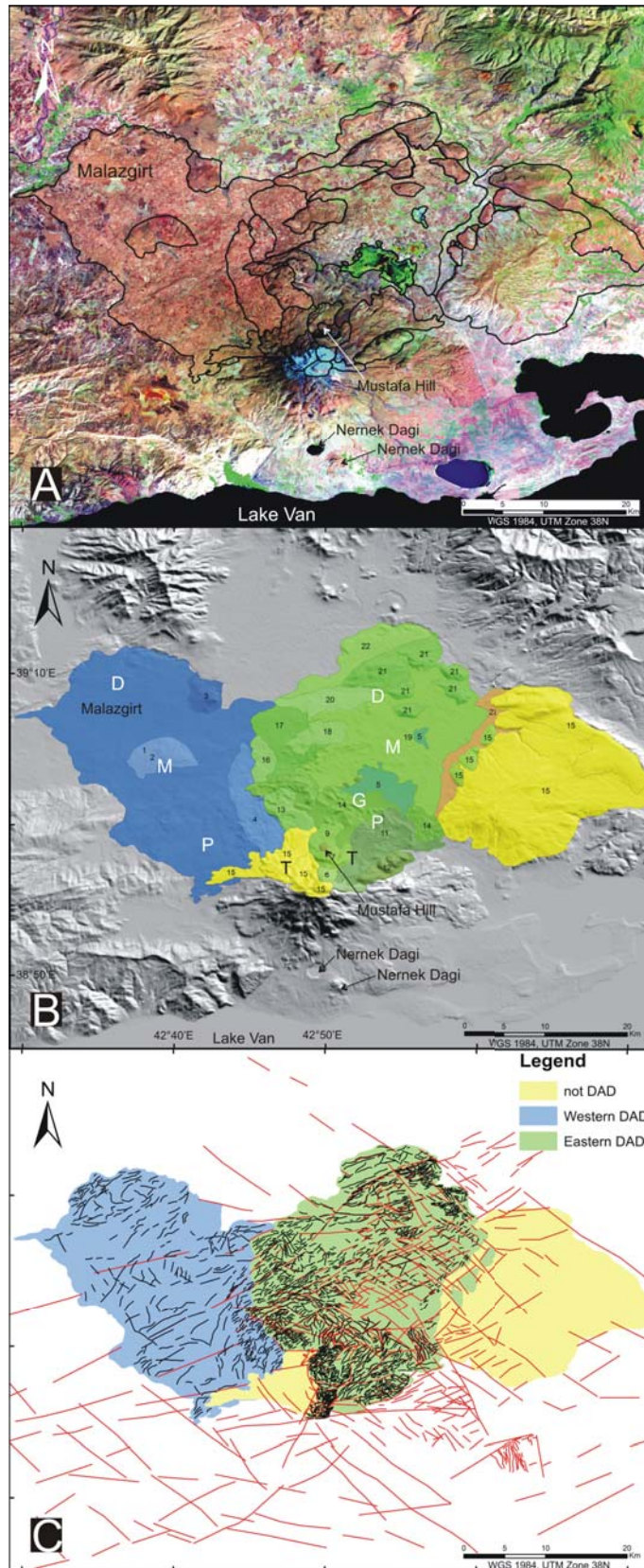
### 6.5.2.1 The Western Süphan Dağı DAD

There are four areas and blocks (Fig. 6.3B, 6.4A) delineated within the western DAD that show varying spectral signatures, surface texture, morphology, and structures: the main body (polygon 1), the blocks (polygons 2 and 3), and the eastern levee (polygon 4). The DAD has a single lobe with irregular edges (Fig. 6.4A). It has a runout of about 36 km towards the northwest direction and is 13 km wide at the narrowest proximal and distal areas and 19 km across in the medial zone. Post-collapse lava flows cover most of the summit down to the piedmont of the volcano. A graben structure separates the translation and proximal depositional zones. On the eastern side of the proximal depositional zone, a levee (polygon 4 in Fig. 6.3B, 6.4A) with an en-echelon structures indicating strike-slip faulting is mapped. Two blocks, polygons 2 and 3 have surface texture that is different from the main body of the DAD (polygon 1, in Fig. 6.3B, 6.4A). The larger block (polygon 2 in Fig. 6.3B, 6.4A) in the medial zone has parallel structures perpendicular to the sliding direction. On the distal portion, a smaller block, polygon 3 (Fig. 6.3B, 6.4A) has smoother surface texture similar to the surface of the landform on the northern side.

In the depositional area of the DAD are at least four major NE structures. Other prominent structures (Fig. 6.3C, 6.4A) delineated include: the strike-slip en-echelon fractures in the eastern proximal edge; the perpendicular to sub-perpendicular normal faults in the proximal zone that exhibit stretching and extension; and the transtensional structures in the medial zone that indicate a dominantly lateral spreading. The dense thrust faults perpendicular to the sliding direction and the probable folds at the front of the distal zone indicate strong frontal deceleration and bulldozing.

### 6.5.2.2 The Eastern Süphan Dağı DAD

The eastern DAD at Süphan Dağı extends 33 km towards the northeast from the volcano and is 19 km, 9 km, and 22 km across in the proximal, distal and medial zones, respectively. It is slightly asymmetric, being broader towards the northeast. This debris avalanche is constrained by the higher elevation on the northern edge and by the sedimentary deposits and landforms (polygon 15 in Fig. 6.3B, 6.4B) on the eastern side. The same post-collapse lava (polygon 15 in Fig. 6.3B) that mantles the collapse zone of the western DAD also covers the western edge of the eastern DAD.



A collapse scar that opens towards the north is evident. On both sides of the translation zone, are remobilised blocks (polygons 9, 7, 6, 12 in Fig. 6.3B, 6.4B). The lateral sides of the source area have lava flows with perpendicular normal faults that extend downslope (Fig. 6.3C, 6.4B). The middle part of the source area is dominated by strike-slip faults, although there is an extensional feature in a transform zone. Further downslope in the proximal zone, there are perpendicular to sub-perpendicular transtensional (normal with strike-slip component) faults. In the proximal depositional zone are ridges oriented perpendicular to the sliding direction. This area is bounded to the north by a graben structure. This structure also bounds the southern end of a lake (polygon 5 in Fig. 6.3B, 6.4B). The structurally controlled lake is part of the medial depositional zone that exhibits a hummocky topography (polygon 19 in Fig. 6.3B, 6.4B). The edges of the deposit on the proximal zone and the shape of the lake indicate a graben within this area formed as the slope gradient changed from a steeper source and translation area to a gentler medial and distal depositional zones just like those in analogue models. The eastern side of the medial zone is dominated by extensional strike-slip faults while its western counterpart is dominated by perpendicular to sub-perpendicular faults. Toward the distal depositional zone are large blocks of hummocks (polygons 21 and 15 in Fig. 6.3B, 6.4B) with compressional structures perpendicular to the sliding direction.

### 6.5.3 Tacna

The Tacna rock avalanche has a runout of about 44 km and it is 8 km at its widest and 3 km at the narrowest in the translation and distal zones, respectively. Major regional structures: the Incapuquio Fault in the source area and the Sama-Calientes Fault System in the distal depositional zone; and a lineament that could be a branch of the Incapuquio Fault cross the DAD. Movement along these faults may have also caused or triggered the slide and may have affected the emplacement and transport direction during

---

Figure 6.3 (*preceding page*): **A** Landsat TM Mosaic with the all the delineated parts of the Süphan Dağı western and eastern DAD. **B** SRTM showing the shaded relief map of Süphan Dağı with its two DAD: western DAD (blue) and eastern DAD (green). The yellow polygon is not part of the DAD and description of each numbered polygon is in the text. **C** The two DAD of Süphan Dağı drawn with the regional (red lines) and localized (in the DAD, black lines) structures. The translation (T), and proximal (P), medial (M) and distal (D) depositional areas are also marked in white ink.

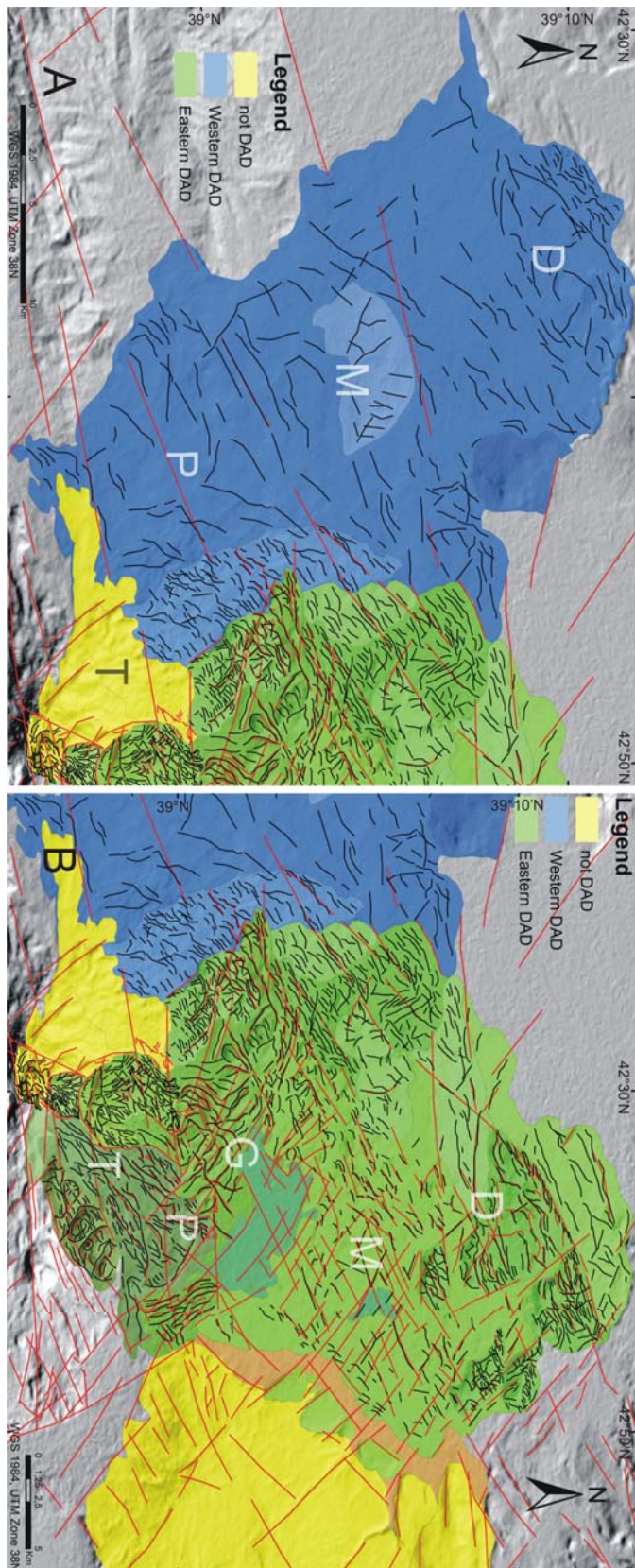


Figure 6.4: The two DAD of Süphan Dağı: **A** the western and **B** eastern DAD. Regional structures (red lines) and the localised faults (black lines), and the translation (T), and proximal (P), medial (M) and distal (D) depositional areas are also shown.

the avalanche (Fig. 6.5).

This DAD is extension dominated as implied by the density and population of strike-slip and normal faults. The thrust faults are only related to the emplacement of later debris and rock materials on top of the earlier deposits from the earlier stages of the collapse.

Six lobes can be traced in the DAD that imply series of collapses that happened during the avalanche (Fig. 6.5B) such as those shown in the long runout avalanche models presented in Chapter 5. The first collapse deposited the three sub-lobes, the longest reached the distal depositional zone, and the other two stopped in the proximal and translation zones. The regional structures (red line in Fig. 6.5A) have influenced the transport and emplacement of the first slide as shown by the abrupt change (red arrow in Fig. 6.5B) in the sliding direction of the debris slide. This collapse is extension-dominated as implied by the density of strike-slip faults (yellow lines in Fig. 6.6B-D) in the middle part of the proximal and medial zones, and levees in the distal zone. Some normal faults are also delineated in the first lobe in the distal depositional zone. Most of them form repeating short ridges elongated perpendicular to the sliding direction that form the rib-ridge morphology. The proximal deposits of the first collapse are mantled by deposits from the third collapse, forming the third lobe that is also mantled by deposits from the fourth collapse except on its distal portion. The ends of these lobes are delineated by the thrust faults at the front and strike-slip faults within the lobe.

The source area (Fig. 6.6A) has two distinct regions: the western and eastern side. The western collapse scar (Fig. 6.5B) has a generally smoother morphology with the fourth to the sixth lobes deposited from the last three collapses of the Tacna slide. From the previous collapses, the flank of this mountain has lost most of the lower material, thus loosening the support and destabilising the eastern adjacent side and forming the normal faults parallel to the main sliding direction. The sliding of the materials in the source area, however, did not quite succeed because of the confinement by the new lobes that were deposited in the sliding direction. This created the repeating horsts and grabens formed from the extension by normal faulting as materials in the eastern side moved towards the west resulting a rib-ridge morphology.

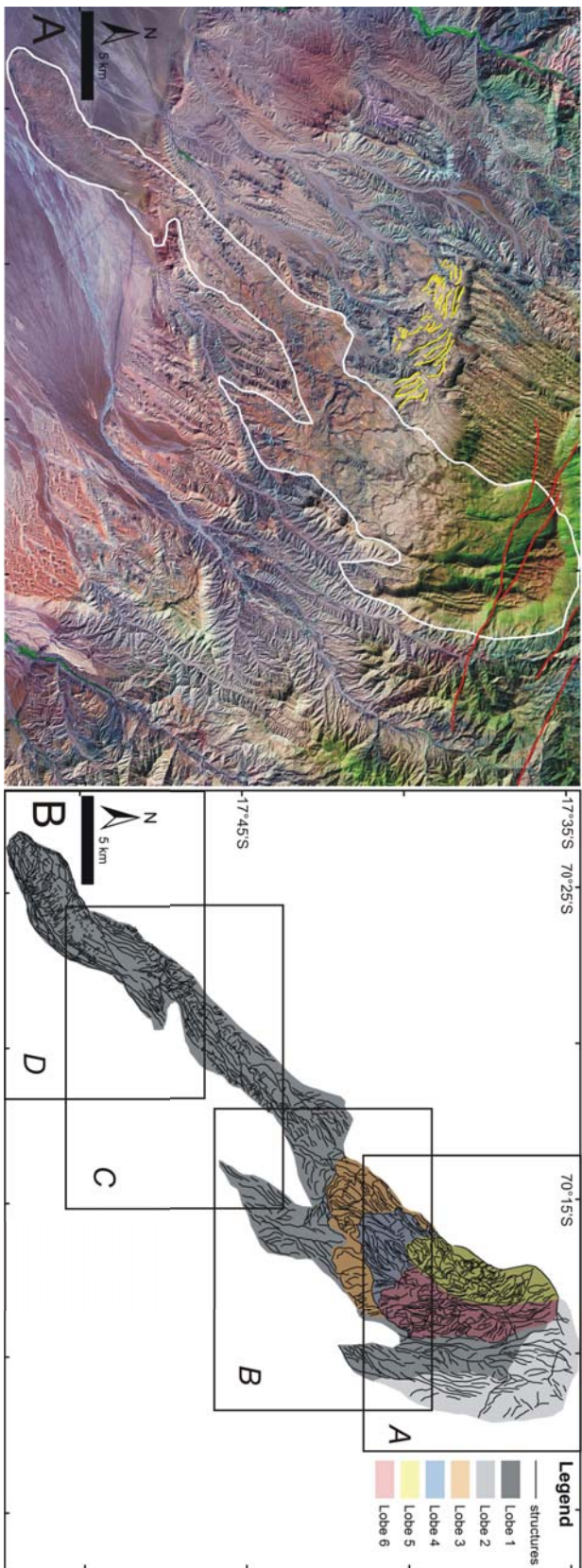


Figure 6.5: The Tacna DAD. **A** Landsat ETM+ image drawn with the extent of the large landslide. **B** shows the lobe traces and the structures for this DAD. Drawn in squares are the source area (**A**), the proximal zone (**B**), the medial zone (**C**), and the distal zone (**D**) presented in more detail in Figure 6.6.

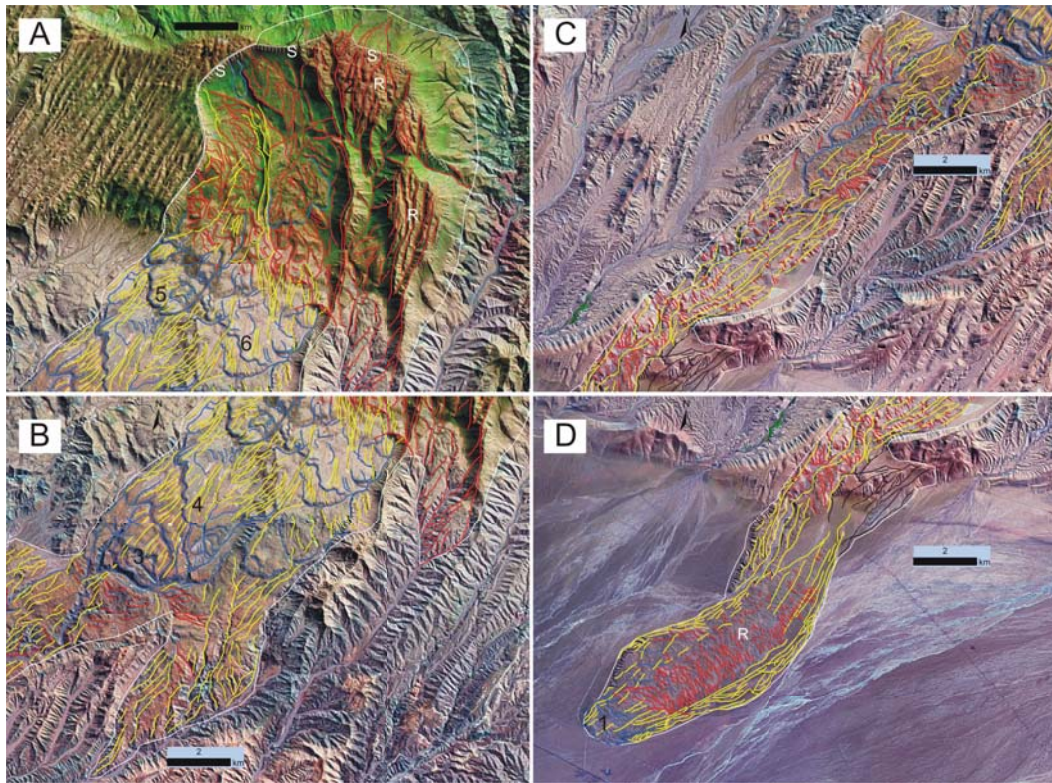


Figure 6.6: Areas in detail for the Tacna DAD. **A** The source region: shows the collapse scar (S) and the normal (red lines) and strike-slip (yellow) faults in the translation zone, the thrust faults (blue lines) that serve as the boundary of the overlying lobes (5) and (6), and the repeating ridges drawn as normal faults that form the rib-ridge morphology (R) of lobe (2); **B** The Proximal zone: also shows the normal, strike-slip and thrust faults bounding lobes (3) and (4); **C** The medial zone showing the same set of faults; and **D** The distal zone, which also forms the head of the long runout slide marked as lobe (1) that shows the same set of faults with strike-slip faults forming its levees and an addition of a set of en-echelon set of fractures that may indicate strike-slip extensional faulting, and the repeating short ridges that are perpendicular to transport direction and form the rib-ridge morphology.

## 6.6 Dynamics and Kinematics based on Morphological and Structural interpretation

### 6.6.1 Cerro Pular-Pajonales

If Salin, Tarque, Agua Delgada, Aracar, and Arizaro volcanoes (Fig. 6.1A) existed before the collapse, these volcano flanks have constrained the spreading of the Cerro Pular-Pajonales DAD. When the Cerro Pular-Pajonales collapsed, debris and rock slid down the steep slope until reaching the piedmont and started to spread at a slower speed on the lateral sides. The smooth-textured surface at the translation zone is a result of the continued sliding of more recent Pular-Pajonales deposits. The abrupt change of slope from the source towards the medial depositional zone created the graben that bounds the southern part of the Salar de Pular.

During its transport, longitudinal spreading waned but lateral spreading continued creating a thicker medial zone. This is shown by the dominance of compressional features on the distal zone with some strike-slip structures near the lake at the medial zone. The thick deposit at the medial zone and the confinement from the southern flank of Aracar volcano contributed to the over-steepened front. This front collapsed and created a secondary collapse in the distal zone dominated by extension. The irregularity of the edges in these zones is attributed to the most recent volcanic deposits that cover some parts of the DAD.

This DAD has similar features as those of analogue slides on curved ramps presented in Chapter 5 of this study. One prominent similarity is the extension-dominated secondary mini slides from the over-steepened accumulation zone in the medial depositional zone that collapsed. Within the irregular and hummocky accumulation zone are the thrust faults and the strike-slip faults in the proximal area where the debris decelerated. Another similar structural feature of this DAD to the analogue avalanches is the graben resulting from the abrupt change of slope from the source towards the depositional zone.

### 6.6.2 Süphan Dağı

Süphan Dağı is located in the SE termination of the Süphan Fault with several faults branching near its vent (Fig. 6.3C, 6.7D) (Adiyaman *et al.*, 1998). Activity along this basement fault may have contributed to the collapses of the volcano as shown by the analogue models of Lagmay *et al.* (2000), Wooller *et al.* (2009), and Mathieu and van Wyk de Vries (2011) (Fig. 6.7A-D). The two collapses could be related to progressive deformation of the edifice by these

underlying faults. Comparison of Süphan Dağı structures (Fig. 6.7D) with the predictive models of fault-driven edifice collapse Wooller et al. (2009) (Fig. 6.7B) suggests that a vertical left-lateral strike-slip fault, with a probable 75° to 85° of obliquity located very near the centre of the cone could have caused the instability of the Süphan Dağı edifice. Based on the analogue models, also, the eastern Süphan Dağı is older than the western DAD.

### 6.6.2.1 The Western Süphan Dağı DAD

The single-lobe indicates that this avalanche was a result of a single collapse and the irregularity of the edges is due to the confinement by the surrounding elevated areas. The surface structures indicate that this DAD is extension-dominated, spreading the debris longitudinally parallel to the transport direction. Confinement on the distal zones resulted in thrust faults as shown in earlier chapters. The two blocks in the medial and distal areas have similar spectral signature and surface texture. There are two possibilities for the origin of these blocks: they could be part of the DAD with the distal block as a hummock pushed towards the edge or they could be more likely older landforms not remobilised by the debris avalanche. The first possibility is due to the NE-trending strike-slip and thrust faults that is evidence that this block has been included in the slide but did not fragment. Although, existing 1:500,000 geological map of the area (<http://www.mta.gov.tr>) shows that these blocks are Pliocene basalts from formed by ancient volcanism in the area and are therefore not part of DAD.

### 6.6.2.2 The Eastern Süphan Dağı DAD

The DAD is extension-dominated until it reached the base of the volcano where compression starts on the western levee of the medial and distal depositional zones. The eastern side of the medial zone, however, is undergoing mostly spreading downslope and extension. This kinematic caused the materials to move further towards the northeast side resulting in an extended tongue-like lobe making the DAD asymmetric to the northeast. This DAD has large blocks on the distal zone (polygon 21, Fig. 6.3B). Based on analogue models presented earlier, blocks of this size are expected on the proximal and medial depositional zones at the farthest. The 1:500,000 geologic map of the area shows these parts as having miocene andesite (<http://www.mta.gov.tr>).

### 6.6.2.3 Lessons Learned

Remote sensing proves to be a necessary step in studying major geologic events such as large landslides and avalanches. Knowledge learned from analogue

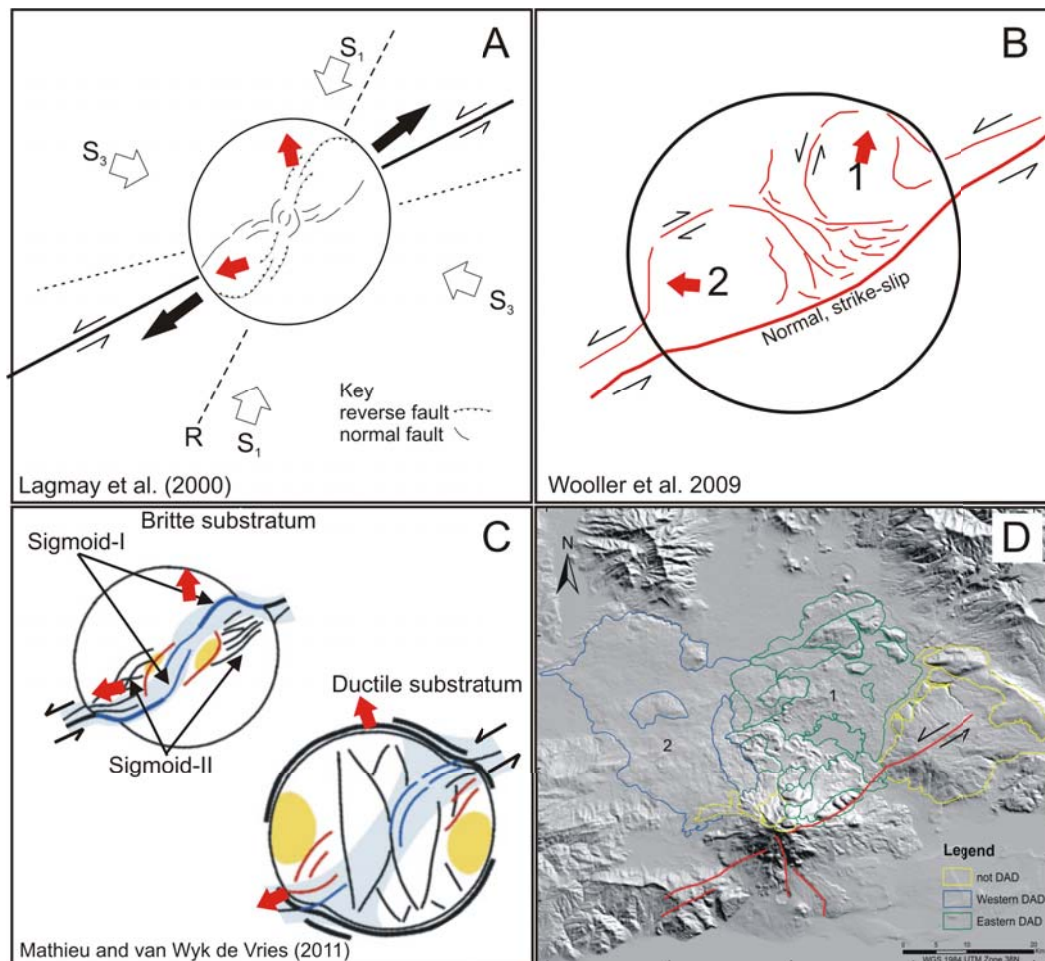


Figure 6.7: Structures of Süphan Dağı as compared to the analogue models. **A** Structures from the analogue model for cones overlying sinistral strike-slip faults by [Lagmay et al. \(2000\)](#). **B** Summary sketch of transtensional deformation of about  $75^\circ$  of obliquity in analogue models from [Wooller et al. \(2009\)](#) with predicted collapse order that is matched by Süphan Dağı. **C** Morphology and strike of structures in left-lateral strike-slip experiments by [Mathieu and van Wyk de Vries \(2011\)](#) showing the locations of the Sigmoid-I faults that curve at the summit of the cone and Sigmoid-II in the upper cone. Figure at the lower left with flower structures in the northern and southern flanks is a cone with the addition of a ductile layer. **D** The structural pattern on the flank of Süphan Dağı are similar to those outlined in (A), (B) and (C) suggesting that a strike slip with dip movement may have led to an instability, and subsequent collapses. The red arrows indicate direction of Mt Iriga collapses.

modelling seems to compliment in the aim of understanding these events. However, as in the case of Süphan Dağı DAD, wherein doubts arise from expected dynamics and kinematics based on analogue modelling and remote sensing, field evidence is as necessary to check the validity of remote sensing results.

### 6.6.3 Tacna

The Tacna long runout slide has six slide waves that formed lobes. The first slide is the longest-reaching and deposited debris all the way to the distal depositional zone, called the Negros Cerillos. It also created two short lobes to the east. The first collapse destabilised the mountain and caused the succeeding slides that mantled the previous deposits with materials forming the later lobes.

These waves of collapses destabilised the eastern adjacent zone in the source area that it extended towards the west forming the rib-ridge morphology from the repeating horsts and grabens. In general, this slide is extension-dominated and a perfect natural prototype for long-runout slides on straight basal plane presented in Chapter 5 of this thesis with compression when the later materials are emplaced on top of the earlier collapse deposits forming the thrust faults.

#### 6.6.3.1 Applications to Geohazard Assessments

The remote sensing work of proposed Tacna DAD (Fig. 6.5A) exhibits how such work becomes necessary for geohazard assessments. On the source area of Tacna DAD, a regional fault crosses upper collapse zone that might have contributed to its collapse. On the western part outside of the collapse zone is a continuation of the regional fault. At the piedmont of the source area is a group of W-E trending faults or folds. An interpretation is that the fault trace at the top is an implication of a collapse that is starting in the area, extension as the source area creeps downward causes compression at the bottom as implied by the series of faults and folds. A triggering event might cause this whole area to experience a large landslide or an avalanche that can reach an oasis further downslope.

## 6.7 Conclusion

This work shows the identification, mapping, and characterisation of the four major DAD in three areas at Cerro Pular-Pajonales (Chile-Argentina), Süphan Dağı (Turkey), and Tacna (Peru). Remote sensing enabled the morphological

and structural mapping and detailed characterisation of some key surface features of the DAD. Availability of DEM data with its high resolution enables the identification of much smaller-scale topographic features (like hummocks) and improves the mapping of structures on the DAD.

The morphological features of the DAD provided information on the DA formation and emplacement. The morphological and structural mapping of DAD can be supplemented and confirmed with field analysis of structures and debris avalanche deposits morphology. And If indeed, the morphology and structures presented here are confirmed in the field, then the method presented here is a low-cost approach for studying flank collapses and mapping DAD in inaccessible areas where vegetation cover and erosion have not yet obliterated the spectral and topographical evidences. This kind of work is helpful in geohazard assessment.

CHAPTER 7

# Summary and future work

---

## 7.1 Introduction

My participation in the Search and Rescue operations for a thousand people buried alive in Guinsaugon, Southern Leyte (Philippines) by a rockslide-debris avalanche has provided me a lesson on the capability of avalanches to cause great human tragedy and property loss. Natural hazards such as large landslides and avalanches are prevalent and pose a day-to-day threat for tectonically active regions such as the Philippines, an archipelago formed by opposing subduction zones and crossed by countless faults and steep mountains. Volcanoes and mountain ranges are spatially distributed according to the subduction and collision zones bounding the archipelago. Philippine volcanoes, whether active, potentially active or inactive all pose great risk to people living nearby. Due to its unique and dynamic setting, causal and triggering factors for catastrophic earth mass movements are present anywhere in the Philippines at any time. This makes the archipelago a good geologic laboratory. Mt Iriga for example, is one of the best places to study DAD not only because of the good preservation but because there is enough erosion and human excavation that exposes their internal structures.

In the end, this study hopes to help mitigate the risks associated with large-scale landslides and avalanches by recognising natural DAD and understanding their kinematics and dynamics. Deposit of such large events is recognised by structural and morphological mapping on the field and complemented by remote sensing. Through laboratory-scale avalanches and landslides, this work explores the role of topographic features and structures such as hummocks, ridges, levees, accumulation zones, and faults in avalanche kinematics and dynamics.

## 7.2 The Philippine Volcanoes

Morphometric analysis of the Philippine volcanoes using MorVolc code and SRTM DEM classified the younger-looking edifices of active and potentially active volcanoes into three classes: cones, subcones, or massifs and a breached edifice subclass that can also belong to either the small or large volcano groups. Cones are higher, steeper, and have regular and circular shape and higher average flank slope than subcones and massifs, although, their basal width, volume and edifice truncation may be the same. Small volcanoes either cones or subcones can grow in height, basal width, and volume into massifs. However, as volcanoes grow, they can experience a flank collapse and generate large landslide or avalanches reshaping the volcano and depositing voluminous debris on its flank. Volcano classification and the evolution trend obtained from

morphometric analysis provide an idea whether or not a volcano flank collapse is expected at certain volcanoes.

### 7.3 Iriga volcano (Philippines) and her 2 DAD

One particular volcano edifice considered in this study is Iriga volcano. It is known for its southeast-elongated collapse scar and DAD. Fieldwork and remote sensing concluded that Mt Iriga has two DAD located oblique to the strike of a main strike-slip fault on which the volcano is built. The failure directions coincide with the predicted avalanche directions on analogue models of combined transtensional faulting and gravity spreading.

The Iriga debris avalanches were generated by the flank collapses caused by the movement of the underlying strike-slip fault and weakening of its southwest edifice that stands on the weak substrata of the Bicol River Basin. The sedimentary substrata at the southwest piedmont of Mt Iriga served as the highly mobile basal layer during the Iriga avalanche. On the other hand, a thick layer of pumice-rich ignimbrite in Buhi DAD2 contributed to its mobility.

Morphological and structural field and remote sensing mapping, and description of the hummock spatial distribution, shape, and orientation and the surface structures of these two DAD reveals information on their avalanche kinematics and dynamics. The DAD1 collapse is extension-dominated in the proximal and medial zones and compression-dominated as it approached the elevated area and water bodies in the distal depositional zone. This is shown by the normal and strike-slip faults mapped in the proximal and medial zones and very dense population of thrust faults on its distal depositional zone. The hummocks in DAD1 are normal and elongated to its transport direction and are bigger in the distal zone. Buhi DAD2, however, underwent progressive spreading until confined and deflected by the opposing Malinao edifice towards the west. This is implied by the progressive decrease in hummock size towards the distal depositional zone, the normal, and strike-slip faults mapped in the DAD surface and some thrust faults in the margins of deflection where the second group of bigger hummocks are delineated.

The morphology, structures, difference in hummock geometry and spatial distribution in both DAD led to studying hummocks and development of structures in large landslides and avalanches. The formation and evolution of hummocks and structures in DAD were explored for their use in understanding avalanche kinematics and dynamics.

## 7.4 Hummocks: How They Form, What They Mean, and Anatomy

Hummocks are topographic features of aerial and sub-aerial large landslides and debris avalanches common in volcanic ones but also relevant to many non-volcanic settings. Large-scale collapses are replicated in these sets of experiments and compared with the natural prototype hummocks at the Iriga DAD to characterise their formation, evolution, spatial distribution; to understand their geometry, surface, and internal structures; and to explore their use as indicators for landslide and avalanche kinematics and dynamics. The analogue model set-up is a hybrid of the previous work that explored the kinematics of rockslides by describing the morphology and structures of the upper brittle layer made of a mixture of sand and plaster from the initiation towards final emplacement. Earlier models simulated a low basal friction contact using a polished surface (Shea and van Wyk de Vries, 2008) and a ductile layer of silicone that simulates basal ductile deformation (Andrade and van Wyk de Vries, 2010). In these experiments, the upper brittle layer undergoes pure shear and the underlying ductile layer by simple shear deformation. The analogue avalanches are in an unconfined transport zone with oil added as lubrication to reduce basal ductile layer friction against the underlying surface and reduce ductile layer viscosity.

In general, landslide and avalanches and hummocks evolve in the same way. Hummocks initially form by extension. As motion continues, individual large blocks develop and move apart resulting in an initial hummock distribution with larger hummocks in the proximal zone and small hummocks at the distal front. As the mass spreads, individual hummocks can undergo progressive breaking and spreads farther apart (Avalanche Class A) and result in small, primary Hummock Type 1a. A possibility of compression at some point (Avalanche Class B) or at the final stages as the avalanche wanes (Avalanche Class C) can result in large, primary Hummock Type 1b and small, secondary Hummock Type 1b, respectively.

Hummock shape and size is a function lithology and initial position in the sliding mass modified by subsequent hummock deformation and break up or merging. Hummock morphology and spatial distribution is dependent on the density of normal, thrust and strike-slip faults, which in turn is a function of strain material properties such as cohesion and the nature of the ductile sliding layer and upper brittle layer.

Hummock structural anatomy is composed of normal faults that become less steep from the middle to the edge and from the upper brittle layer into low-angle detachments at the base, where they merge with the basal shear zone.

Hummock surfaces are destabilised by minor slumping and scree formation.

The layer and structure interface between the upper brittle layer and ductile sliding base control hummock structure. They can have progressive or sharp vertical transitions; original discontinuities in the brittle layer can be preserved; complete disaggregation into blocks with the injection of avalanche matrix can occur; or detachment-type faulting from the combination of low-dipping ductile shear zone and block faulting on the brittle layer can be preserved. The type of stretch structure also depends on the lithology and coherent interface (generally lava flows) such the Lava Topping Hummock at Iriga DAD1 or incoherent interface like the Ignimbrite Topping blocks at Buhi DAD2.

## **7.5 The Development of Structures in Long-Runout Avalanches and Large Landslides**

The internal structures of rockslide-debris avalanche deposits are observed on the surface as faults and folds that can be mapped to determine deformation history and kinematics. These slide experiments of curved and straight ramps try to replicate the reduced basal friction of long-runout debris avalanches and large landslides similar to a highly deformed simple shear layer with plug flow. A detailed description of deposit structures; formation and morphology to investigate transport type, and deformation chronology from slide initiation to runout stopping of avalanches is presented.

Both sets experiments have recurrent morphology and structures on their deposits including: (1) levees on the lateral margins, (2) accumulation zones, (3) subsequent lobes emplaced on top and masking pre-existing structures, (4) secondary ‘mini’ slides, and the (5) thrust-fold, (6) strike-slip faults, and (7) normal fault structures. Over-steepened accumulation zones can destabilise and spread further by secondary ‘mini’ slides. This is important in mountainous avalanches where there are rapid changes in slope. Extension by spreading is shown by the strike-slip and normal faults, while the thrust faults and folds express compression.

Unique to each experiment set-up are morphological features and surface structures such as: (1) terraces or steps, and (2) hummocks in the curved ramp experiments; and the (3) rib-and-ridge structures and (4) transtensional graben in straight ramp experiments. In straight ramp experiments, materials accumulate in the distal zone creating the head of the deposit that implies dominance of extension and spreading by sliding and translation during emplacement. The Storegga slide off the coast of Norway has a long tongue-like shape and runouts with rib-and-ridge morphology.

The sliding base morphology can also influence the emplacement mechanism, morphology, and runout of large landslides and avalanches. Curved ramp slides have fan-shaped depositional area with shorter but wider runout due to the sudden change in the sliding and deposition slopes with accumulation and thickening at where the slope decreases with displacement of coherent blocks creating terraces or steps, and hummocks like in the Guinsaigon rockslide-debris avalanche (Philippines). Straight ramp slides have well-spread, longer and narrower tongue-shaped depositional area with parallel levees or wider proximal zone narrowing towards the distal zone. Accumulation zones can form at the proximal and medial portions with overflows that can mask previously emplaced deposits. Descriptions of these structural features and morphology in large landslides and avalanche deposits give insights on the prediction of runouts and sequence of events to be expected during an avalanche development.

## 7.6 Mapping Remote DAD

Remote sensing and GIS structural and morphological mapping have been used as tools for the identification and delineation of three previously unmapped collapse deposits at Süphan Dağı (Turkey), Cerro Pular-Pajonales (Chile-Argentina), and Tacna (Peru). Although, field data is strongly suggested to supplement such work in these cases much. The necessary information on the causes, triggering and emplacement mechanisms of these DAD can be extracted from remote sensing. Also mapping and detailed description on the recurrent features such as: the collapse scars, DAD extent, levees, hummocks, lobes, ridges, morphological features such as the rib-ridge morphology, accumulation zones, and frontal ‘mini slides’, and structures such as normal, thrust and strike-slip faults can be used to map out DAD in inaccessible areas and explain their landslide kinematics and dynamics.

## 7.7 Future Work

Some interesting points arise for future consideration in this line of study:

1. Use the morphometric analysis supplemented with geological, geochemical, and geophysical data of each volcano to further understand the evolutionary trends and make long-term predictions such as the possibility of Mt Mayon to spread and collapse.
2. Analogue experiments can be set-up to investigate the role of barriers and saturated sliding material or base to the kinematics and transport

mechanism and emplacement of debris during the avalanche. Experiments can also be done to observe and describe fracturing and clast evolution in debris avalanches.

3. Improve the identification, interpretation, and spatial distribution analysis of hummocks and other morphological and structural features by using automated methods for digital image analysis to analyze photos of the model surfaces.
4. Supplement the remote sensing structural and morphological mapping at Cerro Pular-Pajonales (Chile), Süphan Dağı (Turkey), and Tacna (Peru) with field data. Also use the finding to create a more global or solar system-wide inventory of DAD features for VOLGRIPA.
5. Based on the analysis of the morphometry of Philippine volcanoes, Mt Mayon is susceptible to experience a flank collapse at this stage of its development and growth. Also, Mt Mayon is in the same tectonic environment as Iriga volcano, which has already experienced two flank collapses. And so, an assessment for the instability and possibility of future flank collapse at Mt Mayon based on these two points might be helpful for hazards mitigation around the volcano.
6. Structural to dynamics approach as those employed in this study can be used to other volcanoes in the Philippines such as Mt Kanlaon and Mt Apo to gather information on their morphology, stability, and DAD, if indeed they have.



APPENDIX A

**Active and Potentially Active  
Volcanoes in the Philippines**

---

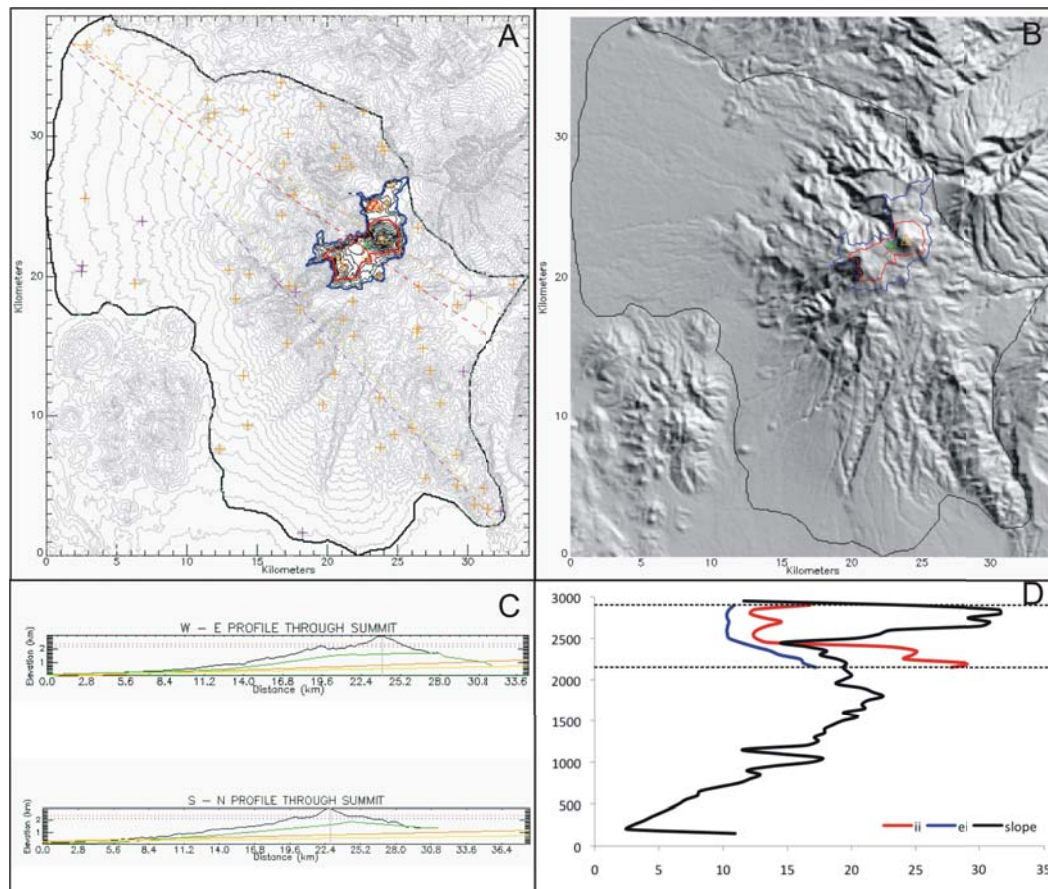


Figure A.1: Apo

Status:	Potentially Active Volcano
Morphometry Type:	Breached edifice
Location (Lat, Long):	6.9874294, 125.27085
Elevation (min, max):	109-2928 m
Basal Area:	765.5 km <sup>2</sup>
Height:	2819 m
Volume:	549 km <sup>3</sup>
Profile shape (height/ base width, summit width/base width):	0.07, 0.12
Slope:	0°-56.13°
Base orientation in azimuth (through the summit, through the base centre):	122°, 137°

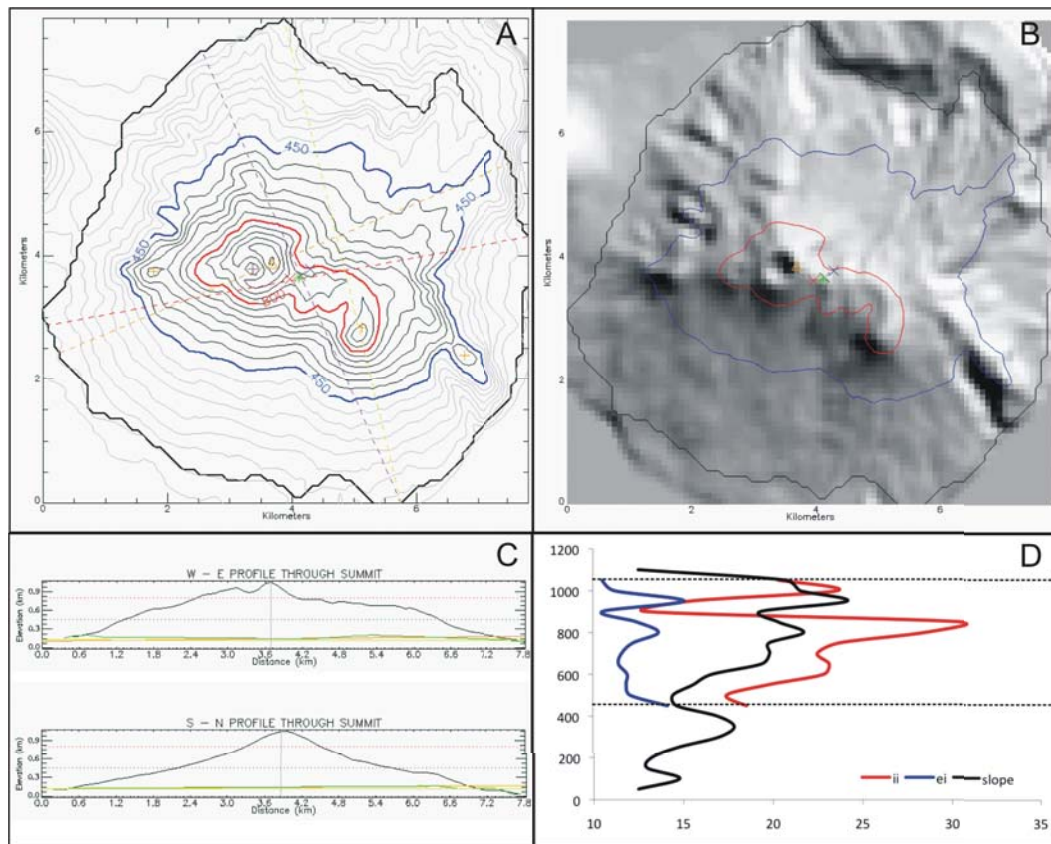


Figure A.2: Babuyan Claro

Status:	Active Volcano
Morphometry Type:	Sub-cone
Location (Lat, Long):	19.523999, 121.95234
Elevation (min, max):	109-1058 m
Basal Area:	43.4 km <sup>2</sup>
Height:	1058 m
Volume:	18 km <sup>3</sup>
Plan shape (ellipticity index, irregularity index):	2.2, 1.24
Profile shape (height/ base width, summit width/base width):	0.12, 0.25
Slope:	0°-50.71°
Base orientation in azimuth (through the summit, through the base centre):	67°, 156°

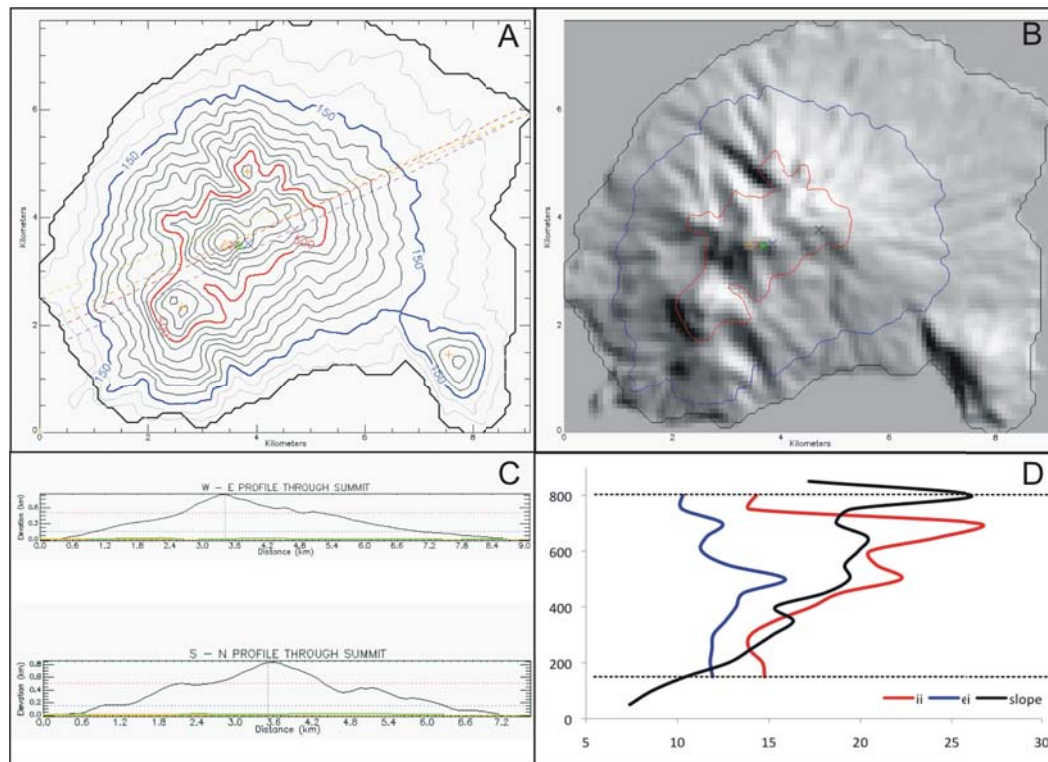


Figure A.3: Balut

Status:	Potentially Active Volcano
Morphometry Type:	Sub-cone
Location (Lat, Long):	5.3973815, 125.37608
Elevation (min, max):	0-837 m
Basal Area:	51.9 km <sup>2</sup>
Height:	837 m
Volume:	11 km <sup>3</sup>
Plan shape (ellipticity index, irregularity index):	1.64, 1.29
Profile shape (height/ base width, summit width/base width):	0.10, 0.32
Slope:	0°-39.21°
Base orientation in azimuth (through the summit, through the base centre):	66°, 63°

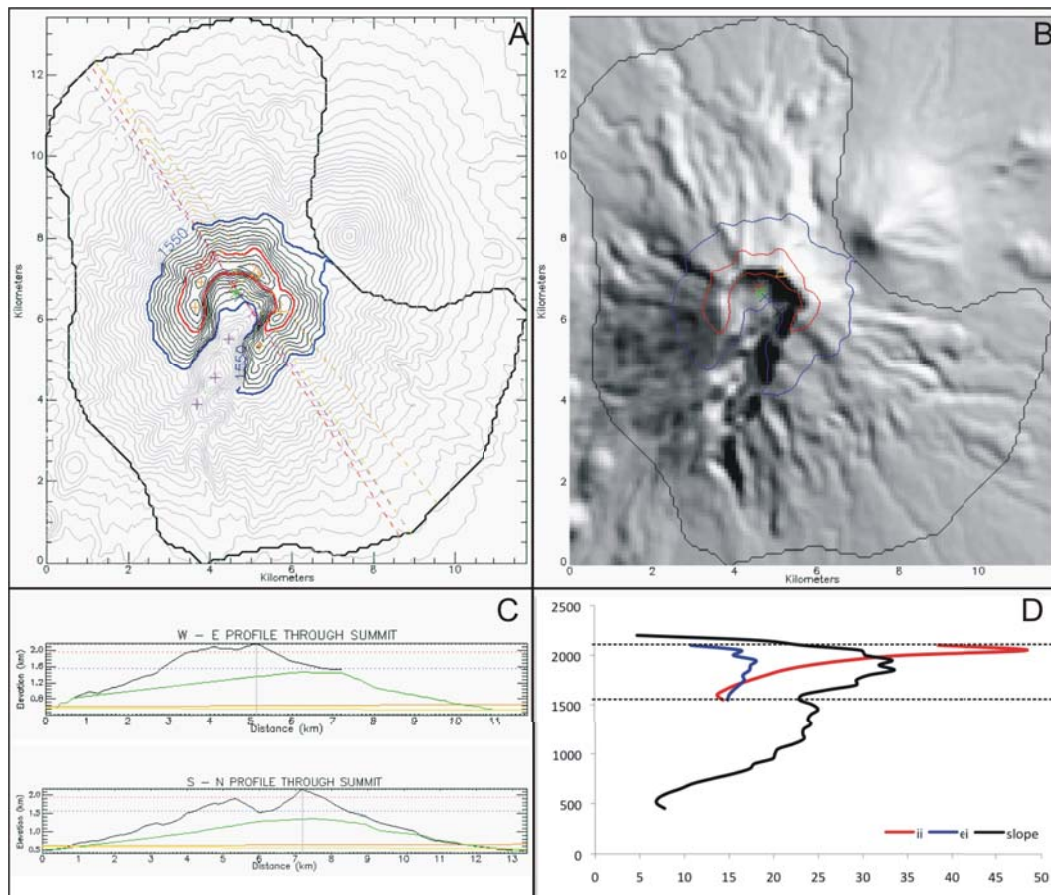


Figure A.4: Banahaw

Status:	Active Volcano
Morphometry Type:	Breached edifice
Location (Lat, Long):	14.067335, 121.4918
Elevation (min, max):	424-2150 m
Basal Area:	97.4 km <sup>2</sup>
Height:	1726 m
Volume:	55 km <sup>3</sup>
Plan shape (ellipticity index, irregularity index):	1.87, 1.64
Profile shape (height/ base width, summit width/base width):	0.14, 0.15
Slope:	0.86°-59.78°
Base orientation in azimuth (through the summit, through the base centre):	142°, 144°

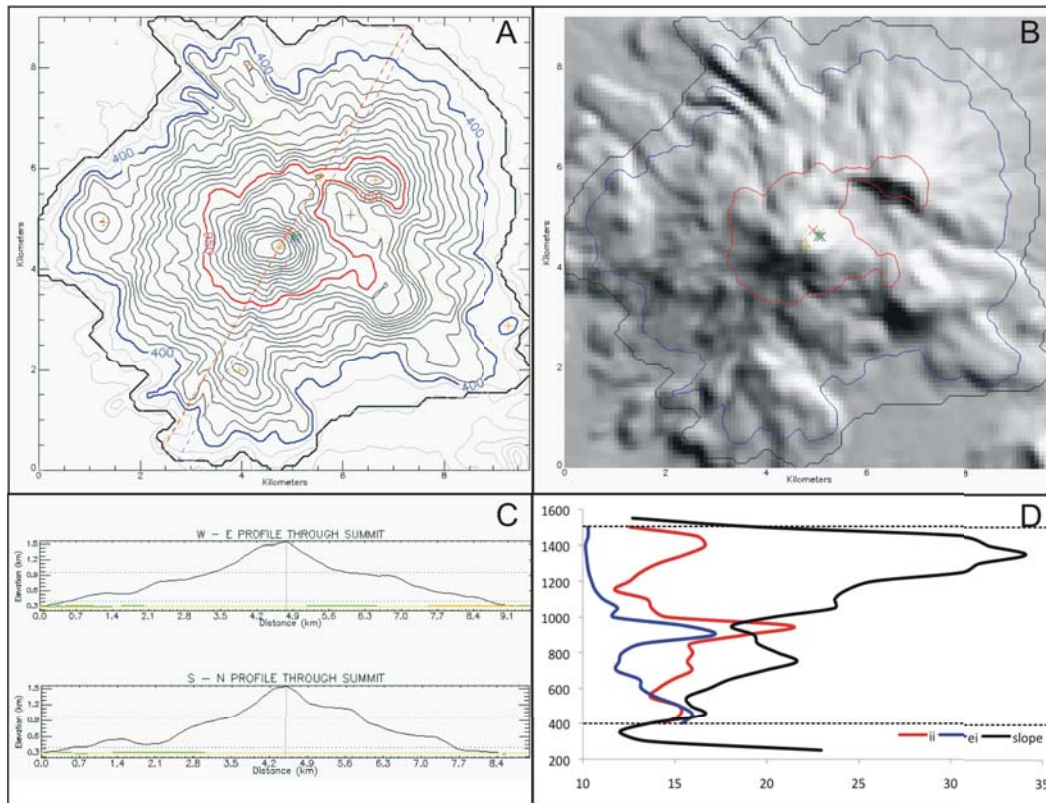


Figure A.5: Bulusan

Status:	Active Volcano
Morphometry Type:	Sub-cone
Location (Lat, Long):	12.768641, 124.05604
Elevation (min, max):	225-1537 m
Basal Area:	62.4 km <sup>2</sup>
Height:	1312 m
Volume:	24 km <sup>3</sup>
Plan shape (ellipticity index, irregularity index):	1.59, 1.41
Profile shape (height/ base width, summit width/base width):	0.14, 0.33
Slope:	0°-41.82°
Base orientation in azimuth (through the summit, through the base centre):	30°, 28°

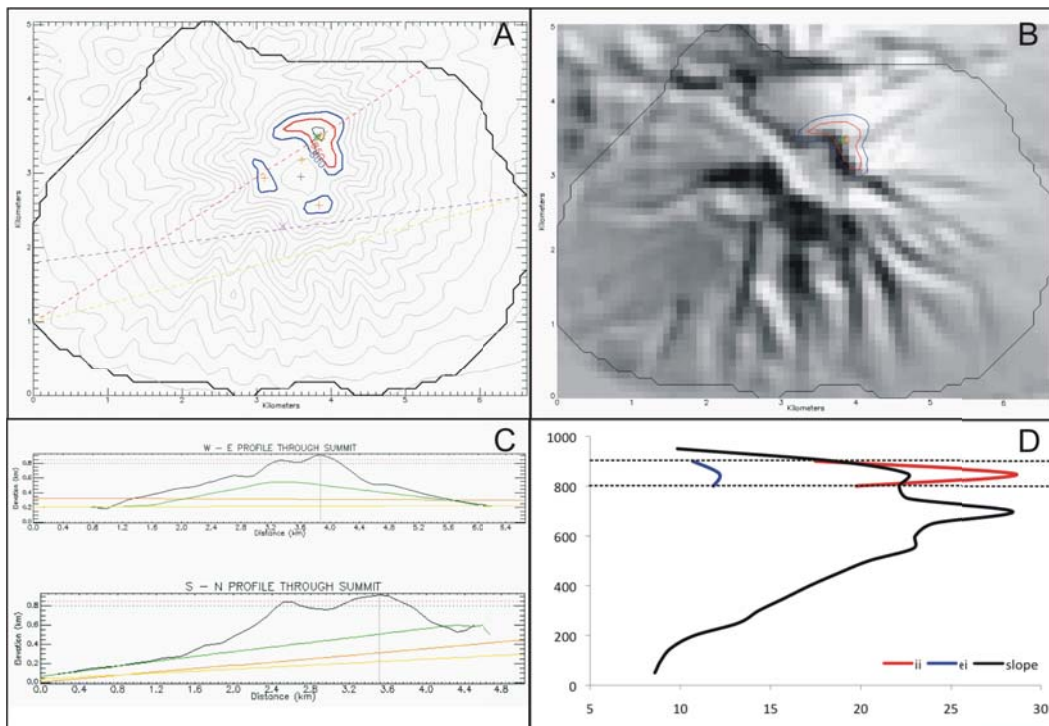


Figure A.6: Cabalian

Status:	Active Volcano
Morphometry Type:	Sub-cone
Location (Lat, Long):	10.284742, 125.21758
Elevation (min, max):	10-910 m
Basal Area:	25.8 km <sup>2</sup>
Height:	900 m
Volume:	9 km <sup>3</sup>
Profile shape (height/ base width, summit width/base width):	0.1, 0.09
Slope:	0.62°-40.63°
Base orientation in azimuth (through the summit, through the base centre):	56°, 82°

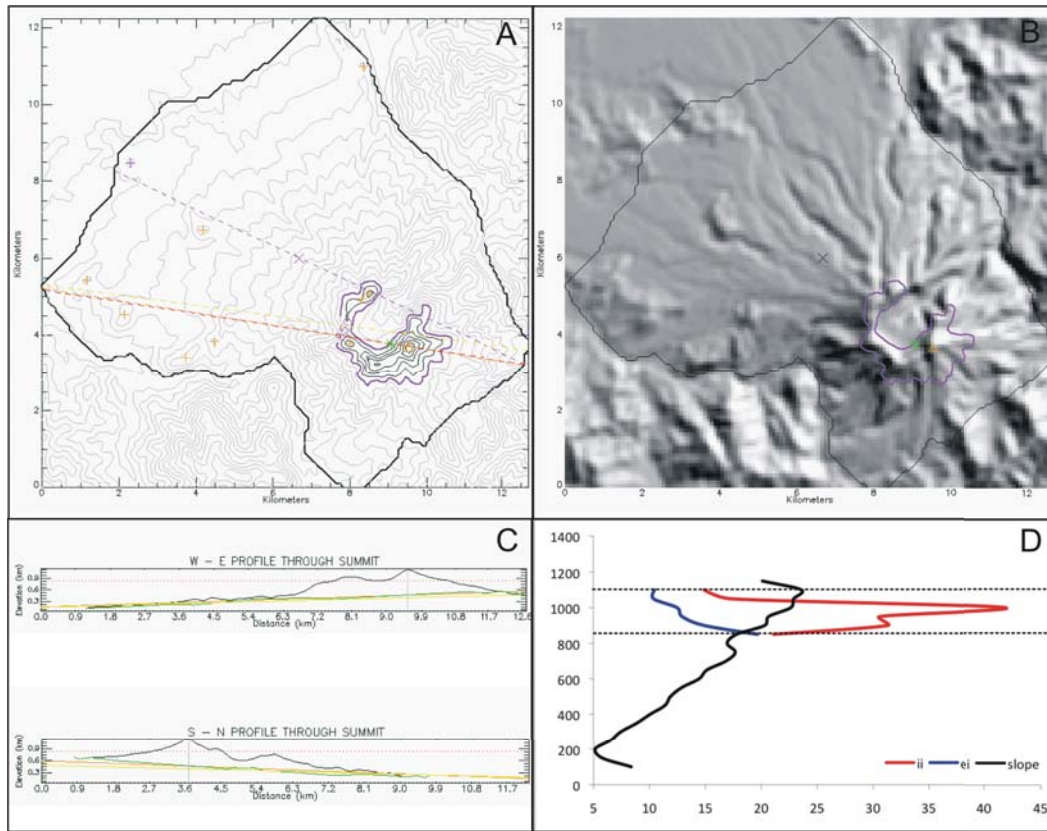


Figure A.7: Cagua

Status:	Active Volcano
Morphometry Type:	Cone
Location (Lat, Long):	18.215435, 122.1196
Elevation (min, max):	59-1141 m
Basal Area:	84.9 km <sup>2</sup>
Height:	1082 m
Volume:	31 km <sup>3</sup>
Profile shape (height/ base width, summit width/base width):	0.07, 0.2
Slope:	0°-39.63°
Base orientation in azimuth (through the summit, through the base centre):	99°, 115°

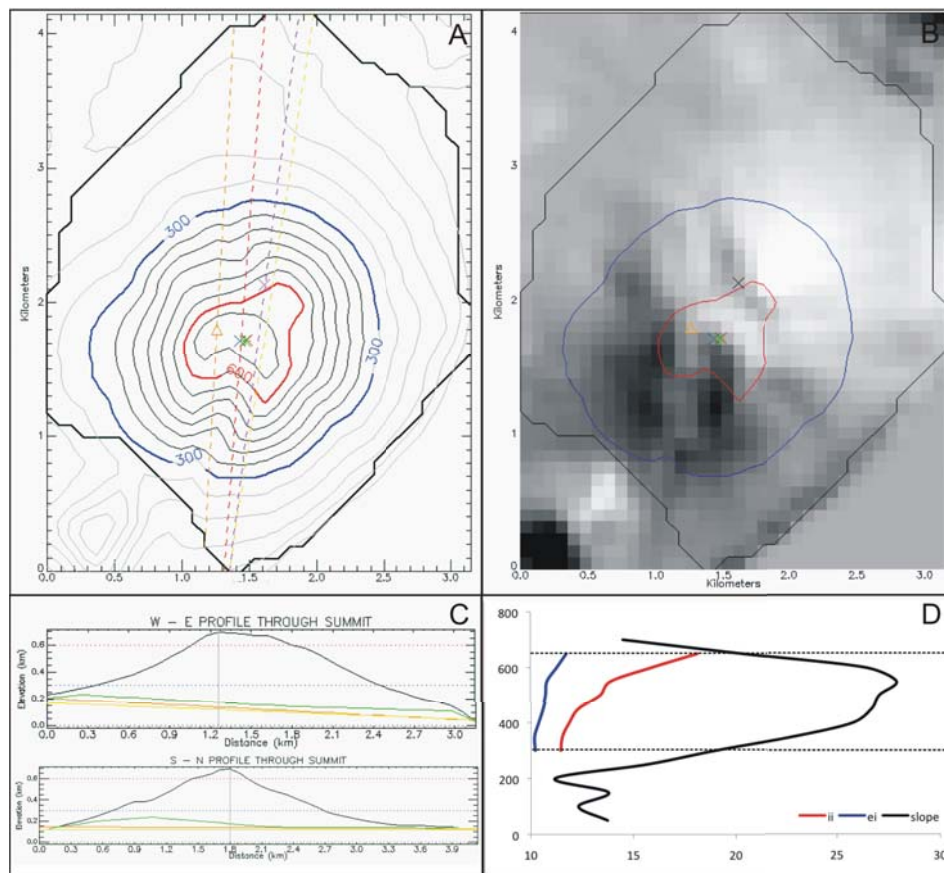


Figure A.8: Camiguin de Babuyanes

Status:	Active Volcano
Morphometry Type:	Cone
Location (Lat, Long):	18.832998, 121.86104
Elevation (min, max):	0-693 m
Basal Area:	9 km <sup>2</sup>
Height:	693 m
Volume:	3 km <sup>3</sup>
Plan shape (ellipticity index, irregularity index):	1.29, 1.06
Profile shape (height/ base width, summit width/base width):	0.16, 0.23
Slope:	0.15°-35.20°
Base orientation in azimuth (through the summit, through the base centre):	3°, 7°

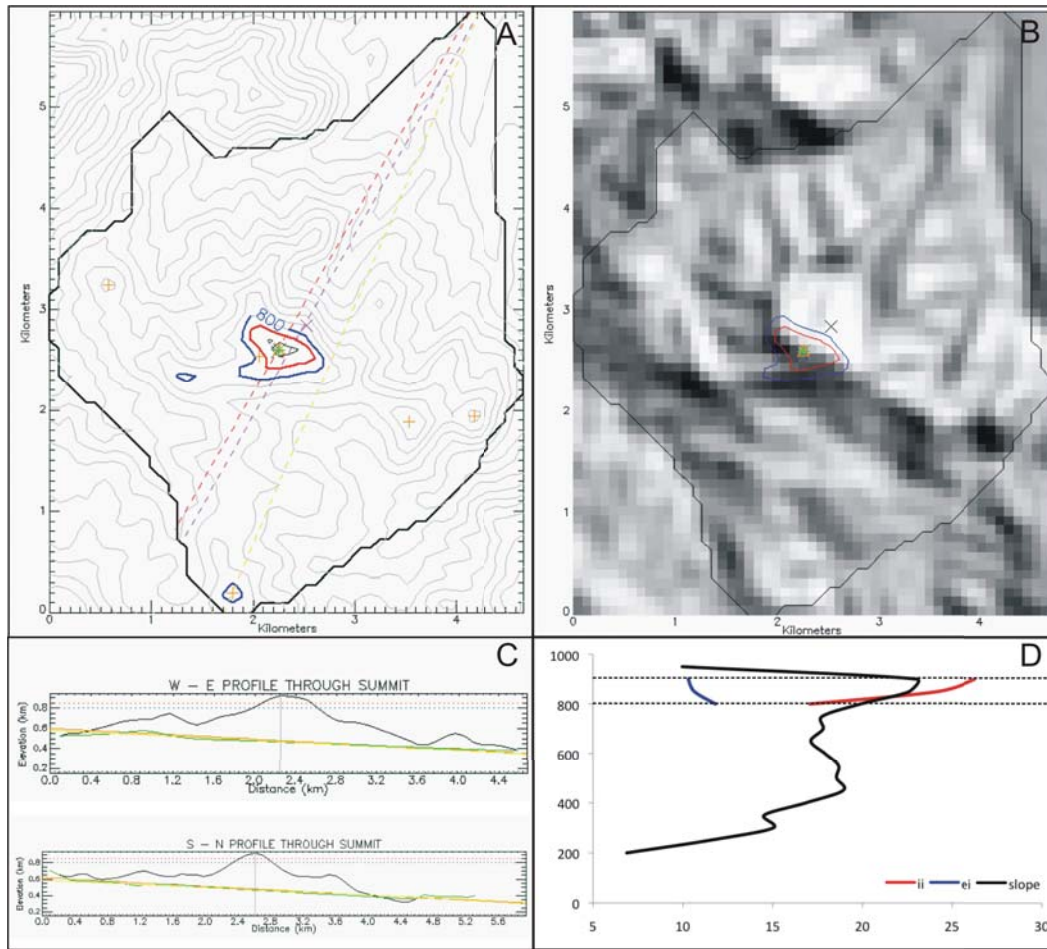


Figure A.9: Cancanaajag

Status:	Potentially Active Volcano
Morphometry Type:	Sub-cone
Location (Lat, Long):	11.06039, 124.77685
Elevation (min, max):	171-919 m
Basal Area:	17.2 km <sup>2</sup>
Height:	748 m
Volume:	6 km <sup>3</sup>
Profile shape (height/ base width, summit width/base width):	0.09, 0.10
Slope:	0.77°-41.92°
Base orientation in azimuth (through the summit, through the base centre):	29°, 29°

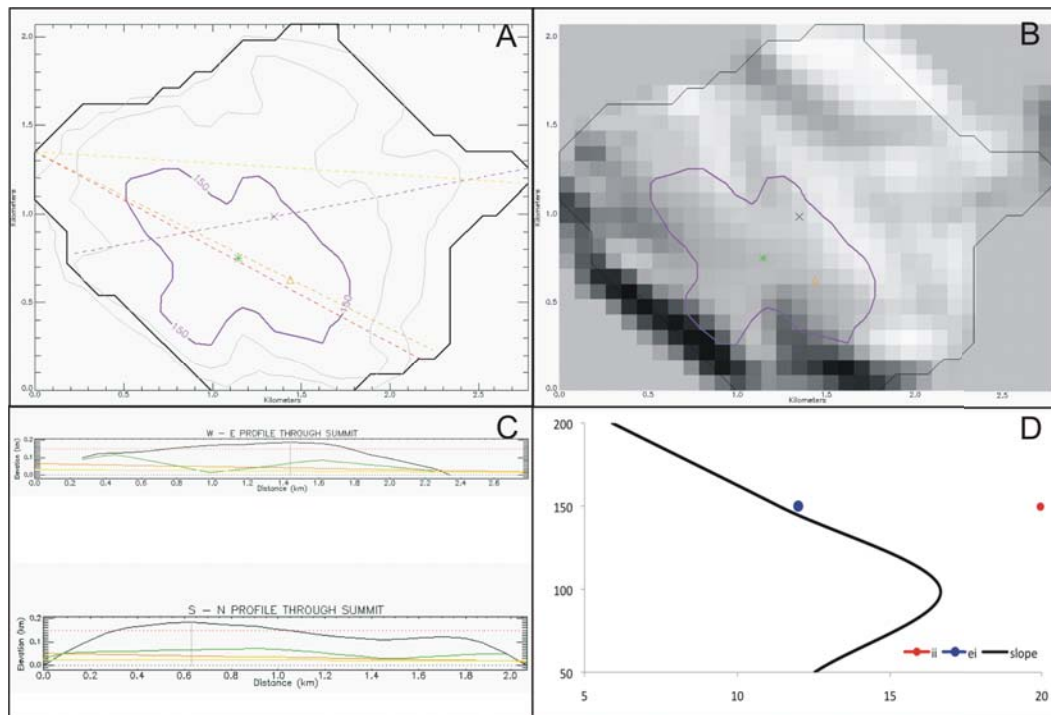


Figure A.10: Corregidor Complex

Status:	Potentially Active Volcano
Morphometry Type:	Sub-cone
Location (Lat, Long):	14.379435, 120.57611
Elevation (min, max):	0-186 m
Basal Area:	3.7 km <sup>2</sup>
Height:	186 m
Volume:	0.4 km <sup>3</sup>
Profile shape (height/ base width, summit width/base width):	0.07, 0.46
Slope:	0°-35.48°
Base orientation in azimuth (through the summit, through the base centre):	116°, 79°

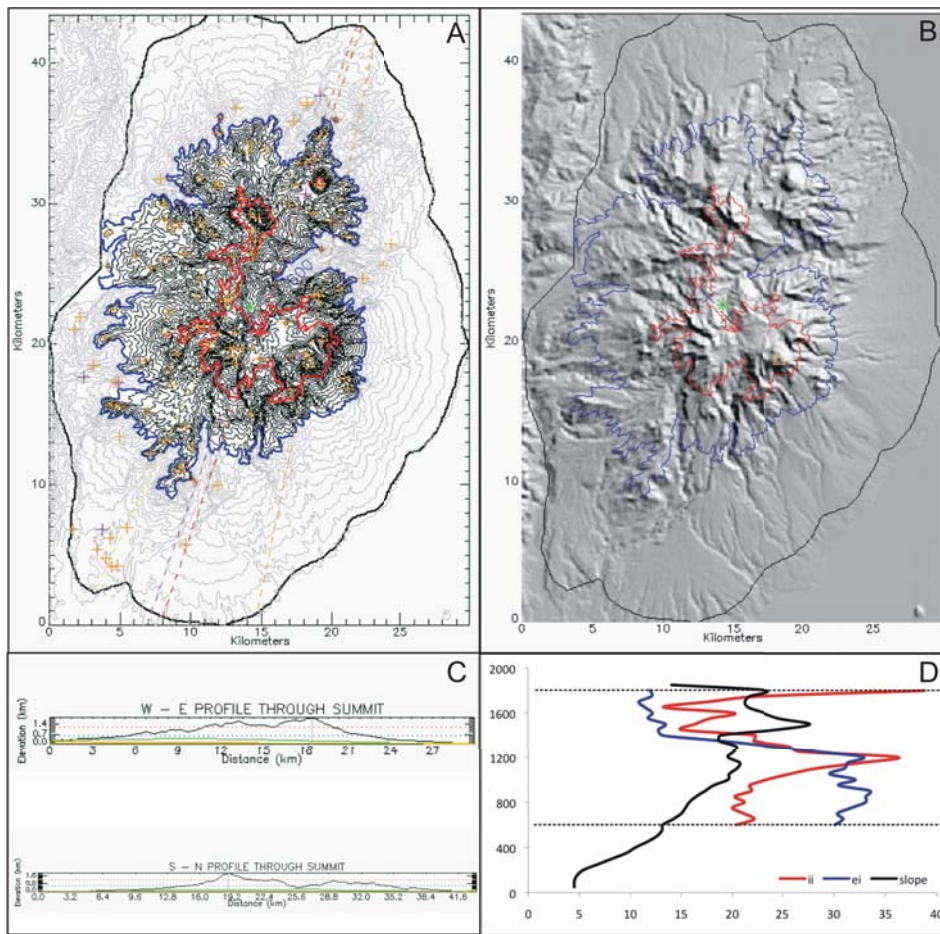


Figure A.11: Cuernos de Negros

Status:	Potentially Active Volcano
Morphometry Type:	Eroded massif
Location (Lat, Long):	9.2446421, 123.17998
Elevation (min, max):	0-1828 m
Basal Area:	938.9 km <sup>2</sup>
Height:	1828 m
Volume:	467 km <sup>3</sup>
Plan shape (ellipticity index, irregularity index):	2.42, 3.15
Profile shape (height/ base width, summit width/base width):	0.05, 0.24
Slope:	0°-61.37°
Base orientation in azimuth (through the summit, through the base centre):	11°, 19°

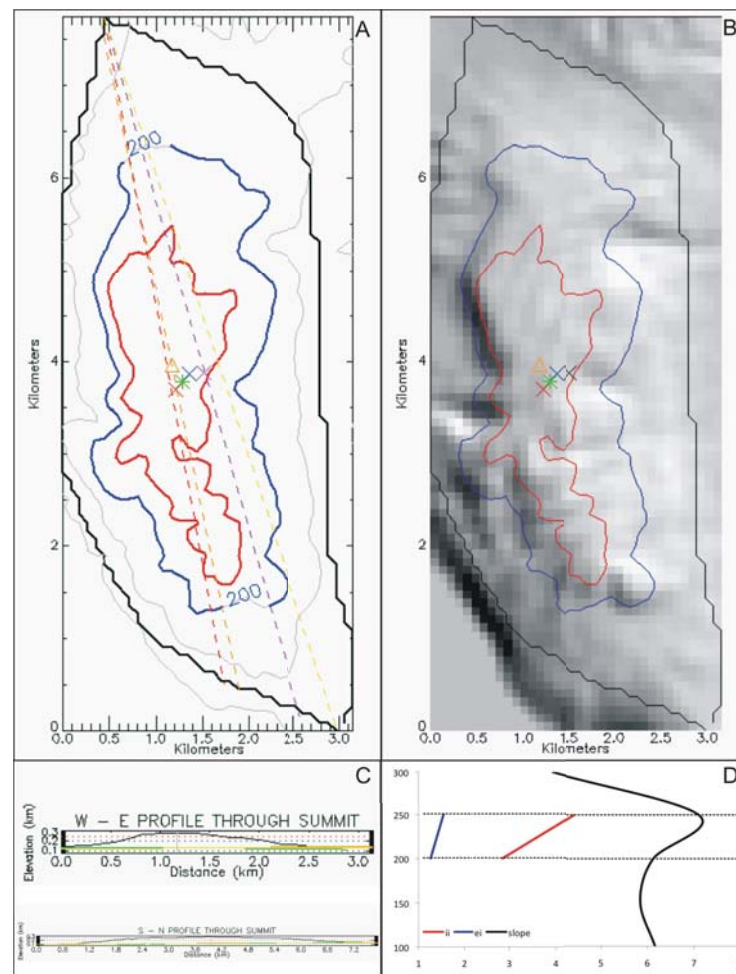


Figure A.12: Didicas

Status:	Active Volcano
Morphometry Type:	Sub-cone
Location (Lat, Long):	19.073477, 121.21454
Elevation (min, max):	96-283 m
Basal Area:	17.6 km <sup>2</sup>
Height:	187 m
Volume:	2 km <sup>3</sup>
Plan shape (ellipticity index, irregularity index):	3.63, 1.08
Profile shape (height/ base width, summit width/base width):	0.16, 0.13
Slope:	0.11°-61.37°
Base orientation in azimuth (through the summit, through the base centre):	168°, 164°

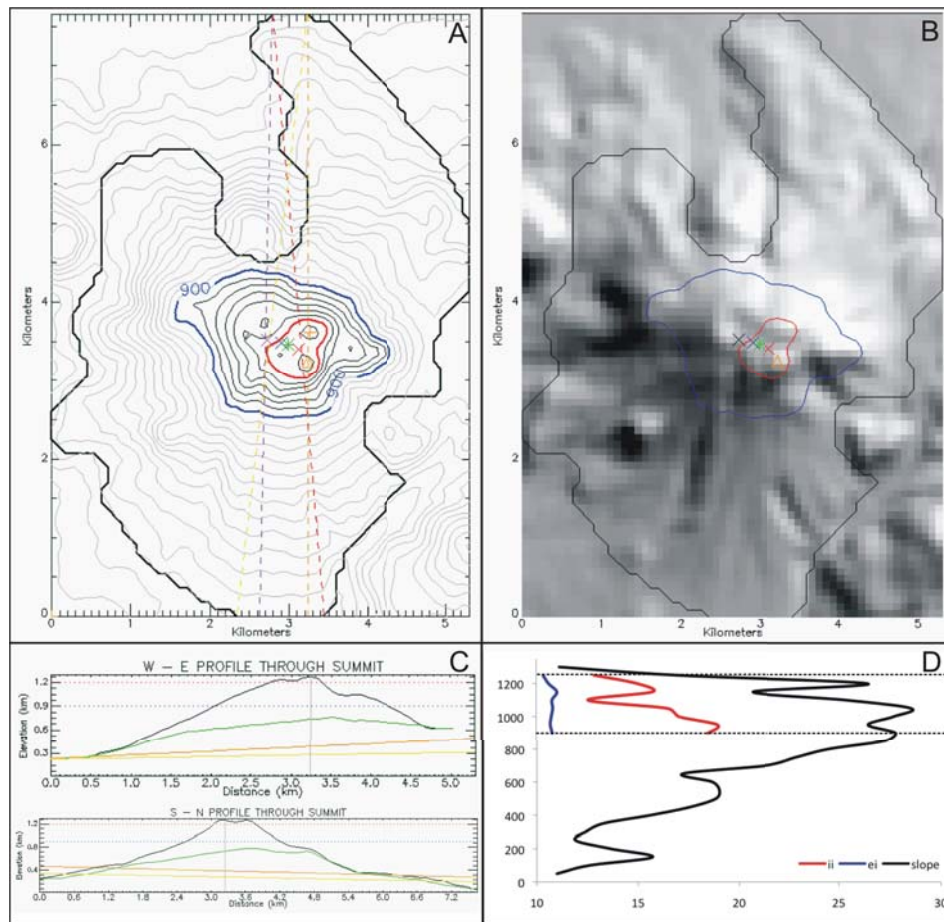


Figure A.13: Hibok-hibok

Status:	Active Volcano
Morphometry Type:	Sub-cone
Location (Lat, Long):	9.1992769, 124.67573
Elevation (min, max):	33-1273 m
Basal Area:	23.9 km <sup>2</sup>
Height:	1240 m
Volume:	13 km <sup>3</sup>
Plan shape (ellipticity index, irregularity index):	1.63, 1.08
Profile shape (height/ base width, summit width/base width):	0.16, 0.13
Slope:	1.21°-46.45°
Base orientation in azimuth (through the summit, through the base centre):	180°, 1°

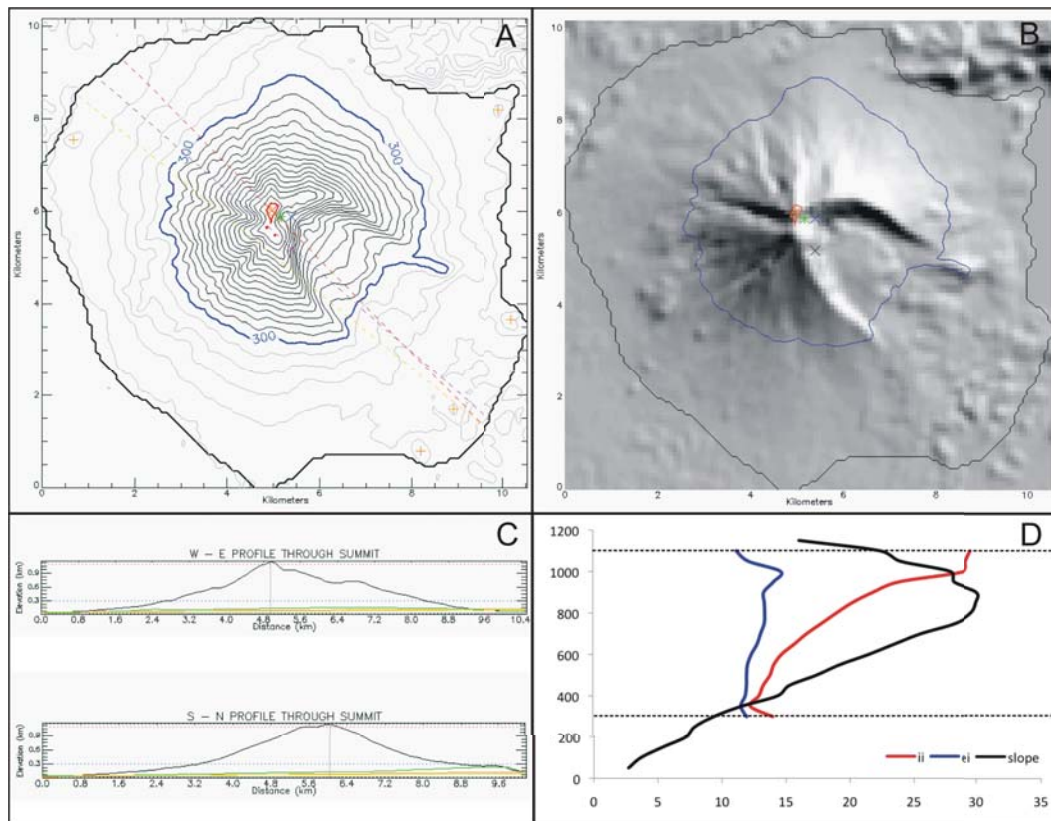


Figure A.14: Iriga

Status:	Active Volcano
Morphometry Type:	Breached edifice
Location (Lat, Long):	13.458041, 123.45038
Elevation (min, max):	28-1149 m
Basal Area:	79.7 km <sup>2</sup>
Height:	1121 m
Volume:	18 km <sup>3</sup>
Plan shape (ellipticity index, irregularity index):	1.87, 1.26
Profile shape (height/ base width, summit width/base width):	0.1, 0.03
Slope:	0°-49.22°
Base orientation in azimuth (through the summit, through the base centre):	135°, 131°

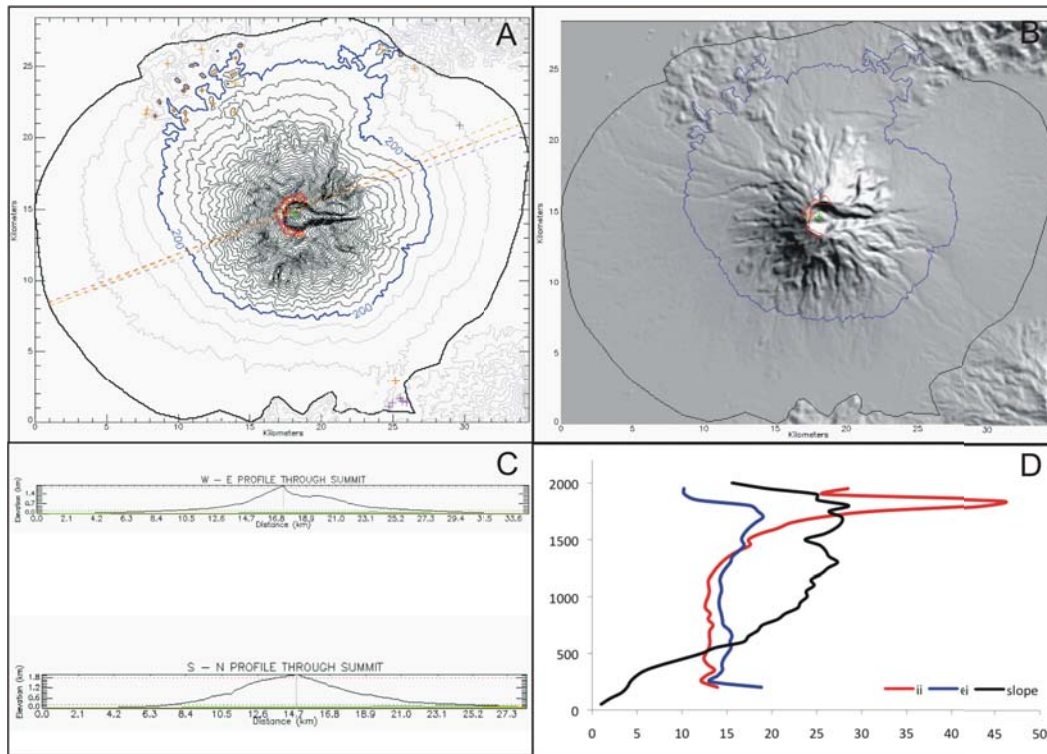


Figure A.15: Isarog

Status:	Potentially Active Volcano
Morphometry Type:	Breached edifice
Location (Lat, Long):	13.658362, 123.37253
Elevation (min, max):	3-1972 m
Basal Area:	753.4 km <sup>2</sup>
Height:	1969 m
Volume:	174 km <sup>3</sup>
Plan shape (ellipticity index, irregularity index):	1.60, 1.55
Profile shape (height/ base width, summit width/base width):	0.1, 0.24
Slope:	0°-54.20°
Base orientation in azimuth (through the summit, through the base centre):	68°, 70°

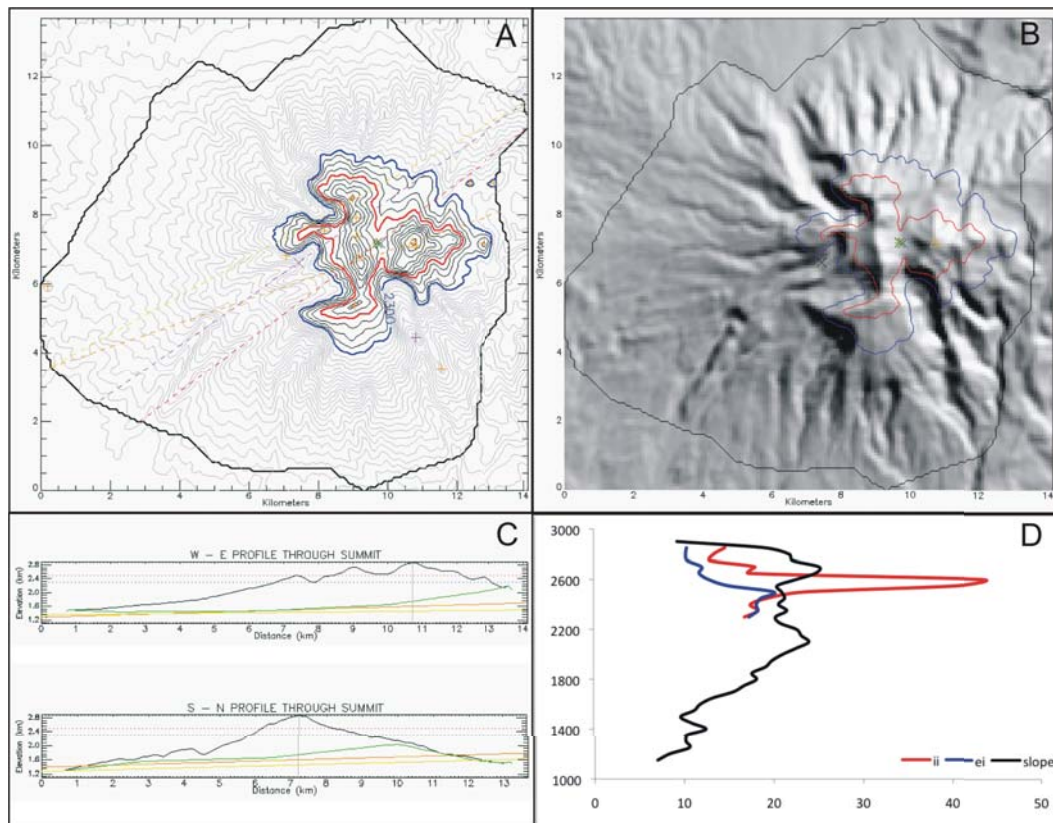


Figure A.16: Kalatungan

Status:	Potentially Active Volcano
Morphometry Type:	Eroded massif
Location (Lat, Long):	7.954539, 124.80169
Elevation (min, max):	1118-2860 m
Basal Area:	136.1 km <sup>2</sup>
Height:	1742 m
Volume:	96 km <sup>3</sup>
Plan shape (ellipticity index, irregularity index):	1.91, 1.85
Profile shape (height/ base width, summit width/base width):	0.10, 0.24
Slope:0.38°-54.48°	
Base orientation in azimuth (through the summit, through the base centre):	71°, 55°

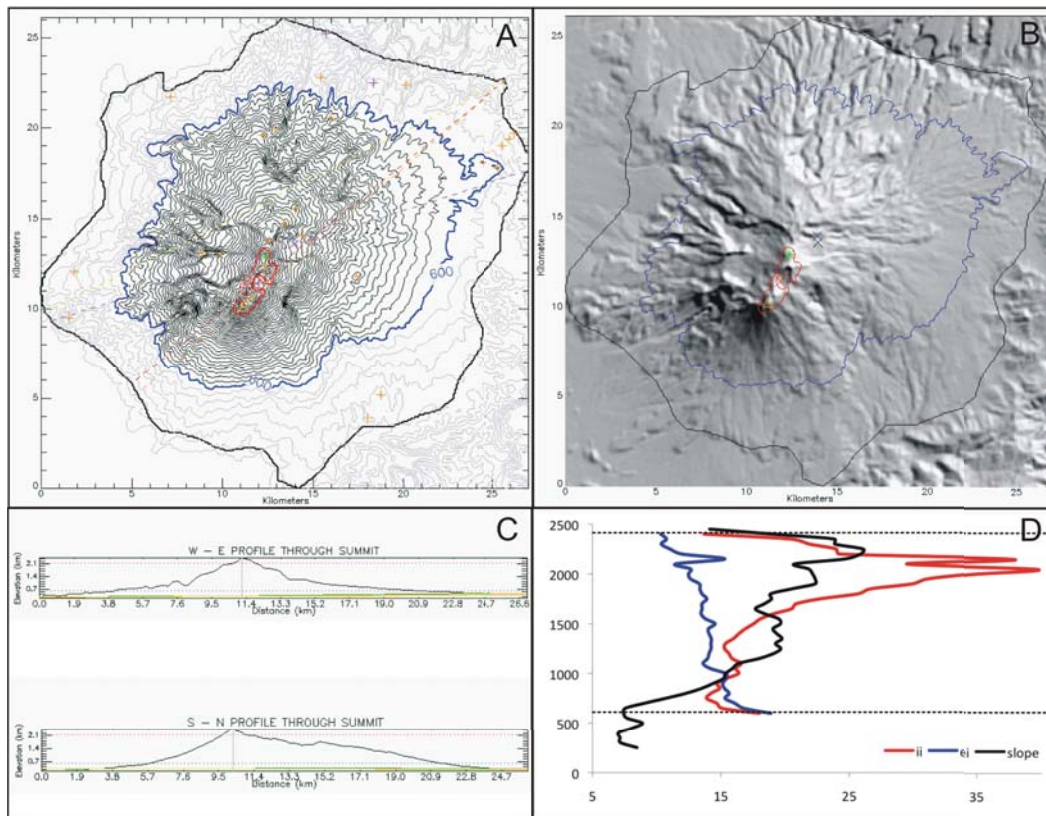


Figure A.17: Kanlaon

Status:	Active Volcano
Morphometry Type:	Breached
Location (Lat, Long):	10.409523, 123.12963
Elevation (min, max):	203-2421 m
Basal Area:	461.5 km <sup>2</sup>
Height:	2218 m
Volume:	251 km <sup>3</sup>
Plan shape (ellipticity index, irregularity index):	2.04, 1.43
Profile shape (height/ base width, summit width/base width):	0.09, 0.08
Slope:	0°-51.83°
Base orientation in azimuth (through the summit, through the base centre):	50°, 73°

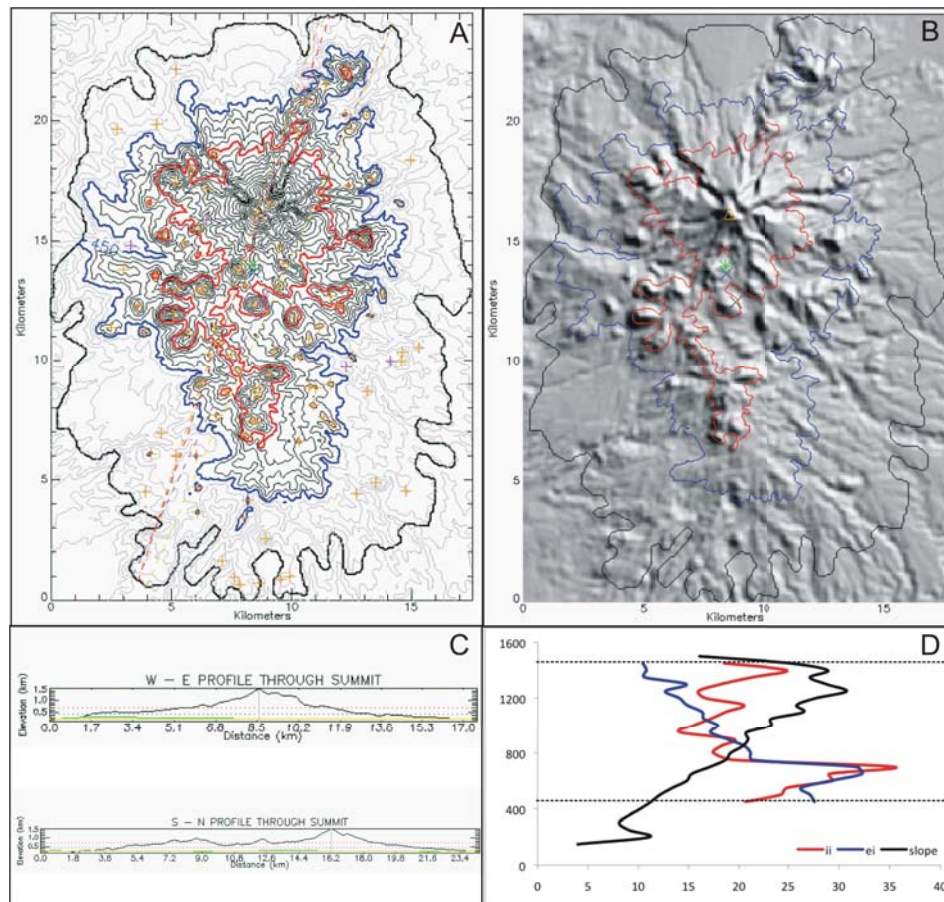


Figure A.18: Labo

Status:	Potentially Active Volcano
Morphometry Type:	Eroded massif
Location (Lat, Long):	14.012547, 122.78718
Elevation (min, max):	144-1482 m
Basal Area:	317.9 km <sup>2</sup>
Height:	1338 m
Volume:	105 km <sup>3</sup>
Plan shape (ellipticity index, irregularity index):	2.73, 2.90
Profile shape (height/ base width, summit width/base width):	0.06, 0.36
Slope:	0°-48.93°
Base orientation in azimuth (through the summit, through the base centre):	18°, 25°

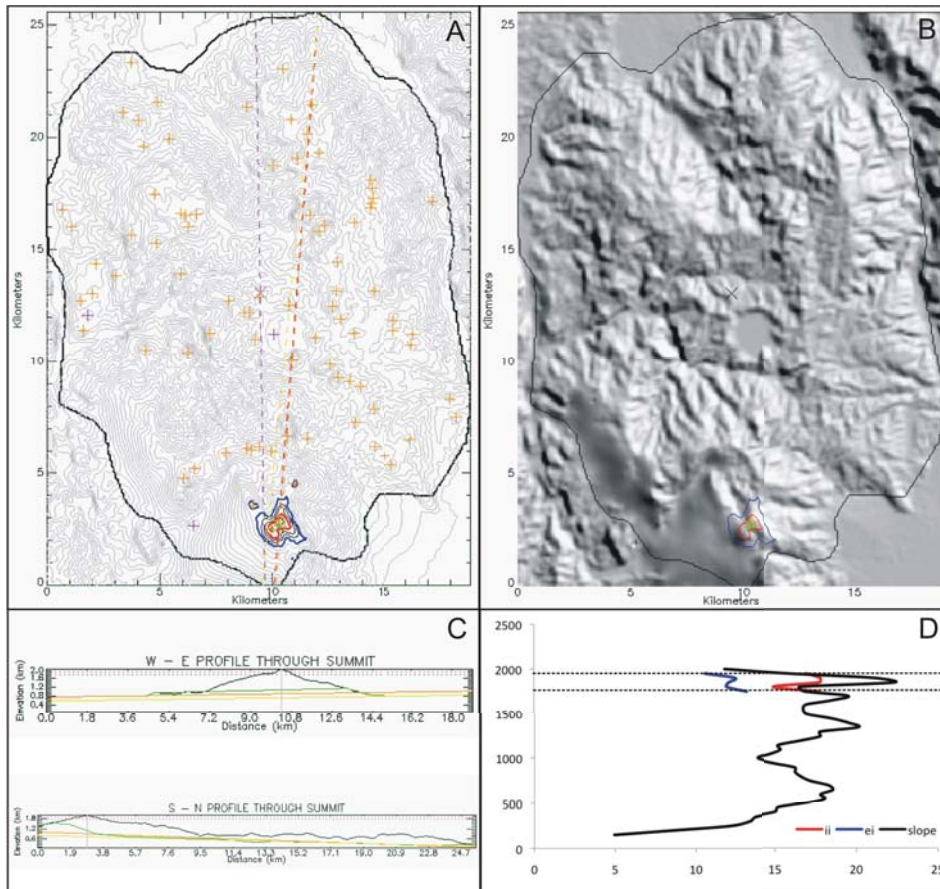


Figure A.19: Leonard Massif

Status:	Active Volcano
Morphometry Type:	Massif
Location (Lat, Long):	7.3179087, 126.06177
Elevation (min, max):	101-1990 m
Basal Area:	366.4 km <sup>2</sup>
Height:	1889 m
Volume:	270 km <sup>3</sup>
Profile shape (height/ base width, summit width/base width):	0.05, 0.04
Slope:	0°-53.97°
Base orientation in azimuth (through the summit, through the base centre):	4°, 179°

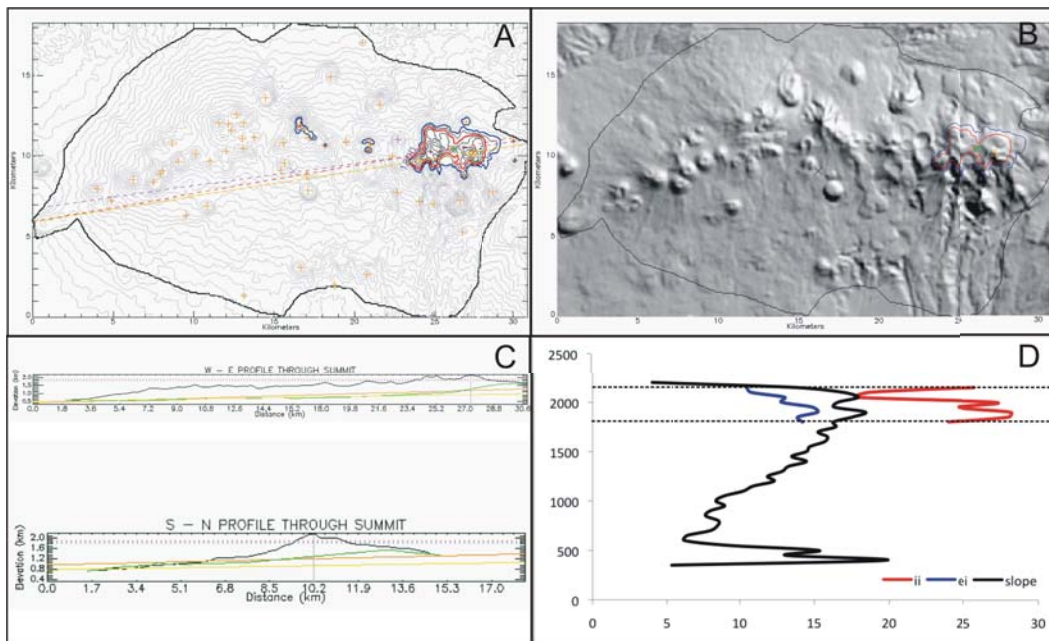


Figure A.20: Makaturing

Status:	Active Volcano
Morphometry Type:	Massif
Location (Lat, Long):	7.6386784, 124.39984
Elevation (min, max):	339-2155 m
Basal Area:	399.9 km <sup>2</sup>
Height:	1816 m
Volume:	307 km <sup>3</sup>
Profile shape (height/ base width, summit width/base width):	0.04, 0.13
Slope:	0°-49.94°
Base orientation in azimuth (through the summit, through the base centre):	81°, 82°

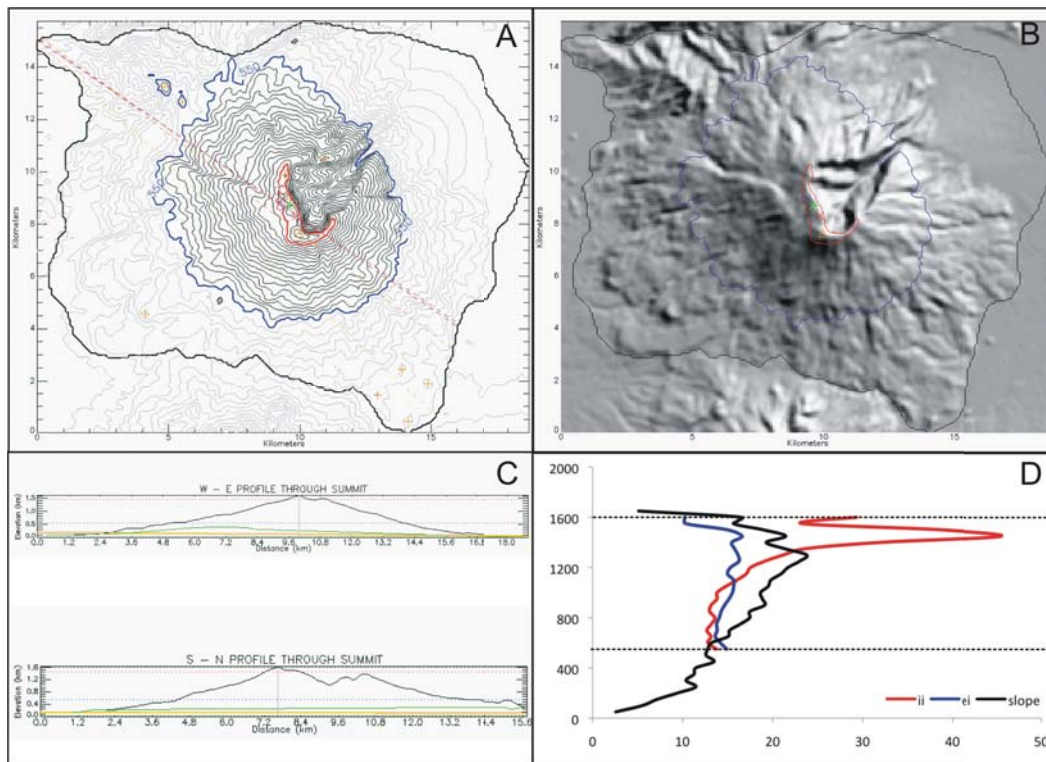


Figure A.21: Malinao

Status:	Potentially Active Volcano
Morphometry Type:	Breached edifice
Location (Lat, Long):	13.402375, 123.60738
Elevation (min, max):	13-1602 m
Basal Area:	210.8 km <sup>2</sup>
Height:	1589 m
Volume:	95 km <sup>3</sup>
Plan shape (ellipticity index, irregularity index):	1.79, 1.50
Profile shape (height/ base width, summit width/base width):	0.09, 0.09
Slope:	0°-55.24°
Base orientation in azimuth (through the summit, through the base centre):	127°, 124°

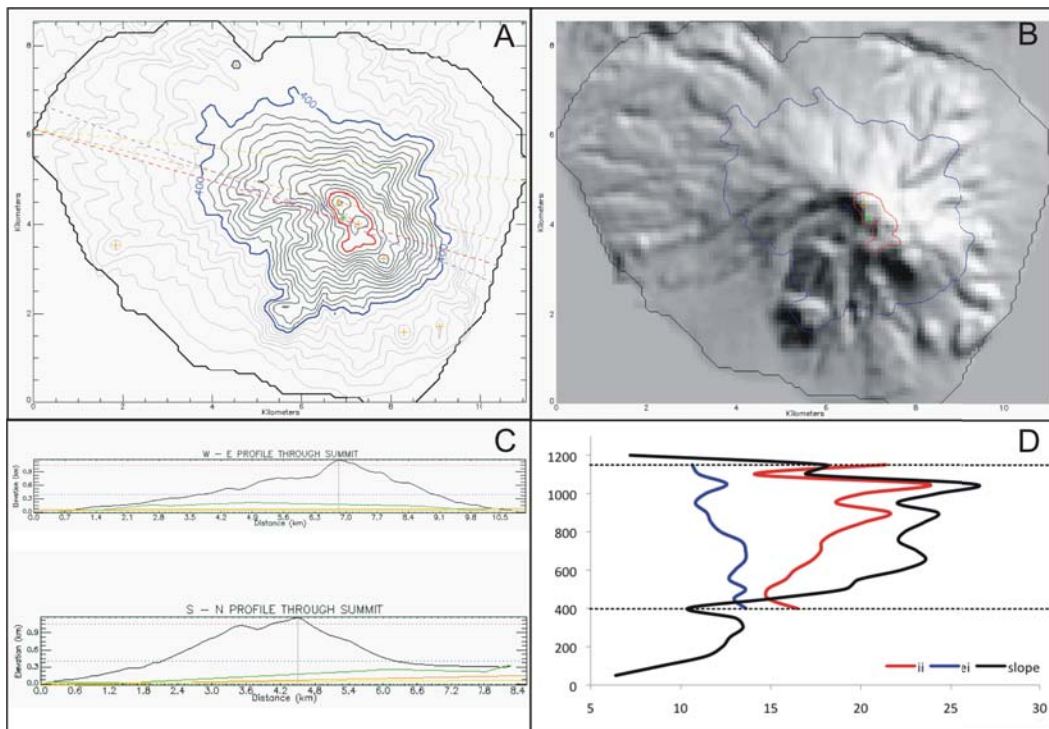


Figure A.22: Malindig

Status:	Potentially Active Volcano
Morphometry Type:	Sub-cone
Location (Lat, Long):	13.240873, 122.01283
Elevation (min, max):	0-1161 m
Basal Area:	70 km <sup>2</sup>
Height:	1162 m
Volume:	22 km <sup>3</sup>
Plan shape (ellipticity index, irregularity index):	1.81, 1.26
Profile shape (height/ base width, summit width/base width):	0.12, 0.10
Slope:	0°-43.37°
Base orientation in azimuth (through the summit, through the base centre):	103°, 111°

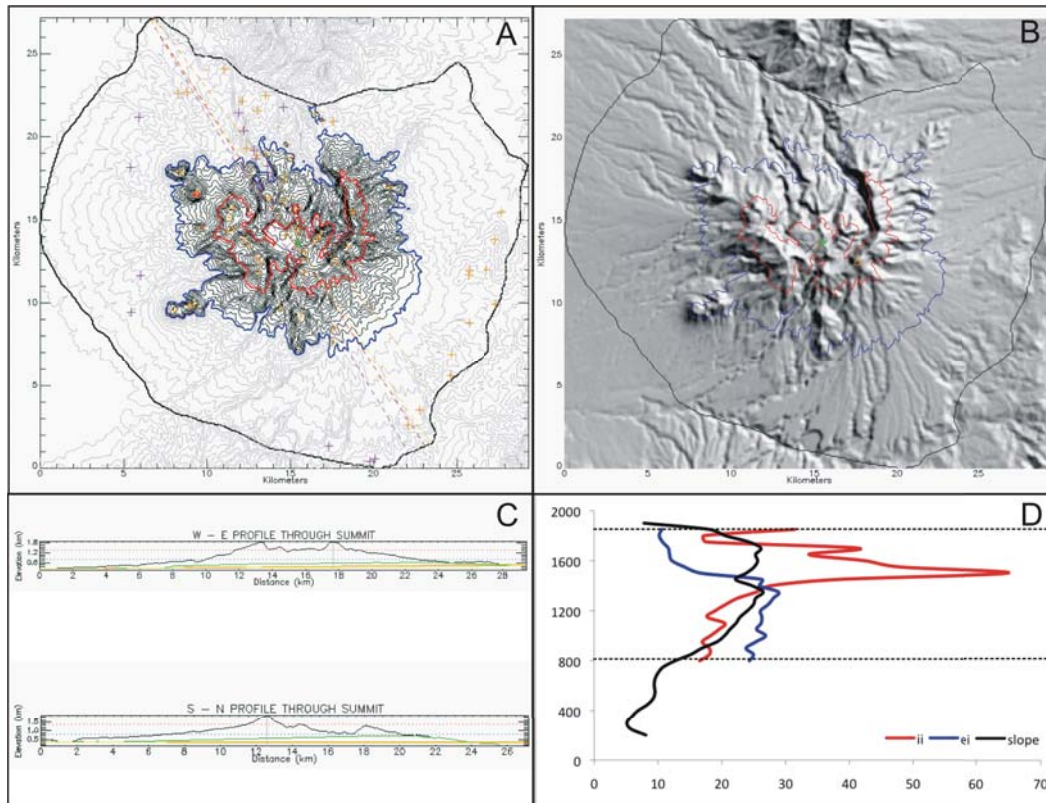


Figure A.23: Mandalagan

Status:	Potentially Active Volcano
Morphometry Type:	Eroded massif
Location (Lat, Long):	10.636564, 123.23505
Elevation (min, max):	166-1854 m
Basal Area:	539 km <sup>2</sup>
Height:	1688 m
Volume:	267 km <sup>3</sup>
Plan shape (ellipticity index, irregularity index):	1.94, 2.61
Profile shape (height/ base width, summit width/base width):	0.06, 0.023
Slope:	0.11°-58.32°
Base orientation in azimuth (through the summit, through the base centre):	144°, 149°

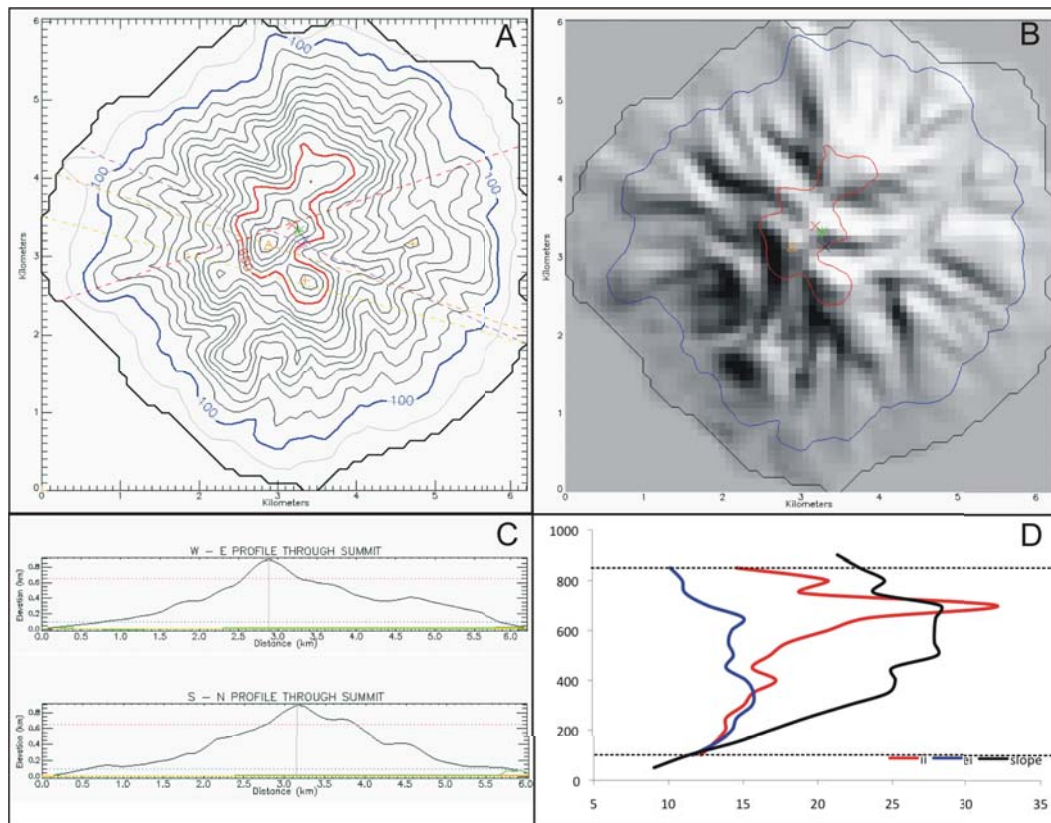


Figure A.24: Maripipi

Status:	Potentially Active Volcano
Morphometry Type:	Sub-cone
Location (Lat, Long):	11.788589, 124.31892
Elevation (min, max):	0-889 m
Basal Area:	27.9 km <sup>2</sup>
Height:	889 m
Volume:	7 km <sup>3</sup>
Plan shape (ellipticity index, irregularity index):	1.63, 1.44
Profile shape (height/ base width, summit width/base width):	0.15, 0.22
Slope:	1.09°-44.11°
Base orientation in azimuth (through the summit, through the base centre):	108°, 114°

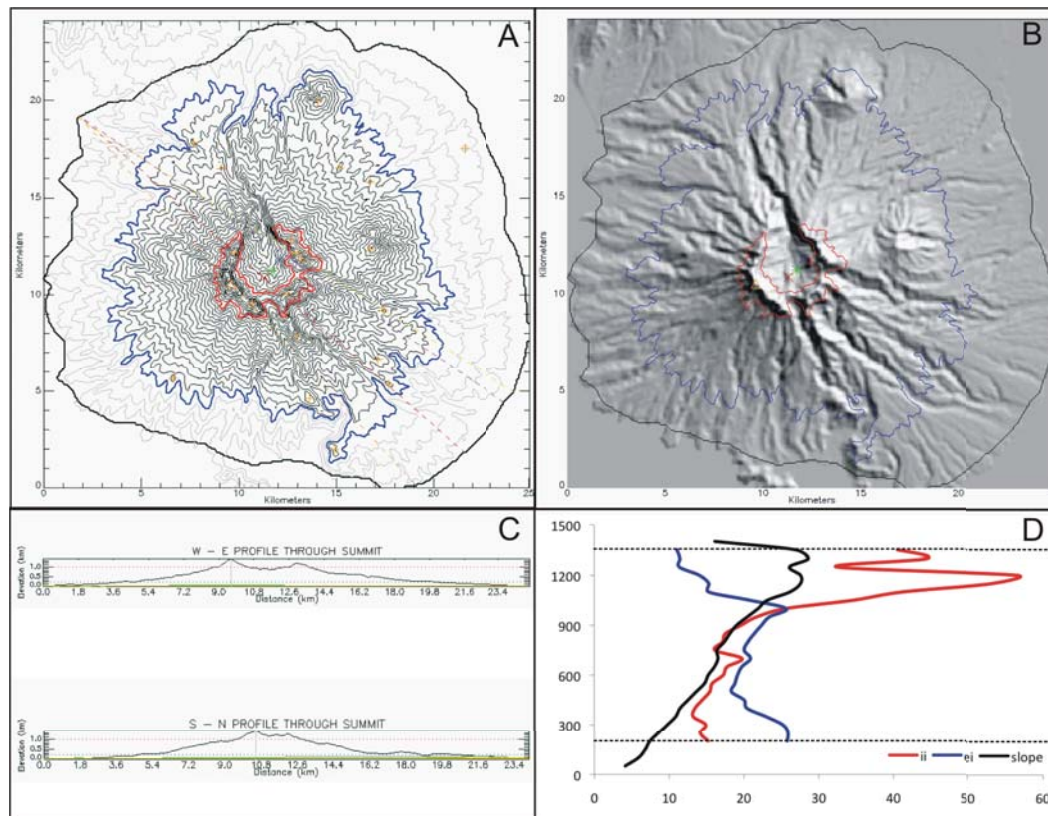


Figure A.25: Mariveles-Limay-Samat

Status:	Potentially Active Volcano
Morphometry Type:	Breached edifice
Location (Lat, Long):	14.51893, 120.46526
Elevation (min, max):	0-1396 m
Basal Area:	457.5 km <sup>2</sup>
Height:	1396 m
Volume:	128 km <sup>3</sup>
Plan shape (ellipticity index, irregularity index):	1.70, 2.17
Profile shape (height/ base width, summit width/base width):	0.06, 0.15
Slope:	0°-55.44°
Base orientation in azimuth (through the summit, through the base centre):	138°, 124°

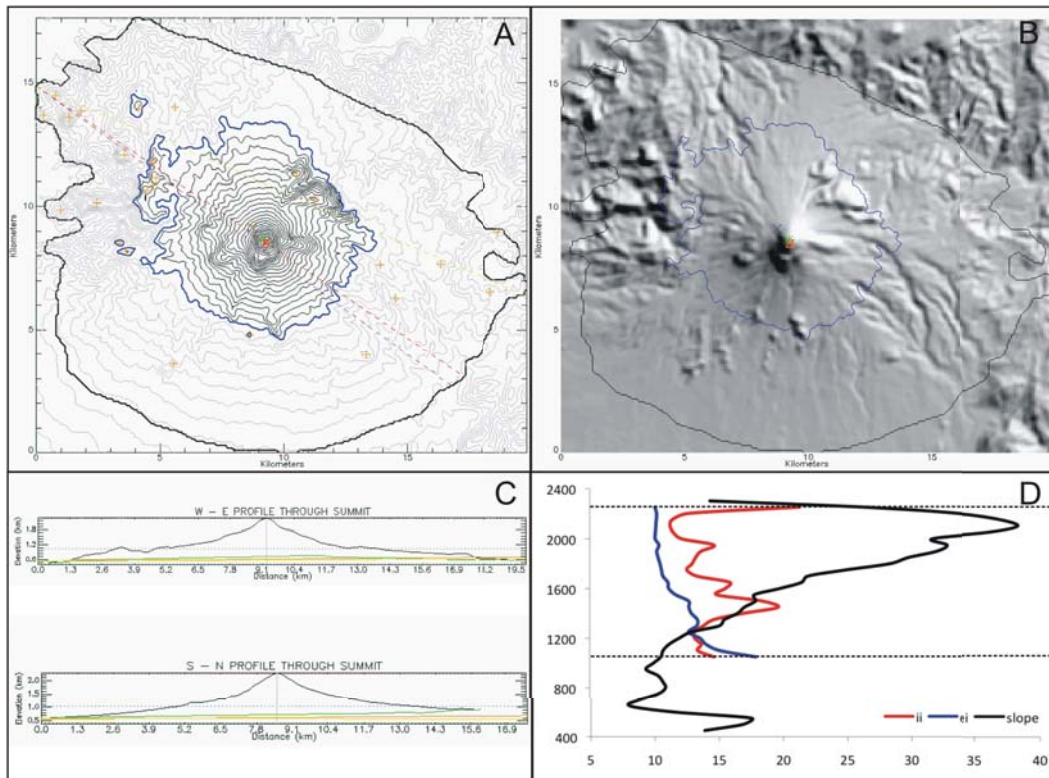


Figure A.26: Matutum

Status:	Active Volcano
Morphometry Type:	Cone
Location (Lat, Long):	6.3602102, 125.07605
Elevation (min, max):	408-2258 m
Basal Area:	241.8 km <sup>2</sup>
Height:	1850 m
Volume:	120 km <sup>3</sup>
Plan shape (ellipticity index, irregularity index):	1.43, 1.18
Profile shape (height/ base width, summit width/base width):	0.09, 0.01
Slope:	0.11°-51.61°
Base orientation in azimuth (through the summit, through the base centre):	124°, 126°

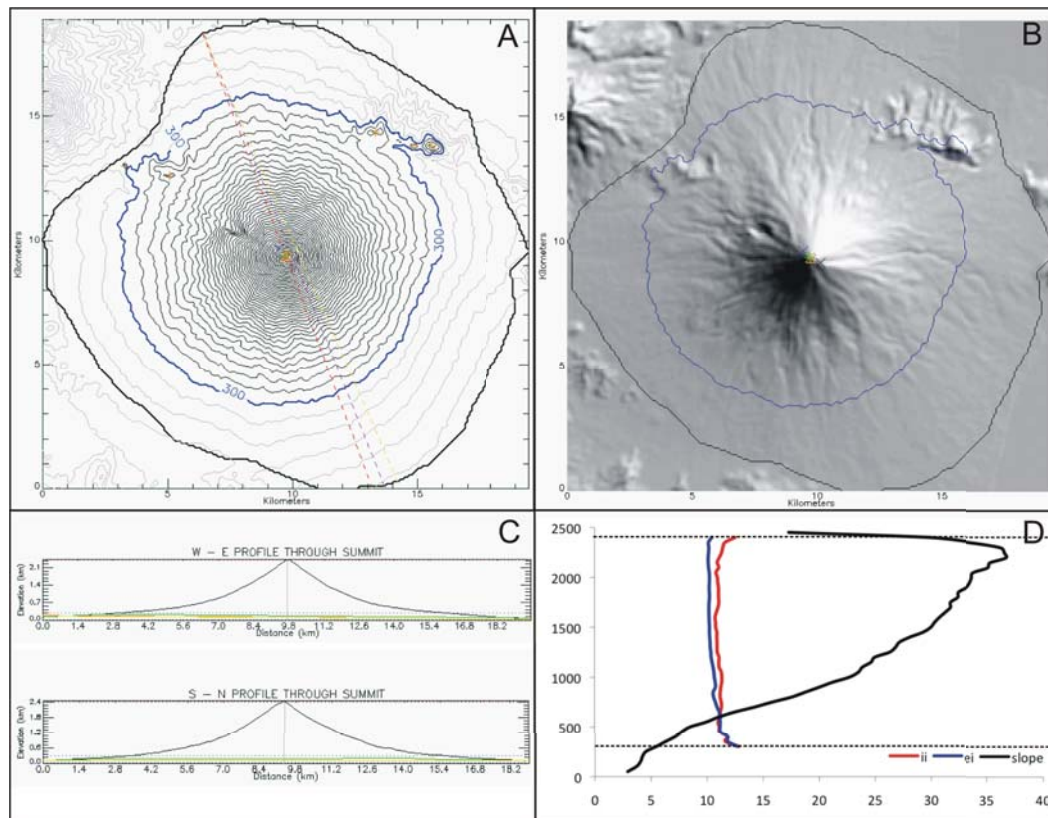


Figure A.27: Mayon

Status:	Active Volcano
Morphometry Type:	Cone
Location (Lat, Long):	13.255697, 123.68511
Elevation (min, max):	4-2420 m
Basal Area:	257.5 km <sup>2</sup>
Height:	2416 m
Volume:	104 km <sup>3</sup>
Plan shape (ellipticity index, irregularity index):	1.2, 1.06
Profile shape (height/ base width, summit width/base width):	0.13, 0.01
Slope:	0.15°-42.53°
Base orientation in azimuth (through the summit, through the base centre):	160°, 158°

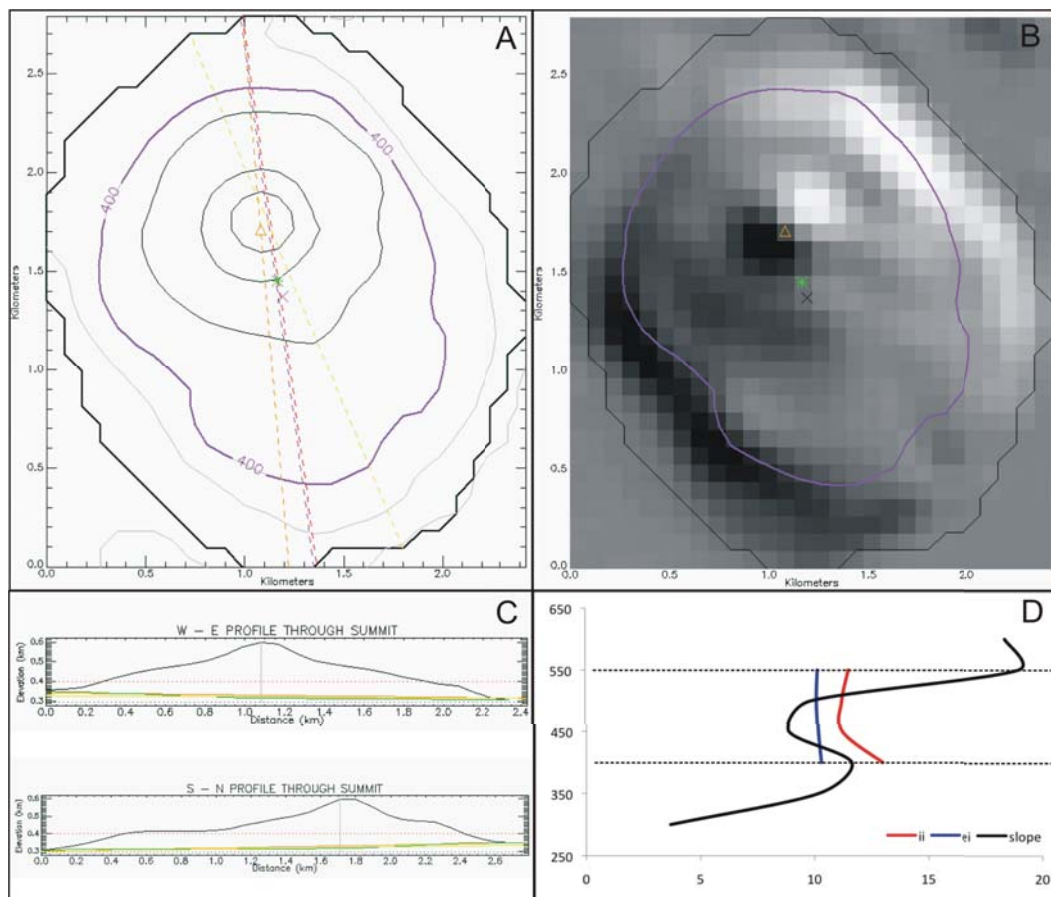


Figure A.28: Musuan

Status:	Active Volcano
Morphometry Type:	Cone
Location (Lat, Long):	7.876002, 125.069
Elevation (min, max):	297-598 m
Basal Area:	5 km <sup>2</sup>
Height:	301 m
Volume:	1 km <sup>3</sup>
Profile shape (height/ base width, summit width/base width):	0.11, 0.72
Slope:	0.54°-28.84°
Base orientation in azimuth (through the summit, through the base centre):	175°, 172°

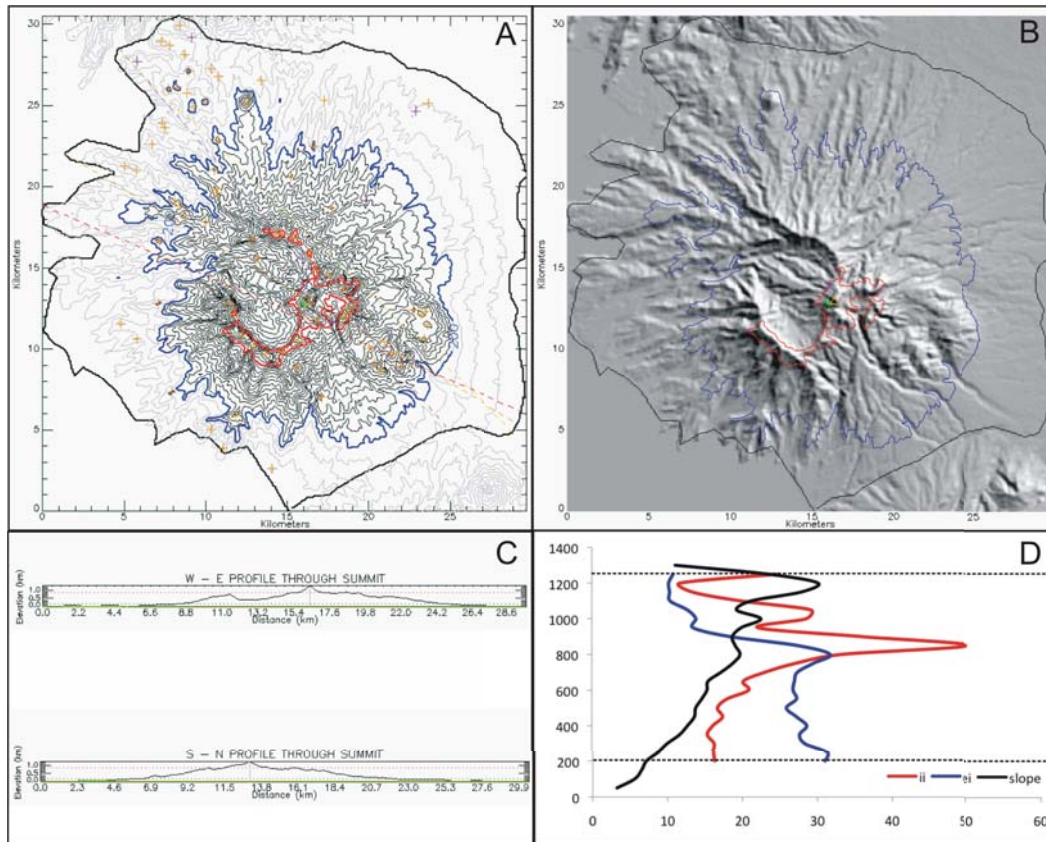


Figure A.29: Natib

Status:	Potentially Active Volcano
Morphometry Type:	Breached edifice
Location (Lat, Long):	14.711715, 120.4004
Elevation (min, max):	0-1253 m
Basal Area:	640.9 km <sup>2</sup>
Height:	1253 m
Volume:	151 km <sup>3</sup>
Plan shape (ellipticity index, irregularity index):	2.19, 2.84
Profile shape (height/ base width, summit width/base width):	0.04, 0.14
Slope:	0°-48.73°
Base orientation in azimuth (through the summit, through the base centre):	121°, 139°

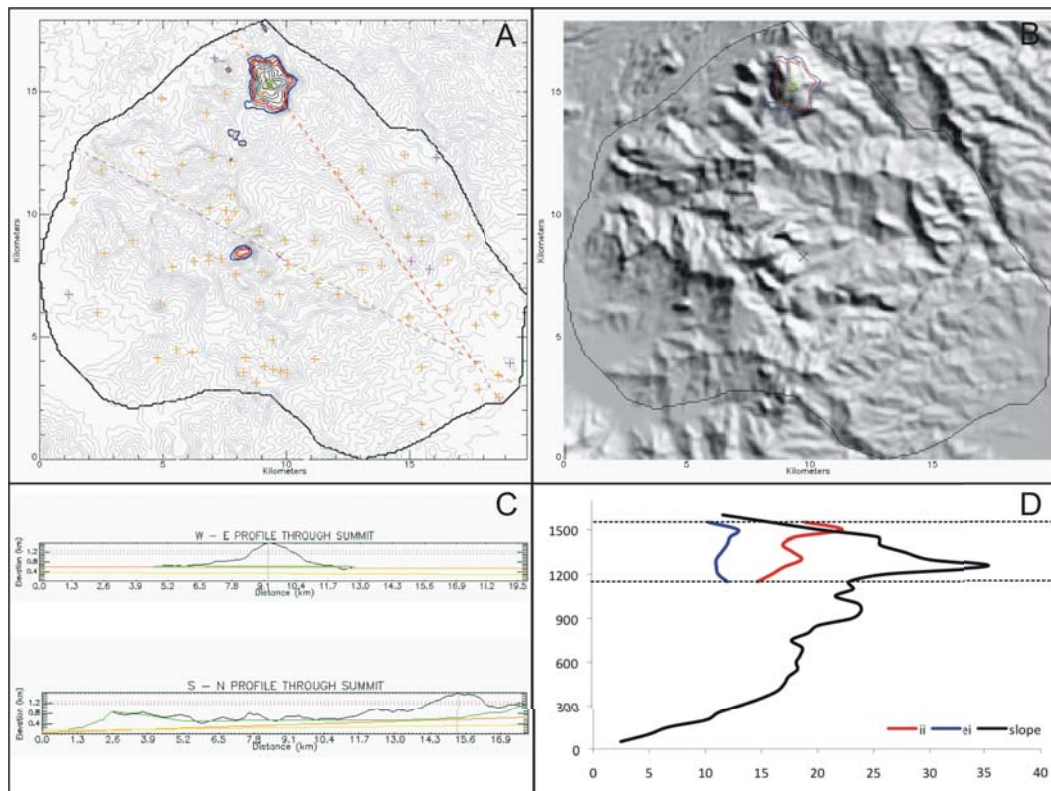


Figure A.30: Negron

Status:	Potentially Active Volcano
Morphometry Type:	Massif
Location (Lat, Long):	15.092623, 120.36738
Elevation (min, max):	35-1558 m
Basal Area:	236 km <sup>2</sup>
Height:	1523 m
Volume:	109 km <sup>3</sup>
Profile shape (height/ base width, summit width/base width):	0.06, 0.10
Slope:	0°-62.36°
Base orientation in azimuth (through the summit, through the base centre):	144°, 118°

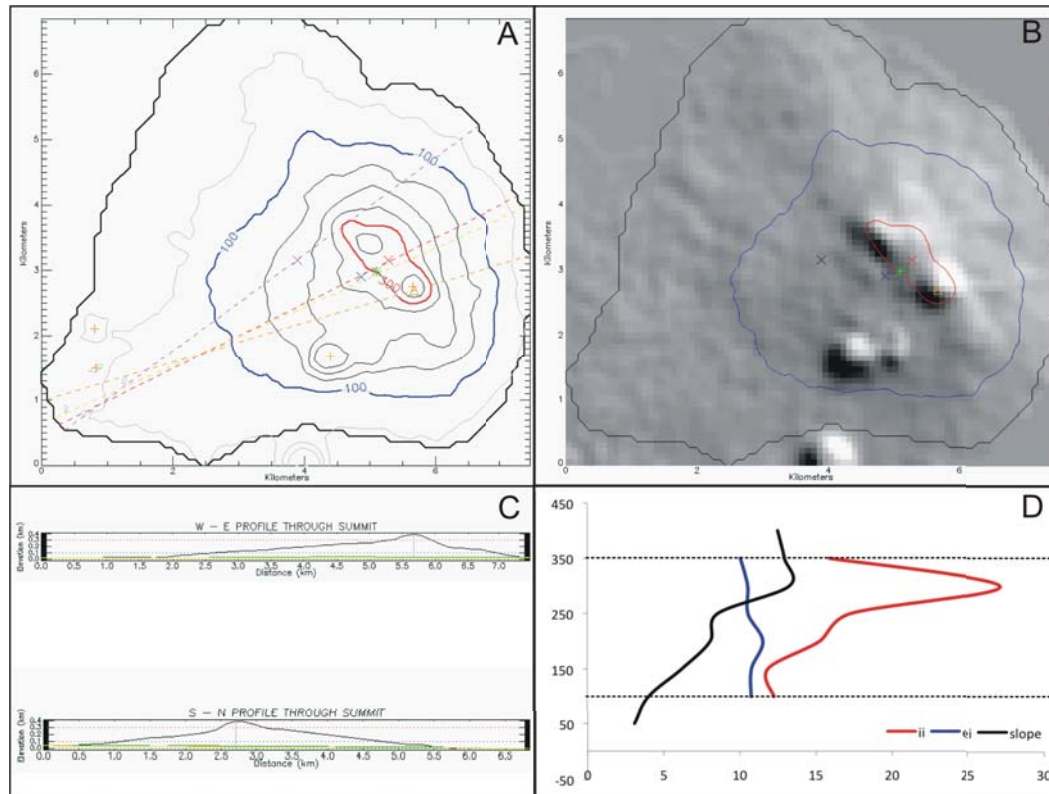


Figure A.31: Parangan

Status:	Potentially Active Volcano
Morphometry Type:	Cone
Location (Lat, Long):	5.9704632, 121.4077
Elevation (min, max):	1-390 m
Basal Area:	36.8 km <sup>2</sup>
Height:	389 m
Volume:	4 km <sup>3</sup>
Plan shape (ellipticity index, irregularity index):	1.67, 1.08
Profile shape (height/ base width, summit width/base width):	0.05, 0.15
Slope:	0°-28.45°
Base orientation in azimuth (through the summit, through the base centre):	73°, 53°

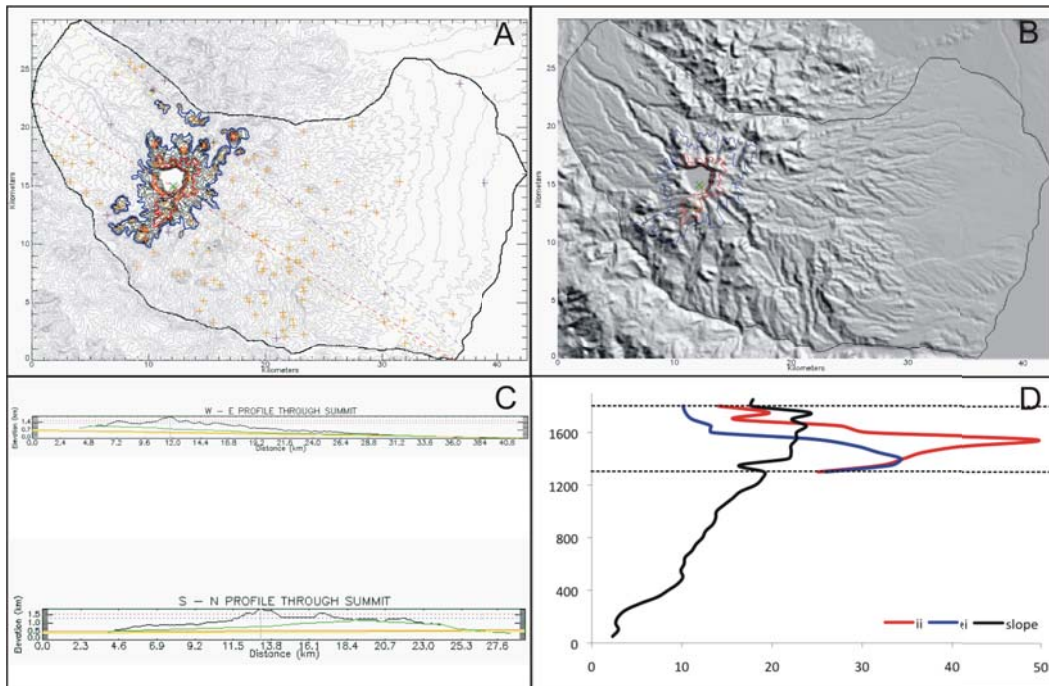


Figure A.32: Parker

Status:	Active Volcano
Morphometry Type:	Massif
Location (Lat, Long):	6.0793874, 124.88636
Elevation (min, max):	0-1849 m
Basal Area:	781.3 km <sup>2</sup>
Height:	1849 m
Volume:	472 km <sup>3</sup>
Plan shape (ellipticity index, irregularity index):	3.67, 2.98
Profile shape (height/ base width, summit width/base width):	0.04, 0.10
Slope:	0°-58.28°
Base orientation in azimuth (through the summit, through the base centre):	119°, 130°

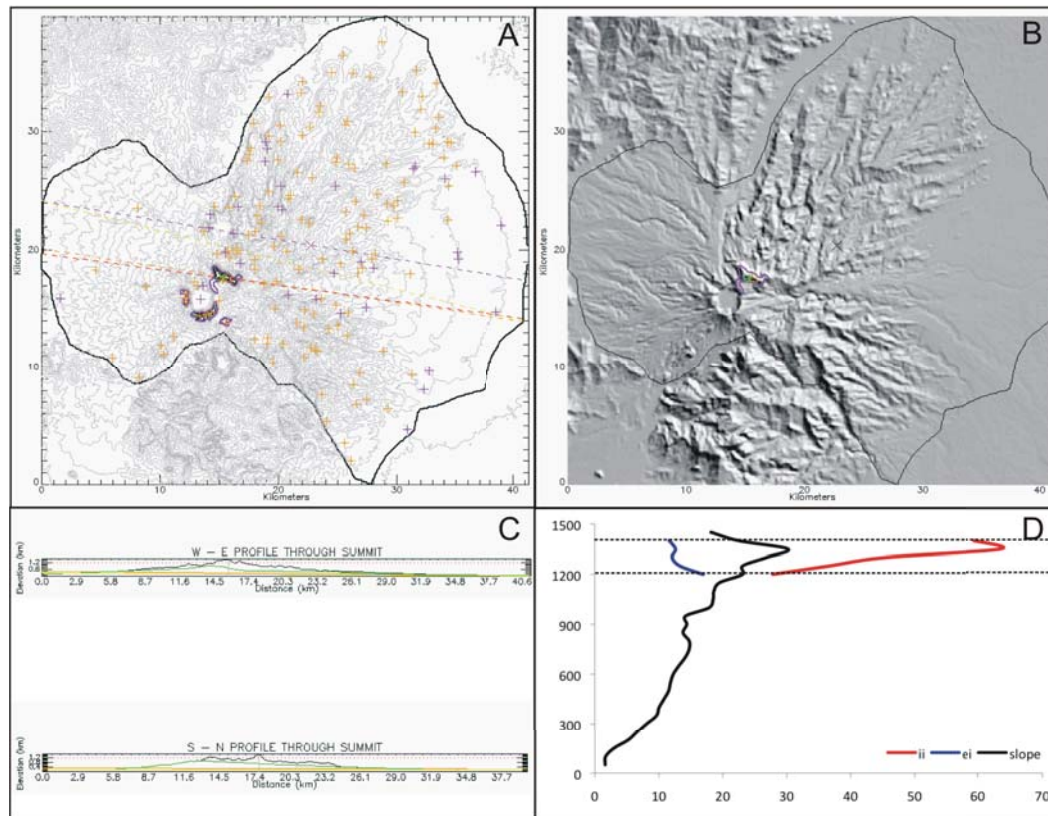


Figure A.33: Pinatubo

Status:	Active Volcano
Morphometry Type:	Massif
Location (Lat, Long):	15.159325, 120.37074
Elevation (min, max):	46-1445 m
Basal Area:	939.2 m
Height:	1399 m
Volume:	301 km <sup>3</sup>
Profile shape (height/ base width, summit width/base width):	0.03, 0.05
Slope:	0°-49.81°
Base orientation in azimuth (through the summit, through the base centre):	99°, 99°

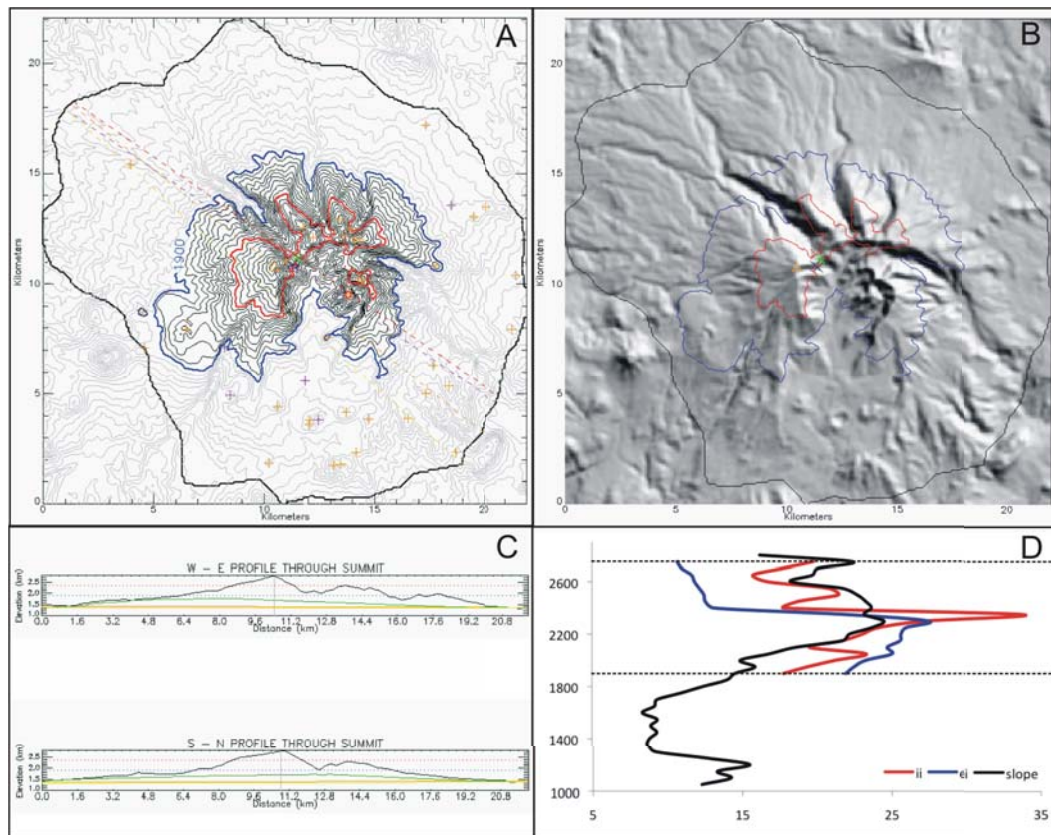


Figure A.34: Ragang

Status:	Active Volcano
Morphometry Type:	Breached edifice
Location (Lat, Long):	7.6904039, 124.50688
Elevation (min, max):	1008-2787 m
Basal Area:	334.6 km <sup>2</sup>
Height:	1779 m
Volume:	236 km <sup>3</sup>
Plan shape (ellipticity index, irregularity index):	2.31, 2.44
Profile shape (height/ base width, summit width/base width):	0.07, 0.20
Slope:	0.11°-52.56°
Base orientation in azimuth (through the summit, through the base centre):	129°, 124°

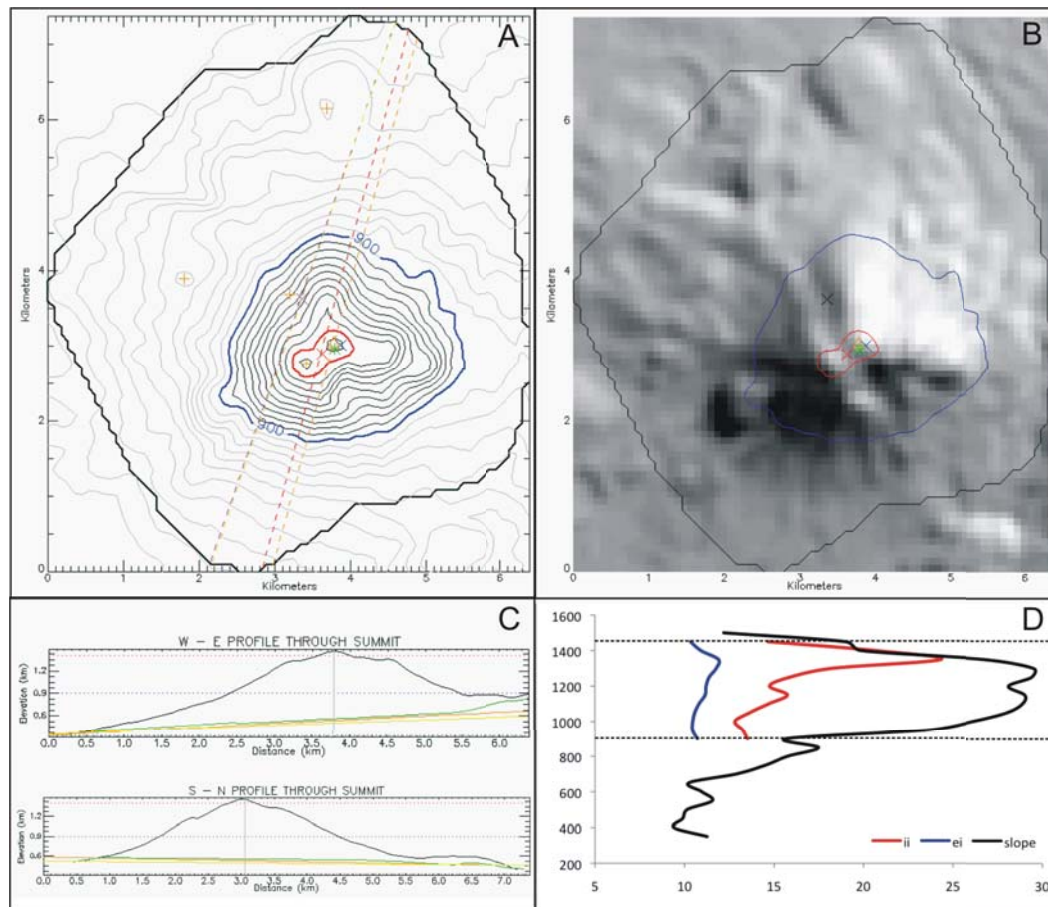


Figure A.35: San Cristobal

Status:	Potentially Active Volcano
Morphometry Type:	Sub-cone
Location (Lat, Long):	14.064475, 121.42598
Elevation (min, max):	330-1467 m
Basal Area:	32.5 km <sup>2</sup>
Height:	1137 m
Volume:	13 km <sup>3</sup>
Plan shape (ellipticity index, irregularity index):	1.61, 1.10
Profile shape (height/ base width, summit width/base width):	0.14, 0.09
Slope:	0.21°-40.43°
Base orientation in azimuth (through the summit, through the base centre):	15°, 19°

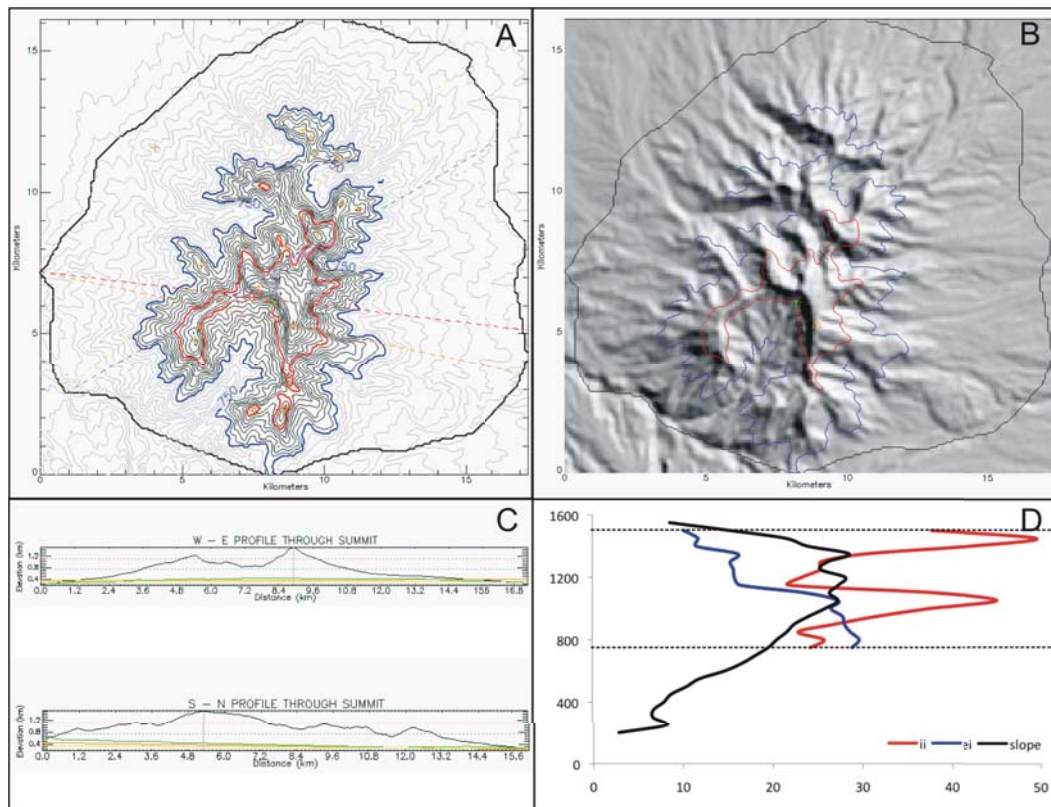


Figure A.36: Silay

Status:	Potentially Active Volcano
Morphometry Type:	Eroded massif
Location (Lat, Long):	10.770056, 123.23268
Elevation (min, max):	198-1508 m
Basal Area:	207.8 km <sup>2</sup>
Height:	1310 m
Volume:	84 km <sup>3</sup>
Plan shape (ellipticity index, irregularity index):	3.16, 2.76
Profile shape (height/ base width, summit width/base width):	0.07, 0.22
Slope:	0.24°-52.12°
Base orientation in azimuth (through the summit, through the base centre):	102°, 60°

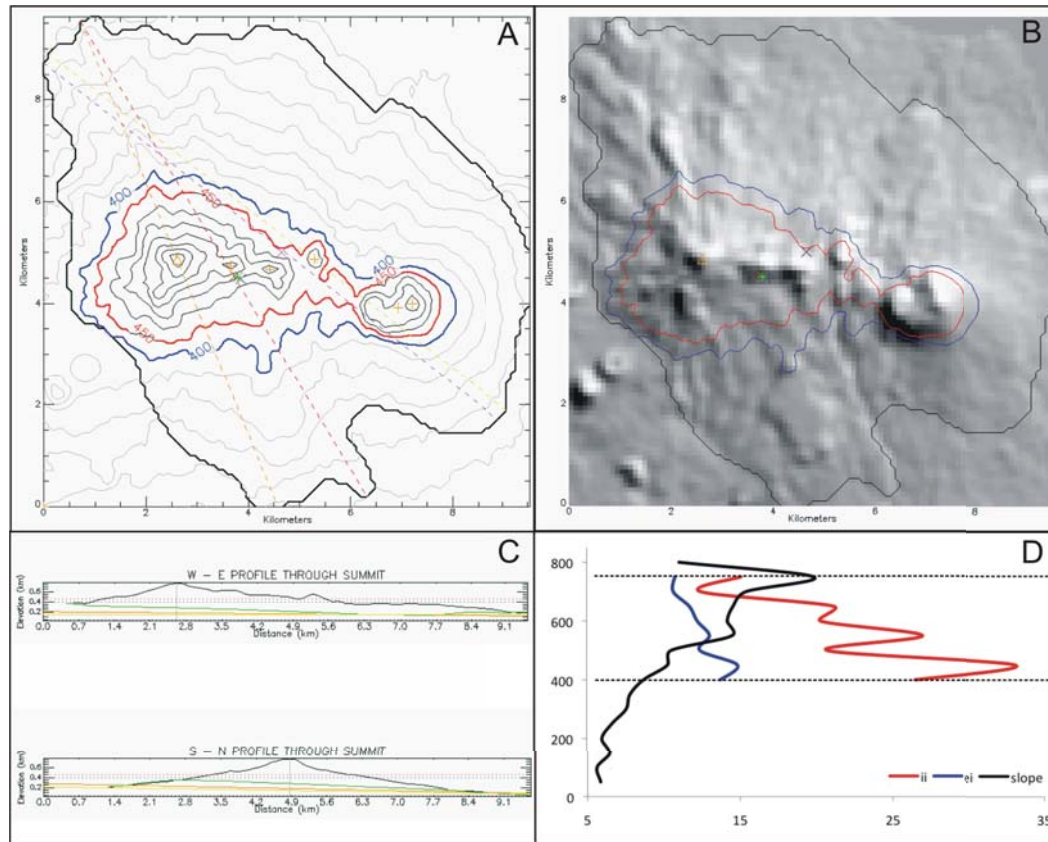


Figure A.37: Sinumaan

Status:	Potentially Active Volcano
Morphometry Type:	Sub-cone
Location (Lat, Long):	6.0370237, 121.09941
Elevation (min, max):	45-764 m
Basal Area:	62.8 km <sup>2</sup>
Height:	719 m
Volume:	17 km <sup>3</sup>
Plan shape (ellipticity index, irregularity index):	2.98, 1.43
Profile shape (height/ base width, summit width/base width):	0.06, 0.42
Slope:	0.15°-33.05°
Base orientation in azimuth (through the summit, through the base centre):	158°, 128°

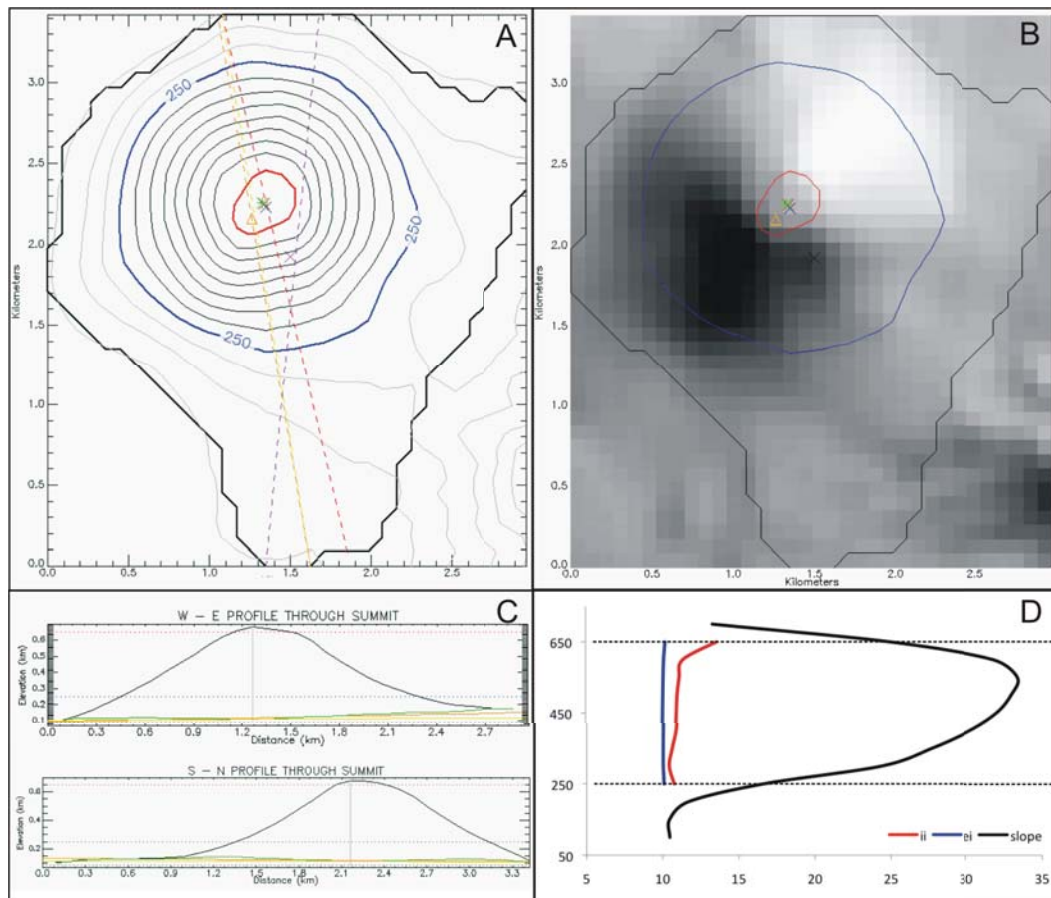


Figure A.38: Smith

Status:	Active Volcano
Morphometry Type:	Cone
Location (Lat, Long):	19.537585, 121.91194
Elevation (min, max):	87-679 m
Basal Area:	6.6 km <sup>2</sup>
Height:	592 m
Volume:	1 km <sup>3</sup>
Plan shape (ellipticity index, irregularity index):	1.12, 1.01
Profile shape (height/ base width, summit width/base width):	0.19, 0.13
Slope:	0.44°-35.31°
Base orientation in azimuth (through the summit, through the base centre):	171°, 5°

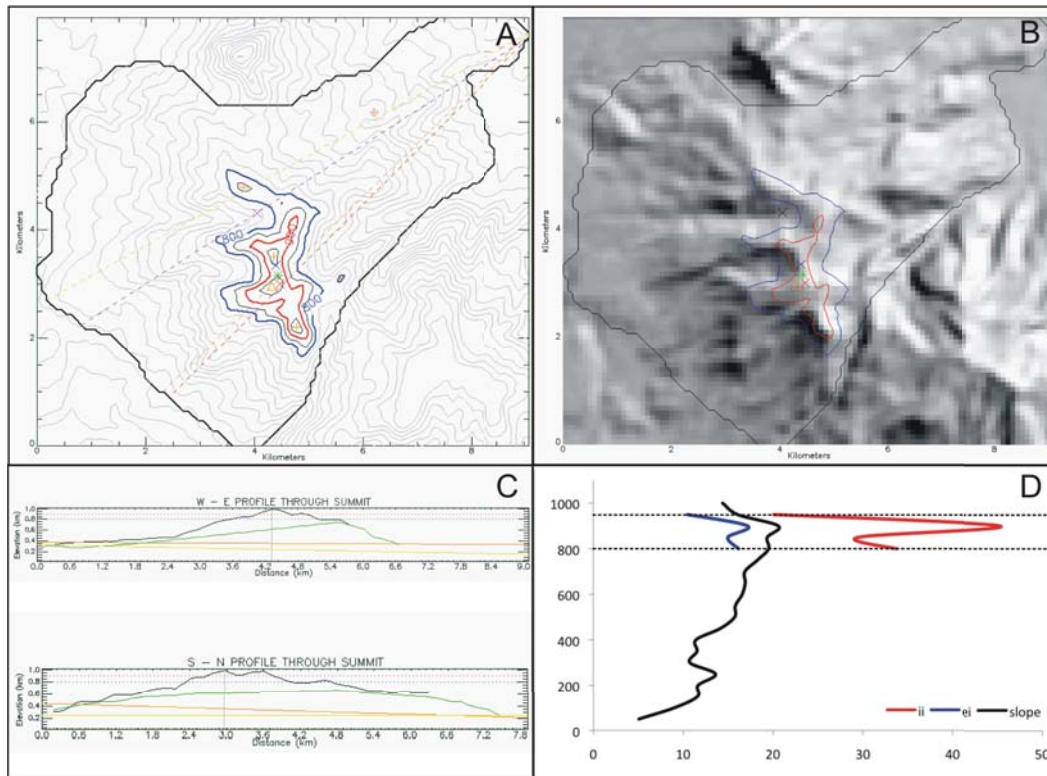


Figure A.39: Vulcan Biliran

Status:	Active Volcano
Morphometry Type:	Sub-cone
Location (Lat, Long):	11.533802, 124.50502
Elevation (min, max):	38-989 m
Basal Area:	39.1 km <sup>2</sup>
Height:	951
Volume:	18 km <sup>3</sup>
Plan shape (ellipticity index, irregularity index):	3.61, 1.61
Profile shape (height/ base width, summit width/base width):	0.09, 0.15
Slope:	0.15°-39.51°
Base orientation in azimuth (through the summit, through the base centre):	46°, 57°

APPENDIX B

# Avalanche class and hummock types

---

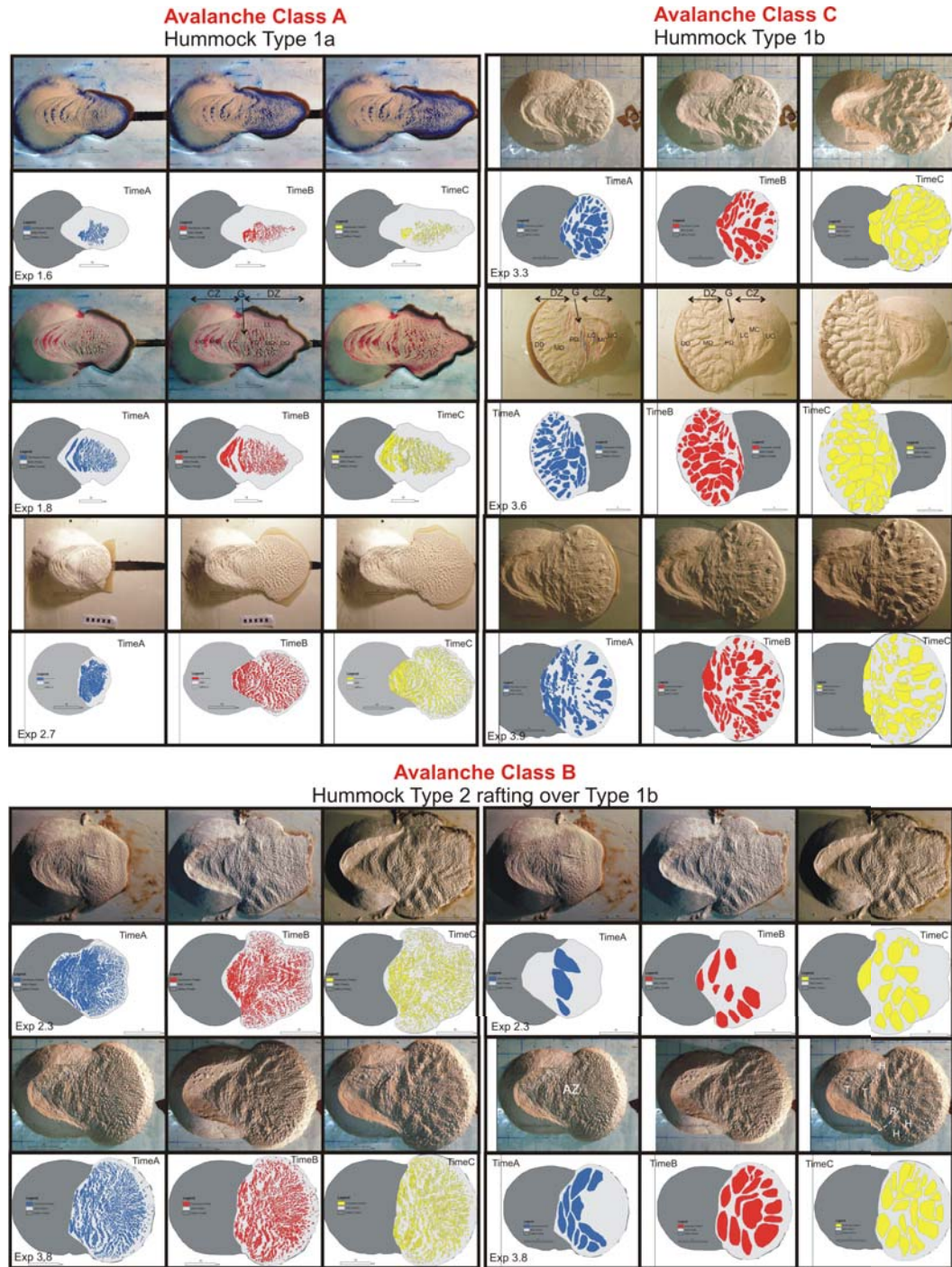


Figure B.1: Chosen analogue models that best represent the recurrent morphology and structures in the three sets of experiments: Set 1, Set 2, and set 3 with their classified avalanche classes and the type of hummocks formed in each of the classes.

APPENDIX C

# Hummock size versus distance

---

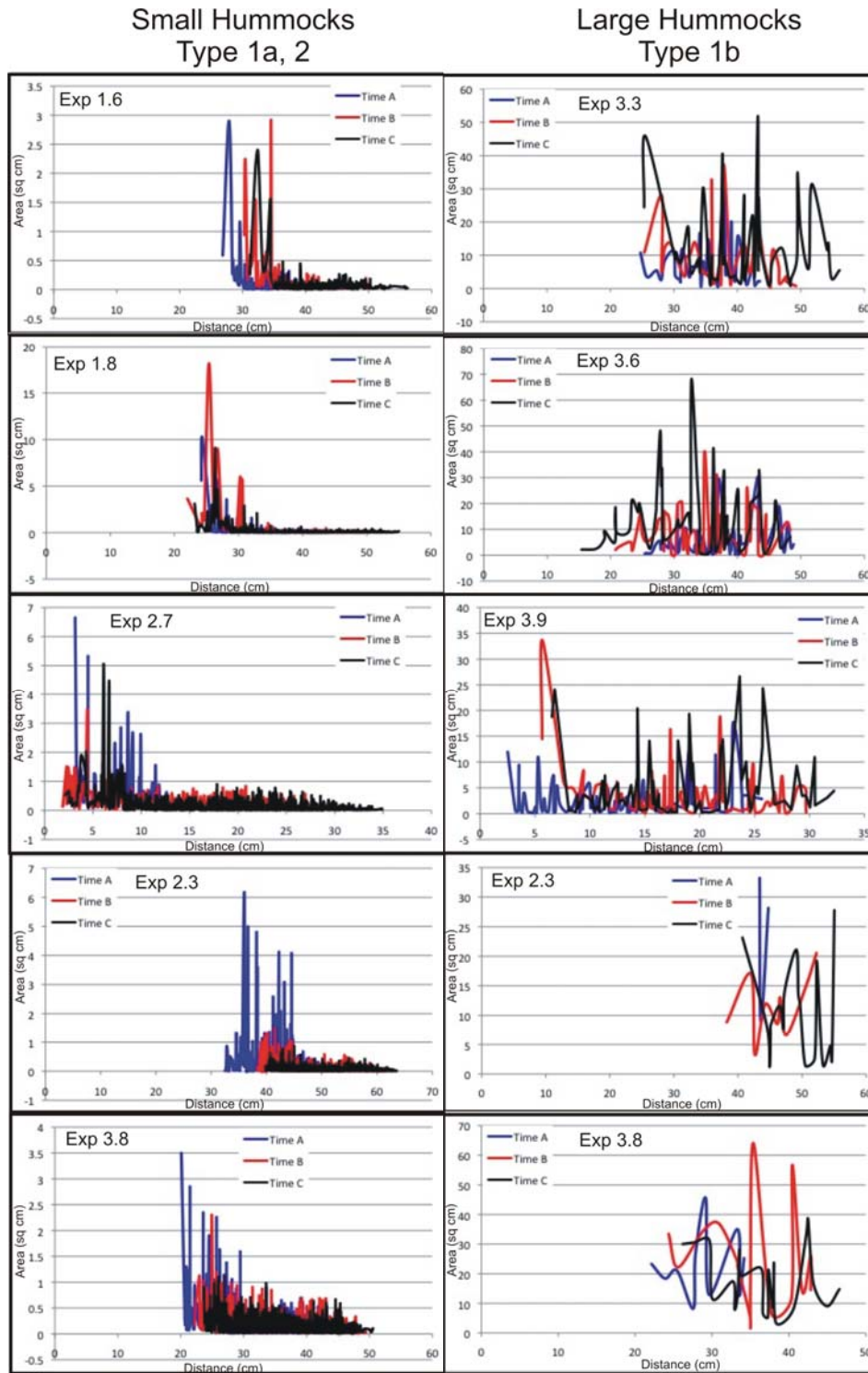


Figure C.1: Line plot of the hummock sizes sorted according to its distance away from the source.

APPENDIX D

# Curved and straight ramp experiments

---

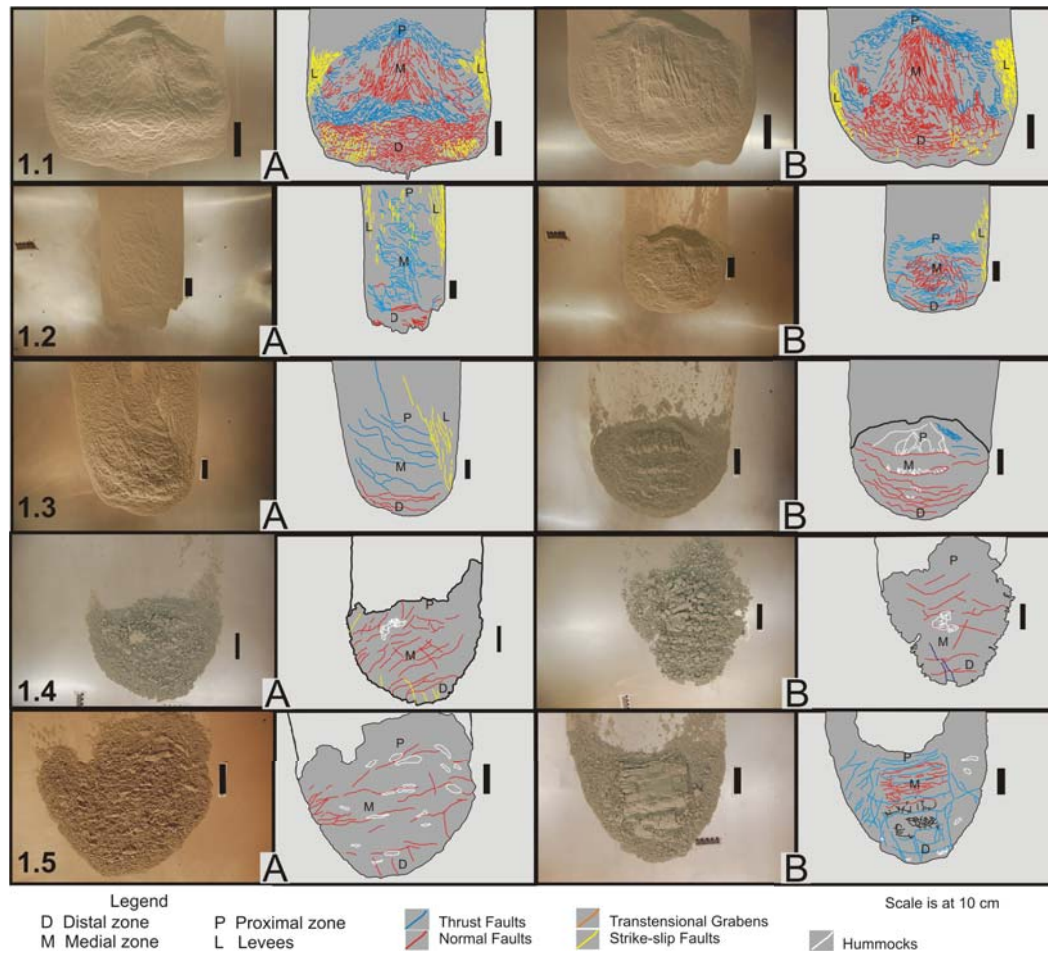


Figure D.1: Analogue slides using the curved ramp, Set 1. Parameters used are presented in Table 2.

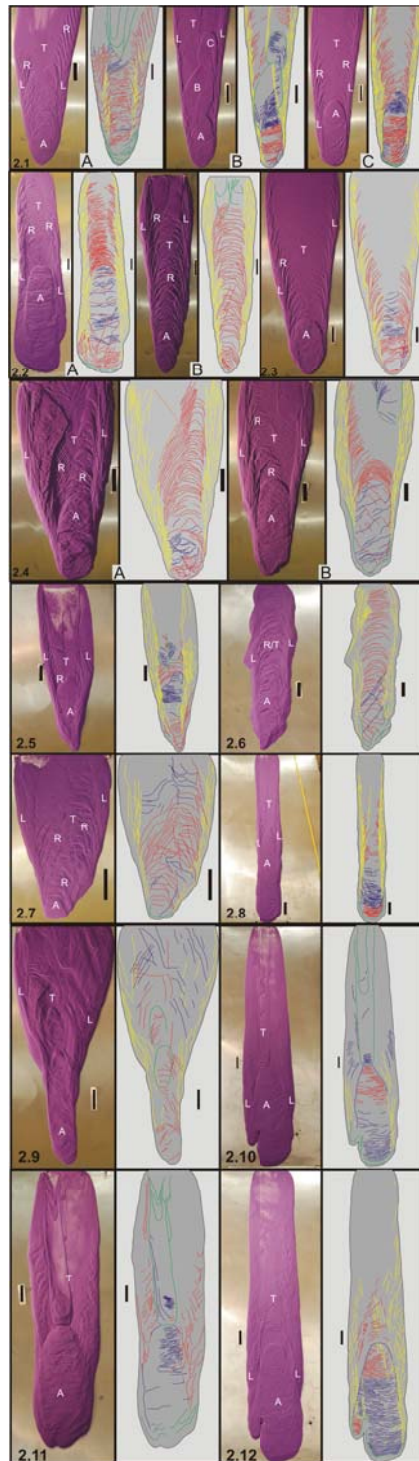


Figure D.2: Analogue slides using the straight ramp, Set 2. Parameters used are presented in Table 3.



# Bibliography

- Abele, G. (1974). Bergstürze in den Alpen. *Wiss. Alpenvereinshefte*, 25:1–230. (Cited on page 83.)
- Adiyaman, O., Chorowicz, J., and Kose, O. (1998). Relationships between volcanic patterns and neotectonics in eastern Anatolia from analysis of satellite images and DEMs. *Journal of Volcanology and Geothermal Research*, 85:17–32. (Cited on pages 137 and 152.)
- Afrouz, A. (1992). *Practical handbook of rock mass classification systems and modes of ground failure*. CRC, London. (Cited on page 59.)
- Aguila, L. C., Newhall, C. G., Miller, C. D., and Listanco, E. L. (1986). Reconnaissance geology of a large debris avalanche from Iriga volcano, Philippines. *Philippine Journal of Volcanology*, 3:54–72. (Cited on pages 25 and 27.)
- Andal, E., Yumul, G., and Listanco, E. (2005). Characterization of the Pleistocene volcanic chain of the Bicol Arc, Philippines: implications for geohazard assessment. *Terrestrial, Atmosphere and Ocean*, 16(4):865–883. (Cited on page 10.)
- Andrade, S. D. and van Wyk de Vries, B. (2010). Structural analysis of the early stages of catastrophic stratovolcano flank-collapse using analogue models. *Bulletin of Volcanology*, 72(7):771–789. (Cited on pages 3, 44, 45, 54, 55, 56, 57, 58, 59, 72, 75, 84, 101, 133 and 160.)
- Arcilla, C., Maximo, R., Vogel, T., Patino, L., Flower, M., and Mukasa, S. (2003). High-Nb Lavas from Northern Palawan: implications for high field strength enrichment in southern Philippine Arc. *EGS - AGU - EUG Joint Assembly*, -1:3451. (Cited on page 11.)
- Atakan, K. and Ojeda, A. (2005). Stress transfer in the Storegga area, offshore mid-Norway. *Marine and Petroleum Geology*, 22(1-2):161–170. (Cited on page 121.)
- Audin, L., David, C., Hall, S., Farber, D., and Hérail, G. (2006). Geomorphic evidences of recent tectonic activity in the forearc, southern Peru. *Analysis*, 61(4):545–554. (Cited on page 138.)
- Aurelio, M. (2000). Tectonics of the Philippines revisited. *Journal of the Geological Society of the Philippines*, 55(3-4):119–183. (Cited on pages 6, 7, 9, 10, 25 and 26.)

- Aurelio, M. A., Barrier, E., Gaulon, R., and Rangin, C. (1997). Deformation and stress states along the central segment of the Philippine Fault: implications to wrench fault tectonics. *Journal of Asian Earth Sciences*, 15(2-3):107–119. (Cited on pages 25 and 44.)
- Aurelio M and R, P. (2002). *Geology and Mineral Resources of the Philippines- Volume 1: Geology*. Department of Environment and Natural Resources- Mines and Geosciences Bureau. (Cited on pages 6 and 7.)
- Bachèlery, P., Robineau, B., Courteaud, M., and Savin, C. (2003). Avalanches de débris sur le flanc occidental du volcan bouclier Piton des Niegues (Réunion). *Bulletin de la Société Géologique de France*, 174:125–140. (Cited on page 3.)
- Balce, G., Encina, R., Momongan, A., and Lara, E. (1982). Geology of the Baguio District and its implication on the tectonic development of the Luzon Cordillera Central. Philippines. Technical report, Bureau of Mines, Manila. (Cited on page 9.)
- Barrier, E., Huchon, P., and Aurelio, M. (1991). Philippine Fault: A key for Philippine kinematics. *Geology*, 19:32–35. (Cited on pages 6, 7, 9 and 26.)
- Bell, F. (2000). *Engineering properties of soils and rocks*. Blackwell, Oxford, 4th edition. (Cited on page 59.)
- Belousov, A., Belousov, M., and Listanco, E. (2011). The youngest eruptions and edifice collapse of Iriga volcano, Philippines. In *IUGG General Assembly*, Melbourne, Australia. (Cited on pages 25 and 27.)
- Belousov, A., Belousova, M., and Voight, B. (1999). Multiple edifice failures, debris avalanches and associated eruptions in the Holocene history of Shiveluch volcano, Kamchatka, Russia. *Bulletin of Volcanology*, 61(5):324–342. (Cited on page 29.)
- Berg, K., Solheim, A., and Bryn, P. (2005). The Pleistocene to recent geological development of the Ormen Lange area. *Marine and Petroleum Geology*, 22(1-2):45–56. (Cited on page 123.)
- Bernard, B., van Wyk de Vries, B., Barba, D., Leyrit, H., Robin, C., Alcaraz, S., and Samaniego, P. (2008). The Chimborazo sector collapse and debris avalanche: Deposit characteristics as evidence of emplacement mechanisms. *Journal of Volcanology and Geothermal Research*, 176(1):36–43. (Cited on page 3.)

- Bernard, B., van Wyk de Vries, B., and Leyrit, H. (2009). Distinguishing volcanic debris avalanche deposits from their reworked products: the Perrier sequence (French Massif Central). *Bulletin of Volcanology*, 71(9):1041–1056. (Cited on pages 2, 25, 28 and 73.)
- Besana, G., Negishi, H., and Ando, M. (1997). The three-dimensional attenuation structures beneath the Philippine archipelago based on seismic intensity data inversion. *Earth and Planetary Science Letters*, 151(1-2):1–11. (Cited on page 12.)
- Borgia, A., Delaney, P. T., and Denlinger, R. P. (2000). Spreading volcanoes. *Annu. Rev. Earth Planet. Sci.*, 28:539–570. (Cited on page 44.)
- Borgia, A., Ferrari, L., and Pasquarè, G. (1992). Importance of gravitational spreading in the tectonic and volcanic evolution of Mount Etna. *Nature*, 357(6375):231–235. (Cited on pages 2 and 24.)
- Brun, J.-P. and Choukroune, P. (1983). Normal faulting, block tilting, and décollement in a stretched crust. *Tectonics*, 2(4):345. (Cited on pages 77 and 78.)
- Bryn, P., Berg, K., Forsberg, C. F., Solheim, A., and Kvalstad, T. J. (2005). Explaining the Storegga Slide. *Marine and Petroleum Geology*, 22(1-2):11–19. (Cited on page 123.)
- Bryn, P., Berg, K., Lien, R., Solheim, A., Ottesen, D., and L, R. (2002). The Storegga geomodel and its use in slide risk evaluation: Geological and geotechnical site investigations in the Storegga Slide area. Offshore Site Investigation and Geotechnics-Diversity and Sustainability. In *The Society of Underwater Technology International Conference*, pages 219–232, London, UK. The Society of Underwater Technology. (Cited on page 123.)
- Bureau of Mines and Geosciences (1963). Geological Map of the Philippines. Scale, 1:1,000,000. (Cited on page 25.)
- Bureau of Mines and Geosciences (1981). Geology and Mineral Resources of the Philippines. Vol.1. Technical report. (Cited on page 25.)
- Cadisch, J. (1944). Beobachtungen im Bergsturzgebiet der Umgebung von Reichenau und Rhazuns. *Eclogae Geol. Helv*, 37:409–412. (Cited on page 83.)
- Calibo, M., Honrado, M., Paguican, E., and Listanco, E. (2009). Monogenetic fields in the Macolod Corridor. In *NIGS Research Symposium 2010: Dangerous Grounds: A Geological Perspective on Philippine Disasters*, Quezon City. (Cited on page 11.)

- Campbell, C. (1989). Self-lubrication for long runout landslides. *Journal of Geology*, 97:653–665. (Cited on pages 4, 54, 101 and 133.)
- Campbell, C. S., Cleary, P. W., and Hopkins, M. (1995). Large-scale landslide simulations: global deformation, velocities and basal friction. *Journal of geophysical research*, 100(B5):8267–8283. (Cited on pages 4, 54, 101 and 133.)
- Capra, L. and Macías, J. (2000). Pleistocene cohesive debris flows at Nevado de Toluca volcano, central Mexico. *Journal of Volcanology and Geothermal Research*, 102(1-2):149–167. (Cited on page 83.)
- Carrasco-Núñez, G. (1993). *Structure, eruptive history, and some major hazardous events of Citlaltépetl volcano (Pico de Orizaba), Mexico*. PhD thesis, Michigan Technological University, U.S.A. (Cited on page 83.)
- Cassie, J. W., Gassen, W. V., and Cruden, D. M. (1988). Laboratory analogue of the formation of molards, cones of rock-avalanche debris. *Geology*, 16(8):735. (Cited on pages 3 and 83.)
- Castillo, P., Rigby, S., and Solidum, R. (2007). Origin of high field strength element enrichment in volcanic arcs: Geochemical evidence from the Sulu Arc, southern Philippines. *Lithos*, 97(3-4):271–288. (Cited on page 11.)
- Castillo, P., Solidum, R., and Punongbayan, R. (2002). Origin of high field strength element enrichment in the Sulu Arc, southern Philippines, revisited. *Geology*, 30(8):707–710. (Cited on page 11.)
- Castillo, P. R., Janney, P. E., and Solidum, R. U. (1999). Petrology and geochemistry of Camiguin Island, southern Philippines: insights to the source of adakites and other lavas in a complex arc setting. *Contributions to Mineralogy and Petrology*, 134(1):33–51. (Cited on page 12.)
- Castillo, P. R. and Newhall, C. (2004). Geochemical Constraints on Possible Subduction Components in Lavas of Mayon and Taal Volcanoes, Southern Luzon, Philippines. *Journal of Petrology*, 45(6):1089–1108. (Cited on pages 9 and 10.)
- Catane, S. G., Cabria, H. B., Tomarong, C. P., Saturay, R. M., Zarco, M. A. H., and Pioquinto, W. C. (2007). Catastrophic rockslide-debris avalanche at St. Bernard, Southern Leyte, Philippines. *Landslides*, 4(1):85–90. (Cited on page 4.)

- Catane, S. G., Cabria, H. B., Zarco, M. A. H., Saturay, R. M., and Mirasol-Robert, A. a. (2008). The 17 February 2006 Guinsaungon rock slide-debris avalanche, Southern Leyte, Philippines: deposit characteristics and failure mechanism. *Bulletin of Engineering Geology and the Environment*, 67(3):305–320. (Cited on pages 4 and 118.)
- Cecchi, E., Wyk de Vries, B., and Lavest, J.-M. (2005). Flank spreading and collapse of weak-cored volcanoes. *Bulletin of Volcanology*, 67(1):72–91. (Cited on pages 4 and 56.)
- Chorowicz, J., Collet, B., Bonavia, F., and Korme, T. (1994). NW to NNW extension direction in the Ethiopian Rift deduced from the orientation of structures and fault slip analysis. *Geological Society of America Bulletin*, 105:1560–1570. (Cited on page 137.)
- Clavero, J., Polanco E., Godoy, E., Aguilar, G., Sparks, R. S. J., van Wyk de Vries, B., de Arce, C. P., and Matthews, S. (2004). Substrata influence in the transport and emplacement mechanism of the Ollague debris avalanche (Northern Chile). *Acta Vulcanologica*, 16(1/2):59–76. (Cited on page 3.)
- Clavero, J., Sparks, R., Huppert, H., and Dade, W. (2002). Geological constraints on the emplacement mechanism of the Parinacota debris avalanche, northern Chile. *Bulletin of Volcanology*, 64(1):40–54. (Cited on pages 3 and 75.)
- Corpuz, E. S. G. (1992). *Petrology and geochemistry of the Central Mindanao Volcanic Arc, southern Philippines*. PhD thesis. (Cited on page 12.)
- Crandell, D. R. (1861). Gigantic debris avalanche of Pleistocene age from ancestral Mount Shasta Volcano, California, and debris-avalanche hazard zonation. Technical report, U.S. Geological Survey. (Cited on page 54.)
- Crandell, D. R., Miller, C. D., Glicken, H. X., Christiansen, R. L., and Newhall, C. G. (1984). Catastrophic debris avalanche from ancestral Mount Shasta volcano, California. *Geology*, 12(3):143. (Cited on page 83.)
- Crippen, R. E. and Blom, R. G. (2001). Unveiling the lithology of vegetated terrains in remotely sensed imagery. *Photogrammetric Engineering and Remote Sensing*, 67(8):935–943. (Cited on page 134.)
- Dade, W. B. and Huppert, H. E. (1998). Long-runout rockfalls. *Power*, 26:803–806. (Cited on pages 48 and 59.)

- David, C., Comte, D., Tavera, H., Audin, L., and Hérail, G. (2004). Crustal seismicity and recent faults in Southern Peru. In *American Geophysical Union, Fall Meeting*. (Cited on page 138.)
- Davies, T., McSaveney, M., and Kelfoun, K. (2010). Runout of the Socompa volcanic debris avalanche, Chile: a mechanical explanation for low basal shear resistance. *Bulletin of Volcanology*, 72(8):933–944. (Cited on page 4.)
- Defant, M. J., Maury, R., Joron, J.-L., Feigenson, M. D., Leterrier, J., Bellon, H., Jacques, D., and Richard, M. (1990). The geochemistry and tectonic setting of the northern section of the Luzon arc (The Philippines and Taiwan). *Tectonophysics*, 183(1-4):187–205. (Cited on page 9.)
- Delcamp, A., van Wyk de Vries, B., and James, M. R. (2008). The influence of edifice slope and substrata on volcano spreading. *Journal of Volcanology and Geothermal Research*, 177(4):925–943. (Cited on page 55.)
- Denlinger, R. and Iverson, R. (2001). Flow of variably fluidized granular masses across three-dimensional terrain: 2, numerical predictions and experimental tests. *Journal of Geophysical Research*, 106(B1):553–566. (Cited on pages 54 and 133.)
- Deplus, C., Le, A., Boudon, G., Komorowski, J.-c., Villemant, B., and Harford, C. (2001). Submarine evidence for large-scale debris avalanches in the Lesser Antilles Arc. *Earth*, 192:145–157. (Cited on page 3.)
- Donnadieu, F. and Merle, O. (1998). Experiments on the indentation process during cryptodome intrusions: New insights into Mount St. Helens deformation. *Geology*, 26(1):79–82. (Cited on pages 2, 24, 56 and 57.)
- Drury, S. (1987). *Image interpretation in geology*. Allen & Unwin, London, UK. (Cited on pages 134, 135 and 136.)
- Drury, S. (2001). *Image interpretation in geology*. Routledge, 3rd edition. (Cited on page 139.)
- Dufresne, A. (2009). *Influence of runout path material on rock and debris avalanche mobility : field evidence and analogue modelling*. Phd thesis, University of Canterbury. (Cited on pages 4 and 54.)
- Dufresne, A. and Davies, T. (2009). Longitudinal ridges in mass movement deposits. *Geomorphology*, 105(3-4):171–181. (Cited on pages 3, 54, 83, 132 and 133.)

- Dufresne, A., Salinas, S., and Siebe, C. (2010). Substrate deformation associated with the Jocotitlán edifice collapse and debris avalanche deposit, Central México. *Journal of Volcanology and Geothermal Research*, 197(1-4):133–148. (Cited on page 4.)
- Elsworth, D. and Voight, B. (1996). Evaluation of volcano flank instability triggered by dike intrusion. In McGuire, W., Jones, A., and Neuberg, J., editors, *Volcano instability on the Earth and other planets*, pages 45–53. Geological Society of London Special Publication. (Cited on pages 2 and 25.)
- Eppler, D. B., Fink, J., and Fletcher, R. (1987). Rheologic Properties and Kinematics of Emplacement of the Chaos Jumbles Rockfall Avalanche, Lassen Volcanic National Park, California. *Journal of Geophysical Research*, 92(B5):3623–3633. (Cited on page 54.)
- Evans, D., Harrison, Z., Shannon, P., Laberg, J., Nielsen, T., Ayers, S., Holmes, R., Hout, R., Lindberg, B., and Hafliðason, H. (2005). Palaeoslides and other mass failures of Pliocene to Pleistocene age along the Atlantic continental margin of NW Europe. *Marine and Petroleum Geology*, 22(9-10):1131–1148. (Cited on page 121.)
- Evans, S. (2006). Single event landslides resulting from massive rock slope failure: Characterising their frequency and impact on society. In Evans, S., Scarascia-Mugnozza, G., Strom, A., and Hermanns, R., editors, *Landslides from Massive Rock Slope Failure*, pages 53–73. NATO Sci Ser IV, Earth Environ Sci, Dordrecht. (Cited on page 119.)
- Evans, S. G., Guthrie, R. H., Roberts, N. J., and Bishop, N. F. (2007). The disastrous 17 February 2006 rockslide-debris avalanche on Leyte Island, Philippines: a catastrophic landslide in tropical mountain terrain. *Natural Hazards and Earth System Science*, 7(1):89–101. (Cited on pages 2 and 4.)
- Færseth, R. B. and Sætersmoen, B. H. (2008). Geometry of a major slump structure in the Storegga slide region offshore western Norway. *Norwegian Journal of Geology*, 88:1–11. (Cited on pages 123 and 126.)
- Francis, P. W., Gardeweg, M., Ramirez, C. F., and Rothery, D. A. (1985). Catastrophic debris avalanche deposit of Socompa volcano, northern Chile. *Geology*, 13(9):600. (Cited on page 53.)
- Francis, P. W. and Wells, G. L. (1988). Landsat Thematic Mapper observations of debris avalanche deposits in the Central Andes. *Bulletin of Volcanology*, 50(4):258–278. (Cited on pages 3 and 134.)

- Friedmann, S. J., Taberlet, N., and Losert, W. (2006). Rock-avalanche dynamics: insights from granular physics experiments. *International Journal of Earth Sciences*, 95(5):911–919. (Cited on page 4.)
- Friele, P. and Clague, J. (2009). Paraglacial geomorphology of Quaternary volcanic landscapes in the southern Coast Mountains, British Columbia. In Knight, J. and Harrison, S., editors, *Periglacial and Paraglacial Processes and Environments*, pages 219–233. Geol Soc Spec Publ London. (Cited on page 119.)
- Friele, P., Jakob, M., and Clague, J. (2008). Hazard and risk from large landslides from Mount Meager volcano, British Columbia, Canada. *Georisk: Assessment and Management of Risk for Engineered Systems and Geohazards*, 2(1):48–64. (Cited on page 119.)
- Galgana, G., Hamburger, M., McCaffrey, R., Corpuz, E., and Chen, Q. (2007). Analysis of crustal deformation in Luzon, Philippines using geodetic observations and earthquake focal mechanisms. *Tectonophysics*, 432(1-4):63–87. (Cited on page 11.)
- Gauer, P., Kvalstad, T. J., Forsberg, C. F., Bryn, P., and Berg, K. (2005). The last phase of the Storegga Slide: simulation of retrogressive slide dynamics and comparison with slide-scar morphology. *Marine and Petroleum Geology*, 22(1-2):171–178. (Cited on page 126.)
- Gervasio, F. (1967). Age and nature of orogenesis of the Philippines. *Tectonophysics*, 4(4-6):379–402. (Cited on pages 6 and 7.)
- Giachetti, T., Paris, R., Kelfoun, K., and Pérez-Torrado, F. J. (2011). Numerical modelling of the tsunami triggered by the Güïmar debris avalanche, Tenerife (Canary Islands): Comparison with field-based data. *Marine Geology*, 284(1-4):189–202. (Cited on page 3.)
- Glicken, H. (1982). Criteria for identification of large volcanic debris avalanche. In *Trans Am Geophys Union*, page 1141. EOS. (Cited on page 83.)
- Glicken, H. (1986). *Rockslide debris-avalanche of May 18, 1980, Mount St. Helens volcano*. PhD thesis, University of California. (Cited on pages 53 and 54.)
- Glicken, H. (1991). Sedimentary architecture of large volcanic-debris avalanches. In Fisher, R. and Smith, G., editors, *Sedimentation in volcanic settings*, pages 99–106. Sepm speci edition. (Cited on page 53.)

- Glicken, H. (1996). Rockslide-debris avalanche of may 18, 1980, Mount St. Helens volcano . Technical report, U.S. Geological Survey. (Cited on pages 28, 43 and 54.)
- Goguel, J. and A, P. (1972). Géologie et dynamique de l'écroulement du Mt. Granier dans le Massif de Chartreuse en novembre. Technical report, Bureau de Recherches Géologiques et Minières. (Cited on page 83.)
- Griggs, E. (1920). Great Mageik slide, Alaska. *Ohio Journal of Science*, 20:325–354. (Cited on page 83.)
- Grosse, P., van Wyk de Vries, B., Euillades, P. A., Kervyn, M., and Petrinovic, I. A. (2012). Systematic morphometric characterization of volcanic edifices using digital elevation models. *Geomorphology*, 136(1):114–131. (Cited on pages 12 and 14.)
- Grosse, P., van Wyk de Vries, B., Petrinovic, I. a., Euillades, P. a., and Alvarado, G. E. (2009). Morphometry and evolution of arc volcanoes. *Geology*, 37(7):651–654. (Cited on pages 2, 12, 13, 14, 18, 135 and 136.)
- Gupta, R. (1991). *Remote sensing geology*. Springer-Verlag, Berlin. (Cited on pages 135 and 136.)
- Guthrie, R. and Evans, S. (2007). Work, persistence, and formative events: The geomorphic impact of landslides. *Geomorphology*, 88(3-4):266–275. (Cited on page 119.)
- Guthrie, R., Friele, P., Allstadt, K., Roberts, N., Evans, S., Delaney, K., Roche, D., Clague, J., and Jakob, M. (2012). The 6 August 2010 Mount Meager rock slide-debris flow, Coast Mountains, British Columbia: characteristics, dynamics, and implications for hazard and risk assessment. *Nat Hazards Earth Syst Sci*, 12:1277–1294. (Cited on pages 119, 121 and 123.)
- Guthrie, R. H., Evans, S. G., Catane, S. G., Zarco, M. a. H., and Saturay, R. M. (2009). The 17 February 2006 rock slide-debris avalanche at Guinsaogon Philippines: a synthesis. *Bulletin of Engineering Geology and the Environment*, 68(2):201–213. (Cited on pages 4 and 118.)
- Heim, A. (1932). *Bergstruz and Menschenleben*. Zurich. Fretz und Wasmuth. (Cited on page 83.)
- Heim, A. (1981). Geologie der Hochalpen zwischen Reußund Rhein. Beitr. Z. Geol. Karte der Schweiz. (Cited on page 83.)

- HK, A. and YP, A. (1980). Seismicity and tectonics of the Philippine Islands. *Journal of Geophysical Research*, 85:3239–3250. (Cited on page 12.)
- Hobbs, W. (1911). Repeating patterns in the relief and in the structure of the land. *Geological Society of America Bulletin*, 22:123–176. (Cited on page 141.)
- Hunger, O. (2006). Rock avalanche occurrence, process and modelling. In Evans, S., editor, *Landslides from Massive Rock Slope Failure*, pages 243–266. Springer, Netherlands. (Cited on page 132.)
- Innocenti, F., Mazzuoli, R., Pasquare', G., Serri, G., and Villari, L. (1980). Geology of the volcanic area north of lake van (turkey). *Geologische Rundschau*, 69(1):292–323. (Cited on page 137.)
- Iverson, R. M. and Denlinger, R. P. (2001). Flow of variably fluidized granular masses across three-dimensional terrain 1. Coulomb mixture theory. *Journal of Geophysical Research*, 106(B1):537–552. (Cited on pages 54 and 133.)
- Kelfoun, K., Druitt, T., Wyk de Vries, B., and Guilbaud, M.-N. (2008). Topographic reflection of the Socompa debris avalanche, Chile. *Bulletin of Volcanology*, 70(10):1169–1187. (Cited on pages 3 and 75.)
- Kelfoun, K. and Druitt, T. H. (2005). Numerical modeling of the emplacement of Socompa rock avalanche, Chile. *Journal of Geophysical Research*, 110(B12):1–13. (Cited on pages 4, 54, 59, 101 and 133.)
- Kerle, N. and van Wyk de Vries, B. (2001). The 1998 debris avalanche at Casita volcano, Nicaragua — investigation of structural deformation as the cause of slope instability using remote sensing. *Journal of Volcanology and Geothermal Research*, 105(1-2):49–63. (Cited on pages 2, 4 and 25.)
- Kervyn, M., Ernst, G. G. J., Klaudius, J., Keller, J., Mbede, E., and Jacobs, P. (2008). Remote sensing study of sector collapses and debris avalanche deposits at Oldoinyo Lengai and Kerimasi volcanoes, Tanzania. *International Journal of Remote Sensing*, 29(22):6565–6595. (Cited on pages 3 and 135.)
- Knittel, U. and Defant, M. J. (1988). Sr isotopic and trace element variations in Oligocene to recent igneous rocks from the Philippine island arc: evidence for recent enrichment in the sub-Philippine mantle. *Earth and Planetary Science Letters*, 87(1-2):87–99. (Cited on page 9.)
- Kruse, F. and Dietz, J. (1991). Integration of diverse remote sensing data sets for geologic mapping and resource exploration. In *SPIE—The International*

- Society for Optical Engineering, Earth and Atmospheric Remote Sensing*, pages 326–337. (Cited on page 133.)
- Kvalstad, T. J., Andresen, L., Forsberg, C. F., Berg, K., Bryn, P., and Wangen, M. (2005). The Storegga slide: evaluation of triggering sources and slide mechanics. *Marine and Petroleum Geology*, 22(1-2):245–256. (Cited on page 123.)
- Lagmay, A., Ong, J., Fernandez, D., Lapus, M., Rodolfo, R., Tengonciang, A., Soria, J., Baliatan, E., Quimba, Z., Uichanco, C., Paguican, E., Remedio, A., Lorenzo, G., Valdivia, W., and Avila, F. (2006). Scientists Investigate Recent Philippine Landslide. *EOS*, 87(12):121–124. (Cited on pages 4 and 118.)
- Lagmay, A., Tengonciang, A., and Uy, H. (2005). Structural setting of the Bicol Basin and kinematic analysis of fractures on Mayon Volcano, Philippines. *Journal of Volcanology and Geothermal Research*, 144(1-4):23–36. (Cited on page 25.)
- Lagmay, A. and Valdivia, W. (2006). Regional stress influence on the opening direction of crater amphitheatres in Southeast Asian volcanoes. *Journal of Volcanology and Geothermal Research*, 158(1-2):139–150. (Cited on page 135.)
- Lagmay, A. M. F., van Wyk de Vries, B., Kerle, N., and Pyle, D. M. (2000). Volcano instability induced by strike-slip faulting. *Bulletin of Volcanology*, 62(4-5):331–346. (Cited on pages 2, 4, 24, 44, 45, 57, 152 and 154.)
- Le Friant, A., Boudon, G., Arnulf, A., and Robertson, R. E. (2009). Debris avalanche deposits offshore St. Vincent (West Indies): Impact of flank-collapse events on the morphological evolution of the island. *Journal of Volcanology and Geothermal Research*, 179(1-2):1–10. (Cited on page 3.)
- Lénat, J.-F., Gibert-Malengreau, B., and Galdéano, A. (2001). A new model for the evolution of the volcanic island of Réunion (Indian Ocean). *Journal of Geophysical Research*, 106(B5):8645–8663. (Cited on page 3.)
- Lillesand, T. and Kiefer, R. (1979). *Remote Sensing and Image Interpretation*. John Wiley and Sons. New York, New York. (Cited on pages 135 and 136.)
- Lipovsky, P. S., Evans, S. G., Clague, J. J., Hopkinson, C., Couture, R., Bobrowsky, P., Ekström, G., Demuth, M. N., Delaney, K. B., Roberts, N. J., Clarke, G., and Schaeffer, A. (2008). The July 2007 rock and ice avalanches at Mount Steele, St. Elias Mountains, Yukon, Canada. *Landslides*, 5(4):445–455. (Cited on page 119.)

- Liu, J. and Mason, P. (2009). *Essential image processing and GIS for remote sensing*. Wiley-Blackwell. (Cited on page 139.)
- Lucchitta, B. K. (1979). Landslides in Valles Marineris, Mars. *Journal of Geophysical Research*, 84(B14):8097–8113. (Cited on page 53.)
- Mangeney, A., Roche, O., Hungr, O., Mangold, N., Faccanoni, G., and Lucas, A. (2010). Erosion and mobility in granular collapse over sloping beds. *Journal of Geophysical Research*, 115(F3):F03040. (Cited on page 116.)
- Mathieu, L. and van Wyk de Vries, B. (2011). The impact of strike-slip, transtensional and transpressional fault zones on volcanoes. Part 1: Scaled experiments. *Journal of Structural Geology*, 33(5):907–917. (Cited on pages 4, 45, 55 and 154.)
- Maury, R. C., Defant, M. J., and Joron, J.-L. (1992). Metasomatism of the sub-arc mantle inferred from trace elements in Philippine xenoliths. *Nature*, 360(6405):661–663. (Cited on page 9.)
- Maury, R. C., Sajona, F. G., Pubellier, M., Bellon, H., and Defant, M. J. (1996). Fusion de la croûte océanique dans les zones de subduction/collision récentes; l'exemple de Mindanao (Philippines). *Bulletin de la Société Géologique de France*, 167(5):579–595. (Cited on page 12.)
- McColl, S. and Davies, T. (2011). Evidence for a rock-avalanche origin for 'The Hillocks' "moraine", Otago, New Zealand. *Geomorphology*, 127(3-4):216–224. (Cited on page 3.)
- McConnell, R. and Brock, R. (1904). The great landslide of Frank, Alberta. Technical report, Canada Department of Interior. (Cited on page 83.)
- McDermott, F., Delfin Jr., F. G., Defant, M. J., Turner, S., and Maury, R. (2005). The petrogenesis of volcanics from Mt. Bulusan and Mt. Mayon in the Bicol arc, the Philippines. *Contributions to Mineralogy and Petrology*, 150(6):652–670. (Cited on page 10.)
- McGuire, W. J. (1996). Volcano instability: a review of contemporary themes. *Geological Society, London, Special Publications*, 110(1):1–23. (Cited on page 2.)
- Mehl, K. W. and Schmincke, H.-U. (1999). Structure and emplacement of the Pliocene Roque Nublo debris avalanche deposit, Gran Canaria, Spain. *Journal of Volcanology and Geothermal Research*, 94(1-4):105–134. (Cited on page 3.)

- Merle, O. and Borgia, A. (1996). Scaled experiments of volcanic spreading. *Journal of Geophysical Research*, 101(B6):13805–13817. (Cited on pages 3, 4, 100 and 102.)
- Middleton, G. and Wilcock, P. (1994). *Mechanics in the Earth and environmental sciences*. Cambridge University Press, Cambridge. (Cited on pages 105 and 106.)
- Mienert, J., Vanneste, M., Bünz, S., Andreassen, K., Hafliðason, H., and Sejrup, H. P. (2005). Ocean warming and gas hydrate stability on the mid-Norwegian margin at the Storegga Slide. *Marine and Petroleum Geology*, 22(1-2):233–244. (Cited on page 121.)
- Mimura, K. and Kawachi, S. (1981). Nirasaki debris avalanche, a catastrophic event at the Yatsugatake volcanic chain, central Japan. In *IAVCEI Symp Arc Volcanism*, page 237 p, Tokyo and Hakone. (Cited on page 83.)
- Mitchell, A., Hernandez, F., and dela Cruz, A. (1986). Cenozoic evolution of the Philippine archipelago. *Journal of Southeast Asian Earth Sciences*, 1(1):3–22. (Cited on page 10.)
- Mollard, J. and Janes, J. (1984). Airphoto Interpretation and the Canadian landscape. (Cited on page 83.)
- Montaldo, A., Vinciguerra, S., Menza, Z., and Patane, G. (1996). Recent seismicity of Mount Etna: implications for flank instability. In McGuire, W., Jones, A., and Neuberg, J., editors, *Volcano instability on the earth and other planets*, pages 169–177. Geological Society of London, special publication edition. (Cited on pages 2 and 25.)
- Moriya, I. (1994). Geomorphology of continental and island volcanoes: development and classification. Technical report, Kanazawa Univ, Dept Geography. (Cited on page 27.)
- Nabholz, W. (1954). Neue Beobachtungen im Bergsturzgebiet südlich von Reichenau-Tamins (Graubünden). *Verh. Naturf. Ges. Basel*, 65(1):67–81. (Cited on page 83.)
- Nygård, A., Sejrup, H. P., Hafliðason, H., and Bryn, P. (2005). The glacial North Sea Fan, southern Norwegian Margin: architecture and evolution from the upper continental slope to the deep-sea basin. *Marine and Petroleum Geology*, 22(1-2):71–84. (Cited on page 121.)

- Oehler, J.-F., Labazuy, P., and Lénat, J.-F. (2004). Recurrence of major flank landslides during the last 2-Ma-history of Reunion Island. *Bulletin of Volcanology*, 66(7):585–598. (Cited on page 3.)
- Paguican, E., van Wyk de Vries, B., and Lagmay, A. (2011). Hummocks in large avalanches; how they form and what they mean. In *EGU*, Vienna. (Cited on pages 53, 74, 77, 84, 85 and 86.)
- Panem, C. and Cabel, A. (1998). Geology of Isarog-Iriga geothermal prospect. Technical report, PNOC-EDC. (Cited on page 27.)
- Pavoni, N. (1968). Über die Entstehung der Kiesmassen im Bergsturzgebiet von Bonaduz-Reichenau (Graubünden). *Eclogae Geol. Helv.*, 61(2):494–500. (Cited on page 83.)
- PHIVOLCS-DOST (2002). *Volcanoes of the Philippines*. PHIVOLCS Press, 2002 edition. (Cited on page 9.)
- Podwysocki, M. H., gal, D. B. S., and Abrams, M. J. . (1982). Use of Multi-spectral Scanner Images for Assessment of Hydrothermal Alteration in the Marysvale , Utah , Mining Area. *Economic Geology*, 78:675–687. (Cited on page 135.)
- Pouliquen, O. and Renaut, N. (1996). Onset of granular flows on an inclined rough surface: Dilatancy effects. *J Physique II*, 6:929–935. (Cited on pages 4, 54, 101 and 133.)
- Procter, J. N., Cronin, S. J., and Zernack, A. V. (2009). Landscape and sedimentary response to catastrophic debris avalanches, western Taranaki, New Zealand. *Sedimentary Geology*, 220(3-4):271–287. (Cited on page 3.)
- Prost, G. (1980). Alteration mapping with airborne multispectral scanners. *Economic Geology*, 75(6):894–906. (Cited on page 135.)
- Pubellier, M., Quebral, R., Rangin, C., Deffontaines, B., Muller, C., Butterlin, J., and Manzano, J. (1991). The Mindanao collision zone: a soft collision event within a continuous Neogene strike-slip setting. *Journal of Southeast Asian Earth Sciences*, 6(3-4):239–248. (Cited on pages 11 and 12.)
- Ramberg, H. (1981). *Gravity, deformation and the Earth's crust*. London Academic Press, London. (Cited on pages 3, 100 and 103.)
- Reid, M. E., Sisson, T. W., and Brien, D. L. (2001). Volcano collapse promoted by hydrothermal alteration and edifice shape, Mount Rainier, Washington. *Geology*, 29(9):779–782. (Cited on pages 2 and 24.)

- Remenyik, T. (1959). Geologische Untersuchungen der Bergsturzlandschaft zwischen Chur und Rodels. *Eclogae Geol. Helv*, 52(1):177–235. (Cited on page 83.)
- Roperch, P., Sempere, T., Macedo, O., Arriagada, C., Fornari, M., Tapia, C., García, M., and Laj, C. (2006). Counterclockwise rotation of late Eocene–Oligocene fore-arc deposits in southern Peru and its significance for oroclinal bending in the central Andes. *Tectonics*, 25(3):TC3010. (Cited on page 138.)
- Rowan, L. and Kahle, A. (1982). Evaluations of 0.46–2.36 micrometer Multi-spectral scanners images of the East Tintic mining district, Utah for mapping hydro-thermally altered rocks. *Economic Geology*, 77:441–452. (Cited on page 135.)
- Sajona, F. G., Bellon, H., Maury, R. C., Pubellier, M., Cotten, J., and Rangin, C. (1994). Magmatic response to abrupt changes in geodynamic settings: Pliocene–Quaternary calc-alkaline and Nb-enriched lavas from Mindanao (Philippines). *Tectonophysics*, 237(1-2):47–72. (Cited on pages 10, 11 and 12.)
- Sajona, F. G., Maury, R. C., Bellon, H., Cotten, J., and Defant, M. (1996). High field strength element enrichment of Pliocene–Pleistocene island arc basalts, Zamboanga peninsula, western Mindanao (Philippines). *Journal of Petrology*, 37(3):693–726. (Cited on page 11.)
- Sajona, F. G., Maury, R. C., Bellon, H., Cotten, J., Defant, M. J., and Pubellier, M. (1993). Initiation of subduction and the generation of slab melts in western and eastern Mindanao, Philippines. *Geology*, 21(11):1007. (Cited on page 12.)
- Sajona F.G., Bellon H., Maury R.C., Pubellier M., Quebral R.D., Cotten J., Bayon F.E., Pagado E., and Pamatian P. (1997). Tertiary and Quaternary magmatism in Mindanao and Leyte (Philippines): geochronology, geochemistry and tectonic setting. *Journal of Asian Earth Sciences*, 15:121–153. (Cited on page 12.)
- Scheller, E. (1970). *Geophysikalische Untersuchungen zum Problem des Taminser Bergsturzes*. PhD thesis, ETH Zurich. (Cited on page 83.)
- Schneider, J.-l. and Fisher, R. V. (1998). Transport and emplacement mechanisms of large volcanic debris avalanches : evidence from the northwest sector of Cantal Volcano Ź France /. *Science*, 83:141–165. (Cited on page 3.)

- Shea, T. and van Wyk de Vries, B. (2008). Structural analysis and analogue modeling of the kinematics and dynamics of rockslide avalanches. *Geosphere*, 4(4):657–686. (Cited on pages 3, 4, 29, 36, 37, 43, 48, 54, 73, 74, 101, 102, 103, 133, 141, 144 and 160.)
- Shea, T., Wyk de Vries, B., and Pilato, M. (2008). Emplacement mechanisms of contrasting debris avalanches at Volcán Mombacho (Nicaragua), provided by structural and facies analysis. *Bulletin of Volcanology*, 70(8):899–921. (Cited on pages 3, 44, 132 and 133.)
- Siebert, L. (1984). Large volcanic debris avalanches: Characteristics of source areas, deposits, and associated eruptions. *Journal of Volcanology and Geothermal Research*, 22(3-4):163–197. (Cited on pages 54, 56, 83 and 133.)
- Siebert, L. (2002). Landslides resulting from structural failure of volcanoes. In Evans, S. and DeGraff, J., editors, *Catastrophic Landslides*, pages 209–235. Geol Soc Am Rev Eng Geol. (Cited on pages 2, 25 and 28.)
- Siebert, L., Beget, J., and Glicken, H. (1995). The 1883 and late prehistoric eruptions of Augustine volcano, Alaska. In Ida, Y. and Voight, B., editors, *Models of magmatic processes and volcanic eruptions*, pages 367–395. J Volcanol Geotherm Res. (Cited on page 54.)
- Siebert, L., Glicken, H., and Ui, T. (1987). Volcanic hazards from Bezymianny- and Bandai-type eruptions. *Bulletin of Volcanology*, 49:435–459. (Cited on pages 83 and 133.)
- Sousa, J. and Voight, B. (1995). Multiple-pulsed debris avalanche emplacement at Mount St. Helens in 1980: Evidence from numerical continuum flow simulations. *Journal of Volcanology and Geothermal Research*, 66(1-4):227–250. (Cited on page 59.)
- Staron, L., Vilotte, J., and Radjai, F. (2001). Friction and mobilization of contacts in granular numerical avalanches. In Kishino, Y., editor, *Powders and Grains*, pages 451–454. Lisse, Swetes and Zeitlinger, Sendai, Japan. (Cited on pages 4, 54, 101 and 133.)
- Stoopes, G. R. and Sheridan, M. F. (1992). Giant debris avalanches from the Colima Volcanic Complex, Mexico: Implications for long-runout landslides (>100 km) and hazard assessment. *Geology*, 20(4):299–302. (Cited on page 132.)
- Strandberg, C. (1967). *Aerial Discovery Manual*. Wiley, University of Michigan. (Cited on pages 135 and 136.)

- Takarada, S., Ui, T., and Yamamoto, Y. (1999). Depositional features and transportation mechanism of valley-filling Iwasegawa and Kaida debris avalanches, Japan. *Bulletin of Volcanology*, 60(7):508–522. (Cited on pages 3 and 54.)
- Teng, L. S. (1990). Geotectonic evolution of late Cenozoic arc-continent in Taiwan. *Tectonophysics*, 183:57–76. (Cited on page 9.)
- Thompson, N., Bennett, M. R., and Petford, N. (2010). Development of characteristic volcanic debris avalanche deposit structures: New insight from distinct element simulations. *Journal of Volcanology and Geothermal Research*, 192(3-4):191–200. (Cited on pages 4 and 56.)
- Tibaldi, A. (2001). Multiple sector collapses at Stromboli volcano, Italy: how they work. *Bulletin of Volcanology*, 63(2-3):112–125. (Cited on pages 2 and 24.)
- Travaglia, C. and Baes, A. (1979). Geology of Sorsogon Province. Technical report, Soil and Land Resources Appraisal and Training Project, Bureau of Soils, UNDP/FAO Programme, Manila. (Cited on page 25.)
- Ui, T. (1983). Volcanic dry avalanche deposits — identification and comparison with nonvolcanic debris stream deposits. *Journal of Volcanology and Geothermal Research*, 18(1-4):135–150. (Cited on page 54.)
- Ui, T. and Glicken, H. (1986). Internal structural variations in a debris-avalanche deposit from ancestral Mount Shasta, California, USA. *Bulletin of Volcanology*, 48(4):189–194. (Cited on page 54.)
- Vallance, J. W. and Scott, K. M. (1997). The Osceola Mudflow from Mount Rainier: Sedimentology and hazard implications of a huge clay-rich debris flow. *Geological Society of America Bulletin*, 109(2):143–163. (Cited on page 83.)
- van Wyk de Vries, B. and Borgia, A. (1996). The role of basement in volcano deformation. In McGuire, W., Jones, A., and Neuberg, J., editors, *Volcano instability on the earth and other planets*, pages 95–110. Geological Society of London, special publication edition. (Cited on page 44.)
- van Wyk de Vries, B. and Francis, P. W. (1997). Catastrophic collapse at stratovolcanoes induced by gradual volcano spreading. *Nature*, 387(6631):387–390. (Cited on pages 2, 4, 24, 43, 44, 56 and 59.)

- van Wyk de Vries, B., Gilbaud, M.-N., Self, S., and Druitt, T. (2002). A brittle crust during the emplacement of the Socompa debris avalanche? In *European Geosciences Union general assembly*, Nice, France. (Cited on page 3.)
- van Wyk de Vries, B., Grosse, P., and Alvarado, G. (2007). Volcanism and volcanic landforms. In Bundschuh, J. and Alvarado, G., editors, *Central America: Geology, resources and hazards, Volume 1*, pages 123–158. Balkema, Netherlands. (Cited on page 2.)
- van Wyk de Vries, B., Kerle, N., and Petley, D. (2000). Sector collapse forming at Casita volcano, Nicaragua. *Geology*, 28:167–170. (Cited on pages 2, 4, 25 and 56.)
- van Wyk de Vries, B., Self, S., Francis, P., and Keszthelyi, L. (2001). A gravitational spreading origin for the Socompa debris avalanche. *Journal of Volcanology and Geothermal Research*, 105:225–247. (Cited on pages 3, 43, 45 and 59.)
- Vidal N. and Merle O. (2000). Reactivation of basement faults beneath volcanoes: a new model of flank collapse. *Journal of Volcanology and Geothermal Research*, 99(1):9–26. (Cited on pages 2, 24 and 57.)
- Voight, B. and Elsworth, D. (1997). Failure of volcano slopes. *Geotechnique*, 47(1):1–31. (Cited on page 133.)
- Voight, B., Glicken, H., Janda, R., and Douglas, P. (1981). Catastrophic rockslide avalanche of May 18. In Lipman, P. and Mullineaux, D., editors, *The 1980 eruptions of Mount St. Helens, Washington*, pages 347–377. U.S. Geological Survey, professional edition. (Cited on page 54.)
- Voight, B., Janda, R., Glicken, H., and PM, D. (1983). Nature and mechanics of the Mount St. Helens rockslide-avalanche of the 18 May 1980. *Geotechnique*, 33:243–273. (Cited on pages 2, 25 and 54.)
- von Poschinger, A. and Kippel, T. H. (2009). Alluvial deposits liquefied by the Flims rock slide. *Geomorphology*, 103(1):50–56. (Cited on page 83.)
- Wadge, G., Francis, P. W., and Ramirez, C. F. (1995). The Socompa collapse and avalanche event. *Journal of Volcanology and Geothermal Research*, 66(94):309–336. (Cited on pages 3, 45, 53 and 134.)

- Wise, D., Grady, L., and Salvini, F. (1985). Topographic lineament domains of the Appalachians. Some new methods and techniques for paleostress analysis. In *International Geoscience and Remote Sensing Symposium*, pages 125–130. (Cited on page 141.)
- Wooller, L., van Wyk de Vries, B., Cecchi, E., and Rymer, H. (2009). Analogue models of the effect of long-term basement fault movement on volcanic edifices. *Bulletin of Volcanology*, 71(10):1111–1131. (Cited on pages 4, 44, 45, 152, 153 and 154.)
- Wooller, L., van Wyk de Vries, B., Murray, J. B., Rymer, H., and Meyer, S. (2004). Volcano spreading controlled by dipping substrata. *Geology*, 32(7):573. (Cited on pages 4, 44 and 56.)
- Wright, R., Garbeil, H., Baloga, S., and Mouginismark, P. (2006). An assessment of shuttle radar topography mission digital elevation data for studies of volcano morphology. *Remote Sensing of Environment*, 105(1):41–53. (Cited on page 136.)
- Yilmaz Y., Guner Y., and Saroglu F. (1998). Geology of the quaternary volcanic centres of the east Anatolia. *Journal of Volcanology and Geothermal Research*, 85(1):38. (Cited on page 138.)
- Yousif, M. and Shedid, G. (1999). Remote sensing signature of some selected basement rock units from the central eastern desert of Egypt. *Egypt J Remote Sensing & Space Sci*, 1:132–141. (Cited on page 134.)
- Yumul, G. P., Dimalanta, C. B., Tamayo, R. A., and Barretto, J. A. L. (2000). Contrasting morphological trends of islands in Central Philippines: Speculation on their origin. *Island Arc*, 9(4):627–637. (Cited on page 9.)
- Yumul, G. P., Dimalanta, C. B., Tamayo, R. a., and Maury, R. C. (2003). Collision, subduction and accretion events in the Philippines: A synthesis. *The Island Arc*, 12(2):77–91. (Cited on page 9.)



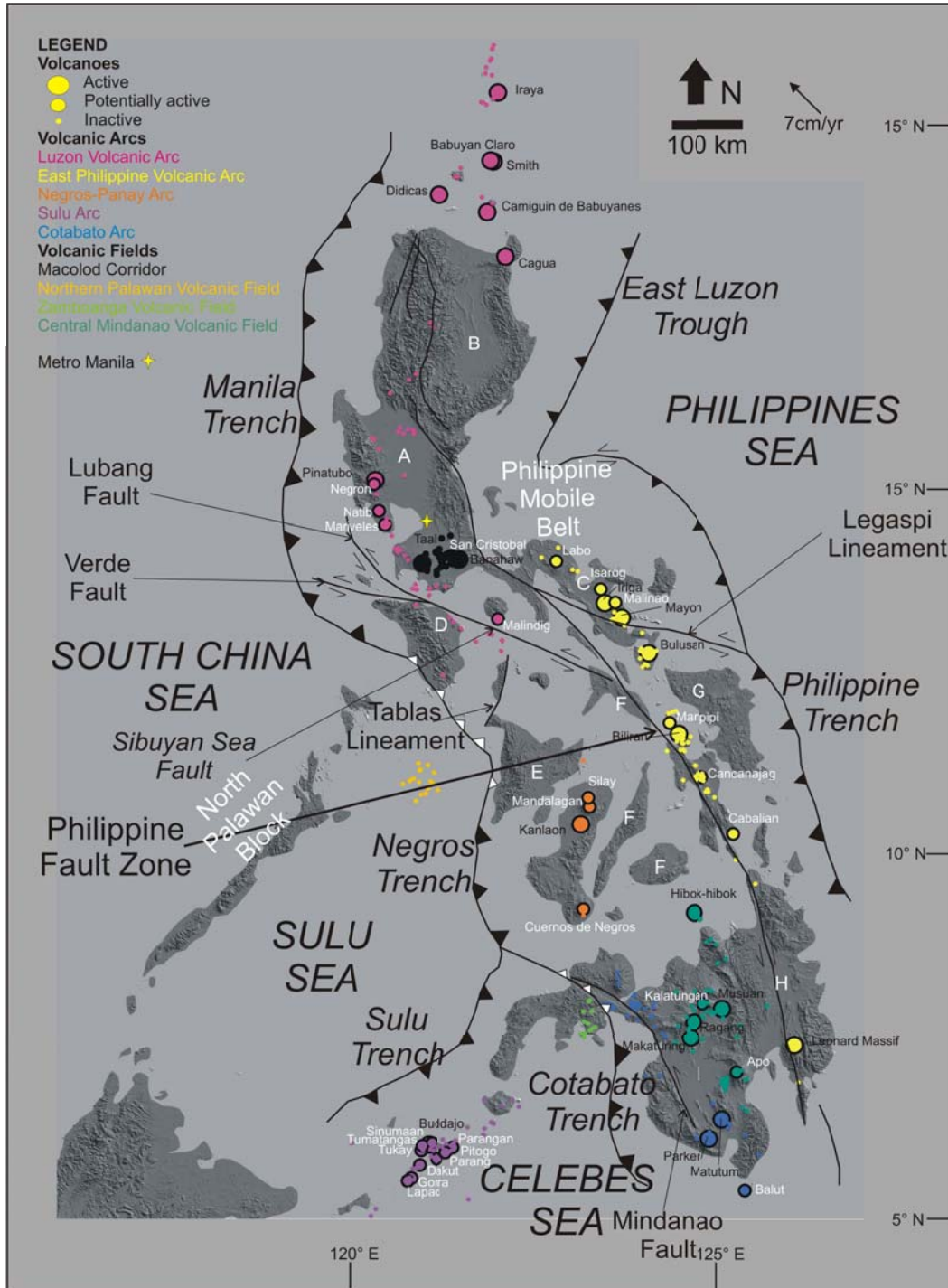
Figure 1.2: My photo during the 2006 Guinsaugon rockslide debris avalanche search and rescue operations.

debris avalanche risks is to learn to recognise the structures, morphology, and surface textures of avalanches and large landslides, and understand their roles and effects in the emplacement and transport mechanisms of such events.

This thesis attempts to use this approach at understanding avalanches. Clear examples of natural DAD structures and morphology at Mt Iriga, Guinsaugon, Mt Meager and Storegga are complemented with those created by laboratory analogue avalanches. In particular, the spatial distribution, formation, evolution, and internal characteristics of hummocks and the development of structures and morphological features in long runout landslides are described in detail.

### 1.3 This Thesis

The dissertation starts with an introduction (Chapter 1) to the tectonics and geology of the Philippines. A major part discussed is on the spatial distribution, morphometry and evolution of the Philippine volcanoes. At the end of



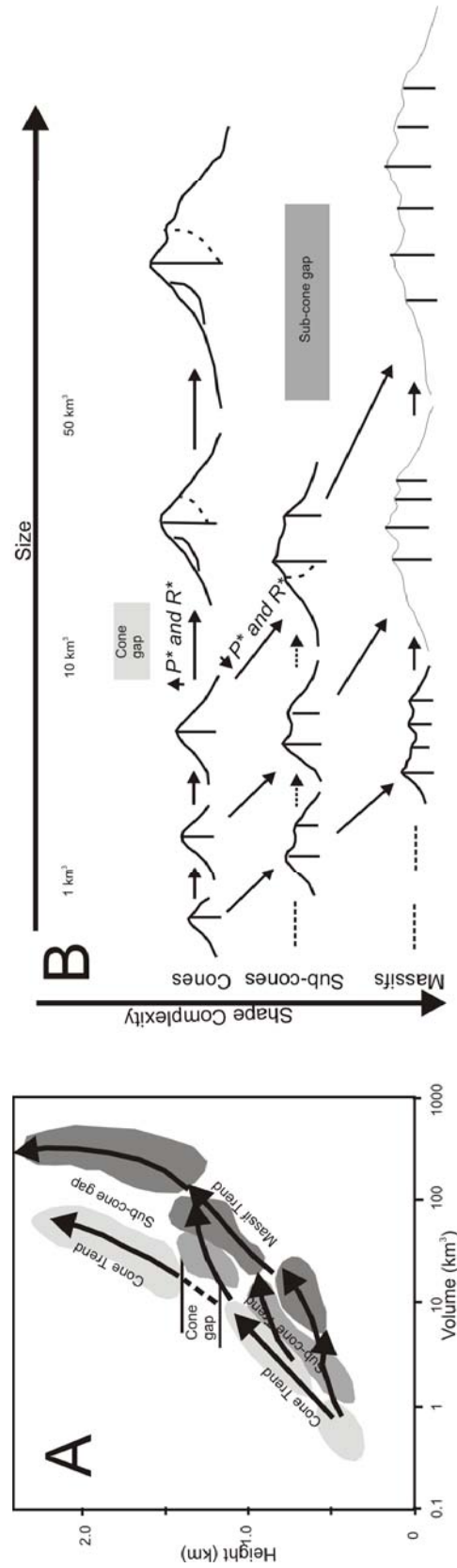


Figure 1.4: Evolutionary trends of the Central American and southern Central Andes volcanic edifices (taken from Grosse et al., 2009). **A** Evolutionary trends of the three main types of volcanic edifices and **B** Evolutionary growth paths starting from small simple cone. P\* is pressure and R\* is resistance balance.

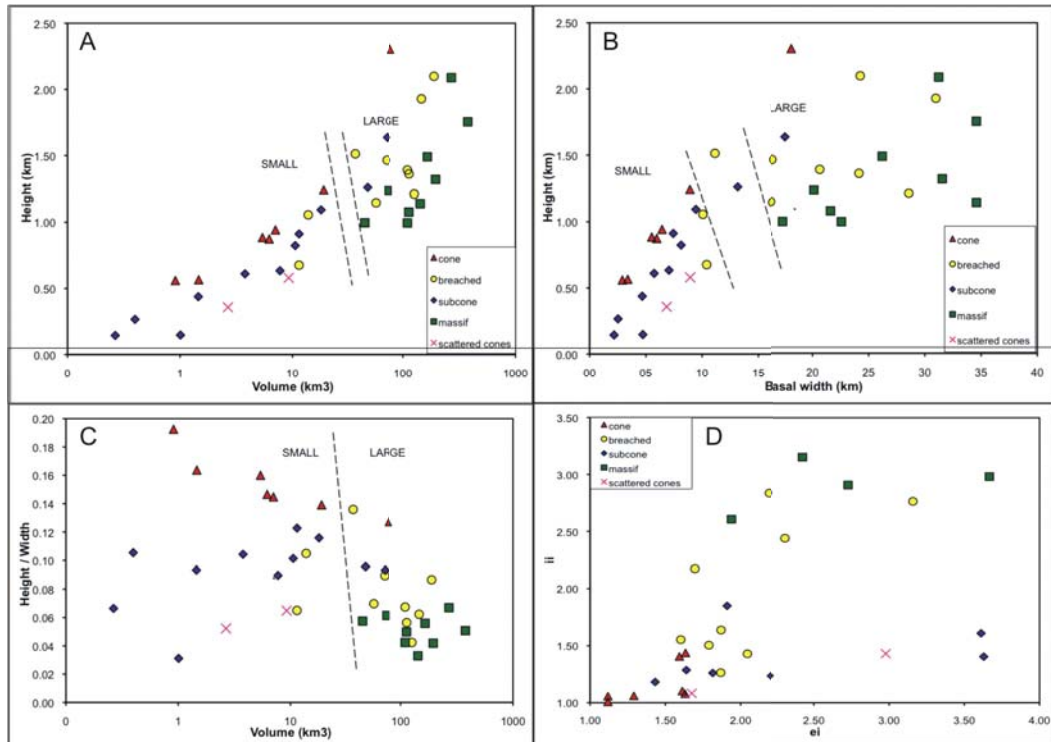


Figure 1.5: Morphometry of Active and Potentially Active Volcanoes in the Philippines. Plot of volcano shape: height against **A** volume and **B** Basal width, and **C** height and basal width ratio against volume. Legend is the same as in A-B and C; volcano complexity: **C** irregularity index against ellipticity index.

$\geq 15$  km and volume  $\geq 30$  km<sup>3</sup>. Two volcanoes, Banahaw and Kalatungan have intermediate basal widths but are large considering their volumes. Their heights are in the higher end of the spectrum for the cone and subcone classes, respectively.

Edifices classified as cones ( $n=7$ ) are steep, with  $H/W_B \geq 0.13$ . They have circular and regular plan shapes, having low  $ei$  (average  $ei$   $\approx$  1.7) and  $ii$  (average  $ii \leq 1.1$ ) values, although two edifices are more irregular, Maripipi, because of strong erosion, and Bulusan as it is a vent of a caldera system. Most cones are small, except for large and very active Mayon.

Massifs ( $n=9$ ) are large volcanoes with low  $H/W_B$  ( $\leq 0.07$ ). Their plan shapes are very irregular (average  $ii < 2.6$ ), with intermediate to high ellipticity (average  $ei < 1.9$ ).

Subcones ( $n=11$ ) have shape parameters with intermediate values. They have  $H/W_B$  ratios mostly between 0.08 and 0.12 and average  $ii$  values between

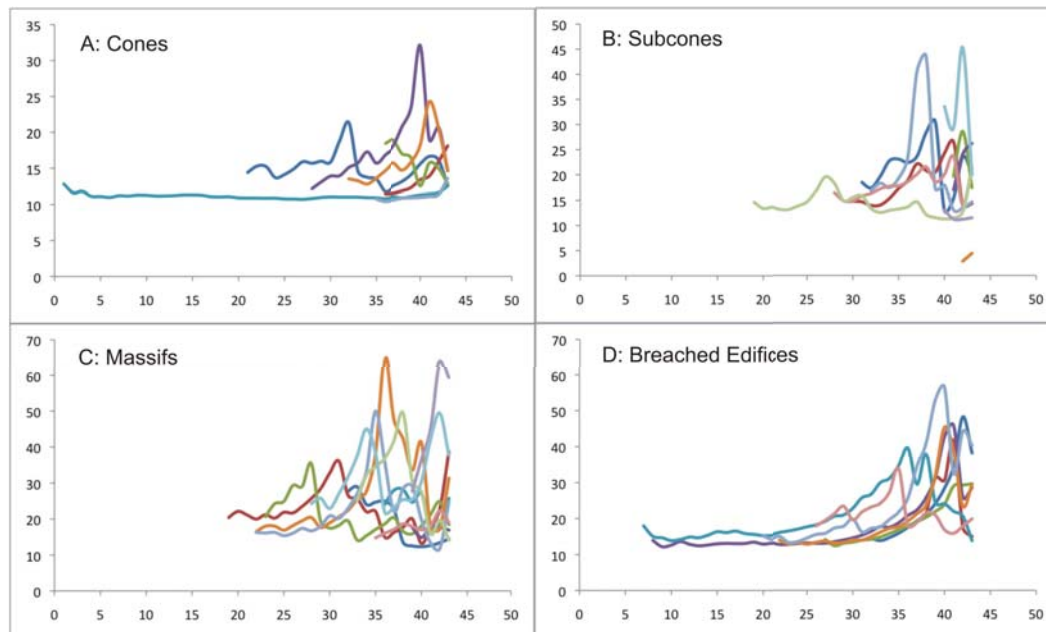


Figure 1.6: Line plot of the summit contours (pegged on the highest elevation contour) vs irregularity index ( $ii$ ). Irregularity Indices of the Summit Contours grouped according to classes: **A** Cones; **B** Subcones; **C** Massifs; and **D** Breached Edifice, a subclass that can include cones, subcones or massifs.

1.2 and 1.8; their average  $ei$  values are very variable. Most subcones are small.

Ten volcanoes have breached edifices, qualitatively defined by collapse scars and horseshoe-shaped summits. These edifices can be grouped into a morphometric subclass; they are edifices belonging to any of the three main classes that show breaching. They have variable  $H/W_B$  ratios mostly below 0.12, within the range of subcones (3 edifices) and massifs (6 edifices); only Banahaw has a high  $H/W_B$  ratio within the range of cones. They have a variable  $ei$  values and intermediate to high  $ii$  values (average  $ii < 1.2$ ). Most breached edifices are large, only Cagua and Iriga are small. It is difficult to distinguish breached edifices quantitatively because their morphometric parameters are variable as a result of their different ‘pre-breaching’ edifice morphologies. Their common feature is the horseshoe shape of their summits. Thus, their uppermost elevation contours generally have very high  $ii$  and  $ei$  values. Figure 1.6 shows height vs  $ii$  graphs of different edifice types. Breached edifices have increasing irregularity towards the summit.

Two small and very low edifices, Parangan and Sinumaan can be considered as a separate class of scattered cones. Makaturing is seen as a large example of this group (see Appendix A).

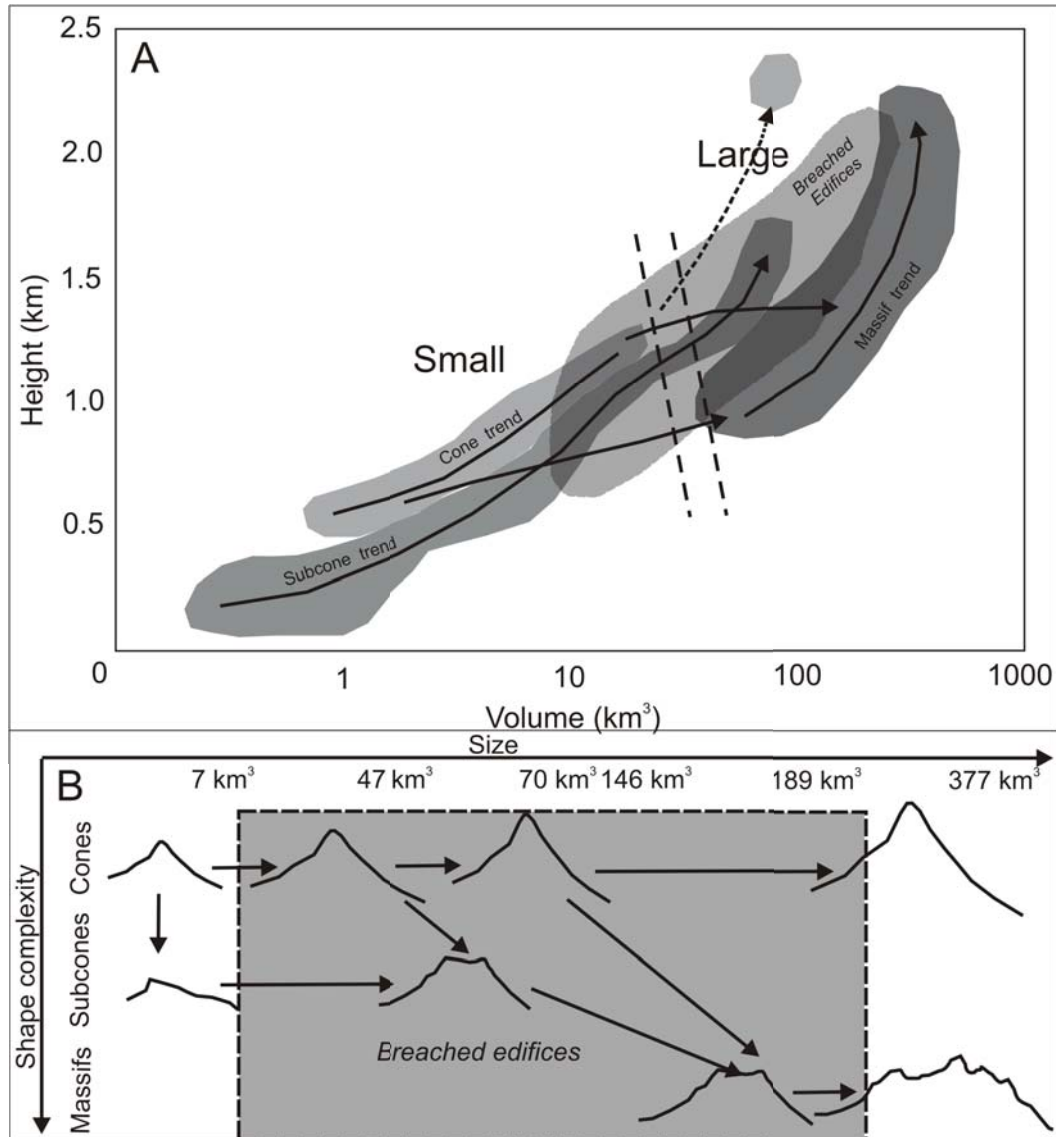
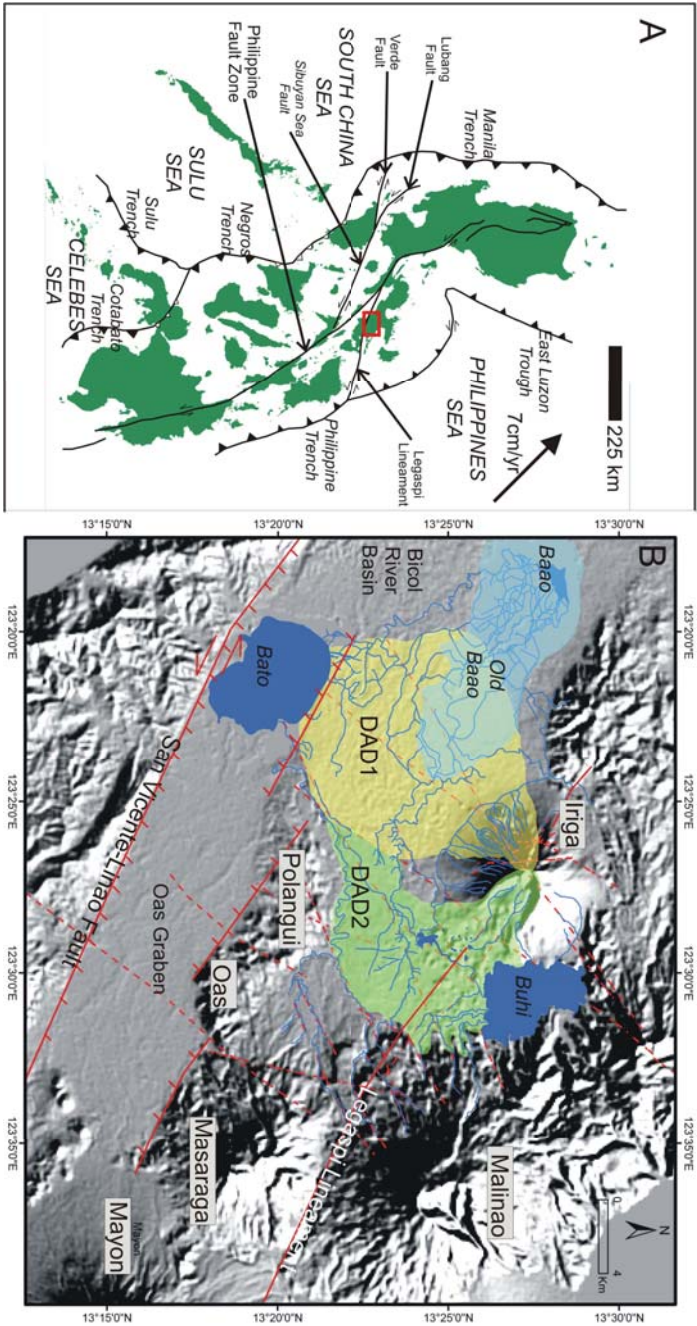
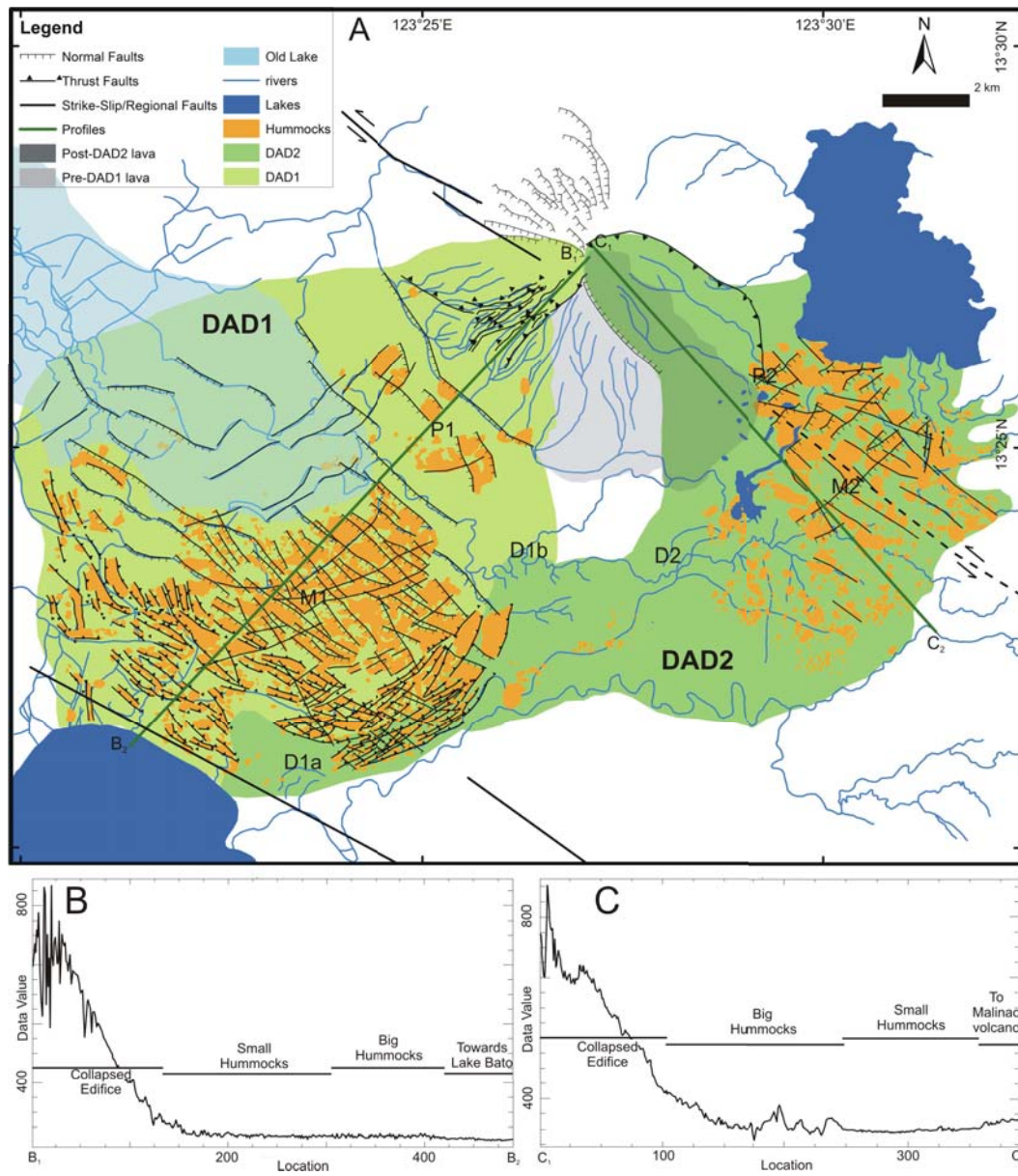


Figure 1.7: Morphometric evolution trends of Philippine volcanoes. **A** Fields of the four main types of volcanic edifices based on the plot of volcano height against volume and **B** possible evolutionary growth paths starting from either a small cone with a single vent or a small subcone with multiple eruption centres or domes (modified from (Grosse et al., 2009)).

Figure 2.1: **A** Tectonic map of the Philippines and the location of Mt Iriga (red box). Structures are from [Barrier et al. \(1991\)](#) and [Aurelio \(2000\)](#). Hachured lines with solid triangles are active subduction zones and those with open triangles are active collision fronts. Arrow indicates the direction and velocity of the Philippine Sea Plate. **B** SRTM shaded relief map of Mt Iriga and vicinity showing its two DAD, Mounts Malinao, Masaraga, Polangui-Oas, Mayon, the Oas Graben, the Lakes Buhí, Bato, Baao and older Baao, the Bicol River Basin (BRB). The regional faults are shown (red polylines): northwest-trending Legaspi Lineament, San Vicente-Linao Fault, the normal faults on the northern boundary of Lake Bato, and the northeast-trending structures.





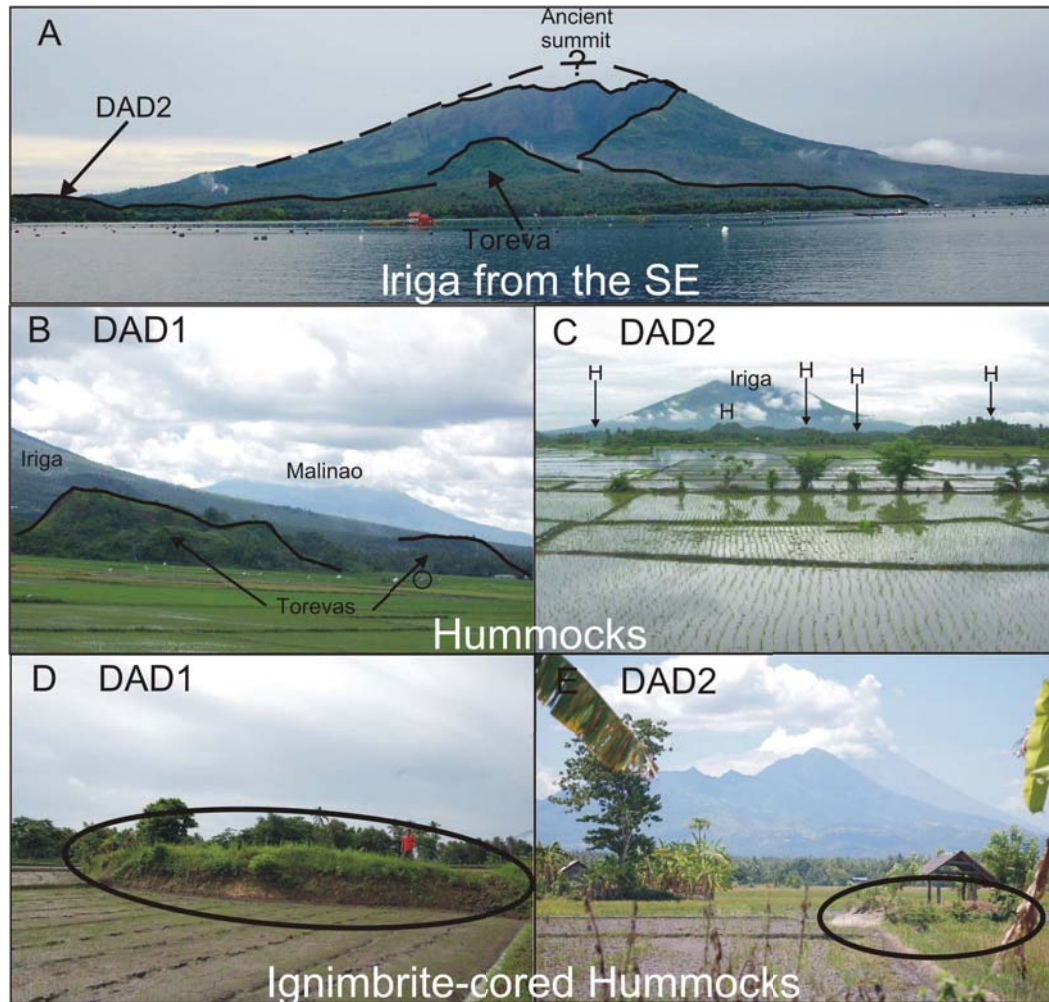


Figure 2.3: **A** View of the southeastern collapse amphitheatre and inferred edifice prior to the first collapse of Mt Iriga. Note the large torevas block on DAD2 standing above the debris field. **B** General view of the DAD1 torevas from the western plains with a small hut (circled) as scale. **C** View from the southeast looking over the saturated surface of DAD2 with the hummocks (H) in the distance. **D** Photo of ignimbrite-cored small hummock (circled) in the eastern part of DAD1. **E** View, looking southeast on DAD2 including a small ignimbrite-cored (circled) hummock sticking out of paddy field with Masaraga and Mayon in the distance.

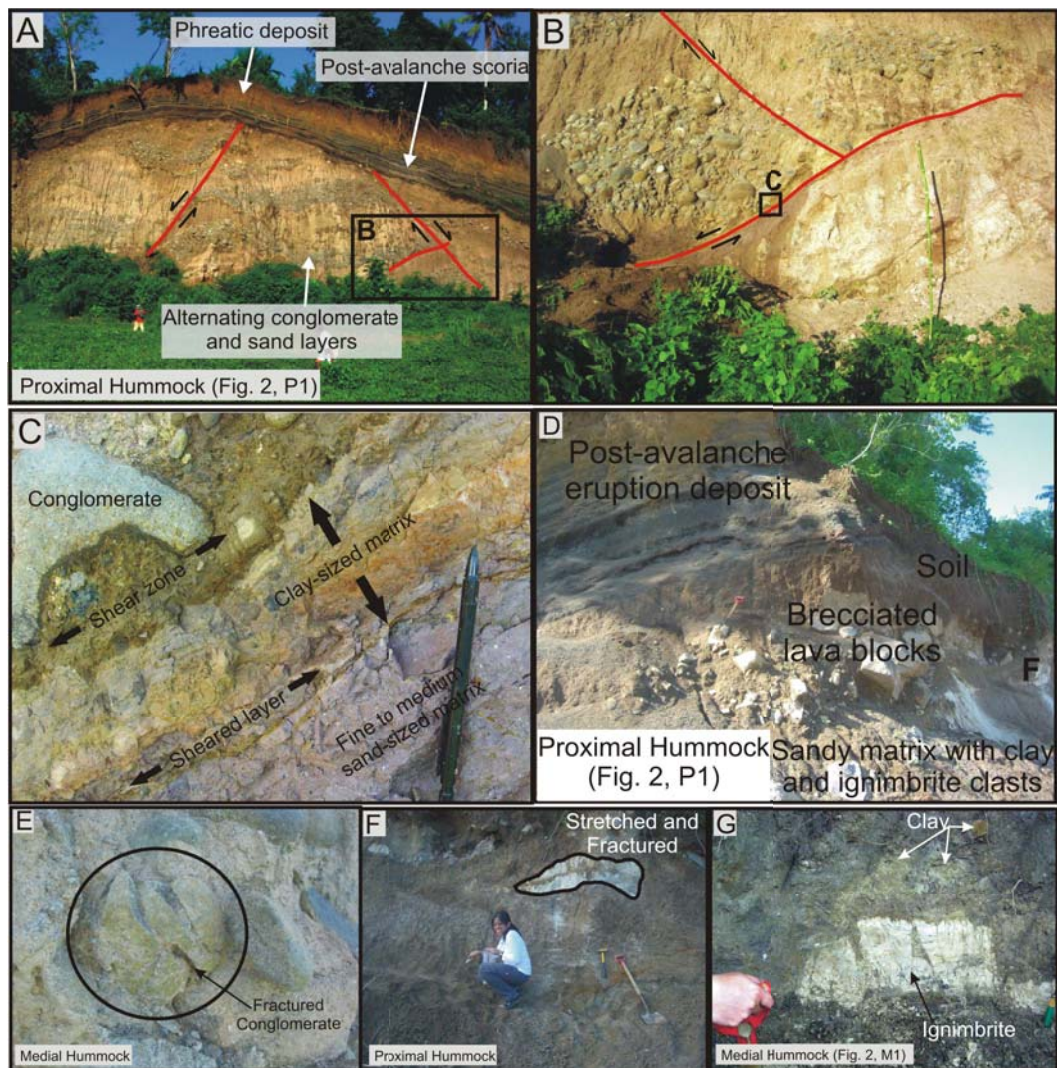
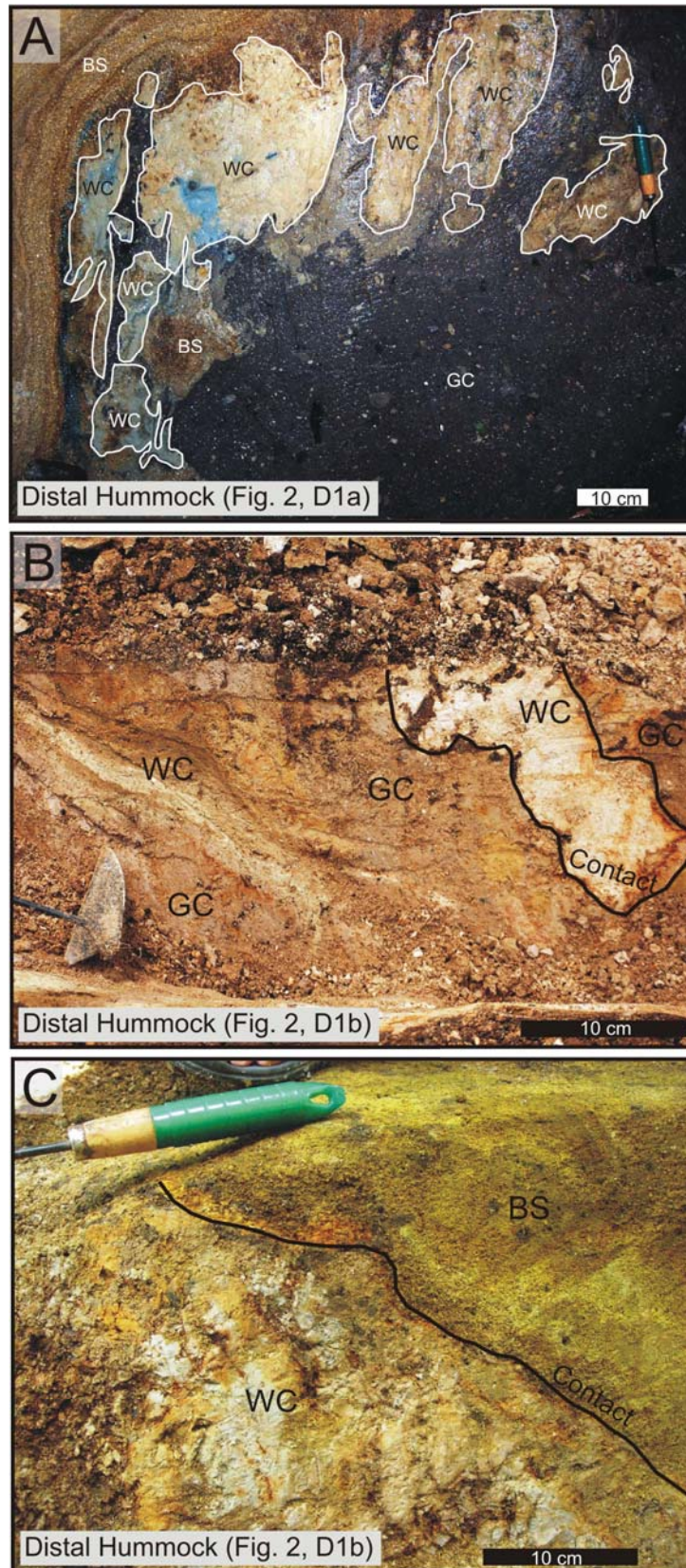


Figure 2.4: DAD1 lithologies and structures. **A** Large proximal hummock of DAD1 that is entirely made of alternating conglomerate and sand layers displaced by normal faults and mantled by post-collapse eruption deposits. **B** Displaced alternating conglomerate and sand layers cut by normal listric that illustrate the extensional dynamics forming the hummocks. **C** Close up of extensional low angle shear zone cutting the lower clay and conglomerate layers. **D** Hummock mantled by alternating scoria deposits and about 0.3 m thick phreatic eruption deposit. A soil layer between the hummock and the alternating scoria signifies that scoria eruptions happened sometime after the avalanche. **E** Fracturing in cobbles near the base of a hummock. **F**, **G** Clasts of stretched and fractured ignimbrite and clay blocks within the DAD.



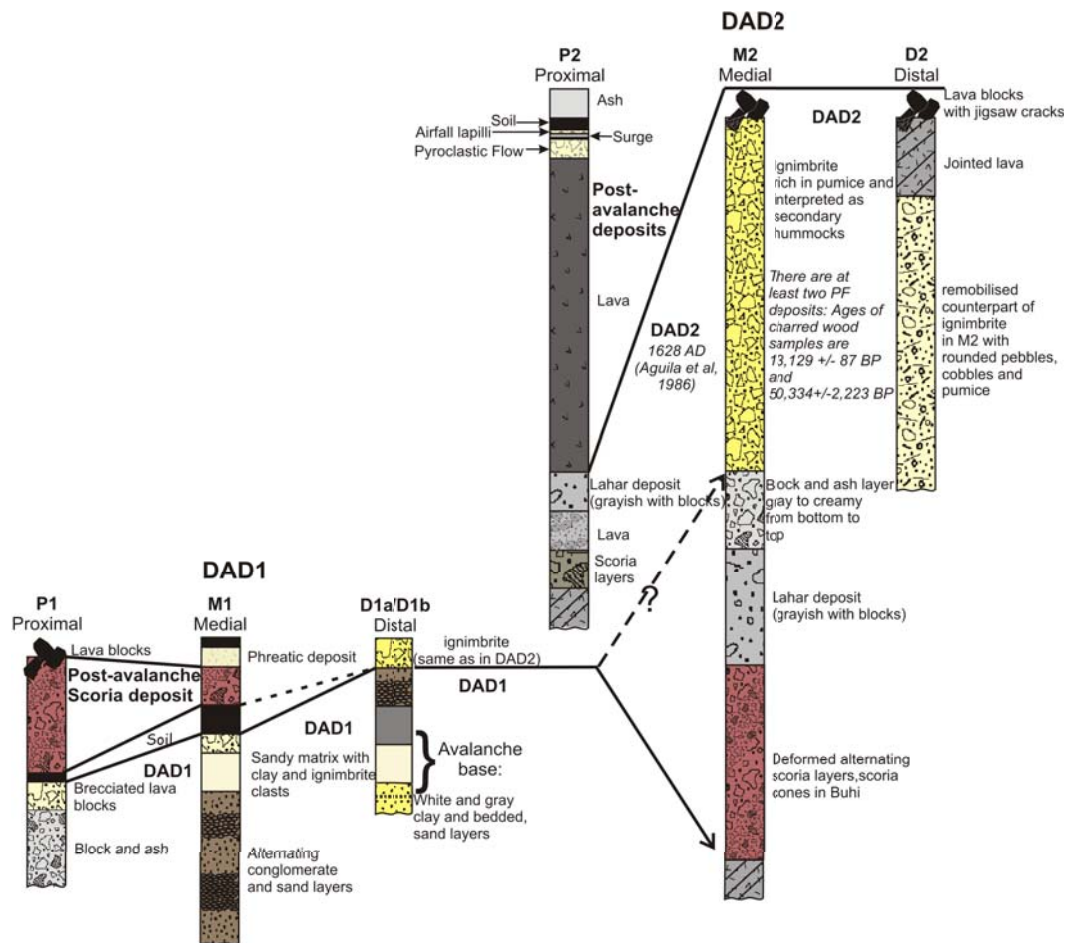


Figure 2.6: Stratigraphic columns and correlations in DAD1 and DAD2 of Mt Iriga with locations plotted in Figure 2.2A.

8 km west of the main body covering an area of about 70 km<sup>2</sup> and leaving a hummock field with small lakes and depressions (Fig. 2.2A). The opposing slope of Malinao volcano has constrained the debris avalanche path (Fig. 2.1B, 2.2A). The source amphitheatre is prominent and fresh. Buhi DAD2 is covered by a thin soil and is not affected by the frequent and widespread floods of the Bicol River Basin because of its higher elevation. Iriga River that drains Lake Buhi has cut a gorge down to the base of the deposit.

The DAD2 hummocks are elongate and mostly oriented parallel to the transport direction. Hummock height and area decrease with distance (Fig. 2.2A, C). Most of them are conical (Fig. 2.3C); some smaller hummocks have flat tops (Fig. 2.3E). One 2.5 km-wide torea block stands at the eastern base of the edifice. The DAD2 topographic profile is dominantly proximally raised, using the classification of Shea and van Wyk de Vries (2008).

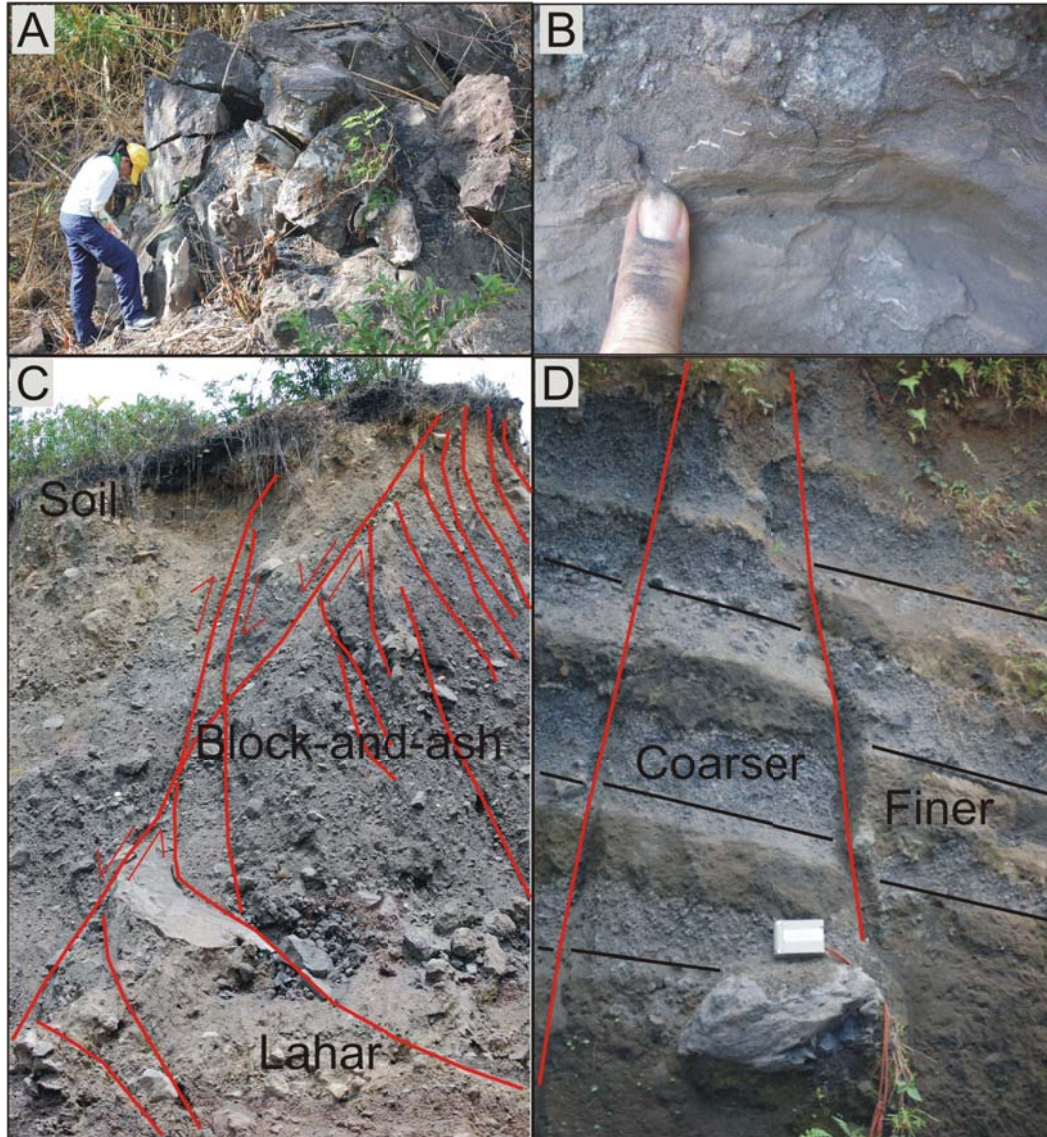


Figure 2.7: Internal deformation within DAD2 hummocks. **A** Large-scale spaced jigsaw cracks in the lava block facies. **B** Small-scale deformation in mixed lahar and block and ash facies. Note the small faults picked out by the white ash layer. **C** Faults in hummocks dissecting the block and ash and lahar layers. **D** Faults displacing layers within scoria cones transported by the avalanche.

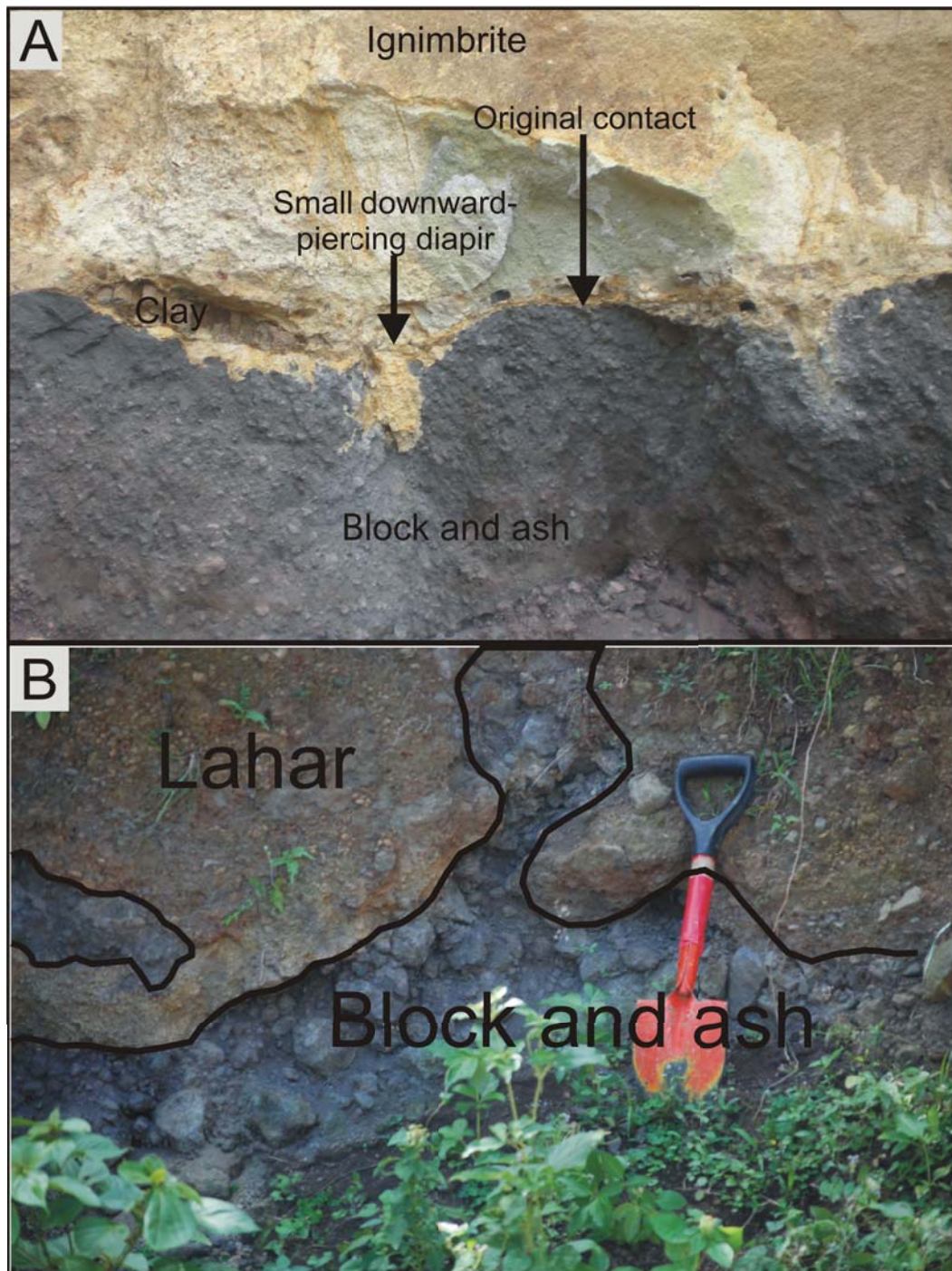


Figure 2.8: Mingling, and limited mixing of units within DAD2. **A** Contact between pumice-rich ignimbrite and block and ash facies, showing small diapirs of the ignimbrite descending into the lower layer, but a general preservation of the contact (small scale deformation in B is within this lower layer). **B** Inter-fingering of the blocky part of the block and ash (lower) layer with the upper laharic layer.

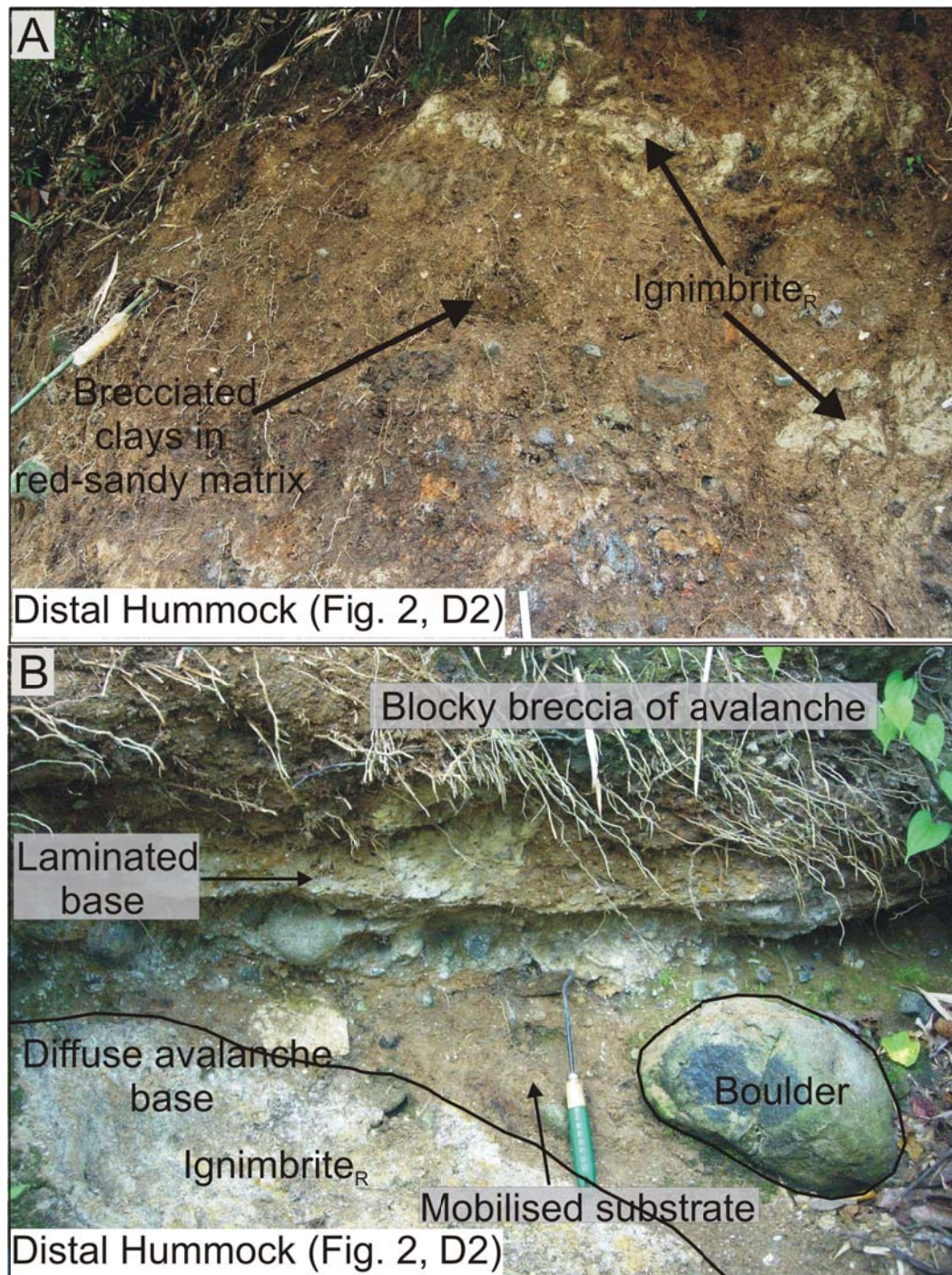


Figure 2.9: **A** The substrate-dominated lower part of DAD2 composed of stretched blocks of remobilised ignimbrite (ignimbrite<sub>R</sub>) seen as clasts with clays, sands and gravel, and no distinct contact. **B** Horizontally-banded base with conglomerates and lahar materials, broken lava, and mixed clay on top of consolidated gravel and pyroclastic flow layers.

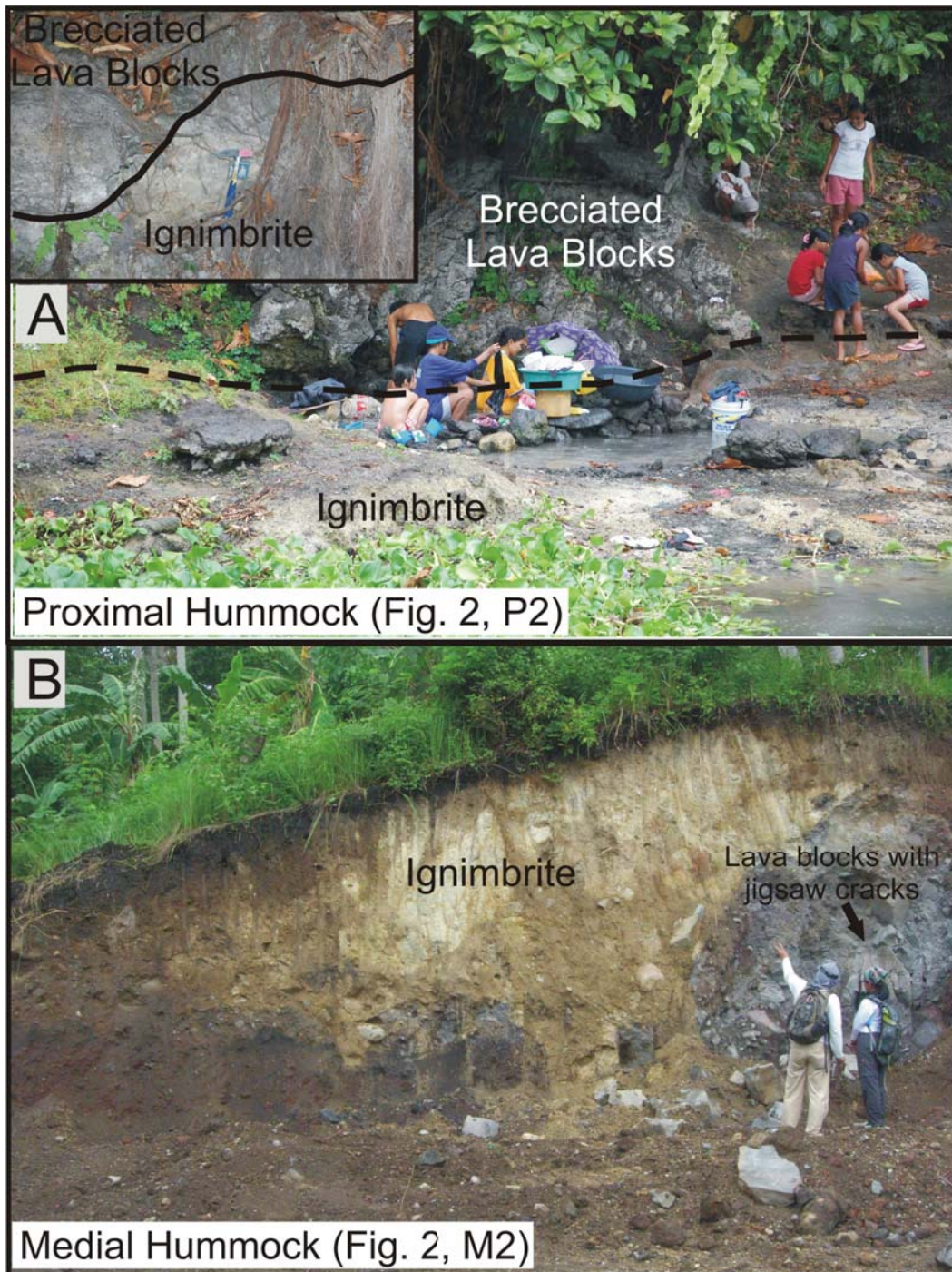
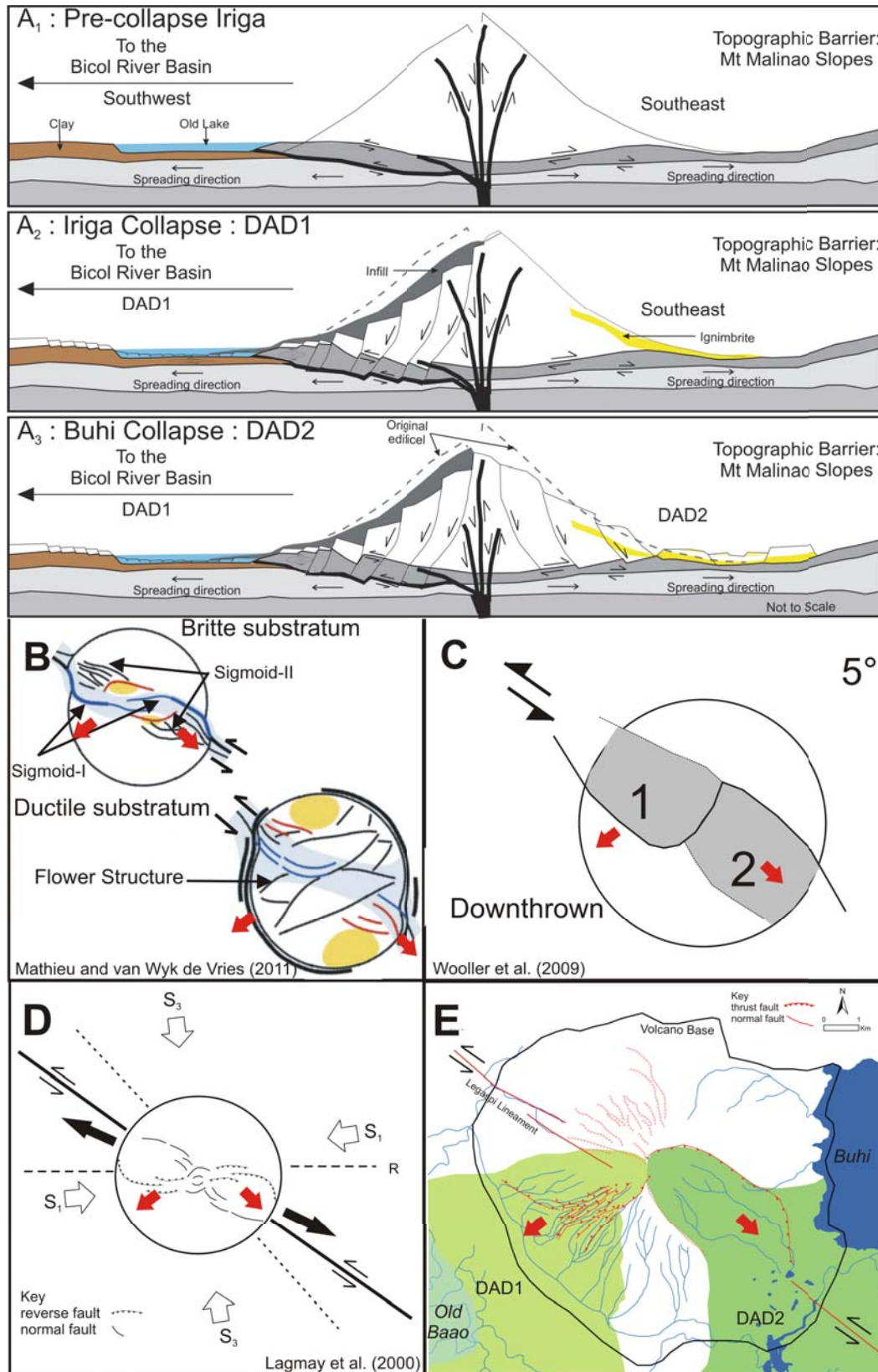


Figure 2.10: Illustration of DAD2 lithologies. **A** The block facies composed of lava blocks overlying (without soil layer) the ignimbrite. Inset shows a detail of hummock dominated by lava breccia and underlying ignimbrite. **B** Lava block inclusions with jigsaw cracks included in the ignimbrite.



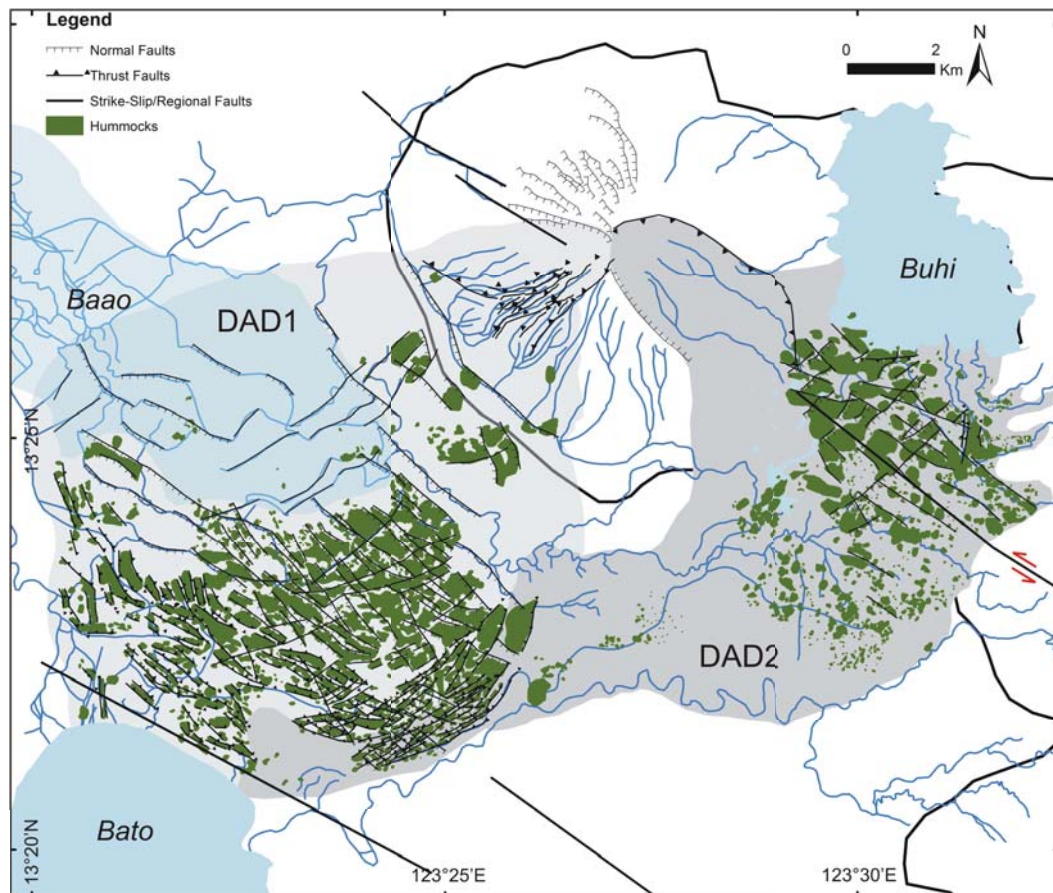


Figure 3.1: Iriga Volcano and her two DADs ((Paguican et al., 2011) showing the regional faults, water bodies: Lakes Baao, Buhi and Bato, hummocks, DAD structures-faults and ridges.

sub-aerial and submarine mass movements on the Earth and also on other planets. They are especially common on volcanic mass movements, for example, the Iriga debris avalanches (Fig. 3.1). The hummock family includes torevas, which are large tilted and rotated blocks left within or at the foot of the failure scar. Torevas can reach up to several kilometers in size and can disaggregate on their downhill sides into smaller hummocks (Francis et al., 1985; Lucchitta, 1979; Wadge et al., 1995). Often steep-sided in the downslope direction, the proximal sides of torevas are often filled in by post collapse material (Glicken, 1991). Downslope of the torevas are smaller hummocks. These can have radial or transverse orientation with respect to the landslide transport direction. This arrangement has been explained to be due to basal shear resistance when hummocks are either slowed and sculpted by adjacent faster moving material parallel to the flow direction (Glicken, 1986, 1991),

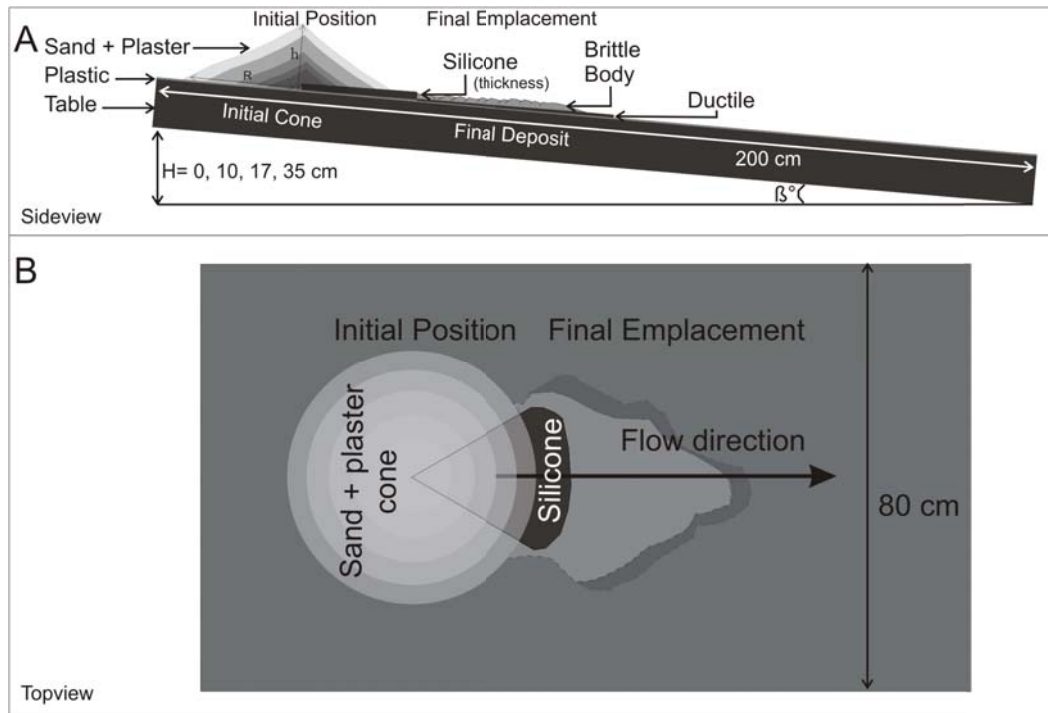


Figure 3.2: Analogue model set-up and illustration of geometrical parameters in **A** vertical view and **B** plan view. Constants and scaling parameter values are given in Tables 3.1 and 3.2.

Sand and plaster represent the edifice, silicone is the underlying ductile strata, and oil (when used) is the highly lubricated sliding base. The sand-plaster mix has cohesion and internal friction scaled to be similar to most rocky materials of volcanic slopes. By adding plaster, cohesion is raised as described by [Donnadieu and Merle \(1998\)](#). The silicone layer simulates the low viscosity basal layer in spreading stratovolcanoes and flank collapses ([Andrade and van Wyk de Vries, 2010](#); [Cecchi et al., 2005](#); [van Wyk de Vries and Francis, 1997](#); [van Wyk de Vries et al., 2000](#); [Wooller et al., 2004](#)). This layer is often consists of mobilized sediments, volcanoclastic, and altered rocks. The oil placed under the silicone in some experiments decreases friction between the sliding basal layer and the plastic sheet, thus speeding up sliding. In such cases, simple shear is concentrated in the oil layer and the rest deforms by pure shear stretching. This layer represents a possibly very low resistance layer that could be present at an avalanche base (e.g. [Siebert, 1984](#); [Thompson et al., 2010](#)).

The failure angle of the landslide (i.e. its initial plan shape) and inclination of transport and depositional areas are also taken into account in the

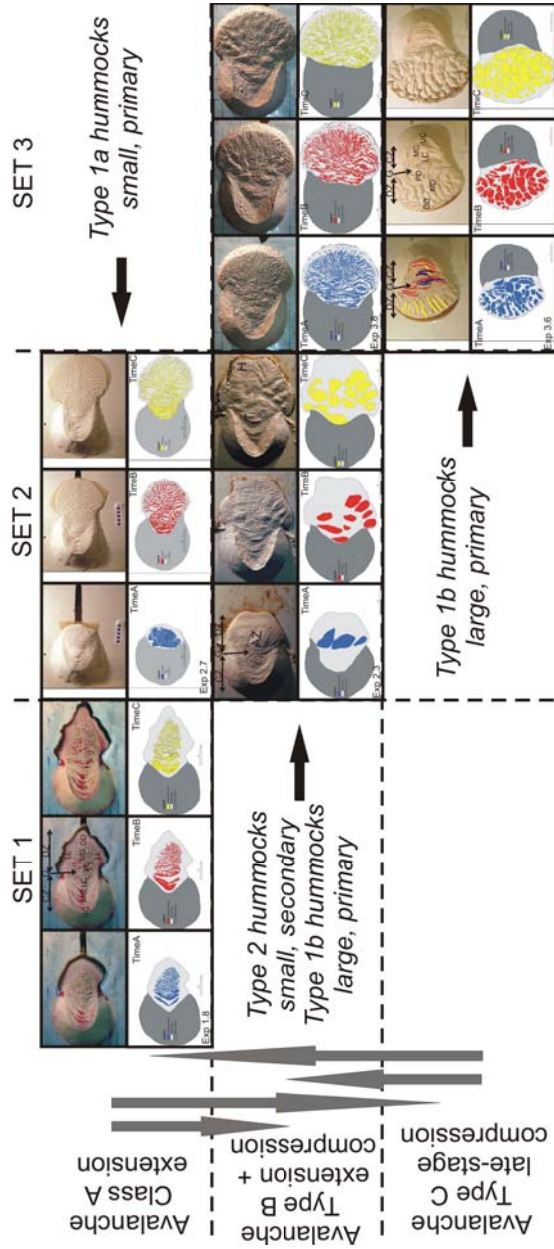


Figure 3.3: Development of analogue avalanches. Five analogue models that represent the three sets of experiments are grouped according to avalanche classes and the resulting hummock types: one for Set 1, two for each Set 2 and Set 3. Avalanches can be of Class A with progressive spreading and extension resulting in progressively broken, primary, smaller hummocks, Hummock Type 1a; Avalanche Class B for progressive spreading with compression in some areas resulting in a wider range of hummock size, Hummock Type 1b and 2; or Avalanche Class C for progressive sliding with late-stage compression resulting in increasing hummock size, Hummock Type 1b. Grey arrows indicate that during an avalanche, hummocks can start big and break during extension or they can merge sometime during its development. For each experiment, three photos representing the avalanche evolution and hummock development are in the first row, with their hummocks, debris field and depositional zone delineations below for statistical analysis of hummock area and spatial distribution. Morphological features are labeled and delineated in some experiments: collapse zone (CZ) and its upper (UC), medial (MD) and lower (LC) areas; depositional zone (DZ) and its proximal (PD), medial (MD) and distal (DD) areas; the graben (G); accumulation zone (AZ) in the PD, MD or DD, ridges (R), torevas (T) and hummocks (H); and the surface structures: normal (red), thrust (blue) and strike-slip (yellow) faults.

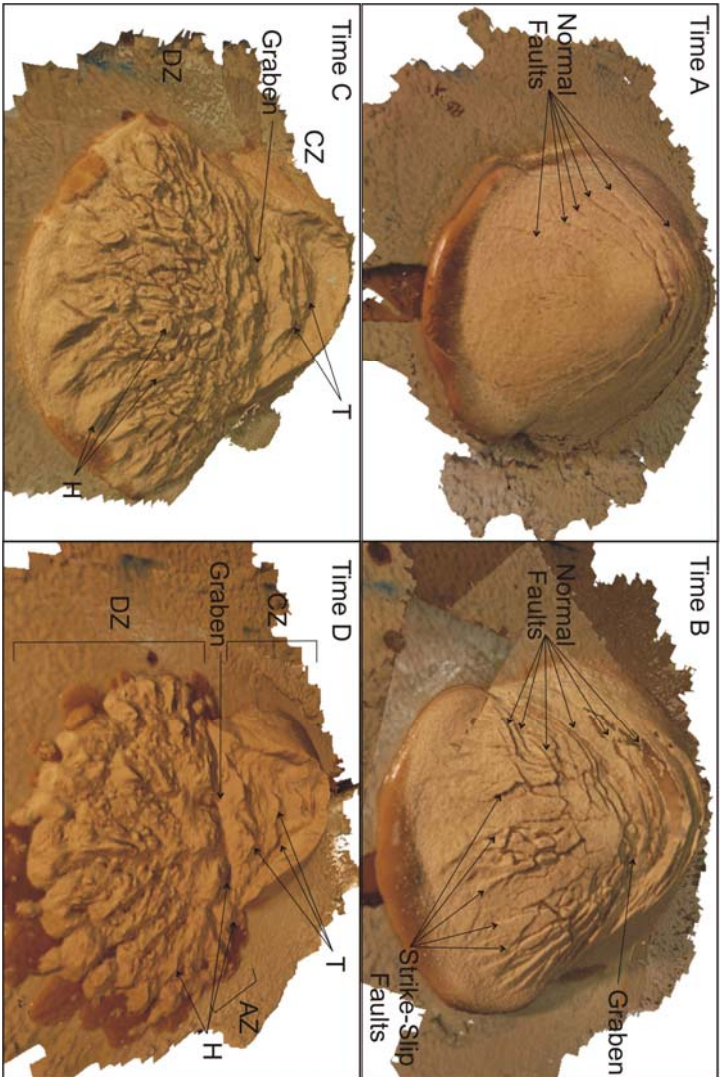
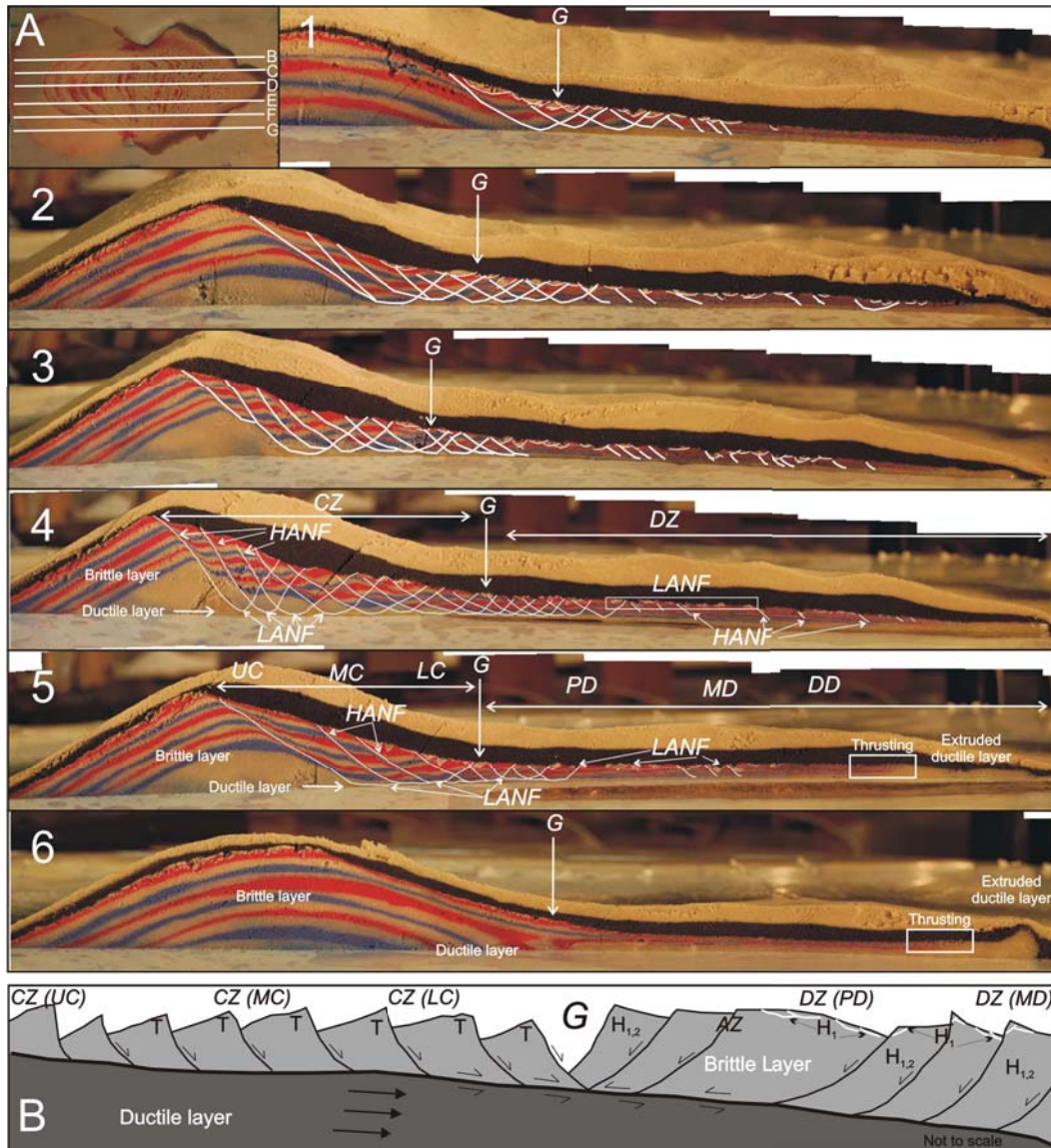


Figure 3.4: A 3D example of structural and morphological development of an avalanche and formation of hummocks during its evolution (ARC 3D webservice by the VISICS research group, Belgium). Time **A** formation of normal faults and movement along these cause edifice extension downwards by sliding; Time **B** collapse of more edifice materials near the summit and formation of more normal faults in the collapse (CZ) and depositional (DZ) zones. Movement along these faults spreads the materials further down with the graben forming as the edifice materials comes out of the amphitheatre limits towards a gentler slope; At Time **C**, torevas (T) formed since the earlier stages are more evident and the materials at the base spreads both to the lateral and downslope direction. Hummocks in the DZ are well formed at this stage; and at Time **D**, the avalanche spreads and hummocks break up.



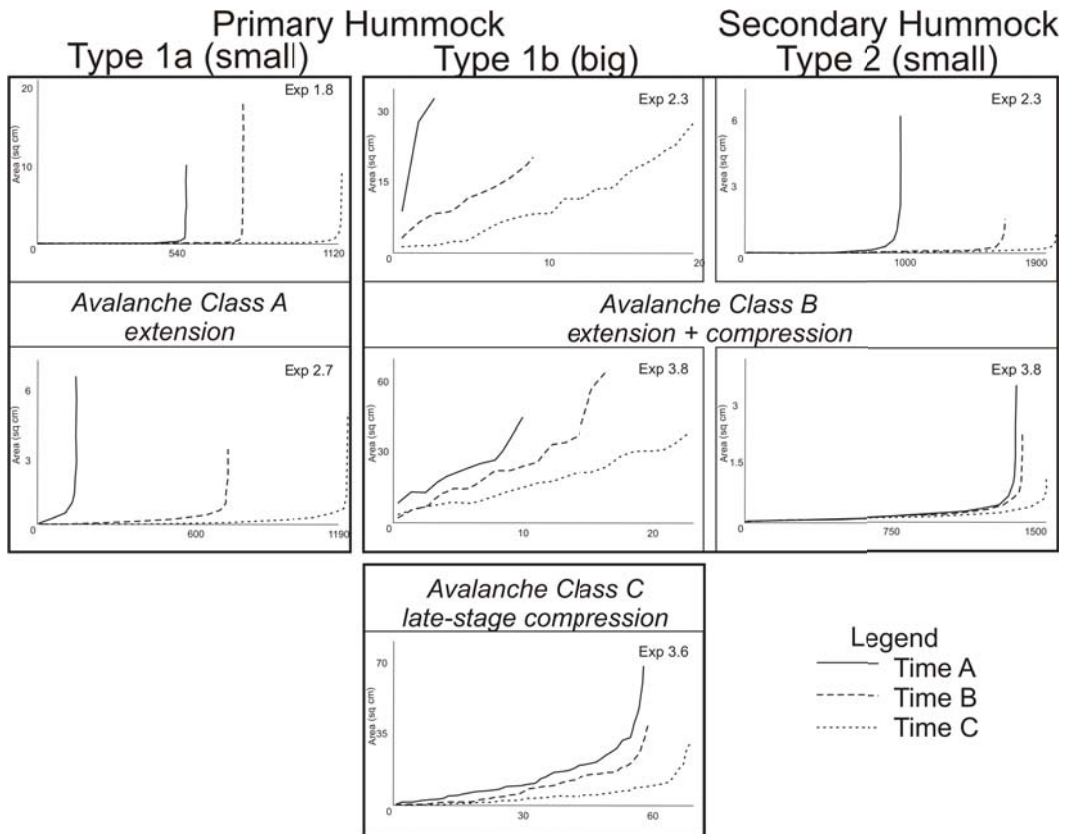


Figure 3.6: Increasing line plot of hummock area. Avalanches can produce either or a combination of a large number of small hummocks or a very low count of big hummocks. Small hummocks, regardless of whether they are primary or secondary can be highly contrasting having mostly of very small and very few large hummocks. Sizes of type 2 hummocks, however, exhibit a gradual change in slope implying that for avalanches that produce larger hummocks (compression-dominated avalanches), their hummocks are of similar sizes during transport.

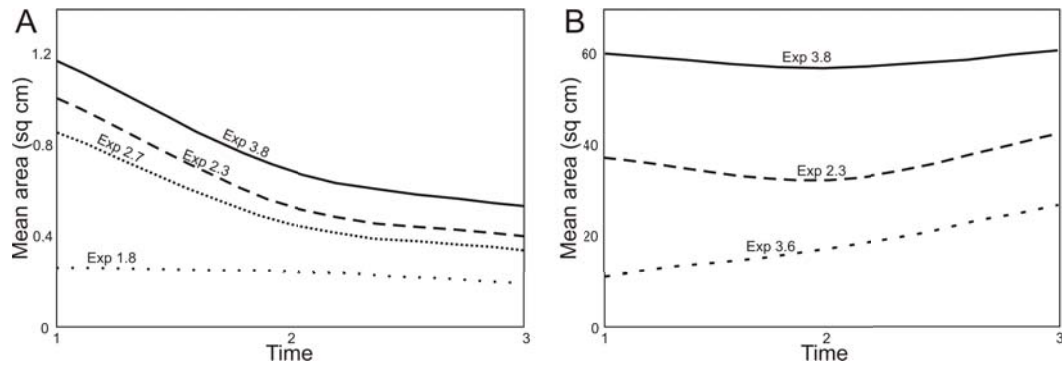


Figure 3.7: Line graph showing mean areas of hummocks with respect to distance from the summit (the greater the time, the farther the hummocks are from the source). Type 1 (A) and Type 2 (B) hummocks will always tend to break up, due to spreading and extension during an avalanche emplacement. However, they can start to merge and form increase in size once undergoes compression.

avalanche) tend to have very high frequency of small and very few big hummocks. This is seen by the very abrupt change in slope on Figure 3.6. Type 1b hummocks (Exp 2.3, 3.8, 3.6) produced by class B and C analogue avalanches (with compression at some point during the avalanche) exhibit gently sloping graphs, indicating that within certain stages during the avalanche, the hummocks are of restricted range of sizes. In general, hummock population may decrease as their size increases or populations increase as they progressively break up.

During an avalanche, types 1a and 2, small hummocks always tend to break-up and disintegrate if they have lower cohesion (Fig. 3.7A, Appendix D) as shown by an overall decrease in hummock size. However, as an avalanche wanes or when cone materials block the spreading of silicone at the front of the avalanche causing compression, hummocks can merge and integrate materials (Fig. 3.7B, Appendix D) forming the larger hummocks during compression. This results in larger hummocks at the medial to distal margins.

### 3.4.6.3 Spatial Distribution

Hummock spatial distribution is recorded by taking the centre of each hummock. The elongation and direction of the ellipse (Fig. 3.8) represents the general direction and orientation in which the hummocks form and separate. In general, this follows the plan view shape of the debris avalanche deposit itself.

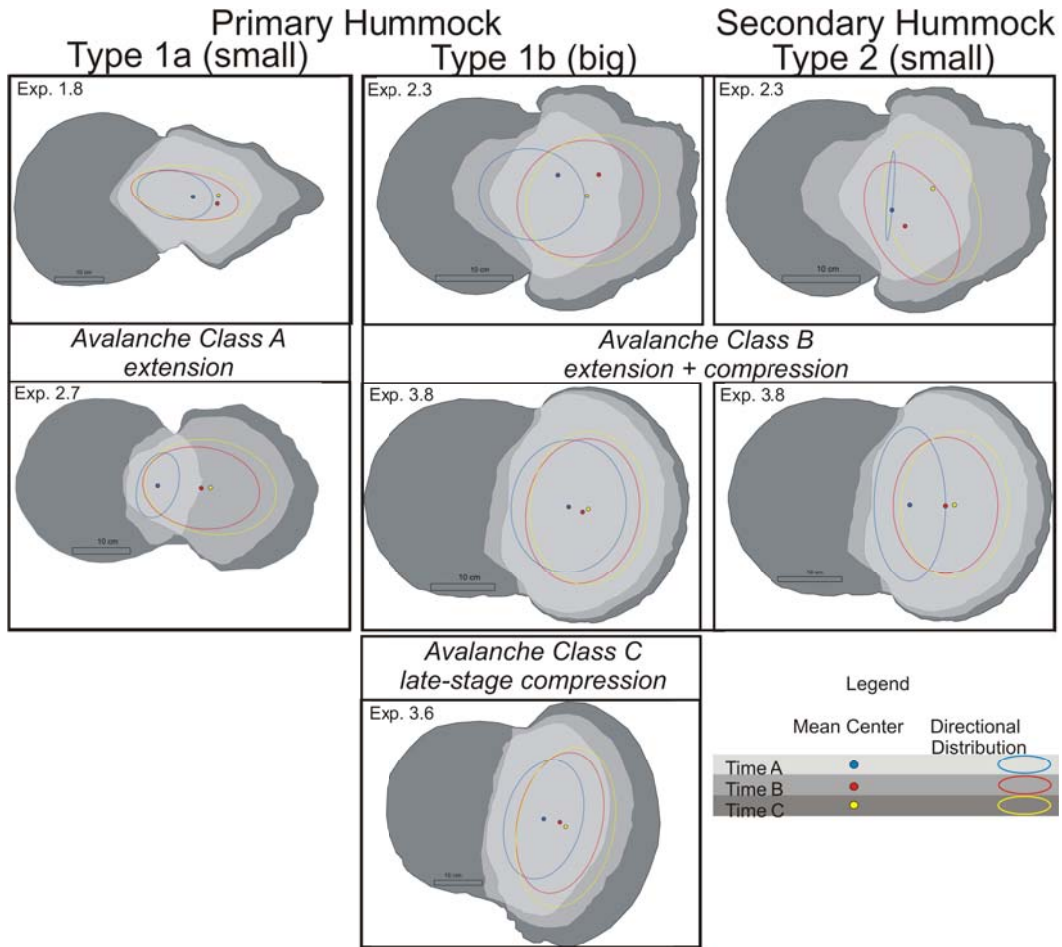


Figure 3.8: Trend of the directional ellipses and mean centers. The directional ellipses show the lateral or longitudinal formation direction of hummocks and the mean centre is the centre point of the central hummock.

The mean centre (Fig. 3.8) shows the point where the central hummock moves at each stage of the experiment. In general, these trends allow visualization of the link between central hummocks, overall direction of movement and avalanche flow direction. The trend in the directional ellipse and mean centre of the hummock areas show that spreading occurs mostly parallel to the long axis, downslope-spreading of the avalanche if the material is less cohesive and lubricated whereas dominantly lateral for high basal friction and more cohesive experiments.

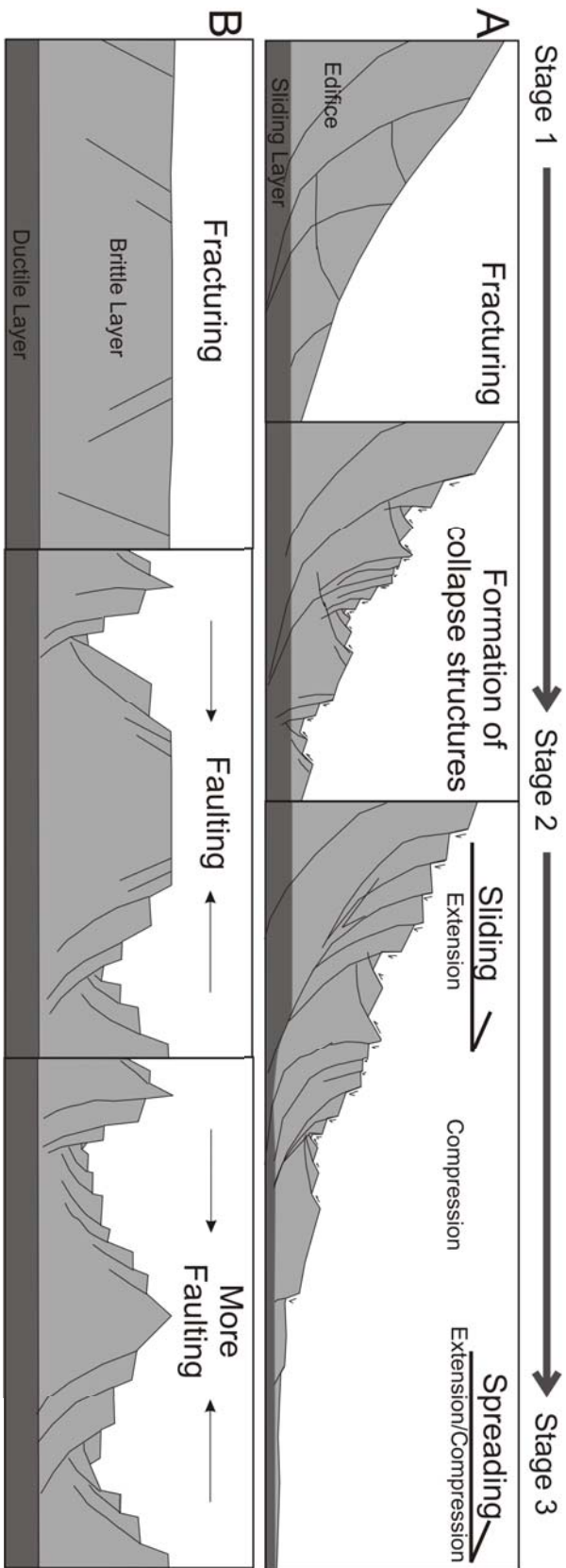
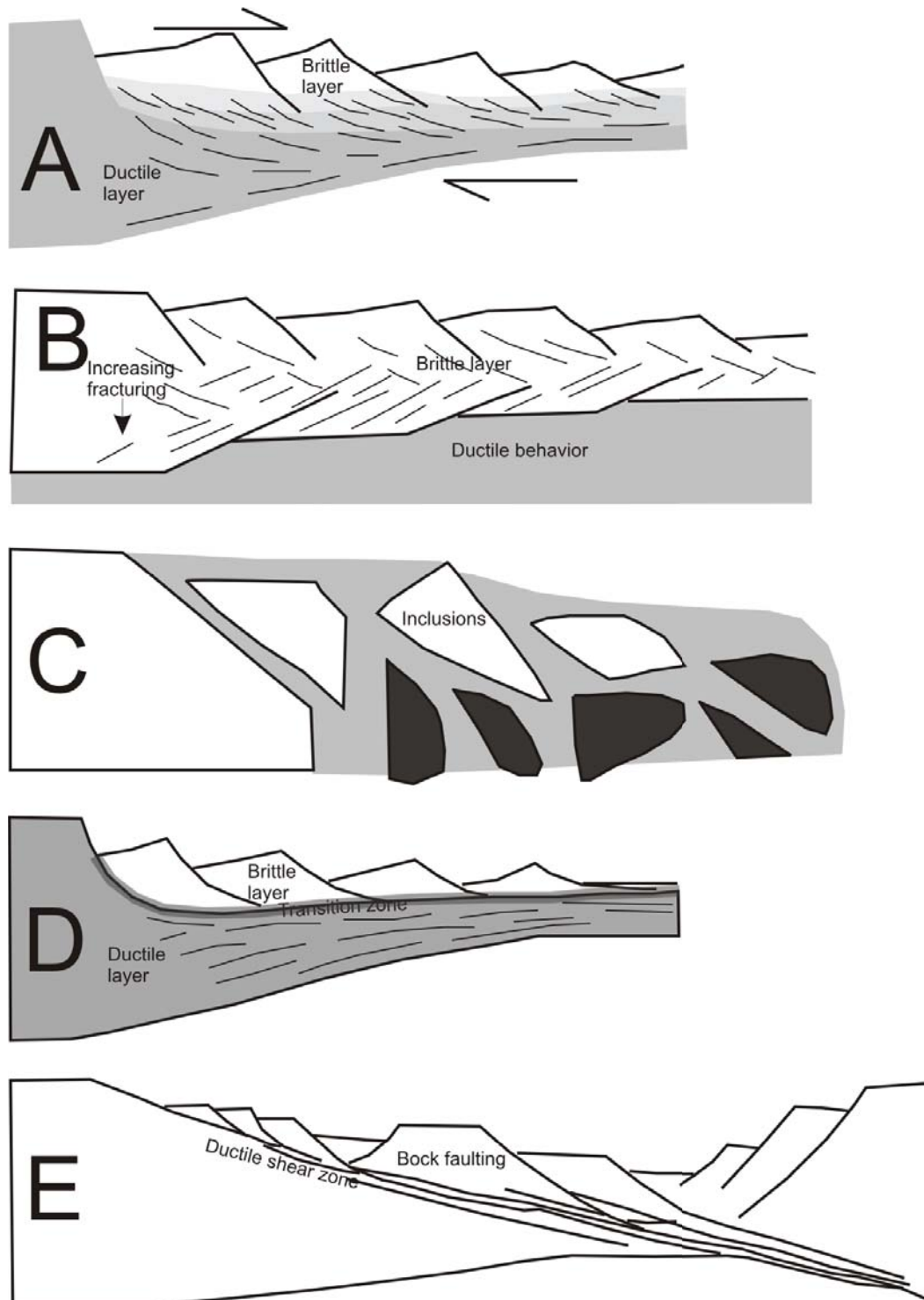


Figure 3.9: The different stages of avalanche emplacement showing an interpretation of hummock formation **A** and degree of faulting **B**.



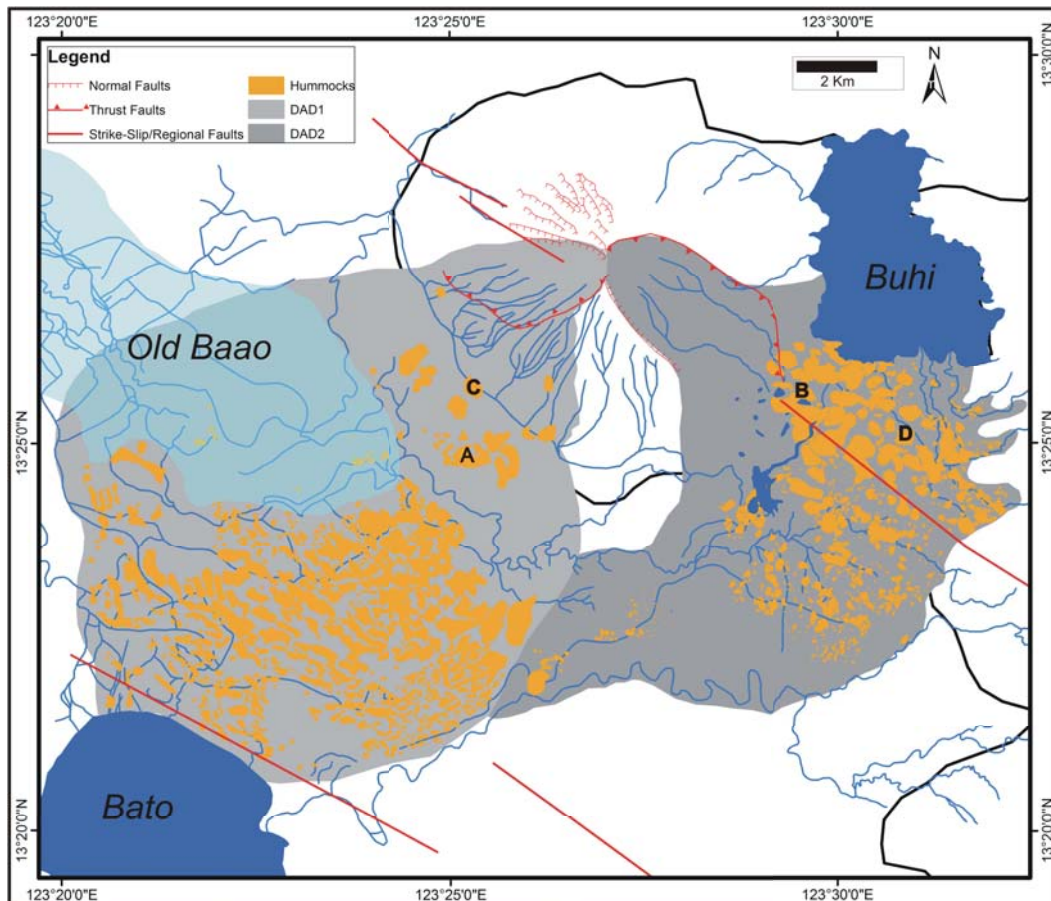


Figure 4.1: Iriga Volcano and her two DADs (Paguican et al., 2011) and the location of featured hummocks. In red polylines are the structures that caused and resulted from the edifice collapses. In blue are the water bodies that have significant roles in the development and emplacement of the avalanches and their hummocks: Iriga river system; and Lakes Old Baao and Bato for DAD1 (yellow polygon) on the southwest and Lake Buhi for DAD2 (green polygon) on the southeast. Locations of the hummocks are shown as A for Lady Backhoe (Fig. 4.4); B for Captain's Slide (Fig. 4.5); C for the Lava Topping (Fig. 4.6); and D for the ignimbrite Topping (Fig. 4.7).

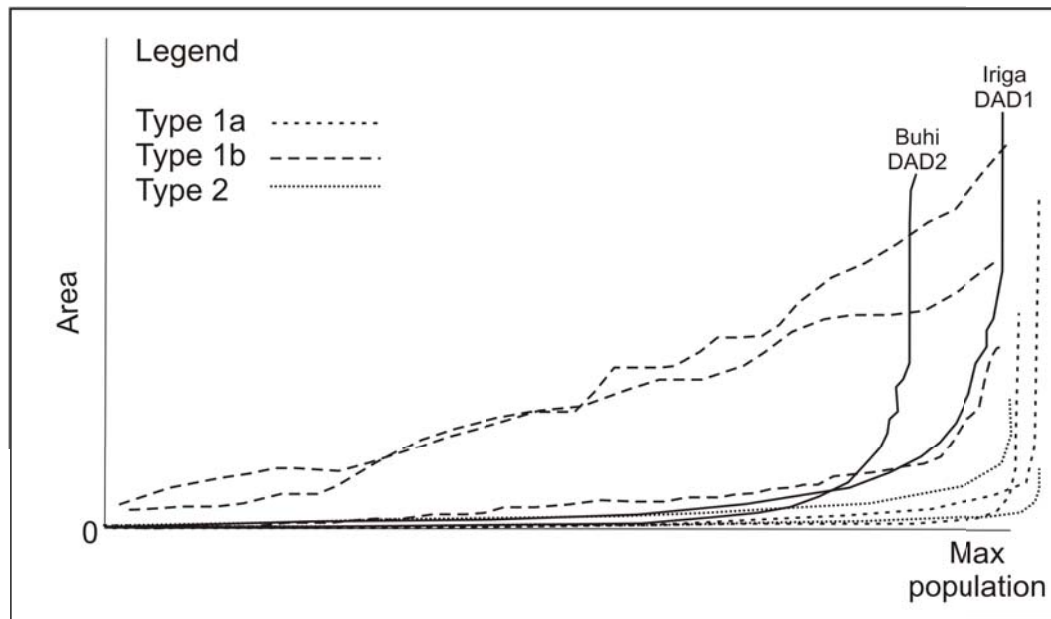


Figure 4.2: Increasing size plot of Iriga DAD1, Buhi DAD2 and analogue avalanche hummocks (previous chapter of this thesis).

of Buhi DAD2, which have the circular base. Based on the hummock elongation direction, those in DAD1 are dominantly perpendicular to flow direction while those in DAD2 dominantly flow parallel except near the deposit edges where the hummocks are randomly oriented. Probably as an effect of DAD2 deflection as it reached the Malinao edifice.

#### 4.4.1 Hummock Exploration and Accounting

A line graph of increasing hummock size for Iriga DAD1 and Buhi DAD2 (Fig. 4.2) yields a pattern that goes well with those plots of analogue hummock models. Iriga DAD1 is dominated by the larger Type 1b hummocks. They are big (several 100s m), and elongated, with relatively gently sloped line plot compared to Buhi DAD2. On the other hand, Buhi DAD2 has characteristics of the small either Type 1a or Type 2 and large Type 1b hummocks. The plot shows a relatively steeper line showing an abrupt change from having a lot of small hummocks to very few big hummocks. Buhi DAD2 has a high number of small hummocks. Most of these are those ignimbrite-cored, secondary hummocks (Type 2) and a few primary large hummocks (Type 1b) especially in the proximal and medial depositional zones.

Plotting the size of hummocks (y) against their distance from the source

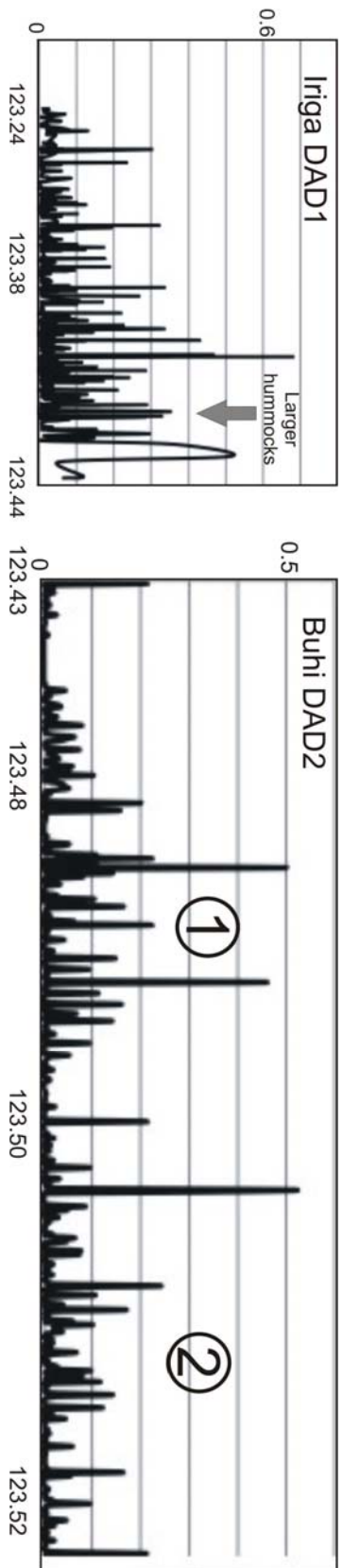


Figure 4.3: Spatial Distribution of Iriga DAD1 and Buhi DAD2 Hummocks showing the change of hummock size ( $y$ ) with respect to its longitudinal location as distance from source ( $x$ ). Iriga DAD1 has larger hummocks in the distal area while Buhi DAD2 has big hummocks in the proximal and medial depositional zones and another group in the distal area.

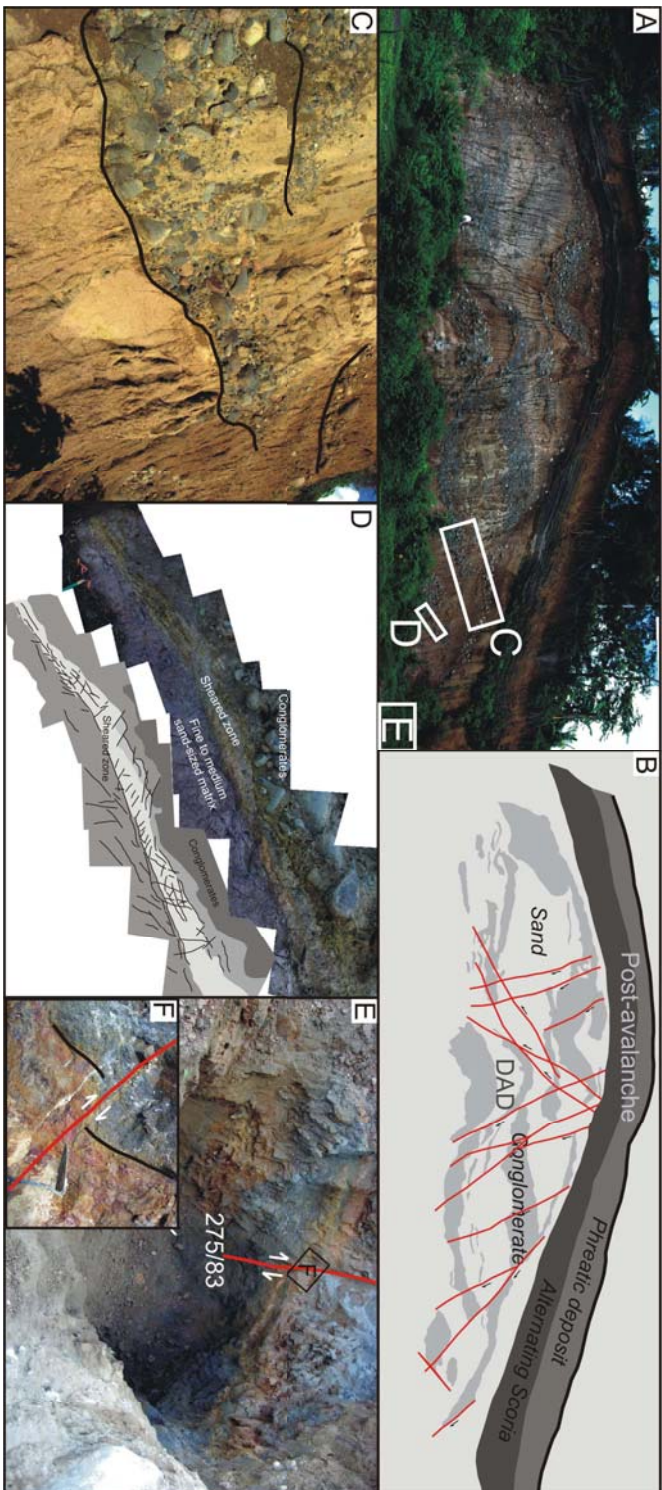


Figure 4.4: The Lady Backhoe's Hummock Faulting (proximal depositional zone, DAD1). **A** is the hummock's vertical cut showing displaced layers of cobbles and sand-sized deposits by the normal faults. Locations of **C**, **D**, and **E** are in white boxes. **B** is a sketch of the internal layers and faults (red polylines) of this hummock. **C** shows the orientation of cobbles as it was originally deposited prior to the avalanche that remobilized them. **D** is a low angle shear zone. It shows the interface between the upper brittle layer and the lower ductile layer of DAD1. **E** is the basal ductile layer of DAD1. It shows that there is continuous deformation under the shear zone shown in **D** and therefore, faults penetrate up to the ductile layer of an avalanche. **F** shows the slickenside in the ductile layer drawn in box **E**.

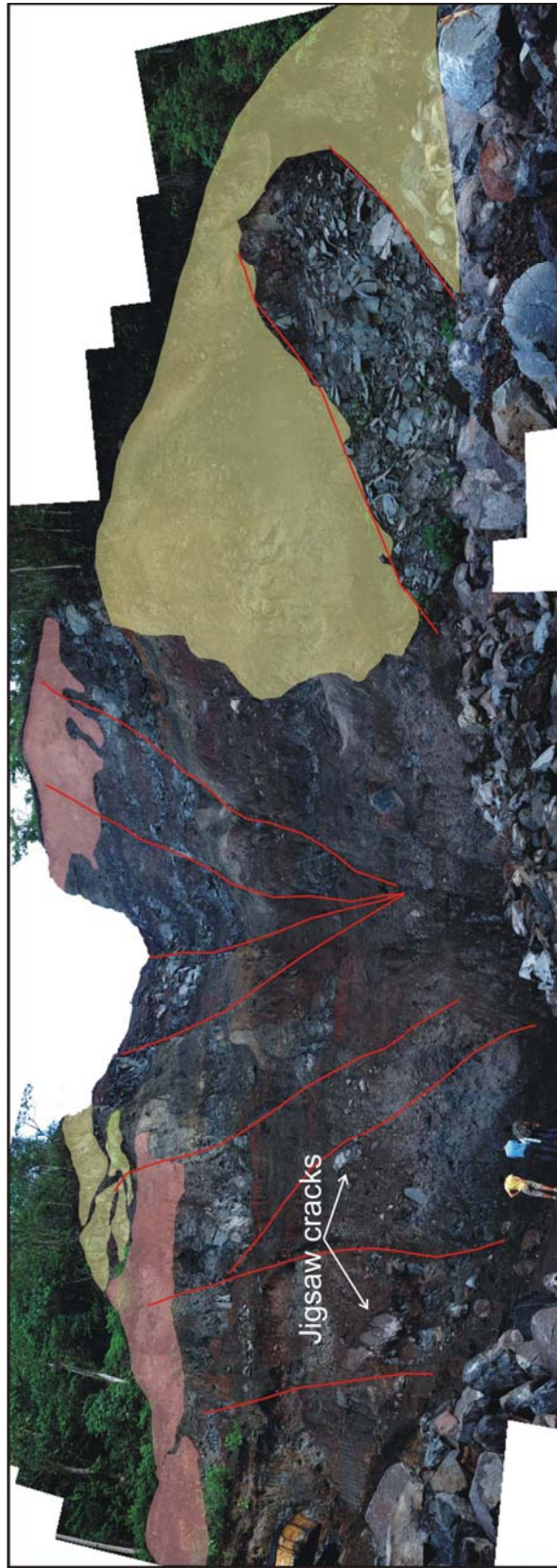


Figure 4.5: The Captain's Slide Hummock (proximal depositional zone, DAD2) showing how normal faults can cause a hummock to break up. In red polylines are some normal faults dissecting the hummock. Movement by extension, sliding for example along these faults, cause the hummock to break up and evolve into smaller hummocks. A hummock is still unstable after its emplacement because of these normal faults.

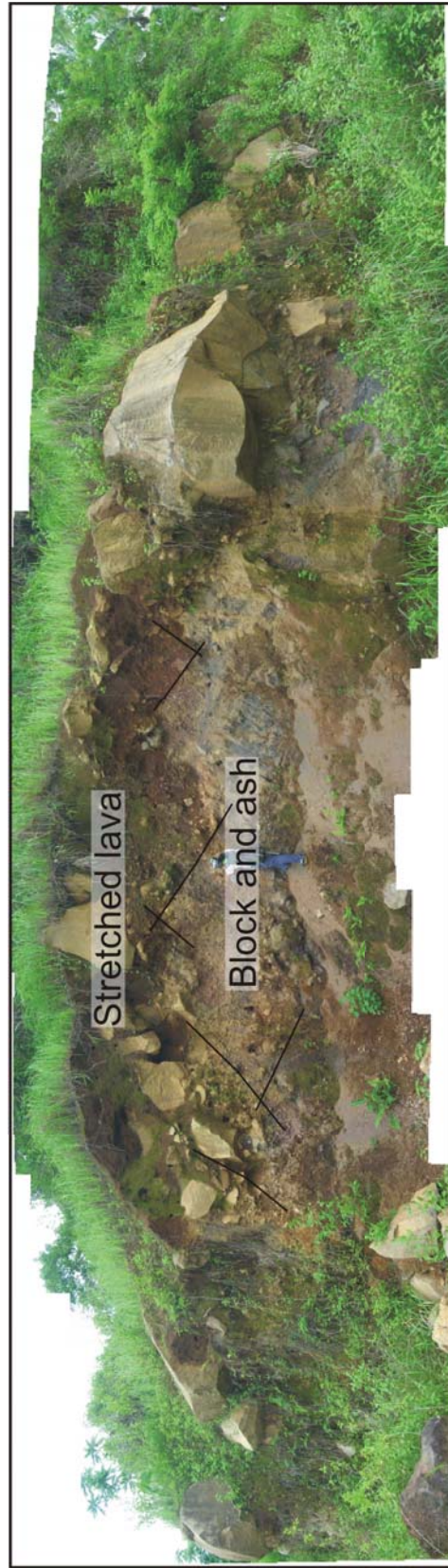


Figure 4.6: The Lava Topping hummock (lower collapse zone, DAD1) shows a coherent interface between the stretched lavas on top and faulted block and ash layer below. These low angle normal faults in black polylines in the block and ash layer accommodated the relative movement of the lavas on top. Here, the stretched lava is considered as a Type 2 hummock floating on top of the block and ash layer.

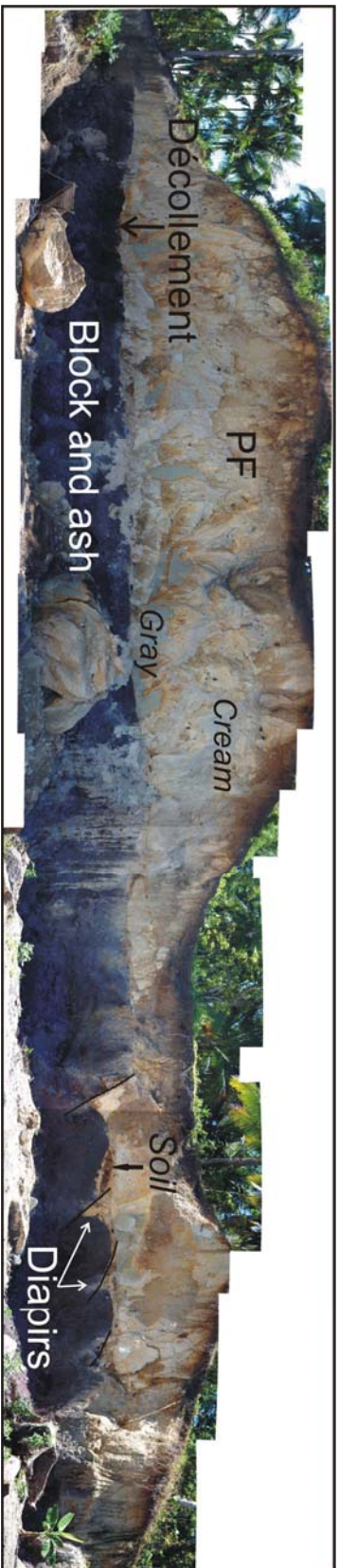


Figure 4.7: The ignimbrite Topping hummock (medial depositional zone, DAD2) shows an incoherent interface between the upper pyroclastic flow deposit layer and the underlying block and ash layer. Extension is by the sliding movement of the overlying deposit. The overlying ignimbrite layer is a Type 2 hummock gliding over the block and ash layer of the DAD during the avalanche.

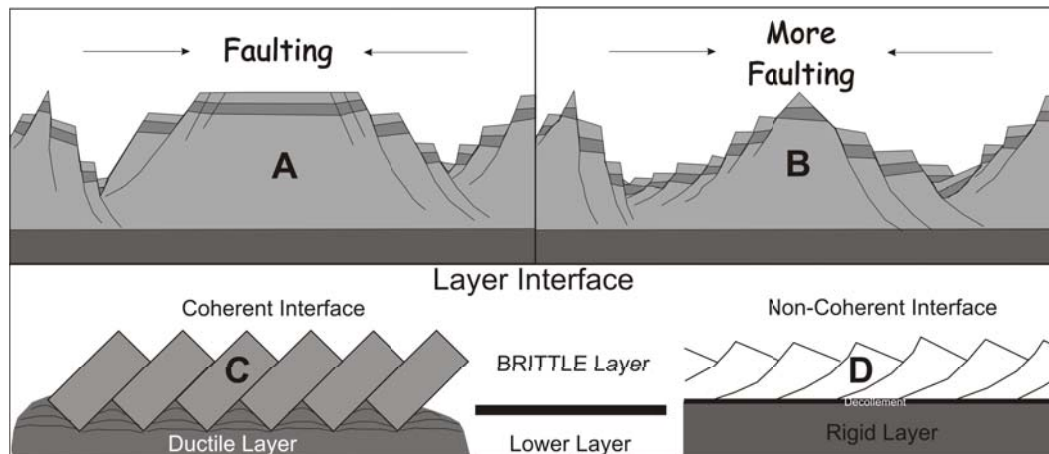


Figure 4.8: The Anatomy of a Hummock. **A** (Case 1, The Lady Backhoe Hummock) and **B** (Case 2, The Captain's Slide Hummock) shows how hummocks evolve from bigger blocks into smaller hummocks and how a primary hummock can be destabilised by increasing fault density and extension during sliding and spreading. **C** (Case 3, The Lava Topping Hummock) and **D** (Case 4, The ignimbrite Topping Hummock) show the types of interface that may exist between the layer boundaries. So far, we only know that non-coherent interface exists in the avalanche (as shown by Hummock 1: The Lady Backhoe) but both can exist for the boundary between a Type 1a or 1b hummocks and a Type 2 hummock (as shown by Hummocks 3 and 4: The Lava Topping and The ignimbrite Topping).

avalanches. Its elongation is dependent on whether there is a uniform extensional forces acting on the hummocks, forming the more rounded-based hummocks such as in Buhi DAD2 or if an avalanche extension is slower in one direction probably by waning extension or compression, and a stronger and lubricated extension on the other direction resulting in elongated hummocks such as in Iriga DAD1.

## 4.6 Conclusions

In conclusion, the internal structures that accommodate the sliding, tilting, and rotation of edifice blocks in avalanches are the same subsurface structures in hummocks only at a more localized level. The normal faults in the hummocks, like in the avalanche are high angle in the upper brittle layer that broadens into shear zone towards the base. They become less steeply dipping from the centre of the hummock towards the edges. If extension is strong

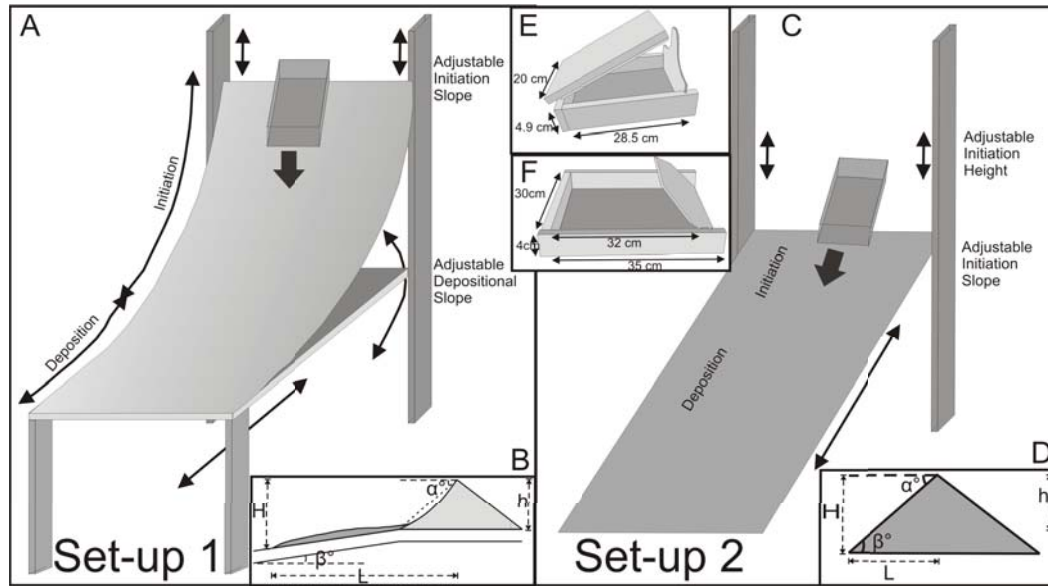


Figure 5.1: Analogue slides set-up. A, B Curved Ramp configuration for Set 1: the initiation and deposition slopes can be varied. C, D Inclined Straight Ramp configuration for Set 2: both the initiation,  $\alpha$  and deposition slopes,  $\beta$  can be changed with height of initiation. E Source Box 1 with a simpler geometry. F Source Box 2 with inclined trapdoor and open lid.

models for a long time (Merle and Borgia, 1996; Shea and van Wyk de Vries, 2008).

### 5.3 Model Set-up

Models must represent the failure, transport, and emplacement plane. Failure occurs on a surface slope that is above or equal to the basal friction angle of the sliding material. The dynamics of the natural basal layer is still not completely understood and is simulated by a low-friction surface of the polished steep ramp.

This study uses the experimental set-up of Shea and van Wyk de Vries (2008) built with flexible 2 mm thick, 150 cm wide, and 300 cm long aluminium sheet (Fig. 5.1). In contrast to the pure sand used previously, we use powder-size ( $< 100 \mu\text{m}$ ) and coloured sand-size spherical glass beads for Set 1 and Set 2, respectively. Unlike sand, this material is sensitive to several factors such as electrostatic interactions and humidity, which introduce a small cohesion and allow for the formation of surface fault scarps. The aluminium sheet has relatively low basal friction angle and does not induce electrostatic interactions

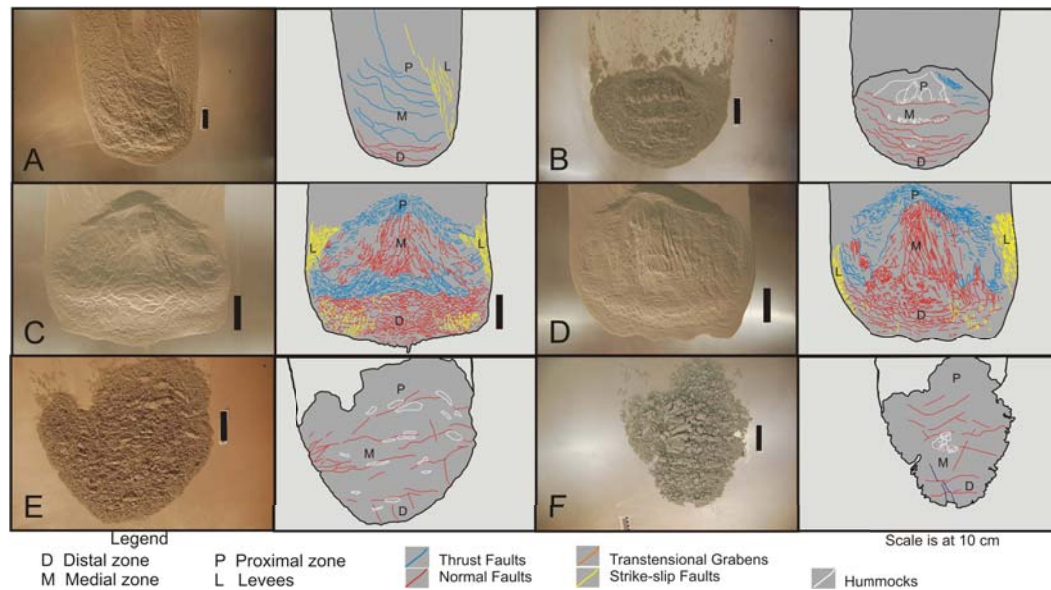


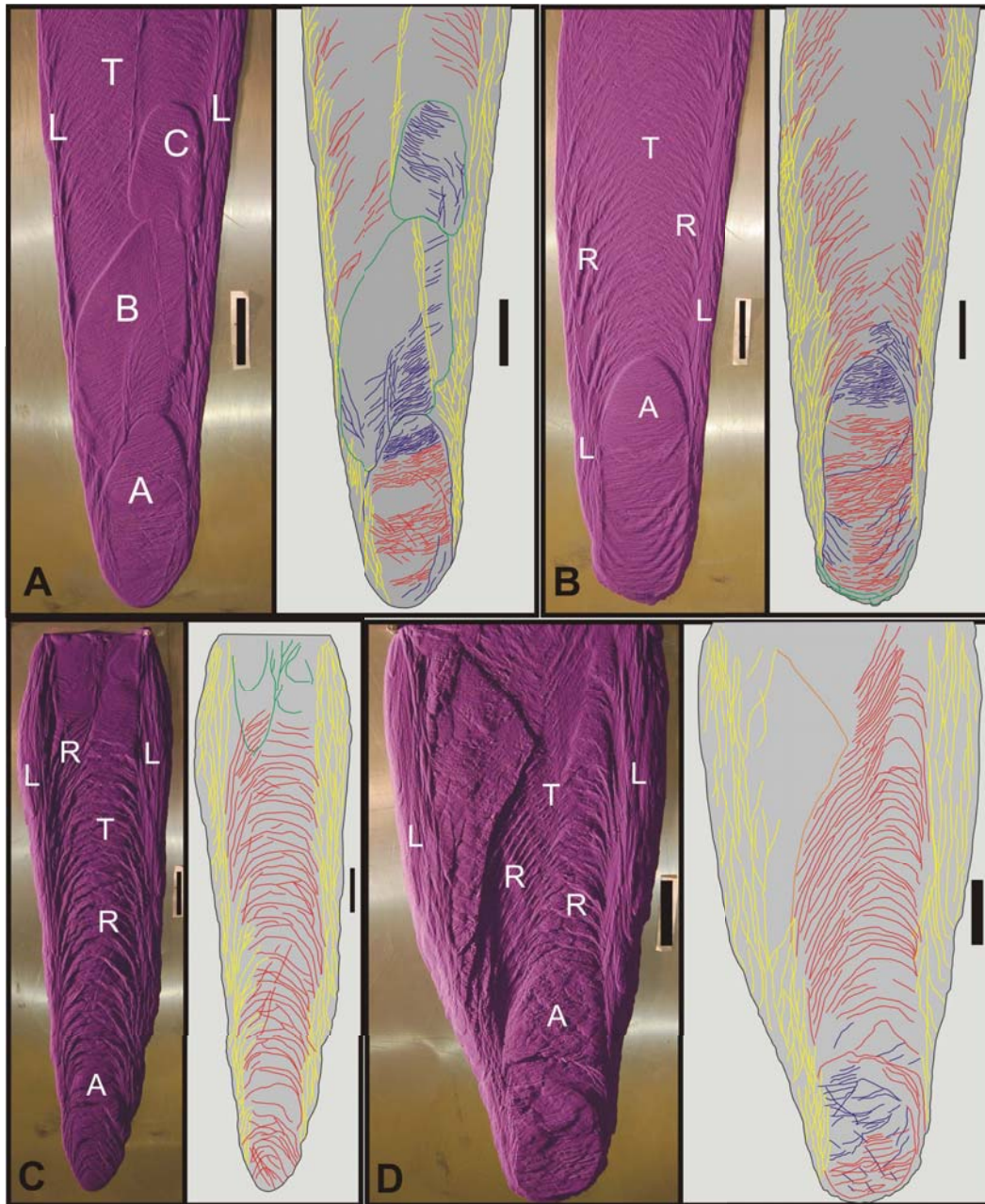
Figure 5.2: Set 1: Curved ramp analogue avalanches using the powder-size glass beads. Source slopes are at 35°, 45°, and 55°; deposition slopes are at 0°, 10°, and 18°; and volume of glass beads at 1000 and 2000 cm<sup>3</sup>

with the sliding material, replicating the equivalent of highly deformed simple shear basal layer in a plug-flow-type configuration (Shea and van Wyk de Vries, 2008).

There are two sets of analogue slides: Set 1 is on a curved ramp (Fig. 5.2, Appendix D) where materials accelerate until they reach a gently sloped depositional surface; and Set 2 on constantly inclined straight ramp (Fig. 5.3, Appendix D) with a more regular slope. Two source boxes of different volumes and dimensions are used: Box 1 (Fig. 5.1E) of simple geometry for better tracking of deformation with straight trapdoor and a compressive lid tightly closed and tied to the lower part, and Box 2 (Fig. 5.1F) with inclined trapdoor and open lid.

## 5.4 Scaling

Geometric and dynamic parameters must be scaled to guarantee maximum similarity between reality and laboratory analogue models. This allows determination of the conditions necessary to ensure proportional correspondence between forces acting in nature and those acting in laboratory environment (Ramberg, 1981). Accordingly, 12 dimensionless numbers serve to compare dynamic and geometric features in both nature and laboratory.



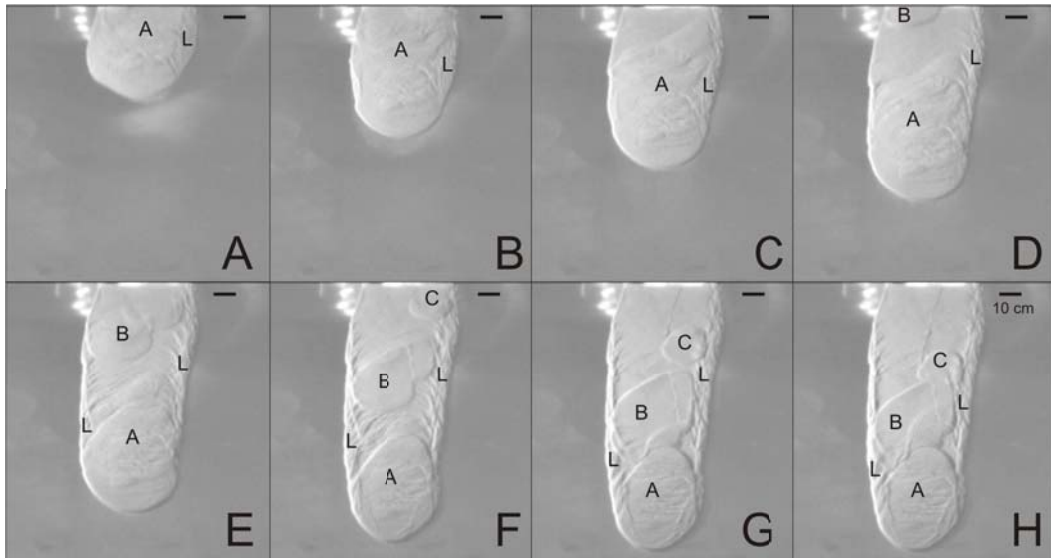


Figure 5.4: Evolution of morphology and development of structures in relatively thinner avalanche deposit showing the formation of an accumulation zone at the distal margin while leaving behind a translation zone in the proximal and medial depositional areas. During release, the materials had a retrogressive discharge as indicated by the pulses. The following is the sequence of structure development for this experiment: A First pulse of materials leave a thick sheet of deposit (A) with radiating structures, strike slip faults formed as the materials are spreading. B Materials continue to slide forming levees (L) with a many strike-slip faults. C Materials spread mostly downwards and to the lateral sides. Oblique strike-slip faults form in the levees. D The sliding of materials towards the front and the pushing of materials at the back causes compressive structures in the middle of the depositional area. Normal faults accommodate sliding in the medial area forming an accumulation zone (A) in the distal part. Meanwhile, a new pulse of material starts to slide (B). E The relatively slower movement of materials at the front than at the middle and back results in an accumulation of materials in the front lobe, now forming its head. As the bulk of deposit is being transported down, movement of the strike-slip with normal movement in the medial area leaves a thin layer of material behind while thrusting materials at the rear portion of the distal head. The new materials from the second pulse (B) also masks previously emplaced deposits in the proximal area. F The distal head slides more slowly, while second pulse materials slides faster by the reduced friction provided by the earlier emplaced material on its base. This results in increased compression between the two lobes. At this point, a third pulse of materials starts to slide down (C). (*continued on next page*)

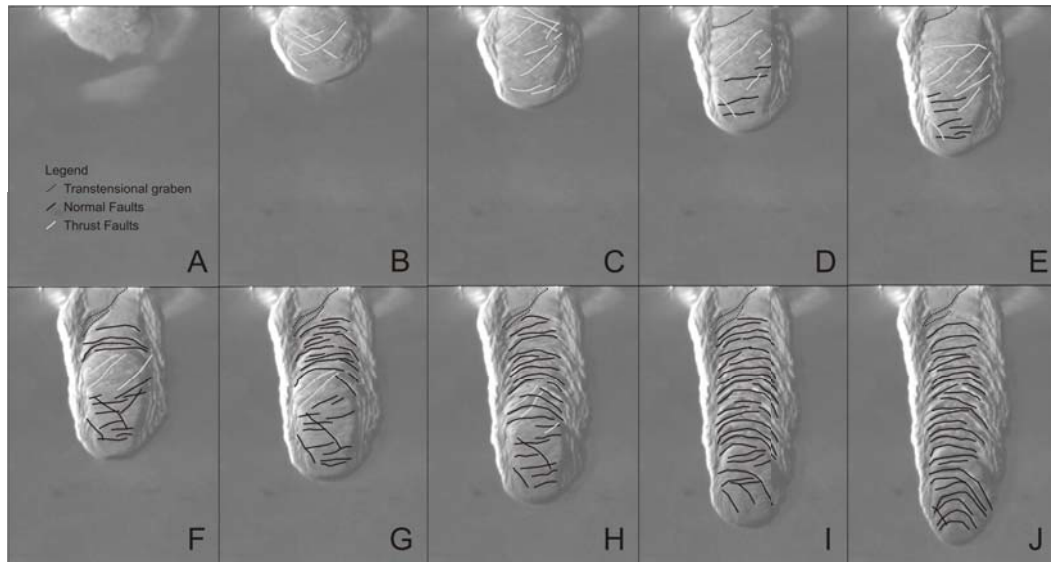
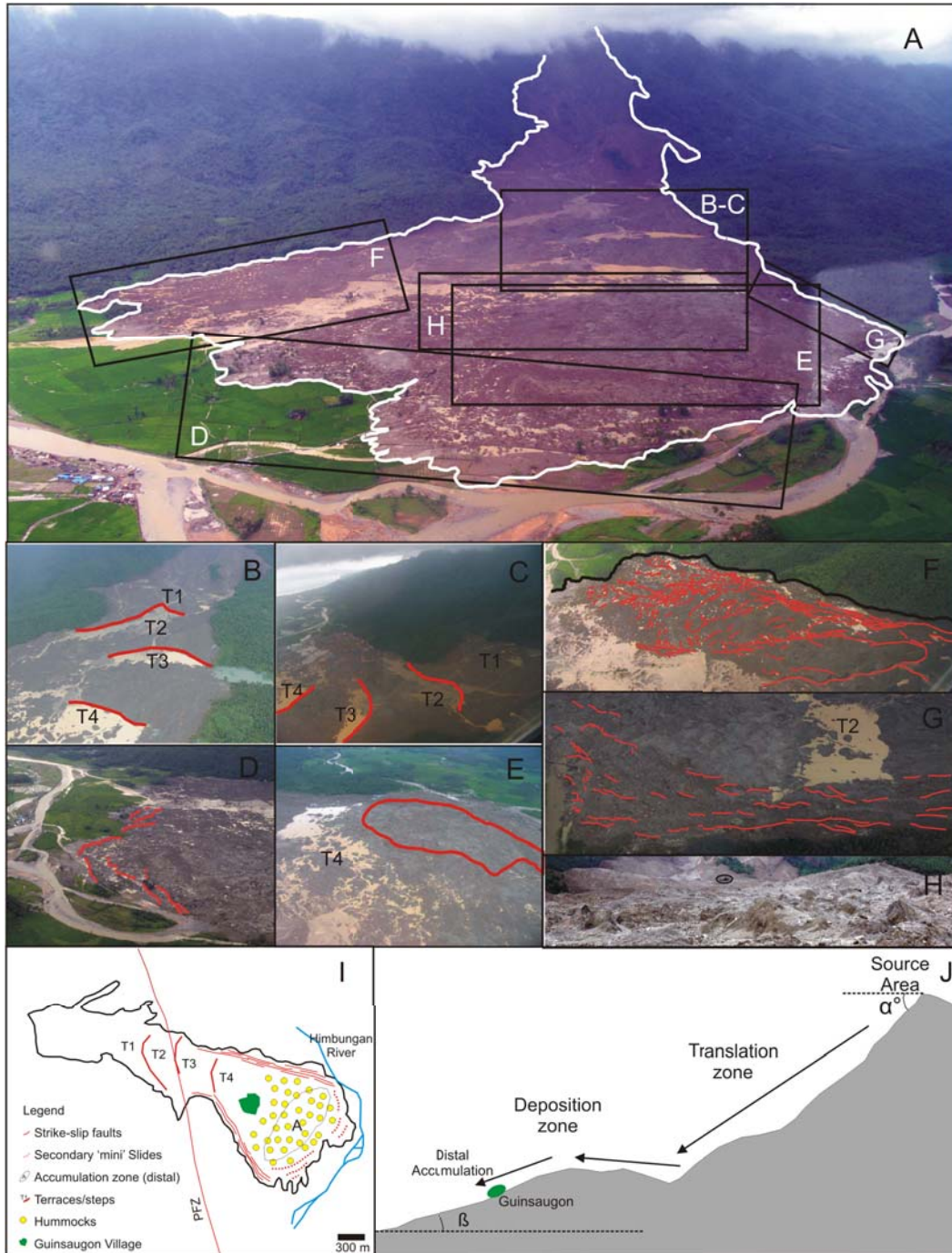
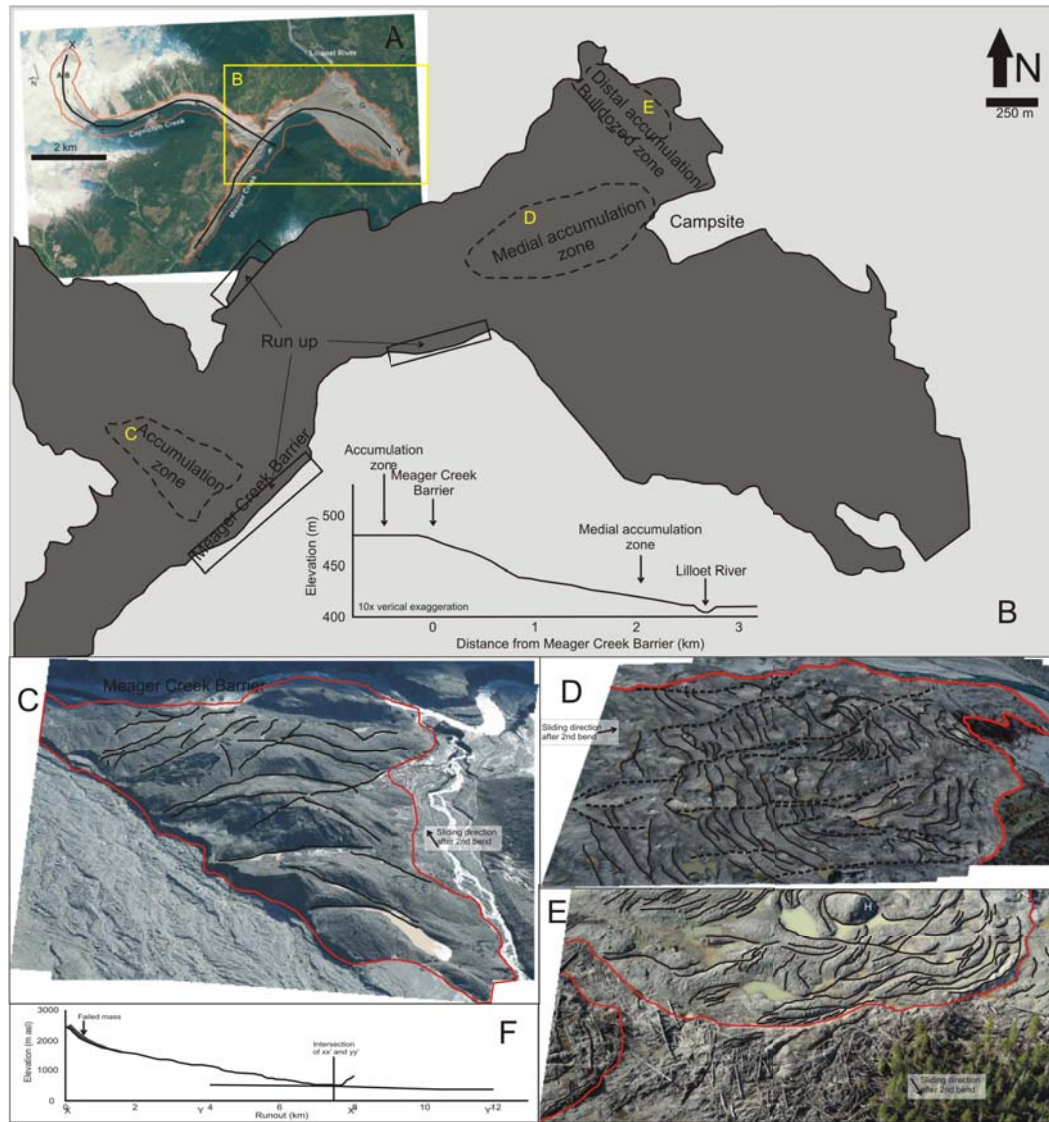
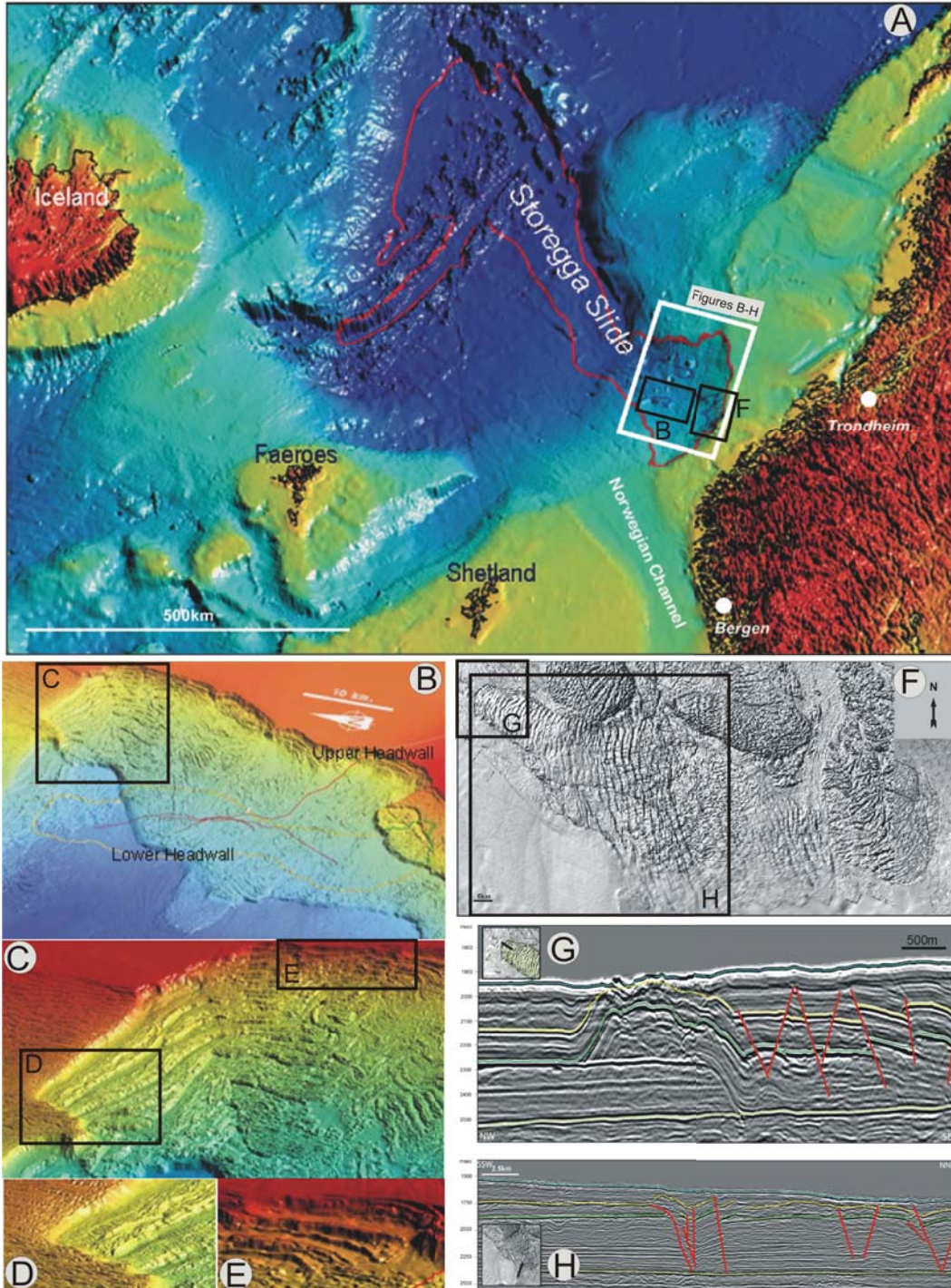


Figure 5.5: Evolution of morphology and development of structures in relatively thicker avalanche deposit. After being released out of the source box, material spreads into a uniformly thick deposit until longitudinal spreading wanes and eventually stops. The evolution and progression of structures is as follows: A After initiation, materials slid forming a lobe at the front. More materials are in the central where there is limited spreading capacity of the materials than at the sides and front. B Compression from the fast-moving rear materials form the oblique structures. Levees (on both lateral sides) with strike slip faults start to form that will remain stable until the end. C More materials slid out of the box resulting in more strike slip faults on both levees. To accommodate the Compression from the rear and shearing at the levees, create oblique structures (thrust faults) in the main body of the slide while the front lobe continuously slides and spreads deposits downward. D A more developed compression structures appears in the main body while normal faults add more extension and spreading at the distal area of the deposit slide. A normal faults that will open up and create a transtensional graben is initiated. E The whole deposit continuous to slide. Just below where the transtensional graben is initiated, continues sliding compresses more materials in the medial area (M) resulting in more thrust faults. More normal faults also develop in the distal area to accommodate spreading of materials downward. *(Continued on the next page)*







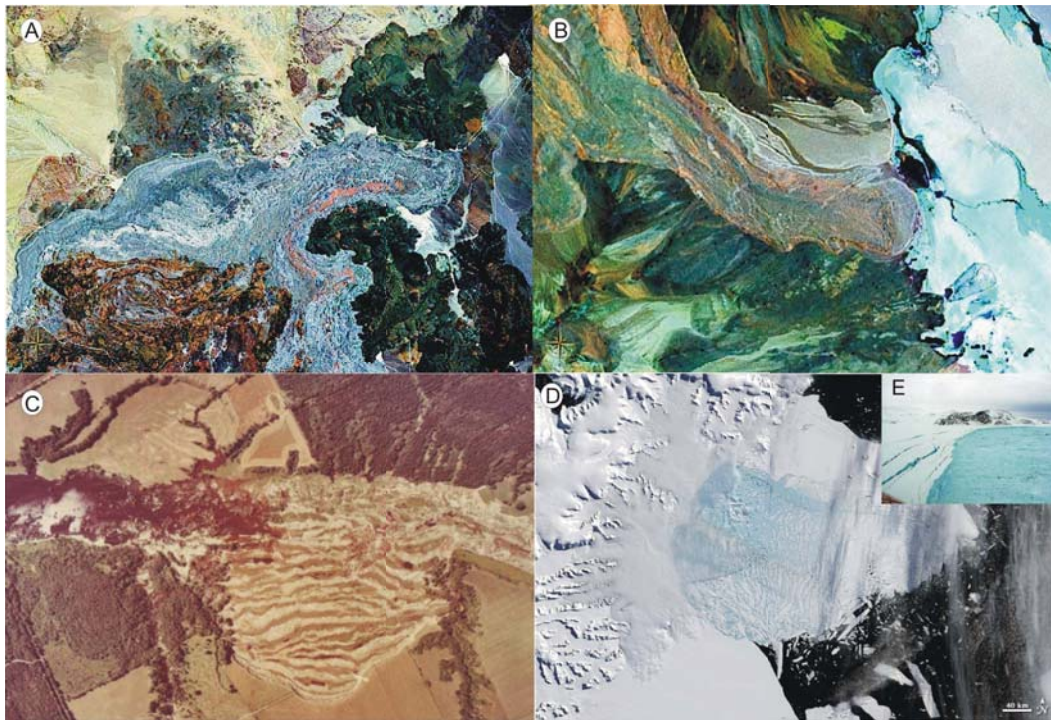


Figure 5.9: Natural examples of the tongue-like long runout deposits and rib-and-ridge morphology formed on a smooth and straight failure surface. Tongue-like long runout deposits at A Llullaillaco southern avalanche and B Socompa rockslide-debris avalanche, and the rib-and-ridge morphology of the C South Nation River slide (Quinn et al. 2011) and D Larsen ice shelf in Antarctica (Quinn et al. 2007). Inset in E is a closer view of the faults that accommodate the breaking and disintegration of the ice shelf.

down. The deposit thus reflects the evolution of the slide. Slides and avalanches on curved ramps (Set 1) and the Guinsaigon rockslide-debris avalanche deposit result into fan-shaped deposits with displacement of coherent blocks creating terraces or steps, and hummocks. Materials start to accumulate at the base of the initiation zone and thicken where the slope decreases (depositional zone) forming the medial accumulation zone. Frontal accumulation during flow occurs as materials at the front move slower relative to those in the medial and proximal zones. This helps maintain a thicker mass that can be remobilised by secondary sliding.

Incoherent and monolithologic materials on a smooth and straight failure surface (Set 2) experiments and the Storegga slide can form the tongue-like longer runouts with rib-and-ridge morphology. The stability of the proximal and instability of the distal sides of the block form transtensional grabens.



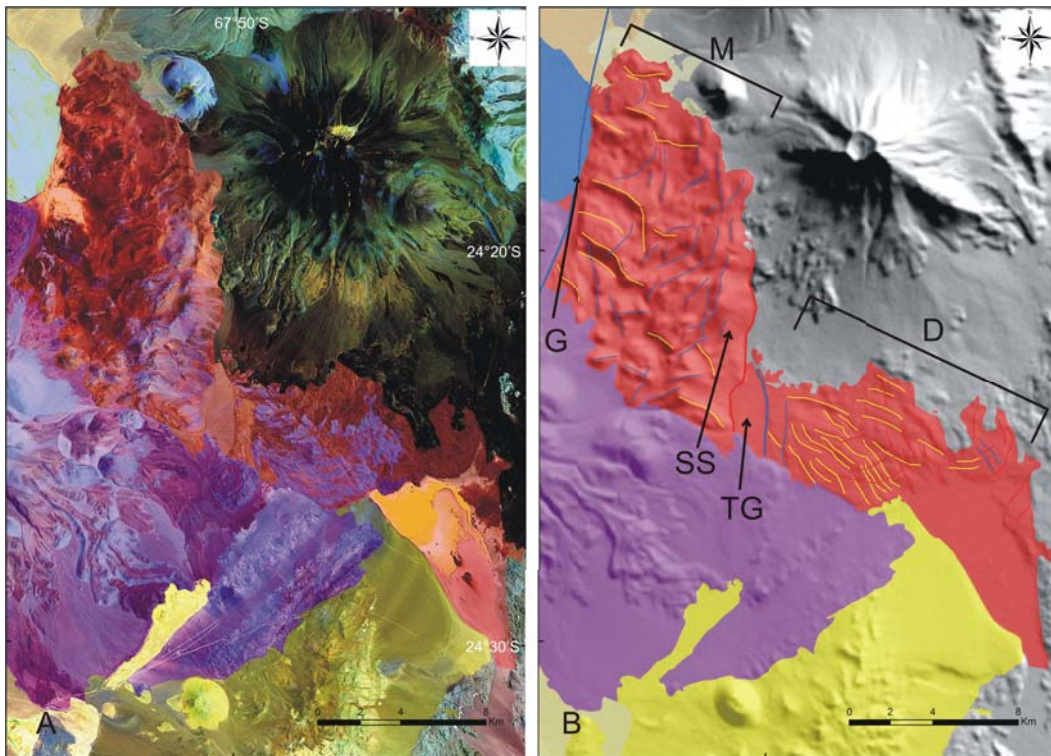
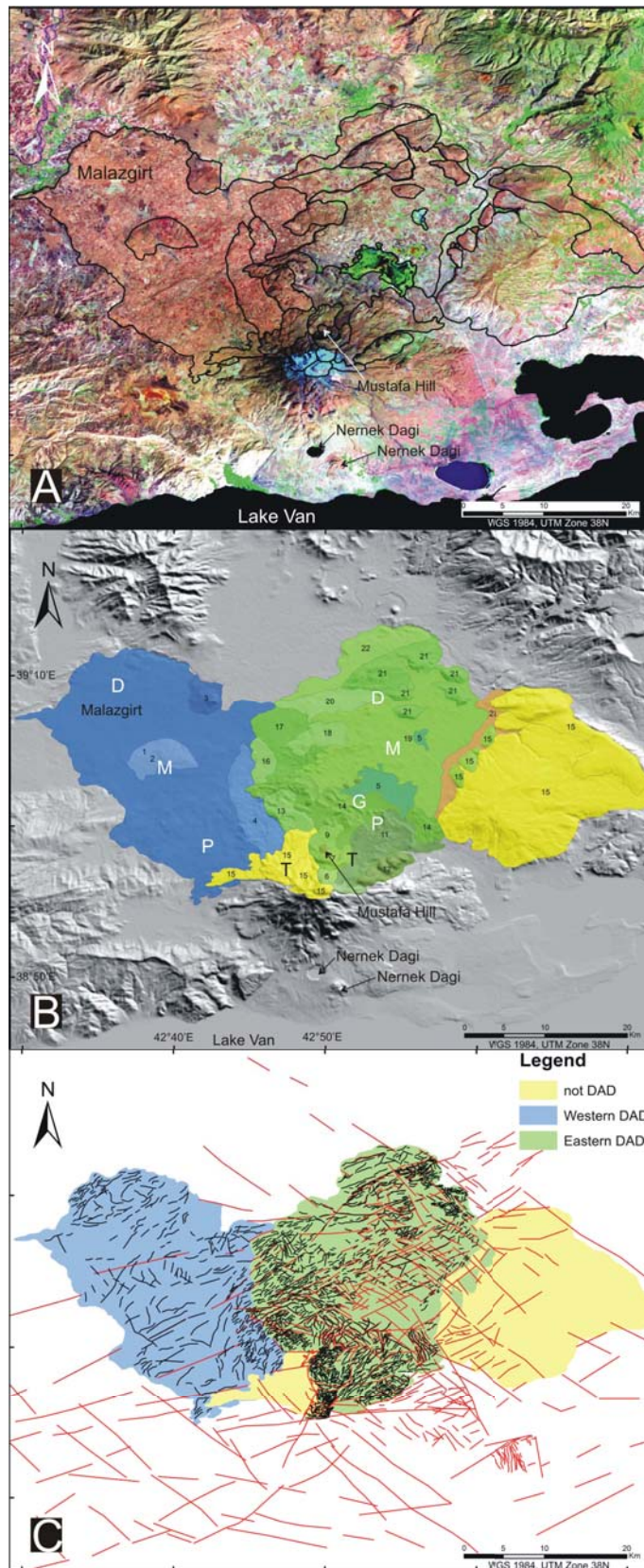


Figure 6.2: Cerro Pular-Pajonales DAD. **A** Landsat ETM+ image of the DAD (in red), showing the hummocky topography in the medial part (upper, left-closer from source) and the smoother, thinner deposit in the distal zone (lower, right-farther from source). **B** DAD draped on a DEM. Structures including the normal (red), thrust (blue), and strike-slip faults (yellow), and the graben (G), secondary slide (SS) and transtensional graben (TG) are drawn.

All geologic and morphologic features and structures such as lava flow and deposits with different spectral signatures and surface textures from its adjacent areas are delineated (Fig. 6.1C). These features are then grouped according to the nearest source area for volcanic deposits (Fig. 6.1B-C). Those left with unique surface texture, morphology and structures similar to those of the natural and analogue DAD are identified to be part of the DAD (red polygon in Fig. 6.1-6.2).

### 6.5.1.1 Geometry of the DAD

For organization of detailed description, the 50-km long Cerro Pular-Pajonales DAD is divided into three zones: the proximal (P), medial (M), and distal (D) areas. Based on the more recent deposits from the surrounding volcanic



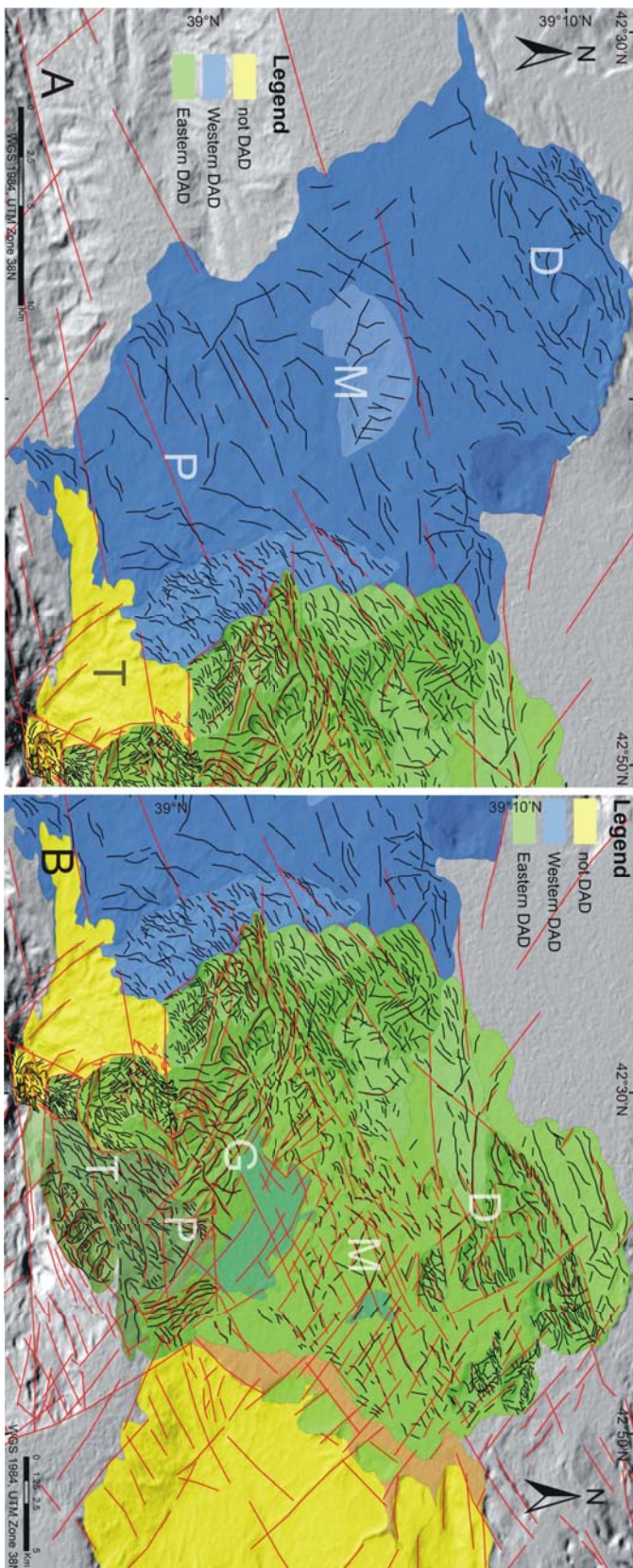


Figure 6.4: The two DAD of Süphan Dağı: **A** the western and **B** eastern DAD. Regional structures (red lines) and the localised faults (black lines), and the translation (T), proximal (P), medial (M) and distal (D) depositional areas are also shown.

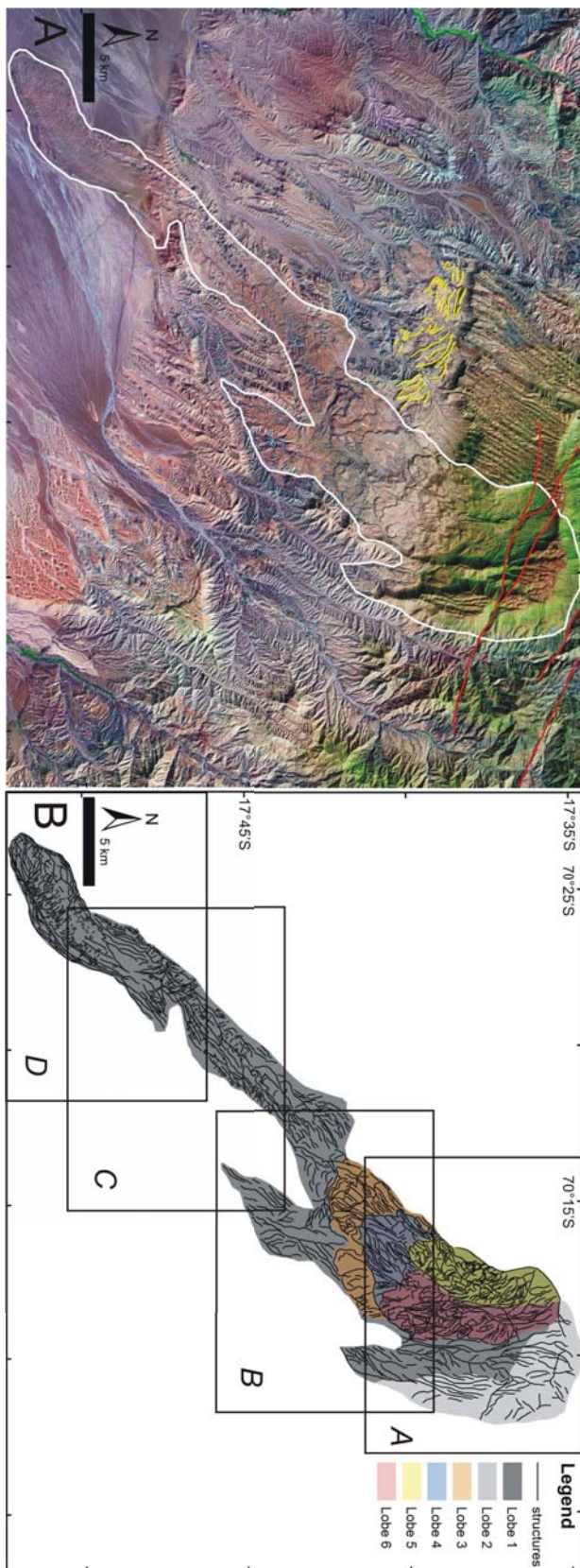


Figure 6.5: The Tacna DAD. **A** Landsat ETM+ image drawn with the extent of the large landslide. **B** shows the lobe traces and the structures for this DAD. Drawn in squares are the source area (**A**), the proximal zone (**B**), the medial zone (**C**), and the distal zone (**D**) presented in more detail in Figure 6.6.

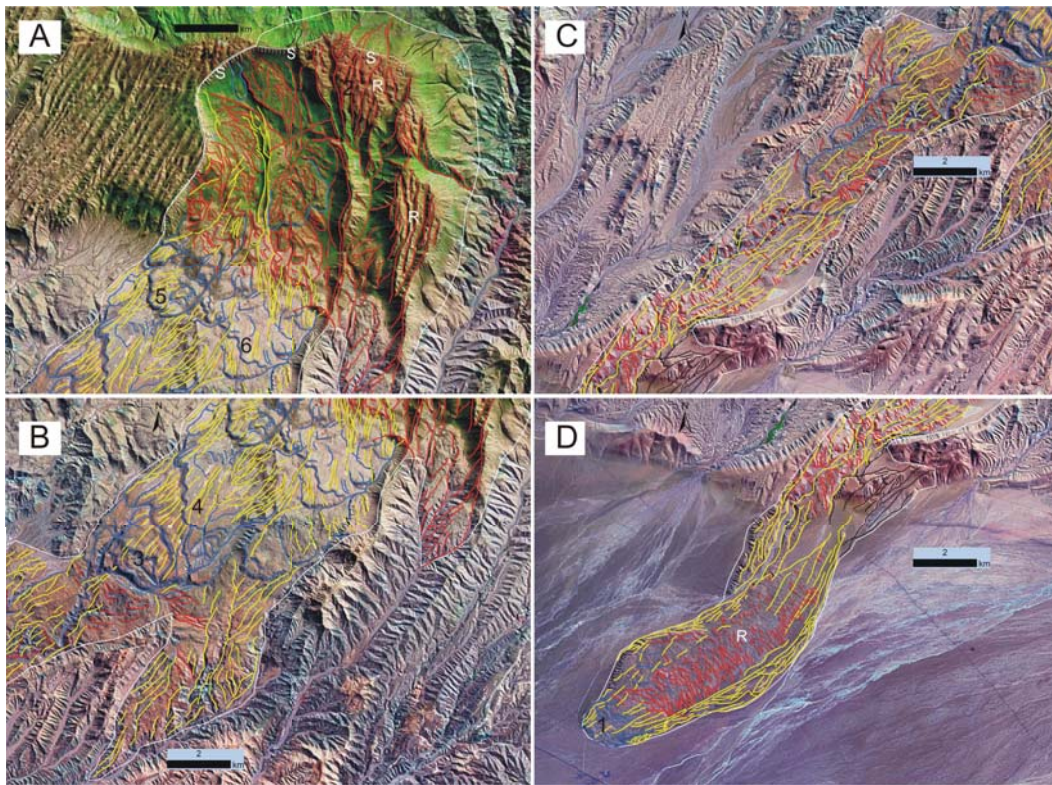


Figure 6.6: Areas in detail for the Tacna DAD. **A** The source region: shows the collapse scar (S) and the normal (red lines) and strike-slip (yellow) faults in the translation zone, the thrust faults (blue lines) that serve as the boundary of the overlying lobes (5) and (6), and the repeating ridges drawn as normal faults that form the rib-ridge morphology (R) of lobe (2); **B** The Proximal zone: also shows the normal, strike-slip and thrust faults bounding lobes (3) and (4); **C** The medial zone showing the same set of faults; and **D** The distal zone, which also forms the head of the long runout slide marked as lobe (1) that shows the same set of faults with strike-slip faults forming its levees and an addition of a set of en-echelon set of fractures that may indicate strike-slip extensional faulting, and the repeating short ridges that are perpendicular to transport direction and form the rib-ridge morphology.

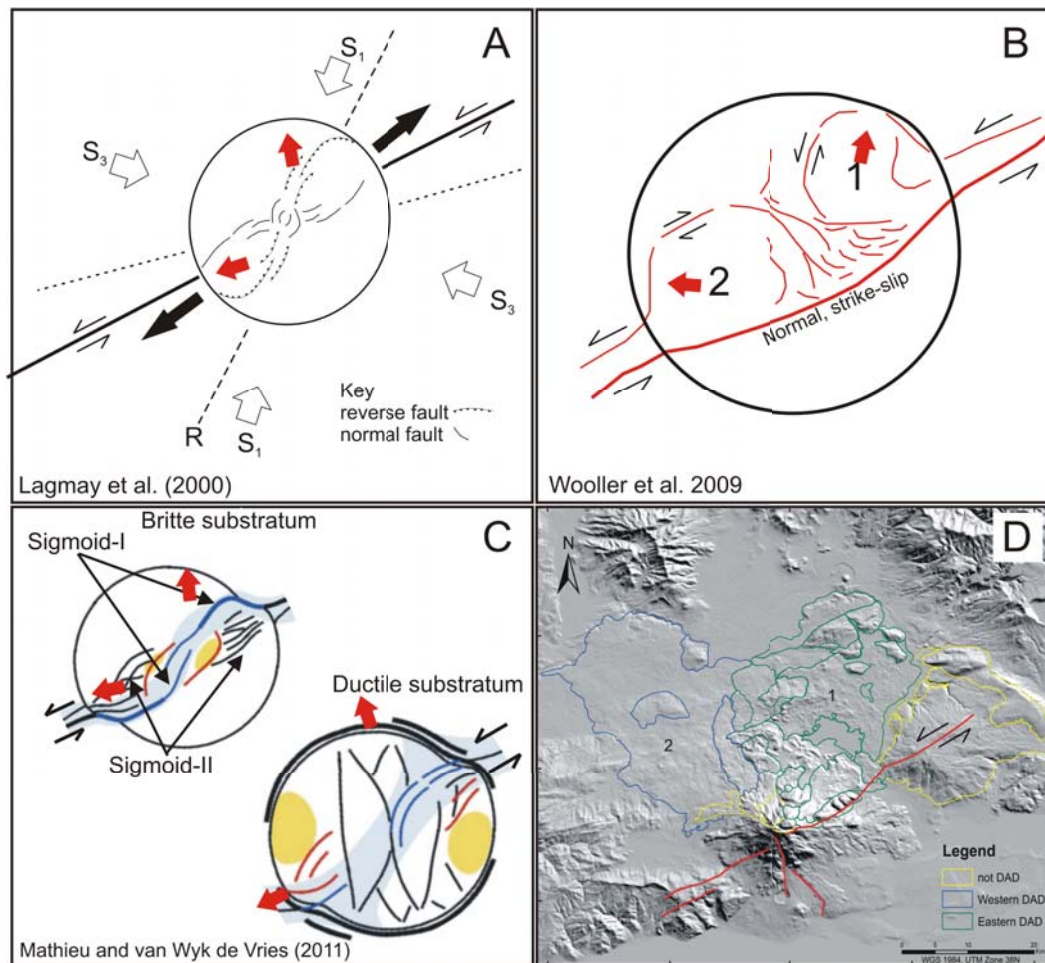


Figure 6.7: Structures of Süphan Dağı as compared to the analogue models. **A** Structures from the analogue model for cones overlying sinistral strike-slip faults by [Lagmay et al. \(2000\)](#). **B** Summary sketch of transtensional deformation of about  $75^\circ$  of obliquity in analogue models from [Wooller et al. \(2009\)](#) with predicted collapse order that is matched by Süphan Dağı. **C** Morphology and strike of structures in left-lateral strike-slip experiments by [Mathieu and van Wyk de Vries \(2011\)](#) showing the locations of the Sigmoid-I faults that curve at the summit of the cone and Sigmoid-II in the upper cone. Figure at the lower left with flower structures in the northern and southern flanks is a cone with the addition of a ductile layer. **D** The structural pattern on the flank of Süphan Dağı are similar to those outlined in (A), (B) and (C) suggesting that a strike slip with dip movement may have led to an instability, and subsequent collapses. The red arrows indicate direction of Mt Iriga collapses.

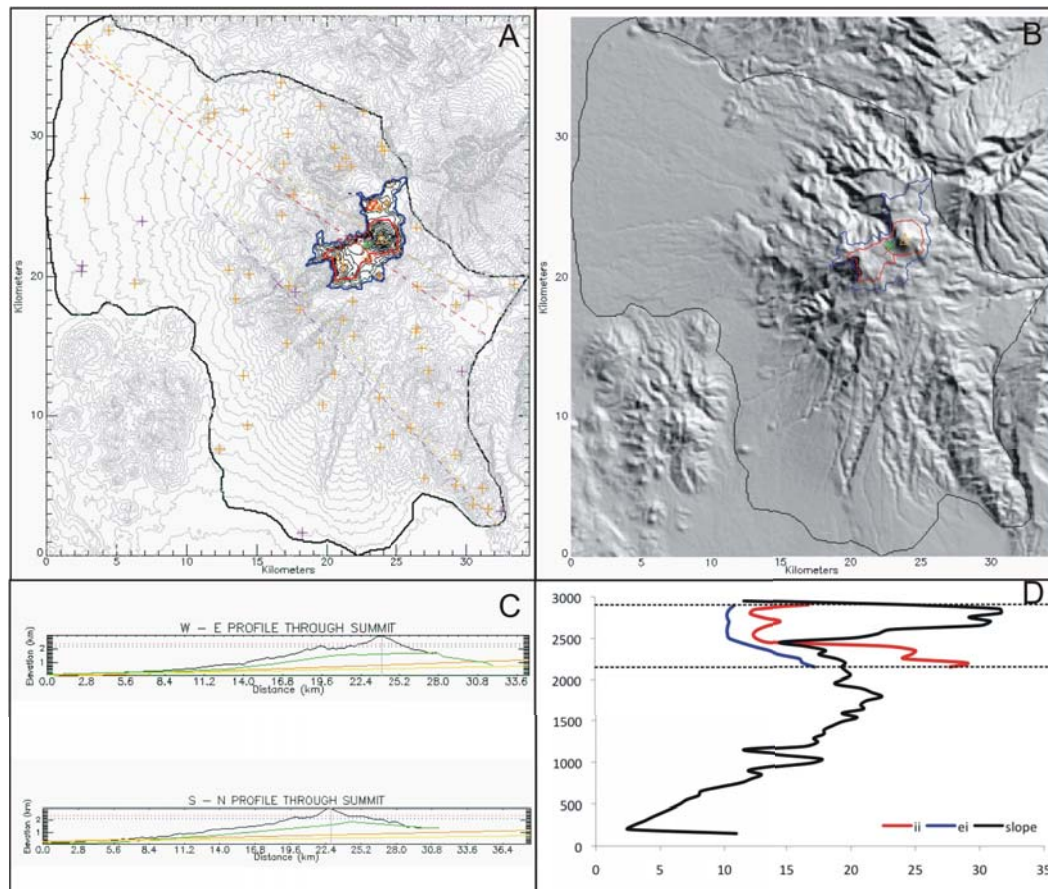


Figure A.1: Apo

Status:	Potentially Active Volcano
Morphometry Type:	Breached edifice
Location (Lat, Long):	6.9874294, 125.27085
Elevation (min, max):	109-2928 m
Basal Area:	765.5 km <sup>2</sup>
Height:	2819 m
Volume:	549 km <sup>3</sup>
Profile shape (height/ base width, summit width/base width):	0.07, 0.12
Slope:	0°-56.13°
Base orientation in azimuth (through the summit, through the base centre):	122°, 137°

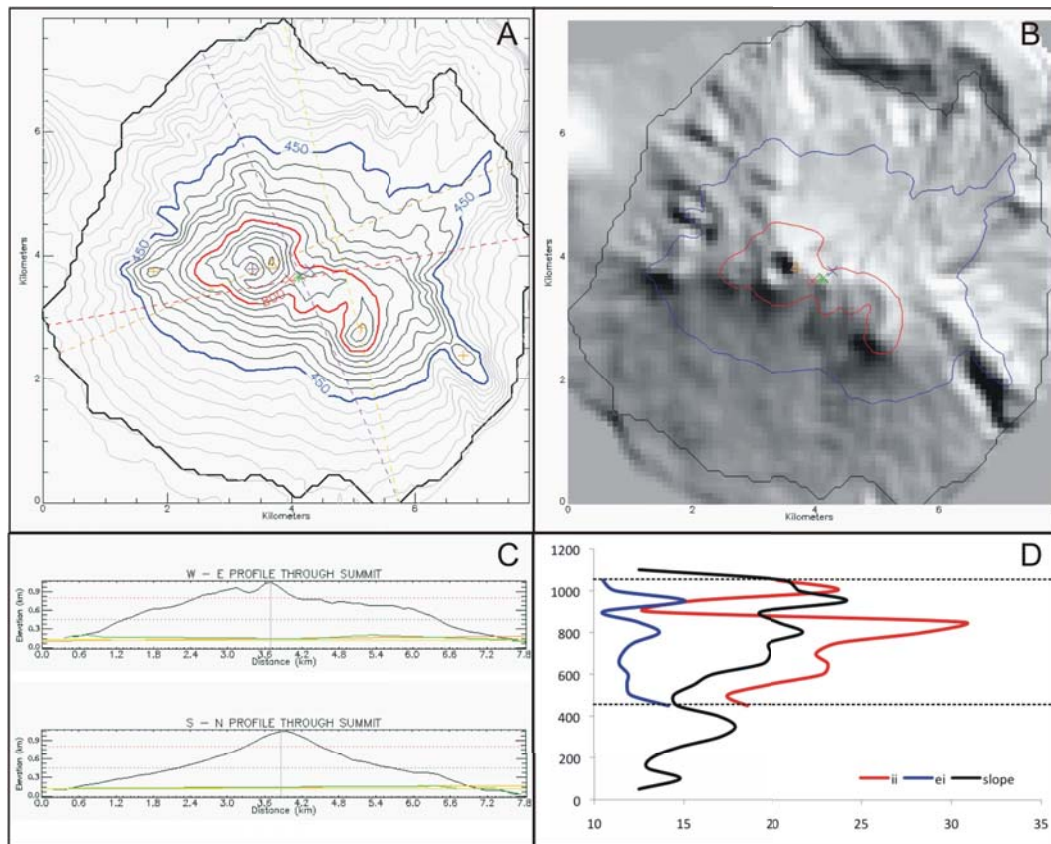


Figure A.2: Babuyan Claro

Status:	Active Volcano
Morphometry Type:	Sub-cone
Location (Lat, Long):	19.523999, 121.95234
Elevation (min, max):	109-1058 m
Basal Area:	43.4 km <sup>2</sup>
Height:	1058 m
Volume:	18 km <sup>3</sup>
Plan shape (ellipticity index, irregularity index):	2.2, 1.24
Profile shape (height/ base width, summit width/base width):	0.12, 0.25
Slope:	0°-50.71°
Base orientation in azimuth (through the summit, through the base centre):	67°, 156°

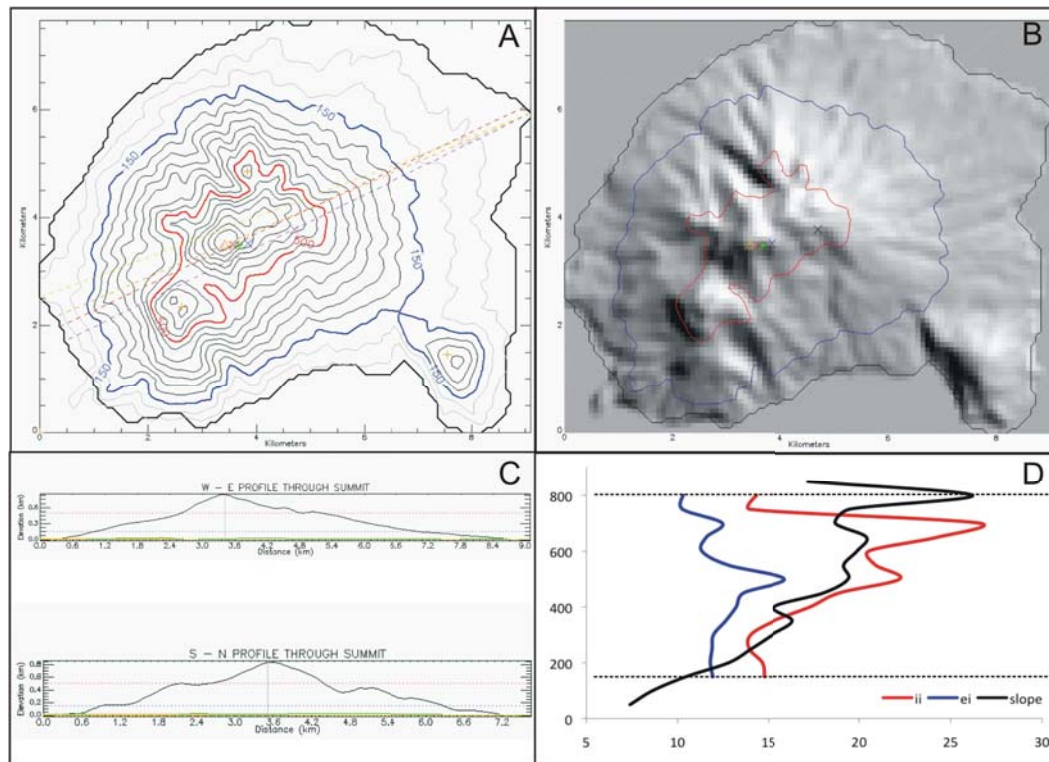


Figure A.3: Balut

Status:	Potentially Active Volcano
Morphometry Type:	Sub-cone
Location (Lat, Long):	5.3973815, 125.37608
Elevation (min, max):	0-837 m
Basal Area:	51.9 km <sup>2</sup>
Height:	837 m
Volume:	11 km <sup>3</sup>
Plan shape (ellipticity index, irregularity index):	1.64, 1.29
Profile shape (height/ base width, summit width/base width):	0.10, 0.32
Slope:	0°-39.21°
Base orientation in azimuth (through the summit, through the base centre):	66°, 63°

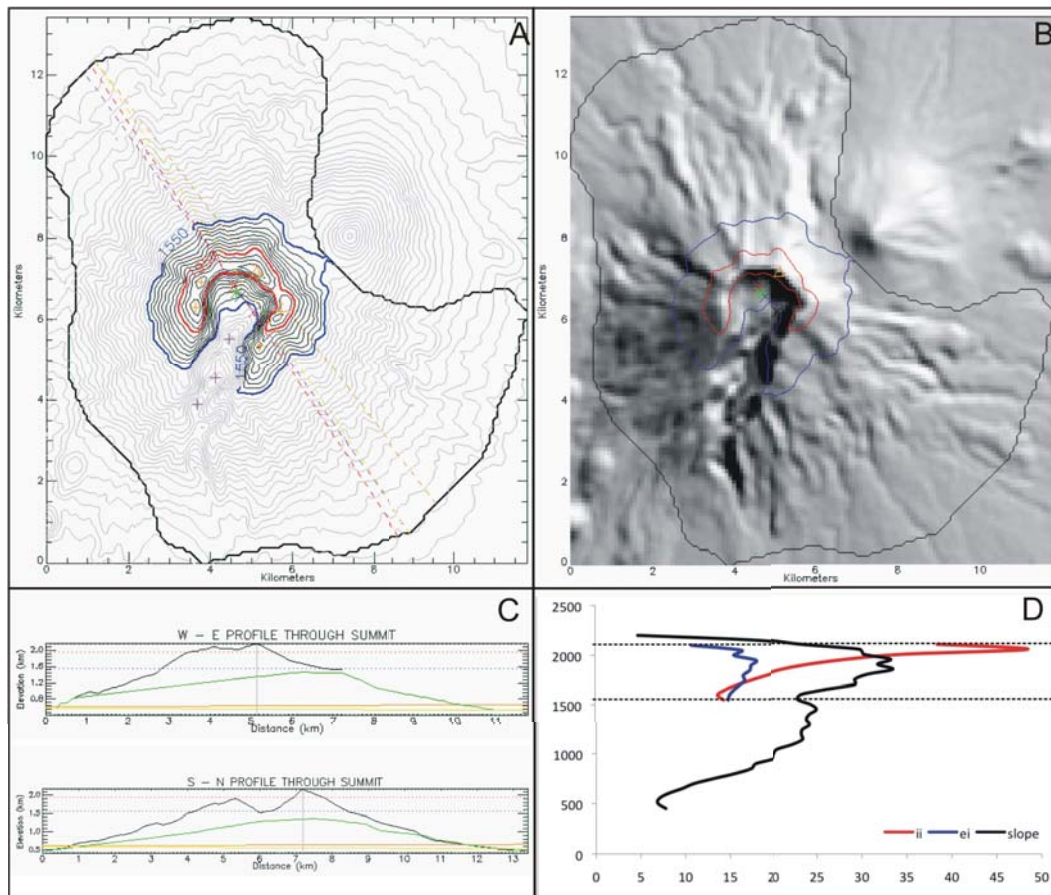


Figure A.4: Banahaw

Status:	Active Volcano
Morphometry Type:	Breached edifice
Location (Lat, Long):	14.067335, 121.4918
Elevation (min, max):	424-2150 m
Basal Area:	97.4 km <sup>2</sup>
Height:	1726 m
Volume:	55 km <sup>3</sup>
Plan shape (ellipticity index, irregularity index):	1.87, 1.64
Profile shape (height/ base width, summit width/base width):	0.14, 0.15
Slope:	0.86°-59.78°
Base orientation in azimuth (through the summit, through the base centre):	142°, 144°

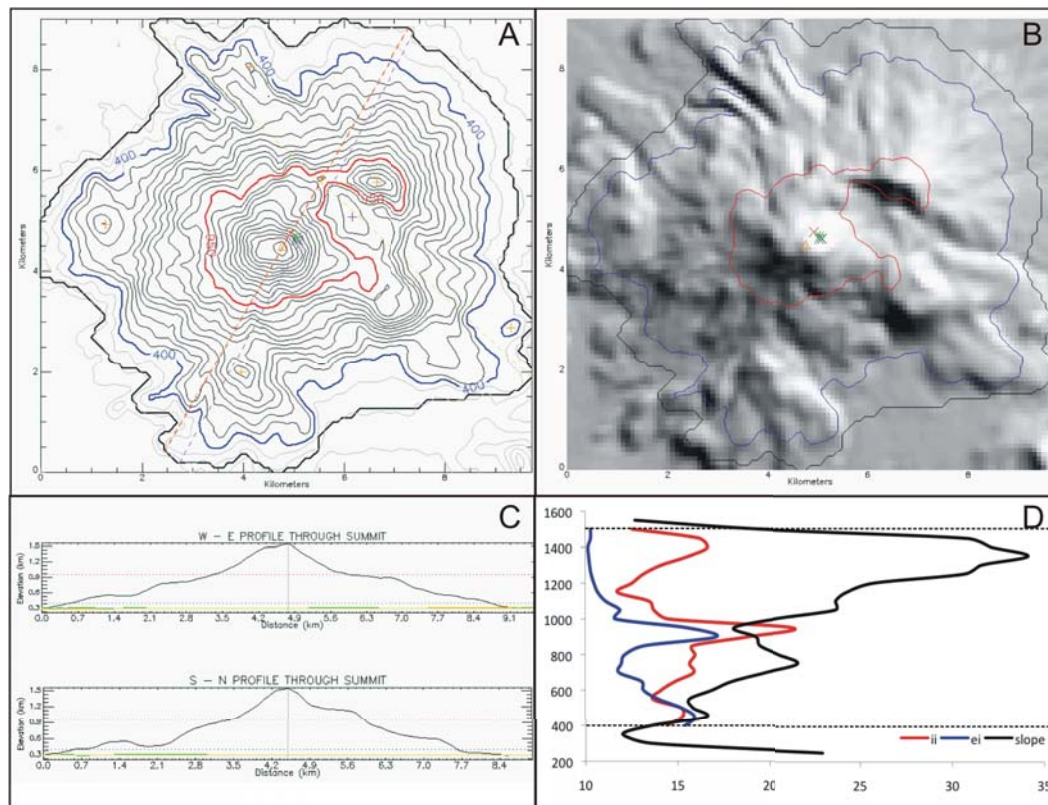


Figure A.5: Bulusan

Status:	Active Volcano
Morphometry Type:	Sub-cone
Location (Lat, Long):	12.768641, 124.05604
Elevation (min, max):	225-1537 m
Basal Area:	62.4 km <sup>2</sup>
Height:	1312 m
Volume:	24 km <sup>3</sup>
Plan shape (ellipticity index, irregularity index):	1.59, 1.41
Profile shape (height/ base width, summit width/base width):	0.14, 0.33
Slope:	0°-41.82°
Base orientation in azimuth (through the summit, through the base centre):	30°, 28°

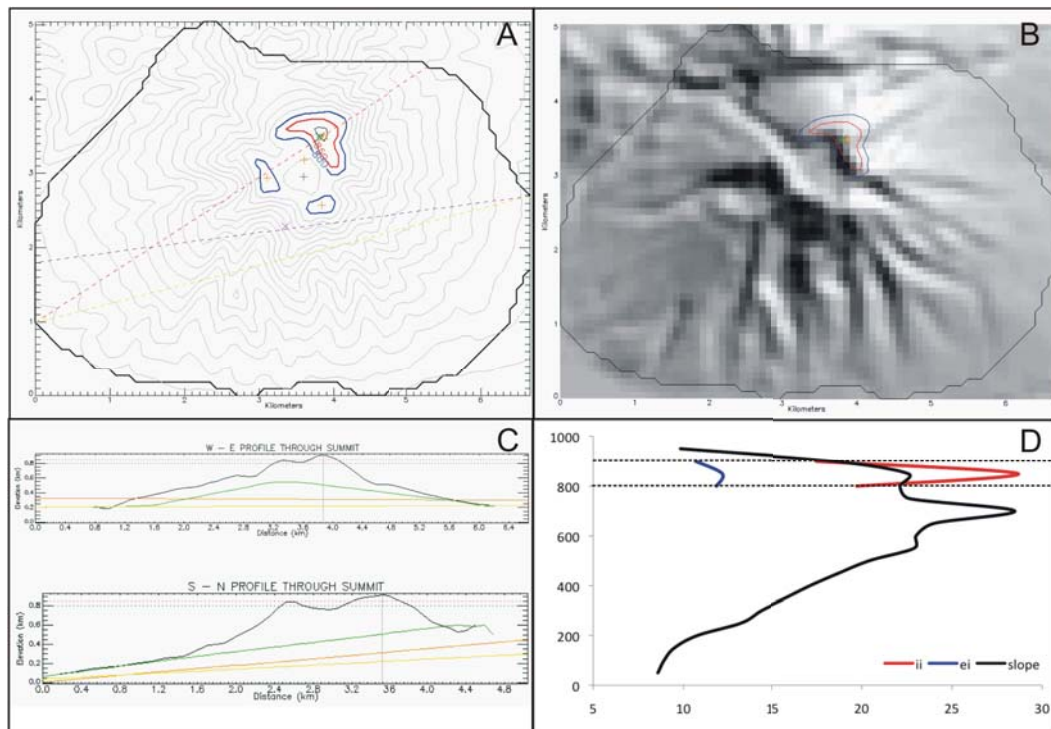


Figure A.6: Cabalian

Status:	Active Volcano
Morphometry Type:	Sub-cone
Location (Lat, Long):	10.284742, 125.21758
Elevation (min, max):	10-910 m
Basal Area:	25.8 km <sup>2</sup>
Height:	900 m
Volume:	9 km <sup>3</sup>
Profile shape (height/ base width, summit width/base width):	0.1, 0.09
Slope:	0.62°-40.63°
Base orientation in azimuth (through the summit, through the base centre):	56°, 82°

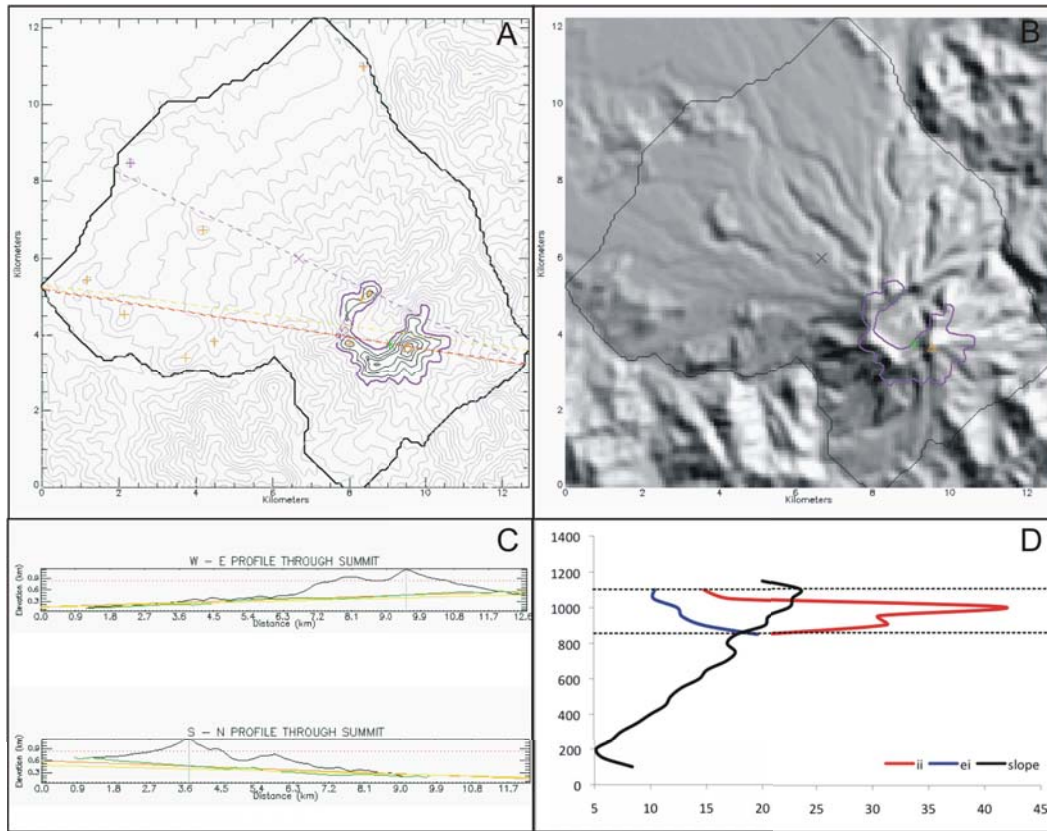


Figure A.7: Cagua

Status:	Active Volcano
Morphometry Type:	Cone
Location (Lat, Long):	18.215435, 122.1196
Elevation (min, max):	59-1141 m
Basal Area:	84.9 km <sup>2</sup>
Height:	1082 m
Volume:	31 km <sup>3</sup>
Profile shape (height/ base width, summit width/base width):	0.07, 0.2
Slope:	0°-39.63°
Base orientation in azimuth (through the summit, through the base centre):	99°, 115°

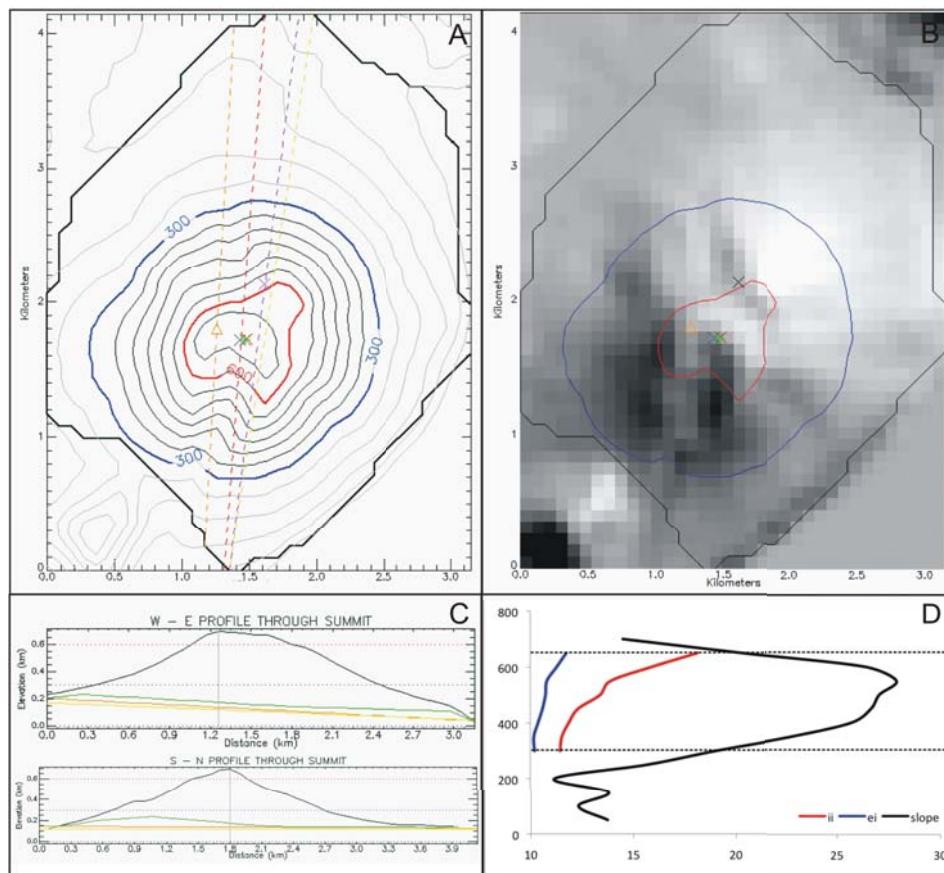


Figure A.8: Camiguin de Babuyanes

Status:	Active Volcano
Morphometry Type:	Cone
Location (Lat, Long):	18.832998, 121.86104
Elevation (min, max):	0-693 m
Basal Area:	9 km <sup>2</sup>
Height:	693 m
Volume:	3 km <sup>3</sup>
Plan shape (ellipticity index, irregularity index):	1.29, 1.06
Profile shape (height/ base width, summit width/base width):	0.16, 0.23
Slope:	0.15°-35.20°
Base orientation in azimuth (through the summit, through the base centre):	3°, 7°

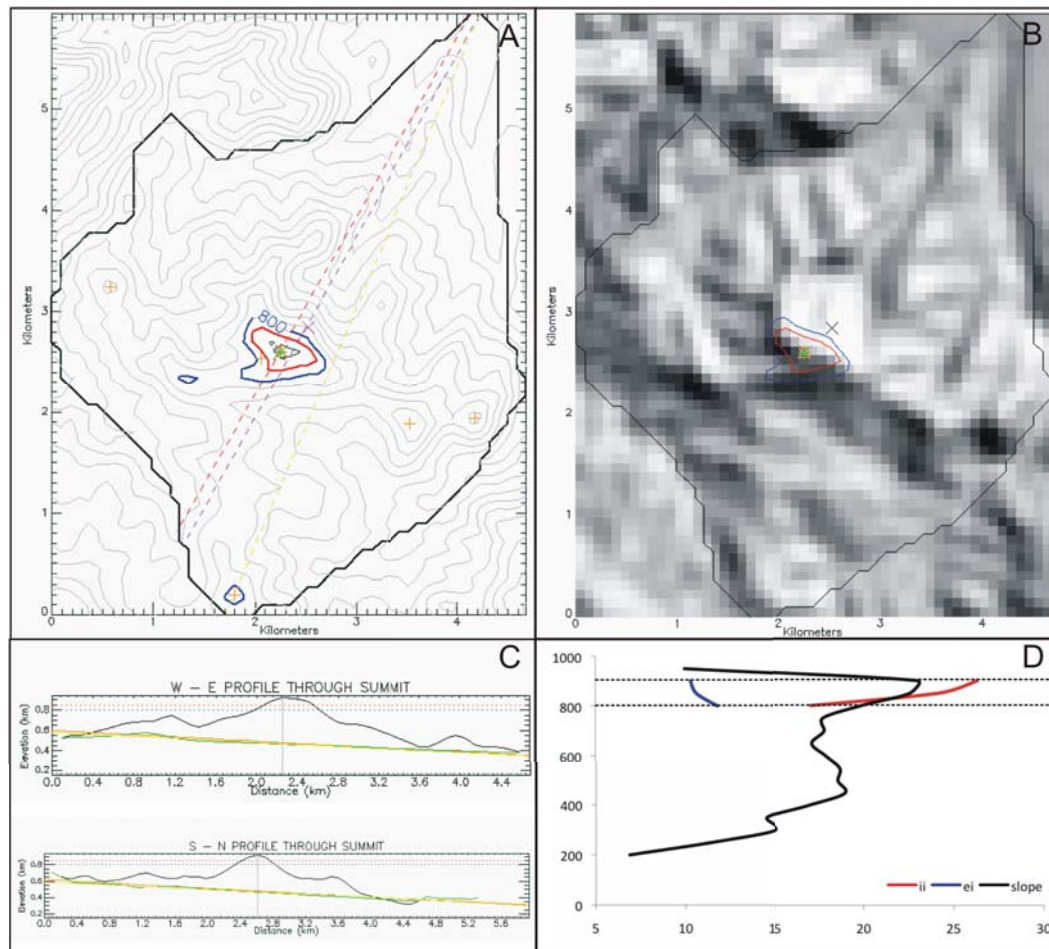


Figure A.9: Cancanaajag

Status:	Potentially Active Volcano
Morphometry Type:	Sub-cone
Location (Lat, Long):	11.06039, 124.77685
Elevation (min, max):	171-919 m
Basal Area:	17.2 km <sup>2</sup>
Height:	748 m
Volume:	6 km <sup>3</sup>
Profile shape (height/ base width, summit width/base width):	0.09, 0.10
Slope:	0.77°-41.92°
Base orientation in azimuth (through the summit, through the base centre):	29°, 29°

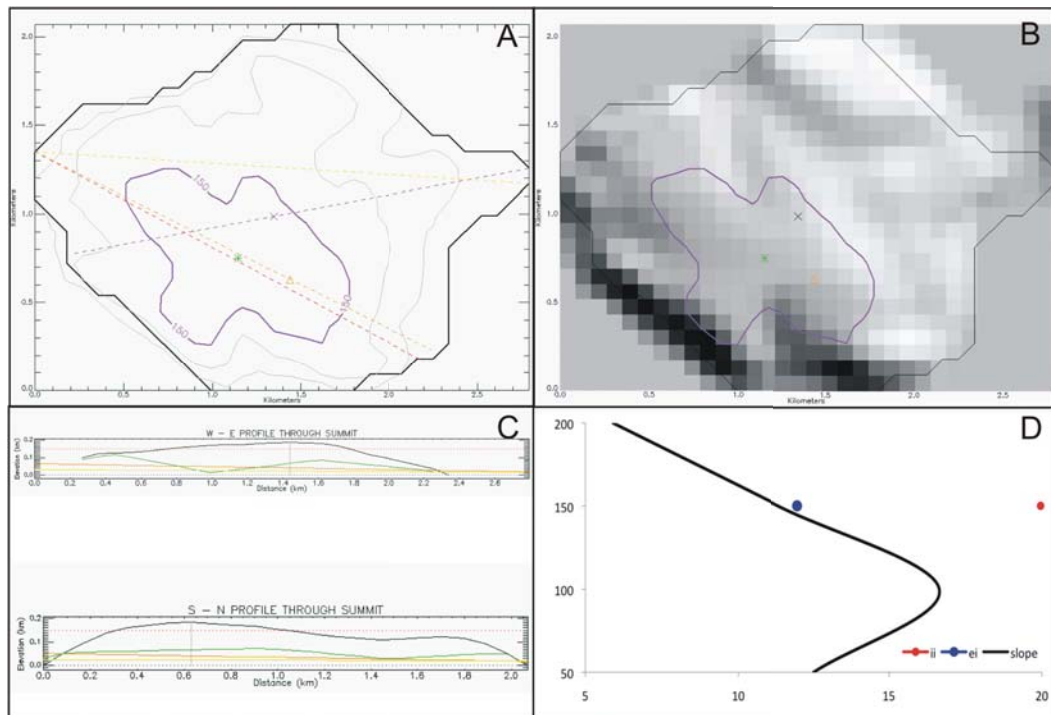


Figure A.10: Corregidor Complex

Status:	Potentially Active Volcano
Morphometry Type:	Sub-cone
Location (Lat, Long):	14.379435, 120.57611
Elevation (min, max):	0-186 m
Basal Area:	3.7 km <sup>2</sup>
Height:	186 m
Volume:	0.4 km <sup>3</sup>
Profile shape (height/ base width, summit width/base width):	0.07, 0.46
Slope:	0°-35.48°
Base orientation in azimuth (through the summit, through the base centre):	116°, 79°

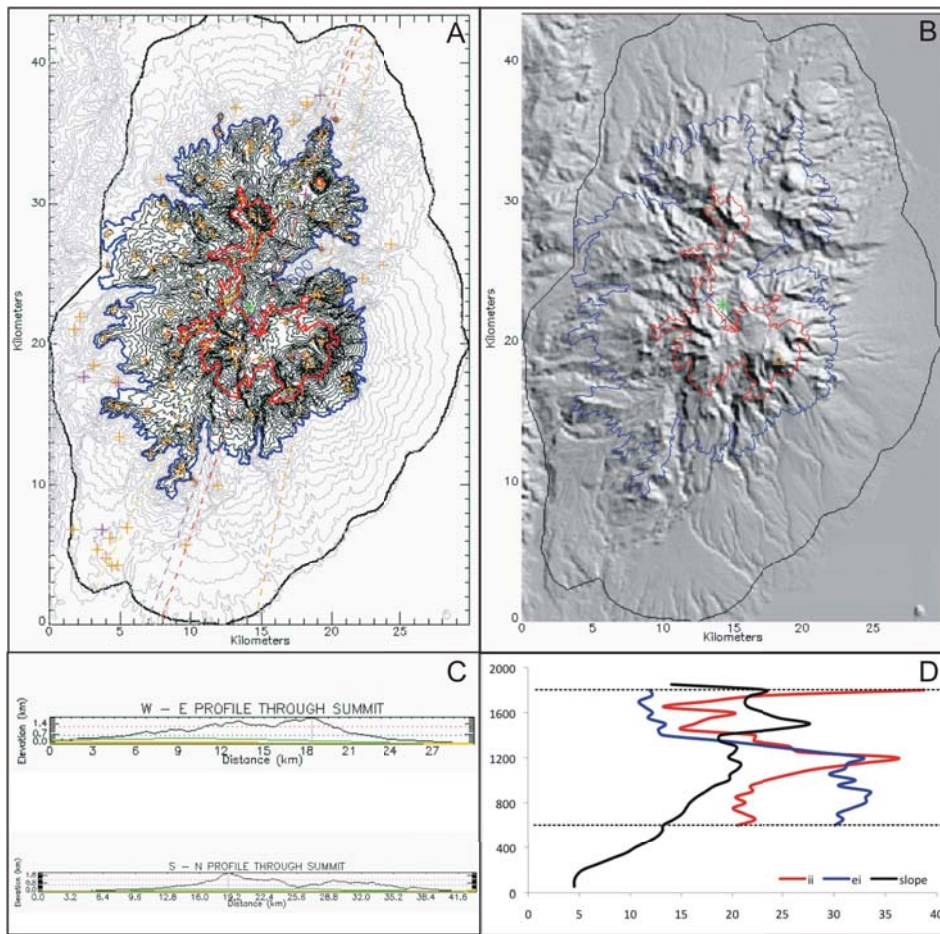


Figure A.11: Cuernos de Negros

Status:	Potentially Active Volcano
Morphometry Type:	Eroded massif
Location (Lat, Long):	9.2446421, 123.17998
Elevation (min, max):	0-1828 m
Basal Area:	938.9 km <sup>2</sup>
Height:	1828 m
Volume:	467 km <sup>3</sup>
Plan shape (ellipticity index, irregularity index):	2.42, 3.15
Profile shape (height/ base width, summit width/base width):	0.05, 0.24
Slope:	0°-61.37°
Base orientation in azimuth (through the summit, through the base centre):	11°, 19°

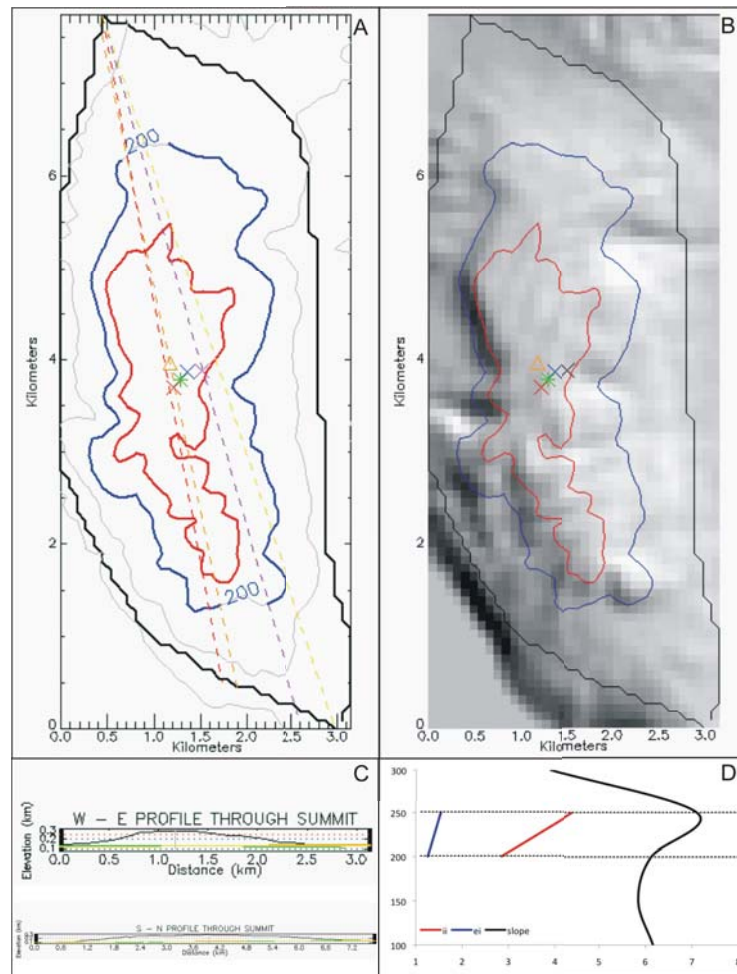


Figure A.12: Didicas

Status:	Active Volcano
Morphometry Type:	Sub-cone
Location (Lat, Long):	19.073477, 121.21454
Elevation (min, max):	96-283 m
Basal Area:	17.6 km <sup>2</sup>
Height:	187 m
Volume:	2 km <sup>3</sup>
Plan shape (ellipticity index, irregularity index):	3.63, 1.08
Profile shape (height/ base width, summit width/base width):	0.16, 0.13
Slope:	0.11°-61.37°
Base orientation in azimuth (through the summit, through the base centre):	168°, 164°

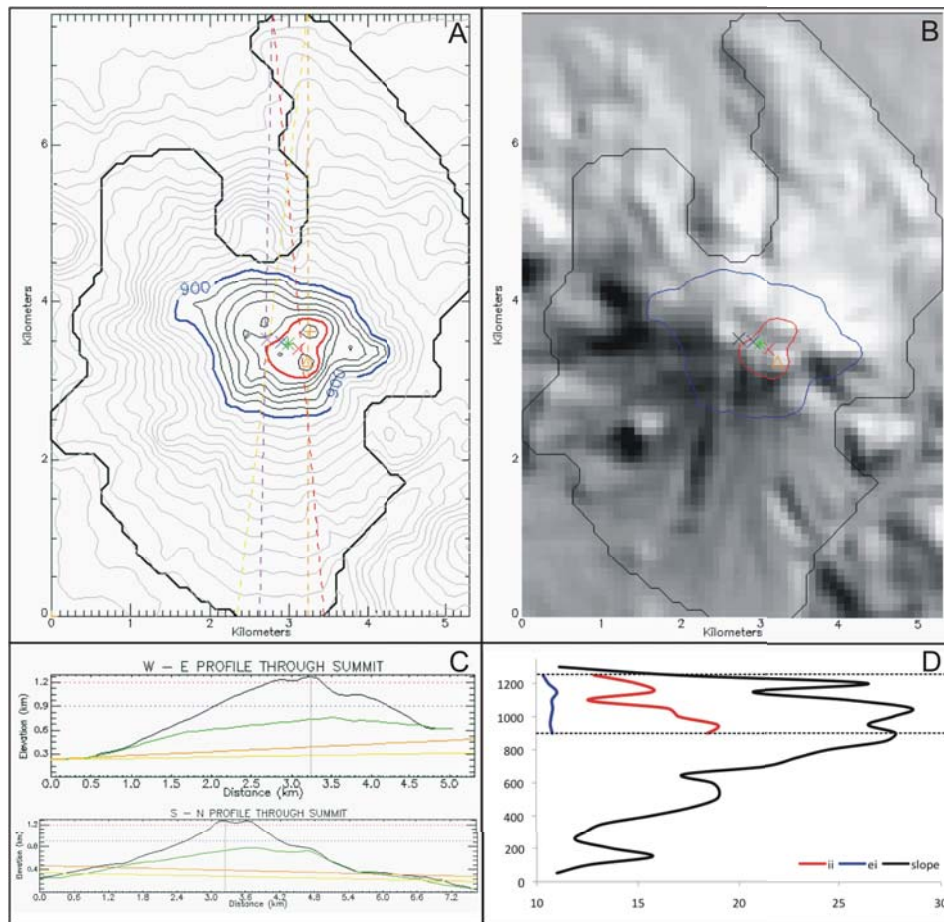


Figure A.13: Hibok-hibok

Status:	Active Volcano
Morphometry Type:	Sub-cone
Location (Lat, Long):	9.1992769, 124.67573
Elevation (min, max):	33-1273 m
Basal Area:	23.9 km <sup>2</sup>
Height:	1240 m
Volume:	13 km <sup>3</sup>
Plan shape (ellipticity index, irregularity index):	1.63, 1.08
Profile shape (height/ base width, summit width/base width):	0.16, 0.13
Slope:	1.21°-46.45°
Base orientation in azimuth (through the summit, through the base centre):	180°, 1°

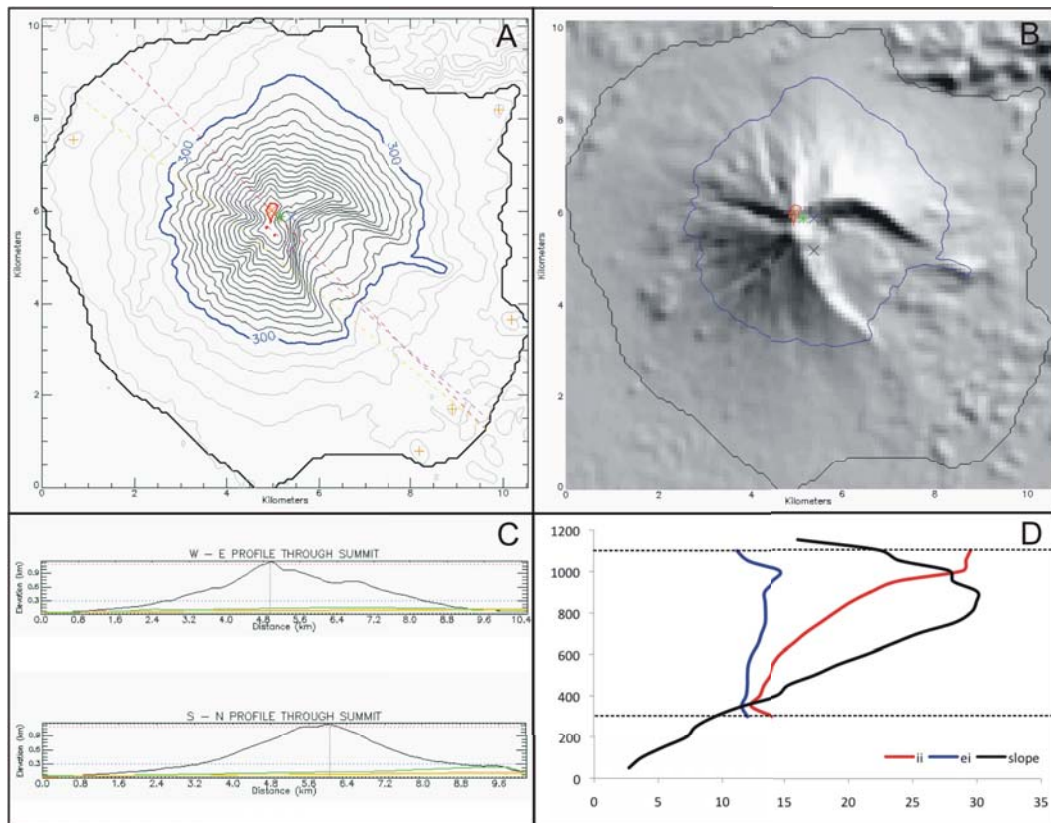


Figure A.14: Iriga

Status:	Active Volcano
Morphometry Type:	Breached edifice
Location (Lat, Long):	13.458041, 123.45038
Elevation (min, max):	28-1149 m
Basal Area:	79.7 km <sup>2</sup>
Height:	1121 m
Volume:	18 km <sup>3</sup>
Plan shape (ellipticity index, irregularity index):	1.87, 1.26
Profile shape (height/ base width, summit width/base width):	0.1, 0.03
Slope:	0°-49.22°
Base orientation in azimuth (through the summit, through the base centre):	135°, 131°

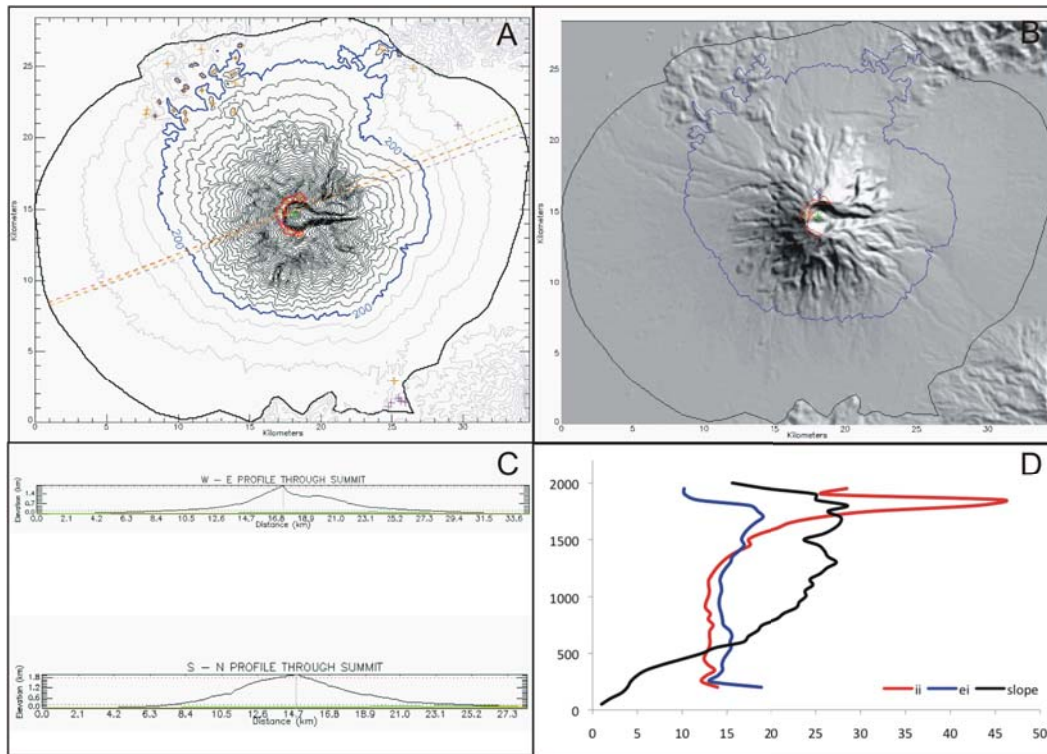


Figure A.15: Isarog

Status:	Potentially Active Volcano
Morphometry Type:	Breached edifice
Location (Lat, Long):	13.658362, 123.37253
Elevation (min, max):	3-1972 m
Basal Area:	753.4 km <sup>2</sup>
Height:	1969 m
Volume:	174 km <sup>3</sup>
Plan shape (ellipticity index, irregularity index):	1.60, 1.55
Profile shape (height/ base width, summit width/base width):	0.1, 0.24
Slope:	0°-54.20°
Base orientation in azimuth (through the summit, through the base centre):	68°, 70°

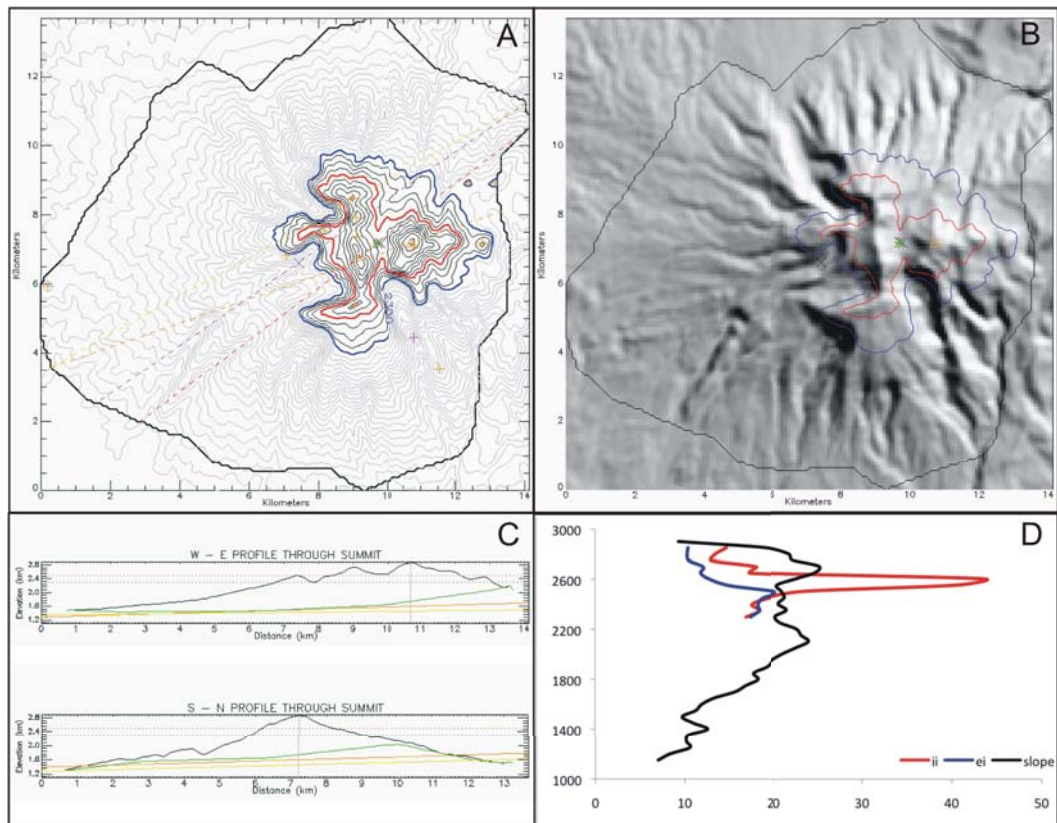


Figure A.16: Kalatungan

Status:	Potentially Active Volcano
Morphometry Type:	Eroded massif
Location (Lat, Long):	7.954539, 124.80169
Elevation (min, max):	1118-2860 m
Basal Area:	136.1 km <sup>2</sup>
Height:	1742 m
Volume:	96 km <sup>3</sup>
Plan shape (ellipticity index, irregularity index):	1.91, 1.85
Profile shape (height/ base width, summit width/base width):	0.10, 0.24
Slope:0.38°-54.48°	
Base orientation in azimuth (through the summit, through the base centre):	71°, 55°

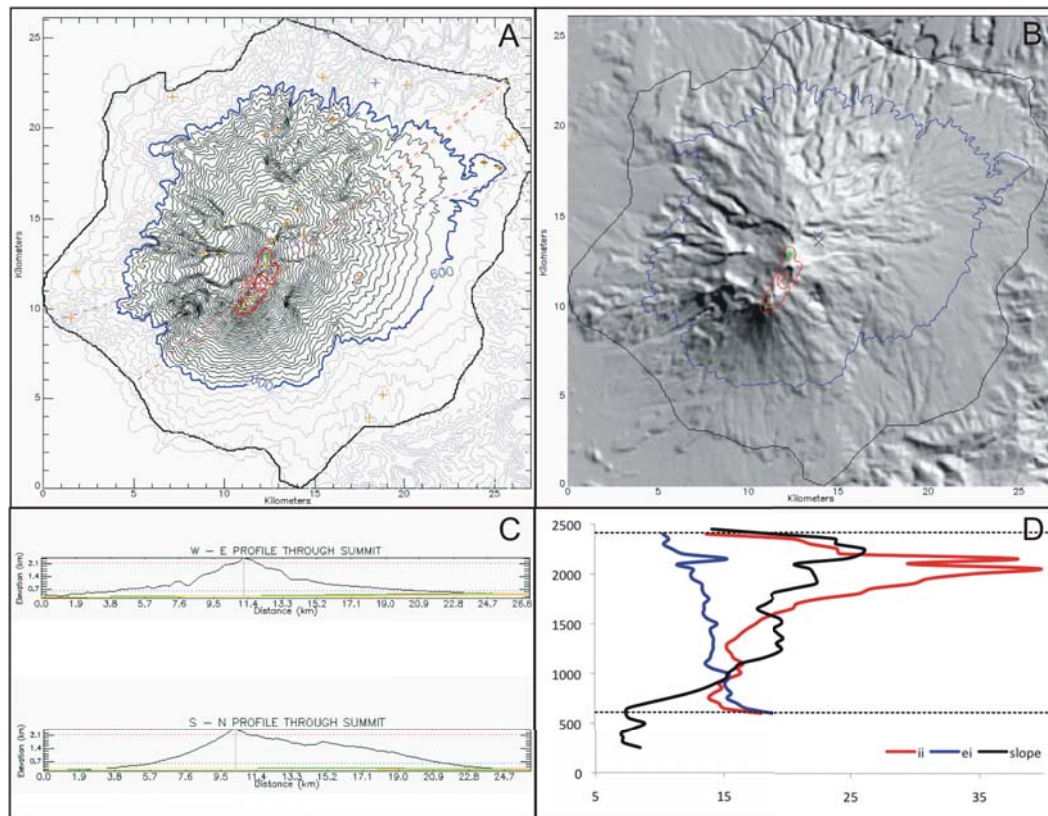


Figure A.17: Kanlaon

Status:	Active Volcano
Morphometry Type:	Breached
Location (Lat, Long):	10.409523, 123.12963
Elevation (min, max):	203-2421 m
Basal Area:	461.5 km <sup>2</sup>
Height:	2218 m
Volume:	251 km <sup>3</sup>
Plan shape (ellipticity index, irregularity index):	2.04, 1.43
Profile shape (height/ base width, summit width/base width):	0.09, 0.08
Slope:	0°-51.83°
Base orientation in azimuth (through the summit, through the base centre):	50°, 73°

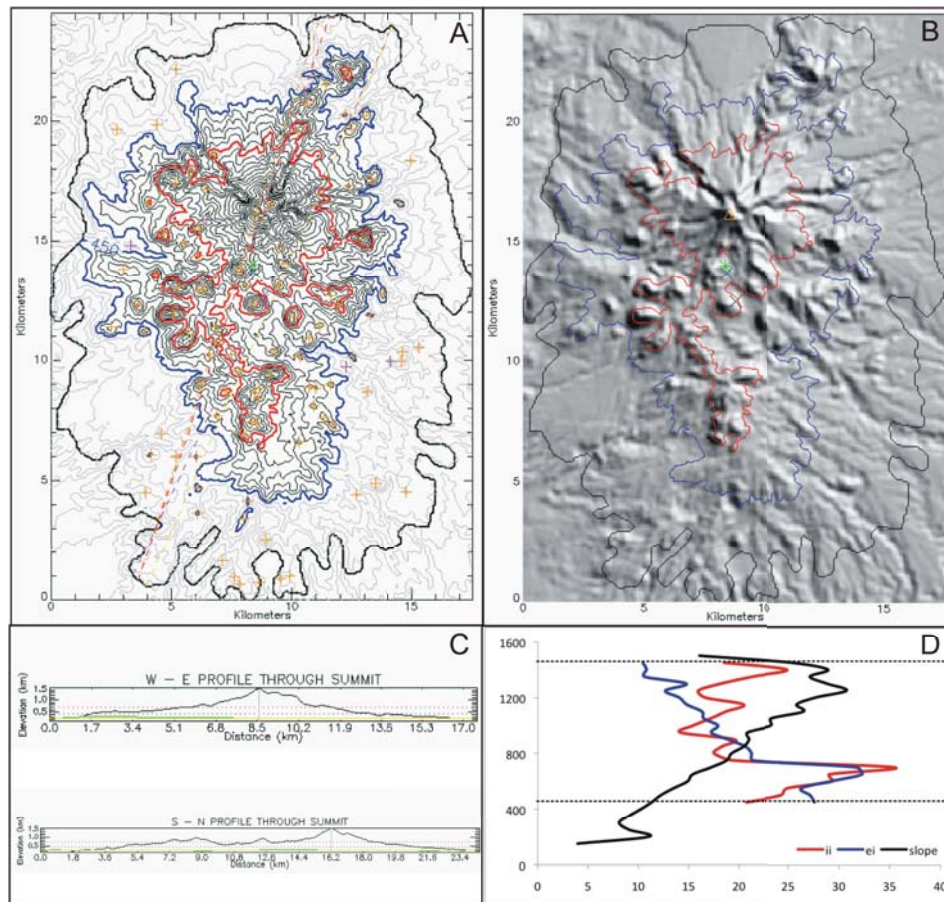


Figure A.18: Labo

Status:	Potentially Active Volcano
Morphometry Type:	Eroded massif
Location (Lat, Long):	14.012547, 122.78718
Elevation (min, max):	144-1482 m
Basal Area:	317.9 km <sup>2</sup>
Height:	1338 m
Volume:	105 km <sup>3</sup>
Plan shape (ellipticity index, irregularity index):	2.73, 2.90
Profile shape (height/ base width, summit width/base width):	0.06, 0.36
Slope:	0°-48.93°
Base orientation in azimuth (through the summit, through the base centre):	18°, 25°

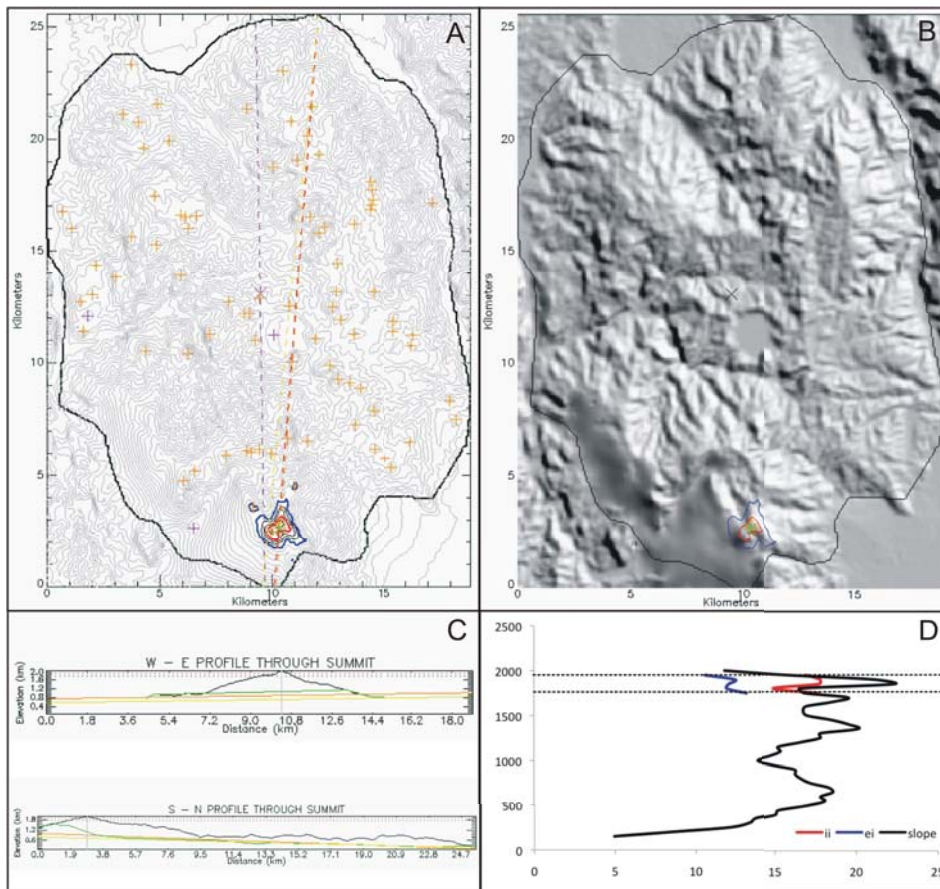


Figure A.19: Leonard Massif

Status:	Active Volcano
Morphometry Type:	Massif
Location (Lat, Long):	7.3179087, 126.06177
Elevation (min, max):	101-1990 m
Basal Area:	366.4 km <sup>2</sup>
Height:	1889 m
Volume:	270 km <sup>3</sup>
Profile shape (height/ base width, summit width/base width):	0.05, 0.04
Slope:	0°-53.97°
Base orientation in azimuth (through the summit, through the base centre):	4°, 179°

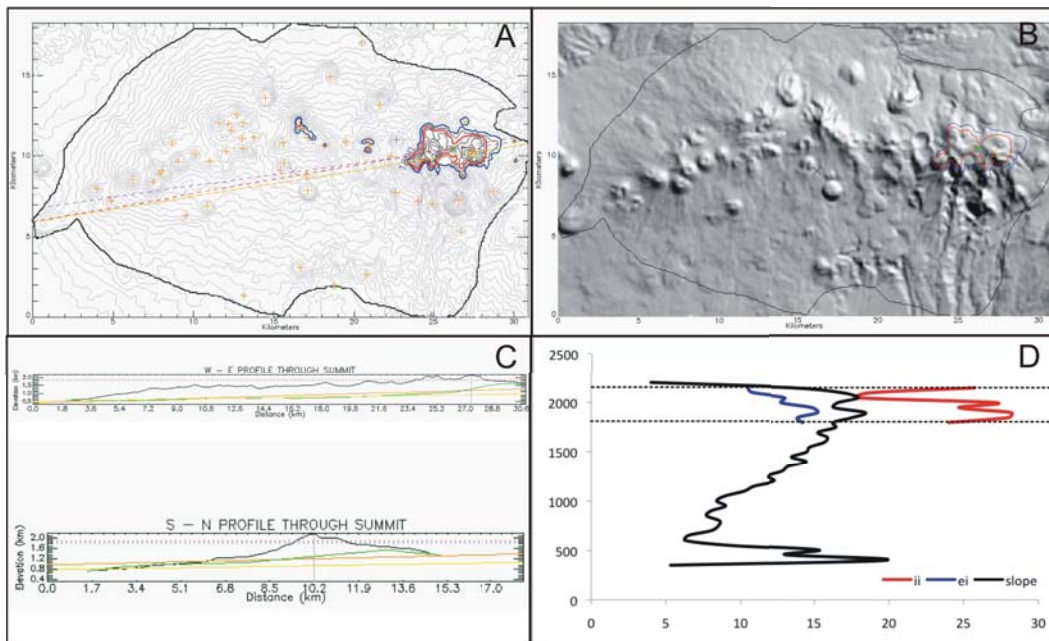


Figure A.20: Makaturing

Status:	Active Volcano
Morphometry Type:	Massif
Location (Lat, Long):	7.6386784, 124.39984
Elevation (min, max):	339-2155 m
Basal Area:	399.9 km <sup>2</sup>
Height:	1816 m
Volume:	307 km <sup>3</sup>
Profile shape (height/ base width, summit width/base width):	0.04, 0.13
Slope:	0°-49.94°
Base orientation in azimuth (through the summit, through the base centre):	81°, 82°

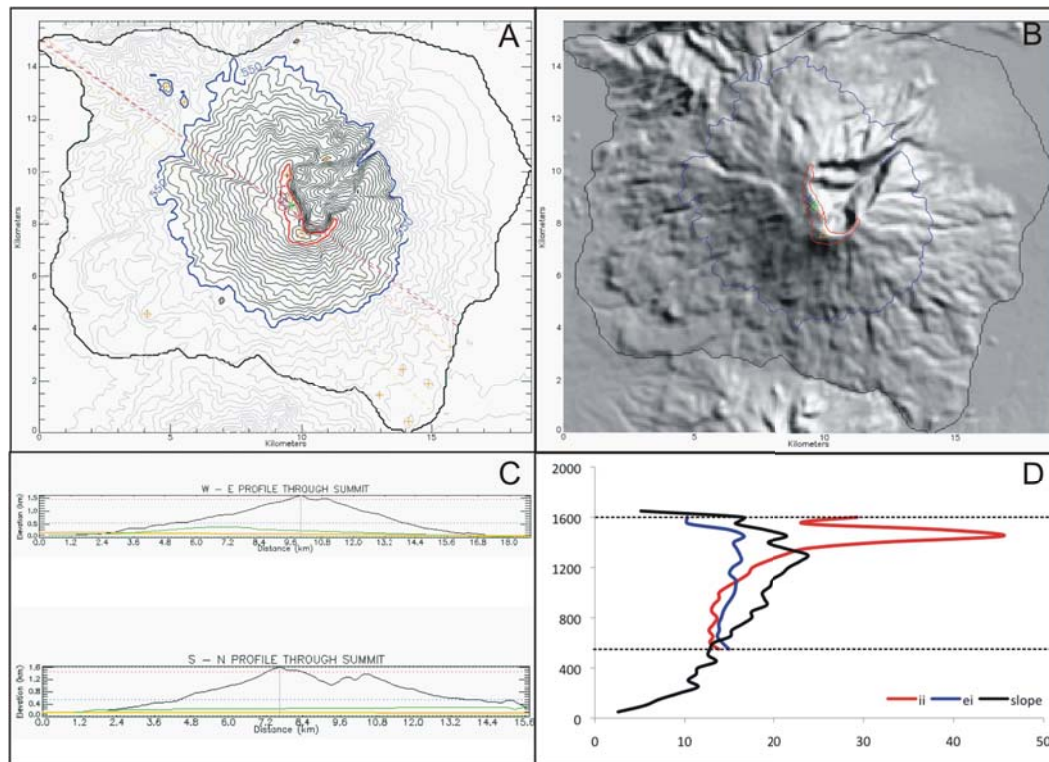


Figure A.21: Malinao

Status:	Potentially Active Volcano
Morphometry Type:	Breached edifice
Location (Lat, Long):	13.402375, 123.60738
Elevation (min, max):	13-1602 m
Basal Area:	210.8 km <sup>2</sup>
Height:	1589 m
Volume:	95 km <sup>3</sup>
Plan shape (ellipticity index, irregularity index):	1.79, 1.50
Profile shape (height/ base width, summit width/base width):	0.09, 0.09
Slope:	0°-55.24°
Base orientation in azimuth (through the summit, through the base centre):	127°, 124°

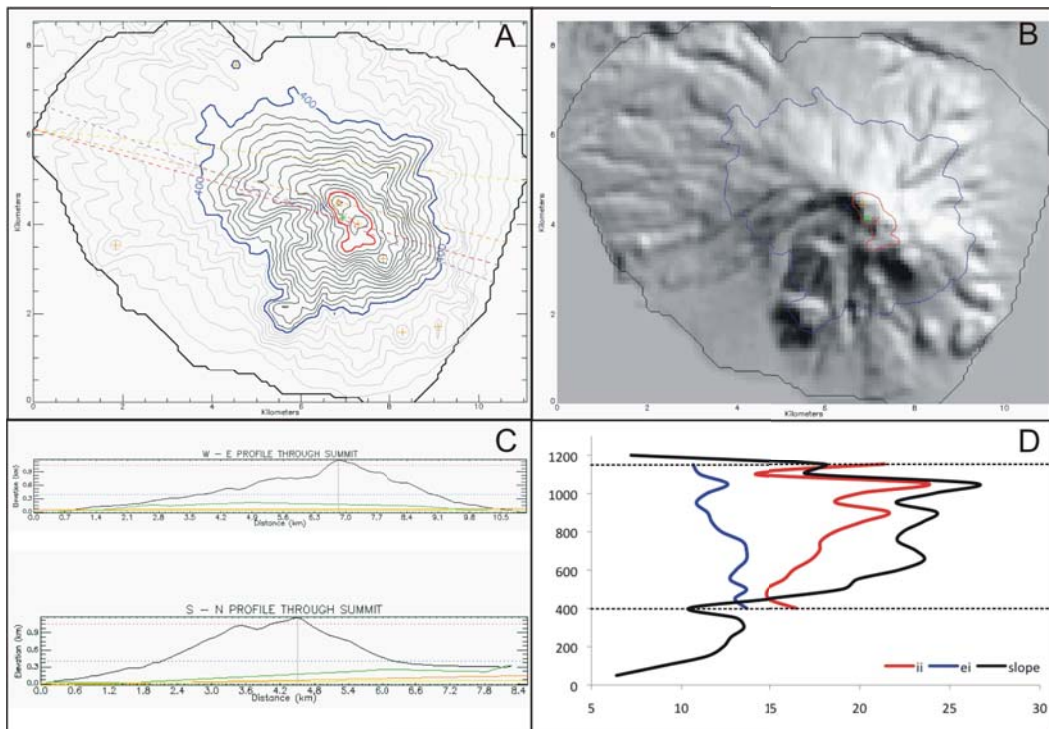


Figure A.22: Malindig

Status:	Potentially Active Volcano
Morphometry Type:	Sub-cone
Location (Lat, Long):	13.240873, 122.01283
Elevation (min, max):	0-1161 m
Basal Area:	70 km <sup>2</sup>
Height:	1162 m
Volume:	22 km <sup>3</sup>
Plan shape (ellipticity index, irregularity index):	1.81, 1.26
Profile shape (height/ base width, summit width/base width):	0.12, 0.10
Slope:	0°-43.37°
Base orientation in azimuth (through the summit, through the base centre):	103°, 111°

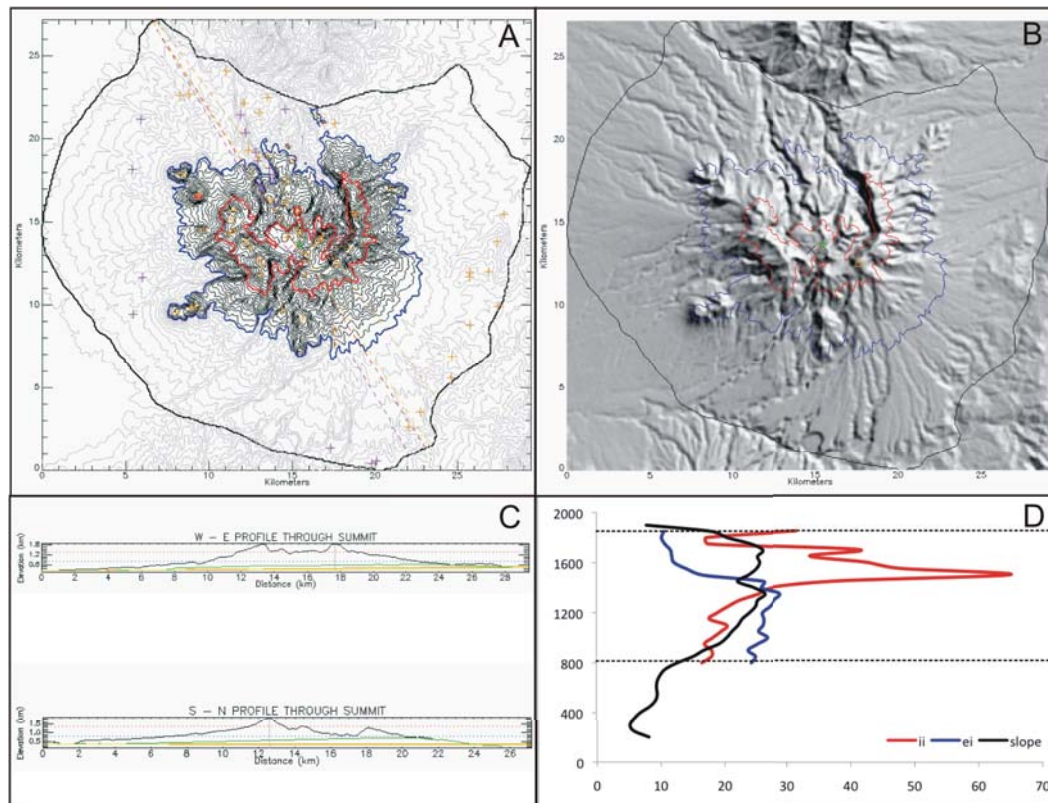


Figure A.23: Mandalagan

Status:	Potentially Active Volcano
Morphometry Type:	Eroded massif
Location (Lat, Long):	10.636564, 123.23505
Elevation (min, max):	166-1854 m
Basal Area:	539 km <sup>2</sup>
Height:	1688 m
Volume:	267 km <sup>3</sup>
Plan shape (ellipticity index, irregularity index):	1.94, 2.61
Profile shape (height/ base width, summit width/base width):	0.06, 0.023
Slope:	0.11°-58.32°
Base orientation in azimuth (through the summit, through the base centre):	144°, 149°

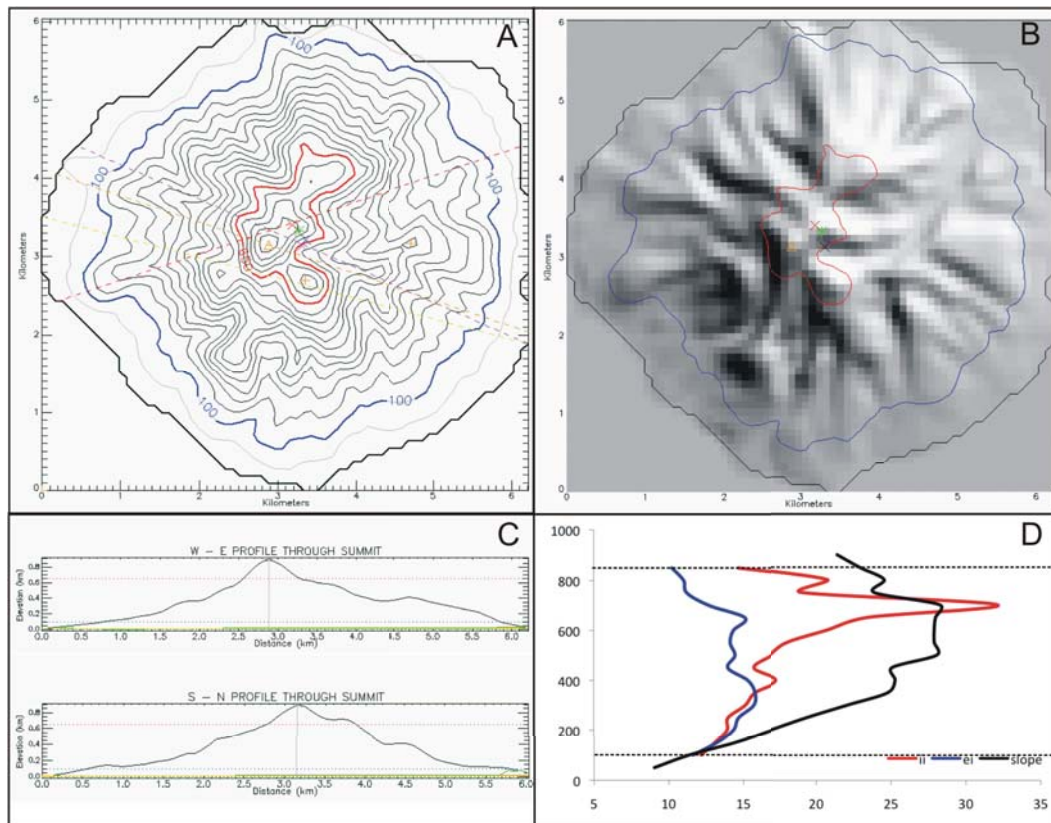


Figure A.24: Maripipi

Status:	Potentially Active Volcano
Morphometry Type:	Sub-cone
Location (Lat, Long):	11.788589, 124.31892
Elevation (min, max):	0-889 m
Basal Area:	27.9 km <sup>2</sup>
Height:	889 m
Volume:	7 km <sup>3</sup>
Plan shape (ellipticity index, irregularity index):	1.63, 1.44
Profile shape (height/ base width, summit width/base width):	0.15, 0.22
Slope:	1.09°-44.11°
Base orientation in azimuth (through the summit, through the base centre):	108°, 114°

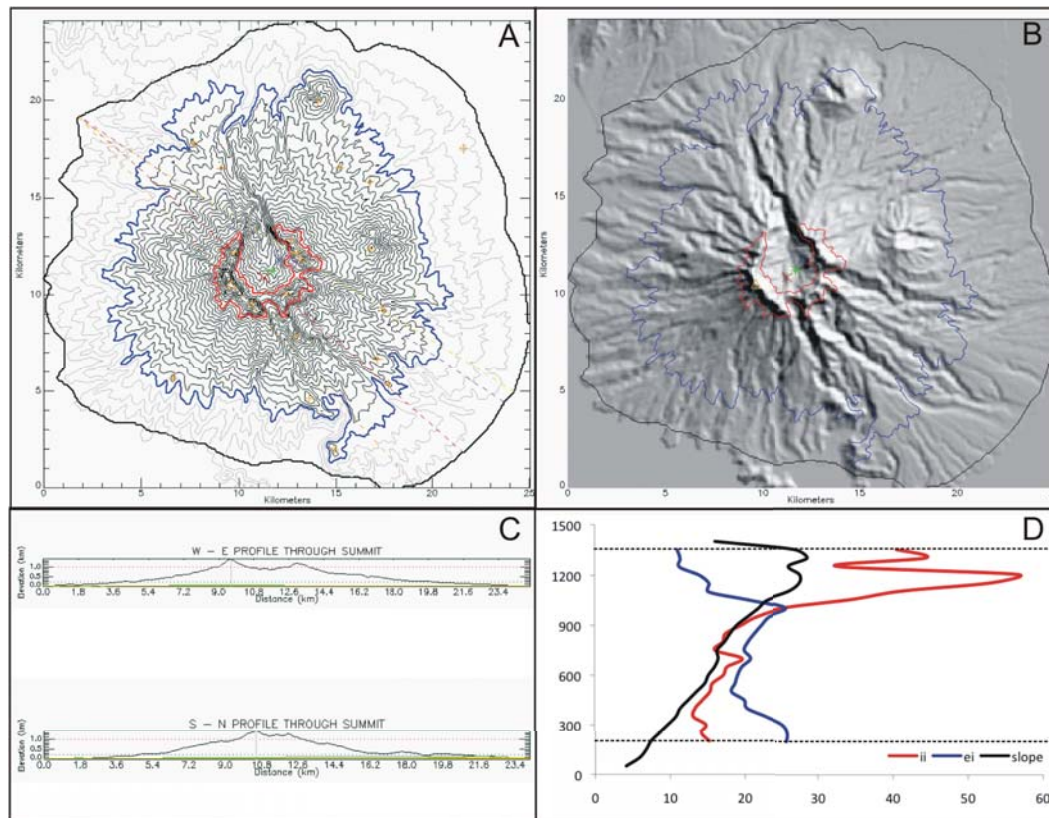


Figure A.25: Mariveles-Limay-Samat

Status:	Potentially Active Volcano
Morphometry Type:	Breached edifice
Location (Lat, Long):	14.51893, 120.46526
Elevation (min, max):	0-1396 m
Basal Area:	457.5 km <sup>2</sup>
Height:	1396 m
Volume:	128 km <sup>3</sup>
Plan shape (ellipticity index, irregularity index):	1.70, 2.17
Profile shape (height/ base width, summit width/base width):	0.06, 0.15
Slope:	0°-55.44°
Base orientation in azimuth (through the summit, through the base centre):	138°, 124°

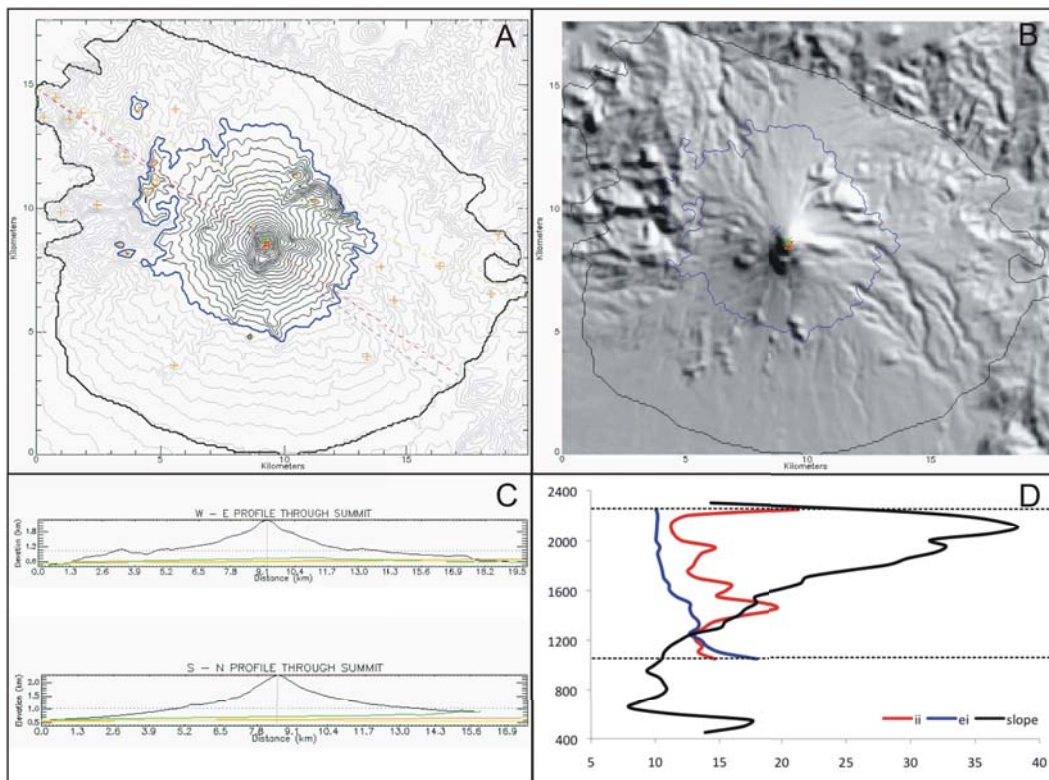


Figure A.26: Matutum

Status:	Active Volcano
Morphometry Type:	Cone
Location (Lat, Long):	6.3602102, 125.07605
Elevation (min, max):	408-2258 m
Basal Area:	241.8 km <sup>2</sup>
Height:	1850 m
Volume:	120 km <sup>3</sup>
Plan shape (ellipticity index, irregularity index):	1.43, 1.18
Profile shape (height/ base width, summit width/base width):	0.09, 0.01
Slope:	0.11°-51.61°
Base orientation in azimuth (through the summit, through the base centre):	124°, 126°

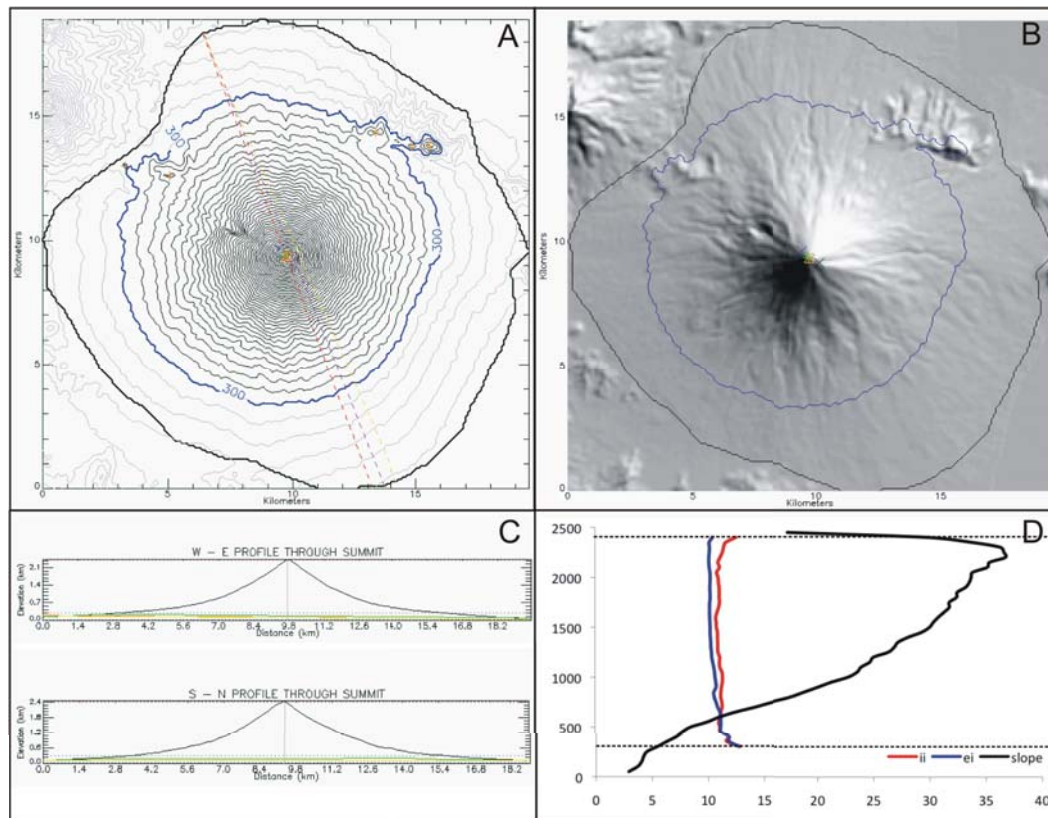


Figure A.27: Mayon

Status:	Active Volcano
Morphometry Type:	Cone
Location (Lat, Long):	13.255697, 123.68511
Elevation (min, max):	4-2420 m
Basal Area:	257.5 km <sup>2</sup>
Height:	2416 m
Volume:	104 km <sup>3</sup>
Plan shape (ellipticity index, irregularity index):	1.2, 1.06
Profile shape (height/ base width, summit width/base width):	0.13, 0.01
Slope:	0.15°-42.53°
Base orientation in azimuth (through the summit, through the base centre):	160°, 158°

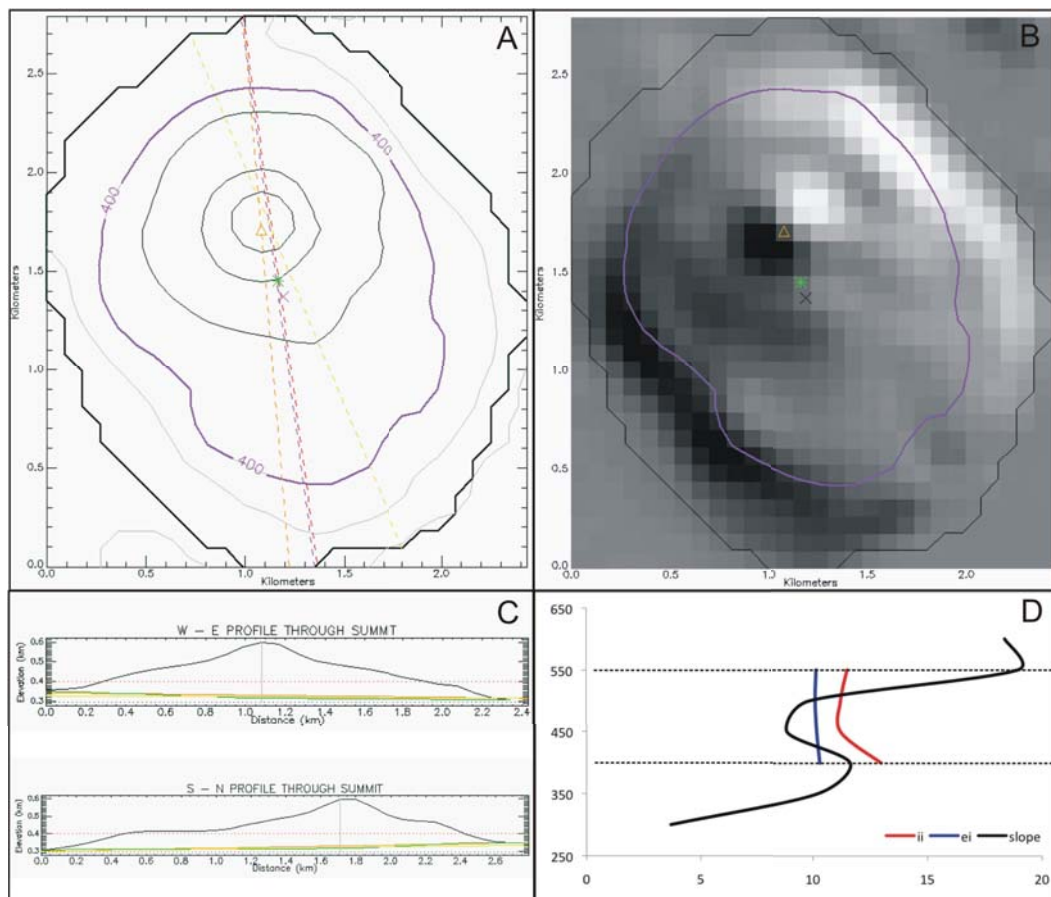


Figure A.28: Musuan

Status:	Active Volcano
Morphometry Type:	Cone
Location (Lat, Long):	7.876002, 125.069
Elevation (min, max):	297-598 m
Basal Area:	5 km <sup>2</sup>
Height:	301 m
Volume:	1 km <sup>3</sup>
Profile shape (height/ base width, summit width/base width):	0.11, 0.72
Slope:	0.54°-28.84°
Base orientation in azimuth (through the summit, through the base centre):	175°, 172°

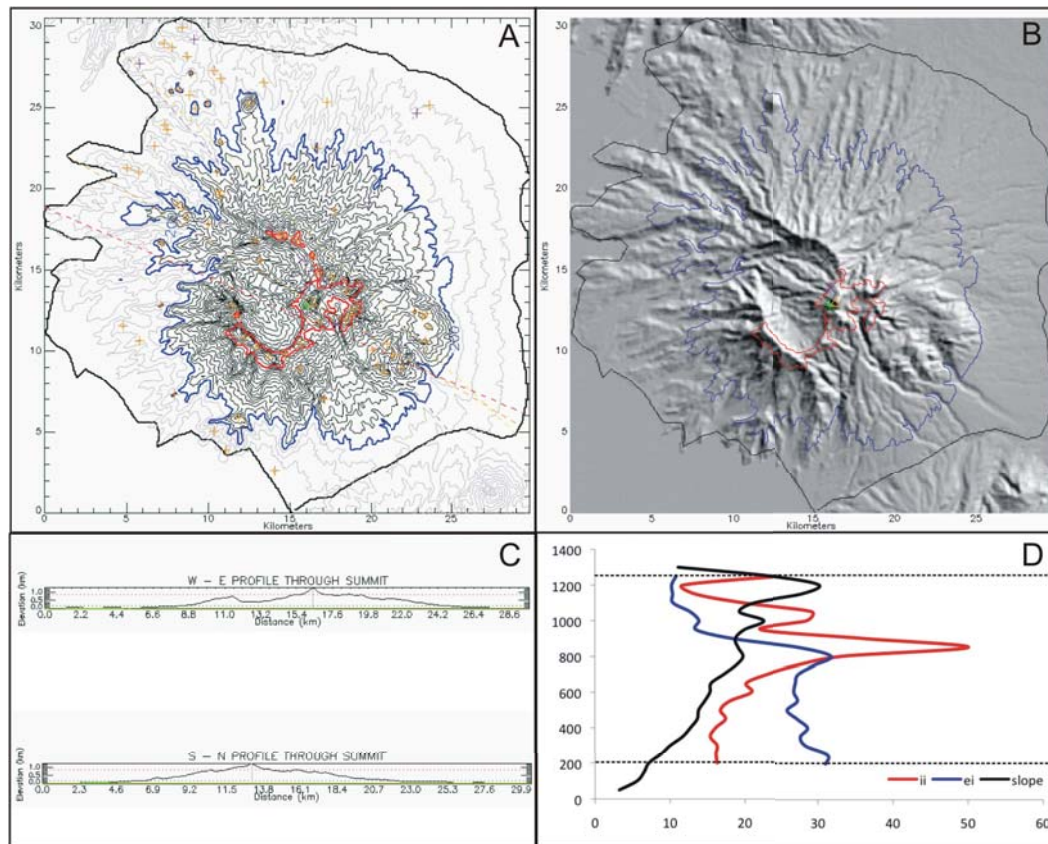


Figure A.29: Natib

Status:	Potentially Active Volcano
Morphometry Type:	Breached edifice
Location (Lat, Long):	14.711715, 120.4004
Elevation (min, max):	0-1253 m
Basal Area:	640.9 km <sup>2</sup>
Height:	1253 m
Volume:	151 km <sup>3</sup>
Plan shape (ellipticity index, irregularity index):	2.19, 2.84
Profile shape (height/ base width, summit width/base width):	0.04, 0.14
Slope:	0°-48.73°
Base orientation in azimuth (through the summit, through the base centre):	121°, 139°

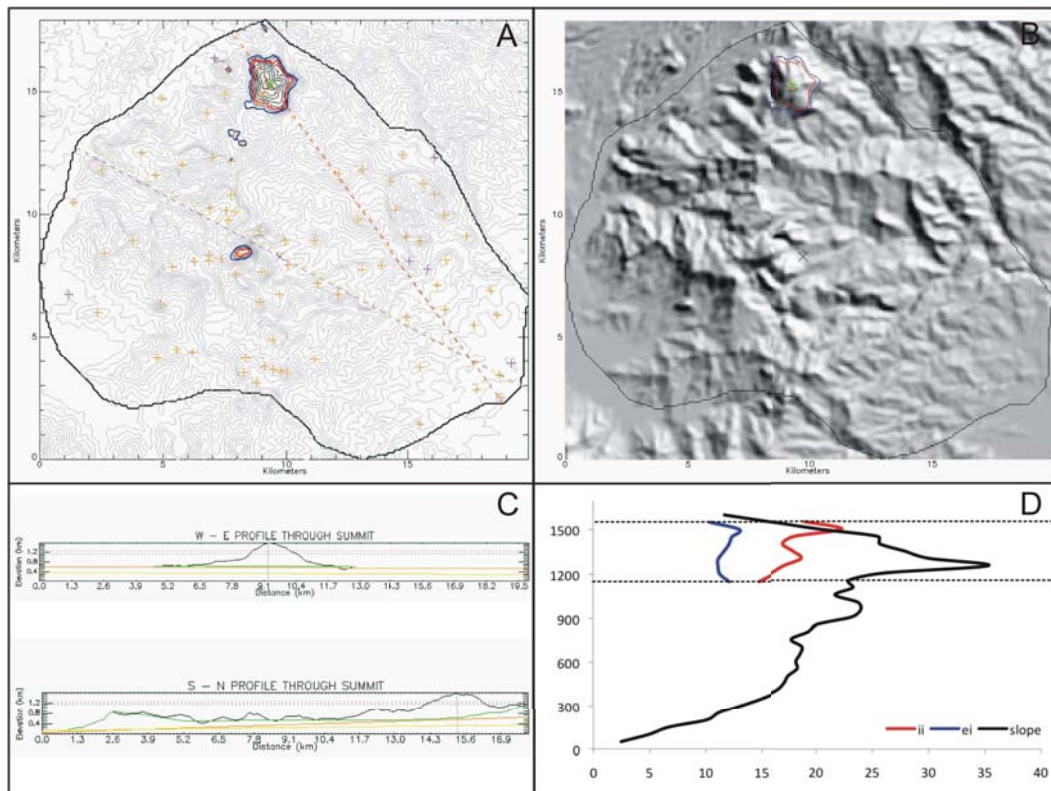


Figure A.30: Negron

Status:	Potentially Active Volcano
Morphometry Type:	Massif
Location (Lat, Long):	15.092623, 120.36738
Elevation (min, max):	35-1558 m
Basal Area:	236 km <sup>2</sup>
Height:	1523 m
Volume:	109 km <sup>3</sup>
Profile shape (height/ base width, summit width/base width):	0.06, 0.10
Slope:	0°-62.36°
Base orientation in azimuth (through the summit, through the base centre):	144°, 118°

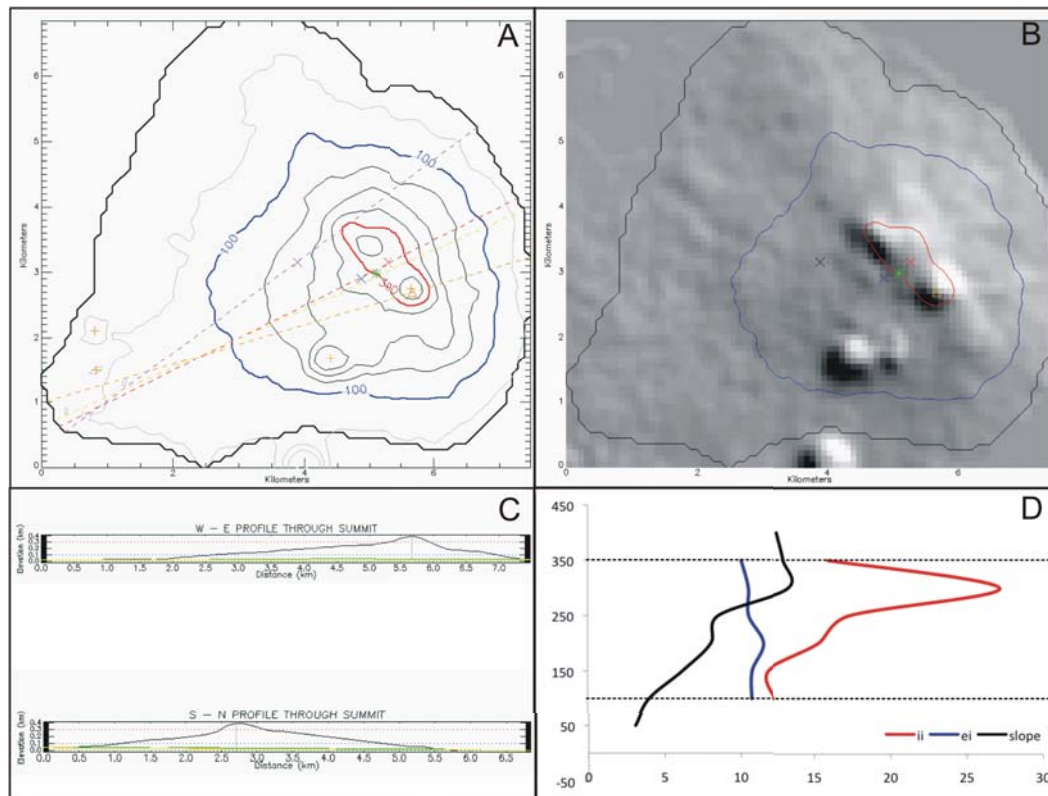


Figure A.31: Parangan

Status:	Potentially Active Volcano
Morphometry Type:	Cone
Location (Lat, Long):	5.9704632, 121.4077
Elevation (min, max):	1-390 m
Basal Area:	36.8 km <sup>2</sup>
Height:	389 m
Volume:	4 km <sup>3</sup>
Plan shape (ellipticity index, irregularity index):	1.67, 1.08
Profile shape (height/ base width, summit width/base width):	0.05, 0.15
Slope:	0°-28.45°
Base orientation in azimuth (through the summit, through the base centre):	73°, 53°

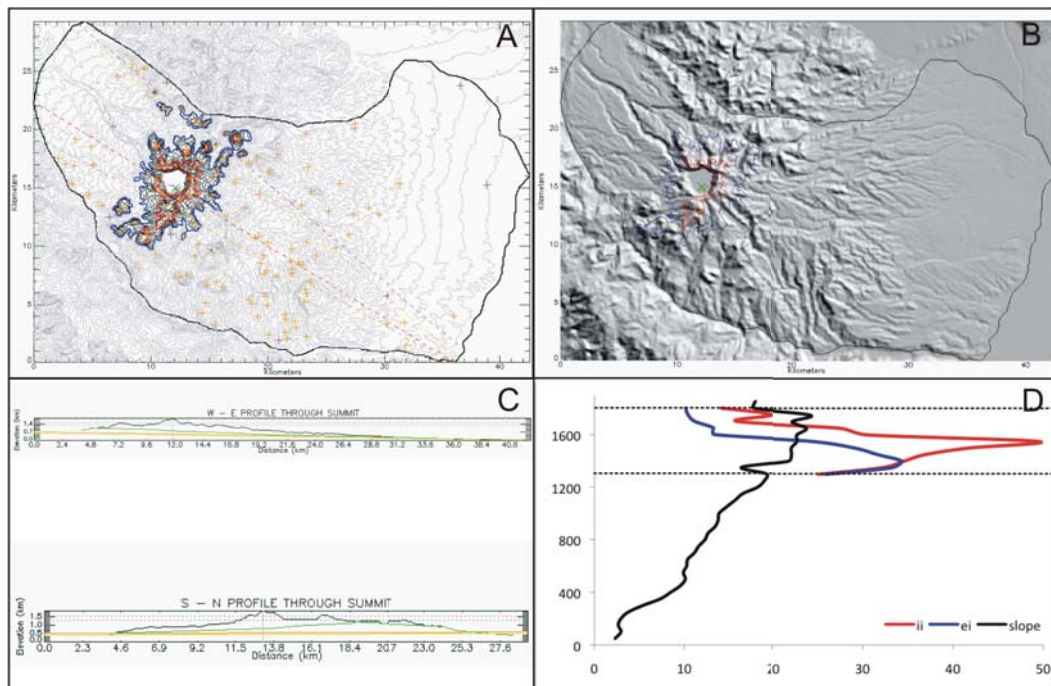


Figure A.32: Parker

Status:	Active Volcano
Morphometry Type:	Massif
Location (Lat, Long):	6.0793874, 124.88636
Elevation (min, max):	0-1849 m
Basal Area:	781.3 km <sup>2</sup>
Height:	1849 m
Volume:	472 km <sup>3</sup>
Plan shape (ellipticity index, irregularity index):	3.67, 2.98
Profile shape (height/ base width, summit width/base width):	0.04, 0.10
Slope:	0°-58.28°
Base orientation in azimuth (through the summit, through the base centre):	119°, 130°

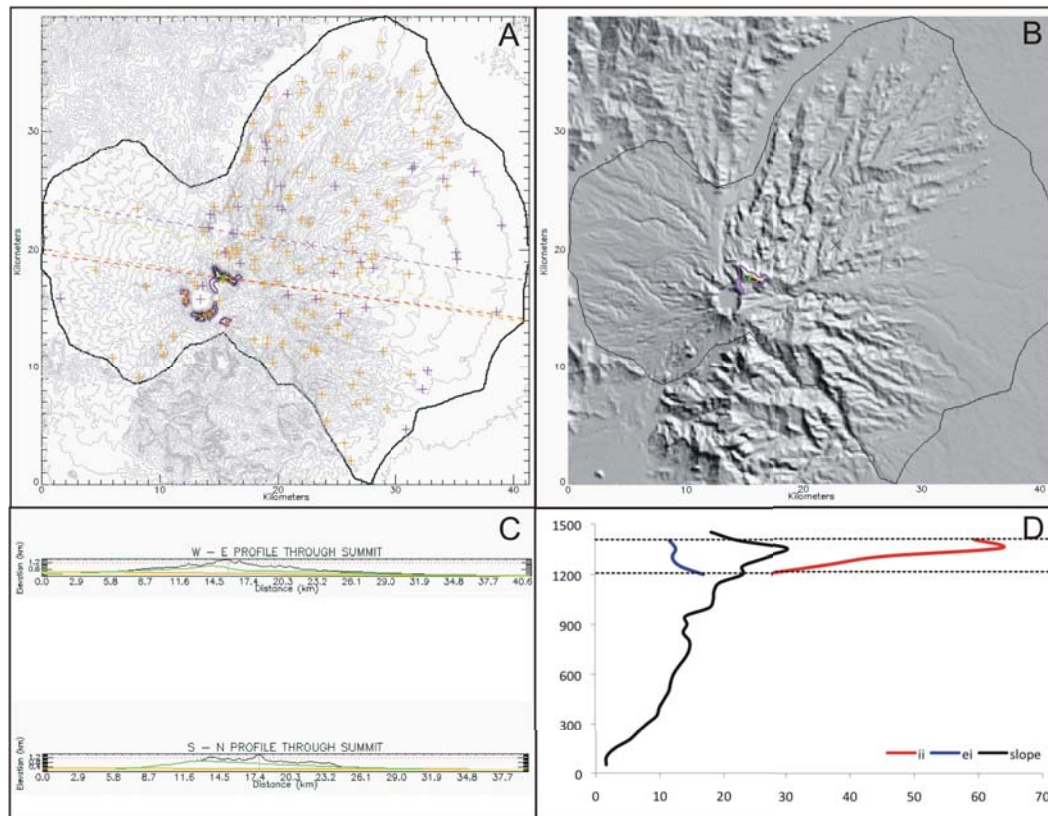


Figure A.33: Pinatubo

Status:	Active Volcano
Morphometry Type:	Massif
Location (Lat, Long):	15.159325, 120.37074
Elevation (min, max):	46-1445 m
Basal Area:	939.2 m
Height:	1399 m
Volume:	301 km <sup>3</sup>
Profile shape (height/ base width, summit width/base width):	0.03, 0.05
Slope:	0°-49.81°
Base orientation in azimuth (through the summit, through the base centre):	99°, 99°

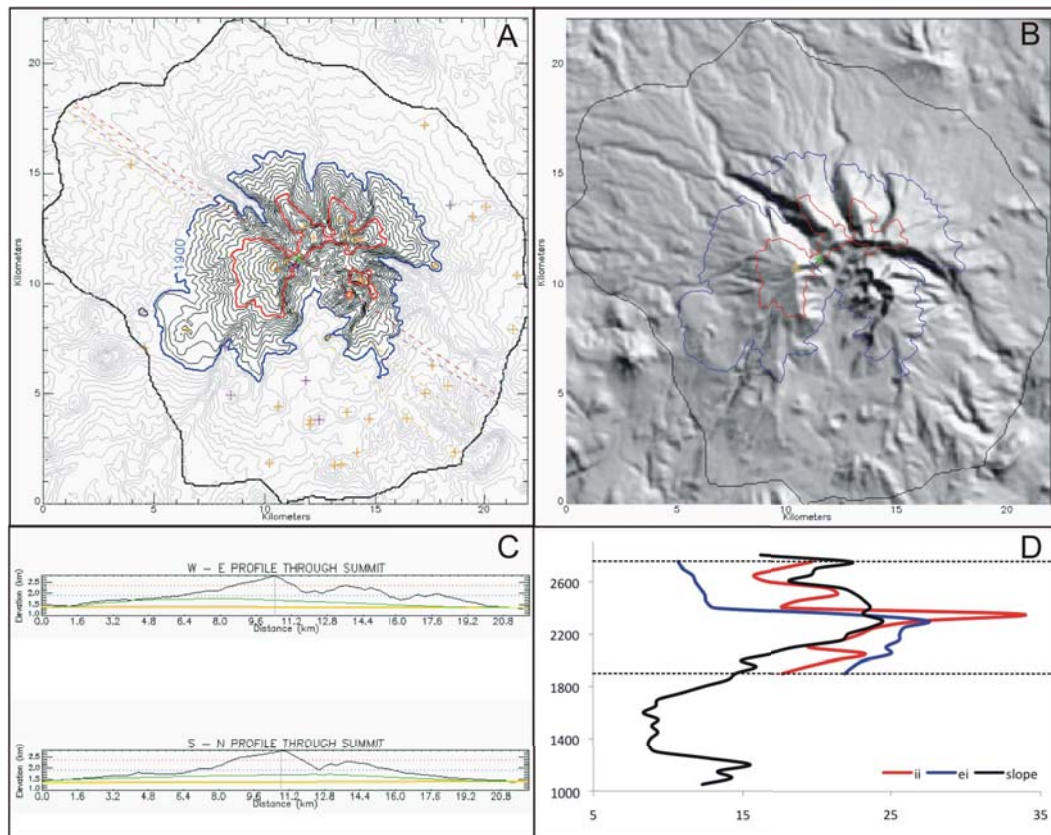


Figure A.34: Ragang

Status:	Active Volcano
Morphometry Type:	Breached edifice
Location (Lat, Long):	7.6904039, 124.50688
Elevation (min, max):	1008-2787 m
Basal Area:	334.6 km <sup>2</sup>
Height:	1779 m
Volume:	236 km <sup>3</sup>
Plan shape (ellipticity index, irregularity index):	2.31, 2.44
Profile shape (height/ base width, summit width/base width):	0.07, 0.20
Slope:	0.11°-52.56°
Base orientation in azimuth (through the summit, through the base centre):	129°, 124°

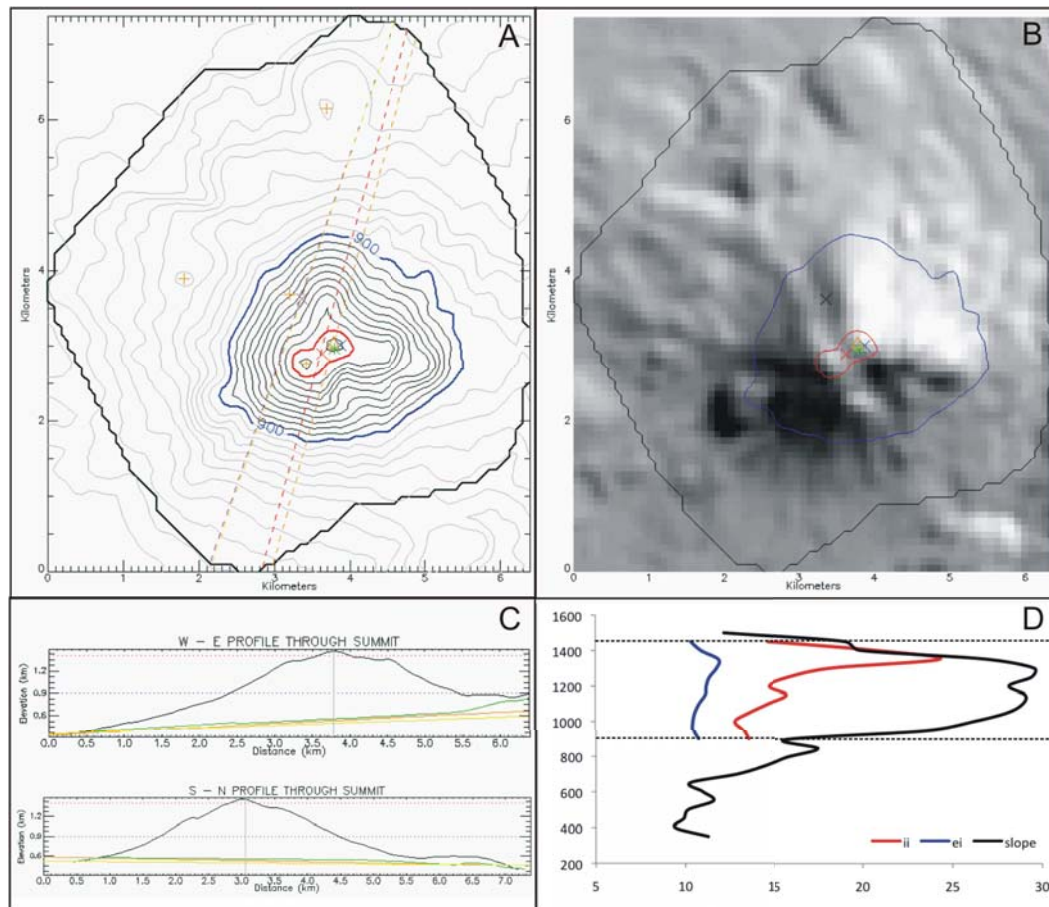


Figure A.35: San Cristobal

Status:	Potentially Active Volcano
Morphometry Type:	Sub-cone
Location (Lat, Long):	14.064475, 121.42598
Elevation (min, max):	330-1467 m
Basal Area:	32.5 km <sup>2</sup>
Height:	1137 m
Volume:	13 km <sup>3</sup>
Plan shape (ellipticity index, irregularity index):	1.61, 1.10
Profile shape (height/ base width, summit width/base width):	0.14, 0.09
Slope:	0.21°-40.43°
Base orientation in azimuth (through the summit, through the base centre):	15°, 19°

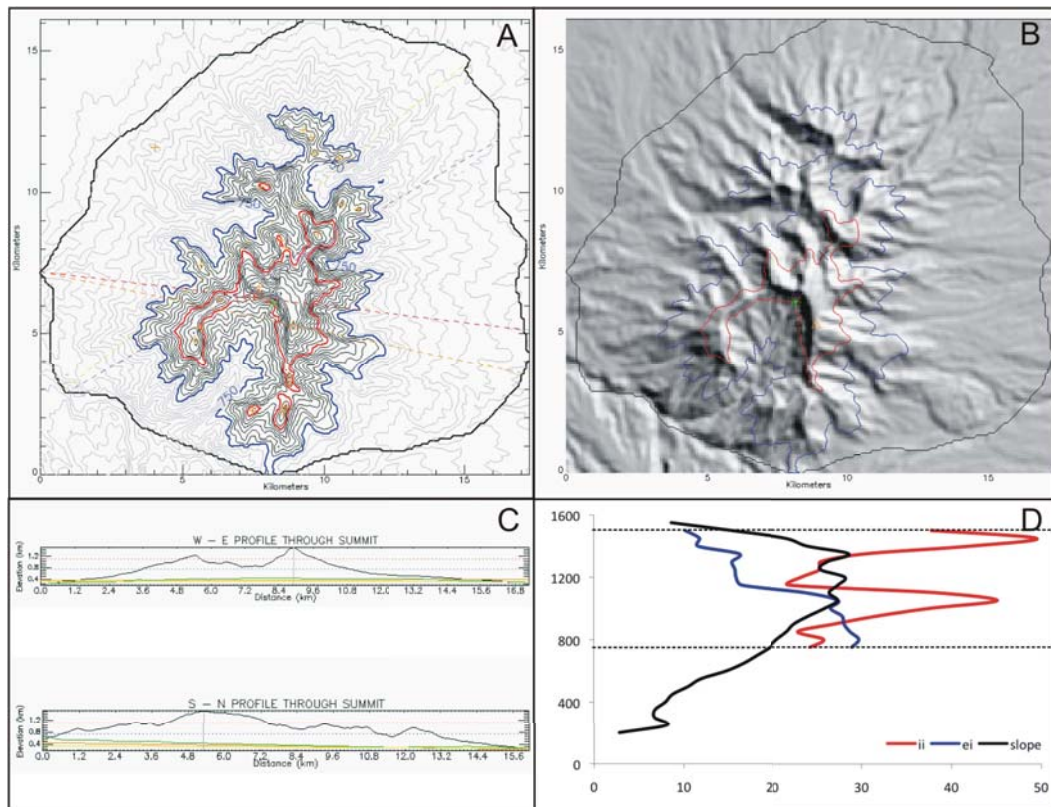


Figure A.36: Silay

Status:	Potentially Active Volcano
Morphometry Type:	Eroded massif
Location (Lat, Long):	10.770056, 123.23268
Elevation (min, max):	198-1508 m
Basal Area:	207.8 km <sup>2</sup>
Height:	1310 m
Volume:	84 km <sup>3</sup>
Plan shape (ellipticity index, irregularity index):	3.16, 2.76
Profile shape (height/ base width, summit width/base width):	0.07, 0.22
Slope:	0.24°-52.12°
Base orientation in azimuth (through the summit, through the base centre):	102°, 60°

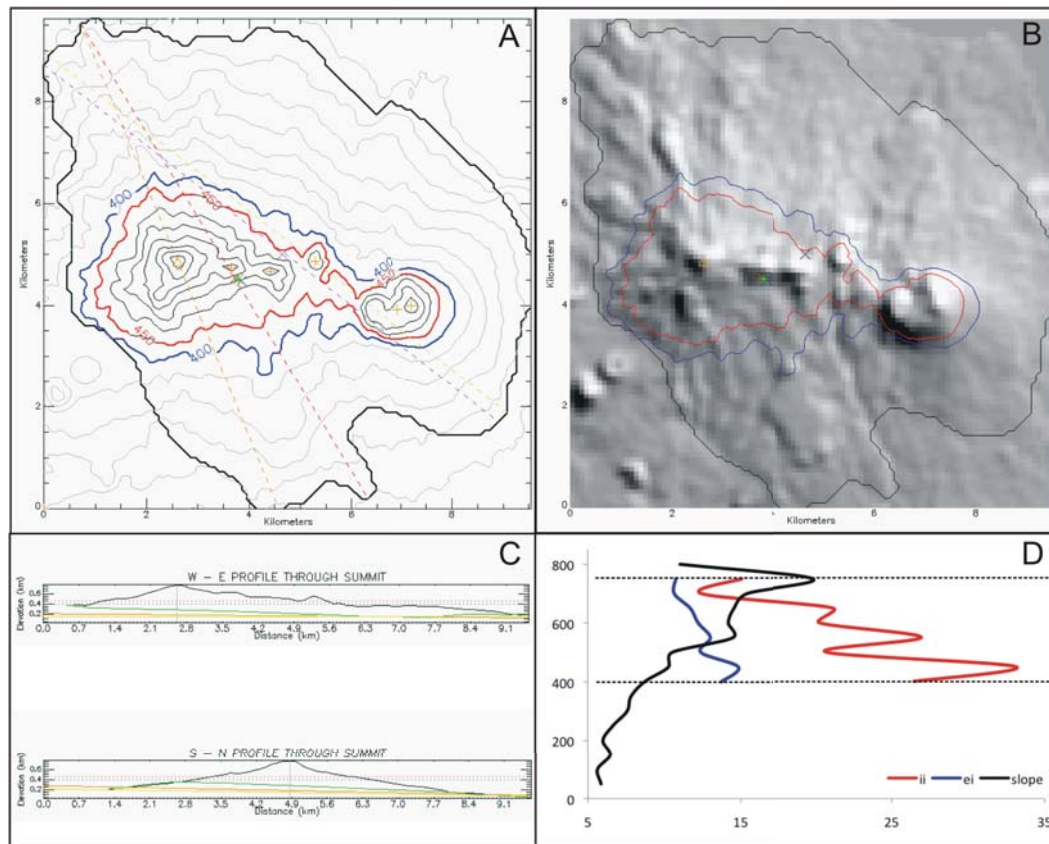


Figure A.37: Sinumaan

Status:	Potentially Active Volcano
Morphometry Type:	Sub-cone
Location (Lat, Long):	6.0370237, 121.09941
Elevation (min, max):	45-764 m
Basal Area:	62.8 km <sup>2</sup>
Height:	719 m
Volume:	17 km <sup>3</sup>
Plan shape (ellipticity index, irregularity index):	2.98, 1.43
Profile shape (height/ base width, summit width/base width):	0.06, 0.42
Slope:	0.15°-33.05°
Base orientation in azimuth (through the summit, through the base centre):	158°, 128°

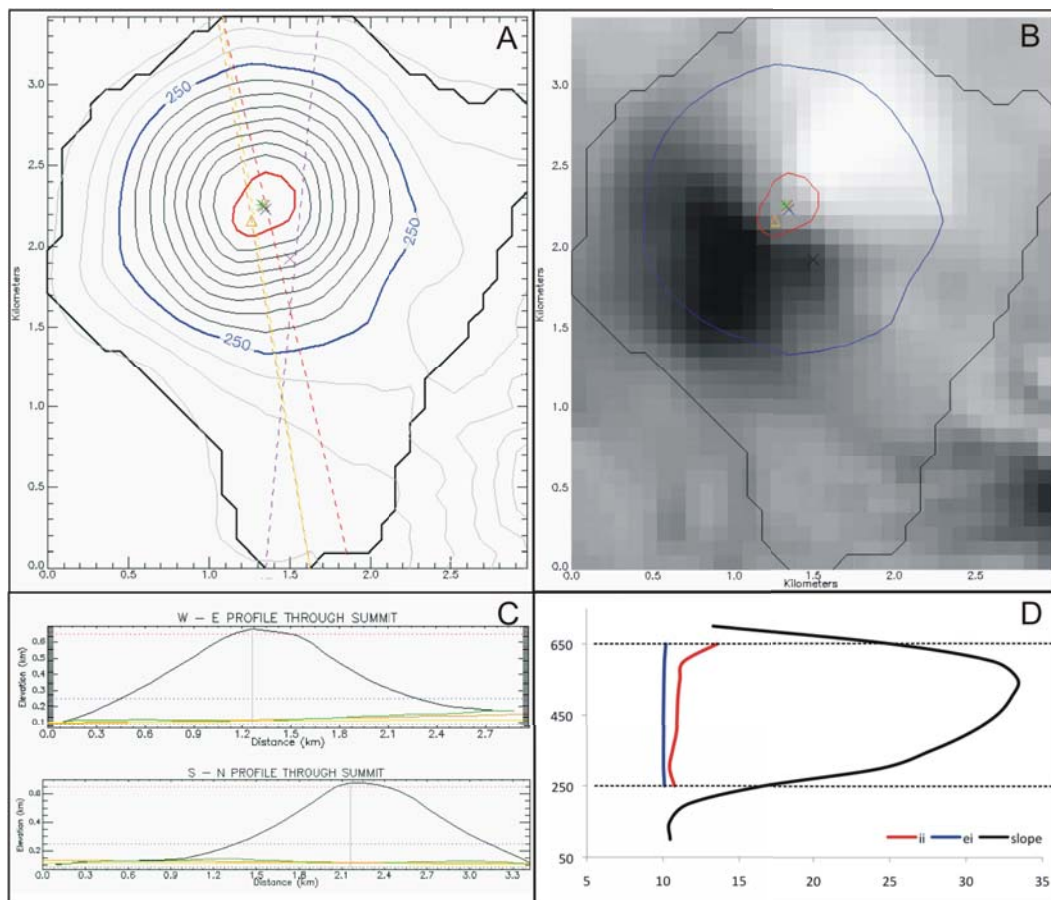


Figure A.38: Smith

Status:	Active Volcano
Morphometry Type:	Cone
Location (Lat, Long):	19.537585, 121.91194
Elevation (min, max):	87-679 m
Basal Area:	6.6 km <sup>2</sup>
Height:	592 m
Volume:	1 km <sup>3</sup>
Plan shape (ellipticity index, irregularity index):	1.12, 1.01
Profile shape (height/ base width, summit width/base width):	0.19, 0.13
Slope:	0.44°-35.31°
Base orientation in azimuth (through the summit, through the base centre):	171°, 5°

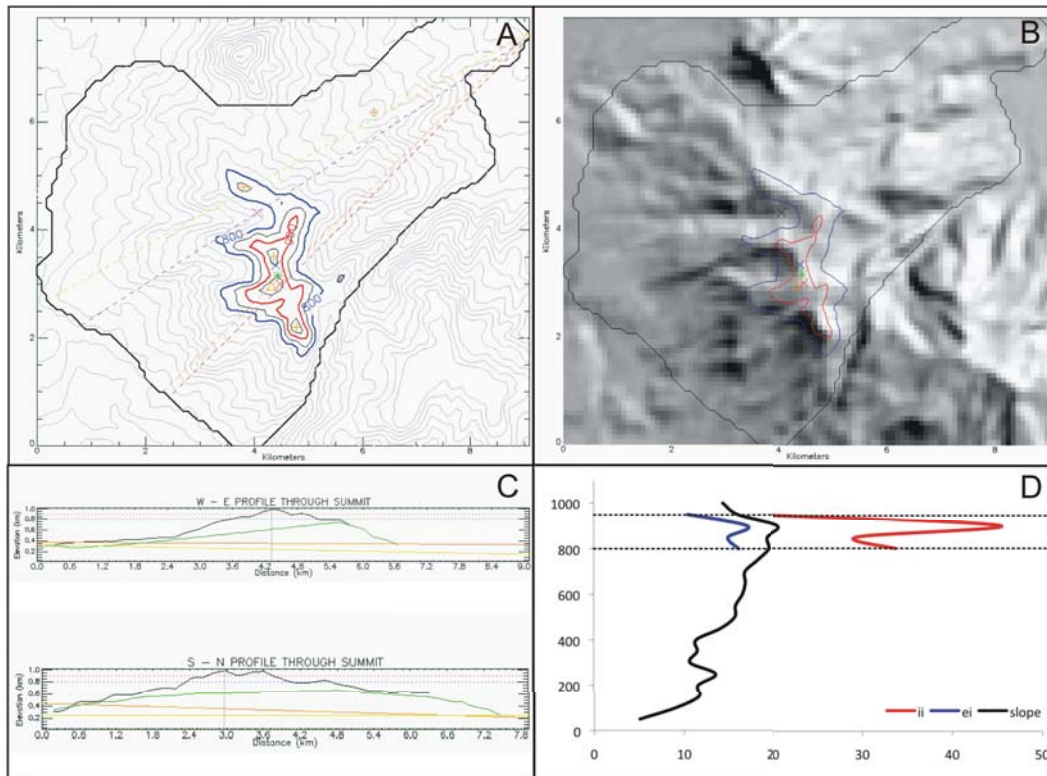


Figure A.39: Vulcan Biliran

Status:	Active Volcano
Morphometry Type:	Sub-cone
Location (Lat, Long):	11.533802, 124.50502
Elevation (min, max):	38-989 m
Basal Area:	39.1 km <sup>2</sup>
Height:	951
Volume:	18 km <sup>3</sup>
Plan shape (ellipticity index, irregularity index):	3.61, 1.61
Profile shape (height/ base width, summit width/base width):	0.09, 0.15
Slope:	0.15°-39.51°
Base orientation in azimuth (through the summit, through the base centre):	46°, 57°

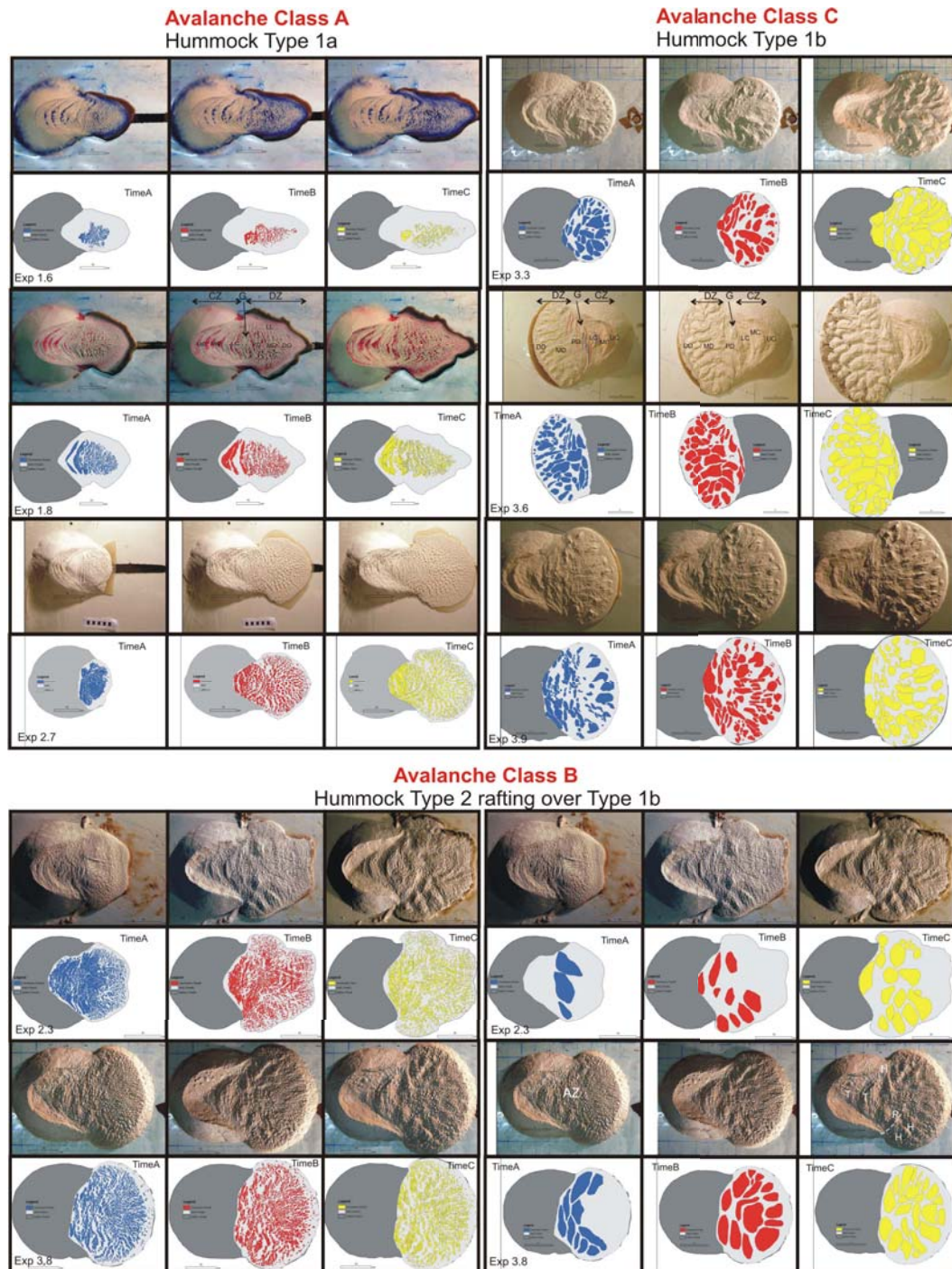


Figure B.1: Chosen analogue models that best represent the recurrent morphology and structures in the three sets of experiments: Set 1, Set 2, and set 3 with their classified avalanche classes and the type of hummocks formed in each of the classes.

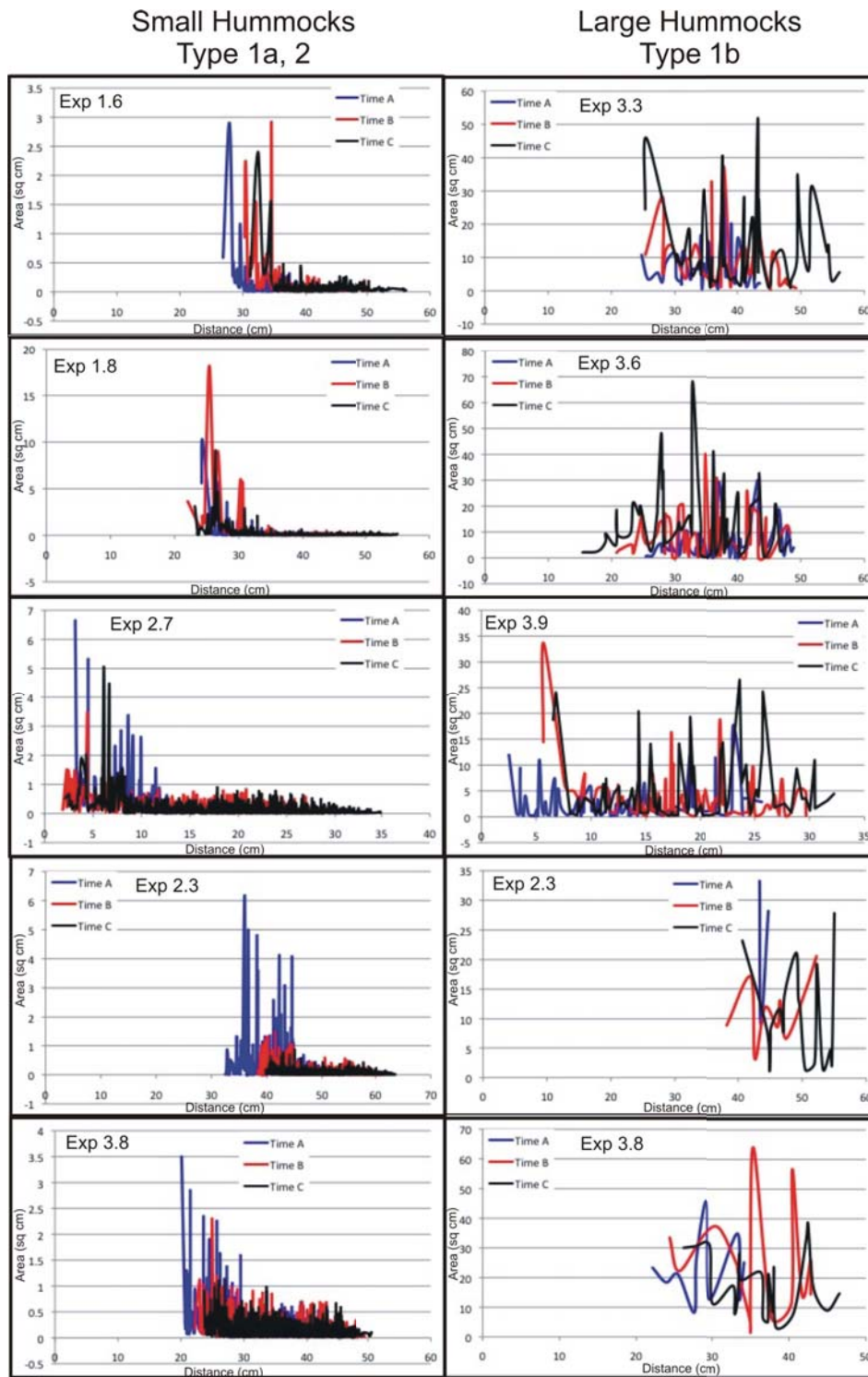


Figure C.1: Line plot of the hummock sizes sorted according to its distance away from the source.

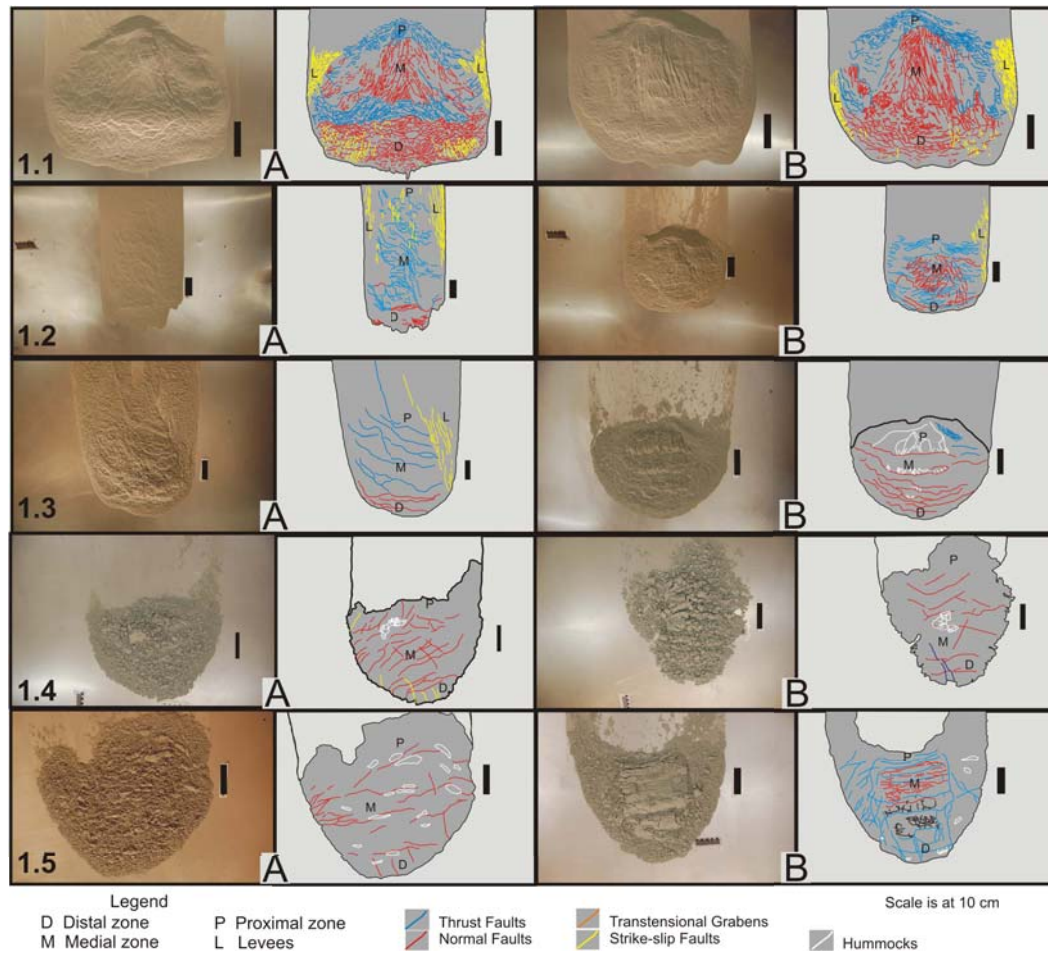


Figure D.1: Analogue slides using the curved ramp, Set 1. Parameters used are presented in Table 2.

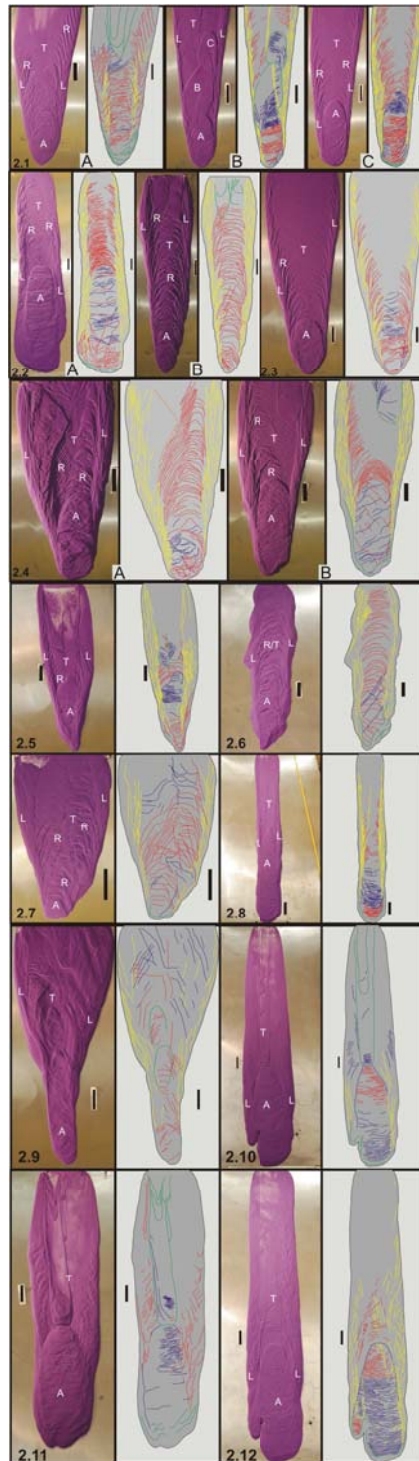


Figure D.2: Analogue slides using the straight ramp, Set 2. Parameters used are presented in Table 3.